SCIENTIFIC DETECTORS FOR ASTRONOMY 2005

JENNA E. BELETIC
JAMES W. BELETIC
PAOLA AMICO
Editors

SCIENTIFIC DETECTORS FOR ASTRONOMY 2005

ASTROPHYSICS AND SPACE SCIENCE LIBRARY

VOLUME 336

SCIENTIFIC DETECTORS FOR ASTRONOMY 2005

Explorers of the Photon Odyssey

Edited by

JENNA E. BELETIC
University of Chicago, U.S.A.

JAMES W. BELETIC
Rockwell Scientific Company, U.S.A.

and

PAOLA AMICO
European Southern Observatory, Chile

Springer

Printed on acid-free paper

Printed in the Netherlands.

TABLE OF CONTENTS

SECTION I: OBSERVATORY STATUS AND PLANS

SECTION II: NON-ASTRONOMICAL APPLICATIONS

SECTION III: CCDs

SECTION IV: CMOS-BASED SENSORS

SECTION V: AVALANCHE PHOTODIODES

SECTION VI: DETECTOR TESTING & CHARACTERIZATION

SECTION VII: ELECTRONICS

FOREWORD

We present the proceedings from the workshop entitled *Scientific Detectors for Astronomy 2005*, a weeklong meeting held in Taormina, Sicily during 19-25 June 2005. This was the sixth workshop of this series, and the fourth with hardcover proceedings. By all measures, this workshop surpassed the previous meetings.

The primary purpose of any technical meeting is the exchange of scientific and engineering information. The meeting was attended by 127 astronomers, scientists and engineers from 21 countries spread across every continent, with representation of all major manufacturers and 36 astronomical observatories. A total of 94 oral and poster papers were presented, of which 87 are contained in these proceedings. A new feature of this workshop was the overview papers of several areas: Ground-based observatories, Space-based observatories, CCDs, and CMOS. Our goal was for these overviews to be true "world views" that combined the expertise of several, often competing, institutions to present basic fundamentals to state-of-the-art material in a pedagogical way. Due to the professionalism and cooperation of the collaborating teams the overview papers were a great success. We are indebted to these authors for giving their time and sharing their knowledge.

The papers presented at the workshop covered the gamut of science, technology and engineering required for developing and using scientific detectors in astronomy. These detectors are the eyes of astronomical instruments, and the performance of an observatory is directly a function of the quality of its detectors. Thus, the workshop began with a day of papers on observatory status and plans, instrumentation, and observing techniques. The next two days of the workshop focused on the primary detector technologies used in astronomy: CCDs and CMOS-based sensors. The size and quality of detectors continues to advance, and these proceedings include several papers from manufacturers presenting their latest products, followed by papers from users who explain how the detectors work in practice. Since CMOS technology is encroaching into domains dominated by CCDs, the workshop was peppered with entertaining sparring between the two camps.

As our sensors are not perfect, an important aspect of our community's work is the testing and characterization of devices, and a day of the workshop concentrated on Sensor Testing. In this area, a breakthrough paper was presented by Gert Finger on the measurement of conversion gain of CMOS-based sensors. We learned that the "photon transfer curve" used to measure

electrons per data number can be in error for some hybrid CMOS arrays. The amount of error depends on the pixel size, the readout design, the detector material and details of hybrid fabrication. After the workshop, many participants hurried back to their laboratories to take their own measurements of this phenomenon.

On the last day of the workshop, we heard presentations on the new generation of control electronics being developed at many institutions. These controllers are required for handling the large amount of readout ports and high data rates of ever larger mosaics of detectors. This session included two papers on ASICs (application specific integrated circuits) that integrate a complete controller onto a silicon chip. ASICs have significantly progressed since the 2002 meeting, having demonstrated performance that convinced NASA to choose ASICs for the control electronics of the James Webb Space Telescope.

The workshop participants were treated to two special presentations. The opening talk of the workshop was given by Roberto Gilmozzi, principal investigator of the OWL 100-meter telescope. Roberto presented a vision of the future of astronomy and the need for square meters of detectors (at a good price!) in the era of extremely large telescopes. Looking into our cultural past, Maurizio Seracini showed how x-ray, visible and infrared sensors are used to assess the provenance and quality of ancient works of art.

As all who attend technical meetings know, the highlights of these meetings are not the formal presentations, but the informal discussions over coffee and dinner. This meeting series addresses that reality with a hotel facility that keeps participants together for meals and a schedule that includes a strong cultural program that exposes the participants to the host region. Activities included a tour of the ancient city of Taormina, an evening trip to a small hilltop town with a pizza dinner under a full moon, and an afternoon trip to a local winery for a tour and classic Sicilian lunch. The conference dinner, held outdoors in a garden by the sea, concluded with an amazing show of fireworks. The program for spouses and guests included two daylong tours to World Heritage sites. Over 60 family members accompanied participants to the meeting, and with children running about during the receptions, the meeting had a very friendly feeling.

The workshop was made possible by the volunteer effort of a large number of people. The Observatory of Catania put in a tremendous amount of effort as the Local Organizing Committee and host institution. We thank their Director, Santo Catalano, for his excellent leadership and we are grateful to all of the observatory staff that helped make this meeting run smoothly.

The Scientific Organizing Committee made significant contributions over the course of 18 months including: selection of the workshop location, definition of the technical programme, chairing of sessions, selection of award winners, and review of papers. We greatly appreciate their dedication and expertise.

This workshop would not have been possible without the tremendous financial and in-kind support of several Italian government organizations and companies from Europe, North America and Hawaii. Many thanks to these sponsors who are listed in the workshop organization pages.

The Hotel Naxos Beach provided us with an excellent facility. We enjoyed comfortable rooms, good food, and the hotel staff were extremely helpful, providing excellent service at every turn. We especially thank Angela Raiti, Massimo Andrighetti, Eva Levander and Gianluca Taglialegne. We also thank Roberta Barbagallo and Lachea Tour for ensuring that bus transport and cultural activities ran like clockwork.

"Mille grazie" to Giovanna Cimino and Giovanni Bonnano for a wonderful partnership over a period of 3 years. We greatly appreciate the personal time and attention they gave to make this workshop an enriching cultural experience for all. We are lucky to have made lifelong friends in the process.

Lastly, we thank the Beletic family who supported this workshop with their energy, time and patience. We also thank Jason Henning for his selfless contributions at critical times.

We hope that you enjoy these proceedings and that you continue to enjoy your adventure as one of the "Explorers of the Photon Odyssey".

Jenna E. Beletic, James W. Beletic and Paola Amico

The editors and the publisher.
(from left to right: Paola Amico, Jenna E. Beletic, Sonja Japenga, James W. Beletic)

WORKSHOP ORGANIZATION

The Scientific Detector Workshop 2005 was made possible by a partnership of institutions, committees, sponsors and individuals who worked together to produce an outstanding technical workshop that brought together the world's leaders in detector technology for astronomy. The parties listed below donated their time, financial support or in-kind contributions, and we are very grateful for their contributions.

Workshop Coordinators

James W. Beletic
Paola Amico

This is the 4th detector workshop organized by James Beletic and Paola Amico. The previous three were held in Germany (1996, 1999) and Hawaii (2002).

Organizing Institutions

Scientific Workshop Factory
Thousand Oaks, California, USA
Istituto Nazionale di Astrofisica - Osservatorio Astrofisico di Catania
Catania, Sicily, Italy

The Scientific Workshop Factory provided overall coordination, development of the scientific programme, and publication of the proceedings. The Observatory was responsible for local organization of facilities, cultural activities, preparation of materials, and support staff during the meeting. This collaboration was very successful and enjoyable. Much credit and "mille grazie" go to the Observatory Director, Santo Catalano, for his leadership.

Lead Coordination in Sicily

Giovanna Cimino
Giovanni Bonanno

Giovanna provided the interface between the organizing institutions, and she planned facility arrangements and cultural activities. Giovanni was the originator of the Sicily meeting concept and he put in a lot of time and effort to make this dream come true.

Scientific Organizing Committee

James W. Beletic, Chair	**Gert Finger**
Paola Amico, Co-Chair	**Alan Hoffman**
Morley Blouke	**Paul Jorden**
Giovanni Bonanno	**Ralf Kohley**
Barry Burke	**Gerry Luppino**
Randall Campbell	**Fernando Pedichini**
Mark Clampin	**Gustavo Rahmer**
Mark Downing	**Doug Simons**

The Scientific Organizing Committee was responsible for the technical content of the workshop. Among their responsibilities were the definition of the scientific programme, chairing sessions, selection of award recipients, and reviewing papers for the proceedings.

Local Organizing Committee

Santo Catalano, Chair	**Piero Massimino**
Giovanni Bonanno, Co-Chair	**Daniela Recupero**
Massimiliano Belluso	**Luigia Santagati**
Antonio Calì	**Salvo Scuderi**
Giovanna Cimino	

The Local Organizing Committee coordinated all aspects of the workshop in Sicily, including meeting facilities, Internet connection, computer support, photography, printing, local souvenirs, registration support and hosting of cultural activities.

Sponsors

e2v technologies	**Fairchild Imaging**
GL Scientific	**Hitec2000**
Istituto Nazionale di Astrofisica	**Medianet Comunicazioni**
Raytheon Vision Systems	**Regione Siciliana**
Rockwell Scientific Company	**SciMeasure Analytical Systems**
ST Microeletronics	**Università di Catania**

The quality of this workshop would not have been possible without the financial and in-kind support from the institutions listed above in alphabetical order. These institutions and companies sponsored facilities rental, workshop receptions, Taormina tour, Internet service, and giveaways such as mugs, portfolios and flavors of Sicily.

WELCOME FROM CATANIA OBSERVATORY DIRECTOR

Presented by Santo Catalano on Monday, 20 June 2005

It is a great privilege and honour, on behalf of the Local Organizing Committee, and as Director of the host institute, to welcome you to the Scientific Detector Workshop 2005 in Taormina, Sicily.

I must confess that when Giovanni Bonanno and Giovanna Cimino proposed hosting the SDW 2005 in Sicily, I was somewhat worried due to the particular characteristics of this workshop series. My concern grew when I discovered that Sicily had indeed been chosen. However, my apprehension vanished when I met our partners Jim Beletic and Paola Amico. I realised that together we were capable of organizing a superior scientific meeting.

I am very proud and happy to see the number and diversity of attendees, who have travelled from as far as Australia, China, Chile and Hawaii. I imagine that for some of you Sicily is a remote island and Catania an unknown city. Therefore, let me express my personal gratitude to the members of the Scientific Organizing Committee for choosing Sicily as the host of the SDW 2005. This is an important opportunity for us, not only for awareness of leading scientists and engineers of our observatory and detector group, but also for the exposure of the vast cultural and historical heritage of Sicily.

This workshop would not have been possible without the support of local sponsors and institutions. We are very grateful to acknowledge the vital financial support from our National Institute for Astrophysics (INAF), whose President Prof. Piero Benvenuti is in attendance today. I also wish to thank several local sponsors, institutions and companies who contributed additional funds and technology to this meeting: the President of Regione Sicilia for his high patronage, the Rector of Catania University, ST Microelectronics of Catania, Hitec 2000, the Soprintendente ai Beni Culturali e Ambientali from Messina, and Medianet Comunicazioni. The secretariat office, the internet connection, airport logistics, and having things run smoothly at the Naxos Beach Resort during the meeting is the result of the hard work and dedication of a number of people from our Observatory who I wish to specially thank: M. Belluso, A. Calì, A. Costa, A. Giuffrida, P. Massimino, D. Recupero, G. Santagati. I would also like to thank our students K. Biazzo, S. Billotta, D. Gandolfi, and L. Spezzi for their help during the meeting, and Mrs. Roberta Barbagallo from Lachea Tour and Giovanna Cimino for their excellent assistance.

I wish all of you a very fruitful meeting and hope that you enjoy your stay in Sicily. I assure you that we will do our best to make this an unforgettable meeting.

Santo Catalano, Director
INAF-Osservatorio Astrofisico di Catania

MAP OF SICILY

Catania	INAF-Osservatorio Astrofisico di Catania
Hotel Naxos Beach	Workshop location
Taormina	Monday walking tour
Forza d'Agrò	Tuesday pizza dinner
Caltagirone*	Wednesday guest tour (ceramics)
Piazza Armerina*	Wednesday guest tour (mosaics)
Murgo Winery	Thursday lunch
Siracusa*	Friday guest tour
Mt. Etna	Saturday tour – active volcano
Agrigento*	Saturday tour – Valle dei Templi (Greek ruins)

* World Heritage site

LIFETIME ACHIEVEMENT AWARDS

A special aspect of this workshop is that we recognize leading members of our community by naming an asteroid after them. These individuals have made substantial contributions over the course of their career and continue to be active leaders in our field.

These asteroids were discovered by Alain Maury and his colleagues at the OCA-DLR Asteroid Survey at Caussols. We thank them for the gift of these asteroids. The official citations, which are registered with the Minor Planet Center, are found below.

Barry Burke, CCD Designer Extraordinaire   **# 20405** (1998 QP6)

Barry Burke (b. 1941), of MIT Lincoln Laboratory, has spent his career designing many of the world's best CCD sensors, including the 2K×4K devices that are used in many of the leading ground-based observatories and the arrays for the LINEAR Project that has discovered the most asteroids to date. His designs include orthogonal transfer, anti-blooming, electronic shutter and many of the lowest noise amplifiers ever made.

Gert Finger, IR Detector Meister   **# 21369** (1997 NO4)

Gert Finger (b. 1951), of the European Southern Observatory, applies his ingenuity in detector characterization and optimization to develop the highest quality infrared systems for astronomy. He uses his world-leading expertise to continually set new standards for "lowest noise" performance, and freely shares his knowledge with observatories and manufacturers worldwide.

Alan Hoffman, IR Detector Pioneer   **# 20259** (1998 FV10)

Alan Hoffman (b. 1948) has led the development of infrared detectors at Raytheon Vision Systems, whose InSb and HgCdTe detectors are in state-of-the-art instrumentation at major ground and space observatories. He has shared his expertise by training a generation of scientists and engineers via his IR detector course, which he has taught for the past 11 years.

Michael Lesser, Dr. CCD Quantum Efficiency   **# 20399** (1998 OO)

Michael Lesser (b. 1960), of University of Arizona Steward Observatory, is best known for his pioneering work in high quantum efficiency CCDs. His techniques for thinning, backside passivation and anti-reflection coating have been key to the high performance achieved in sensors made for the Hubble Space Telescope and many ground-based observatories.

SDW2005 Award Recipients

At the end of every Scientific Detector Workshop, the Scientific Organizing Committee selects those participants who have used their unique "faculties" to contribute to our meeting. With these awards we recognize scientific insight, a love of the oral spotlight, and the biggest array that views the night. We applaud these individuals for their talents.

Best Paper	Gert Finger
Best Poster	Maureen Ellis
Dream On	Roberto Gilmozzi
Most Original Idea	Craig Mackay
Best Presentation	Doug Simons
Lowest Noise	Simon Tulloch
Biggest Array	Brian McLeod
Most Likely to Succeed	Olaf Iwert
Jim Janesick Most Amazing	John Tonry
Longest wavelength	Maureen Ellis
Broadest bandwidth	M. Bonner Denton
Most futuristic	Bernie Rauscher
Young Achiever	Fabrice Christen
Roger Smith Most Loquacious	Roger Smith
Most Dedicated SOC Member	Ralf Kohley
Meister Procrastinator	Mark Clampin
Al Fowler "Sampling" Epicurean	Manfred Meyer
Gerry Luppino Best Sales Pitch	Markus Loose
Most Dedicated Attendee	GL Scientific
Most Congenial	Peter Moore
Something from Nothing	Tim Hardy

LIST OF PARTICIPANTS

This list of participants includes all persons who attended the Scientific Detector Workshop in Taormina, Italy during 19-25 June, 2005. We list the affiliations and E-mail addresses of the participants at the time of publication of the proceedings so that the most recent contact information is available to readers. Note that a few of these affiliations do not match the affiliations listed in the papers since some of our itinerant community have changed employers between attendance at the workshop and the publication of the proceedings.

Acosta Pulido, José Instituto de Astrofisica de Canarias, Spain
    jap@ll.iac.es

Amico, Paola European Southern Observatory, Chile
    pamico@eso.org

Atwood, Bruce Ohio State University, USA
    atwood@ohstpy.mps.ohio-state.edu

Baade, Dietrich European Southern Observatory, Germany
    dbaade@eso.org

Balard, Philippe Observatoire de Marseille, France
    philippe.balard@oamp.fr

Balestra, Andrea European Southern Observatory, Germany
    abalestr@eso.org

Baril, Marc Canada France Hawaii Telescope, USA
    baril@cfht.hawaii.edu

Beigbeder, Francis Observatoire Midi-Pyrénées, France
    francis.beigbeder@bagn.obs-mip.fr

Beletic, James Rockwell Scientific Company, USA
    jbeletic@rwsc.com

Beletic, Jenna University of Chicago, USA
    jbeletic@uchicago.edu

Berry, Paul University of Durham, UK
    paul.berry@durham.ac.uk

Bezawada, Nagaraja UK Astronomy Technology Centre, UK
    nnb@roe.ac.uk

Bleau, Charlie SciMeasure Analytical Systems, USA
    charlie.bleau@scimeasure.com

Blouke, Morley Ball Aerospace & Technologies Corp., USA
    mblouke@ball.com

Bonanno, Giovanni INAF/Osservatorio Astrofisico di Catania, Italy
    gbo@oact.inaf.it

Bonati, Marco California Institute of Technology, USA
    mbonati@astro.caltech.edu

Bortoletto, Fabio   INAF/ Osservatorio Astronomico di Padova, Italy
                          bortoletto@pd.astro.it

Bradley, Ryan   GL Scientific, USA
                          ryanbradley@glscientific.com

Branigan, Neil   e2v technologies, UK
                          neil.branigan@e2v.com

Bredthauer, Richard   Semiconductor Technology Associates Inc., USA
                          r.bredthauer@sta-inc.net

Buey, Jean-Tristan   Observatoire de Paris-Meudon, France
                          jean-tristan.buey@obspm.fr

Burke, Barry   MIT Lincoln Laboratory, USA
                          bburke@ll.mit.edu

Campbell, Randall   W. M. Keck Observatory, USA
                          randyc@keck.hawaii.edu

Carter, David   South African Astronomical Observatory, South Africa
                          dbc@saao.ac.za

Christen, Fabrice   Kapteyn Astronomical Institute, Netherlands
                          fchriste@astro.rug.nl

Clampin, Mark   NASA Goddard Space Flight Center, USA
                          mark.clampin@nasa.gov

Copeland, Keith   Spectral Instruments, USA
                          kcopeland44@yahoo.com

Cosentino, Rosario   INAF Telescopio Nazionale Galileo, Spain
                          cosentino@tng.iac.es

Craven-Bartle, Thomas Anoto AB, Sweden
                          tcb@anoto.com

Cumani, Claudio   European Southern Observatory, Germany
                          ccumani@eso.org

Darson, David   L'Ecole Normale Superieure – Paris, France
                          david.darson@lpa.ens.fr

Deiries, Sebastian   European Southern Observatory, Germany
                          sdeiries@eso.org

Denton, M. Bonner   University of Arizona, USA
                          mbdenton@u.arizona.edu

Diaz Garcia, José Javier Instituto de Astrofisica de Canarias, Spain
                          jdg@iac.es

D'Odorico, Sandro   European Southern Observatory, Germany
                          sdodoric@eso.org

Dorn, Reinhold   European Southern Observatory, Germany
                          rdorn@eso.org

Downing, Mark   European Southern Observatory, Germany
                          mdowning@eso.org

DuVarney, Ray	SciMeasure Analytical Systems, USA *phsrcd@physics.emory.edu*
Duvet, Ludovic	ESA/ESTEC, The Netherlands *ludovic.duvet@esa.int*
Earle, Colin	Fairchild Imaging, USA *colin.earle@fcimg.com*
Ellis, Maureen	UK Astronomy Technology Centre, UK *mae@roe.ac.uk*
Evans, Geoffrey	South African Astronomical Observatory, South Africa *gpe@saao.ac.za*
Feautrier, Philippe	Observatoire de Grenoble, France *Philippe.Feautrier@obs.ujf-grenoble.fr*
Figer, Donald	Space Telescope Science Institute, USA *figer@stsci.edu*
Finger, Gert	European Southern Observatory, Germany *gfinger@eso.org*
Gach, Jean-Luc	Observatoire de Marseille, France *gach@oamp.fr*
Gago Rodriguez, Fernando	Instituto de Astrofisica de Canarias, Spain *fgago@iac.es*
Geimer, Christoph	European Southern Observatory, Germany *cgeimer@eso.org*
Gigante, José	Instituto de Astrofisica de Canarias, Spain *gigante@iac.es*
Gilmore, Kirk	Stanford Linear Accelerator Center, USA *dkg@slac.stanford.edu*
Gilmozzi, Roberto	European Southern Observatory, Germany *rgilmozz@eso.org*
Goodsall, Tim	University of Oxford, UK *txg@astro.ox.ac.uk*
Guillaume, Christian	Centre National Recherche Scientifique, France *Christian.Guillaume@oamp.fr*
Haddad, Nicolas	European Southern Observatory, Chile *nhaddad@eso.org*
Hall, Donald	Institute for Astronomy, University of Hawaii, USA *hall@ifa.hawaii.edu*
Hanna, Kevin	University of Florida, USA *hanna@astro.ufl.edu*
Harding, Paul	Case Western Reserve University, USA *paul.harding@case.edu*
Hardy, Tim	Herzberg Institute of Astrophysics, Canada *tim.hardy@nrc-cnrc.gc.ca*

Harris, Fred   U.S. Naval Observatory, USA
                           fhh@nofs.navy.mil

Hartmann, Robert   PNSensor, Germany
                           robert.hartmann@pnsensor.de

Hello, Yann   Observatoire de Paris- Meudon, France
                           yann.hello@obspm.fr

Henning, Jason   University of Chicago, USA
                           jhenning@uchicago.edu

Hill, Robert   SSAI / Goddard Space Flight Center, USA
                           hill@tophat.gsfc.nasa.gov

Ho, Kevin   Canada France Hawaii Telescope, USA
                           ho@cfht.hawaii.edu

Hoffman, Alan   Raytheon Vision Systems, USA
                           ahoffman@raytheon.com

Holtom, Ralph   e2v technologies, UK
                           ralph.holtom@e2v.com

Ives, Derek   UK Astronomy Technology Centre, UK
                           dji@roe.ac.uk

Iwert, Olaf   European Southern Observatory, Germany
                           oiwert@eso.org

Japenga, Sonja   Springer Science and Business Media, Netherlands
                           sonja.japenga@springer-sbm.com

Jorden, Paul   e2v technologies, UK
                           paul.jorden@e2v.com

Joven, Enrique   Insituto de Astrofisica de Canarias, Spain
                           enrique.joven@iac.es

Karcher, Armin   Lawrence Berkeley National Laboratory, USA
                           akarcher@lbl.gov

Kohley, Ralf   Grantecan, Spain
                           ralf.kohley@iac.es

Kolbe, William   Lawrence Berkeley National Laboratory, USA
                           wfkolbe@lbl.gov

Kramm, J. Rainer   Max-Planck-Institut für Sonnensystemforschung, Germany
                           kramm@mps.mpg.de

Labiche, Jean-Claude   European Synchrotron Radiation Facility
                           labiche@esrf.fr

Lamontagne, Robert   Université de Montréal, Canada
                           lamont@astro.umontreal.ca

Lapeyrere, Vincent   Observatoire de Paris- Meudon, France
                           vincent.lapeyrere@obspm.fr

Lizon a l'Allemand,   European Southern Observatory, Germany
   Jean Louis   *jlizon@eso.org*

Loose, Markus	Rockwell Scientific Company, USA
	mloose@rwsc.com
Love, Peter	Raytheon Vision Systems, USA
	pjlove@raytheon.com
Lumb, David	European Space Agency, Netherlands
	dlumb@rssd.esa.int
Luppino, Gerald	GL Scientific, USA
	ger@glscientific.com
MacDougal, Michael	Aerius Photonics, USA
	macdougal@aeriusphotonics.com
Mackay, Craig	Institute of Astronomy, University of Cambridge, UK
	cdm@ast.cam.ac.uk
MacQueen, Phillip	University of Texas at Austin, McDonald Observatory, USA
	pjm@wairau.as.utexas.edu
McLeod, Brian	Smithsonian Astrophysical Observatory, USA
	bmcleod@cfa.harvard.edu
Mehrgan, Leander	European Southern Observatory, Germany
	lmehrgan@eso.org
Meyer, Manfred	European Southern Observatory, Germany
	mmeyer@eso.org
Moore, Peter	National Optical Astronomy Observatory, US
	pmoore@noao.edu
Morris, David	e2v technologies, UK
	david.morris@e2v.com
Motter, Garry	SciMeasure Analytical Systems, USA
	garry.motter@scimeasure.com
Mueller, Philip	Universität Bonn, Germany
	philipp@astro.uni-bonn.de
Pedichini, Fernando	INAF / Osservatorio di Roma, Italy
	pedik@mporzio.astro.it
Philbrick, Robert	Ball Aerospace & Technologies Corp., USA
	rphilbri@ball.com
Philip, A.G. Davis	Institute for Space Observations, USA
	agdp@union.edu
Phillips, John	Eastman Kodak Company
	john.phillips1@kodak.com
Pool, Peter	e2v technologies, UK
	peter.pool@e2v.com
Prigozhin, Gregory	Massachusetts Institute of Technology, USA
	gyp@space.mit.edu
Rahmer, Gustavo	California Institute of Technology, USA
	grahmer@astro.caltech.edu

Rauscher, Bernard	NASA Goddard Space Flight Center, USA *bernard.j.rauscher@nasa.gov*
Reif, Klaus	Universität Bonn, Germany *reif@astro.uni-bonn.de*
Reiss, Roland	European Southern Observatory, Germany *rreiss@eso.org*
Reyes, Javier	European Southern Observatory, Germany *jreyes@eso.org*
Riopel, Martin	Université de Montreal, Canada *riopel@astro.umontreal.ca*
Robberto, Massimo	European Space Agency, stationed in USA *robberto@stsci.edu*
Rondi, Sylvain	Observatoire Midi-Pyrénées, France *rondi@bagn.obs-mip.fr*
Roth, Martin	Astrophysikalisches Institut Potsdam, Germany *mmroth@aip.de*
Salmon, Derrick	Canada France Hawaii Telescope, USA *salmon@cfht.hawaii.edu*
Schmidt, Ricardo	Cerro Tololo Inter-American Observatory, Chile *rschmidt@ctio.noao.edu*
Seracini, Maurizio	Editech Srl, Italy *seracini@editech.com*
Simons, Douglas	Gemini Observatory, USA *dsimons@gemini.edu*
Sinclaire, Peter	European Southern Observatory, Chile *psinclai@eso.org*
Sirianni, Marco	European Space Agency, stationed in USA *sirianni@stsci.edu*
Slaughter, Charles	Spectral Instruments, USA *cslaughter@specinst.com*
Smith, Roger	California Institute of Technology, USA *rsmith@astro.caltech.edu*
Song, Qian	National Astronomical Observatories, CAS, China *sq@bao.ac.cn*
Speziali, Roberto	INAF / Osservatorio di Roma, Italy *speziali@mporzio.astro.it*
Strada, Paolo	ESA/ESTEC, Netherlands *paolo.strada@esa.int*
Suntharalingam, Vyshnavi	MIT Lincoln Laboratory, USA *vyshi@ll.mit.edu*
Tecza, Matthias	University of Oxford, UK *mtecza@astro.ox.ac.uk*

Tonry, John Institute for Astronomy, University of Hawaii, USA
jt@ifa.hawaii.edu

Tufts, Joseph University of Texas at Austin, McDonald Observatory, USA
grin@astro.as.utexas.edu

Tulloch, Simon Isaac Newton Group of Telescopes, Spain
smt@ing.iac.es

Vu, Paul Fairchild Imaging, USA
paul.vu@fcimg.com

Ye, Binxun National Astronomical Observatories, CAS, China
bxye@bao.ac.cn

Zhao, Zhaowang National Astronomical Observatories, CAS, China
skyccd@bao.ac.cn

THE NERD GALLERY

José Acosta Pulido

Paola Amico

Bruce Atwood

Dietrich Baade

Philippe Balard

Andrea Balestra

Marc Baril

Francis Beigbeder

James Beletic

Jenna Beletic

Paul Berry

Nagaraja Bezawada

Charlie Bleau

Morley Blouke

Giovanni Bonanno

Marco Bonati

Fabio Bortoletto

Ryan Bradley

Neil Branigan

Richard Bredthauer

Jean-Tristan Buey

Barry Burke

Randall Campbell

David Carter

Fabrice Christen

Mark Clampin

Keith Copeland

Rosario Cosentino

Thomas Craven-Bartle

Claudio Cumani

David Darson

Sebastian Deiries

M. Bonner Denton

José Javier Diaz Garcia

Sandro D'Odorico

Reinhold Dorn

Mark Downing

Ray DuVarney

Ludovic Duvet

Colin Earle

Maureen Ellis

Geoffrey Evans

Philippe Feautrier

Donald Figer

Gert Finger

Jean-Luc Gach

Fernando Gago
Rodreiguez

Christoph Geimer

José Gigante

Kirk Gilmore

Roberto Gilmozzi

Tim Goodsall

Christian Guillaume

Nicolas Haddad

Donald Hall

Kevin Hanna

Paul Harding

Tim Hardy

Fred Harris

Robert Hartmann

Yann Hello

Jason Henning

Robert Hill

Kevin Ho

Alan Hoffman

Ralph Holtom

Derek Ives

Olaf Iwert

Sonja Japenga

Paul Jorden

Enrique Joven

Armin Karcher

Ralf Kohley

William Kolbe

Rainer Kramm

Jean-Claude Labiche

Robert Lamontagne

Vincent Lapeyrere

Jean Louis Lizon
l'Allemand

Markus Loose

Peter Love

David Lumb

Gerald Luppino

Michael MacDougal

Craig Mackay

Philip MacQueen

Brian McLeod

Leander Mehrgan

Manfred Meyer

Peter Moore

David Morris

Garry Motter

Philipp Mueller

Fernando Pedichini

Rob Philbrick

A.G. Davis Philip

John Philips

Peter Pool

Gregory Prigozhin

Gustavo Rahmer

Bernard Rauscher

Klaus Reif

Roland Reiss

Javier Reyes

Martin Riopel

Massimo Robberto

Sylvain Rondi

Martin Roth

Derrick Salmon

Ricardo Schmidt

Maurizio Seracini

Douglas Simons

Peter Sinclaire

Marco Sirianni

Charles Slaughter

Roger Smith
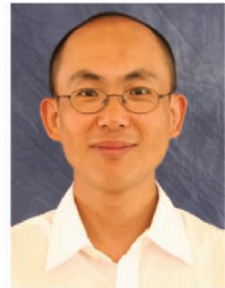
Qian Song

Roberto Speziali

Paola Strada

Vyshnavi
Suntharalingam

Matthias Tecza

John Tonry

Joseph Tufts

Simon Tulloch

Paul Vu

Binxun Ye

Zhaowang Zhao

REFERENCE PLOTS AND COLOR FIGURES

The following plots contain data fundamental to scientific detectors used in astronomy. The reference plots include:

- Blackbody emission curves for the ultraviolet through infrared wavelengths for objects with temperatures from 250K to 6000K
- Transmission of light through the Earth's atmosphere
- Detector wavelength ranges
- Absorption depth of light in silicon
- Absorption depth of light in HgCdTe

We thank the following persons for their contributions to these plots:

Barry Burke	MIT Lincoln Laboratory
Paul Vu	Fairchild Imaging
Jason Henning	University of Chicago
Alan Hoffman	Raytheon Vision Systems
Paul Jorden	e2v technologies
Donald Lee	Rockwell Scientific Company

Blackbody Emission Curves
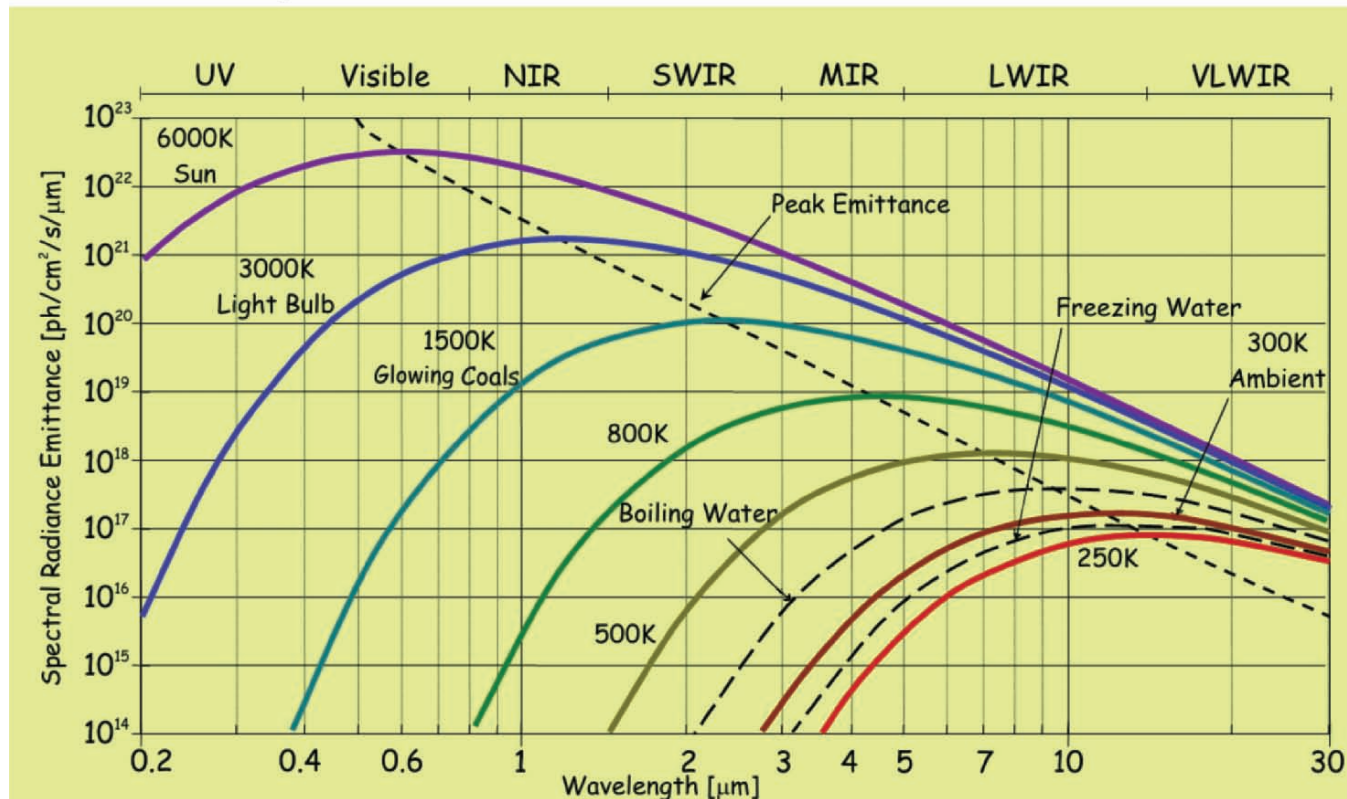
Atmospheric Transmission

Detector Wavelength Ranges

Name	Hard X-Ray	Soft X-Ray	Vacuum UV	UV	Visible	SWIR	MWIR	LWIR	VLWIR

| λ [μm] | 10^{-6} | 10^{-4} | 0.01 | 0.2 0.4 | 0.9 | 2.5 | 5 | 10 | 100 |

Detector Type

- 10^{-5} — Silicon (CCDs & CMOS) — 0.1
- 0.4 — Substrate removed HgCdTe
- 0.9 — HgCdTe — 19
- InSb — 5.5
- 4 — SI:As

Photometric Bands

Johnson UBVRI

Infrared JHK L M N Q

Name-λ_c	U_J-0.36	B_J-0.44	V_J-0.55	R_J-0.7	I_J-0.88	J-1.25	H-1.65	K-2.2	L-3.5	M-4.8	N-10.6	Q-21
Bandpass [μm]	0.07	0.1	0.09	0.22	0.24	0.3	0.35	0.4	1.0	0.6	5.0	11.0
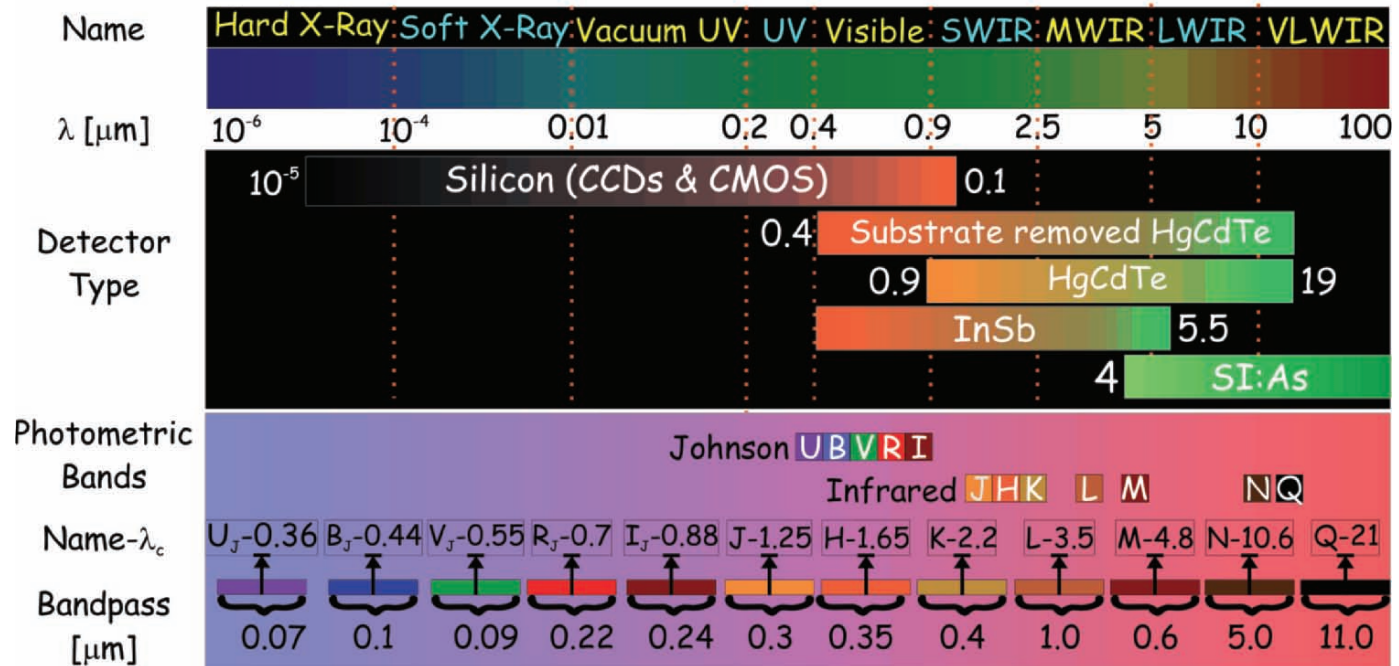
Absorption Depth of light in Silicon

Absorption Depth of light in HgCdTe

Backside surface of a CCD42-80 2Kx4K CCD that demonstrates e2v's new graded thickness anti-reflection coating. See the paper by Kelt, et al. for more information.

One of the first images taken with the MMT Megacam, the largest operational focal plane array in astronomy. See the paper by McLeod, et al. for more information.

COLOR PHOTO GALLERY

Forza d'Agró, site of the Tuesday pizza dinner.

Mark Downing enhances the spectacular sunset
with a glass of fine Murgo champagne.

Mariana Casal, Claudio Cumani and William Kolbe enjoy the great service
and delicious food at the Sunday evening reception.

A plate of cannoli that soon disappeared at the Thursday winery lunch.

Morley and Kay Blouke enjoy Sicilian cuisine at the Murgo Winery.

Workshop attendees are entertained by traditional music and dance
at the Friday night "Festa Paesana" (Town Festival).

Fred Harris, conference scribe, shows his expertise
on a keyboard not attached to a computer.

The French quarter at the Festa Paesana.
(Balard, Darson, Gach, Feautrier, Labiche, Buey, Rondi, Guillaume, Beigbeder)

Marc Baril smashes readout noise,
while Paul Berry anxiously awaits his turn.

The workshop included roundtables,
such as the CMOS vs. CCD "Spaghetti Western".

The flags of the 21 countries represented by
workshop participants graced the assembly hall.

The lovely town of Forza d'Agró hosted the Tuesday night pizza dinner. In this town the alleys are too narrow for vehicles so donkeys are used to transport household goods and laboratory equipment.

The most preserved Greek temple in the world, the Temple of Concordia, was just one of several sites visited during the Saturday Agrigento trip. The other Saturday trip was to the top of Mt. Etna (see below).

Pizza dinner in Forza d'Agró town plaza.

The view of Taormina from Forza d'Agró.

The bay of Giardini Naxos, site of the workshop hotel.

Exuberant guests enjoying the Friday trip to Siracusa
with special escort Doug Simons (far right).

Workshop participants debate how long it will take for Peter Love (second from right) to share his pizza in Forza d'Agró.

Colorful gifts on sale in Taormina.

SECTION I:

OBSERVATORY STATUS AND PLANS

SCIENCE, TECHNOLOGY AND DETECTORS FOR EXTREMELY LARGE TELESCOPES

Roberto Gilmozzi
European Southern Observatory

Abstract: *The second decade of the third millennium will hopefully see a new generation of extremely large telescopes. These will have diameters from 30 to 100 meters and use advanced adaptive optics to operate at the diffraction limit in order to detect astronomical objects that are impossible to observe today, such as earth-like planets around nearby stars and the earliest objects in the Universe. Even for small fields of view, the requirements for detectors are daunting, with sizes of several gigapixels, very fast readout times and extremely low readout noise. In this paper I briefly review the science case for ELTs and the requirements they set on telescopes and instruments, and report on the status of the OWL 100 m telescope project and the challenges it poses.*

Key words*:   Extremely Large Telescopes, OWL 100m telescope, gigapixel detectors.*

1.   INTRODUCTION

The decade 2010-2020 will see the maturity of the current generation of telescopes (VLT, Keck, Gemini, Subaru, LBT, GTC, HET, SALT, Magellan, etc.) equipped with a second generation of instruments often performing at the diffraction limit through advanced Adaptive Optics (AO). Interferometry will have come out of its infancy to operate in the faint object regime (K~20) and to produce astrometric results in the micro-arcsecond range (1 μas resolution resolves 2 mm details at the distance of the moon, although astrometric accuracy is not the same as imaging capability, which remains about 2 m at the moon for the VLT Interferometer, VLTI). ALMA will provide mm and sub-mm astronomers with a facility "equivalent" to

optical ones (both in terms of service offered to the community and of resolution and sensitivity). Space missions like the James Webb Space Telescope JWST, the X-ray satellite XEUS, the Terrestrial Planet Finder TPF/Darwin precursor missions and others will explore the heavens from above the atmosphere, exploiting the freedom from turbulence, sky absorption and gravity. And a new generation of ground-based optical/ near infrared 30 to 100-m telescopes may open a completely new window on the Universe and produce unprecedented results (with resolution of milli-arcseconds and sensitivity hundreds or even thousands of times beyond what is available today).

The new telescopes, collectively known as ELTs (Extremely Large Telescopes) all try to break one or both of the traditional laws of the art of telescope making: the *cost law* ($\propto D^{2.6}$) and the *growth law* (the next generation telescope is twice as large as the previous one). The rationale for breaking the growth law comes from the science cases. The motivation for beating the cost law is key to obtaining funding.
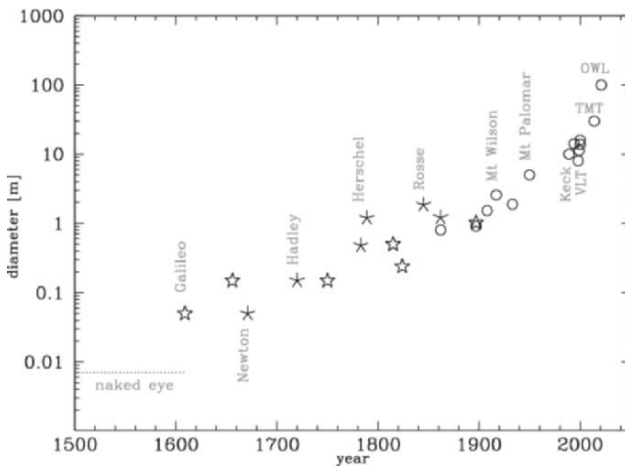
Figure 1. Brief history of the telescope. *Stars*: refractors, *asterisks*: speculum reflectors, *circles*: glass reflectors. A few telescopes are named.

Figure 1 shows the history of the telescope diameter, with a few future telescopes (the Thirty Meter Telescope TMT and the 100-m OWL) added for reference. There are two aspects that are immediately evident: (1) "local" scatter notwithstanding, the trend of diameter increase has remained substantially constant since Galileo (doubling every 50 years or so) and (2) the *quantum jump* between a 10-m and a 100-m telescope is similar to that between the night-adapted naked eye and the first telescope, which certainly

bodes well for the potential for new discoveries. During the 20th century there has been some acceleration, with the doubling happening every 35 years: see e.g. the "California progression" with the Hooker [2.5 m, 1917], Hale [5 m, 1948], and Keck [10 m, 1992] telescopes.
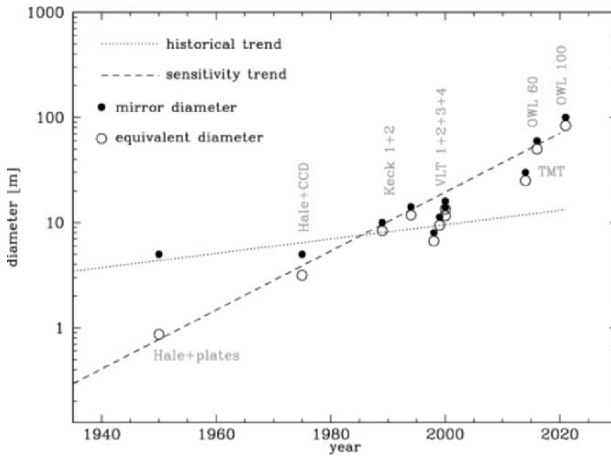
Figure 2.   Recent history of improvement in sensitivity of telescopes expressed in "equivalent diameter of a perfect telescope" = $\sqrt{(\eta D^2)}$, with η the telescope overall efficiency (the dashed line is an aid to the eye, not a fit).

One point that perhaps is not immediately evident, though, is that in the last 50 years there has been a larger increase in telescope sensitivity due to improvements in detectors than to increases in diameter (see Fig. 2). Now that detectors efficiencies approach 100%, *large improvements can be obtained only through large increases in telescope diameter*. For example, at the times of photographic plates, with efficiency of a few percent, even the 5-meter Hale telescope was only equivalent to a 1-meter "perfect" telescope (i.e. one with 100% efficiency).

2.   THE SCIENCE CASE

Table 1 gives an overview of some of the science cases developed in the framework of the OPTICON working group on ELT science. Projecting our scientific expectations 10-15 years in the future is prone to error, so that at times it looks as if extending the "discovery space" may be the dominant driver. However, there are a few cases that in my opinion are particularly significant in determining the requirements for the designs, and in pushing

the instrumental parameter space (instruments are an integral part of the telescopes, and sometimes as complex): the quest for terrestrial planets (possibly also for exo-biospheres) in extra-solar systems (see Fig. 3); the study of stellar populations in a large sample of the Universe (including in elliptical galaxies, missing today – often referred to as "Virgo or bust!"); the still mysterious relation between matter, dark matter and dark energy (with their link to particle physics); the star formation history of the Universe and the evolution of the cosmos from big bang to today; the first objects and the epoch of re-ionization (primordial stars and their role); the *direct* measurement of the deceleration of the Universe (with no assumptions, no extrapolations, no models). In the following I discuss one science case, to show the requirements it sets for the next generation of ELDs (extremely large detectors).
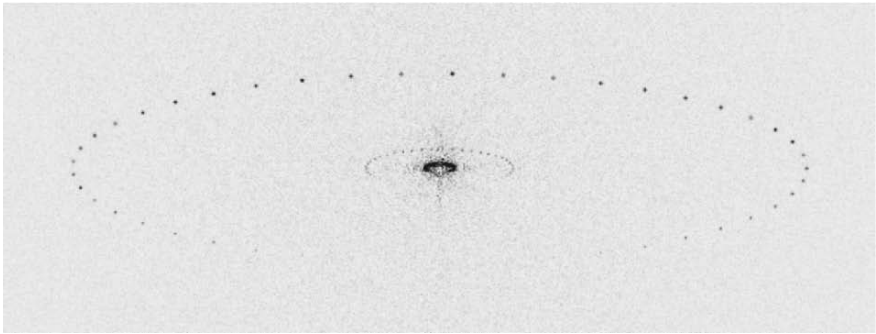
Figure 3. Simulation of the solar system at 30 light years as seen by OWL. The Earth and Jupiter are shown at different positions in their orbits. Note the phase effect (they are not visible when their illuminated hemisphere looks away from us).

Table I. Summary of science cases (adapted from the book "The Science Case for the European ELT", Isobel Hook (Ed), published by OPTICON)

Are there terrestrial planets orbiting other stars?	Direct detection of earth-like planets in nearby extra-solar systems and a first search for bio-markers (e.g. water and oxygen) may become feasible.
How typical is our Solar System? What are the planetary environments around other stars?	Direct detection of proto-planetary disks will become possible around many nearby very young stars. In mature planetary systems, detailed spectroscopic analysis of Jupiter-like planets, determining their composition and atmospheres, will be feasible. Study of the planets and small bodies in our Solar System will complement space missions.

When did galaxies form their stars?	When and where did the stars now in galaxies form? Precision studies of individual stars determine ages and the distribution of the chemical elements, keys to understanding galaxy assembly and evolution. Extension of such analyses to a representative section of the Universe is the next challenge in understanding the visible Universe.
How many super-massive black holes exist?	Do all galaxies host central monsters? When and how did super-massive black holes form and evolve in the nuclei of galaxies? Extreme resolution and sensitivity is needed to extend these studies to normal and low-mass galaxies in order to address these key puzzles.
When and where did the stars and the chemical elements form?	Can we meet the grand challenge to trace star formation back to the very first star ever formed? By finding and analyzing distant galaxies, gas clouds, and supernovae, the history of star formation and of the creation of the chemical elements can be fully quantified.
What were the first objects?	Were stars the first objects to form? Were these first stars the source of the ultraviolet photons which re-ionized the Universe some 200 million years after the Big Bang, and made it transparent? These objects may be visible through their supernovae/hypernovae or their surrounding ionization zones.
How many types of matter exist? What is dark matter? Where is it?	Most matter does not emit any electromagnetic radiation and can be identified only through its gravitational pull on surrounding visible objects. By mapping the detailed growth and kinematics of galaxies out to high redshifts, we can observe dark-matter structures in the process of formation.
What is dark energy? Does it evolve? How many types are there?	Direct mapping of space-time topology, using the most distant possible tracers, is the key to defining the dominant form of energy in the Universe. This is arguably the biggest single question facing not only astrophysics but also fundamental physics as a whole.
Extending the age of discovery	In the last decades astronomy has revolutionized our knowledge of the Universe and established it as the ultimate physics laboratory. The next big steps are likely to be discoveries of unimagined new physical processes.

2.1   The cosmic supernova rate at high redshift

I have chosen to discuss this science case in some detail (rather than the perhaps more exciting ones of the terrestrial exo-planets or the direct detection of the cosmic deceleration that I also described in my talk) because it gives a clear example of the kind of detectors we need to achieve the

science objectives OWL will make possible. Some details on the other cases may be found in the paper by Sandro D'Odorico in these proceedings.

The detection and the study of high redshift (z) supernovae (SNe) is important not only because their use as calibrated standard candles allows measurements of the acceleration of the Universe and to probe the different cosmological models, but also because the evolution of the cosmic SN rate provides a direct measurement of the cosmic star formation rate.
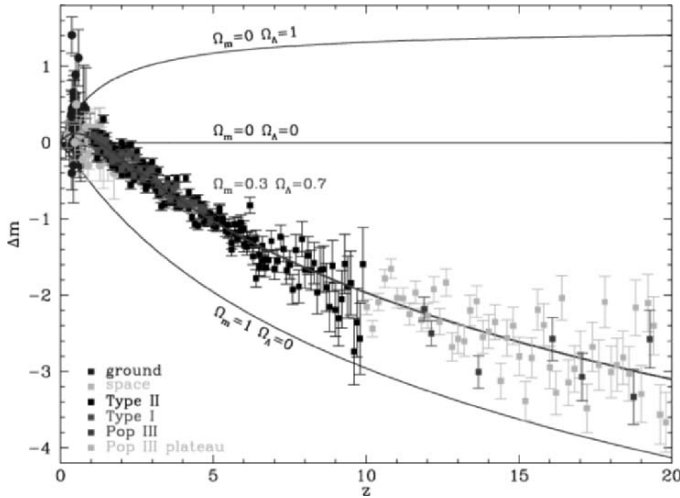
Figure 4. Simulation of OWL observations of SNe. The points between z = 0 and z = 1 are actual observations, the black points to z = 10 are core-collapse supernovae (Type II and Ib/c), the dark gray points between z = 1 and z = 5 are Type Ia SNe (binary systems). The SNe above z = 10 are hypothetical SNe from the very first generation of stars in the Universe. The curves represent models of the Universe. The simulation is based to today's "favorite" model, but the OWL observations will determine if a different one is should be considered.

SNe are enormously energetic explosions that can be seen at large distances in the Universe. They come from different physical mechanisms: core-collapse explosion of massive stars at the end of their 'life' (due to the star having consumed all its usable nuclear fuel), or thermonuclear explosion of a white dwarf in a binary star system (due to its accreting matter from the companion to above a critical threshold). These different types of SNe have specific signatures that allow astronomers to distinguish among them. Determining their rate at various redshifts (i.e. at various look back times) will tell us about the distribution of their parent stars, from which we can

deduce the history of star formation, one of the critical elements to understand the evolution of the Universe from the initial fireball to today.

Figure 4 is a simulation that Massimo della Valle and I did a couple of years ago, showing the expected results of OWL observations based on some assumptions on the SN rates valid in the far Universe (extrapolated from our knowledge up to redshift $z = 1$) and on the current best knowledge of the "model" describing the Universe. The anticipated quality of the data is such that if it turns out that a different model would describe better the Universe, it would immediately be shown by the data.

To obtain this data set one needs a substantial amount of observing time, and a reasonable field of view. The data shown in Fig. 4 require that one find the SNe with a suitable search strategy, characterize them (to know what their "intrinsic" luminosity is, and at which redshift they are), and follow them during their light curve (to be sure that they are detected at their maximum light). All this translates into about 120 nights observing in the J, H and K infrared bands with a field of view of 2×2 arcminutes sampled at the half the diffraction limit (1.6 mas at J). In other words, one would need a 75K×75K detector (more than 5 Gpixel, about 1 m^2 if the pixels are 15 μm in size). Ways to resize the science case may possibly be found, whereby the observations are made sampling the focal plane in a smart way, or taking a longer time with a smaller field of view, or accepting a less optimal sample statistics. But one thing is certain: to avoid that the detectors cost more than the telescope (!) we need to find ways to decrease the costs from the current 10 ¢/pixel to below 1 ¢/pixel. A breakthrough may come from the fact that by next decade the request for pixels will have increased more than 100-fold with respect to today, and this will probably require some paradigm shifts (e.g. the development of a new mass production, cost saving approach).

3.   THE OWL TELESCOPE CONCEPT

Since 1997, ESO has been developing the concept of a ground-based 100-m class optical telescope. It has been named OWL for its keen night vision and for being OverWhelmingly Large (showing either the *hubris* of astronomers or their distorted sense of humor). The challenge and the science potential are formidable and highly stimulating: a 100m diffraction-limited optical telescope would offer 40 times the collecting power of the whole VLT with the milliarcsecond imaging resolution of the VLTI.

A few principles, mostly borrowed from recent developments in the art of telescope making, hold the key to meet the difficult OWL requirements: optical segmentation as pioneered by the Keck, massive production of standardized mirrors from the Hobby-Eberly, active optics control and

system aspects from the VLT. The most critical development is diffraction-limited imaging in "large" fields (a few arcminutes in the near-IR). This is the goal of the so-called multi-conjugate adaptive optics concept, whose principles and applications have been already demonstrated (ESO is building MAD, an MCAO demonstrator, to see first light at the VLT in 2006). Tremendous pressure is building to implement this capability into existing large telescopes, and rapid progress in the underlying technologies is taking place, e.g. fabrication of low-cost deformable mirrors with tens of thousands actuators from integrated circuits techniques.
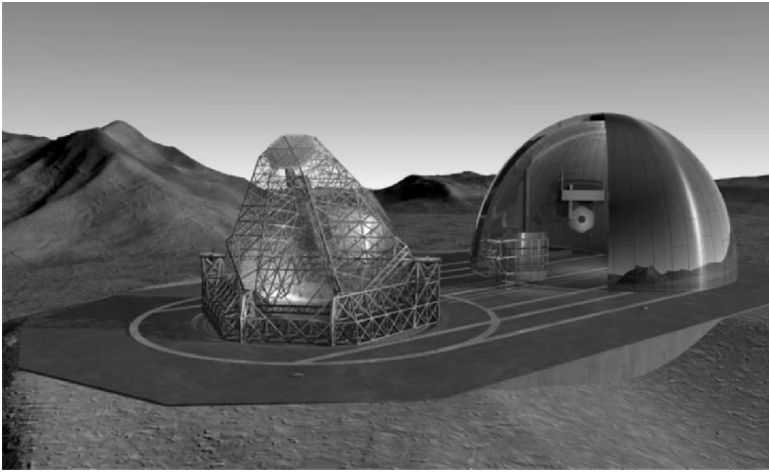
Figure 5. Layout of the OWL observatory.

The evolution of the OWL telescope design has been marked by a few key trade-offs and subsequent decisions: (i) Segmented primary and secondary mirrors, segment dimension < 2-m; (ii) Optical design, spherical primary mirror solution; (iii) Non-adaptive main telescope optics (2 mirrors in the corrector, however, have been identified as adaptive mirrors, conjugated at 0 and 8km) (iv) Implementation of active optics and field stabilization; (v) Alt-az mount. Several optical designs have been explored, from Ritchey-Chrétien solutions to siderostats with relatively slow primary mirrors. It has been found that cost, reliability, fabrication and telescopes functionality considerations point towards a spherical primary mirror solution. In terms of fabrication, all-identical spherical segments are ideally suited for mass-production and suitable fabrication processes recommended by potential suppliers are fully demonstrated. In a modified version, these processes could also be applied to aspheric segments, however with a substantially higher cost (more complex polishing, lower predictability, tighter material requirements).

The current baseline design is based on a spherical primary mirror solution, with flat secondary mirror and aspheric, active corrector (see Fig. 6). The flat secondary mirror also has a major advantage in terms of decenters (cm rather than μm), which are evidently crucial with a structure the size of OWL's. Several mount options have been assessed, from a classical alt-az solution to de-coupled primary and secondary mirror structures. Cost and performance considerations point clearly towards the alt-az solution (see observatory layout in Fig. 5). The current baseline design is modular i.e. the structure is made of (nearly) all-identical, pre-assembled modules. This crucial feature allows for major cost savings.
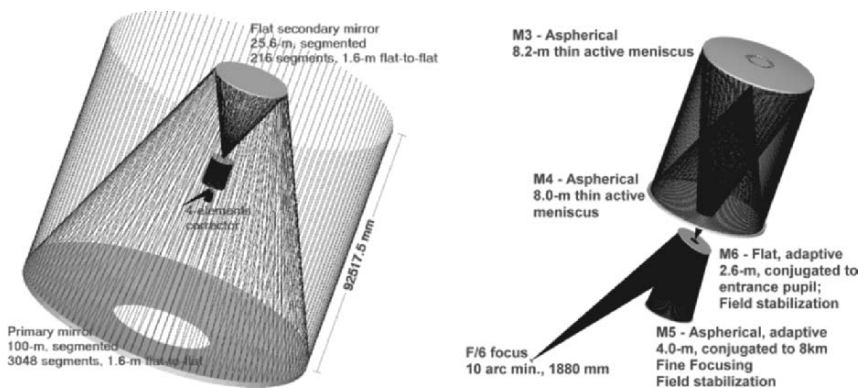
Figure 6. OWL baseline optical design.

There is no provision for a co-rotating enclosure, the advantage of which is anyway dubious in view of the enormous opening such enclosure would have. Protection against adverse environmental conditions and excessive day-time heating would be ensured by a sliding hangar, whose dimensions may be unusual in astronomy but actually comparable to or lower than those of large movable enclosures built for a variety of applications. Mirror covers sliding into the structure would provide segments cleaning and handling facilities, and local air conditioning if required.

Relevant site aspects are more complex than with previous telescope generations, mainly because of adaptive optics, telescope size, and the higher impact of seismic activity on cost and safety. AO implies, in particular, that the function of merit of the atmosphere cannot be described by a single parameter (seeing). Better understanding of site quality in relation to climatology is also essential.

Cost estimates (more than half of which supported by industrial studies) indicate that the required capital investment could be around 1 billion Euros.

Compared to "classical" telescope cost factors, substantial cost reduction occurs with the main optics (fabrication processes adapted to mass-production), the telescope structure (very low mass in proportion to dimensions, mass-produced modules), and the enclosure (reduced functionality, no air conditioning). Schedule estimates indicate that technical first light could occur within 8-9 years after project funding. Allowing for 2.5 years integration and verification of the IR adaptive module(s) the telescope could already deliver science data in the IR within 11 years after project go-ahead, with unmatched resolution and collecting power. Full completion would occur about 15 years after project start.

OWL is undergoing conceptual design review at the end of 2005. The so-called OWL Blue Book is a report detailing the studies during this phase and will be publicly available after the review.

4.   CONCLUSIONS

Several projects in the optical and near infrared, both in space and on the ground, are currently underway for deployment in the second decade of the third millennium. Their scientific goals open new and exciting avenues of research that are outside the reach of current instrumentation. The detection of earth-like exo-planets and possibly of biospheres, the study of the first building blocks of stars and galaxies and their evolution, the direct measure of the deceleration of the Universe, all have driven the technical requirements to unprecedented levels, and the sensitivity increase of the new generation of telescopes with respect to the previous one will be one never seen before in astronomy.

ELTs are what "ground-based" astronomers and engineers are working on now with a view to build (at least one of) them by the next decade. Although many technical challenges remain to be solved and funds need to be found, the possibility that OWL may become a reality is far more likely today than it was when the discussions started a few years ago. The industries that built the VLT have not found any obvious showstoppers, and even adaptive optics (which we consider a "go/no-go" milestone for the entire project) is developing at a pace that allows some cautious optimism. Ten years from now, turning OWL to some nearby earth-like planet, or to the far reaches of the Universe may not be as wild a dream as it was yesterday.

To achieve the science goals, OWL or any other ELT will of course need the most advanced, large, fast readout, extremely low noise detectors, at affordable prices (i.e. at least 10 times cheaper than today), and at the tune of several gigapixels per instrument.

Jim et al, your task for the next 10 years is set!

INSTRUMENTS, DETECTORS AND THE FUTURE OF ASTRONOMY WITH LARGE GROUND BASED TELESCOPES

Douglas A. Simons[1], Paola Amico[2,3], Dietrich Baade[3], Sam Barden[4], Randall Campbell[5], Gert Finger[3], Kirk Gilmore[5], Roland Gredel[6], Paul Hickson[7], Steve Howell[8,20], Norbert Hubin[3], Andreas Kaufer[3], Ralf Kohley[9], Philip MacQueen[10], Sergej Markelov[11], Mike Merrill[8], Satoshi Miyazaki[12], Hidehiko Nakaya[12], Darragh O'Donoghue[13], Tino Oliva[14], Andrea Richichi[3], Derrick Salmon[15], Ricardo Schmidt[9], Hongjun Su[16], Simon Tulloch[17], Maria Luisa García Vargas[9], R. Mark Wagner[18], Olivier Wiecha[19], Binxun Ye[16]

[1]Gemini Observatory, [2]W.M. Keck Observatory, [3]European Southern Observatory, [4]Anglo Australian Observatory, [5]Stanford/SLAC, [6]Calar Alto Observatory, [7]University of British Colombia, [8]National Optical Astronomy Observatory, [9]GranTeCan/ Instituto de Astrofisica de Canarias, [10]University of Texas, [11]Russian Academy of Sciences, [12]Subaru Telescope, [13]South African Astronomical Observatory, [14]INAF/ Telescopio Nazionale Galileo, [15]Canada France Hawaii Telescope, [16]National Astronomical Observatories, CAS, [17]ISAAC Newton Group/ Instituto de Astrofisica de Canarias, [18]Large Binocular Telescope Observatory, [19]Lowell Observatory, [20]WIYN Observatory

Abstract: *Results of a survey of instrumentation and detector systems, either currently deployed or planned for use at telescopes larger than 3.5 m, in ground based observatories world-wide, are presented. This survey revealed a number of instrumentation design trends at optical, near, and mid-infrared wavelengths. Some of the most prominent trends include the development of vastly larger optical detector systems (>10^9 pixels) than anything built to date, and the frequent use of mosaics of near-infrared detectors – something that was quite rare only a decade ago in astronomy. Some future science applications for detectors are then explored, in an attempt to build a bridge between current detectors and what will be needed to support the research ambitions of astronomers in the future.*

Key words: *survey, cost, market share, future science, galactic center, dark matter, dark energy.*

1.   OVERVIEW

For the most part, a typical astronomical instrument is a one-of-a-kind, highly specialized assemblage of optics, mechanisms, electronics, and control systems that work together as a system to capture information in the focal plane of a telescope and translate it into the images and spectra astronomers use everyday to explore the universe. In many ways, the astronomical research potential of modern observatories is defined and constrained by the instrumentation developed within the astronomy community and commercial manufacturers. Most instruments are built within relatively small labs, located in universities or various research institutions while most detectors are built by commercial entities since the technology, infrastructure, and expertise needed to generate modern array detectors is fairly unique to commercial enterprises. The complex "marriage" between astronomical instruments and the detector systems they incorporate therefore represents a crucial interface between intrinsically disparate entities, driven by a range of interests and motivations, that overlap in the arena we call astronomy. While it is fair to say that most established commercial providers of detectors have a reasonable understanding of the astronomical community as a business client, and astronomers in general have a reasonable understanding of what current detectors can do, bridging the gaps between these communities is important to help ensure the future viability of this research / business relationship. This paper is intended to help bridge that gap, to convey current trends in astronomical instrumentation and the detectors they rely upon, and extrapolate to the extent practical future trends in astronomy that will impact development plans of detector manufacturers.

To characterize existing and planned instrumentation in astronomy, the authors conducted a fairly extensive survey of the ground-based astronomical community. Responders were located around the world, including China, Australia, North and South America and of course Europe at large. To help keep the quantity of information provided manageable, the survey was limited to observatories housing telescopes with apertures of 3.5 m or greater. Each of these observatories was sent a questionnaire to fill-out and return. The data was merged into a single database that could be easily interrogated to identify globally significant trends. In some cases we relied on information published in the web sites of the observatories polled to complement the data provided through the questionnaire. Accordingly, this paper does not attempt to describe in detail all of the instruments represented in this poll. The detailed results of the survey are shown in the Appendix, printed in the back of the book. These results can be used to assess the types of instrumentation used by a wide range of major

observatories. The reader is encouraged to contact the observatories listed in this survey directly if comprehensive information about any particular instrument is needed.

2. SURVEY DETAILS

Through the aforementioned survey, a variety of information was collected about instruments and the detectors they incorporate. In summary this information includes:

- Instrument name
- Observing Modes
- Start of operations
- Wavelength Coverage
- Field of View
- Instrument cost
- Multiplex gain
- Spatial/Spectral resolution
- # Detectors
- Detector Format

- Buttability
- Pixel size
- Pixel scale
- Electronics
- Noise
- Readout Time
- Dark Current
- Full well
- Cost per pixel
- Detector size

A total of 25 institutions (see Table 1 for a complete list) were contacted and information was received on over 200 instruments in the optical, near, and mid-infrared wavelength range. All institutions that feature at least one telescope larger than 3.5 m have been included, with the exceptions of the Starfire (3.7 m) and AEOS (3.5 m) telescopes, which belong to the US Air Force, and the ARC Apache Point Observatory 3.5 mt telescope. All scientific astronomical instruments, which are in use or being planned for the near future, have been listed while technical/facility instrumentation and detector systems (such as guider systems and Avalanche Photodiode-based instruments) have been left out. While certainly not 100% complete, this survey is broad enough to identify statistically meaningful trends about instrument designs, capabilities, and of course detector systems used in modern astronomy. As a technical resource the survey data in the Appendix is likely unique in astronomy.

All of this information was loaded into a database that was queried to analyze various parameters. For example, it was possible to assess how many optical and infrared pixels are in use now and planned to be deployed soon, what are the most common designs and operating modes used and planned, and what is the market share for optical and infrared detector manufacturers. These results and others are described in more detail in Section 3.

Table 1. List of the Institutions/Observatories which were polled for the survey. The grey cells indicate telescopes currently being built or planned. #×Size indicates the number of mirrors time their size in meters.

Institution	Telescope	# ×Size
Anglo Australian Observatory (AAO)	Anglo Australian Telescope (AAT)	3.9
Caltech	Hale/Palomar	5
California Association for Research in Astronomy (CARA)	Keck I and II	2 x 10
Carnegie Observatories (OCIW)	Magellan Telescope	2 x 6.5
Canada France Hawaii Telescope (CFHT) Observatory	CFHT	3.6
European Southern Observatory (ESO)	Very Large Telescope VLT1,2,3,4	4 x 8.2
	ESO 3.6mt	3.6
	NTT	3.5
	Visible and Infrared Telescope for Astronomy (VISTA)	4
Gemini Observatory	Gemini North and South	2 x 8.1
HET Consortium	Hobby Eberly Telescope (HET)	
Istituto Nazionale di AstroFisica (INAF)	Telescopio Nazionale Galileo (TNG)	3.6
ISAAC Newton Group	William Herschel Telescope	4.2
Large Binocular Telescope (LBT) Observatory	LBT	2 x 8.4
Max Planck Institut fuer Astronomie (MPIA)	Calar Alto	3.5
National Astronomical Observatory of Japan (NOAJ)	Subaru Telescope	8.2
National Optical Astronomy Observatory (NOAO)	Southern Astrophysical Research SOAR CTIO	4.1
	Blanco CTIO	4
	Mayall Kitt Peak	4
Russian Academy of Sciences (RAS)	Bolschoi/SAO	6
Smithsonian/Arizona (MMT Cons.)	Multi Mirror telescope (MMT)	6.5
UK PPARC	United Kingdom InfraRed Telescope (UKIRT)	3.8
University British Colombia	Large Zenith Telescope (LZT)	6
Wisconsin Indiana Yale NOAO (WIYN) Consortium	WIYN Kitt Peak	3.5
Discovery Communications Inc/Lowell Observatory	Discovery Channel Telescope (DCT)	4
Giant Magellan Telescope (GMT) Consortium	GMT	7 x 8.4
Instituto de Astrofisica de Canarias	Grantecan (GTC)	10.4
National Astronomical Observatory of China	LAMOST	6.4 (4)
Large Synoptic Survey Telescope (LSST) Corporation	LSST	8.4
South African Astrophysical Observatory	South African Large Telescope (SALT)	10.4

3. CURRENT INSTRUMENTS

Instrumentation in astronomy can be broadly categorized according to functionality (spectroscopy vs. imaging), spectral and spatial resolution, etc. The following section summarizes the results of the survey according to these various categories, identifying major trends where evident. Possible explanations for these trends are also offered.

3.1 Wavelength Coverage

As shown in Figure 1, despite advances that are now well established in near and mid-infrared detectors systems, ground based astronomy remains primarily an optical scientific endeavor. One is tempted to claim this is cost related, since optical detectors generally remain significantly cheaper per pixel than their infrared counterparts. However, this would be an over simplification of a fairly complex situation involving cost, the availability of instruments to conduct research, and even sociology. Large format near-infrared detectors, which to first order "behave" like CCDs from the perspective of scientists, have been available for more than a decade and while there is undoubtedly a trend to migrate into the 1-2.5 µm regime from the optical, that migration has been fairly slow. Ultimately, this is probably due to both historical trends and the availability of instruments on the numerous small telescopes that are used for graduate-level research.
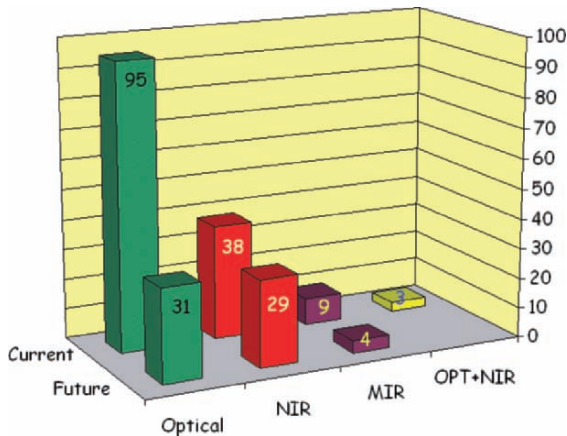
Figure 1. An overview of optical, near and mid-infrared instruments, both current and planned, is shown.

Generations of astronomers remain today that only knew optical detector systems (including photographic plates) when they became grounded in a

particular branch of astronomy, and they have remain focused on the same type of research over the years, only branching out into other wavelength regimes recently and in some cases reluctantly. More recently, many astronomers within the past couple of decades have trained on relatively small telescopes with equally small budgets that could not afford to invest in the advanced infrared detector systems, custom array controllers, cryogenic opto-mechanical systems, etc. These are required to enter the infrared "business". This trend is declining as more major facilities open the infrared windows to astronomers. Furthermore, expertise on the part of the astronomer needed to operate these often more complex instruments (involving such techniques as chopping and special processing steps) are increasingly provided by dedicated staff astronomers. This allows the research astronomer to focus on the scientific interpretation of data, rather than the subtleties of acquiring it.

Taken at face value, Figure 1 suggests that detector manufacturers should not seriously pursue infrared (particularly mid-IR) detector development, given the demonstrated low market share of this technology. This would be a mistake though, since it does not factor in future research trends in astronomy. Larger telescopes are now enabling observations to ever more distant targets that were simply unreachable by previous generation (4 m and smaller) telescopes. Of course these more distant targets are increasingly redshifted due to the expansion of the universe, and many of them are redshifted out of the optical and into the near-infrared, which in turn triggers the need to switch to the small family of near-infrared detectors available today. This is an indisputable trend – research in cosmology will inevitably push back to find the first luminous objects in the universe, which can only be seen in the infrared thanks to their enormous distances and redshifts.

3.2   Modes

The instruments sampled represent an impressive array of capabilities distributed around the world. Many naturally contain more than one primary functional mode and many are highly specialized instruments designed to observe targets using novel or unconventional techniques. Figure 2 shows the breakdown of instruments commonly in use in astronomy today, sorted by operating mode and wavelength.

Not surprisingly a significant fraction consists of direct imagers and single slit conventional spectrometers. The vast majority of the single slit spectrometers surveyed also support direct imaging, no doubt because target acquisition typically involves imaging a field before the slit is located precisely on the sky.
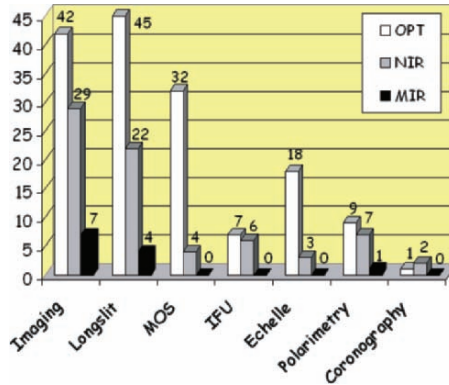
Figure 2. The distribution of observing modes across currently deployed instruments in the survey.

A number of integral field spectrometers were reported, which provide both imaging and spectroscopy across the instrument's field of view. This type of instrument invariably suffers from a lack of detector "real estate", given the intrinsically highly multiplexed nature of its data structure. Another instrument that offers considerable multiplex gains is the multi-object spectrometer (MOS). The popularity of this type of spectrometer has increased radically over the past 10-15 years since it is particularly efficient for complex target-rich fields like galaxy clusters or star formation regions.

Figure 3 shows the distribution of observing modes across future instruments.
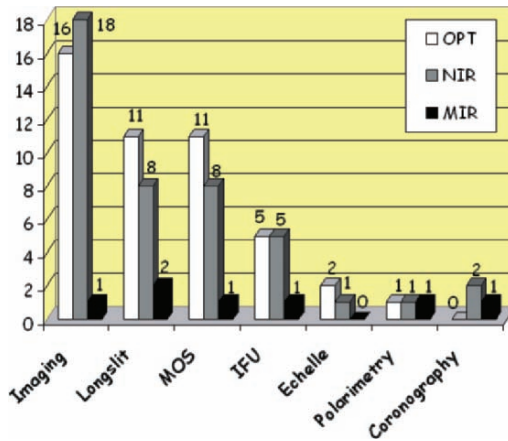
Figure 3. Future instrument types are summarized, again broken into optical, near, and mid-infrared categories.

Imaging and long-slit spectroscopy appear to be the "mainstay" instruments in the near future. Interestingly, instruments offering greater

multiplex gains are gaining popularity. Figure 3 demonstrates an increase in MOS and IFU based instruments being deployed in the future. Also, though highly specialized, note the increased deployment of coronagraphs in the future. This no doubt reflects an increase in interest in planet/disk observations in modern astronomy as well as advances in adaptive optics.

3.3   Spatial Resolution

The distribution of spatial resolutions instruments tend to use is shown in Figure 4. Working from left to right in this plot, the instruments using very fine plate scales are generally fed by AO systems, which of course typically yield near diffraction-limited point spread functions (PSFs) that are nearly an order of magnitude smaller than seeing limited PSFs. Interestingly, if the same poll were cast a decade ago, the plot in Figure 4 would not have included many instruments with plate scales measured in units of milli-arcseconds simply because adaptive optics was not widespread enough to drive the development a significant population of AO specialized instruments.
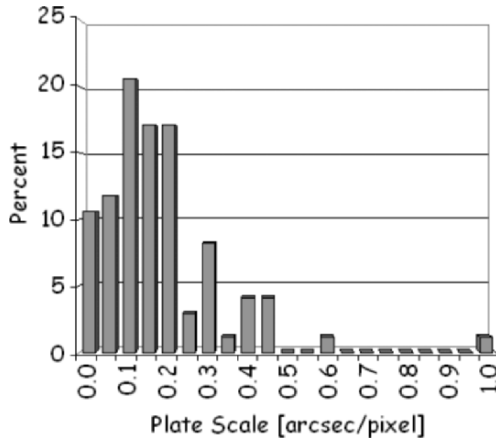
Figure 4. The distribution of plate scales for all of the instrumentation sampled in the survey.

Today, however, AO systems are becoming commonplace and modern research is conducted at spatial resolutions that were previously impossible to achieve. The peak in the distribution at ~0.1" is a bit surprising. On the assumption that most instruments are sampling seeing limited images (~1") at the Nyquist limit, a peak closer to ~0.5" is expected. The dearth of instruments using large pixels (>0.5") is probably due to a bias built into the survey, which was restricted to 3.5 m telescopes or larger. If it included the large number of ~1-3 m telescopes in use today, which are often wide field

systems, the right end of the histogram in Figure 4 would have included many more instruments.

3.4 Field of View

Like so many other wavelength dependent instrument properties, field of view varies widely between optical, near, and mid-infrared instruments. As seen in Figure 5, there is an enormous range of fields that instruments cover but invariably the smallest field instruments operate at either mid-infrared wavelengths or use AO systems. in fact there is a fairly staggering factor of $\sim 10^8$ between the largest field optical imagers planned and the smallest imagers currently in use. For mid-infrared systems, this is primarily driven by the small mid-infrared detectors presently available, though there are ancillary reasons like the maximum practical chop-throw possible with the large secondary mirrors needed on 8-10 m class telescopes. Again, AO imagers must use extremely fine plate scales to adequately sample an AO corrected focal plane, and hence tend to have small fields when the maximum size NIR detector has been (until recently) 1024^2.
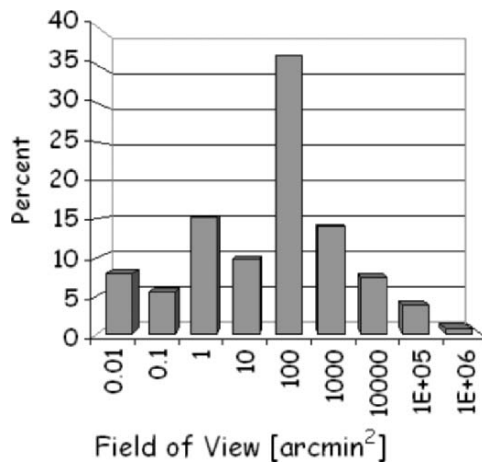
Figure 5. A clear peak in the field of view of most instruments at ~100 arcmin2 was found in the survey.

In the middle of the pack, large field mosaic based near-infrared imagers are now coming on-line. While small compared to the largest field optical imagers, this next-generation of imagers will enable important new scientific frontiers with wide and deep surveys (see Sec. 4 for details). The high end in Figure 5 is defined by wide field optical imagers that are becoming increasingly popular, including on telescopes too small to be included in this

survey. For example, wide field imagers like ESO's OmegaCAM and WFI and University of Hawaii Institute for Astronomy's Pan-STARRS, represent state-of-the-art optical imagers.

3.5 Detector Systems

Given the previous top-level summary of instrumentation sampled in this survey, we will now shift to the detector systems used in these instruments. This includes both the detectors and advanced array controllers needed to readout signals recorded by contemporary detectors.

3.5.1 Array Controllers

Given the common need to readout array detectors with a controller, the range of controllers built in astronomy over the past few decades is remarkable. Manufacturers historically do not market controllers with the detectors they supply, leaving it to the customer to find or develop in-house their own controllers. This has led over the past few decades to a myriad of controllers in astronomy, based upon a wide range of evolving technologies. The previous decade saw controllers based on transputer or DSP technology that required fairly unique skills to program and maintain, occupying considerable amounts of rack space to generate a 16 or 32 channel system. More recently controllers based upon fast PCI processors and broadband fiber links are becoming available, which are cheaper (since they are based on PC technology), require much less space, dissipate far less heat, and are easier to program. The future points to further miniaturization as ASIC technology slowly but surely emerges with the promise of reducing controllers to a minimum of small components.

As shown in Figure 6, no single vendor has attempted to meet all the needs of astronomy. The readout requirements of such different detector architectures as mid-infrared IBCs and CCDs are obviously different (speed, clocking patterns, noise performance, etc.). However having a small/unified set of array controllers that are affordable, broadly supported, and readily available would no doubt be embraced by many observatories strapped with the complications of maintaining nearly as many types of array controllers as they have instruments. That said the bulk of the market share is currently occupied by controllers made by San Diego State University (Bob Leach). The next most common controllers in use today are those made by ESO (FIERA for the optical and IRACE for the infrared detectors). The ~30% share in the "Others" category testifies the large number of custom made systems, each of them present in quantities too small to plot separately.
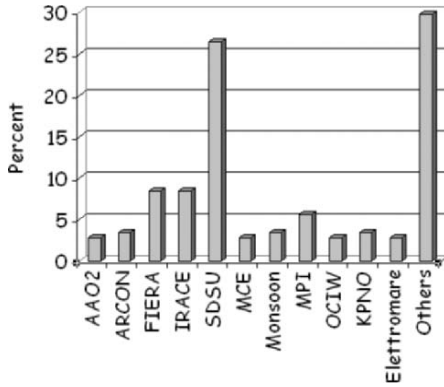
Figure 6. Among the "brand names", the San Diego State University by Bob Leach is the most popular controllers.

3.5.2 Number of Pixels per Focal Plane

Some of the most interesting results of the survey are encapsulated in Figures 7 and 8. These histograms show the number of pixels per focal plane at optical and infrared (near plus mid-infrared) wavelengths for both current and future instruments. Adding the pixels in Figure 7 leads to a total of ~2.2 Giga-pixels in use today in astronomy. As shown in Figure 7, most optical and infrared systems use focal planes in the 1-10 Mpixel range and the vast majority of current NIR focal planes are well below 10 Mpixel in size. Focal planes well beyond that size are only populated by optical sensors (CCDs), again no doubt due to cost and complexity constraints.
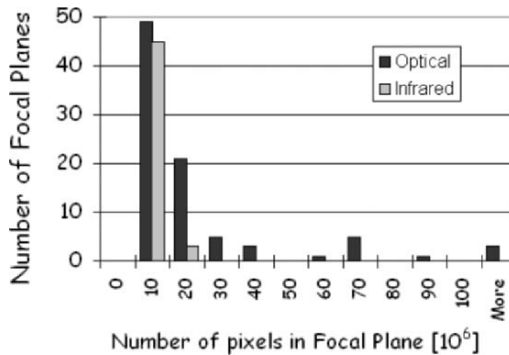
Figure 7. Contemporary distribution of optical and infrared pixels across all of the instruments sampled.

Looking forward, Figure 8 shows the future growth of large CCD mosaics in astronomy. The science drivers behind this are explained in Sec.

4. Of particular note is the peak in the "more" category, which reflects the upsurge in development of Giga-pixel class CCD focal planes intended for ultra-wide field surveys in the near future. In the same vein, notably absent are comparably large infrared focal planes which regrettably remain beyond the reach of astronomers. Amazingly, the future instruments sampled here include a staggering ~7×10^9 pixels in planned instrumentation, ~90% of which is in the form of CCDs in the "more" category. This means a nearly four-fold increase in detector "real estate" will be realized in the next decade compared to what is now available to astronomers using ground based instrumentation.
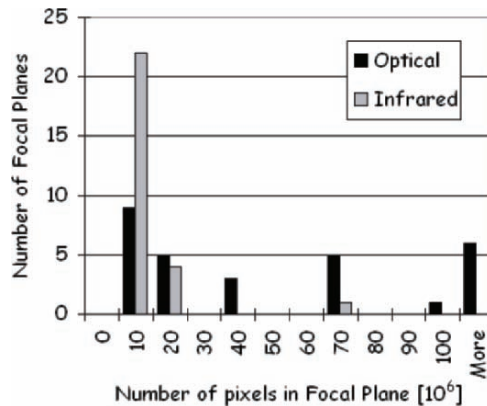
Figure 8. Distributions of optical and infrared pixels for future/planned instruments.

3.5.3   Cost per Pixel

The data provided in this area is relatively scant given the number of instruments sampled. Nonetheless, results are consistent with what has been anecdotally recognized for a long time – the cost per infrared pixel is nearly an order of magnitude higher than the cost per CCD pixel (typically ~1-3¢/pixel). The situation is even worse when comparing CCDs with mid-infrared detectors, which have far fewer pixels yet retain a comparable cost to near-infrared arrays. While this is no doubt attributable to the much higher complexity associated with infrared arrays, the cost "challenge" of infrared arrays is an inhibiting factor in astronomical research. As mentioned before, this is certainly at least partially responsible for the fewer number of infrared instruments available to astronomers today. This in turn limits the scientific research capacity of astronomers, particularly those without access to large modern facilities. Breaking the cost curve for infrared arrays remains one of the key challenges in the future development of this technology.

Without a major cost reduction, it will probably prove impossible to finance the Giga-pixel class focal planes that are being designed with CCDs today. Table 2 lists average instrument costs provided through the survey. It is notoriously difficult to make "apples-to-apples" comparisons in instrument costs, given the different methods used to account for labor and various indirect costs. With this caveat in mind, the principal conclusion from Table 2 is that next-generation optical instruments will be much more expensive due to the use of much larger CCD focal planes. While infrared instruments will become more expensive, with a cost increase of ~25%, the ~16% cost increase foreseen in optical instruments is not foreseen in the infrared. Again this is due to the large cost per pixel for infrared detectors, which effectively prohibits development of enormous infrared focal planes. Another possible effect seen here could be "market saturation", i.e., it is simply very difficult to raise large amounts of money for a single instrument.

Table 2. The current and future median instrument costs derived from the survey are listed.

	Optical	**Infrared**
Current	$400,000	$3,750,000
Future	$6,600,000	$5,000,000

3.5.4 Typical Mosaic Building Blocks

The unit detector or building block used to assemble large scale mosaics varies radically from optical to mid-infrared detectors. As shown in Figure 9, the most currently popular CCD format has dimensions of 2048×4096, and these are typically buttable on 2 or 3 sides.
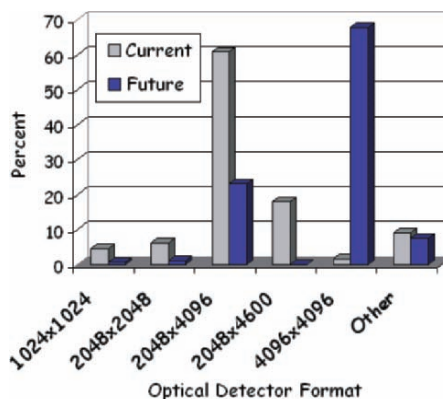
Figure 9. The most popular current and future CCD building blocks used in astronomy.

In some cases optical instruments have incorporated 4096×4096 monolithic detectors. In contrast, only one of the various near-infrared

instruments sampled incorporated a 256×256 detector. The majority of near-infrared instruments in use today rely upon 1024×1024 arrays, with a significant fraction using the more recent generation 2048×2048 buttable devices just now becoming available. Finally, the handful of mid-infrared instruments in the survey principally used 240×320 format devices, with only 1 using an older 128×128 detector. None of these devices are readily buttable.

From the instrument builder's perspective, while the availability of large format single detectors has and will continue to be important, what is arguably just as important is the possibility of making these devices buttable. What has long been possible with CCDs has only recently become possible in the near-infrared. This single advancement in technology makes it possible to build truly enormous focal planes without relying upon the development of ever larger monolithic structures. From a pure marketing perspective, this area is one in which infrared vendors have been slow to recognize the sales potential of providing not just bigger detectors, but detectors that the customer can combine to make instruments previously impossible to build. From a science perspective, this has enormous implications, as it facilitates the development of instruments such as: wide field imagers, cross-dispersed spectrometers covering large wavelength ranges, adaptive optics imagers which rely on large numbers of small pixels to sample an exquisitely fine focal plane, or ELTs that simply need enormous focal planes that scale with the rest of the telescope.

Though the natural tendency may be to develop ever larger infrared arrays, it has already been demonstrated that the $\sim 2048^2$ building blocks offered by CCDs can be used effectively to build enormous mosaics.
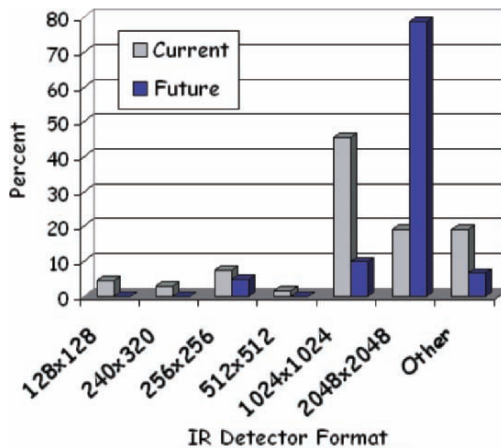
Figure 10. The most popular current and future infrared arrays used in astronomy.

While near-infrared instrument builders will no doubt use larger monolithic arrays (as demonstrated Figure 10), the real breakthrough in infrared detector technology from the astronomer's perspective has been the advent of buttable infrared arrays, from which larger mosaics can be built. Nonetheless, for future ELT applications, where the focal plane is intrinsically large and the detector package must expand correspondingly, detector costs must fall radically. If not only a small portion of an ELT's focal plane that cost ~$1B to produce will be adequately sampled with a detector system. Infrared array manufacturers are quick to accentuate that costs will fall if the number of devices built increases. While no doubt true, this trade space remains to be explored and will be the subject of considerable dialog as the ambitions of astronomers drive the development of ever larger infrared sensors.

3.5.5   Manufacturers

A unique aspect of the survey is that it allows a fairly comprehensive assessment of market shares for the various manufacturers of astronomical detectors. The situation is fairly simple for the current crop of mid-infrared instruments, where Raytheon dominates the market, though it remains comparatively small and specialized. This field remains challenging to support from an observatory perspective, though scientifically it remains one of the most "target rich" in astronomy. In the near-infrared most instruments operate from 1-2.5 μm and use Rockwell detectors. In fact over 1/2 of all infrared arrays in use are made by Rockwell. This should also remain true in the near future. The instruments in the 1-5 μm range typically use Raytheon detectors. With only a few exceptions, these two manufacturers dominate the infrared astronomy market today – a situation that has existed for the better part of 2 decades (see Figure 11).
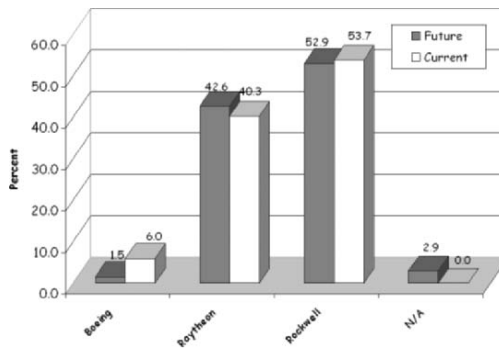
Figure 11.   The market share for various infrared array manufactures, both for current and future instruments.

In the optical, there are more manufacturers today providing high quality CCDs to astronomy. That said, the bulk instruments sampled use e2v detectors, with SITe/Tektronix coming second, closely followed by MIT/LL. Loral, and a handful of other manufacturers follow. e2v is still dominating the future market share according to our survey, though a large fraction of the surveyed future market, as testified by the larger percent of N/A entries for the future, remains uncommitted. This is principally due to the detectors, (over 200), foreseen for the LSST. The vendor has not yet been selected. It is also important to note that this survey only included science detectors, some of which are used for wavefront sensing and none for technical purposes. A large number of these small format high speed CCDs are used in astronomy but for the purposes of this survey were not included. Figure 12 shows the market share for various CCD manufactures, both for current and future instruments.
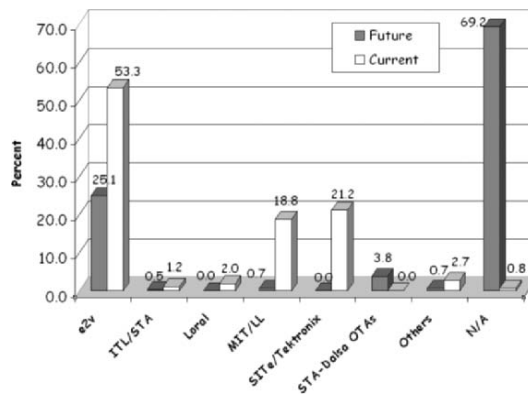
Figure 12. Market share for various CCD manufactures is plotted, both for current and future instruments.

4. FUTURE SCIENCE – FUTURE DETECTORS

This section describes future science and the detectors we will use as our conduit to discovery. Many of the future technology demands of astronomy are intrinsically uncertain since they will be linked to the scientific opportunity of our time, whatever that time may be. Forecasting discoveries about the universe is fraught with risk and is more the subject of science fiction than science fact. Nonetheless, it is useful to assess some of the major research themes in astronomy today as a means to determine, in broad brush terms, where forefront research is headed. Likewise, it is important to examine past discoveries to gauge the pace at which astronomers have made discoveries, so we can extrapolate ahead to where we hope (if not expect) to be in roughly a decade.

4.1 A "Golden Age of Astronomy"

It has no doubt been said countless times over past few centuries, during the time since the invention of the telescope when "modern" astronomy was arguably born, that we live in a golden age of discovery in astronomy. This is natural in a field of science that has truly unbounded potential for discovery. While geologists catalog a finite supply of rocks, entomologists classify insects on the verge of extinction, and meteorologists seek to perfect ever more complex models of the same terrestrial atmosphere, astronomers look to the sky each night examining celestial objects that have never been seen before, conducting experiments on grand scales that no earth-bound laboratory could ever host, hypothesizing about nothing less than the ultimate origin and destiny of the universe. In such a rich research environment, all generations of astronomers count themselves among the lucky few who have witnessed and participated in a "golden age" of discovery.

So what makes the current golden age unique? For millennia questions of innate interest to humans have remained, including questions such as "does life exist elsewhere", "what is the universe made of", and "what did everything originate from"? These questions have stood the test of time as insurmountable monuments in the face of ever more sophisticated scientific assaults. What makes our generation of astronomers unique is that, unlike all previous generations, we are actually on the verge of answering these questions. The 21st century will, in all likelihood, be identified as the era that the first extra-solar *terrestrial* planets were found, some perhaps harboring the unmistakable spectral signatures of biospheres. It will also be the century in which we come to terms with a new and deep understanding of the bulk of the matter and energy in the universe – basic entities which we do not even begin to grasp now. Of course the 20th century was filled with important discoveries in astronomy, including the expansion of the universe, the discovery of the faint highly red-shifted microwave whispers of the Big Bang, and the detection of such bizarre beasts as black holes, which defy the space-time fabric of Einstein's theoretical invention. While all important – and more such discoveries await today's intrepid legion of astronomers – what is probably more significant is that through these discoveries we have come to recognize how little we actually know about the universe. This renewed introspection about our realm of existence almost has religious overtones due to the profound nature of the discoveries awaiting us. It nonetheless remains firmly grounded in the tried and true principles of science that have carried us this far quite faithfully. Furthermore, we have no reason to expect that the advances in technology which have taken us this far

in astronomy won't propel us to much greater heights in our tireless quest of discovery.

We also live in an age when, for the first time, the fields of physics and astronomy are becoming inextricably linked. Modern physicists are becoming increasingly reliant on the ultimate particle accelerator, the Big Bang, to understand the nature of matter and energy under the most extreme conditions, which only existed in the first instant after the universe exploded into reality. It was in this singular regime in the entire history of the universe that matter and energy were merged into a shared state and, over time, evolved into the stars, planets, radiation, gas, dust, thermal energy, etc., that we now struggle to understand and link. The path physicists must take in the quest for their "holy grail", a unified theory of everything, is being paved by astronomers. Interestingly, astronomers and physicists have stumbled upon the same path in recent years albeit from separate directions. This isn't due to some complex set of sociological or technology driven reasons. It is much simpler. It is because we are all compelled to answer the same questions – "are we alone", "what is the universe made of", and "what did everything originate from"?

Events like the merging of physics and astronomy, inner recognition of how little we know about the universe through the discovery of some of its most precious secrets, and a technology revolution that is yielding tools of discovery unlike any conceived by our ancestors, are all signs that this age is truly unique. This age is "golden".

4.2   The Galactic Center – A Case Study in Technology Driving Science

The center of our galaxy has remained an enigma for decades. It was first discovered in the early 20th century that we live in a galaxy, which must have a core like those we see in galaxies around us. Detecting that core has been a challenge. At optical wavelengths it is obscured by at least 30 magnitudes due to intervening dust along the plane of the galaxy. Even the cumulative light from billions of stars along the line of site to the Galactic center cannot penetrate to our position in the galaxy. As a result, the advent of recording devices like photographic plates, photoelectric sensors, and even CCDs, were of little use in observing the Galactic center.

The era of Galactic center research began in earnest only with the use of infrared sensors. These first seriously emerged in the 1960's in astronomy and led to pioneering research which was later perfected with "advanced" infrared optimized telescopes and observing techniques in the 1970's. The challenge in using these sensors was to detect targets that were millions of times fainter than the thermal glow of the earth's atmosphere. This required

techniques that previous generations of optical astronomers never encountered. It was only through rather ingenious techniques involving fast chopping on the sky and lock-in amplifiers to sample and subtract several times a second object from sky beams that background removal to the level of about 1 part per million was possible.

Figure 13 shows a watershed result in the early days of infrared astronomy, which involved the use of some of the first simple single element PbS infrared detectors in astronomy. This is the discovery strip chart of the Galactic center, which is seen as a blip toward the left of the chart. This first faint infrared signal from the Galactic center sparked a revolution in this field of astronomy and soon led to the first crude maps of the complex star field circling the chaotic central gravitational well of the Milky Way. These maps were made by step-scanning the telescope across the field (see Figure 14) and led to the discovery of massive young stars orbiting the Galactic center, their formation mechanism still unknown in the highly dynamic and energetic region which characterizes the core of our Galaxy. It wasn't until the 1980's that the first infrared arrays were used to image the Galactic center from the summit of Mauna Kea. Images were obtained utilizing a detector multiplex gain that at the time only optical astronomers had tasted through their much larger format CCDs, which were of course still blind to the radiation from the ~10 kpc distant stars in the Galactic center. It was then possible to achieve in a matter of minutes with an array detector what previously took hours through tedious step-scanning techniques, which were susceptible to the vagaries of seeing, humidity, and photometric conditions while discrete observations were being compiled into maps. Suddenly it became "easy" to achieve impressive results in infrared astronomy. Information could be extracted much faster through direct infrared imaging than ever before, and astronomers finally had the upper hand in studying the Galactic center. When used in infrared spectrometers, these new arrays allowed spectroscopic studies of the stars in the Galactic center for the first time, revealing unusual populations of stars unlike those in our immediate neighborhood. More importantly, these studies strongly suggested the presence of an unseen extremely massive object or cluster of dark objects that were clearly dominating the local dynamics of the visible stars in the Galactic center. An unseen monster was lurking in their midst.
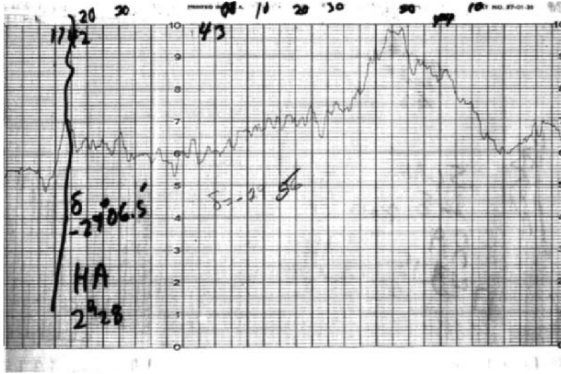
Figure 13. The discovery strip chart of the Galactic center by Becklin et al. [1] is shown. Adapted from McLean [2].
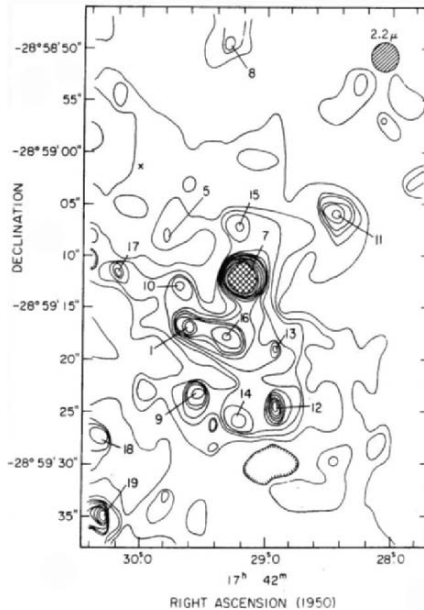
Figure 14. Soon after the discovery of the center of the Galaxy, Becklin and Neugebauer [1] made the first maps by step scanning the telescope beam across the field.

In the beginning of the next decade the push was on at telescopes around the world for ever higher resolution images of the Galactic center. This was performed using larger format infrared detectors and techniques like "shift and add", various deconvolution algorithms (all fraught with problems to some extent), speckle observations, and even lunar occultations with fast arrays to meticulously drill-down to finer spatial resolutions. Sites like

Mauna Kea had the advantage in the early 1990's, thanks to the intrinsically better seeing offered by the smooth high altitude slopes of this volcano situated in the middle of the Pacific. The next breakthrough came in the mid to late 1990's, when the first adaptive optics systems were used to make observations with nearly an order of magnitude higher resolution than anything achieved before. Though these AO systems relied upon visible sensors to lock onto natural guide stars and compensate for atmospheric turbulence, fortuitously, a foreground star along the line-of-sight to the Galactic center provided astronomers with the "break" they needed to use AO systems with Galactic center observations. Finally, in the late 1990's and early 2000's, the use of AO systems on the 8-10 m class telescopes of the time put astronomers "over the top" – they were at last armed to probe the dynamics of the core of our galaxy on spatial scales comparable to our own solar system but a distance of nearly 30,000 light years. From this great distance, using infrared detectors then containing over a million pixels, astronomers could map with exquisite precision the motions of stars as they danced around an unseen companion. Using nothing more than orbital measurements and Kepler's Laws, it was possible to directly measure the mass of the unseen companion, proving that a black hole with a mass well over a million times that of our sun resides at the center of the Milky Way [3]. These observations led to an even more spectacular result though, as serendipity came into play and astronomers imaged a bright flash from the exact location of the black hole. This was soon recognized as the signature of hot gas as it spiraled under the black hole's inexorable pull, through its event horizon (see Figure 15), and slipped into a space-time singularity that still defies our understanding of physics. The stuff of science fiction just became science fact.
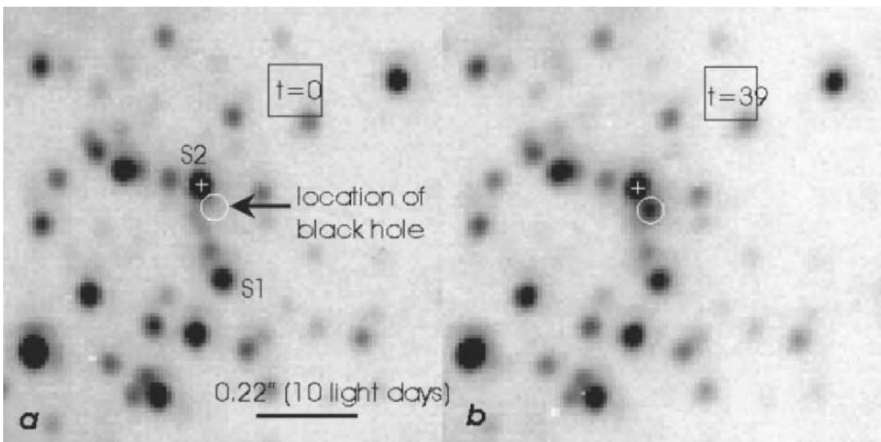
Figure 15. The flare from matter falling into the black hole at the center of the galaxy is shown in these 2 frames recorded at the VLT. Adapted from Genzel et al. [4].

None of this would have been possible without the advent of infrared array technology. In the ~25 year history of infrared observations of the Galactic center, technology laid the course of discovery from a blip on a strip-chart to movies of matter falling into the abyss of a super-massive black hole. The engineers, technicians, material scientists, physicists, etc. that are collectively responsible for the advent of infrared arrays deserve as much credit for these discoveries as the astronomers who made these remarkable observations over the past couple of decades. Amazingly, this same technology path is advancing our capabilities at an exponential rate. What took 25 years to achieve before might only take a decade in the future as our understanding of the universe accelerates forward. As a case-study, Galactic center research beautifully illustrates where we've been and how fast we're going. We know our trajectory, but what lies ahead on the horizon?

4.3   Future Research Tools and Trends

As mentioned before, predicting scientific breakthroughs on timescales of decades is about as uncertain as long range weather or economic forecasting. To do so requires that we assess some of the main trends in astronomy now, look at near term technology developments, and make a measured extrapolation into the future. There are several trends in astronomy that lend themselves to this sort of analysis, including forefront research in cosmology, new wide field observatories, and new Extremely Large Telescopes (ELTs). It is useful to assess them one at a time, explore how they are connected, and where those connections will take astronomy in the next decade.

Much of modern research in cosmology involves either counting and characterizing large numbers of galaxies or pushing with extremely deep concentrated observations in "pencil" surveys to probe to the edge of the visible universe. Unraveling large scale structure and finding the origins of structures on the vast scale of the cosmos offer key insights into the early epochs of the universe. Figure 16 illustrates the star formation history of the universe, which was biased quite heavily toward the first few billion years after the Big Bang. In other words, despite the on-going star formation activity that is prevalent in large numbers of galaxies today, on average, the stars found in our galaxy were born not long after the universe formed, at a time when the distance between these stars was much closer than we witness today. Soon after the Big Bang but prior to the initial period of rampant star formation, the universe was actually a much simpler realm to understand. Distinct structures that we recognize today, like galaxies, stars, and planets, did not exist during the first few hundred thousand years after the Big Bang.

Instead the universe was filled with a high temperature plasma, cooling as the universe expanded, filled with simple particles (protons and electrons) that were awash in a sea of radiation. This harsh environment resembled the blinding interior of a star more than the dark cold space we gaze upon at night. In this fully ionized state, photons traversing the universe did not get very far without scattering off the unbound particles that sped around at high speed. In time, with the expansion of the universe came cooling, and for the first time protons and electrons were traveling slowly enough that they could couple in the presence of their mutually attracting electric fields. Thus began the so-called "Dark Age" in the primitive universe. Photons could travel for great distances without interacting with matter and if someone were present to witness this phase transition of recombination across the universe, they would have watched a remarkable change as the "lights went out" in all directions. We see this transition now in the form of Cosmic Microwave Background (CMB) radiation, which is the highly red-shifted radiation leaving this last scattering surface as particles in the universe coalesced and freed photons to travel unhindered across space.
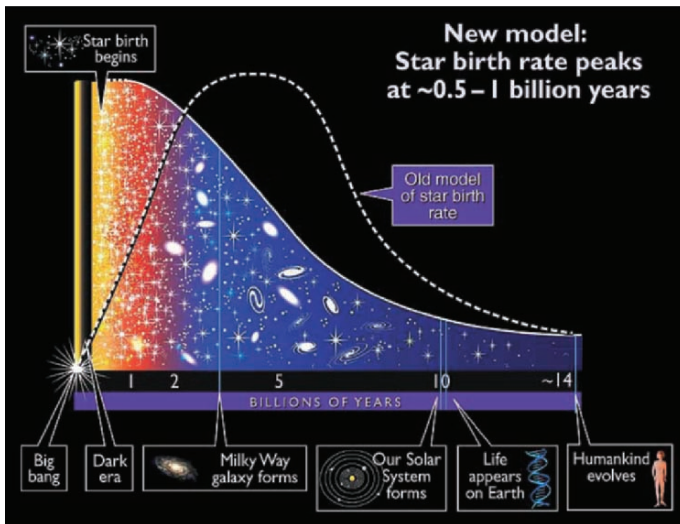
Figure 16. The star formation history of the universe is illustrated, as well as important milestones in the evolution of the universe, from the Big Bang to the current epoch. Credit: A. Feild (STSci).

It is important to realize that at this point, no stars have formed. There are no self-luminous bodies, only expanding and cooling gas with intermittent eddies and ripples of local density enhancements. The term Dark Age is apt, because we are thoroughly "in the dark" about what happened next in the development of the universe. Clearly, stars must have formed at some point but the formation mechanism in these unique conditions is poorly

understood at best. We also know that these first stars did not survive in great numbers, since they would have been metal free (metals were only formed through stars, not the Big Bang), yet we see metals in all of the stars observed to date. In addition, the universe must have been flooded with enough UV radiation to return back to an ionized state, which in turn suggests a radiation source consistent with massive stars at some point in the early universe. While we can look back across time to the CMB and study this event through ever more detailed satellite observations, somewhere in the foreground lie the first stars and one of the great quests in astronomy is to find them. At least a couple of things are sure about what will be required to detect these mysterious objects. It will (1) either take a large ground based or space based telescope and (2) observations will have to be made in the near-infrared, since light from these stars will be so highly red-shifted that the peak in their spectral energy distributions will fall in the 1-2 µm range. CCDs will be of no use in this quest – like the Galactic center, this cutting-edge research will rely exclusively on infrared array technology.

There are applications for CCDs in similarly grandiose future explorations of the universe. These applications will be based upon observations of galaxies that are much closer in space and time than the so-called first light targets mentioned before. Surveys to date have employed 8-12 CCDs in a single mosaic and have been used to map large swaths of the sky to measure the three-dimensional distribution of galaxies. The surveys of the future will be far greater in scope and include observations of the entire sky on short timescales to detect synoptic phenomena that current relatively narrow field telescopes are effectively blind to. Science applications of such observations are manifold and include mapping the structure of galaxies across a ~1000 deg^2 field and using weak lensing as a probe of dark matter across the voids between the galaxies spread across the universe. This application is particularly important, as it stands to "shed light" on one of the greatest mysteries of the universe. Observations of the motions of stars and gas in galaxies have long been known not follow the speeds expected, given the amount of luminous matter present in these galaxies and simple gravitational laws. A nearly endless string of theories has been postulated in recent decades about what this so-called missing mass is, ranging from failed stars (brown dwarves) to exotic massive particles that have the bizarre property of not interacting with radiation. Thus far, none have been proven to account for dark matter. Since astronomers rely almost exclusively on studying the radiation from distant objects to learn about the universe, they are at an enormous disadvantage in studying dark matter, which appears to be oblivious to all forms of radiation. It does interact gravitationally with normal or baryonic matter though. Thus far one of the best probes of the nature of dark matter has been gravitational lensing as light passes through

dark matter clumps to map out its spatial distribution. In massive galaxy clusters this is relatively easy to do. However, to map the distribution of dark matter across the entire cosmos requires imaging field galaxies across great expanses of space to detect minute deformation in the shapes of galaxies that is characteristic of intervening dark matter. The objective of such measurements is to measure the temperature and clumpiness of dark matter with high fidelity over various spatial scales. These data can be used to constrain the multitude of theories in astronomy which attempt to explain dark matter. Ultimately, the importance of dark matter lies not just in the enigma which it poses, but in its overwhelming quantity, because dark matter is by far the dominant form of matter in the universe. What we know as normal or baryonic matter, and learned about in high school chemistry through the periodic table, has little to do with dark matter. Stars, planets, and even humans are the exception in a universe dominated by dark matter.

The enormous surveys planned to probe weak lensing across the sky will require Giga-pixel class focal planes that sample 2-3 degrees of the sky in a single observation. Figure 17 shows some examples of the new observatories planned that will rely exclusively on camera systems incorporating $>10^9$ pixels. To reduce the overhead of such enormous data streams to acceptable levels will require the use of advanced high speed and highly multiplexed array controllers. These are capable of reading out enormous focal planes in just seconds – something that many modern controllers cannot achieve with much smaller mosaics.
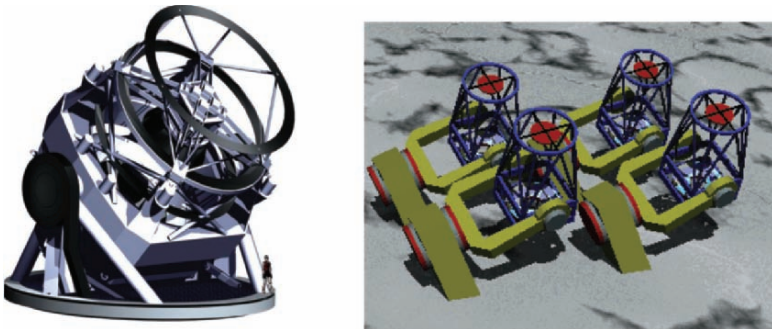
Figure 17. A couple examples of next-generation observatories employing Giga-pixel class optical focal planes: *(left)* the LSST and *(right)* Pan-STARRS.

Another great mystery of our time is dark energy – a more recent discovery that arguably has even deeper consequences for the universe than dark matter. Observations of supernovae during the past decade have been used to measure the expansion rate of the universe. In essence, a certain type of supernova is a fairly accurate "standard candle", hence measuring the brightness of supernovae as a function of red-shift is a gauge of their

distances. Though simple in concept these measurements require considerable finesse to properly deal with systematic uncertainties, not to mention an unorthodox technique in which large telescopes (necessary to measure the spectra of distant supernovae) are called into service on very short notice to measure spectra during the early peak phase in their apparent brightness evolution. As shown in Figure 18, these measurements indicate a slow roll-off in the measured brightness of supernovae compared to what is expected, demonstrating that they are further than expected and that the universe is in fact expanding at an accelerating rate. This discovery has triggered an enormous amount of research in astronomy, as the search continues for the source of energy behind this expansion. Like dark matter, the underlying physics behind dark energy remains essentially unknown, though theoreticians have characteristically left us awash with possibilities. Like the early days after the discovery of the Big Bang, a broad range of theories were posed in astronomy to explain the earliest moments in the universe. However it was not until follow-up observations, particularly by COBE and WMAP, that the vast majority of these theories were ruled out, leaving us with the demonstrably sound theoretically basis we have today for the origin of the universe. New observations will be used to systematically reduce the theoretical possibilities behind dark energy. In the process, they will leave us with a much more complete picture of our universe.
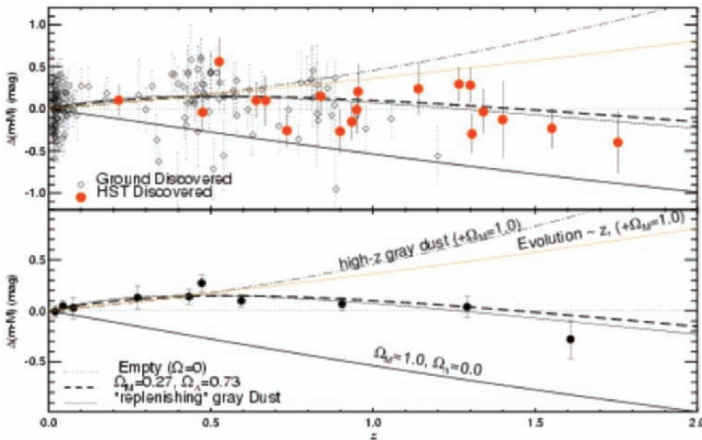
Figure 18. Adapted from Riess et al. [5], the downturn in the brightness of supernovae at large red-shifts indicates the acceleration of the universe.

Dark energy has a number of important implications, beyond opening new avenues of physics. For example, prior to this discovery it was understood that the universe is slowly decelerating from its initial expansion, with progressively finer measurements used to pin-down this expansion rate.

With dark energy the ultimate fate of the universe now appears to involve ultimately shearing apart the large scale structures we commonly see today, like galaxies, stellar clusters, and even stars and planets. Beyond the obvious question of where this energy comes from is that of why did it begin to dominate the energy density of the universe ~5 Gyr ago. Prior to that time the universe was a matter dominated realm but now dark energy accounts for ~70% of the energy density content of the universe. This even has certain anthropic implications, since it appears impossible for life to exist early in the universe (insufficient time for stars to form, which generated the heavy elements necessary for life), and it appears impossible for life to exist late in the universe due to its accelerated expansion. Hence we appear to live in a unique phase over the lifetime of the universe.

Key to understanding dark energy will be a range of observations made over the next decade by various instruments. Among these will be next-generation wide field spectrometers offering the same sorts of enormous multiplex gains over current spectrometers as the imagers of tomorrow. Figure 19 shows a couple of examples of optical spectrometers that will provide nearly an order of magnitude multiplex gain over any astronomical spectrometers existing today.
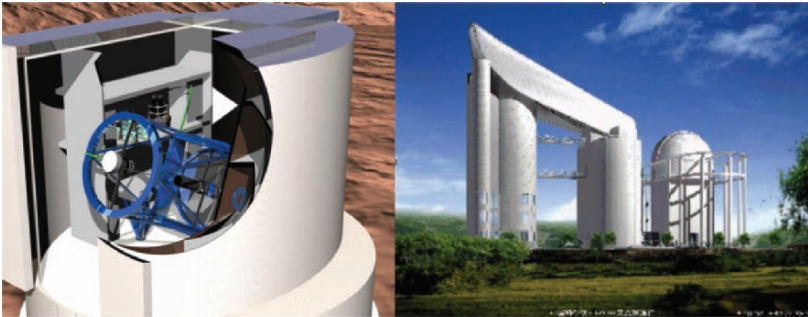
Figure 19. Next-generation spectrometers with multiplex gains are nearly an order of magnitude greater than anything available today. *(left)* The Gemini/Subaru WFMOS, shown deployed on Subaru. *(Right)* LAMOST, which is being built in China.

One way such spectrometers may be used for dark energy measurements is to make large scale measurements of the 3D distribution of galaxies at different epochs to evaluate the time-evolution of the expansion of the universe using a "standard ruler" metric. Specifically, after the Big Bang there were low-level local density peaks that propagated across the then highly-compact universe at the speed of sound. The physics behind the propagation of sound waves in the fluid medium of the early universe is quite simple, since structure was nearly absent and the universe existed in a

very well mixed and uniform phase. As mentioned before, when the universe went dark, due to the temperature and pressure dropping to the point that neutral atoms could form, is the time when these physical over-densities were frozen into the tapestry of matter, forever acting as the seeds of collapse for the largest structures in the universe. Evaluation of the power spectrum of spatial structure in the CMB reveals that most structure existed on the ~1° scale at this point in the evolution of the universe (see Figure 20).
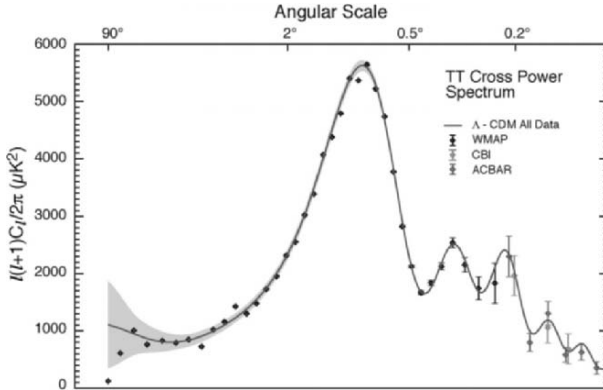
Figure 20. Adapted from Bennett et al. [6], these oscillations on the power spectrum of structure in the universe, as derived from CMB observations, demonstrate a "preferred" spatial scale or standard ruler in the universe.

Thereafter in time, or at closer distances in our line-of-sight to the edge of the universe, emission that we detect is essentially due to stars associated with galaxies, all of which formed in clusters with some typical spatial scale. This is where the next generation of highly multiplexed spectrometers come into play. These machines will be used to map out the three-dimensional structure of the universe across vast regions of space. Evaluating the spatial power spectrum of these enormous distributions of matter (galaxies) will yield a set of baryonic power spectrum "wiggles" which are the tell-tale signatures of the initial seeds of structure, dating back to the so-called dark ages in the history of the universe. This characteristic spatial scale or "standard ruler" is essentially an invariant metric unless the fabric of space-time is changing over time due, for example, to dark energy. By measuring the length of this standard ruler at different epochs or look-back times in the universe, it will be possible to measure the time-evolution of dark energy to much higher fidelity than any measurement achieved to date, thereby providing important clues about its origin and nature.

5.   COMMON THREADS – BRIDGING TODAY'S CAPABILITIES WITH TOMORROW'S NEEDS

The previous section provides the reader with a glimpse of what discoveries await astronomers in their collective quest for answers to core questions in astronomy. It will doubtless be a "golden age", though we recognize tomorrow's astronomers will likely make the same claim, when their "time" to conquer the unseen truths of our universe arrives. Answers to questions like "are we alone", "what is the universe made of", and "what did everything originate from" will naturally lead to more questions and it would be naïve to assume that even more profound questions will not emerge as our understanding of the universe deepens. We will not know what questions to even ask though in the decades ahead until we answer those before us now. That is the nature of science though. As we use the tools at our disposal to study our surroundings we "simply" let the data dictate our path, even though we remain substantially clueless about our ultimate destination.

The bold new directions of astronomy will drive detector technology in equally bold new directions. The need for ever wider and deeper optical surveys to probe cosmology questions demands ever larger optical detectors that are buttable (preferably on 4 sides) and can be mounted in mosaics that are larger than even the largest photographic plates ever used in astronomy. These Giga-pixel class focal planes will require controllers that are highly multiplexed in order to maintain low readout overheads, incorporating hundreds of data channels that can read-out a billion pixels in only seconds. This new generation of detectors will also require storage systems and pipeline processing equipment to efficiently and automatically extract information that exceeds anything commonly used in today's modern observatories, yielding many TB of data each night. These focal planes will likely consist of large numbers of either $2K \times 4K$ or $4K \times 4K$ detectors, though even larger monolithic structures are under development and may become available on useful timescales for the fabrication of these large focal planes. CCDs will probably be the detector of choice, given their established track record, high quantum efficiency, and relatively low cost. New developments that will factor into these massive focal planes include the use of orthogonal transfer CCDs, which will allow real-time image stabilization (tip/tilt) as charge is shuffled along rows and columns in concert with turbulence in the atmosphere. The use of CMOS-based devices, similar to the now familiar architectures used for infrared arrays but using silicon as a detector substrate, will also inevitably come into use. Here, one of the main challenges will be to lower the cost of these next-generation optical sensors to the same level (~1¢/pixel) level as CCDs – a non-trivial extrapolation given the much more complex architectures of CMOS devices.

In the infrared, trends needed to support the science goals outlined above will be, quite simply, to make them perform and cost more like CCDs in many respects. As explained previously, observations of extremely deep objects (e.g., "first light" stars) will be in the 1-2 µm range since they are so highly red-shifted. This means ground based observations will likely have to be made between the numerous atmospheric OH lines, unless advanced multi-line optical filters can be produced that efficiently reject these lines (currently under development). In any event, these deep observations either between or absent OH emission lines will make the sky at NIR wavelengths nearly as dark as it is at optical wavelengths, meaning near-infrared detectors will not be background limited unless they achieve dark currents and read-out noises that are comparable to what CCDs produce today. Having devices that are buttable will be crucial (again at least 3 sided, preferably 4 sided) in the fabrication of the immense NIR focal planes envisioned to critically sample the large focal planes of tomorrow's ELTs. Even more importantly, lowering the per-pixel-cost of these detectors down by a factor of 5-10 will be needed to make such large infrared focal planes affordable.

Whether it is in the optical or infrared, astronomers have an insatiable appetite for larger format, lower noise, and lower cost detectors. Ultimately photon-counting arrays, which boast zero read-noise, that also have nearly 100% quantum efficiency over broad bands, remain the tacit design target for all science arrays in astronomy. If they could also resolve the energy levels of the photons striking each pixel, the staggering complexity of modern imagers and spectrometers could be essentially eliminated in tomorrow's astronomical instruments. That is the subject of a future conference though.

6.   ACKNOWLEDGEMENTS

7.　　REFERENCES

[1] Becklin, E.E, and Neugebauer, G., 1975, Astrophys. J. **200**, L71.

[2] McLean, I.S., 1994, *Infrared Astronomy with Arrays*, Kluwer Academic Publishers, London, plate 1.

[3] Ghez, A.M. et al., 2000, Nature **407**, p. 349.

[4] Genzel, R. et al., 2003, Nature **425**, p. 934.

[5] Riess, A.G., et al., 2004, Astrophys. J. **607**, p. 665.

[6] Bennet, C.L., et al., 2003, Astrophys. J. S. **148**, p. 1.

The award for Best Presentation is given to
Doug Simons by Jenna and James Beletic.

Peter Moore asks where to insert the battery, while Gustavo Rahmer
gleefully reads the poem on the workshop pen.

Ralph Holtom contemplates future sales as Paul Jorden and Neil Branigan endure
another "amazing" tale by Gerry Luppino.

REQUIREMENTS ON ARRAY DETECTORS FROM OWL INSTRUMENT STUDIES

Sandro D' Odorico
European Southern Observatory

Abstract: *The scientific aims and characteristics of seven possible instruments for the OWL 100 m telescope are summarized. The different instruments are designed to operate in wavelength ranges from 400 nm to 850 μm offering different configurations for imaging and spectroscopy. The requirements for the active area and properties of the detectors by the different instrument concepts are presented. Reasonable extrapolation of today's detector technology could satisfy all of the main instrument needs, but cost per unit and capability to supply devices in large quantities with homogeneous, guaranteed performance will be critical issues.*

Key words: *Detector arrays, Overwhelming Large Telescope (OWL), instruments.*

1.   INTRODUCTION

ESO is completing a concept study report for a 100 m telescope called OWL, the OverWhelming Large telescope, by the end of 2005. The study encompasses internal and industrial studies on various telescope subsystems which have been pursued over the last 4 years and will present a comprehensive concept of the OWL Observatory. Within this effort, beginning in 2004, a set of instrument concept studies has been launched by ESO in collaboration with several external institutes. Of the seven studies now coming to conclusion, 5 have external P.I.s and 2 have been led by ESO. In this phase of the OWL project, the studies had the following goals:

- to support the principal OWL science cases with actual instrument concepts
- to verify interfaces and operation scheme of the telescope design
- to ensure the feasibility of instrument concepts and identify needs and required R&D for the different subsystems

The instruments offer various modes of observing in imaging and spectroscopy, and cover different wavelength bands from the blue to sub-millimeters. They are well representative of the different possible modes of operation of OWL. The sample of instruments is, however, by no means exhaustive. It was not the goal of this phase of study to cover or even establish priorities among the various instrumental options. In the selection of the initial instrument concepts to be investigated, ESO has been guided by science cases which have been made for OWL.

The short time frame available for the studies (less than 1 year) has constrained the choice of groups to ones which had both the necessary expertise and the manpower. In this paper, I have extracted basic information on the instrument detectors from the draft reports of the studies to provide a first overview of the requirements in this field.

2.   OWL INSTRUMENTATION AND THEIR DETECTOR ARRAYS

2.1   Overview of OWL Instruments

Table 1 identifies the seven OWL instruments which have been studied and provides basic information on their capability.

2.2   CODEX

CODEX, the Cosmic Dynamics Experiment, is a high resolution spectrograph (R ~ 150,000) operating within the wavelength range of 400-700 nm with very high, long term stability of the wavelength scale. Its main scientific aim is to measure the expected wavelength shifts of spectral features of light emitted at high redshift to probe the evolution of the expansion on the universe directly. With an accuracy of ~1 cm/s in the velocity scale and using a time interval of about 10 years, the instrument will be able to directly measure the dynamics of the universe and probe the effect of the elusive dark energy [1].

Instrument	Wave range	Main Capability	Primary Science Goals	Institutes	Externally Responsible	Responsible at ESO
CODEX	0.4-0.7 µm	High velocity accuracy, visual spectrograph	To measure the dynamics of the Universe	ESO, INAF-Ts, Geneve Obs, IoA Cambridge	=	L. Pasquini
QUANTEYE	0.4-0.8 µm	Photometry at 10^{-3} -10^{-9} second resolution	Astrophysical phenomena varying at sub-msecond time scale	Padova Univ., Lund University	C.Barbieri, D. Dravins	R. Fosbury
EPICS	0.6-1.9µm	Camera-Spectrograph at diffraction limit	Imaging and spectroscopy of earth-like planets	ESO & ext. consultants	=	N.Hubin
MOMFIS	0.9-2.5 µm	Near IR spectroscopy using many deployable IFUs	Masses of high z galaxies, regions of star formation, GC stars	CRAL, LAM, OPM	J.G. Cuby	M. Casali
ONIRICA	0.9-2.5 µm	NIR Imaging Camera on a field of 1x1 / 2x2 arcmin	Faint stellar and galaxy population	INAF- Arcetri Heidelberg MPIfA	R. Ragazzoni	E. Marchetti
T-OWL	2.5-27 µm	Thermal, Mid Infrared Imager and Spectrograph (tbc)	Search, study of planets, high redshift Hα galaxies	MPIfA Heidelberg Leiden, ASTRON, ESO	R. Lenzen	H.U. Kaeufl
SCOWL	250-450-850 µm	Imaging at sub-millimeter wavelengths	Surveys of dusty regions, of extrag. fields for star-forming galaxies	ATC	I. Egan, B.Dent	R. Siebenmorgen

Table 1. OWL instrument concept studies.

The present instrument concept (matched to a 60 m telescope) foresees the light of the target to be relayed by an optical fiber or an optical train to 6 echelle spectrographs located in a temperature-stable laboratory outside the OWL platform. Each spectrograph has a detector area of 120 × 120 mm, or an 8K × 8K mosaic of devices with 15 μm pixels. If the current standard format of 4K × 2K pixel chips is used, the required detector estate corresponds to ~50 devices, a number comparable to large imaging mosaics now in use or in development. In the spectral range of the spectrograph, 400-700 nm, state-of-the-art CCDs already reach the required QE ≥ 90%. Other crucial performance parameters for CODEX are a low number of device defects, low readout noise (RON) and dark current. Preliminary calculations for the main application of CODEX indicate that a RON ≤2 e$^-$/pixel and a dark current ≤10^{-3} e$^-$/pixel/sec would be acceptable. Both values are within the performance characteristics of state-of-the-art silicon devices.

2.3   QUANTEYE

The proposed instrument aims at offering the highest time resolution achieved so far in optical astronomy, going far below today's millisecond in the domain of micro and nanosecond astrophysics. Approaching the quantum optical limit, new types of photon phenomena, not previously investigated in astronomy, may become observable [2]. Today's high time resolution instruments use either CCDs (limited to a fastest frame rate of 1 ms) or various photon-counting devices as detectors, which are limited by the maximum sustained photon-count rate. QUANTEYE is designed to observe stellar sources at the center of the field and a reference object in the field. The detector will consist of an array of photo-counting avalanche diodes which will fully utilize OWL's collecting power for photon count rates up to GHz. The current concept is based on the use of 2 sparse-geometry arrays of 10 × 10 Silicon SPAD, Single-Photon Avalanche Diodes [3]. SPAD arrays are not yet in operation, but there is a reasonable extrapolation from simpler, well-tested devices. There is potentially more than one supplier. Time tagging should be provided by an atomic clock with at least 100 ps accuracy.

2.4   EPICS

One of the primary science goals of OWL is the detection and possibly characterization by spectroscopy of an earth-like planet. This objective is a strong driver for the maximum size of the primary mirror of OWL because it calls for extreme angular resolution and photon collecting power. The

instrument to achieve this goal, EPICS, is still being defined. Three main capabilities are being explored: differential imaging in the J band, polarimetry in the R-I bands, and integral field spectroscopy in J band [4]. The instrument will also need a dedicated AO system to complement the standard ones associated with the telescope. Table 2 summarizes the preliminary requirements for the detectors.

Table 2. Detector requirements for EPICS.

Mode	Field (arcsec)	Pixel Scale (mas)	Total Array Estate
Differential Imaging (J)	4×4	0.5	2 (8K×8K) HgCdTe
Polarimetry (R, I)	2×2	0.5	8K×4K , frame transfer CCD
IFS (J band , R= 10-50)	2×2	0.5	8K×8K mosaic, HgCdTe
Wav. Sensor for EXAO	=	=	3K×3K CCD mosaic, ~1 KHz (Shack-Hartmann)

2.5   ONIRICA

ONIRICA [5] is the large field imaging camera of OWL, designed to operate in the NIR where AO systems can achieve or approach the diffraction limit of the telescope and thus fully exploit its capability. The selected detectors are large NIR arrays (HgCdTe). The number is dictated by the field to be covered and the desired sampling. The present optical concept of OWL offers a diffraction-limited central field of 3 arcmin diameter, but realistic assumptions on the performance of the first generation AO systems make it doubtful that the diffraction-limit will be achieved over the entire 3 arcmin field. However, it is reasonable to expect that high quality images can be achieved over this entire field. A first layout of ONIRICA foresees a central field of ~ 30" diameter sampled at 1 mas/pixel (Nyquist sampling in the K band) and an outer field of ~3'× 3' sampled at 10 mas. This configuration would imply 15×15 $2K^2$ NIR arrays with 18 µm pixels (or possibly 8×8 $4K^2$, e.g., with 12 µm pixel) for the central field and of the order of 9×9 $2K^2$ for the outer field. This adds up to ~300 of the currently rather expensive HgCdTe arrays. The actual need will be determined by the final configuration of the telescope and by the result of more extended simulations of the AO performance. The science case will have to be correspondingly adjusted with an eye to the predicted performance of the JWST. A reduction of the current price/unit of the NIR arrays is required to make the instrument cost affordable.

2.6   MOMFIS

Performance simulations show that medium resolution spectroscopy in the NIR (J, H, K) could be advantageous with respect to an equivalent spectrograph at the JWST. This is possible if a significant fraction of the flux of compact sources can be kept within diameters which are intermediate between optimal seeing and the diffraction limit. The main science case for the MOMFIS study [6] aims at exploiting this capability for the spectroscopy of faint, high redshift galaxies. The instrument concept foresees Multi-IFU systems which can be positioned on the targets over at least a 3' diameter field and is supported by a "local" AO correction. Each IFU unit would have ~30 × 30, 30 mas pixels (1" × 1" field). With this configuration the required number of $2K^2$ arrays (HgCdTe) would be ~50 to cover the three bands in parallel at R ~4000.

2.7   T-OWL

This instrument is designed to work in the 3-27 µm region. At this wavelength thermal emission and atmospheric absorption play the most important role. The main potential competitor is the JWST, which can be outperformed for specific applications if the diffraction limit of the large OWL diameter is fully exploited. The current study [7] has thus far developed the imaging camera design. The wavelength range is split by a dichroic in the 3-5 µm and 7-25 µm bands. A science field of 15" × 15" would imply the use of 4 $2K^2$ InSb arrays (sampling 3.5mas @ 3-5 µm) and of 4 1K × 1K SiAs arrays (sampling 7 mas @ 7-27 µm).

2.8   SCOWL

This concept study has explored the advantages and the feasibility of building a SCUBA-2 like sub-millimeter instrument for OWL. The basic instrument requirements for this instrument call for a resolution ≤2" and a field of 2' × 2' [8]. With these characteristics, SCOWL can complement the small field, very high resolution work of ALMA and operate mainly in survey mode. The baseline detectors being considered for SCOWL are Transition Edge Sensors (TES) hybridized to a Superconducting Quantum Interference Device (SQUID) multiplexer, as under construction for SCUBA-2. For SCOWL, 4 SCUBA-2 sub-arrays would be needed (each is a mosaic of 4 41 × 32 pixel arrays). Each detector must be optimized for a specific sub-millimeter band. Expanding the SCUBA-2 detector size would

involve facing a number of challenges in current technology and new development work.

An alternative to the TES detectors are the so-called KIDs (Kinetic Inductor Detectors), which are being developed by a number of international groups. In a few years this technology could be sufficiently developed and tested to be scaled to large format arrays which would be required in SCOWL. Their main potential advantages with respect to TES detectors are a simpler manufacturing process, lower heat load and the possibility to populate the field of view more densely, increasing the survey efficiency.

3.   2-D DETECTORS FOR ACTIVE AND ADAPTIVE OPTICS WAVEFRONT SENSING AND TELESCOPE TRACKING

An overview of the detector requirements for the OWL project would not be complete without accounting for the detector systems used for tracking, active and adaptive wavefront sensing. All these functions are essential to control the telescope and to reach and maintain the image quality on which the science case of OWL is based. In the current OWL concepts there are 6 focal stations on the telescope structure which can be addressed by proper rotation of the M6 mirror. Every station will eventually be equipped with its adapter/rotator hosting a number of sensing probes which can reach different points in the FoV. The preliminary concept of the adapter/rotator includes six probes for tracking and active optics and up to six probes for AO wavefront sensing. In the first type, the beam will be split by dichroics as in the VLT adapters. Tracking will be performed on relatively standard imaging CCDs of modest format ($1K \times 1K$) while the active optics and segment phasing control will be achieved via Shack-Hartmann pattern sensing on ~$2K \times 2K$ CCDs read at 1 Hz frequency. For the 6 AO wavefront sensors in the adapter, the preferred format is 500×500 pixel CCDs to be read at 500 Hz with close-to-zero noise. The total number of devices required will initially be approximately 30. NIR arrays ($1K \times 1K$) for wavefront sensing in the NIR might be also required, but only for special applications.

4.   ACKNOWLEDGEMENTS

The information on the instrument concepts and their detectors has been provided by the P.I. (see Table 1) in advance of the completion of their

study. I am very grateful to them for the use of their preliminary results for this review.

5.   REFERENCES

[1]   Pasquini, L. and CODEX Team, 2005, *CODEX Concept Study,* OWL-CSR-ESO-00000-0160.

[2]   Dravins, D., Barbieri C., Fosbury R.A.E., Naletto G., Nilsson R., Occhipinti, T., Tamburini, F., Uthas H., Zampieri L., 2005, *QUANTEYE, Quantum Optics Instrumentation for Astronomy,* OWL-CSR-ESO-00000-0162.

[3]   Bonanno, G., et al., 2005, *SPADA: An Array of SPAD Detectors for Astrophysical Applications*, these proceedings.

[4]   Hubin, N., Kasper, M., Verinaud, C. and EPICS Team, 2005, *EPICS: Earth-Planet Imaging Camera and Spectrograph*, OWL-CSR-ESO-00000-0166.

[5]   Ragazzoni, R. and Consortium Team, 2005, *ONIRICA, OWL NIR Imaging Camera,* OWL-CSR-ESO-00000-0165.

[6]   Cuby, J.G., Kneib J.-P., Prieto, E., and Consortium Team, 2005, *MOMFIS, Multi Object, Multi Field Imaging Spectrograph,* OWL-CSR-ESO-00000-0164.

[7]   Lenzen,R. and Consortium Team, 2005, *T-OWL, Thermal Infrared Instrument for OWL,* OWL-CSR-ESO-00000-0161.

[8]   Atad, E., Dent, B., Egan, I., Ellis, M., Gostick, D., Kelly, D., 2005, *SCOWL, SCUBA for OWL,* OWL-CSR-ESO-00000-0163.

Simon Tulloch, Peter Sinclaire, Roberto Gilmozzi and Sandro D'Odorico (left to right) enjoy the pizza dinner, but none more so than Roberto.

PAN-STARRS AND GIGAPIXEL CAMERAS

John L. Tonry[1], Peter M. Onaka[1], Barry Burke[2], Gerard A. Luppino[1]
[1]Institute for Astronomy, University of Hawaii, [2]Lincoln Laboratory, Massachusetts Institute of Technology

Abstract: *The Pan-STARRS project will undertake repeated surveys of the sky, finding "Killer Asteroids" and everything which moves or blinks, as well as building an unprecedentedly deep and accurate image of the sky. The key technology for this is the next generation of large format cameras, which will offer an order of magnitude improvement in size, speed, and cost relative to existing instruments. This is achieved in part by the integrated design of telescope, detectors, controllers, software, and scientific direction.*

Key Words: *Pan-STARRS, OTA, gigapixels.*

1.   INTRODUCTION

The Pan-STARRS project [1] will revolutionize astronomy, mapping the entire visible sky to unprecedented depth and precision (1% photometry in 5 colors, 5 mas astrometry). The most unusual target, however, is the transient universe. We will search continuously for everything which blinks or moves for the operational lifetime, and we expect to find killer asteroids down to 300 m diameter, KBOs, supernovae, variable stars, microlensing events, extrasolar occultations, AGN, etc.

The Pan-STARRS project will build four identical telescopes of 1.8 m aperture and 3 deg field of view. To sample the large image produced by the optics, we are building four cameras, each of which comprises 1.4 billion pixels subtending 0.26 arcsec. The short exposures required to capture moving objects requires a total readout time of 3 seconds at 5 e⁻ read noise. The requirements of pixel count and readout time has compelled us to design

a new detector called the Orthogonal Transfer Array (OTA), and a new controller.

The modular nature of the Pan-STARRS project permits us to begin with one telescope, which in presently under construction on Haleakala, Maui. This Pan-STARRS 1 (PS1) will enable us to shake down the telescope, detectors, and pipeline, and get a jump on the science while we are carrying out the careful and thorough site assessment necessary to determine whether Pan-STARRS 4 (PS4) should be sited on Mauna Kea, Hawaii. We expect first light for PS1 in January 2006 and in 2009 for PS4.

The limitations of space in this publication preclude any discussion of the Pan-STARRS science or software, and we will concentrate on the camera and controllers. Another paper in this volume [2] covers the detectors in more detail, or see Kaiser [3].

2.   THE PAN-STARRS TELESCOPES

The optical design of the telescope is relatively straightforward. It is essentially a Ritchey-Cretien telescope with a 3 element corrector. There are the usual challenges with aspheres, baffling, etc., which we believe should not be major problems. The image size budget is driven by the excellent seeing on Mauna Kea (free air median seeing of 0.5-0.6 arcsec), and should not degrade the PSF significantly. The filters are large (500 mm diameter), and will comprise the standard SDSS *g*, *r*, and *i* filters, with a *z* filter which differs in that it is cut off at 915 nm, and a *y* filter which extends from 965 to 1025 nm. The filter changer is a simple stack of three slides, each carrying a filter at each end and an open aperture in the middle. The University of Bonn is fabricating the large shutter.

The focal plane is 400 mm wide and will be curved with a radius of 470 m (see Fig. 1). We expect to build an atmospheric dispersion compensator (although PS1 will initially be built without an ADC), which is a drop-in replacement for the first lens of the system. The ADC consists of a prism which rotates between two other wedged lenses, all of which are immersed in Siloxane oil to suppress ghosting. We will not depend on the telescope to maintain a good collimation for long periods of time. The primary mirror will be actuated to compensate for offsets in the vertical direction as well as a 12-point astigmatism correction. The secondary will be mounted on a hexapod for all five degrees of freedom.

We are designing a calibration system, which should enable us to reach 1% photometric accuracy. This system comprises a flatfield screen which we can be illuminated with monochromatic light and monitored with a calibrated photodiode. Thus we should be able to characterize the throughput of the entire optical system on a weekly basis. This will also give us flatfield

images that we can match to any spectral energy distribution of interest. In particular we should be able to simulate the night sky emission and build an artificial fringe image for subtraction. We will also have a sky monitor telescope which will give us a minute-by-minute measure of the transparency. It will have a spectroscopy channel to monitor atmospheric absorption and emission as a function of wavelength on a minute-by-minute basis in the direction that Pan-STARRS is pointing. The low resolution spectra from the monitor telescope will provide a high resolution theoretical model of the atmospheric behavior.
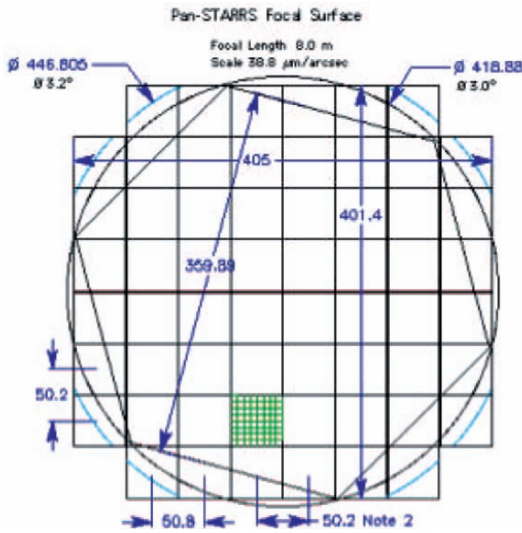
Figure 1. The Pan-STARRS focal plane with detector layout, 3 deg circle of good focus, hexagonal tile, and 1.65 deg circle for wavefront sensing.

The focal plane will be equipped with two wavefront sensors. A deployable Shack-Hartmann sensor illustrated in Fig. 2 can be brought out over the focal plane to perform a detailed analysis of wavefront tilts when a bright star is steered onto its entrance aperture.

There will also be continuous wavefront sensing available from an apparatus just outside of the 3 degree field of view. This curvature sensing apparatus consists of a converging lens and block of calcite which makes simultaneous above- and below-focus images of all the stars present. These donuts are very sensitive to wavefront errors, and can be analyzed to reveal errors in secondary displacement and tilt. We expect to read out these curvature sensing images every 30 seconds along with the science data, and have information immediately available about the state of focus and collimation of the telescope. With proper choice of the optical axis of the calcite, we can arrange for the two star images to be adjacent to one another

at a convenient separation. The introduction of the calcite would ordinarily put the balanced pair of donuts below the nominal focal plane, and since we want this apparatus to be parfocal with the rest of the field of view, we introduce a converging lens (see Fig. 3).
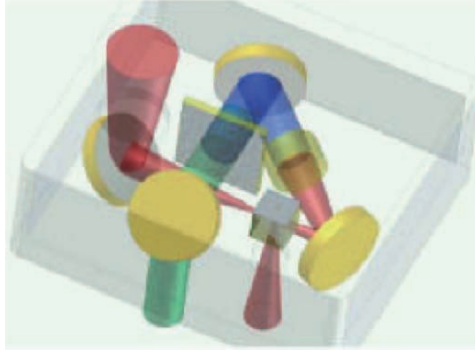
Figure 2. The Pan-STARRS Shack-Hartmann wavefront sensor folds the light in such a way that it is parfocal with the science images. The sensor unit is deployed above the huge focal plane which serves as its detector. The apparatus also provides an out-of-focus pupil image and carries LEDs and calibrated photodiodes for purposes such as monitoring QE or window fog.
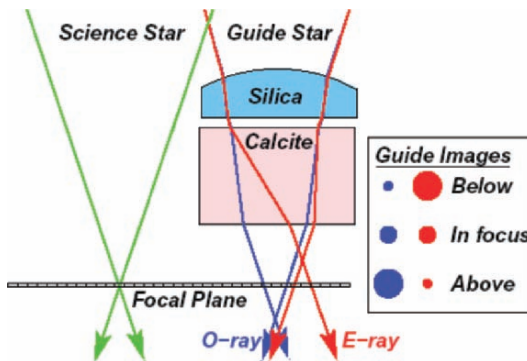
Figure 3. This schematic diagram shows how a calcite block and converging lens can provide above- and below-focus images which provide focus and collimation information. We will employ at least two of these units above the Pan-STARRS focal plane, just outside of the 1.5 deg radius.

3.   THE PAN-STARRS CAMERAS

The camera will be constructed in three steps. Our first step was to build two test cryostats which could in principle hold a 3 × 3 array of close-packed OTAs for 200 Mpixels, but we are using these cryostats for device testing.

The OTAs are four-side buttable, so for testing we normally mount them in a handling bracket. The test cryostats can carry a loose-packed 2 × 2 array of OTAs (90 Mpixels) on handling brackets.

The next step is "Test Camera 3" (TC3), which is almost an exact quarter of the "Giga-pixel Camera 1" (GPC1). This camera will be a 4 × 4 array of OTAs, closely packed onto a silicon carbide (a good CTE match to silicon, thermal conductivity, and stiffness) focal plane, which has been figured to the curvature required by the optics. The close packed array of devices connects via flexprint to a rigidflex board below. Four devices in a line are bussed out together, and the rigid flex passes through a slot in the cryostat wall with epoxy potting making a vacuum seal. One of the main advantages of the potted rigidflex is the elimination of hand wiring.

TC3 will have two controller boxes, each holding 4 controller boards. Each board provides 16 channels for 2 OTAs, so the system will have a total of 128 readout channels and 360 Mpixels. A CTI cryocooler will cool the focal plane instead of the Cryotigers used by TC1 and TC2. We will gain experience in the thermal management of the focal plane and devices, which is extremely important because at 1 µm the QE will vary by about 1% per degree.

TC3 will also incorporate both wavefront sensors, the deployable Shack-Hartmann apparatus and the continuous curvature sensing optics. TC3 will be used for first light on PS1, and will be populated with the development Lot 1 OTAs which are already in hand. The data from TC3 will provide an excellent data stream for shakedown of the Image Processing Pipeline (IPP). When the PS1 telescope is operating reliably (~June 2006) we will replace TC3 with GPC1.

The full-scale Gigapixel camera, illustrated in Fig. 4, with a focal plane of some 1.4 billion pixels spanning 40 × 40 cm, is essentially four close-packed copies of TC3. The final lens in the optics is the cryostat window.

4.   THE PAN-STARRS CONTROLLER

The controller we are developing for Pan-STARRS must be very fast, high density, and low power. This is an ideal application for one or more ASICs, but in our judgment ASICs do not yet have the maturity to field a system in the next few years. We have therefore elected to build a new controller around the best discrete parts we can presently find. Our goal is to meet the performance requirements while trying maintain simplicity and low cost. Our basic controller, illustrated in Fig. 5, is a PC board which is 3 U wide and about 16 cm long. It dissipates about 15 watts.
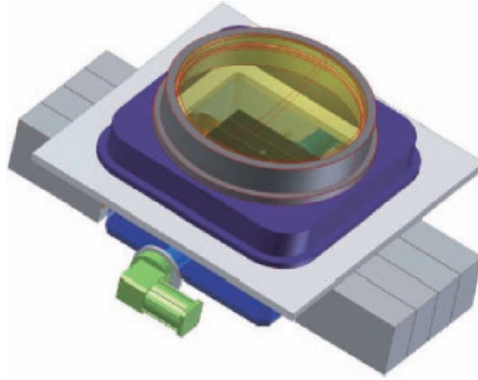
Figure 4. A solid body rendering of the Pan-STARRS Giga-pixel Camera, complete with L3 cryostat window and 8 controller boxes.
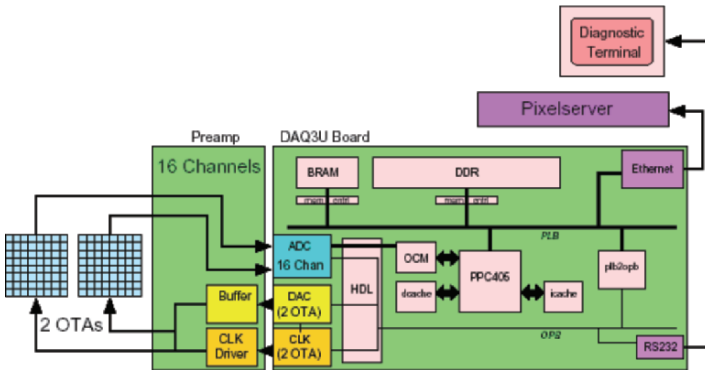
Figure 5. This figure illustrates schematically how 2 OTAs (16 channels) are connected to a preamp board and a DAQ3U board, and how these are interfaced to a generic pixelserver running Linux.

This "DAQ3U" board has an FPGA for communications, clock and bias generation, signal chain operation, and arithmetic operation on digital samples. One design requirement that makes our controller unique is the need for independent control of the OT readout and correction for each OTA. This requires a design that is easy to program and communicate with, and the FPGA selected has an integral hardcore CPU.

A 16 channel preamplifier/buffer board is paired with its corresponding DAQ3U board to run 2 OTAs. Two of these board pairs are assembled to run a row of 4 OTAs. Two sets of these pairs are placed into individual sub-chassis to run 8 OTAs. The sub-chassis are assembled 4 wide into a frame that sits on either side of the cryostat. This frame is exactly the same width as the two rows of OTAs being served, so that the detector/controller combination can be extended indefinitely.

The DAQ3U board also hosts 1 Gbit ethernet fast enough to read out and deliver data in real time to a pixelserver host computer, which can use a conventional ethernet interface card. We use standard internet protocols for communications. We also provide 256 Mbyte of on-board ECC memory (standard commercial laptop memory), which enables us to read two entire OTAs (50 Mpixels) and begin another exposure before dumping the data to the pixelserver. Although the Gbit ethernet bandwidth is adequate to read out an OTA within 3 seconds, we would be vulnerable to latencies on the pixelserver. We can imagine modes in which the need to dump more than 16 bits per pixel may arise. It therefore seems prudent to provide on-board memory to maximize flexibility and robustness.

The DAQ3U is implemented as a 14 layer printed circuit board with 50 ohm controlled trace impedance and matched length on critical digital and analog traces. Multiple ground planes are also employed for noise shielding. Version 2 of this board will be split into a mother/daughter board configuration that splits digital and analog functions, and increases the channel density from 12 to 16. The PCB has multiple fine pitch (1 mm) ball grid array components with as many as 896 balls per device. We have also paid attention to the lengths and impedances of the lines on the rigidflex board which connect the OTAs to the controllers.

The preamplifier design is extremely simple to save space. Each channel amplifies, provides a DAC based offset voltage and filters the video output. There are no dual slope integrator or clamp and sample circuits. We have tried both DC and AC coupling the OTA outputs into the preamps, and are presently getting better performance with AC coupling because it is easier to take out the cell-to-cell offsets. Analog voltage levels are provided via Analog Devices AD5532 DACs (32 outputs at 14 bit resolution) current buffered by separate driver ICs. Note that we also have to provide relatively unusual, large negative biases of about -40V for the detector substrate bias.

A full 64 OTA mosaic will have 512 video outputs requiring very fast, high density ADCs. We selected the Analog Devices AD9826 which offer three channels of 16 bit A/D and CDS, at speeds up to 12 MHz for a single channel and 5 MHz for all three channels simultaneously. We have done extensive testing of the AD9826 by building a daughter board, which replaces the Datel 937 ADC used on an SDSU video board, leaving the other channel alone for comparison. Our experiments indicated that the AD9826 is as linear and accurate as the Datel A/D. The AD9826 has no problems with sampling a single channel at 10 MHz, but the AD9826 has 3 ADU of noise. This noise appears to be uncorrelated so it can be reduced by multiple samples. The AD9826 data sheet lists a cross-talk between channels of 72 dB, which is not good enough to run individual CCD amplifiers through different channels, and we have elected to use one channel of the AD9826 per CCD amplifier.

We do not use the conventional technique of dual slope integration to reduce bandwidth and noise, nor do we use the CDS function in the AD9826. Instead, we digitize many samples on every pixel (typically four per pedestal and four per signal) and do digital arithmetic in the FPGA: sum four signal samples, subtract four pedestal samples, divide by four. The oscilloscope trace in Fig. 6 shows an example of a video signal and the four samples we make of the pedestal and signal levels. This serves both to reduce the A/D noise to 2 ADU as well as averaging down the detector noise. We have tested the noise performance of the controller using a low-noise CCID20 which has about 2.1 e⁻ noise when read out using an SDSU controller at high gain and 160 kpix/sec. The timing illustrated in Fig. 6 achieves 3.8 e⁻ read noise at a pixel rate of 530 kpix/sec. We expect that we can do improve this by steering the samples between clock transitions and careful bandwidth tuning of the stages leading up to the A/D. It is also possible to use the FPGA to weigh different samples for additional improvement.
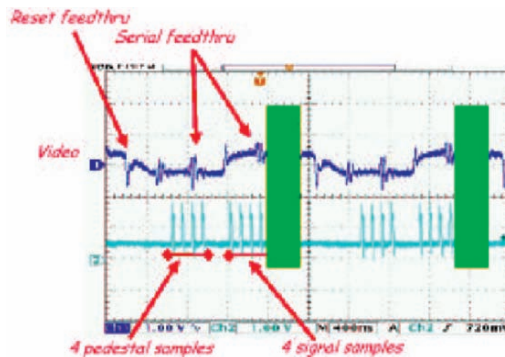
Figure 6. This oscilloscope trace illustrates how we take 4 samples on the video pedestal and four on the signal of each pixel. The resulting samples are digitized and added, subtracted, and scaled by 4 by the FPGA before delivery to the pixelserver.

One of the real strengths of the Pan-STARRS project is that the development of detectors, controller, and software are all happening in conjunction and synergistically. For example, we will be transitioning to a 2-phase serial register to reduce the clock feedthrough and produce faster and cleaner video. We are nearing completion of the design of a revised controller and preamp board, and expect to implement them in time for TC3 and PS1 in January 2006.

5. CAMERA SOFTWARE

The software architecture for the Pan-STARRS camera is very modular and powerful. Each PowerPC core on each DAQ3U board runs a server program which accepts commands to change voltages, change readout parameters, read out the CCD, etc. We assign a 1U rack-mounted generic Linux box ("pixel server") to every pair of DAQ3U boards, and each of these runs software that communicates with its DAQ3U servers and in turn responds to commands from an overall controlling process run on the "Conductor" computer. The conductor process is responsible for synchronizing all the different OTAs - designating which cells are reading out guide stars, calculating OT shifts, triggering readouts, etc. We will also have a camera datastore, with 30 TB of disk. This will reside on the mountain and have a capacity to buffer a few days' worth of observing in case the fiber to the IPP goes down. The conductor process is also responsible for maintaining a metadata database, communicating with the telescope system, and receiving commands from the observing sequencer.

The Image Processing Pipeline (IPP) for Pan-STARRS must be both extremely sophisticated and robust. The basic steps include:

- Acquire four images of the same field from the four telescopes
- Perform the usual "instrument signature removal" of bias subtraction, flatfielding, and removal of bad pixels and cosmic rays
- Identify stars, create a map from each image to a global coordinate system, and warp images to the global coordinate system
- Sum the four images in an optimally weighted way
- Match the PSF of this sum to the PSF of an archival, deep sky image and subtract this static sky image
- Search the difference image for significant changes: moving objects, transient objects
- Add moving and transient object detections to the database; process moving objects to match up with orbits of known objects; generate alerts for transient objects
- Add the summed image into the growing static sky image; process the summed image and the static sky image for various science clients such as parallax/proper motions, variable object light curves, etc.
- Update the database of objects: add new objects, add attributes to known objects

The two enormous challenges of the IPP are data volume (we will ingest about 10 TB per night and we must either keep up in real time or fall hopelessly behind), and the need to get the reductions right the first time (we will create petabytes of reduced data per year and we do not plan to archive even the reduced data, let alone the raw data). Fortunately, PS1 will only

generate data at a quarter of the rate, and at startup we will have empty disks, so we will be able to save those data for a year or two and reprocess many times until we have the pipeline right.

6.   SUMMARY

The Pan-STARRS project will open up new vistas in science, both synoptic and static. In truth, Pan-STARRS is an obvious project which was waiting for Moore's law to overtake the size of the universe. At the same time it is presenting new challenges and opportunities for very large, very high performance detectors, controllers, and software. We feel very privileged to be entrusted with the resources and freedom to set a standard which we hope will be inspiring for many years.

7.   ACKNOWLEDGEMENTS

8.   REFERENCES

[1] http://pan-starrs.ifa.hawaii.edu.
[2] Tonry, J., et al., 2005, *Orthogonal Transfer Array*, these proceedings.
[3] Kaiser, N., 2004, *Pan-STARRS: a wide-field optical survey telescope array*, Proceedings of the SPIE, Vol. **5489**, p. 11-22.

THE LARGE SYNOPTIC SURVEY TELESCOPE

My Instrument is Bigger than Yours

D. Kirk Gilmore

Stanford Linear Accelerator Center (SLAC)/Kavli Institute for Particle Astrophysics and Cosmology (KIPAC)

Abstract: The Large Synoptic Survey Telescope (LSST) will be a wide-field telescope facility that will add a new capability to astronomy. The LSST will provide unprecedented 3-dimensional maps of mass distribution in the Universe, in addition to traditional images of luminous stars and galaxies. These mass maps can be used to better understand the nature of the newly discovered and mysterious "dark energy" that is driving the accelerating expansion of the Universe. By looking at the entire accessible sky every few nights, the LSST will provide large samples of events that we now only rarely observe and will create substantial potential for new discoveries.

The LSST telescope, with its 8.5 m primary mirror and fast f/1.25, 3-mirror design, offers unique design challenges driven by requirements for fast "slew and settle" time, tracking accuracy, and tight alignment tolerances. It must be possible to point the telescope quickly (<5 sec) and repeatedly to adjacent field locations. The LSST camera is a wide-field optical (0.35-1 μm) imager designed to provide a 3.5 degree FOV with better than 0.2 arcsecond sampling. The detector format will be a circular mosaic providing approximately 3.2 Gigapixels per image. The camera includes a filter mechanism and shuttering capability. It is positioned in the middle of the telescope where cross-section area is constrained by optical vignetting and heat dissipation must be controlled to limit thermal gradients in the optical beam.

The LSST will produce the largest non-proprietary data set in the world, and this data set will be made accessible through the Virtual Observatory (VO). The "open data" approach, with no proprietary data or science, is a precedent-setting aspect of the LSST project.

Key words: LSST, large focal plane, dark matter, survey.

1.   LSST CAMERA

1.1   Overall Description

The LSST camera is a wide-field optical (0.4–1 µm) imager designed to provide a 3.5° FOV with better than 0.2 arcsecond sampling ([1], see Fig. 1). The image surface is flat with a diameter of approximately 64 cm. The detector format will comprise a mosaic of 16 Mpixel silicon detectors providing a total of approximately 3.2 Gpixels. The camera includes a filter changing mechanism and shutter. It is positioned in the middle of the telescope where cross-section area is constrained by optical vignetting and heat dissipation must be controlled to limit thermal gradients in the optical beam. The camera must produce data of extremely high quality with minimal downtime and maintenance.
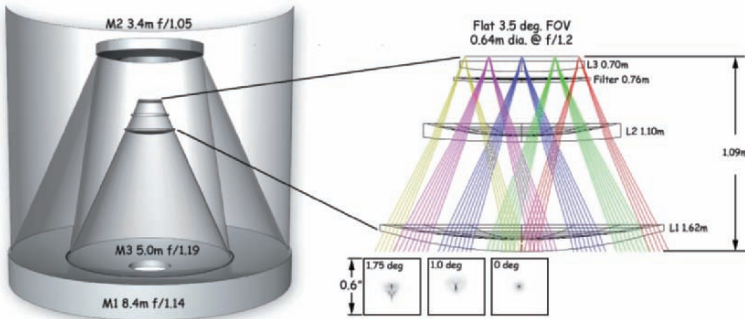
Figure 1. The LSST optical design.

The focal plane array operates at a temperature of approximately −100°C to achieve the desired detector performance. The focal plane array is contained within an evacuated cryostat, which incorporates detector front-end electronics and thermal control. The lens L3 serves as an entrance window and vacuum seal for the cryostat. Similarly, the lens L1 serves as an entrance window and gas seal for the camera housing, which is filled with a suitable gas to provide the operating environment for the shutter and filter change mechanisms. The filter carousel can accommodate 5 filters for rapid exchange without external intervention.

The camera mechanical mount (see Fig. 2) provides proper support and registration to the telescope and incorporates provisions for adjusting camera position and orientation to compensate for alignment variations with telescope elevation. In addition, the camera axial position must be adjusted to optimize focus at different filter wavelengths (the axial position of L2 is similarly adjusted). Additional camera interfaces include electrical power,

thermal cooling, and fiber optic connections for control and data interfaces. The following sections describe these features in detail and discuss the considerations leading to the current design conclusions.
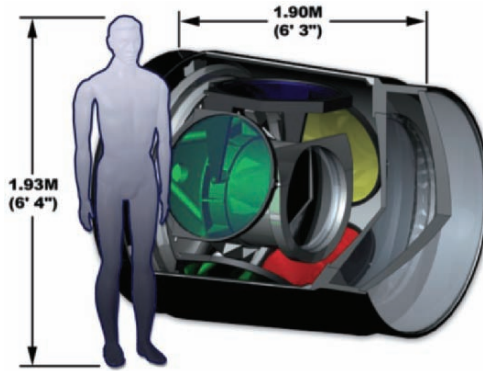
Figure 2. LSST camera.

2.   SENSOR DESIGN

2.1   Requirements and Design Approach

The LSST science goals lead to a set of challenging performance requirements for the focal plane sensors, as shown below in Tables 1 and 2.

Of central importance are high Quantum Efficiency (QE) extending into the near infrared and small contribution to the instrument Point Spread Function (PSF) budget. The requirement for a large $A\Omega$ leads to a large focal plane area, which can be economically realized only by using silicon as the sensor material. To achieve high QE in the near-IR, the sensor must be thick because the absorption depth of silicon increases rapidly in this wavelength range. However, increasing detector thickness degrades the spatial resolution of the sensor due to two effects. Diffusion of the photo-generated charge increases due to longer transit time to the collecting electrode. Thick sensors also require sufficient substrate bias to fully deplete the device; otherwise, lateral diffusion in the undepleted field-free region severely degrades the PSF. A second cause of PSF broadening results from the fast focal ratio of the LSST optics (f/1.2). For red wavelengths where the absorption length is long, the light becomes defocused before it is fully absorbed, further broadening the PSF. Other less pronounced drawbacks of thick sensors include higher dark current and increased contamination from cosmic rays.

Table 1. LSST sensor requirements.

Science Requirement	Design Implications
High QE out to 1000nm	thick silicon (> 75 μm)
PSF << 0.7"	high internal field in the sensor high resistivity substrate (> 5 kΩ·cm) high applied voltages (> 50 V) small pixel size (0.2″ = 10 μm)
Fast f/1.2 focal ratio	sensor flatness < 5μm peak-to-valley focal plane package flatness < 10 μm p-to-v package with piston, tip, tilt adjustable to ~1 μm
Wide FOV	3200 cm^2 focal plane > 200-CCD mosaic (~16 cm^2 each) industrialized production process required
High throughput	> 90% fill factor 4-side buttable package, sub-mm gaps
Fast readout	highly-segmented sensors (~6400 output ports) > 150 I/O connections per package

Table 2. LSST sensor requirements.

	Allowable range	Target	Units
Pixel size	8 – 12	10	μm
Flatness deviation	10	5	μm
Aggregate fill factor (entire array)	90	95	%
Frame read time	3	2	s
Read noise	10	6	e$^-$
Full well	70000	90000	e$^-$
Output-output crosstalk	.05	.01	%
Nonlinearity	7	5	%
Dark signal (95th percentile)	4	2	e$^-$ s^{-1}
Charge memory	.05	.02	%
QE at 400nm	55	60	%
QE at 600 nm	80	85	%
QE at 800 nm	80	85	%
QE at 900 nm	60	85	%
QE at 1000 nm	25	45	%

2.2 Sensor Format, Readout Speed, and Readout Segmentation

The LSST focal plane has a number of requirements and desired characteristics that preclude the use of any existing sensor design ([2], see Table 3). In addition to the need for extended red response and small point spread function, the fill factor, full well capacity, and readout speed and read noise of the sensor have the most impact on LSST science performance. Due to the large (~3200 cm^2) imaging area of the focal plane, a large number of individual sensor units will need to be produced. Thus, reliability, reproducibility, and compatibility with industrial fabrication methods are of paramount importance as well.

The proposed approach to address these issues is a large format CCD with highly segmented readout. Large formatting will minimize the number of gaps between sensors in the assembled mosaic. To provide for a 2 sec readout of the entire focal plane, it will be necessary to have multiple outputs per CCD operating in parallel. As the number of outputs per CCD is increased, the readout speed per output can be reduced, thus minimizing the noise bandwidth. However, a correspondingly higher number of electronic signal processing channels will be required. Output-to-output crosstalk must be minimized, and reaching the required level is expected to be a challenge for the electronics development.

A further advantage of segmentation is that it can be used to reduce the impact of bloomed charge from bright stars. In a 15 sec LSST exposure the charge from 16th magnitude and brighter stars will exceed the pixel full well capacity, resulting in blooming up and down the column. By choosing an appropriate segmentation the length of the affected columns can be kept small, so blooming from a bright star is contained to within no more than .005% of the imaging area. Segmentation also substantially reduces the power dissipation of the clock drivers.

It is assumed that the LSST sensors will be developed and produced by a commercial vendor or vendors. However, using expertise that exists within the collaboration a "strawman" design [3] of a large format, highly segmented CCD design has been produced and will be discussed in detail in Sec. 3. The geometry of the frontside electrodes has been chosen to be consistent with contemporary CCD technology. It is anticipated that this strawman design can be used as a starting point for negotiations with potential CCD vendors leading to a contract for the production of the first prototypes.

Table 3. LSST sensor design parameters.

Parameter	Value
Pixel size	10 μm
Format	4000×4000 pixels
Segmentation	Eight 4000×500 pixel sub-arrays, 4 outputs each
Total no. of output amplifiers	32
Anticipated gain	$3 - 5$ μV/e$^-$
Parallel clocking	4-phase (4 poly layers)
Serial clocking	3-phase
Contiguous column length	500 pixels (100 arcsec)
Guard ring	100 μm
Pin count	208
Fill factor	96.5%

3.   ELECTRONICS

The LSST focal plane represents a quantum leap in size and scope over those in use in telescopes today. While both CMOS/PIN diode image sensors and CCDs remain under consideration, we restrict our attention here to the CCD option and for this design option. The readout electronics (see Fig. 3) support 4K × 4K CCD sensors with 32 output ports per device (see Figures 4 and 5). With the exception of the front end module, comprising the front end signal processing electronics, the remaining downstream electronics could also accommodate a CMOS image sensor array.

The combined requirements of large size, high dynamic range, low noise, and rapid readout time, dictates a highly segmented focal plane with approximately 6,400 readout ports. This dictates a high degree of integration for both the front end electronics, those which process the CCD output signals and provide clocks, and the back end, which digitize the data, buffers it, and transmits it off-camera via optical fiber.

A basic choice must be made to distribute functionality either within the camera inner cryostat or outside it. A design with most of the electronics outside cryostat would afford greater accessibility at the expense of a much higher number of cryostat electrical penetrations. An analysis of connector requirements indicates that for a system with two hundred 16 Mpixel CCDs, about 20,000 cryostat penetrations would be required. To avoid this excessive number of penetrations, a much more highly integrated strategy with considerable electronics within the cryostat is preferred.

A second design driver is the low noise requirement, and in particular, low feedthrough of digital activity back to the sensitive analog signals from

the CCDs. This dictates front end electronics located very closely to the CCD ports with digital activity somewhat removed. It also dictates use of low-level differential signaling both for analog and digital data transmission.

Finally, the entire LSST focal plane will be synchronous in operation, which means that clocking for all sensors in the array will be synchronous to the level of some tens of nanoseconds. This assures repeatability and robustness against feedthrough and pickup. Timing generation will take place within the timing/control crate under the command of the off-camera control system.
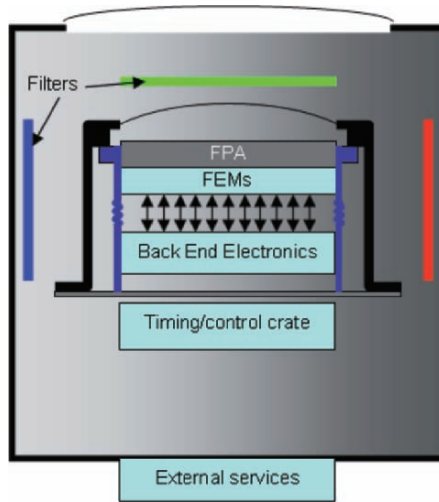
Figure 3. LSST electronics.
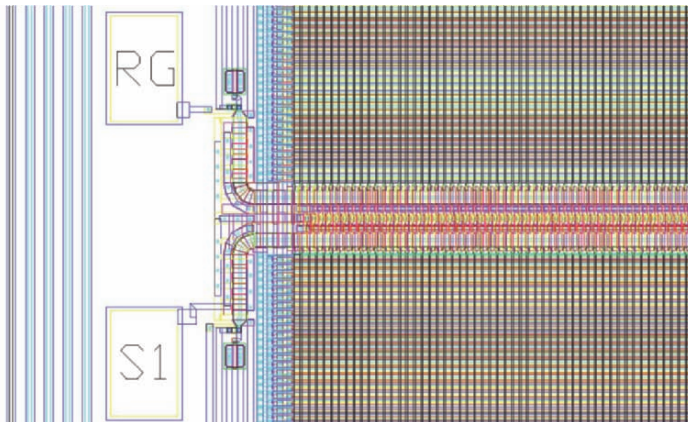
Figure 4. LSST sensor segment layout.

```
Format: 8 X (4 X 2000 X 250) = 16.000E6
Size:   40.660 X 40.797 mm
Fill factor:  96.46 %
```
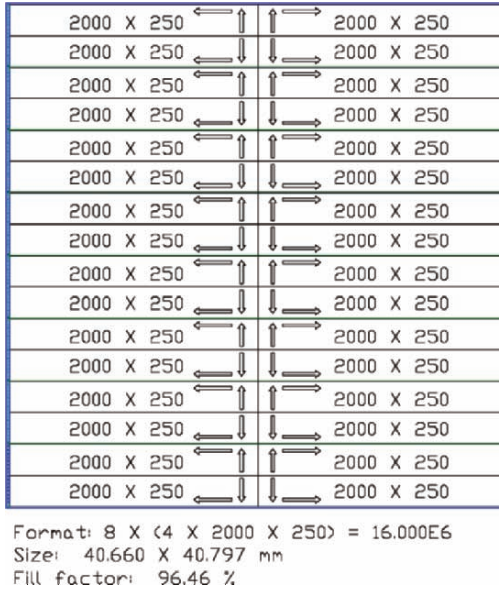
Figure 5. LSST CCD layout.

4.   CCD VS PIN-CMOS TECHNOLOGY SELECTION

Both CCD and hybrid-CMOS technologies offer advantages and disadvantages. The most significant advantages of PIN-CMOS would be operating the camera without a mechanical shutter and windowing. However, silicon PIN-CMOS devices with the required area and small pixel size have not been proven in astronomy applications. In addition, technical issues regarding the achievement of a reliable production process for large format and fine-pitched hybrid arrays, and the cost and limited number of potential suppliers also present special challenges for LSST. At this stage, we are pursuing the development of CCDs as the baseline, with CMOS as the backup. A vendor information package for the sensors has been prepared and was distributed to both CCD and CMOS vendors in 2005. A request for proposals (RFP) to develop LSST sensors has been issued to both CCD and CMOS vendors. The technology down select will be made when we have made an evaluation of responses to the RFP.

5. TESTING PROGRAM

Testing will be concentrated on the most challenging parameters, which are the key objectives of the R&D program:

- direct measurement of PSF due to charge diffusion (e.g., ≤3 µm rms)
- properties of multiport readout, such as readout noise (≤5 rms e⁻) and crosstalk (<10–3) at the required readout speed (2 s)
- QE vs. wavelength (e.g., ~25–45% at 1000 nm)
- optical quality measurements of sensor flatness (<5 µm peak-to-valley).

Conventional phase measuring interferometry will be used to measure sensor flatness [1]. It is assumed that the sensors will be fabricated in an industrial process due to the large number required, e.g., ~250–300 including spares. As a part of the manufacturing process most of the basic functional testing is expected to be done by the manufacturer(s).

6. REFERENCES

[1] LSST Corporation, *The Large Synoptic Survey Telescope Design and Development,* proposal submitted to the National Science Foundation, December 2003, pp. J–22, J–23.

[2] Groom, D.E., et al., 1999, *Quantum efficiency of a back-illuminated CCD imager: An optical approach,* Proc. SPIE, vol. **3649**, pp. 80–90.

[3] *CCD Strawman Design*, http://www.inst.bnl.gov/~poc/LSST/strawman_geary.doc.

[4] *Study of Silicon Sensor Thickness for LSST*, http://www.inst.bnl.gov/~poc/LSST/Study%20of%20sensor%20thickness.doc.

John Tonry exudes the confidence of someone who knows that his Pan-STARRS camera will be the first gigapixel imager on the sky.

Suffering from jet lag and lost luggage, Kirk Gilmore, who represented the LSST, is overwhelmed by John Tonry's talk.

OPTICAL DETECTOR SYSTEMS AT THE EUROPEAN SOUTHERN OBSERVATORY

Dietrich Baade & Optical Detector Team
European Southern Observatory

Abstract: *An introductory overview of recent, current, and future optical detector projects at ESO is given.   These projects fall into 3 categories: (i) commissioning of detector systems with their host instruments (FLAMES, HARPS, VIMOS, and UVES blue upgrade) and VLT 2nd generation instruments (MUSE and X-shooter), (ii) the wide-angle mosaic imager OmegaCAM, and (iii) projects with a preparatory component for OWL (adaptive optics and the New General detector Controller, NGC, for both optical and infrared instruments).   Their main characteristics, objectives, and realization are briefly described.*

Key words: *CCDs, detector controllers, adaptive optics, cryostat operation.*

1.   INTRODUCTION

   In the 3 years since our previous status report [1], three themes have dominated the work of the Optical Detector Team (ODT) at ESO. As always, the first and main theme is the support of instrument development for ESO's La Silla Paranal Observatory (ESO established a formal policy that the detector systems for all ESO instruments are developed and built by ESO). This entailed the completion and commissioning of FLAMES, HARPS, and VIMOS, the upgrade of the blue detector in UVES, and the preparation for MUSE and X-shooter as 2nd generation VLT instruments. The second theme, although logically only a subset of the first category, has been the wide-angle CCD mosaic camera OmegaCAM, owing to the large dimensions and complexity of the project. The third domain is VLT projects

with preparatory elements toward Extremely Large Telescopes (ELTs). Since ELTs are fundamentally dependent on the performance of Adaptive Optics (AO), there is a gradual shift in emphasis from scientific imaging to signal sensing applications. Another key stepping stone in this context will be ESO's New General detector Controller (NGC).

In principle, a 4th pillar should be contributions to the operation of ESO's La Silla Paranal Observatory. However very low downtime of the ODT systems deployed there and competent on-site support make this a very minor field of activity.

2.   MULTI-CONJUGATE ADAPTIVE OPTICS DEMONSTRATOR (MAD)

As enabling technology for ELT's, MAD [2] tests two different advanced AO concepts (Shack-Hartmann and layer-oriented) for a field of view as large as one arc minute. This requires the simultaneous usage of several reference sources in the field, which are natural stars in the case of this prototype system. One method employs 2 detector heads, whereas the other employs 3 to be operated in tightly intertwined loops with frame rates of up to 400 Hz. Since only one of the systems will be used at a time, one FIERA is sufficient to support them. The total peak pixel rate is several Mpixel/s and so exceeds the original specification for ESO's standard CCD controller, FIERA [3], by a few factors. Nevertheless, the read noise is less than ~7 e[-] for each of the 5 identical e2v CCD39 systems with 80×80 pixels and 2-stage Peltier cooling.

MAD will be commissioned jointly with the accompanying CAMCAO camera, which deploys a Hawaii-2 detector at the beginning of 2006. The MAD detector system is described in more detail by Reiss et al. [4].

3.   A 2ND GENERATION ADAPTIVE OPTICS DETECTOR

Advanced AO systems for 8 m telescopes are based on at least 1000 degrees of freedom. As one degree of freedom requires 6×6, if not 8×8, pixels, detectors for these advanced AO systems require in the order 200 pixels on a side. Since the associated higher spatial frequencies also demand faster temporal sampling, at least 1000 frames/s is mandatory. As a result, the number of photons contained in each space-time pixel is so reduced that the ability to detect single photons becomes vital even with very large telescopes. In spite of very short exposure times, dark current is another

concern because the use of high-efficiency cooling systems is excluded due to the need to freely position AO units in the field of view.

Numerous European astronomical institutions, including ESO, have joined forces in the OPTICON network to apply for funds from the Commission of the European Union in support of the massive R&D work needed to master the above challenges. The resulting grant was supplemented by ESO and so permits the development of a custom-designed detector. L3Vision™ technology from e2v was chosen as the baseline, which was expanded to a split frame transfer chip design and 8 outputs to satisfy the high speed requirements. The first of these systems will be used with HAWK-I, a wide-field IR imager; MUSE (Sect. 5) requires the next four.

More in-depth information about the resulting CCD220, including a number of special options, and cross-references to other publications under the same OPTICON umbrella can be found in Downing et al. [5].

4.   THE OMEGACAM WIDE-ANGLE CAMERA

The heart of the detector system of this $1^{\circ} \times 1^{\circ}$ wide-angle imager [6] for the VLT Survey Telescope (VST; [7]) is a $16K \times 16K$ mosaic of 32 e2v CCD44-82 chips. But the detector system is much more than a passive photon sensor. It must also provide positional and wavefront information for the telescope's tracking and active optics systems respectively. To this effect, two auxiliary pairs of $2K \times 4K$ CCDs are installed on the mosaic baseplate. Compared to conventional beam-splitter solutions, this has the added the following advantages: (a) by using the same filter, the same passband is used for science imaging, autoguiding, and active optics control, while (b) the flux of the guide stars does not have to be shared between different tasks. Moreover, the detector system controls the instrument shutter [8].

OmegaCAM was designed with a stringent set of technical specifications. Perhaps, the requirement of a very small back focal distance had the single largest impact, which necessitated (i) that the instrument to be partly surrounded by the M1 cell of the telescope and (ii) that the detector head be deeply imbedded in the instrument. This imposed difficult geometrical constraints on the detector head electronics. The obligatory use of FIERA instead of a purpose-designed controller is an obvious constraint in the areas standardization and maintenance on Paranal, but was not a booster of the overall design. The mass and volume of the three FIERA and three power supply boxes (two each for the mosaic and the other one for the auxiliary CCDs) are tangible evidence of the limitations of the project.

Substantial challenges also resulted from the survey-specific requirements that observations over the whole accessible sky and at least 10 years will still be highly homogeneous. These include very careful shielding against stray light, excellent planarity of the mosaic and its alignment with other critical planes, precise centering of the dewar entrance window (which serves as a field flattening lens), homogeneous thermal control, no cross talk between unit detectors, etc. Moreover, OmegaCAM must be very reliable because it will be the only instrument on the VST. A failure of this instrument will inevitably imply an idle telescope.

Very careful planning and faithful adherence to the approved plans have helped substantially limit the number and severity of problems at later stages of the project. Because of the amount of liquid nitrogen and the large number of CCDs (the replacement of which following an accident would probably take at least 2 years), much attention has been paid to the safety of operations staff as well as the equipment itself.

Iwert et al. [9] give a broad account of the history and status of the OmegaCAM detector system (the commissioning is expected for the first half of 2006). The liquid nitrogen-based, innovative cooling system, which combines the simplicity of a bath cryostat with the effectiveness of a continuous-flow cryostat, is detailed in Lizon and Silber [10] while methodological spin-offs from the extensive testing of the unit CCDs are developed by Christen et al. [11, 12].

5. MULTI-UNIT SPECTROSCOPIC EXPLORER (MUSE)

Twenty-four integral field units will enable this spectrograph [13] to take a full celestial inventory over a field of view of 1 armin^2, with an adaptive optics-supported spatial sampling of 0.2 arcsec, and out to a redshift of 6. On the VLT Nasmyth platform, there will be a battery of 24 separate detector systems with 4K × 4K unit detectors (or 2 × 1 mosaics of 2K × 4K detectors) with 15-micron pixels. Given the objectives for the range in redshift, high red response is project critical. Equally important is that each unit detector system contributes as little to the total mass and volume as possible. Parts must be machined such that they can be assembled without much measuring and adjusting. ESO's new VLT 2nd generation detector head will address these points. With most possibilities for failure replicated 24 times, reliability is another design driver. Finally, MUSE will be the first optical instrument to be equipped with the New General detector Controller (NGC; Sect. 8). A prototype detector system must be ready in 2006 whereas

the whole instrument will be installed at the VLT in 2011. Further information about MUSE is provided by Reiss et al. [14].

6.   X-SHOOTER

X-shooter [15] will be the first instrument at ESO to bridge the 1-micron barrier. Its simultaneous wavelength coverage of nearly one dex from 0.3-2.4 micron will be affected by two optical arms (with an e2v CCD44-82 in the blue arm and an MIT/LL CCID-20 in the red arm) and one IR arm (Rockwell Hawaii-2 RG). With no user definable parameters (except for coordinates and exposure time), X-shooter will be especially suited to respond rapidly, over an extreme wavelength range, and at medium spectral resolution to ephemeral or highly variable point sources.   For the two optical arms, two independent virtual cameras will be defined by software on one shared FIERA hardware. Following the final design review in the summer of 2005, the instrument will be commissioned in 2008.

7.   CRYOSTAT CLEANLINESS AND CONTROL

7.1   Plasma Cleaning

Contamination is one of the biggest threats to any optical detector system. It is a textbook example of problems that are better prevented than solved. This is easily possible prior to assembly. However if the dewar must be reopened again later, this is where the dilemma begins. On the one hand, there is a significant risk of contamination. However, cleaning by means of the conventional washing and baking not only disrupts the project schedule but can also open a Pandora's box of new problems because disassembling and re-integrating a detector system poses a large variety of risks.

In ESO's experience, plasma cleaning is the ideal method that not only excels as a preventive measure but is extremely effective at cleaning fully assembled cryostats. Only the detectors need to be removed because they may not withstand the high field strengths. If electronics boards can be easily removed, this is also recommended. The wall of the vessel can be used as one of the electrodes, and the plasma can be ignited and observed through the dewar entrance window. One full cleaning cycle of a large cryostat such as the one of OmegaCAM [10] only takes about 10 minutes. There are no operating costs.

The method is explained, and tests and results are described, in Deiries, et al. [16].

7.2   H₂O Exorcism

The ODT test bench permits two $2K \times 4K$ CCDs to be tested simultaneously. When it was used to bake (60ºC, 24 h) and oxygen-flush a MIT/LL CCID-20 device, it was decided to install one of the OmegaCAM CCDs for comparison. As expected, the low-frequency response non-uniformity in the UV of the latter device was removed and the lower-sensitivity regions were lifted to the higher sensitivity level of the other regions, which remained essentially unchanged. To our surprise, the QE between 300 nm and 550 nm of the OmegaCAM chip improved by a factor of up to 1.5, which was uniform over the chip surface and only depended on wavelength.

The limited experience obtained thus far suggests the following: The UV quantum efficiency of the OmegaCAM detector can be toggled between a low and a high state. The low state is assumed when the detector is kept under normal atmospheric conditions for sometime. Baking under vacuum conditions (10^{-4} mbar) does not bring any improvement but combined with oxygen at 1 bar it does. During subsequent storage for 2 months at 10^{-4} mbar and -120ºC no significant degradation could be detected.

Further tests showed that the same effect as with pure oxygen can be achieved with clean, dry air. This could mean that the improvement in UV QE is not due to a chemical reaction but that the baking removes substance from the CCD surface that is not easily re-adsorbed in the presence of gas. A plausible candidate for this substance is water. The tests will be repeated under more rigorously controlled conditions and will be extended to plain nitrogen in particular.

7.3   New House-Keeping Unit PULPO2

The novel concept of the OmegaCAM dewar and its large size [10] suggested that one should utilize a large number of temperature sensors for diagnostic purposes (vertical temperature stratification and horizontal homogeneity across the mosaic) although only 4 PT100's are used for actual thermal control. To this end, based on the well-proven PULPO house-keeping unit, an all new PULPO2 was developed, which also features enhanced heating capabilities for both normal operation and contamination-preventing warm-up in case of a loss of vacuum or cooling. Other essential features are the associated issuing of alarm signals to the Paranal Central

Alarm System and the precise shutter timing. More information can be found in Geimer, et al. [17].

8.   NEW GENERAL DETECTOR CONTROLLER (NGC)

Between 1998 and 2008, a total of 30 FIERA and IRACE [18] systems will have been deployed at ESO's La Silla Paranal Observatory for optical and infrared detector systems respectively. Good performance and high reliability (the combined downtime of the FIERA hard- and software is of order 0.5%) have been demonstrated in more than 10,000 nights of scientific operation. On June 30, 2005, the ESO Science Archive Facility held a total of 4.4 million raw files from the La Silla Paranal Observatory, of which nearly 100,000 were acquisition images, suggesting that a similar number of targets and fields having been observed.

Nevertheless, the above sections have already identified some limitations of FIERA. These partly exist in a similar way for IRACE, with the additions of the following: mass, volume, heat dissipation, insufficient range and swing in voltage for more advanced detectors such as fully depleted CCDs, speed, number of channels, system noise, obsolete components, etc.

In response to these and further challenges resulting largely from adaptive optics and interferometry, ESO has decided to design and build a new-generation detector controller that not only satisfies the above requirements but will also be color blind and so serve both optical and IR detector systems. This also acknowledges the fact that two parallel successes may result in a larger total personal satisfaction but also incur two costs.

Because of its broad range of applications, the system is called New General detector Controller (NGC). A 4-channel prototype of the hardware has already successfully 'seen' first light with a 256×256 PICNIC array from Rockwell as well as with a CCD44-82 device from e2v. The detailed quantitative characterization and improvement, the design and integration of a 34-channel acquisition board, the extension to the needs of adaptive optics [19], and the development of the associated control software [20], which will include a substantial complement of test software, etc. will take most of the coming 3 years.

NGC will be in operation until at least 2015 when the construction of the Overwhelmingly Large Telescope (OWL) could commence. It will pave the way of detector control into the ELT era, at which time it will become clear what role ASICs will play and whether and where CMOS devices can replace CCDs.

A both wider and deeper overview of the NGC hardware is available in Meyer, et al. [21].

9.   REFERENCES

[1]   Baade, D., et al., 2004, Kluwer, ASSL Vol. 300, p. 197.
[2]   Marchetti, E., et al., 2004, Proc. SPIE, Vol. 5490, p. 236.
[3]   Beletic, J.W., Gerdes, R., Duvarney, R.C., 1998, Experimental Astronomy, 8, 13.
[4]   Reiss et al., these proceedings.
[5]   Downing et al., these proceedings.
[6]   Kuijken, K., et al., 2004, Proc. SPIE, Vol. 5492, p. 484.
[7]   Capaccioli, M. et al., 2005, The ESO Messenger, No. 120, p. 10.
[8]   Reif et al., these proceedings.
[9]   Iwert, O. et al., these proceedings.
[10]   Lizon, J.L., Silber, A., these proceedings.
[11]   Christen, F., et al., these proceedings.
[12]   Christen, F., et al., these proceedings.
[13]   Bacon, R., et al., 2004, Proc. SPIE, Vol. 5492, p. 1145.
[14]   Reiss, R., et al., MUSE, these proceedings.
[15]   Dekker, H., and D'Odorico, S., 2005, The ESO Messenger, No. 120, p. 2.
[16]   Deiries, S., et al., these proceedings.
[17]   Geimer, C., et al., these proceedings.
[18]   Meyer, M. et al., 1998, Proc. SPIE, Vol. 3354, p. 134.
[19]   Reyes, J., et al., these proceedings.
[20]   Cumani, C., et al., these proceedings.
[21]   Meyer, M. et al., these proceedings.

THE UKIRT WIDE FIELD CAMERA

Derek Ives
United Kingdom Astronomy Technology Centre

Abstract: *The Wide Field Camera (WFCAM) has recently (in 2004) been commissioned at the United Kingdom Infra Red Telescope (UKIRT) in Hawaii. The complete system consists of a new IR camera with integral autoguider and a new tip/tilt secondary mirror unit. The optical system operates over 0.7-2.4 μm and has a large corrected field of view with a 0.9° diameter. The focal plane is sparsely populated with 4 2K×2K Rockwell HAWAII-2 detectors, giving a pixel scale of 0.4 arcsec/pixel. A separate autoguider CCD is integrated onto the focal plane unit. This paper summarises the performance of the camera system and more specifically reports on some of the lesser known IR detector characteristics, such as the reset anomaly and inter-channel cross talk.*

Key words: *HAWAII-2 arrays, detector characteristics, reset anomaly, inter-channel cross talk.*

1.   INTRODUCTION

The Wide Field Camera (WFCAM) is mounted in a forward Cassegrain position in front of the UKIRT primary mirror on its lifting plug. The vacuum vessel is approximately 1 m in diameter and 3 m long. The overall length to the field lens is ~5 m and the overall mass of the instrument is ~1.5 tonnes. A two stage closed cycle cooler is used. The first stage cools the majority of the instrument (radiation shield, support structure, tertiary mirror) to ~120 K. The second stage cools the focal plane unit to ~70 K. Figure 1 shows the instrument as mounted in its final position on the telescope. Key operating parameters and specifications of WFCAM are listed in Table 1. The four IR detectors and autoguider CCD are positioned at the focal plane and closely packed. This can be seen in Figure 2. This

presented a challenge due to the lack of space around the detectors for positioning components and connectors. The allowed footprint for each IR detector PCB is only slightly larger than the ZIF socket holding the detectors themselves. A flexi-rigid design was used for each detector PCB with flexible sections linking the main board section to connectors for the outputs/biases and clocks.

Table 1. Key instrument design parameters

Detector	4 × Rockwell HAWAII-2 PACE, 2×2 array, 94% spacing of active areas
Pixel scale	0.4 arcsec/pixel
Field of view	0.933° (single exposure, diagonal)
Image Quality	MTF > 0.5 at 1.2 cycles/arcsecond
Filters	Broad band - Y (1.00-1.07 µm), J98 (1.17-1.33 µm), H98 (1.49-1.78 µm), K98 (2.00-2.37 µm) Narrow band - H2 (2.122 µm)
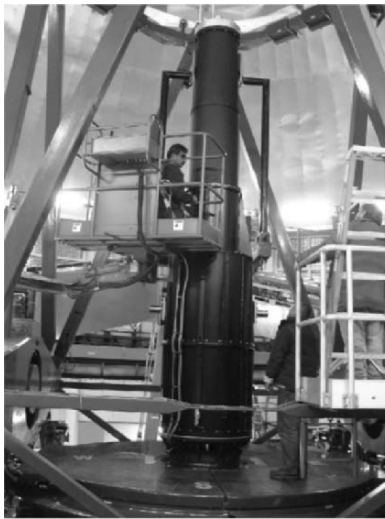
Figure 1. WFCAM mounted on telescope.

Figure 2. The final focal plane assembly.

The four IR detectors are each controlled using their own 32 channel ARC-III controller. The controllers are highly synchronized using a master clock and frame start pulse scheme to ensure that they clock the arrays at exactly the same time to avoid clock coupling between detectors. However, the autoguider CCD is operated asynchronously to the IR detectors. We typically run this E2V47-10 device at 100-200Hz windowed frame rates to feed corrections to our tip-tilt secondary mirror system. We do not see any

clock coupling between the autoguider clocks and the IR detectors even though the devices are mounted in close proximity to each other. We did mount the CCD completely inside a "Faraday" enclosure, even coating the window with Indium Tin Oxide on both sides. We mounted the window using an electrical gasket to the rest of the enclosure. We reduced all the CCD clock swings to the minimum voltage required for correct operation. This does reduce full well, but this is not an issue for our autoguider system.

2.   STANDARD DETECTOR CHARACTERISTICS

We have characterised 7 detectors for the project. A summary of the typical performance parameters for all the detectors is given below for completeness.

Operating temperature	- 75 K
Pixel rate	- 180 kHz
Frame readout time	- 0.73 s
Detector bias (Vreset)	- 1.0 V
Transimpedance	- 3.6 μV/e$^-$
Gain change v. Signal	- ~2%(10-90% full well)
Read noise (pixel-to-pixel)	- 15 e$^-$ (rms)
Full well	- 180 ke$^-$
Non linearity	- ~2%(10-90% full well)
QE (JHK)	- >80% reported

3.   OTHER DETECTOR CHARACTERISTICS

The remaining sections focus primarily on lessons learnt from operating these detectors. Some of features of these detectors have been previously described in other publications but I felt it worth revisiting from a slightly different perspective and describe what was seen with the particular detectors on our project.

3.1   Reset Anomaly

The reset anomaly has been described numerous times at other conferences [1,2]. The chief component of the reset anomaly is a large intensity ramp at one edge of each quadrant. The edge where the reset anomaly is largest is also where the array readout electronics are located. A typical Correlated Double Sample (CDS) bias frame from one of our detectors is given in Figure 3, showing the typical profile from the edge

inwards. The ramp drops from approximately 1000 ADU from the edge to 0 ADU near the centre. This is typical for most devices; however we have also seen devices where the maximum value of the profile is at least a factor four to five improved. More of a concern is the instability of this profile across the detectors for consecutive reads. In standard observing we subtract a dark and bias frame flattening the profile. However we find that when we subtract consecutive CDS images the profile does not flatten out, but is unstable. Figure 4 shows the images and profiles for three consecutive CDS frames, subtracted from each other as described.

Solutions for this have been reported elsewhere [2]. These usually consist of running read or reset frames that have the same execution time as real reads and are then be dumped. However, for our wide field imager we typically only do simple correlated double samples, an extra frame time would reduce the readout efficiency by 33%. Our solution is, therefore, to perform extremely fast reads of all the pixels in the array using standard read routines. However we do not settle or digitize for each pixel. This typically takes approximately 0.1 s to complete. We do this twice only after the resetting of the array, which adds 0.2 s to our CDS time of 1.4 s. This process is therefore more than twice as efficient as other methods for reducing the reset anomaly.
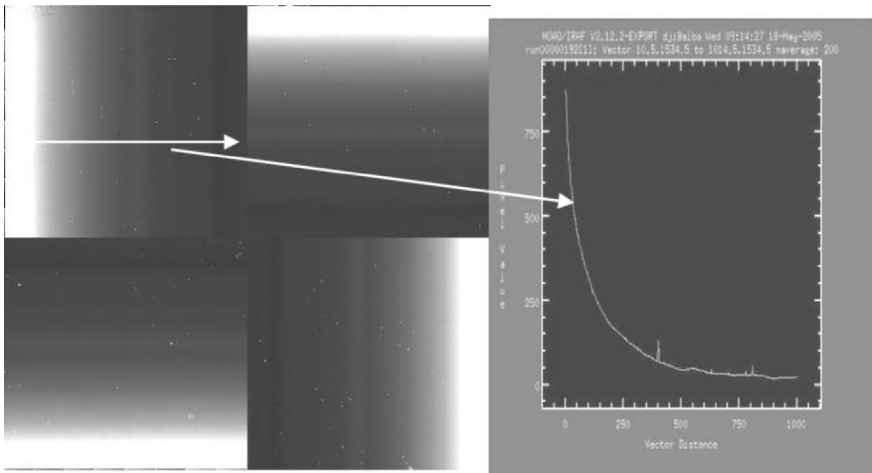
Figure 3. CDS bias frame showing reset anomaly profile.
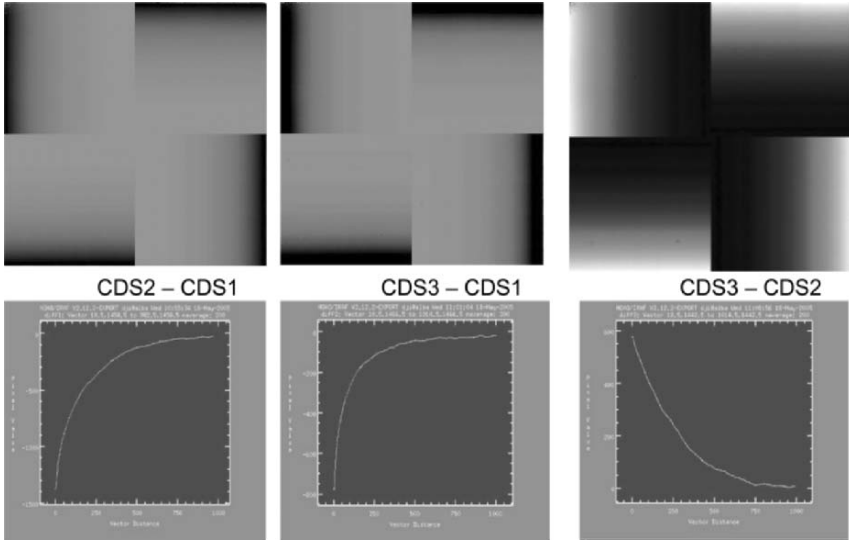
Figure 4. CDS subtracted frames, indicating instability caused by reset anomaly.

3.2 Low Frequency Banding

Once the reset anomaly fix has been implemented, another issue with subtracted CDS frames arises. This is low frequency banding [1]. This banding is shown below in Figure 5.
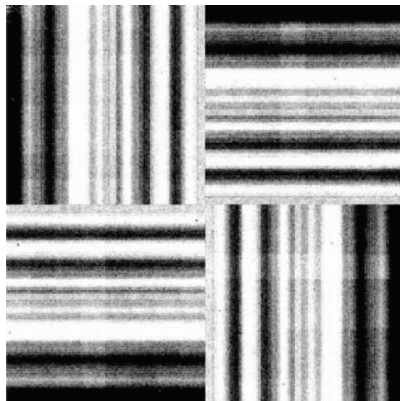
Figure 5. CDS subtracted frames, with fix for reset anomaly implemented.

In our system the bands are +/-20e p-v. As reported in previous papers this banding can be corrected using the average of a few columns for one

quadrant to flatten the image. In Figure 5 we see that the peaks and valleys occur at exactly the same places in the four quadrants of the detector so the correction from one quadrant can be used to correct the other three quadrants also. In our system we synchronise the readout for four detectors and see low frequency banding on all four detectors. However the peaks and valleys occur at different places on the different detectors. Thus each detector must be corrected separately.

On an imager such as WFCAM, in a crowded star field, there may be many stars near the edge of the detector which would not then allow this edge to be used for the correction described. It may therefore be sensible to design an under scan region onto each detector. This could take the form of a simple mask which sits above the detector as part of a radiation shield and blanks off a few columns of one quadrant of each detector on a mosaic.

3.3 Inter Quadrant and Channel Cross Talk

We have seen inter quadrant cross talk on our detectors where a hot spot or projected image on one quadrant has "ghost" images on the other three quadrants. We were able to completely eliminate this type of cross talk by separating the analog supplies for each quadrant of the detector. However we do still see inter channel cross talk, where a hot spot on one of the eight outputs on a quadrant will produce "ghosts" on the other seven outputs of the same quadrant of a detector. The ghost images at either side of the projected spot are approximately 0.1% of the projected spot level and spots further away from the projected spot and either side of it are at the 0.02% level.

4. ACKNOWLEDGEMENTS

5. REFERENCES

[1] Finger, G., Dorn, R.J., Hoffman, A.W., Mehrgan, L., Meyer, M., Moorwood, A.F.M., Stegmeir, J., 2002, *Readout techniques for drift and low frequency noise rejection in infra red arrays*, Scientific Detectors for Astronomy, p. 435.

[2] Riopel, M., Doyon, R., Nadeau, D., Marois, C., 2002, *An optimized data acquisition system without reset anomaly for the HAWAII and HAWAII-2 arrays*, Scientific Detectors for Astronomy, p. 453.

SYSTEM DESIGN OF DETECTOR SYSTEMS FOR A MAJOR CHINESE MULTI-OBJECT SPECTROSCOPIC SKY SURVEYOR

Binxun Ye and Binhua Li
Research Labs for Astronomy, National Astronomical Observatories, CAS

Abstract: *Based on a comprehensive description of the Major Chinese Multi-Object Spectroscopic Sky Surveyor Project and its requirements for the detector systems, recent system design work was introduced to emphasize some special considerations. With a reflective Schmidt-type camera in the spectrograph, which was configured such that CCDs must be in the middle of the optics and confined between two cross beams, the cryostats were physically limited. In addition, CCD chips had to be positioned 6 mm behind the field lens with ±0.10 mm accuracy. To operate 32 CCD cameras in a limited space in total darkness and an air-tight environment, a variation of a recently developed Astronomical Array Control & Acquisition System was adopted. This model allowed all the controls and acquisition done via LAN to meet the control and data flow requirements defined by the Observing Control System (OCS-1) of the project.*

Key words: *MOS, detector system, CCD camera, system design.*

1. INTRODUCTION

The ambitious project to build a Large Sky Area Multi-Object Fiber Spectroscopic Telescope (LAMOST) is in development in China [1]. The project aims to unveil the large scale structure of the universe through spectroscopic surveys of extra-galactic objects, and the structure of the galaxy by stellar spectroscopic survey.

The telescope was configured as a 4 meter meridian Schmidt system with an active reflective corrector to obtain a 5 degree FOV. 4000 optical fibers will be applied on the focal plane to feed light to the spectrographs. It will take galactic spectra of 2×10^7 and stellar spectra of 1×10^8 objects down to a magnitude of 20.5 in 3 years, covering the spectral range of 390-900 nm with a resolution of about 1 nm. Completion of the telescope is foreseen in 2007 and will be installed at the Xinglong station (117º34'.5E, 40º23'.5N) of the National Astronomical Observatories, surveying the sky north of -10º.

2.   THE SPECTROGRAPHS

The optical configuration of the low resolution spectrograph is basically a Schmidt system. No matter plane, aspheric, or VPHG grating has been selected [2]. For 4000 fibers, 16 such spectrographs are required. Each spectrograph is built upon a 1.3×2.2 meter vibration-isolated optical table. A dichroic beam filter reflects the blue light (370nm ~ 590nm) from the collimator to the blue wing camera while the red light (570nm ~ 900nm) transmits through a dichroic filter and then feeds red wing camera optics. Such arrangement leads folding beams which prevent any extension of the camera header along the axial direction of the camera optics. Limitations arise from the obstruction within the Schmidt optics of the camera, causing all dimensions of the camera header to be limited to 100×100×100 mm or less. Fibers are aligned at the focus of the collimator mirror. Light exiting the fiber should be at f/5 from telescope, but expands to f/4 due to focal ratio degradation. A mechanical slit was placed at the opening of the fiber line. When observing bright star objects, the slit could be cut in half for higher spectral resolution. A shutter for controlling the exposure also resides there.

3.   SYSTEM DESIGN OF THE CAMERA SYSTEMS

Due to delays in the development of the detector system, the design philosophy of the camera system will adhere to simple configurations. These are practical and dedicated designs for reliable operation based on a clear definition of interfaces to the spectrograph and Observing Control System (OCS-1) of the project.

3.1   Basic Design Parameters

Numerous rounds of talks were made with the project team to understand their scientific requirements in depth, and these translated to technical

requirements. The general technical requirements for the detector system are shown in Table 1.

Table 1. General technical requirements of the camera systems.

Spectral	A pair of cameras to cover the spectral range of 390nm ~ 900nm with resolution of 9 Å at the dispersion of 80Å/mm; each spectrum is of 112 μm high and 250 spectra per a CCD frame.
Photonic	The image of a φ320 μm fiber at the CCD surface is an elliptical shape with 100 μm at spectral dispersion and 120 μm elongating in the space direction. For observing a $20^m.5$ galaxy with 1.5 hour exposure, the average photons falling onto the CCD surface is ~1571 with 16562 from the sky and should yield SNR=12; while for a 17^m star at reduced fiber aperture, 12019 star photons fall onto the CCD with 5043 from sky for a SNR of 92. In all the cases, 1% linearity is expected.
Dimensional	The outline of the camera header inserted into the Schmidt optics must be within 100×100×100 mm; section areas of connecting cold fingers and harness must be minimized to reduce the obstruction loss of the optical rays. CCD surface must be positioned exactly 6 mm behind the field lens with a tolerance of ±0.1mm.
Operational	Camera headers and controllers will be operated in a remote, hard-to-access room. All the control commands and data flow are obtained via LAN. Maintenance service will also be limited hence high reliability is required.

3.2   CCD chip

A CCD203-82-1 CCD chip made by e2v technologies was selected for the cameras. This chip's characteristics meet the requirements of the system, and were also adopted for the budget reasons. Table 2 offers specifications that are closely related to our system design.

3.3   Cooling

A mixed-gas Joule-Thomson (J-T) cryo-refrigerator (MJTR) built by The Technical Institute of Physics and Chemistry (TIPC) [3], will be integrated into the camera head for cooling the CCD device. It can cool the chip to -120ºC with a high coefficient of power (COP > 0.15). High reliability and easy operation was another consideration in adopting this cryo-refrigerator for long life and low maintenance. TIPC will also engage in the detailed dewar design and the mechanism to ensure precision positioning of the CCD chip. A detailed document describing the requirements of the cryostats for the detector system was filed with TIPC along with a management plan. Table 3 shows the major requirements.

Table 2. Specification of the System Design.

		For blue cameras	For red cameras
Type number		CCD203-82-1-C60	CCD203-82-1-C59
Format		4096×4096	
Pixel size		12μm×12μm	
Q.E.	350nm	40%	N/A
	400nm	75%	20%
	600nm	80%	80%
	700nm	50%	80%
	800nm	15%	80%
	1000nm	N/A	10%
Readout Noise		5e @200Khz, 8e @1 Mhz	
CTE		Both parallel and serial: 0.999999	
Dark current@173K		10 e⁻/hr max.	
Non-linearity		1% max.	
Number of functional outputs		4	
Serial register dump drain		yes	
Deferred charge		3e⁻ max.	
Surface flatness		±15μm	

Table 3. Major requirements of the system.

Camera header dimensions	100×100×100 mm	
Camera header weight	<3000g	
Camera header out finish	black	No scattering
Vibration induced from compressor	< 1μm	Any freq.
Environments	20°C ±1°C/day, 60% humudity	
CCD Working Temp.	-100°C*±0.1°C within 24 hours dT/dt<0.05°C/hr; RS422 output of the temperature; Cooling and heating at a rate of <1°C /min	working temp. can be set between 80°C and 120°C
Extra cold surface	For trapping residual contaminants	No frost on the surface of the field lens
Vacuum	~10⁻⁶ Torr	

3.4   Controller

A modified version of the Astronomical Array Controlling and Acquisition System (AACAS) was recently developed by Research Labs for Astronomy. NAOC is the CCD controller of the detector system (see [4] for details). Figure 1 concisely demonstrates the system design work.
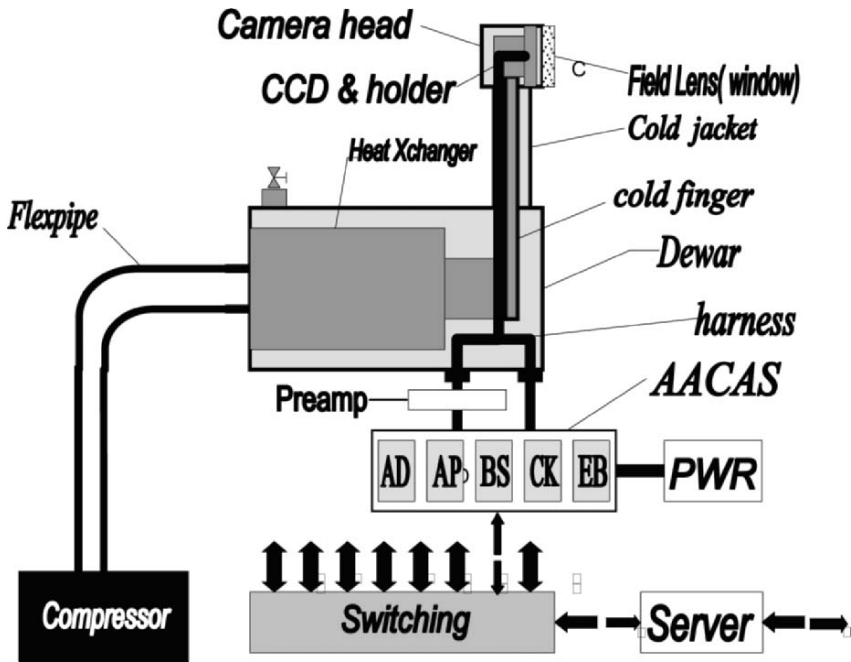
Figure 1. **AD**: A/D converter, **AP**: Analog processor, **BS**: bias voltages, **CK**: clocks, **EB**: embedded processor, **PWR**: power supply unit.

4.   REFERENCES

[1] Su, Hongjun, Cui, X., 2002, *LAMOST Projects and its current status*, Proc. of SPIE, Vol. **4837**, p. 4.
[2] Zhu, Yongtian, Xu, W., 2000, *Low Resolution Spectrograph for LAMOST*, Optical and IR Telescope Instrumentation and detectors, lye, M., Moorwood, A. F. .M. (eds.), Proc. of SPIE, Vol. **4008**, p. 141-147.
[3] Wu, Jianfeng, 2005, private communication.
[4] Zhao, Zhaowang, 2005, *Astronomical Array control & Acquisition System at NAOC*, these proceedings.

Binxun Ye and AG Davis Philips demonstrate the international comraderie that is a hallmark of this workshop.

The workshop participants rest their feet and learn about Taormina's history while sitting on ancient seats in the Teatro Greco (Greek Theatre).

NEAR DIFFRACTION LIMITED VISIBLE IMAGING ON 10 M CLASS TELESCOPES WITH EMCCDs

Craig D. Mackay
Institute of Astronomy, University of Cambridge

Abstract: *Lucky Imaging is the only method of generating near diffraction limited imaging from the ground in the visible over arc minute fields of view. This paper examines the methods used and results obtained on a 2.5 m telescope. It will also discuss a novel approach using techniques borrowed from radio aperture synthesis techniques, which should allow near diffraction limited images to be obtained in the visible with 10 m class telescopes. The technique uses an array of photon-counting EMCCDs using Lucky Image Selection. The paper begins by describing the design and construction of a camera dedicated to the operation of EMCCDs at high pixel rates in photon counting modes.*

Key words: *EMCCD controller, Lucky Imaging, high resolution imaging, adaptive optics.*

1.   INTRODUCTION

We have developed a new technique of achieving high angular resolution imaging from the ground, which we call "Lucky Imaging". We accomplish this by running a camera at speeds high enough to freeze the atmospheric seeing. Provided the telescope being used is not too large, there is a finite probability that the phase errors that normally degrade the image will spontaneously become close to zero and a near-diffraction limited image will be obtained. By looking at a reference star within the field of view images may be graded according to a variety of quality criteria. The best images are selected and combined to produce a much higher resolution image than would be possible if all the images had been used. The technique has been

made possible by the development of EMCCDs, which are essentially conventional CCDs with additional amplification stages in the output register. This allows considerable levels of gain to be achieved before the on-chip output amplifier. The consequent reduction in equivalent readout noise enables Lucky Imaging without the enormous noise penalties that are normally associated with the addition of large numbers of conventional high-speed CCD images. The core of our Lucky Imaging camera system is the CCD camera and its controller. We will describe in some detail the design criteria that were used and are, we feel, most appropriate to cameras using EMCCDs in high-gain mode accounting for individual photons.

2.   A NEW CAMERA FOR EMCCDs

We have developed a new camera specifically for driving EMCCDs at pixel rates up to 35 MHz in photon counting mode. There is considerable variance in the amplitude of each photon event. This relaxes the requirement to design very high precision electronics compared to driving a conventional slow-scan wide dynamic range camera. Our design uses a Kodak KSC-1000 sequencer that provides control flexibility at pixel rates of 4-60 MHz. We have used the latest integrated circuits developed for commercial digital camera use extensively. These include high-speed clock drivers and integrated CCD signal processors that provide preamplifier, double correlated sampling, and analogue to digital conversion in a single low-cost package. Generally we have found the performance of these devices to be extremely good.

The most novel aspect of an EMCCD controller design is the high-voltage clock driver. The e2v technologies devices require a voltage swing in excess of 40 V. The manufacturers suggest using a sinusoidal driver which can be designed to minimise power consumption. However, such a circuit needs to operate continually, which is not simple unless it was designed in association with the sequencer architecture. The other possibility is to use a switch circuit. Figure 1 shows the general layout we have found successful. It is essential that the two enhancement mode FETs are closely matched. If the two transistors are turned on simultaneously for only a nanosecond the currents are extremely high, causing components to emit a lot of noxious smoke. This schematic uses some of the components and structure suggested on the datasheet for the Texas Instruments TC285 Impactron device. Note, however, that their suggested transistors are not very well matched causing the circuit to perform less well than expected. The devices shown in Figure 1 are manufactured by Vishay-Siliconix. Careful attention to layout and thermal management is essential. The schematic shown provides a 40 V square wave with a rise time of 12-15 ns.
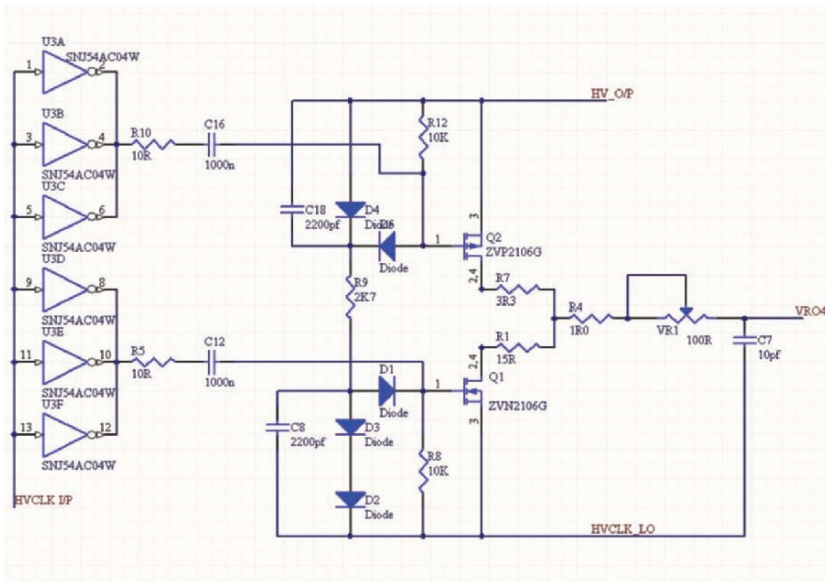
Figure 1. The schematic of the high-voltage clock driver used for EMCCDs in the present controller design.

3. LUCKY IMAGING: PERFORMANCE SUMMARY

A telescope is an instrument that deflects rays of light from a distant star or galaxy to form a sharply defined focused image. In space, a telescope will produce an image whose resolution is only limited by the diameter of the telescope, mirror quality, and the wavelength of light focused. In the case of a ground-based telescope, however, refractive index fluctuations in the atmosphere cause light to be deflected slightly so the focused images become slightly fuzzy. Atmospheric fluctuations change fairly rapidly, on timescales of tens of milliseconds, causing the quality of the focused image to change rapidly. By using a high-speed camera we can choose the images that are least affected by the atmosphere and combine them to give a much higher resolution image then if they were simply added together irrespective of their quality. By doing this we are selecting those fortunate moments when fluctuations in the atmosphere are at a minimum. This is what we call "Lucky Imaging". Lucky Imaging techniques may be used for both astronomical observations with telescopes and for ground-ground imaging, such as surveillance work with long focus lenses.

Lucky Imaging is not a novel idea. It was originally suggested by Fried and these principles have been used extensively by amateur astronomy communities who have been able to take very high quality images of bright objects such as Mars and the other planets. The results of Lucky Imaging can

be quite dramatic. The effects of atmospheric density fluctuations cause limitations in the detection of detail. Using a large diameter telescope will allow one to gather more light, but will not increase the detail in the image once a certain size has been reached. This depends on local atmospheric conditions, which vary daily, and the wavelength of light used. For typical atmospheric seeing of about one arc second this limits the maximum (uncorrected) resolution to that obtained in the visible with a telescope of only 10 cm diameter. With Lucky Imaging we can increase the maximum resolution that can be achieved from the ground by factors of as much as 5-7. With a ground based 2.5 m telescope we can match the resolution obtained by the 2.5 m Hubble Space Telescope, at a tiny fraction of the cost.

4.   HIGH RESOLUTION IMAGING ON 10 M CLASS TELESCOPES

Using Lucky Imaging we have been able to produce images which approach Hubble resolution from the ground. The possibility of exceeding this resolution from the ground is scientifically interesting- something which should be possible simply by using larger diameter telescopes. Unfortunately, the probability of the phase averaging out vanishes with bigger telescopes and different approaches must be used. Adaptive optics have been utilized extensively on larger telescopes with rather limited and relatively disappointing success. Our Lucky Imaging studies have shown that the nature of atmospheric turbulence is much more complicated than traditionally assumed by the builders of AO instruments. The phase across the aperture often has quite significant steps in many places, which are impossible to follow with a correction element that must be continuous at each point. Our conclusions from Lucky Imaging are that those parts of the aperture that have essentially unusable phase structure should be temporarily excluded from the imaging process. In principle, this could be performed with a Lucky Imaging system behind an adaptive optics unit. Another approach would be to break up the aperture and monitor the quality of imaging through each component part before allowing it to be used in the final image synthesis. We believe this approach will be most successful in allowing routine high resolution imaging from the ground on 10 m class telescopes. The methodology for this is shown in Figure 2.

If we imagine a segmented telescope, such as the Keck telescope, we can direct three telescope elements onto a single detector. Provided these elements are correctly phased (and this is not difficult to achieve), the detector will view the normal star field with every unresolved object such as stars crossed with Michaelson interference fringes representing interference between the light from each element in the triad.
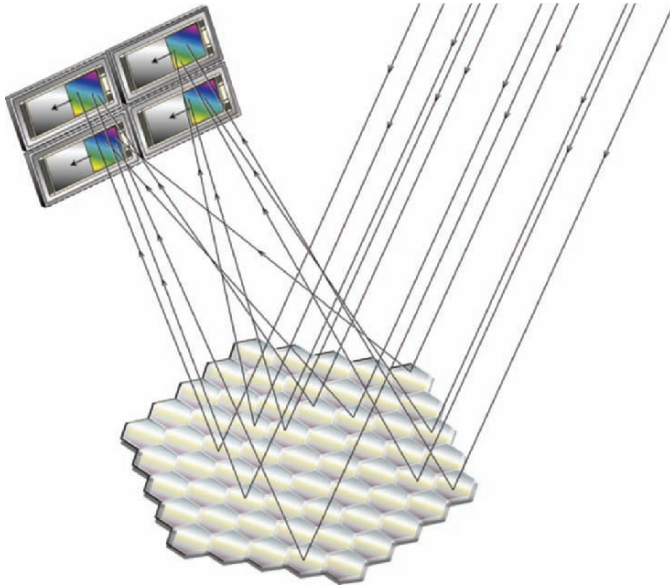
Figure 2. The light from sets of three or four apertures is combined to provide constructive interference on each individual detector.

Atmospheric fluctuations will cause the fringe pattern visibility to change from moment to moment. We use Lucky Imaging techniques to allow us select the moments of highest visibility. As with conventional Lucky Imaging we require a reference star in the field that is bright enough to allow us measure the fringe visibility. Such a star would typically have a limiting magnitude of approximately V=16.5. We can use the moments fringe visibility is reduced by compensating the detected fringe visibility in proportion to the loss in visibility on the reference star. What is detected is three components of the Fourier transform of the two-dimensional sky brightness distribution.

Each set of three elements of the telescope is directed to a different EMCCD detector system, which will then detect a further three components of the Fourier transform of the sky brightness distribution. At the end of the Lucky Imaging exposure we will have a good measure of all necessary components to undertake a successful Fourier inverse transform and generate a high resolution output image. The technique is essentially identical to that used by radio astronomers who use radio aperture synthesis to make high-resolution maps of the radio sky. They use the technique because they require telescopes many kilometres in diameter to achieve good resolution. We realise that we cannot rely upon the telescope to combine different parts of the wavefront entering the telescope because the corrugations in the wavefront make it impossible for the telescope to produce a high-resolution

image. We are monitoring the quality of the phase front in different parts on a moment to moment basis and only using those moments when the wavefront within each of our three elements can provide a good, sharp image. Other sets of three elements will have good moments at different times, but eventually they will be able to determine what is true wavefront.

5.   CONCLUSION

EMCCDs show considerable promise for revolutionising the business of achieving high resolution imaging from the ground. We have used Lucky Imaging technique successfully on 2.5 m class telescopes and believe that the methods described above will allow similar results to be obtained at high resolution on larger telescopes.

6.   ACKNOWLEDGEMENTS

All the observations described above were made with the Nordic Optical Telescope, operated on the island of La Palma jointly by Denmark, Finland, Iceland, Norway, and Sweden, in the Spanish Observatorio del Roque de los Muchachos of the Instituto de Astrofisica de Canarias.

7.   REFERENCES

More information about Lucky Imaging and the results obtained may be found on the Lucky Imaging web site at: http://www.ast.cam.ac.uk/~optics/Lucky_Web_Site/index.htm

NOD & SHUFFLE 3D SPECTROSCOPY
3 years experience with PMAS at Calar Alto Observatory

Martin M. Roth[1], Nicolas Cardiel[2], Javier Cenarro[3], Detlef Schönberner[1], Matthias Steffen[1]

[1]Astrophysikalisches Institut Potsdam, [2]Calar Alto Observatory, [3]Universidad Complutense de Madrid

Abstract: *We present first results from nod & shuffle 3D spectroscopy, obtained with the PMAS instrument at the Calar Alto 3.5 m telescope in southern Spain. The nod & shuffle technique for accurate sky background subtraction has proven essential for the spectroscopy of faint surface brightness objects, which would otherwise be unobservable with conventional techniques. We present results from two applications: (1) measuring the line strengths of the calcium triplet lines in the optical near infrared for stellar population studies in elliptical galaxies, and (2) measuring faint diagnostic lines in the haloes of planetary nebulae to study the mass loss history of stars at the AGB. We present work in progress for these projects, which have yielded reliable Ca triplet gradient in an elliptical galaxy (NGC221) out to one effective radius for the first time, and unprecedented sensitivity in the case of haloes of planetary nebulae.*

Key words: *Integral field spectroscopy, calcium triplet, elliptical galaxies, haloes of planetary nebulae, AGB mass-loss history.*

1.   INTRODUCTION

PMAS, the Potsdam MultiAperture Spectrophotometer, is an integral field ("3D") spectrograph, which has been in operation at the Calar Alto 3.5 m Telescope since 2001 [1]. The instrument is optimized for the UV-visual wavelength range from 0.35 to 1 µm, and offers two different integral field units (IFUs): a fiber-coupled lens array (LARR) for contiguous, seeing-limited sampling with 16×16 spatial elements (spaxels), covering a field-of-view

(FOV) from 8×8 arcsec^2 to 16×16 arcsec^2, depending on the choice of magnification, and a bare fiber bundle (PPAK) with projected fiber diameters of 2.7 arcsec, covering a hexagonal footprint of 65×74 arcsec. While the FOV of the LARR IFU is relatively small in comparison with other existing instruments, it has demonstrated excellent sampling properties, enabling PMAS to record the point-spread-function of point sources with a centroiding accuracy on the m.a.s. level. PPAK, however, is presently the largest FOV IFU available worldwide. Combined with the large light-collecting area of its spaxels (2.7 arcsec fibers), it is an ideal instrument for low surface brightness objects, surpassing even 8 m class telescopes with conventional slit spectrographs and other integral field spectrographs [2].

The fiber spectrograph has a field of view of 60×60 mm^2, which is ideally suited for a 4K×4K 15 μm detector, providing 4096 pixels in the spectral direction, and the same number along the spatial direction. This is rather generous for the relatively small number of 256 spectra of the lens array, and sufficient for the 331 spectra of the PPAK IFU. The spacing for the former is 14 pixels per spectrum, which allows for an extra spectrum between each pair of nominal spectra without introducing significant crosstalk. Given this arrangement of spectra for the lens array IFU, a special variant of Nod & Shuffle (N&S) spectroscopy proposed by Glazebrook & Bland-Hawthorn, which makes use of this space, was introduced at the previous detector workshop SDW2002 [3]. The PMAS variant simply shifts the entire CCD image by 7 rows up and down the parallel charge transfer direction between sky and object exposures, thus resulting in an interlaced pattern of object and sky spectra (Figure 1).
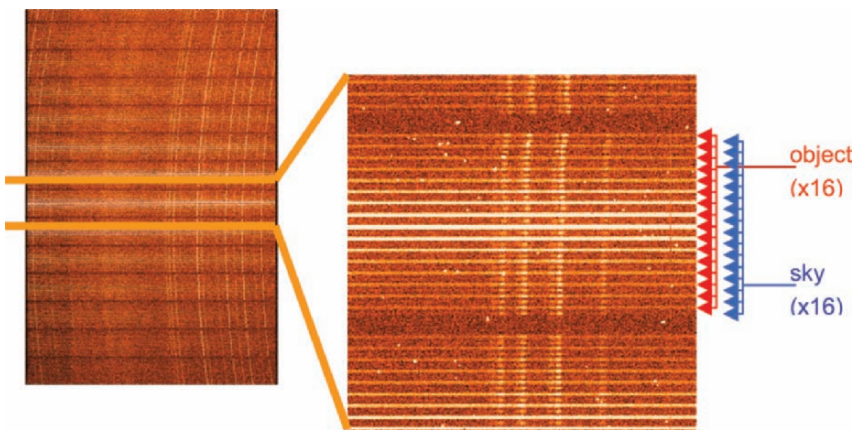
Figure 1. The interlaced N&S scheme used for the PMAS LARR IFU.

This arrangement has the advantage of 100% detector efficiency for object+sky spectra, as opposed to 66% of the conventional technique, which uses one third of the available detector space as storage area. Also, the charge transfer occurs over just 7 rows, reducing sensitivity to low charge transfer efficiency. This new interlaced N&S mode of operation was commissioned at Calar Alto in 2002 and is now available for common user programs. Here we describe the first results from two applications: (1) measuring the line strength of the Calcium triplet lines in the optical near infrared for stellar population studies in elliptical galaxies, and (2) measuring faint diagnostic lines in the haloes of planetary nebulae, to study the mass loss history of stars at the AGB.

2. THE CALCIUM TRIPLET IN ELLIPTICAL GALAXIES

As proposed by Dressler [4], the Ca II triplet lines at 8498Å, 8542Å, and 8662Å can be used as excellent diagnostic tools for measuring the kinematics and metallicity in elliptical galaxies. Such data would provide important observational tests for theoretical scenarios of galaxy formation and evolution. In this context, it would be particularly important to measure the lines' strength as a function of galactocentric radius. However, the Ca II lines are located in a wavelength region which is heavily affected by bright OH night sky lines, rendering the spectroscopy of faint surface brightness regions unreliable, i.e. in particular at large radii, which would be necessary for the determination of a line strength gradient. The situation is illustrated with an example for the dwarf elliptical NGC221 (M32), shown in Figure 2 as a 2MASS image at 1.2 μm (obtained from NASA/IPAC), and a corresponding surface brightness plot obtained as a horizontal cut through the center of the galaxy. The two crosses indicate positions of the center and of the effective radius, where the surface brightness drops by more than two orders of magnitude.

First of all, 3D spectroscopy provides a significant advantage over classical slit spectroscopy, since binning of spaxels can be used to improve the Signal-to-Noise Ratio (SNR) in low brightness regions quite dramatically ([5], see Figure 3). Secondly, spectroscopy in the faint outskirts of the galaxy will be sensitive to systematic errors occurring during the process of sky background subtraction, in particular at the wavelengths of bright night sky emission lines [6]. This is where the N&S beam switching technique provides an invaluable gain over the conventional method of obtaining object and blank sky frames at different times, as the quasi-simultaneous

N&S exposure of object and sky can be evaluated with practically zero residuals, even at the brightest sky lines (see Figure 4).
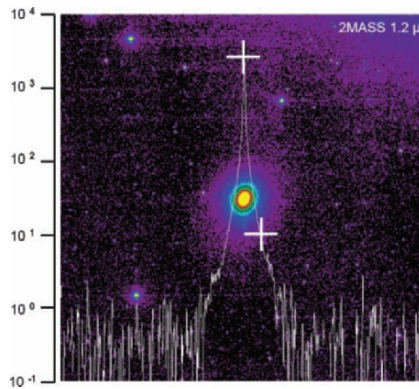
Figure 2. 2MASS image and surface brightness profile of NGC221.
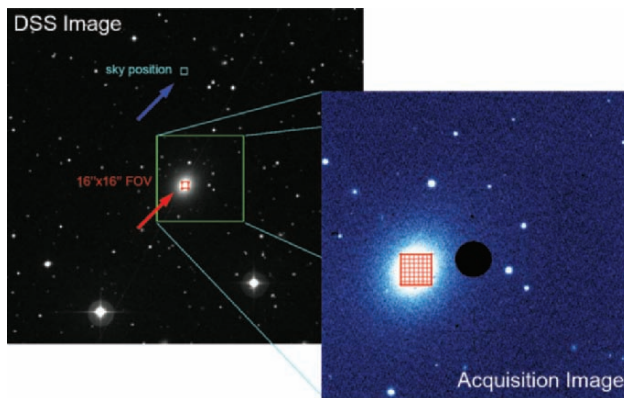
Figure 3. IFUs allow the coadding of several spatial elements to improve the SNR. Sky spectra are obtained at a blank field near the object. N&S observations involve telescope offsets form object to sky, and vice versa, while shuffling charge on the CCD as shown in Figure 1.

In a project by J. Cenarro (PI), N. Cardiel, and collaborators, to study calcium triplet gradients in elliptical galaxies, PMAS data for a total of 11 objects have been obtained from 3 observing runs in August 2003, January 2004, and May 2005. Here we present first results for the galaxy NGC221. Figure 5 shows the Ca II line strengths as a function of radius as obtained from *single spaxels* (from the center to ~ 4") , from *coadding 15-17 spaxels* (the 5 plots symbols with small error bars between 4" and 10"), and by *coadding*

the entire IFU (256 spectra) at 36" (one effective radius). Note that binning improves the SNR significantly at 4"< r < 10", even when the surface brightness has decreased with regard to the inner region. This is particularly obvious in the outer bin at 36", where a nominal SNR gain of 16× has been achieved. The error bar is of the same order of magnitude as for the central unbinned spectrum. Clearly, opening the slit to a width of 16 arcsec to achieve the same effect would be impractical for conventional spectroscopy. Translating the SNR gain into light collecting power, the equivalent in terms of telescope size would be a 14 m telescope (as opposed to the 3.5 m telescope used for these observations!).
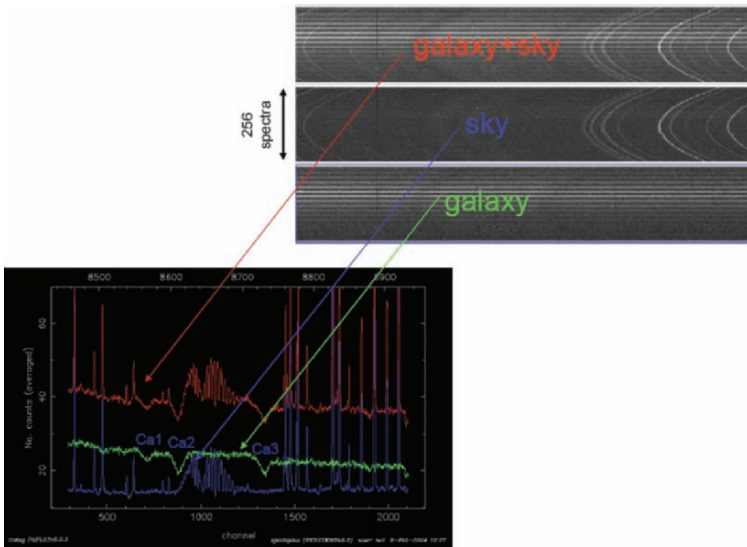
Figure 4. Sky subtraction with N&S spectroscopy, example for NGC221. The subtraction of sky from galaxy+sky is performed arithmetically at the level of corresponding CCD pixels, which have experienced nearly identical optical transmission and atmospheric observing conditions between object and sky subexposures (for technical details [3]). Data reduction and analysis performed with the *reduceme* package of Cardiel [7]. Note: This plot is shown in color in the reference plot section in the front of these proceedings.

To our knowledge, this the first time that a reliable Ca II gradient with accurate sky subtraction has been measured for an elliptical galaxy. The surprising result is that the abundance gradient is *flat*, which is in contrast with the known Mg index gradient for this galaxy [7]. Work is in progress to reduce and analyze the full sample of objects, to investigate whether this is a

peculiar property of NGC221, or whether other objects show the same phenomenon. We conclude that this is a most striking and unexpected first result, which may have a significant impact on the understanding of stellar populations in elliptical galaxies, and scenarios of galaxy evolution in general.
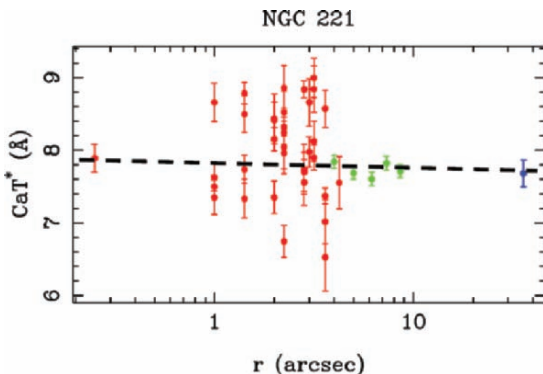
Figure 5. Ca II line strength as a function of radius for NGC221.

3.   FAINT HALOES OF PLANETARY NEBULAE

Planetary nebulae (PNe) indicate that the last phases of stellar evolution of low to intermediate mass stars (up to 8 solar masses), when the star has consumed all of its fuel for nucleosynthesis, move to a position in the HRD diagram on the tip of the Asymptotic Giant Branch (AGB), where it is extremely luminous, yet has a low surface temperature and looses copious amount of matter through strong dust-driven stellar winds. This mass-loss phase is of considerable interest for our quantitative understanding of the cycle of matter in galaxies, and the enrichment of the interstellar medium. However, the theory of mass-loss on the AGB is complicated, involving chemical processes of production and destruction of dust, stellar pulsations, and so forth. To date, different treatments of these problems have only provided largely discrepant predictions, which is why observational tests are badly needed. The PN phase, however, which follows the final period at the tip of the AGB, offers a unique diagnostic opportunity. The nebula forms when the remainder of the star shrinks and heats to temperatures of between 10^4 to 10^5 K and thus ionizes the previously ejected matter. Measuring the temperature, density, and chemical composition as a function of radius throughout the nebula, would, in principle, allow one to study the different

shells as fossil records of the mass-loss history over long periods of time. While the inner parts of PNe are usually bright in a rich spectrum of emission lines and well accessible for plasmadiagnostic tools. The most interesting early phases of mass-loss are recorded in the extremely faint *haloes* of PN, which have typically surface bright-nesses on the order of 10^{-17} to 10^{-18} erg/cm^2/sec/arcsec^2 or fainter, even for the most prominent lines like e.g. Hα, or [O III] 5007 Å. For the same reasons as explained in Sec. 2, we have employed the PMAS LARR IFU and the N&S mode of observation to increase sensitivity and sky subtraction accuracy for this challenging task, which would otherwise require substantial dark time at 8-10 m class telescopes with conventional slit spectrographs for any hope for success. Figure 6 illustrates, for an extreme case, the contrast between the faint halo emission lines (bottom spectrum), which measure on the order of 1/100 of the sky continuum, which essentially is a solar spectrum with a wealth of absorption lines (top), e.g. the prominent Ca H+K feature, and many others.
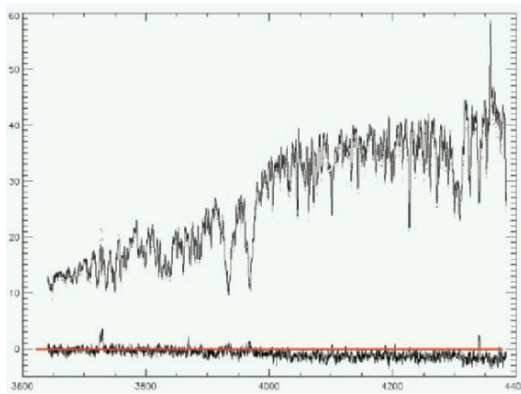
Figure 6. Sky spectrum in the blue (top), object (bottom).

These spectra are extreme in the sense that the observations were obtained 4 days from a full moon, i.e. very strongly background-limited. However, the example demonstrates the power of binning and N&S spectroscopy. As shown in Figure 7, the blue spectra obtained from the halo region outlined in the insert of Figure 8 (reconstructed map in [O II] 3727/3729 Å), where the PMAS guiding camera frame (narrowband Hα) shows no trace of emission, are just presenting noise, if only a single spaxel is selected (top panel).
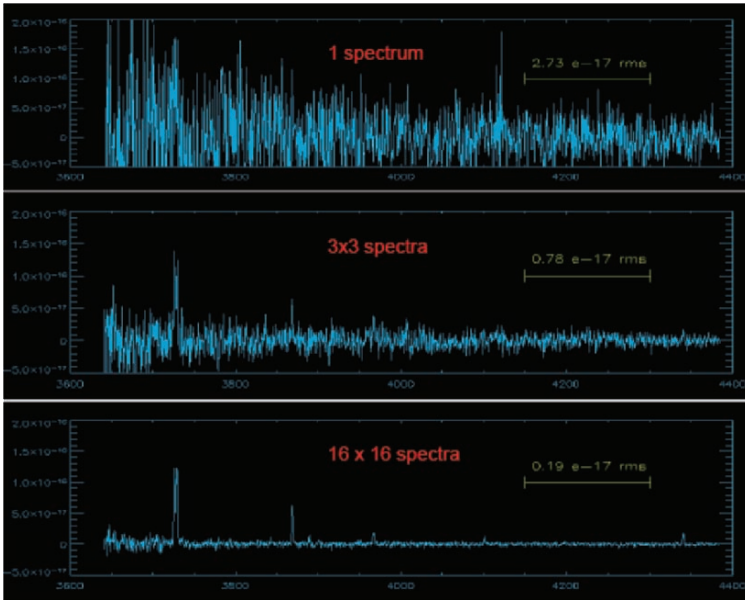
Figure 7.   Signal-to-noise gain with binning of spatial pixels. *(top)* Single spaxel, *(middle)* 9
spaxels, *(bottom)* 256 spaxels. The gains are 3, and 16, respectively.
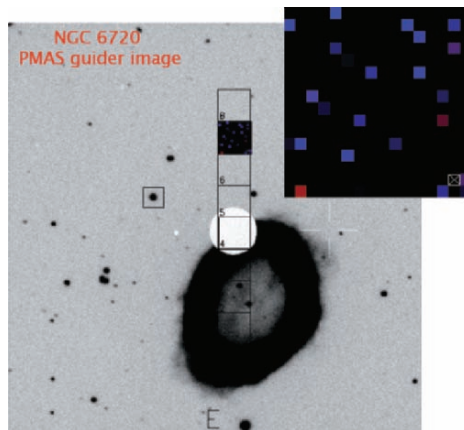
Figure 8. Halo of NGC6720, observed with PMAS IFU.

Coadding 3×3 spaxels in the same region immediately improves the SNR
by a factor of 3. When finally collapsing the entire IFU into a single

spectrum, a SNR gain of 16× is achieved, now revealing the faint emission lines of [O II], [Ne III], Hγ, etc. Note that the final spectrum exhibits a r.m.s. of 2×10^{-18} erg/cm^2/sec/arcsec^2, which is very faint considering that the spectrum was obtained with a total on-target exposure time of 3600 s near full moon. Note also that the data were obtained in N&S mode, which proved crucial for obtaining the required sky subtraction accuracy to significantly better than 1%. We have obtained comparison sky spectra *without* N&S, showing that the sky varied in intensity and colour on the order of several percent within less than 1800 s. A peculiar problem presented the presence of terrestrial emission lines, e.g. Hg 4358 Å, which completely jeopardized any attempt to measure the important nearby, but faint, diagnostic [O III] 4363 Å line that was completely swamped by a strong Hg line residual when subtraction the comparison sky exposure in the conventional way. However, as can be appreciated from the bottom panel of Figure 7, the spectrum resulting from N&S observing is completely consistent with random background noise, without any apparent sky line residuals. Although we were unable to recover the [O III] 4363 Å line owing to its faintness and the continuum sky noise floor near full moon, we estimate that with 2-3 hours of observing under grey to dark conditions the line will become measurable. In addition to our example of NGC6720, we have obtained data from 3 observing runs in Feb. 2003 and Aug. 2004 for a total of 6 PNe, with more observations expected in September 2005.

4.   SUMMARY

We have obtained low surface brightness 3D spectroscopy using PMAS at the Calar Alto 3.5m telescope for two scheduled programs (early type galaxies, PN haloes), demonstrating that N&S with IFUs is indeed capable of achieving extremely accurate sky subtraction with a sensitivity surpassing 8-10 m class telescopes, whenever spaxel binning is employed. Our results also suggest new avenues to efficient use of large telescopes for faint surface brightness spectroscopy even under grey and bright night sky conditions.

5.   REFERENCES

[1] Roth, M., et al. 2005, PASP **117**, p. 620.
[2] Verheijen, M., et al. 2004, AN **325**, p. 251.
[3] Roth M., et al., 2004, Proc.Scientific Detectors for Astronomy, Amico, P., Beletic, J. W., Beletic, J.E., Kluwer, Dordrecht.
[4] Dressler A. 1984, ApJ **286**, p. 97.
[5] Cappellari, M., Copin, Y., 2003, MNRAS **342**, p. 345.

[6] Glazebrook K., Bland-Hawthorne J. 2001, PASP **113**, p. 197.

[7] Cardiel, N., 1999, PhD Thesis, Universidad Complutense de Madrid.

[8] Sanchez-Blazquez, P., 2004, PhD Thesis, Univ. Complutense de Madrid.

Martin Roth enjoys speaking German in Italy with Rainer Kramm and Sebastian Deiries, while overlooking the sea at the plaza in Forza d'Agró.

Nicholas Haddad, Sandro D'Odorico, Gustavo Rahmer and Olaf Iwert play "musical shoes", and it appears that Gustavo has lost.

DETECTOR SYSTEMS FOR THE MODS SPECTROGRAPH

Bruce Atwood, Daniel Pappalardo, Mark A. Derwent, Thomas P. O'Brien
Ohio State University

Abstract: *The detector plan for the four cameras on the work-horse spectrograph of the world's largest optical telescope, the Large Binocular Telescope, is presented. The two cameras of MODS 1 will be outfitted for initial deployment in November, 2006 with 4K×4K detectors processed by the University of Arizona Imaging Technology Laboratory. A custom run of 8192×2880 detectors is in preparation. These larger detectors will be used for MODS 2 and retrofits to MODS 1. The dewar and electronics design are outlined. Projections of the limiting magnitude for the completed spectrograph at S/N=5 and 10 are given.*

Key words: *Large Binocular Telescope (LBT), spectrograph, MODS.*

1.   INTRODUCTION

MODS, fully described by Osmer [1] and Byard [2], will be the work-horse optical spectrograph on the 11.8 m equivalent diameter LBT [3] over the wavelength range of 300 to 1000 nm with resolutions, as we purchase a full compliment of gratings, of 2000 to 16000.

2.   THE MODS DESIGN

It is said that in optical design anyone can add surfaces, the trick is to take them out while still getting the job done. Minimizing the number of surfaces reduces cost and increases throughput. We have adopted a very simple, traditional design for astronomical grating spectrographs: a

decentered paraboloid collimator and a Schmidt camera. A removable dichroic beam splitter located just behind the slit directs the incoming light to separate red ($\lambda > 500$ nm) and a blue ($\lambda < 500$ nm) channels. The red and blue optimized collimators produce a 230 mm diameter beam for the red and blue four-position grating turrets. Dispersed light travels from the gratings to red and blue cameras that, while similar in design, use different materials, coatings and prescriptions. MODS includes full multi-slit capability over the arc-min field with a 25 position mask interchange mechanism. Also included are flat field and wavelength calibration systems and a guide and wavefront-sensing camera, which provides the signal to the LBT active optics system.

The opto-mechanical modules are supported on a welded steel space frame. While the frame is designed to have low hysteresis, displacement of the spectra on the detectors due to the variable gravity vector and thermal gradients would be unacceptable. An image motion compensation system, described by Marshall [4], is included to reduce this flexure to an acceptable level. An IR reference beam is launched from the telescope focal plane and passes through all the optics of the spectrograph with the exception that strikes a small "by-pass" grating mounted in a hole in the main gratings. A germanium quad cell in the detector plane generates an error signal which steers the collimators to maintain the spectra in a fixed location on the detectors.
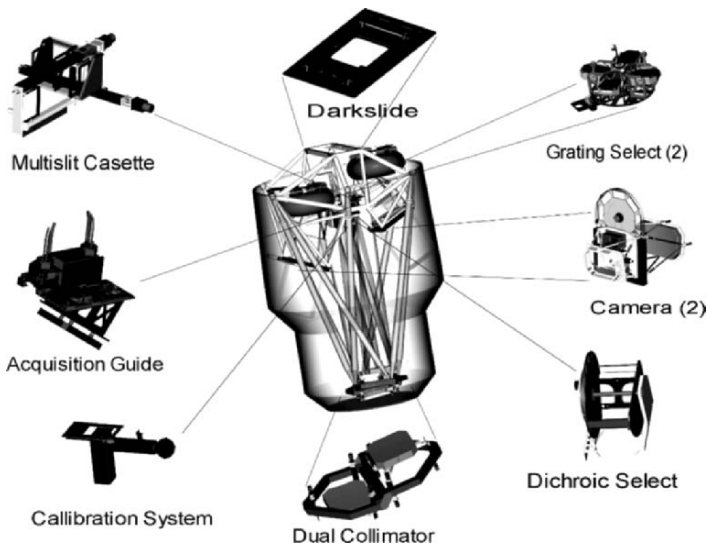
Figure 1. A computer model of the structure and the 10 sub-assemblies of MODs.

A total of 30 stepper motors are used to position the optics. All motors are driven by controllers from Micro-Lynx. Mechanism positions are sensed with proximity switches. Linear motions are accomplished with ball screw slides that include spring-applied/electrically-released breaks. A computer model of the structure and the 10 sub-assemblies is shown in Figure 1.

All mechanisms have been fabricated and are now in testing. The collimator, camera mirrors and small optics are complete. The camera correctors are in fabrication. On site commissioning will begin in the 3rd Q 2006.

3.   THE CAMERAS

Historically, cameras for astronomical spectrographs have needed faster f-ratios as telescope size has increased. This simply reflects that the desired slit width in arc-sec and physical pixel size remained relatively constant. LBT and MODS represent a significant departure from this trend in two ways. LBT (and many of the current generation of telescopes) will produce seeing-limited images that are significantly smaller than previous images. The basic seeing limited-slit width for MODS is 0.6 arc-sec. The MODS cameras have a large focal plane, 120×43 mm, and will be outfitted with detectors with high pixel count, 4096×4096 initially and 8192×2880 when our custom detectors are ready. This allows us to bin pixels for low resolution work in average conditions and still operate at higher resolutions, both spatial and spectral, when conditions warrant. In addition, since LBT is an adaptive optics telescope, MODS has been designed to take advantage of modes such as ground-layer correction by providing scales as fine as 0.12 arc-sec/pixel. The combination allows us to use a relatively slow f/3 camera. The decentered Schmidt design has the advantages of no vignetting and ghosts from the detector are not returned to the grating. The computer model of the MODS blue cameras is shown in Figure 2. Figure 3 shows a picture of the one of the cameras, without optics, on its handling cart. The support structure of four spectrograph cameras [5] consists of a center bulkhead, which mounts to the spectrograph structure, and cells for the primary mirror and corrector which are attached to the center bulkhead with a thermally compensated truss system. The center bulkhead holds the filter wheel and the shutter.
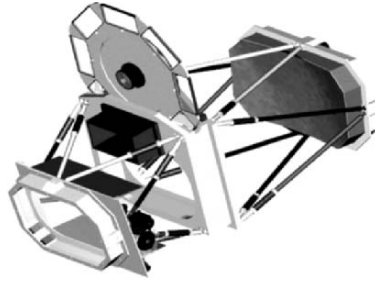
Figure 2. The computer model of the MODS blue cameras.
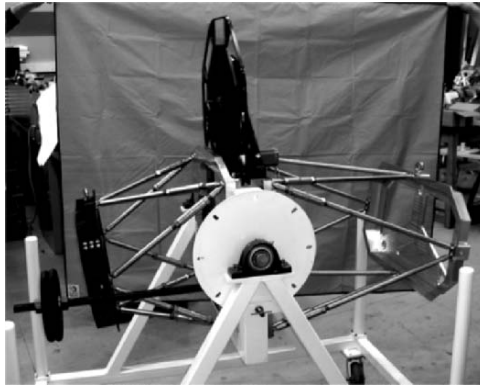
Figure 3. A picture of the one of the cameras, without optics, on its handling cart.

4.   MODS DEWARS

The dewar for the MODS camera, now out for bid, is shown in Figure 4. The design philosophy is described by Atwood [6]. An 8 liter capacity LN2 tank will give a hold time >30 hours. A cold link connects the LN2 reservoir to the detector box which will house either the 4K×4K or 8K×3K CCD. Vacuum is maintained by a cold charcoal to pump N2 and O2 and room-temperature zeolite to keep the interior of the dewar dry even when warm. The zeolite is mounted on the inside of an access port so that it can be changed without disassembling the dewar. The camera field flattener lens is the vacuum window. A convectron gauge is included to measure pressures from atmospheric to ~1mTorr while an ionization gauge is used from 10 mTorr to high vacuum.

Figure 4. The dewar for the MODS camera, now out for bid.

5. FIRST LIGHT AND CUSTOM DETECTORS

MODS will be initially commissioned with 4K×4K STA0500A CCDs, thinned, coated and packaged by the University of Arizona's Imaging Technology Laboratory. The development of these devices is described by Lesser [7] and Bredthauer [8]. The quantum efficiency of both the red and blue detectors is shown in Fig. 5. A schematic of the 8K×3K detector, now in development at the Imaging Technology Laboratory and Scientific Detector Associates, is shown in Fig. 6. The custom detector will include ability for use in split frame-transfer mode, with a removable light shield for the storage section to allow reading of a previous exposure while exposing on the center half. This mode comes at the expense of using only ½ the total slit length. The custom device will have 32 floating gate amplifiers, 8 on each corner, which will be used in two modes. For fast readout, each pixel will be read from a single amplifier, but 32 pixels will be read simultaneously. We anticipate that reading the entire device, with no binning, will take less than 20 seconds. By reading each pixel with 8 amplifiers and averaging the signals we expect a reduction of the read noise of about a factor of ~2.8. In addition, a conventional floating diffusion amplifier will be located in each corner as a risk mitigation measure.

6. ELECTRONICS

The control electronics is based on the Ohio State ICIMACS which is described by Atwood [9] and Atwood [10]. The 32 channel clock bias board, shown in Figure 7 with 8 channels installed, will essentially remain unchanged while the post-amplifier daughter boards will include on-board ADCs. The sequencer is being ported from the ISA bus to PCI.
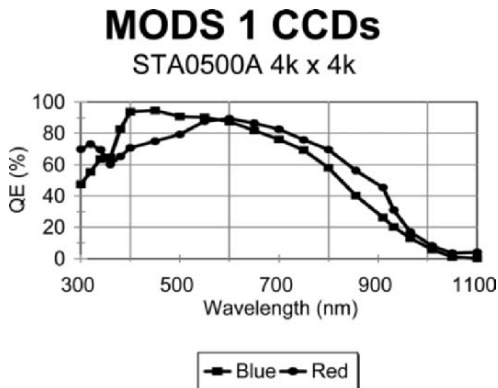
Figure 5. The quantum efficiency of the both the red and blue detectors.
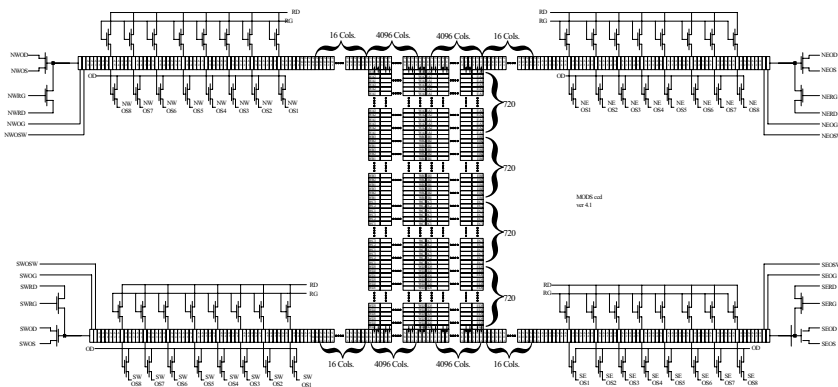
Figure 6. A schematic of the 8K×3K detector, now under development with the Imaging Technology Laboratory and Scientific Detector Associates.
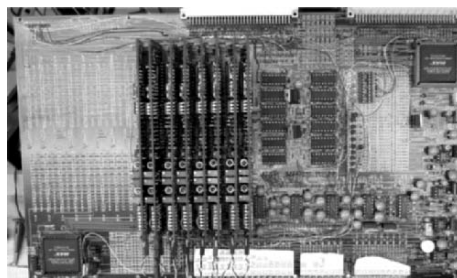
Figure 7. The 32 channel clock bias board.

7.   EXPECTED PERFORMANCE

The expected limiting magnitudes for S/N=5 and 10 from 1 hour exposures as a function of read noise in a single pixel are presented in Figures 8 and 9. Included are the effects of sky noise, readout noise, combining the signal from the two MODS, the size of a resolution element, and system throughput. In addition to plots for resolution of 2000, 8000, and 16,000, calculations were done for slit widths of 0.6 arc-sec, 0.3 arc-sec and 0.15 arc-sec, which correspond to admitting sky light from 0.36, 0.09 and 0,0225 arc-sec^2.
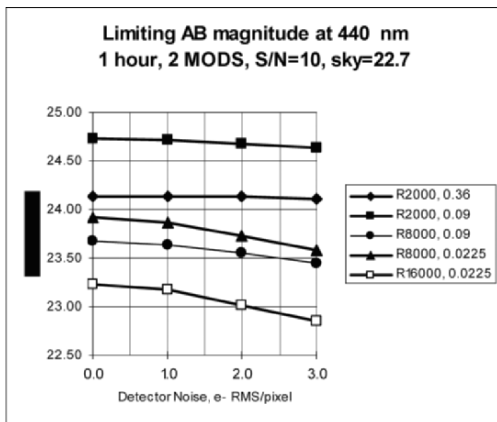
Figure 8. The expected limiting magnitudes for S/N=5 and 10 from a 1 hour exposures as a function of read noise in a single pixel.
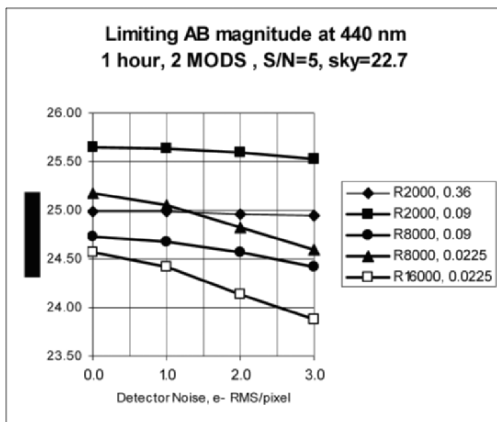
Figure 9. The expected limiting magnitudes for S/N=5 and 10 from a 1 hour exposures as a function of read noise in a single pixel.

8. REFERENCES

[1] Osmer, P.S., et. al., 2000, Proc. SPIE **4008**, p. 40.
[2] Byard, P.L., O'Brien, T. P., 2000, Proc. SPIE **4008**, p. 934.
[3] http://medusa.as.arizona.edu/lbto
[4] Marshal, J.L., Atwood, B., Byard P.L., DePoy D.L., P. O'Brien T.P., Pogge R.W., 2004, Proc. SPIE **5492**, p. 739
[5] Atwood, B., O'Brien, T.P., 2003, Proc. SPIE **4841**, p. 403.
[6] Atwood, B. et al., 2000, Further Developments in Scientific Optical Imaging, M. Bonner Denton (ed.), The Royal Society of Chemistry, Cambridge, UK, p. 176.
[7] Lesser, M. and Bredthauer R., 2000, Further Developments in Scientific Optical Imaging, M. Bonner Denton (ed.), The Royal Society of Chemistry, Cambridge, UK, p. 111.
[8] Bredthauer, R., 2005, these proceedings,
[9] Atwood, B. et al., 1998, Proc. SPIE **3355**, p. 560.
[10] Atwood, B. et al., 2000, Further Developments in Scientific Optical Imaging, M. Bonner Denton (ed.),The Royal Society of Chemistry, Cambridge, UK, p. 80.

This workshop was graced by the company of two of the Atwood girls, Bruce's wife Ana Maria and his daughter Stephanie. Here, Ana Maria toasts Bruce and Mark Downing, while in the background the SciMeasure gang scopes out new customers.

RECENT PHOTON COUNTING DEVELOPMENTS AT THE OBSERVATOIRE DE MARSEILLE

Philippe Balard[1], Philippe Amram[1], Olivier Boissin[1], Jacques Boulesteix[1], Olivier Daigle[2], Jean-Luc Gach[1], Olivia Garrido[1], Olivier Hernandez[1,2], Michel Marcelin[1]
[1]Observatoire de Marseille, [2]Laboratoire d'Astrophysique Expérimentale

Abstract: *We present a new generation photon counting system based on a full software centering system developed at the Observatoire de Marseille. Since the photon counting systems were developed, several improvements have been made on the camera head, whereas centering systems have evolved somewhat slower. The major improvement made on the presented photon counting system is the use of a fast software algorithm for running on a standard PC computer. This system exhibits outstanding photon counting capacity compared to previous hard-wired or DSP-based centering systems, as well as a remarkable cost / performance ratio.*

Key words: *photon counting, centroiding, fast CCDs, GbEthernet, frame acquisition.*

1.   INTRODUCTION

   Photon counting systems have been in use at the Observatoire de Marseille for more than 2 decades. However, a new generation of GaAs and GaAsP photocathodes with high Quantum Efficiency (QE), and proximity-focused image intensifiers without image distortion has been introduced. These are associated with fast frame readout rate and large-format CCDs that can be used as detectors behind the image intensifier, leading to large-format IPCS [1]. This paper will present the evolution of the system over the last few years [1]. Section 2 will describe the camera head and cooling system,

section 3 the acquisition path, and section 4 the centroiding system. Finally, future developments will be discussed in section 5.

2.   CAMERA HEAD AND COOLING SYSTEM

The camera head is composed of a GaAs proximity-focused two-stage microchannel plate (MCP) image-intensifier tube, optically coupled to a 1K×1K 60 frames per second (fps) CCD. The CCD can work in 1K×1K mode (12 µm pixels) at 60 fps or in 2×2 binning mode, 512×512pixels at 100 fps (24 µm pixels). Each photon interacting with the photocathode is amplified up to $10^6 \sim 10^7$ times by the image intensifier, producing a signal much larger than the internal noise of the CCD.

The head was previously cooled by a Ranque-Hilsch vortex tube. A vortex tube uses compressed air as a power source and produces hot air from one end and cold air from the other, with no moving parts. Differential temperatures close to 70°C are possible between compressed air and cold air. Hence, the flow of cold air passes through the cryostat chamber in front of the GaAs proximity-focused image-intensifier tube. The unused calories are directed toward a heat exchanger to cool compressed air before it travels through the vortex tube. The system has implemented at various telescopes, including CFHT in Hawaii and the ESO 3.6 m telescope of La Silla in Chile.

Although remarkably efficient in cooling, this system has several drawbacks. The first is the need for compressed, dry air in large quantities (300 l/min at 8 bar pressure), which in turn requires a suitable compressor and air dehydrator on site, adding about 150 kg to the weight of the system.

The new system uses Peltiers to generate enough cooling to maintain a –30°C temperature at 20°C ambient, using water to pull out the excess heat towards an external water/air exchanger. The cold is confined within the camera head, reducing the thermal loss to a minimum. Due to this redesigned camera head and cold finger, the system is more compact than the previous one with the Ranque-Hilsch tube. The external compressor, dehydrator and expansion tank have all been replaced by a small forced air flow heat exchanger that fits in a standard 19" rack, removing the need for the long plumbing that was used to carry the compressed dry air. Overall, this new head makes the system highly transportable and more reliable than before.

3. IPCS DATA ACQUISITION PATH

Contrary to classical imaging, photon counting needs to be fast to avoid the stacking of events as much as possible. Two photons (or more) falling on the same pixel during a single frame are usually counted as a single event, which leads directly to a severe loss in QE. The mean fraction of missed photons, *M,* can be evaluated assuming a Poissonian process for the photon emission with Eq. 1:

$$M = 1 - \frac{1 - e^{-\lambda}}{\lambda} \tag{1}$$

where λ is the mean number of photons expected during the resolved period of the detector. To counteract that phenomenon it is necessary to use a fast CCD as shown in Fig.1.
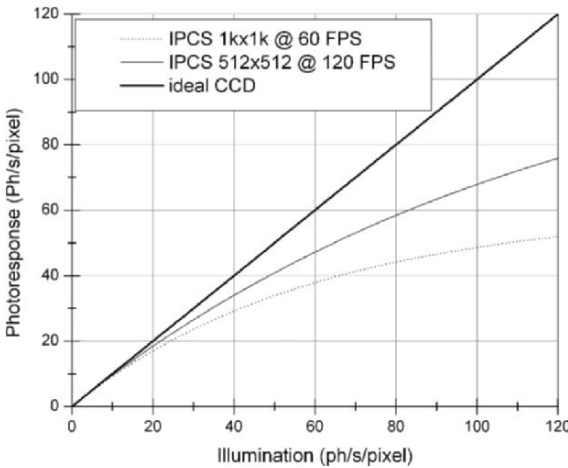
Figure 1. Photoresponse of an IPCS pixel with respect to illumination.

This need for speed leads to naturally high data rates. The previous camera we used was a 1K×1K, 40 images per second (fps) CCD. Sampled at 8 bits per pixel this sustains a flat 40MB per second datarate. Moving this amount of data from the telescope to the host computer was not completely trivial as LVDS signaling only allows for 5 m cables with our data rate. This problem was solved by designing a point-to-point dedicated 1.5 Gbits/s transmission over optic fibers. Signal from the camera was transferred over

the fiber link, then back into LVDS before acquisition by the host computer using a DSP-based frame grabber.

The new system uses a 1K×1K camera at 60 fps (operation at 512×512, 100 fps is also possible) CameraLink standard. As the connectivity changed, this led to a redesign of the linking between camera and host, as well as a 50% increase in data transmission rates.

In the last couple of years we have seen gigabit ethernet over twisted pair become more and more mainstream, up to the point where it is now included in almost every motherboard on the market. With data rates up to 100 MB/s, Gb Ethernet is a viable solution to carry image data up to about 80 MB/s (to take network overhead into account), provided the data moves on a dedicated line that has no other traffic.

We replaced the dedicated point-to-point Fiberoptic link by a CameraLink / GbEth. translator that connects to an ubiquitous Cat. 5e or 6 twisted pair cable, allowing for very easy maintenance and replacement of failing parts from anywhere in the world.

Image acquisition in itself is also simplified. Whereas previous systems had to use frame grabbers to obtain image data, the new one simply uses the network adapter from the motherboard, making again for a much easier to replace acquisition computer should the need arise. It even allows for operation from a laptop computer.

4.   SOFTWARE ACQUISITION AND CENTROIDING

Photon counting using MCPs concerns speed in the analysis of images. The data rates are high so the computing needs to be fast. Initially automatic systems used hardwired circuits to perform centroiding. Then DSP-based systems became available, allowing for more counting capacity and arbitrary impact shape.

The processing power of computers has greatly improved in the past years, and it has become possible to replace 14 DSPs with a single CPU. Using the prior TMS320C80 multimedia video processor with 4 previously state-of-the-art (ca. 1999) DSP we used to manage a counting capacity of 1.6×10^4 impacts per second. These were scalable as we added more processors, but with the challenge of fitting all the boards inside the computer.

Using a single processor at 3.0 GHz with hyperthreading, (which is hardly state of the art nowadays), the new acquisition software we can handle a load of 1.5×10^6 impacts per second, 2 orders above what was the previous limit. Moreover, the 1.5 million impacts per second figure is a limitation of the CCD itself rather than processing power. At these light

levels the impacts begin to stack on our camera, leading to *less* events as light increases. This shows that, using fully software centroiding, the limiting factor for photon counting becomes the camera, not the processing power.

The acquisition software obtains the image from whatever source is available (Frame Grabber, Ethernet link, test image). A 1-bit image is then produced according to the detection level at which a pixel is considered valid. This 1-bit image selects the pixels to be used in the centroiding, which is based on the actual value (8 or 16 bits or more) of the pixels, leading to a more precise positioning of the event as the previous system that simply used binary data. The event's position is computed using a center-of-gravity computation, weighted by the actual pixel value.

As for the previous system, the acquisition software is fully capable of operation in multiprocessor computers, being heavily multithreaded it is particularly well suited for operation on dual-core processors.

Another advantage of using a fully software solution, coupled to Ethernet acquisition, is that it is easy to make the system more powerful: just replace the computer. It is the same in case of hardware failure: just plug in another computer, install the software and continue operation. It is also approximately 1 order cheaper than DSP-based systems due to the absence of an expensive frame grabber inside the host.

5.   FUTURE DEVELOPMENTS

We reduced size, optimized and simplified cooling, added 2 orders in counting capacity, divided costs by an order and added reliability and capability of upgrades. The next improvements we foresee are as follows.

For faint fluxes (in processing, anything below 2×10^5 impacts/s can be considered faint), where the system is nearly at idle levels one could imagine replacing the easy-to-compute center of gravity centroiding by a Gaussian fit, this would allow for intra-pixel accuracy. Adding even *more* counting capacity, by using more powerful processors (like a dual-core 64-bit processor, or several) could lead to interesting investigations at the limit between photon counting and classical imaging. It may be possible to do photon counting at light levels previously judged too high, gaining the absence of read noise of photon counting.

6.   REFERENCES

For more information on photon counting cameras, see the following papers:

[1] Blazit, A., Bonneau, D., Koechlin, L., & Labeyrie, A. 1977, ApJ, 214, L79.
[2] Blazit, A. 1985, in ESA Colloq. on Kilometric Optical Arrays in Space, ed. N. Longdon & O. Melita (ESA SP-226; Cargèse: ESA), 155.
[3] Boksenberg, A. 1977, in IAU Colloq. 40, Astronomical Applications of Image Detectors with Linear Response, ed. M. Duchesne & G.Lelièvre (Paris: l'Observatoire de Paris-Meudon), 13.
[4] Boulesteix, J., & Marcelin, M. 1980, in ESO Leiden Workshop on two-dimensional Photometry, ed. P. Crane & K. Kjär (Garching, ESO), 119.
[5] Foy, R. 1988, in Proc. 9th Santa Cruz Summer Workshop in Astronomy and Astrophysics, ed. L. Robinson (Berlin: Springer), 589.
[6] Gach J-L, Darson D., Guilllaume C., Goillandeau M., Cavadore C., Boissin O., Boulesteix J. 2003, PASP 115, p. 1068.
[7] Thiebaut, Eric; Abbe, L.; Blazit, Alain; Dubois, Jean-pierre; Foy, Renaud; Tallon, Michel; Vakili, Farrokh. CPng: a high sensitivity photon-counting camera 2003 SPIE.4841 p 1527.

Good conversation and great cheer can always be found at the "French Quarter"
(see also p. lviii).

A CMOS SENSOR FOR SOLAR OBSERVATION
CALAS (Camera for the Large Scales of the Solar Surface)

Francis Beigbeder, Sylvain Rondi, Nadège Meunier and Michel Rieutord
Observatoire Midi-Pyrénées (OMP), Laboratoire d'Astrophysique

Abstract: *CALAS is an instrument whose purpose is to observe a large field of view with a very high spatial resolution at the highest temporal cadence, so as to ideally sample the Earth atmospheric distortion. The aim of this project is the study of the dynamics of solar supergranulation. It will be installed on the "Lunette Jean Rösch" (a 50 cm diameter refractor) at the Pic du Midi Observatory.*

We chose a 3952×4064 pixel monolithic CMOS detector, and in this paper explain the reasons to use such a detector for this niche of solar observation. We also briefly describe the controller, acquisition system and opto-mechanical parts of the instrument. More information on the project can be found at http://bass2000.bagn.obs-mip.fr/calas/.

Key words: *FillFactor,y CMOS, Active Pixel Sensor (APS), IBIS16000, ARC GenII controller, CORECO X64-LVDS PCI-X frame grabber.*

1.   SCIENTIFIC GOALS

The origin of supergranulation (convective or not), a dynamic pattern at the 30 Mm scale at the surface of the Sun, is still much debated. Among various possible approaches, one way to study supergranulation is to observe the horizontal motions of granules.

Furthermore, the turbulent properties of granulation and supergranulation remain to be studied in detail. It is therefore crucial to study the dynamics of the solar surface over a very wide range of scales, from a fraction of Mm to sample granules to several hundred Mm to observe many supergranules.

A combination of a very large field-of-view (in order to see as many supergranules as possible), a very high spatial resolution (to sample granules

with a high accuracy) and a high cadence (to enable the removal of Earth atmospheric distortion) is necessary to study this pattern in detail [1, 2].

The main objective of CALAS is to allow the sampling of granules with a high spatial resolution on a 10'×10' field-of-view (~ 300 supergranules) as a step towards a covering of the whole solar surface (30' arcminutes).

2.   DETECTOR

We need a detector that meets the following requirements: large field (~10'×10'), high resolution (0.14"), and high cadence (readout time less than 0.5 second), but also very short exposure time (a few milliseconds). We considered CMOS detectors for some of their intrinsic qualities: fast readout, easy control and potentially low cost. Furthermore we plan to build a mosaic that will cover the entire Sun (30'×30') with the same resolution, which requires a 165 Mpixels detector. For low exposure time an electronic shutter is essential as it is impossible to have a large and fast mechanical shutter with a sufficient MTBF for a continuous acquisition. Low power consumption is also advantageous for a mosaic.

We chose the IBIS16000, a 3952×4064 CMOS Active Pixel Sensor from Fillfactory (see Fig. 1). When processed with the tower TS50 TLMDP method this sensor has a pixel size of $12×12$ μm^2 and on chip double sampling correction circuitry to remove the fixed pattern noise caused by non-uniformities in threshold voltages of the readout electronics [3,4].

The sensor is read out through four parallel analog outputs, which can be multiplexed to one single output. The gain of the output amplifiers is digitally controllable by the user.

This sensor has three transistor active pixels with maximized fill factor. It allows several options: subsampling readout modes in x and y, rolling shutter, programmable gain and offset output voltage.
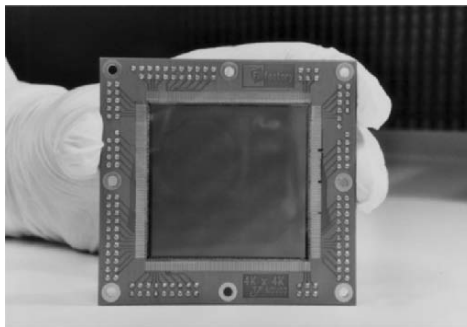
Figure 1. Fillfactory IBIS16000 CMOS detector.

Table I shows characteristics given by the manufacturer. We intend to confirm theses with a complete characterization of this detector in the near future.

Table I. IBIS16000 Characteristics

Resolution	3952×4064
Pixel size	$12 \times 12 \ \mu m^2$
Spectral sensitivity	400 – 1000 nm
Peak QE * fill factor	> 40% in 550 - 650 nm
Fill factor	> 70%
Photodiode capacitance	25 fF
Conversion gain	8.3 μV/e-
Output voltage swing	1.6 V
Full well charge	240000 e-
Linear full well charge	160000 e-
Temporal noise at 21°C	60 e-
Signal to noise ratio	4170:1, linear: 2800:1
Dark current at 21 °C	120 pA/cm2, 900 e-/s
Pixel rate	10 MHz
Outputs	4 or 1 (multiplexed)
Frame rate	2.5 frames/s
Supply Voltage	5 V
Reset Voltage	6 V
Power dissipation	250 mW

3.   CONTROLLER

To control the CMOS sensor we use a customized timing board of a classical ARC GenII controller. We have developed a four-channel analog converter and LVDS interface board (see Fig. 2).

This unique architecture allows us to link the ADC output to the acquisition system (4×10 MHz) in parallel, avoiding the rate limitation of the normal ARC controller link to the host (12.5 MHz).

The DSP code allows us to read the detector with global or rolling shutter and generates the control signals for the frame grabber.

Figure 2. Test controller, analog & timing board.

4.   ACQUISITION SYSTEM

The acquisition system consists of a work station under Windows XP equipped with a CORECO X64-LVDS PCI-X frame grabber, and a 64-bit image acquisition board for parallel output, digital cameras. It allows image transfer to host memory at a rate of 528 MB/s. Used here with four 14-bit taps configuration it is able to unscramble the incident data online.

We plan to have a Network Attached Storage (NAS) with several Tera Bytes of capacity to save a run of 2 or 3 days of observation.

5.   OPTICAL PATHS

This instrument will present two optical paths in parallel (see Fig. 3):

- Direct imagery, in G-band (430.5 nm) allowing the tracking of granules and network bright points (a proxy for magnetic flux tubes). A 2.7 times enlargement of the focal image is made with two doublets.
- Magneto-Optical Filter (MOF) imagery [5] that will permit to get both a Dopplergram and a magnetogram of the solar surface, using four individual images, in a Potassium line at 770 nm. The same enlargement (2.7 times) of the image is achieved with three doublets and a triplet, as the beam needs to go through the two 100×25mm cells of the MOF (see Fig. 4).
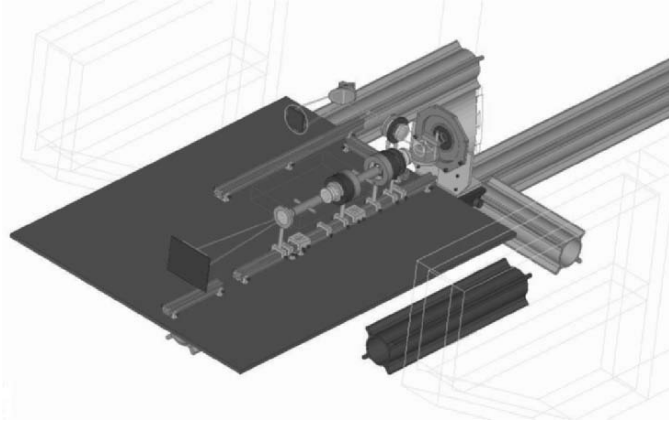
Figure 3. Opto-mechanical design.

Figure 4. Optical beam of the MOF channel.

6. REFERENCES

[1] Meunier, N., Rieutord, M., and Beigbeder, F., 2003, F., *CALAS: a Camera for the Large Scales of the Solar Surface,* Semaine de l'Astrophysique Française, Bordeaux, June 16-20-2003, Combes, F., Barret, D., Contini, T. and Pagani, L., (editors), (EDP-Science Conférence Série, 2003), p. 93.
[2] Meunier., M., Rondi, S., Tkaczuk, R., Beigbeder, F., and Rieutord, M., 2004, *CALAS a Camera for the Large Scales of the Solar Surface*, 22th Sacramento Peak Solar Workshop, October 2004, (in press).

[3] Meynants, G., Dierickx, B., and Scheffer, D., 1998, *CMOS Active Pixel Image Sensor with CCD performance*, AFPAEC Europto/SPIE, Zurich, 18-21 May 1998; proc. SPIE, vol. **3410**, pp. 68-76.

[4] Dierickx, G., Meynants, G., and Scheffer, D., 1997, *Offset-free Offset Calibration for APS,* IEE CCD & AIS workshop, Brugge, Belgium, 5-7 June Procceedings*,* p. R13.

[5] Cacciani, A., Varsik, J., and Zirin, H., 1990, Solar Phys. **125**, 173.

Francis Beigbeder prepares for the pizza eating contest.

PLASMA CLEANING
A New Method of Ultra-Cleaning Detector Cryostats

Sebastian Deiries, Armin Silber, Olaf Iwert, Evi Hummel, Jean Louis Lizon
European Southern Observatory

Abstract: *First results are reported from the application of a plasma-based method to ultra-clean detector cryostats. The device used is a LFG40 controller from Diener electronic in conjunction with a Kendro VT6060M vacuum oven. This technology considerably extends and enhances the cleaning methods used by ESO as described at SDW2002 [1]. While it cannot replace these earlier methods, it requires their previous application. Its virtues are speed and ease of application. Particularly attractive is the possibility of treating a previously cleaned or lightly contaminated cryostat without prior disassembly (but with detectors removed), e.g., after it has been re-opened for corrective action.*

This paper describes the principles of plasma cleaning, its general technical realization, practical applications, and possibilities for adaptation to specific needs. Various qualitative and quantitative measures of the efficiency are presented and as an example of successful plasma-cleaning: the very large OmegaCAM cryostat [2].

Key words: *Cleaning, contamination, CCD cryostat, plasma, UV sensitivity.*

1.   INTRODUCTION

Detector cryostats are often affected by contamination, which can especially decrease the blue and ultra-violet sensitivity of CCD detectors. Infrared detectors seem to be less sensitive to contamination, but there is no alternative to an ultra-clean detector cryostat. Conventional cleaning methods like mechanical and chemical cleaning followed by a baking procedure give good results [1]. However, while investigating processes followed in industry we found that ultra-cleaning can only be obtained by a final cleaning step of plasma cleaning.

Plasma cleaning is an easy, inexpensive method requiring simple installations. It is low risk and excellent cleaning results can be obtained within a few hours of receiving the necessary equipment.

2.   CONVENTIONAL CLEANING

Conventional cleaning of detector cryostats consists of mechanical rough cleaning by tissues or other tools followed by ultrasonic cleaning with special detergents [1]. The parts are then rinsed in de-mineralized water or bathed in acetone and/or alcohol, dried and baked to their individual maximum temperature up to 160ºC in a vacuum oven.

Experience shows that residuals and traces of organic contaminations on surfaces and in cavities remain even after this rigorous process. These can affect the detector performance after left cold for several months of operation at the telescope site.

3.   PLASMA CLEANING PROCESS

Plasma cleaning is suitable for removing very thin films, especially hydro-carbonates and oxides, which remain after conventional cleaning. It is important to choose the correct plasma gas, as gases react and work in different ways at removing contaminants. Oxygen removes contaminants by oxidation and reduction (see Fig. 1). Other neutral gases like Argon clean by sand-blasting surfaces.

4.   REALIZATION OF PLASMA CLEANING

An existing vacuum oven (Kendro VT6060M) was modified by introducing a high voltage anode through a vacuum feed-through at the backside (see Fig. 2). A strong dry vacuum pump (Alcatel ACP28) was used to quickly pump the insides of the oven to approx. 0.1 mbar. Ambient air or gas from a bottle (we tried synthetic air, oxygen or Argon) produces a constant gas stream regulated by the oven gas valve through the oven giving a pressure of 0.1–1 mbar. This is the optimum pressure to ignite the plasma with the connected LFG40 plasma controller from Diener Electronic [3]. Oxygen is the best cleaning gas for aluminium and stainless steel parts. Hydrogen is best for cleaning of noble metals. However, ambient air is sufficient for a good cleaning of most materials. Normal cleaning time takes no longer than 10 minutes.
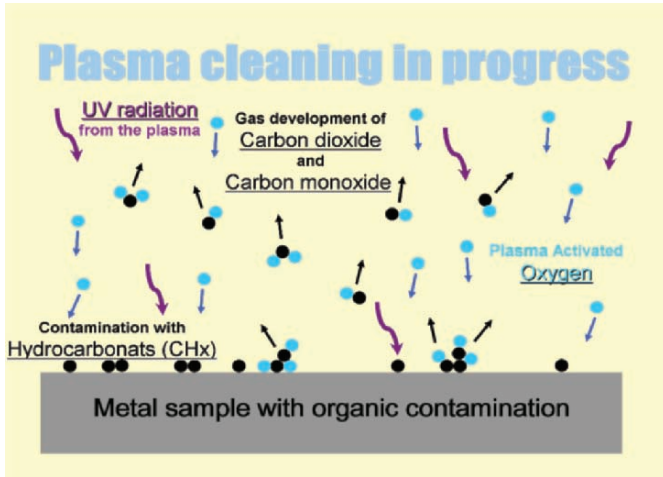
Figure 1. Oxygen ions of the plasma react with hydrocarbon contaminants to produce carbon monoxide and carbon dioxide, which can be pumped away.
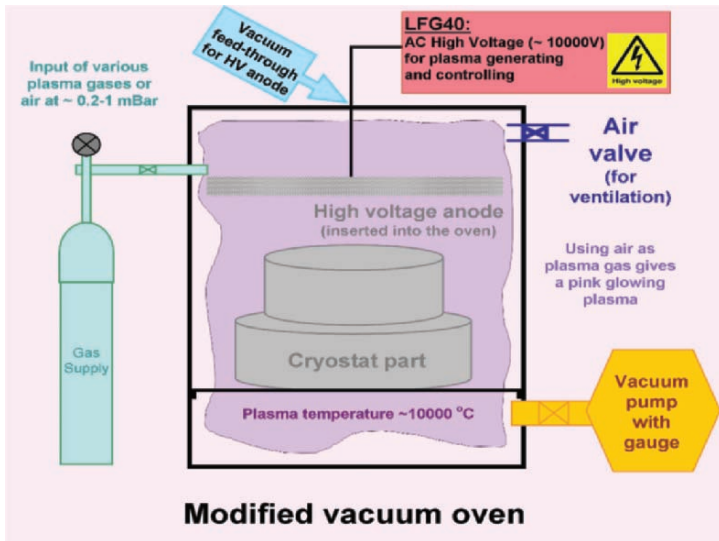
Figure 2. Plasma cleaning using a modified vacuum oven.

5.   PLASMA CLEANING IN READY ASSEMBLED CRYOSTATS

Another very useful application is igniting the plasma in an already assembled detector cryostat. This is possible with an additional transformer

and high voltage anode simply glued to the entrance window of the cryostat (see Fig. 3). This technique is extremely useful to maintain optimum cleanliness after a short opening of the cryostat for minor modifications. Without this special plasma cleaning technique it would not have been possible to clean the OmegaCAM cryostat due to its large volume (approx. 120l volume). There was no alternative to this internal plasma ignition technique. After some minutes of ignition, the entire OmegaCAM cryostat was filled with violet-colored magic glowing plasma (see Fig. 4).
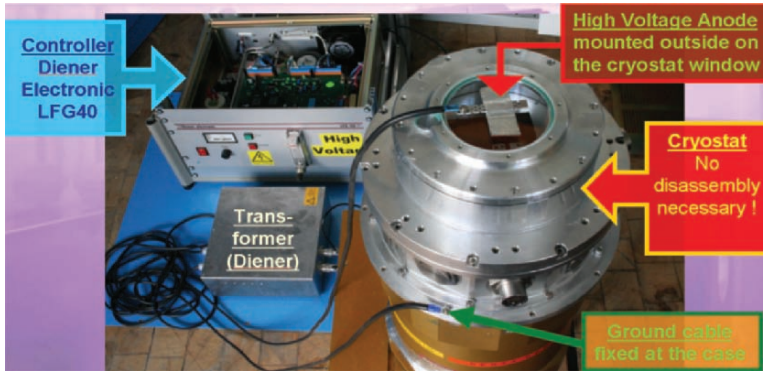
Figure 3. Special arrangement: plasma ignition inside a ready assembled cryostat.
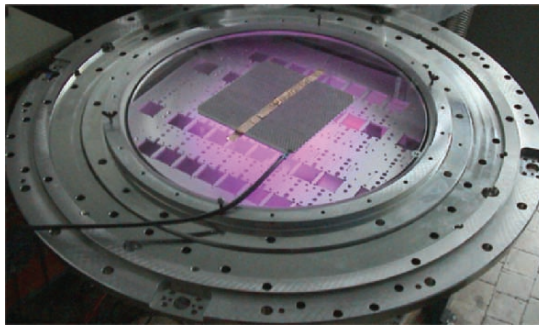
Figure 4. OmegaCAM cryostat during plasma cleaning.

6.   TEST OF PLASMA CLEANING RESULTS

Water drop method:
A contaminated sample shows a round water drop on its surface due to surface tensions created in the water by the contaminants. After plasma

cleaning there is little or no adhesion on the surface due to the lack of contaminates so no water drop develops and the water simply flows away.

End vacuum test:

A cryostat after plasma cleaning reaches a much better end-vacuum after 1 hour of pumping. In our tests, a much lower pressure of 5.0E-5 mbar was obtained after plasma cleaning compared to 1.0E-3 mbar before plasma cleaning.

Mass-spectrometer test:

A mass-spectrum was taken of a sample contaminated with a typical thin film of workshop oil before and after plasma-cleaning. The resulting two spectrums (see Fig. 5) show that most of the lines above masses of 50 amu are reduced significantly. Previous experience shows that unwanted contaminants mainly consist of elements and molecules with masses above 50 amu.
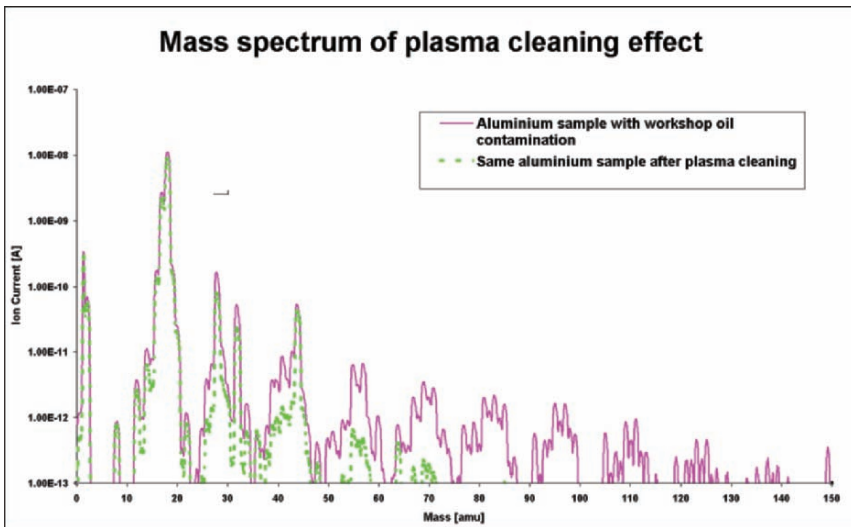
Figure 5. Mass-spectrum of sample before and after plasma-cleaning.

7. COSTS AND CONSTRAINTS

The cost of plasma cleaning equipment is low, especially if one can refurbish an existing laboratory vacuum oven and/or if one can use an existing vacuum pump. The annual maintenance costs are negligible.

Procurement costs:

Vacuum oven	~8000 EUR
Diener Electronic	
LFG40 Plasma Controller	~5000 EUR
Diener Electronic Converter	1000 EUR
Vacuum pump Alcatel ACP28	7000 EUR

Maintenance:

Electrical costs per cleaning process	0.20 EUR
Costs of special gases	~200 EUR per annum
Maintenance	~100 EUR per annum

Stainless steel and aluminum can be plasma cleaned for up to an hour. However, more than satisfactory cleaning results can be obtained within 10 minutes of cleaning.

Noble metals should not be cleaned longer than 10 minutes in ambient air and oxygen or else they become black. Hydrogen gas is an alternative for longer cleaning of these materials.

Plastic materials and PCBs should not be plasma cleaned longer than 10 minutes or surface damage (melting) may result. The plasma cleaning process works by producing temperatures in excess of 10,000°C in the first molecular layers of the sample to "burn" away contaminants. The sample remains hand-warm in its interior. This "burning" could damage plastic materials when exposed too long to the plasma. At present no damage has been observed to electronic components on PCB boards, however, we have yet to clean highly static sensitive active components like operational amplifiers. Before assembled cryostats are cleaned, detectors are removed to reduce risk of damage or irreversibly degrading of their performance. The plasma treatment induces strong electrical field and high surface temperatures which could damage the fine surface structures of detectors. We would welcome any working CCD sample from a manufacturer interested in tests with this cleaning procedure for our future testing. Maybe with plasma cleaning the quantum efficiency of the detector could be improved.

All plasma cleaned pieces should be handled using standard clean room conditions, otherwise the plasma-cleaning will need to be repeated. For safety reasons, personnel should not be exposed to the exhaust gas coming from the vacuum pump, plasma filled oven or cryostat. The UV radiation emitted from the plasma is harmless as it is fully absorbed by the oven window. The high voltage cables of the plasma devices should be handled following standard electrical safety procedures.

8.   CONCLUSIONS

Plasma cleaning is shown to be an easy and effective method in achieving ultra high cleaning results for detector cryostat components and/or complete assembled cryostats when used in addition to conventional cleaning processes. It is a fast cleaning process and has even been applied successfully to the very large OmegaCAM cryostat.

9.   ACKNOWLEDGEMENTS

I want to thank Mark D. Downing for "polishing" my English in this paper.

10.   REFERENCES

[1] Deiries, S., et al., 2004, *Ultra-clean CCD Cryostats – CCD contamination can be kept under control*, Scientific Detectors for Astronomy, Kluwer Academic Publishers.
[2] Iwert, O., et al., The *OmegaCAM 16K×16K CCD detector system for the ESO VST*, these proceedings.
[3] More information about the Plasma cleaning process and about custom made and standard plasma cleaning devices are available from Diener Electronic at http://www.dienerelectronic.de/en/index.html

A body at the cemetery in Forza d'Agró was suspiciously fresh.

Gert Finger (top) and Mike Lesser proudly display their asteroid citations (see Lifetime Achievement Awards on p. xxiii). Mike could not attend the workshop, but was presented his asteroid in Tucson, Arizona by his observatory director.

THERMAL MODELING OF THE WIDE-FIELD INFRARED CAMERA FOR THE CFHT

Philippe Feautrier[1], Eric Stadler[1] and Pascal Puget[2]
[1]Laboratoire d'Astrophysique de Grenoble, [2]LESIA

Abstract: *In the past decade, new tools have emerged in the arena of thermal modeling. These modeling tools are rarely used for cooled instruments in ground based astronomy. In addition to an overwhelming increase computer capabilities, these tools are now mature enough to drive the design of complex astronomical instruments, in particular if these instruments must be cooled. This is the case of WIRCam, the new wide-field infrared camera recently installed on the CFHT on the Mauna Kea summit. This camera uses four 2K×2K Rockwell Hawaii-2RG infrared detectors and includes 2 optical barrels and 2 filter wheels. This camera is mounted at the prime focus of the 3.6 m CFHT telescope. The mass to be cooled weighs close to 100 kg. The camera uses a Gifford Mac-Mahon closed-cycle cryo-cooler to avoid strenuous daily re-fillings on the telescope due to the camera location. This paper presents the thermal model of the camera using finite-element analysis under the I-deas software. The capabilities of the I-deas thermal module (TMG) are demonstrated for our particular application. Predicted performances (cool down time, warm-up time, and mechanical deformations) are presented and compared to measurements.*

Key words: *Thermal modeling, finite element analysis, cryogenic, infrared, camera.*

1.   GENERALITIES ABOUT THE WIRCAM THERMO-MECHANICAL DESIGN

WIRCam (Wide-field InfraRed Camera, see Fig. 1) is the second instrument of the "Wide Field Imaging Plan" of the Canada France Hawaii Telescope, providing a 20.5×20.5 arc minute field of view in the infrared

(0.9-2.4 µm). This will complete the infrared aspect of the MegaCam instrument which has been operational on the CFHT since January 2003.

This innovative instrument is based on four Hawaii 2RG detectors arrays developed by Rockwell in a close buttable package. WIRCam uses the special guiding capability of these arrays. Details of this instrument are described in Puget, et al. [1]. This camera is placed on the prime focus of the 3.6 m CFHT telescope in order to benefit from the simple opto-mechanical design of a wide-field camera. The camera uses a Gifford Mac-Mahon closed-cycle cryo-cooler to avoid strenuous daily refillings on the telescope due to poor accessibility because of the camera location. Moreover, it is necessary to define the thermo-mechanical design to meet the stringent stability requirements of the optical design with minimal thermal losses. This allowed the correct choice of cryo-cooler and to predict the cryogenic performances of the camera: permanent regime, temperature regulation needs, cooling performance, cryostat warming design, cryogenic margin, etc. The provision of excess cooling power was not possible due to weight constraint on the camera of 250 kg from the focusing unit features of the telescope.
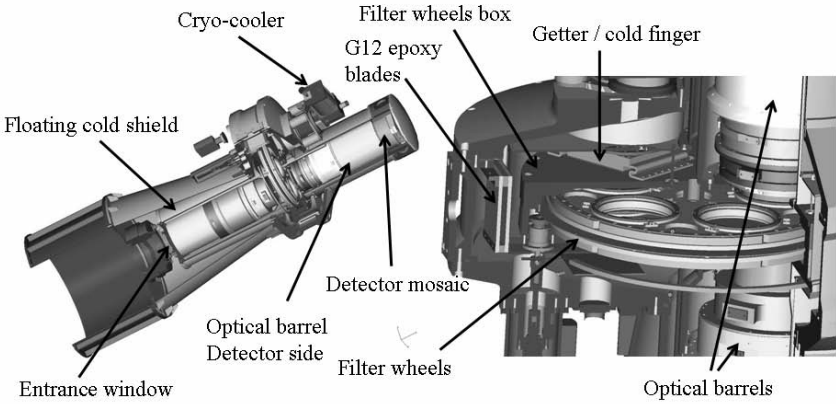
Figure 1. Overall views of the WIRCam cryovessel 3D mechanical model.

The focusing unit, attached to the prime focus upper end, is used to focus the instrument on the telescope. Thermal simulations are also used to assist in the mechanical design and demonstrate the achievement of the required low temperature of the detectors during the design phase.

As the cryo-cooler must be easily dismounted for maintenance operations, cooling power is transmitted by a system of two cones fitted

together, one male and one female, made of OFHC copper with exactly the same shape. The thermal link between the two cones is enhanced by using ultra-high vacuum grease manufactured by Pfeiffer vacuum. A tunable load between the two cones is applied by a system of titanium springs. They provide the required load while minimizing thermal leaks between ambient and colder temperatures. The cold structure is attached to the warm part of the cryostat by ten G12 composite twin blades. This design minimizes thermal leaks while achieving the required stiffness.

Figure 2 shows the WIRCam cryovessel during the cryovessel integration at the CFHT on the Mauna Kea summit in December 2004.
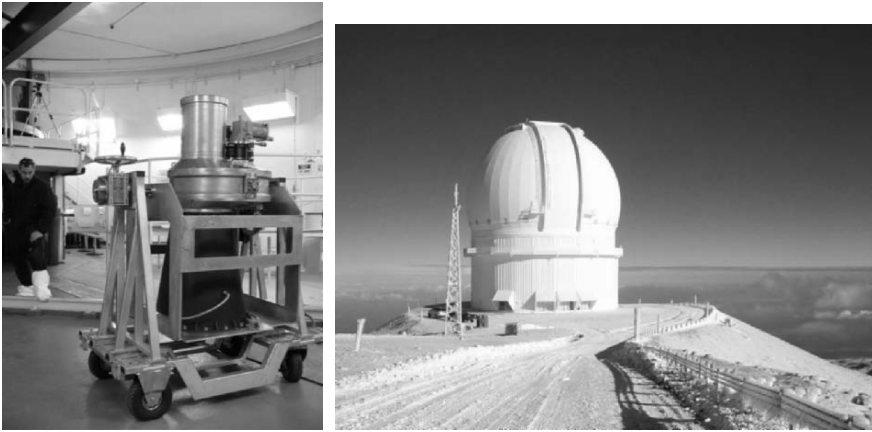
Figure 2. (left) View of the WIRCam cryovessel during the camera integration on the CFHT telescope (December 2004). *(right)* View of the CFHT telescope in December 2004 during the WIRCam cryovessel integration on the Mauna Kea summit.

2.   THERMAL MODELING

2.1   Generalities on the WIRCAM Thermal Simulations

All WIRCam thermal simulations [2] were performed using I-deas/TMG software module provided by the UGS software editor, now distributed as a module of "I-deas ® NX Series" called "NX MasterFEM TMG Thermal". We used version 9 of I-deas under a Windows 2000 operating system. TMG is the thermal module integrated inside the I-deas software distribution. I-deas was also used for the 3D mechanical design of WIRCam and for the finite element analysis of the mechanical deformations and constraints computations.

2.1.1   Physical parameters variation

Using the WIRCam thermal model, variations of the following parameters with temperature are considered:
- cooling power of the cryo-cooler cold head
- specific heat of the materials (used for the transient analysis)
- thermal conduction of the material (used for the conduction computation)

On the other hand, the emissivity of the radiative surfaces is treated as constant.

2.1.2   Computation and simulation method

Finite Element modeling was used to calculate temperatures using Ideas-TMG. The number of elements of the thermal model is ~60000. With a   2 GHz Pentium IV CPU, computing time is ~90 minutes for a steady state analysis and ~8 hours for a transient analysis of the thermal model.

Before meshing the 3D model for the thermal simulations, the model is cleaned of all details that have no effect on the thermal performances, for example, small holes, screws, and small details compared to the overall geometry of the model. Mechanical links with screws or glue are not meshed, they are modeled by so-called "thermal coupling".

2.2   Transient analysis and Comparison with the Measured Temperature in the WIRCam Cryovessel on the Telescope

The WIRCam cryovessel was integrated at the CFHT in December 2004. Cryogenic tests were performed and temperatures were monitored during the cryostat cool-down. In the meantime, a transient analysis of the thermal model was computed. The hypotheses of the thermal model are identical to the experimental conditions on the Mauna Kea summit:
- Air pressure: 620 mbar.
- Outside air temperature: 19°C.
- Camera pointing in vertically (orientation of the gravity vector in the software).

Figure 3 compares the thermal model to the measurements of the current system for different parts of the cryostat. The getter temperature and the optical barrel (detector side) temperature measurements are compared to the thermal model. Figure 3 shows a reasonably good agreement between the thermal model and the measurements. This clearly validates the interest in thermal modeling for this kind of instrument. In particular, the barrel

temperature as a function of time is well fitted by the thermal model. The deviation between the thermal model and the measurements is higher for the Getter, because there are interfaces in the cold finger that are not fully described. Nonetheless, the global behavior of the model reflects with a relatively good accuracy the measurements.
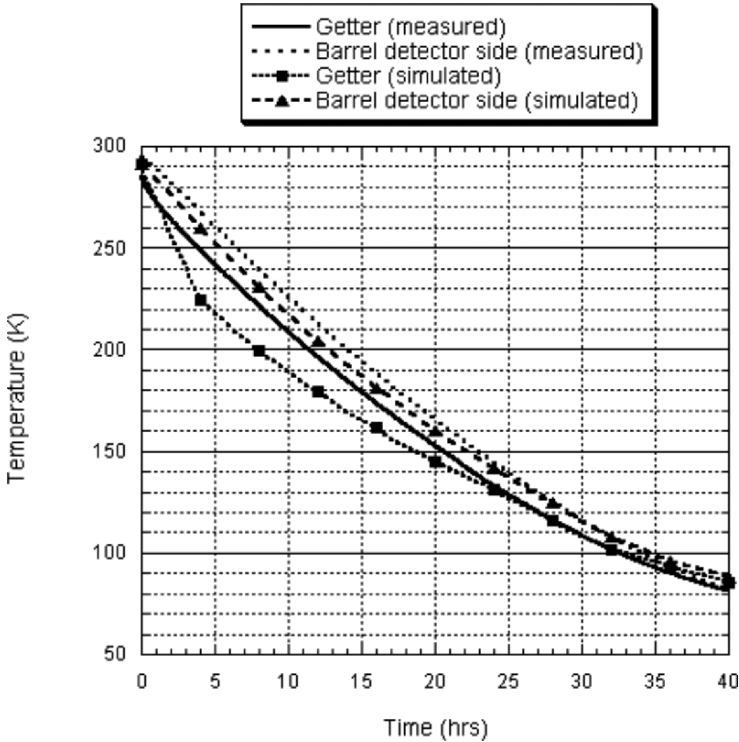
Figure 3. Comparisons between the WIRCam thermal model and the measured temperatures profile as a function of time during the cooling down at the Mauna Kea summit. The getter and the optical barrels temperatures are presented here.

3. CONCLUSIONS

This paper demonstrates the interest of thermal simulations in the system design of cooled instruments in astronomy. We used computing tools based on a single software distribution: I-deas version 9 for the 3D mechanical design and FEA together with the integrated TMG module thermal

modeling. This integrated software solution enhances the efficiency of the simulations. It also avoids unproductive steps and possible translation errors in the system modeling.

Thermal modeling allows the right system choices to be made and to predict system behavior before building the instrument. The accuracy of thermal models is poorer than the FEA accuracy of mechanical models but sufficient to avoid surprises during the instrument integration. Even with these kinds of simulations, some margins still must be considered in terms of cooling performances in order to satisfy the system requirements.

The cryogenic tests on sky allowed us to validate the thermal model of WIRCam, the next wide-field infrared camera for the CFHT. The WIRCam is now at its last steps of integration. The cryovessel includes the optical barrel and the science grade mosaic. The camera will available by the second semester of 2005.

4. ACKNOWLEDGEMENTS

5. REFERENCES

[1] Puget, Pascal, et al., 2004, *WIRCam: the infrared wide field camera for the Canada France Hawaii Telescope*, Proc. SPIE Int. Soc. Opt. Eng. **5492**, p. 978.
[2] Feautrier, Philippe, et al., 2004, *Interest of thermal and mechanical modeling for cooled astronomical instruments: the example of WIRCam*, Proc. SPIE Int. Soc. Opt. Eng. **5497**, p. 149.

COOLING SYSTEM FOR THE OMEGACAM CCD MOSAIC

Jean Louis Lizon and Armin Silber
European Southern Observatory

Abstract: *To optimize dark current, sensitivity, and cosmetics, the OmegaCAM detectors need to be operated at a temperature of 155 K. The detector mosaic, with a total area of 630 cm^2 directly facing the dewar entrance window, is exposed to a considerable heat load. This optimization can only be achieved with a high performance cooling system. This paper describes the cooling system, which is built to make the most efficient use of the cooling power of liquid nitrogen. This is done by forcing nitrogen through a series of well designed and strategically distributed heat exchangers. Results and performance of the system recorded during the past months of system testing are presented.*

Key words: *CCD cryostat, cooling.*

1. INTRODUCTION

The 2.6 m VLT Survey Telescope will be equipped with the optical wide-angle camera OmegaCAM. This camera has a field of view and pixel scale that perfectly match VST and Paranal seeing, respectively. OmegaCAM will be mounted in the Cassegrain focus, and the focal plane is populated with a mosaic of thirty-two 2K×4K CCDs with 4 identical auxiliary CCDs for autoguiding and image analysis. For the optimal trade-off between dark current, sensitivity, and cosmetics, these detectors need to be operated at a temperature of 155 K.

The detectors cover 630 cm^2 and must, for obvious reasons, face the dewar entrance window, which is in direct contact with the ambient air and temperature. Through this window, the detector is exposed to a considerable

radiation heat load of roughly 30 Watts. This is factor dominates thermal balance. However a detailed analysis shows that all other contributions (thermal conductance through the mechanical support structures and cables, dissipation in the electronics, etc.) add up to the same amount, bringing the total heat load to 60 W.

Various cryo-cooling systems were considered, but none were obviously suitable to this task. Eventually, a decision favoring liquid nitrogen (LN2) was made, because ESO has a long experience with CCD cooling using bath cryostats. However, from the Wide Field Imager (WFI), OmegaCAM's predecessor mounted on the 2.2 m telescope at La Silla, we knew that in the case of large heat loads, a plain bath cryostat to directly heat-sink the mosaic would not be efficient enough. The most important limitation is the large change in cooling power with nitrogen level in the tank. This required developing a new system. It still uses an internal storage tank but employs a sophisticated flow of liquid nitrogen in order to be independent of filling level and telescope position.

2.   DESIGN

Figure 1 schematically illustrates the principle, which permits the heat to be extracted where it is required (at the level of the detector mosaic) and makes optimal use of the enthalpy.
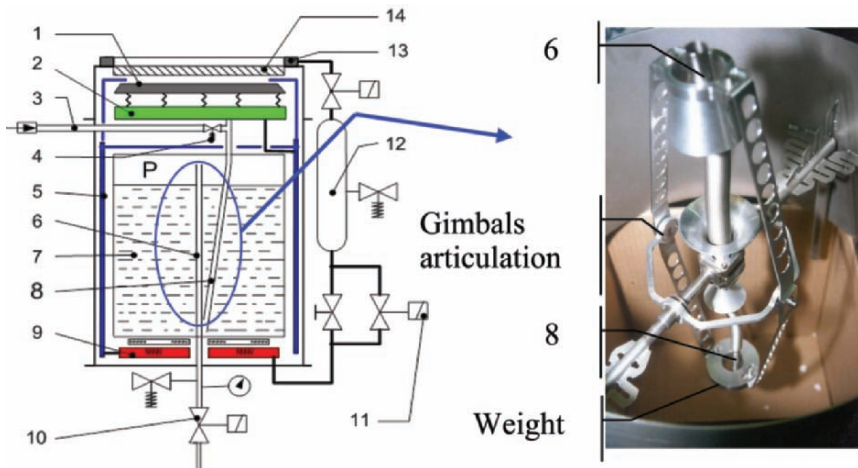
Figure 1. Cryogenic principle with detail of the anti-overflow.

Internal pressure (P), forces the LN2 to flow from the storage tank (7) through pipe (8) to and through a heat exchanger (2) which is in direct

thermal contact with the mosaic base plate (1). The heat exchanger consists of three parallel bars to ensure good temperature homogeneity across the mosaic. After absorbing the heat load, the gasified nitrogen circulates through a special annular heat exchanger (5), which acts as radiation shield for the storage tank. A final heat exchanger (9) is used to (electrically) heat the gas to room temperature. The gas is captured in a small tank (12) after exiting the instrument. At this point the gas is now warm and perfectly dry and can serve a second purpose and be safely blown over the dewar entrance window to prevent the condensation of air humidity.

The thermal regulation employs a valve (11), which is supervised by a PID controller in order to maintain constant operating temperature of the heat exchanger (2). The refilling of the internal tank is done from a standard 120 liter storage tank via a vacuum-insulated line. When the latter is connected to refilling tube (3), this is detected by a proximity sensor, and a valve (10) is opened in order to depressurize the internal tank so that the filling can begin. The valve is automatically closed when the tank is full (which is reported by a temperature sensor). The refilling port is fitted with a small spring loaded valve which is activated by the end of the refilling tube. This maintains the operating pressure when removing the tube.

The tank has been dimensioned to contain 40 liters for a hold time of 30 hours, making refilling only necessary once per day. Thanks to a special anti-overflow system, which allows the cooling tube (8) to be permanently at the lower position (in the liquid) and the vent tube (6) to be permanently at the highest position (in the gas), 90% of this capacity can be used without spilling (up to the nominal pointing limit of 60 deg zenith distance).

A dedicated thermal clamp has been designed to allow easy separation of the detector head from the cooling system. Figure 2 (left) shows the top of the cooling system with the 12 thermal clamps and (right) the bottom of the mosaic plate with the 12 thermal heat-sinking points.
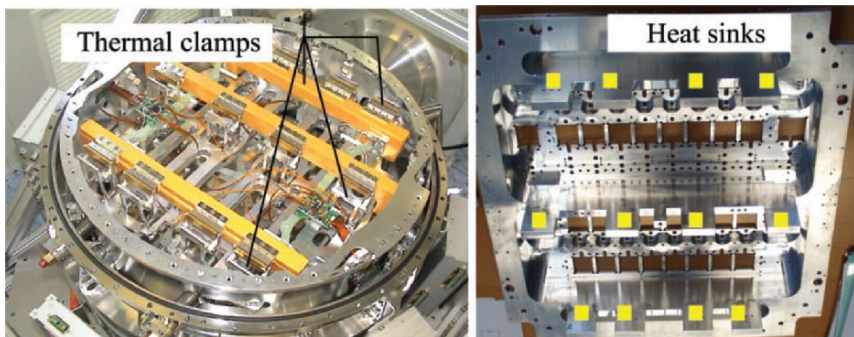
Figure 2. *(left)* Thermal clamps and *(right)* heat sinks.

3.   STATUS AND PERFORMANCE

The integration of the cooling system was essentially complete one year ago (see Fig. 3). Before integrating the science array, it was tested intensively (flexure, leaks, spilling, LN2 flow, etc.). The results are very satisfying. The performance is well within the specifications with the mosaic reaching a temperature to within ±1 K even below the nominal operating temperature (128K for 155K specified). The hold time is ~40 hours.

Figure 3. Cooling system.

4.   ACKNOWLEDGEMENTS

We would like to thank everyone who gave us the opportunity to develop this system. Special thanks to Olaf Iwert who, as project manager of the detector system, put the necessary pressure on us to build a good and well optimized system. Thanks to Dietrich Baade who is responsible for OmegaCAM and head of the Optical Detector Team (ODT) and gave us his trust. Thanks to Jesper Thillerup who helped with the integration and supervised the development of the cooling controller by an external contractor, all other ODT staff. And last, but not least, Guy Hess who carefully designed the detector head.

5.   REFERENCES

[1] Iwert, O., et al., *The OmegaCam 16K×16K CCD detector system for the ESO VST*, these proceedings.
[2] Capaciolli, M. et al., 2002, Proc. SPIE, **4836**, 43.
[3] Kuijken, K. et al., 2002, The ESO Messenger, **110**, 15.

BONN SHUTTERS FOR THE LARGEST MOSAIC CAMERAS

Klaus Reif[1], Günther Klink[1], Philipp Müller[2] and Henning Poschmann[1]
[1]Sternwarte of the Univ. of Bonn, [2] Radio Astron. Inst. of the Univ. of Bonn

Abstract: *Bonn shutters have been developed and implemented in various CCD camera systems with apertures ranging from 110 mm×110 mm (BUSCA, Calar Alto Observatory) to 370 mm×292 mm (OmegaCam, ESO/Paranal).*

Larger shutters with apertures of up to 480 mm×480 mm (for Pan-STARRS) are now in development. The principles of operation are basically contiguous. The key performance parameter is high timing precision which reduces exposure non-homogeneities to less than 1 msec, i.e. <0.1% at 1 sec exposure time. In this paper we report the current status of this technology, as well as new requirements and challenges.

Key words: *CCD mosaics, CCD cameras, exposure shutters.*

1. INTRODUCTION

Camera exposure shutters with apertures in excess of 100 mm are hard to find on the "market". They are practically unavailable if very short exposure times (< 0.1 seconds) and/or photometric performance is required. Typical problems with common iris-type shutters are exposure time errors of several 10 msec and exposure non-uniformities of the same order of magnitude.

We have been confronted with these questions during the development of BUSCA, a 64 Megapixel camera for simultaneous imaging at four wavelengths [1,2]. A shutter was required with an aperture of 110 mm×110 mm that could provide very short exposure times <10 ms and exposure non-homogeneities of no more than 1 msec (i.e. < 0.1% at 1 sec).

Our initial designs were influenced by typical misconceptions about exposure shutters, for example,: i) a shutter is a mechanical device, ii) short exposures need very fast operations or movements, iii) only movements with highly constant speed guarantee uniform exposures, iv) because of these, lifetime and MTBF are real issues. Thus we made a few deviations before arriving at the relatively simple design that is now characteristic of Bonn Shutters [1,3]:

- The shutter system combines precision mechanics, micro controller based electronics and firmware for movement and overall control.
- Short exposure times and exposure homogeneity are achieved by precise control of the movement of two independent blades. The acceleration phase can even take place in the shutter aperture.
- These blades run impact-free on industry quality linear ball bearings. There is no contact between the blades and the bearings. Constant performance over several million operations can be expected.

2. "CAN YOU MAKE IT BIGGER!?"

While we were learning our shutter lessons in Bonn, around the world the silicon-filled portions of focal planes were growing thanks to CCD mosaics. Among the common challenges of developers was the "big shutter problem". As we realized these demands, we began working on large-scale versions of our shutter mechanics design. A shutter with a 200 mm square aperture was designed and built for the 8K×8K mosaic camera 90PRIME at the 90 inch telescope of Steward Observatory at Kitt Peak [4]. Two smaller shutters were built for instruments on the Spanish GTC 10 m telescope on La Palma. A complete list of all Bonn Shutters that were built or are in development is given in Table 1.

A real challenge was the request of the OmegaCam consortium to design and build a "Bonn Shutter" with an aperture of 370 mm×292 mm for the 256 Megapixel instrument [5]. It turned out that the design can even be scaled to this large format with the preservation of high photometric quality. Residual non-homogeneities are below 1 msec [3]. Shutters of similar and larger size (SkyMapper, ODI@WIYN) have been designed and are under development. The largest shutter under development in 2005 has an aperture of 480 mm×480 mm. This huge device will cover the Gigapixel focal plane of the Pan-STARRS prototype telescope (PS1) [6].

Table 1. Bonn shutters that have been built or are in development.

Aperture Format (mm)	Camera, Instrument	Telescope	Observatory	Status
110×110	BUSCA	CAHA 2.2m	CAHA	in operation
200×200	90PRIME	Steward Observatory 90inch	Kitt Peak	in operation
150×150	ELMER	GTC (10m)	Roque de los Muchachos	in operation
125×125	OSIRIS	GTC (10m)	Roque de los Muchachos	integr.
370×292	OmegaCam	VLT Survey Telescope (2.6m)	ESO/Paranal	in operation
200×200	QUOTA (ODI-Testsystem)	WIYN (3.5m)	Kitt Peak	delivered
480×480	PS1-prototype Camera	Pan-STARRS Prototype Telescope (1.8m)	LURE/Haleakala	constr.
450×450	OneDegreeImager (ODI)	WIYN (3.5m)	Kitt Peak	constr.
280×280	SkyMapper Camera	SkyMapper Telescope (1.3m)	Siding Spring Observatory	constr.
480×480×4	Pan-STARRS Camera	4 Pan-STARRS Telescopes (1.8m)	Univ. of Hawai'i Mauna Kea	request

3.   NEW CHALLENGES

The ever increasing size of CCD mosaics has led to new requirements and challenges. The new huge survey cameras with focal planes of up to one Gigapixel will nevertheless be mounted at small or medium sized telescopes (e.g. 1.8 m for Pan-STARRS, 1.3 m for SkyMapper). This leads to very tight constraints with respect to weight and other parameters. One of the consequences of these restrictions is that the classical instrument housing is omitted or reduced. This means that the shutter envelope may become part of the instrument envelope, and it must provide some of the corresponding functionality (e.g. mechanical support, air-tightness).

3.1   Shutter "Thinning"

Due to limited back focal distances, the shutter height (or thickness) is a concern. The only distinctive visible feature of the OmegaCam shutter (apart from its size) is that the two small boxes covering the motors had to be

omitted, transforming the new Bonn Shutters into flat slabs. In one case (ODI, 450 mm×450 mm) the shutter was not thin enough. To meet space constraints along the optical path the central portion received "extra thinning" (35 mm total).

3.2   Blade transfer performance and "pull out" time

Despite increased size, the new half-meter-class shutters have the same photometric performance (homogeneity) as smaller devices, particularly at short exposure times. Some of the survey observations are planned as rapid exposure sequences with short exposure times. To minimize overhead times, shutter blade movements must be fast, yet still very precise and always impact-free. Idle shutter times (i.e., the time between the "exposure end" and the next "start" signal) of about 1 sec are required.

3.3   Spectral IN-Sensitivity Range

Shutters for CCD cameras will block electromagnetic waves from the UV to the NIR. Thus, a somewhat surprising requirement for the PS1 shutter was to cover the wavelength range usually of interest to radio-astronomers. The background for this is the very high level of radio frequency interference due to strong radio transmitters at Haleakala, Hawaii. The shutter must provide RFI shielding for the detector system. To achieve this, an aluminum foil of sufficient thickness (n times "skin depth") will be embedded in the shutter blade with good electrical contact to the shutter envelop.

4.   CONCLUSIONS

Bonn Shutters have been built in various dimensions and are now in use in many different places (see Fig. 1). Their applications range from single detector focal planes to the largest mosaics with several 10^8 CCD pixels. Independent of their size they share similar performance parameters.
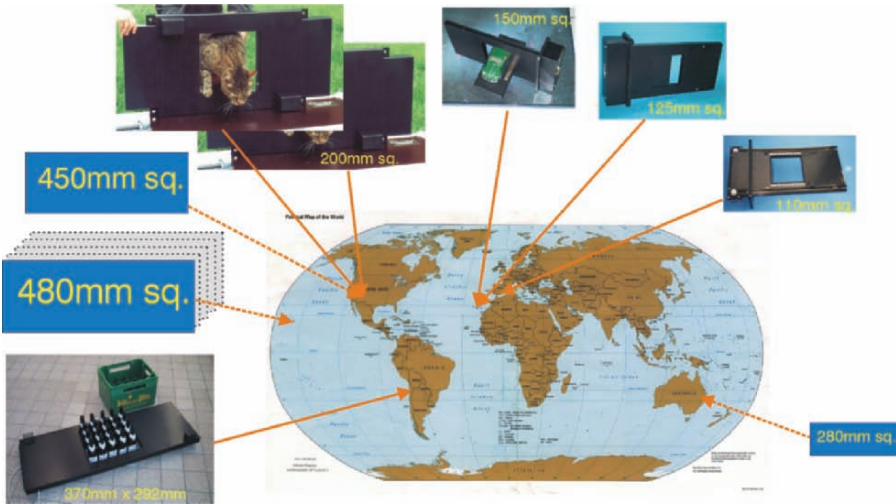
Figure 1. Location of observatories where Bonn Shutters are used or will be used. Numbers give the shutter aperture sizes. Pictures show shutters that are already "delivered". See Table 1 for further details.

5.   REFERENCES

[1] Reif K., Bagschik K., de Boer K.S., Schmoll J., Müller Ph., Poschmann H., Klink G., Kohley R., Heber U., Mebold U., 1999, *BUSCA, a telescope instrumentation for simultaneous imaging in four optical bands*, Proc. SPIE Vol. **3649**, pp. 109-120.
[2] Reif, K., Cordes, O., Poschmann, H., Müller, Ph., 2001, *BUSCA's first Calar Alto campaigns: A 64 Megapixel CCD-Camera System for the 2.2m Telescope*, http://webserv.caha.es/newsletter/news01a/busca/
[3] Reif, K., Klink, G., Müller, Ph., Poschmann, H., 2004, *THE OMEGACAM SHUTTER: A low acceleration impact-free device for large CCD mosaics,* in 'Scientific Detectors for Astronomy: The Beginning of a New Era', P. Amico, J.W. Beletic, & J.E. Beletic (eds), Astrophysics and Space Sciences Library (Kluwer: Dordrecht), Vol. **300**, pp. 367-370.
[4] http://compton.as.arizona.edu/90prime
[5] Nicklas H.E., Harke R., Wellem W. Reif K., Kuijken K., Muschielok B., Cascone E., 2002, *OmegaCAM - Technical Design and Performance,* Proc. SPIE Volume **4836** p. 199-205.
[6] Tonry, J., 2005, *Pan-STARRS and its Gigapixel Cameras*, these proceedings.

Barry Burke says to Klaus Reif (with back to camera), "Klaus, if these CMOS guys get going we will lose our large mosaic jobs. No need for shutters is a powerful argument for using CMOS in wide-field imagers!"

SLICING THE UNIVERSE
CCDs for MUSE

Roland Reiss[1], Sebastian Deiries[1], Jean Louis Lizon[1], Manfred Meyer[1], Javier Reyes[1], Roland Bacon[2], François Hénault[2], Magali Loupias[2]
[1]European Southern Observatory, [2]CRAL - Observatoire de Lyon

Abstract: *MUSE, the Multi Unit Spectral Explorer, is a 2nd generation instrument for the VLT. It is built by a consortium of European institutes and ESO. MUSE consists of 24 Integral Field Units each equipped with its own cryogenically cooled CCD head. The detector is 4096×4096 with 15 μm pixels.*

In this paper we discuss CCD requirements and give an overview of the design status of the detector system. Due to the large number of units, each must be simplified to save cost and man power, and increase reliability. We present a novel preamplifier for use inside the compact detector head with pulse tube cooling. Adaptations of ESO's New General detector Controller (NGC) are presented.

Key words: *CCD, cascode amplifier, detector controller, instrument, pulse tube.*

1.   OVERVIEW

MUSE is an integral field spectrometer mounted at the Nasmyth focus of one of the VLT telescopes. Figure 1 shows the tentative optical configuration. The Fore Optics (FO) split a large field of view into 24 sub-fields. 24 Integral Field Units (IFU) provide the spectral decomposition of the sub-fields. The IFUs include an Image Slicer Subsystem (ISS), Spectrometer Subsystem (SPS) and an Instrument Detector Subsystem (IDS). The spectral coverage of MUSE is 465 to 930 nm, the total field of view in wide field mode is 1×1 arcmin^2, and 7.5×7.5 arcsec^2 in narrow field mode. The total weight of the instrument will be approximately 7 tons. Commissioning of MUSE is planned for 2011.
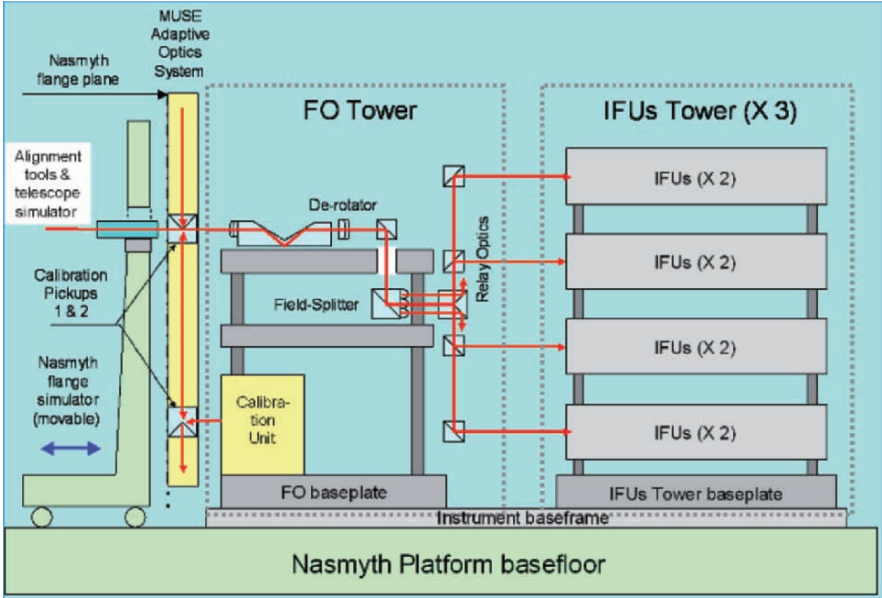
Figure 1. MUSE optical configuration.

2.   CRYOGENICS

The 24 detectors are housed in 24 separate cryostats, which are cooled using separate low frequency Pulse Tube Heads (PTH). The 24 PTHs are custom made and powered by two Coolpack 6000 compressors from Leybold. The prototype cooler has been developed in collaboration with the Service Basse Temperature from the CEA Grenoble. The actual performance of the prototype is 4 Watts at 120 K and a Helium flow rate of 100 l/s. The design is driven by the tight space and weight constraints of MUSE. Figure 2 shows a prototype of the new compact CCD head, which will also be the standard head for future optical ESO instruments.
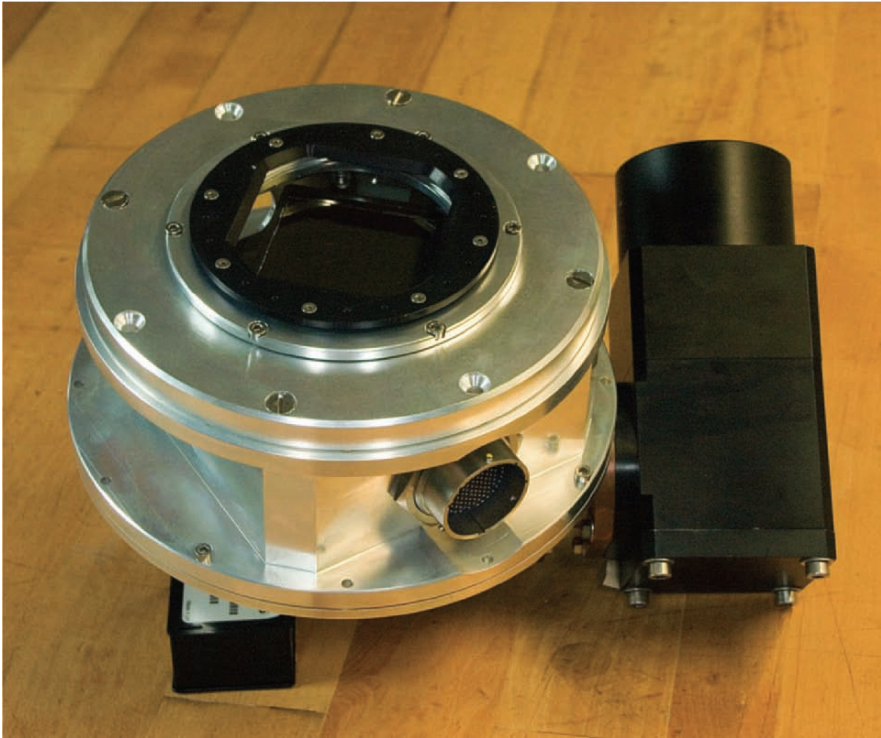
Figure 2. CCD head prototype.

3. CCD HEAD ELECTRONICS

The first buffer stage for the CCD outputs is a cascode stage with two low noise JFETS Q1 and Q2 (see Fig. 3). Q1 acts as a source follower with a gain slightly below 1. Because the resistors R1 and R2 are equal, the signal voltages across R1 and R2 are also equivalent, but with opposite phase. R3 and R4 provide the DC bias for Q2. The advantage of this circuit is a gain two times higher when compared with a single buffer stage. As a benefit the circuit delivers a differential output signal. L1 is a common mode choke to improve noise immunity. Q3 is the usual JFET current source to set a proper load current (1 to 2.4 mA) on the CCD output.

The subsequent video processing stage consists of a differential input amplifier with a line clamp circuit. Further video signal processing methods are currently under investigation. Options under consideration are:

- Classical clamp-and-sample, similar to the circuit used in FIERA [1], where the sampling is actually performed by the Analog-to-Digital Converter (ADC).
- Sample-hold stage with a subsequent differential amplifier to subtract the sampled reference level from the signal level. The resulting signal is then sampled and converted by the ADC.
- Sampling of reference and signal level with the same sampling ADC and subtraction by software (Digital Double Sampling).
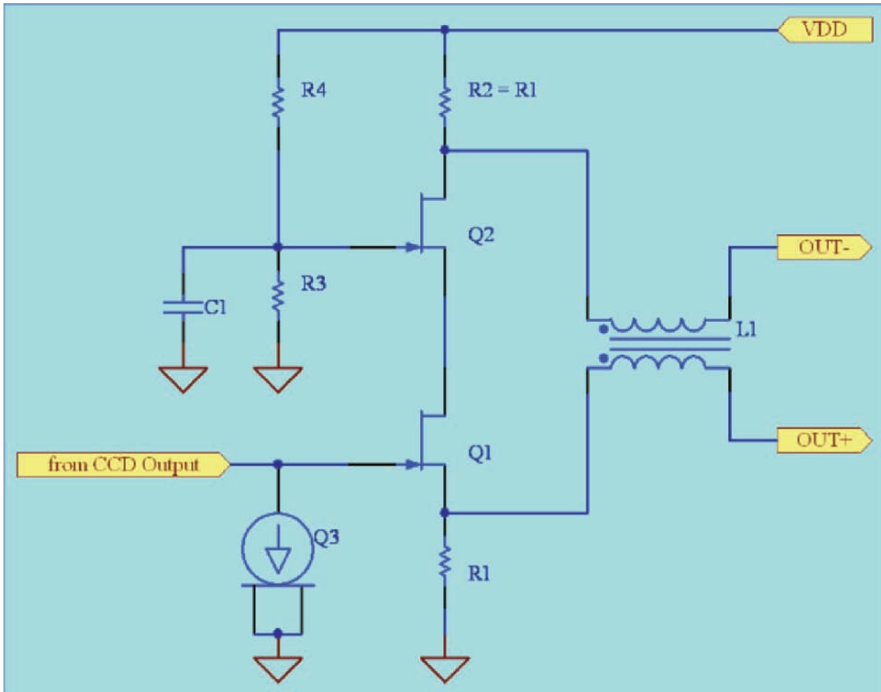
Figure 3. Cascode CCD buffer stage.

4. DETECTOR CONTROLLER

Due to the large number of units, each must be simplified to save cost and man power, and increase reliability. ESO's New General detector Controller (NGC) will be used for MUSE. NGC has been selected because of its compact size and low power consumption. Each of the 24 CCDs is driven by a single board containing 4 video channels, 20 bias and 16 clock sources. One controller unit will contain 4 such boards (see Fig. 4). In total 6

NGCs are required to operate the 24 CCDs. A detailed description of NGC can be found in Meyer, et al. [2].
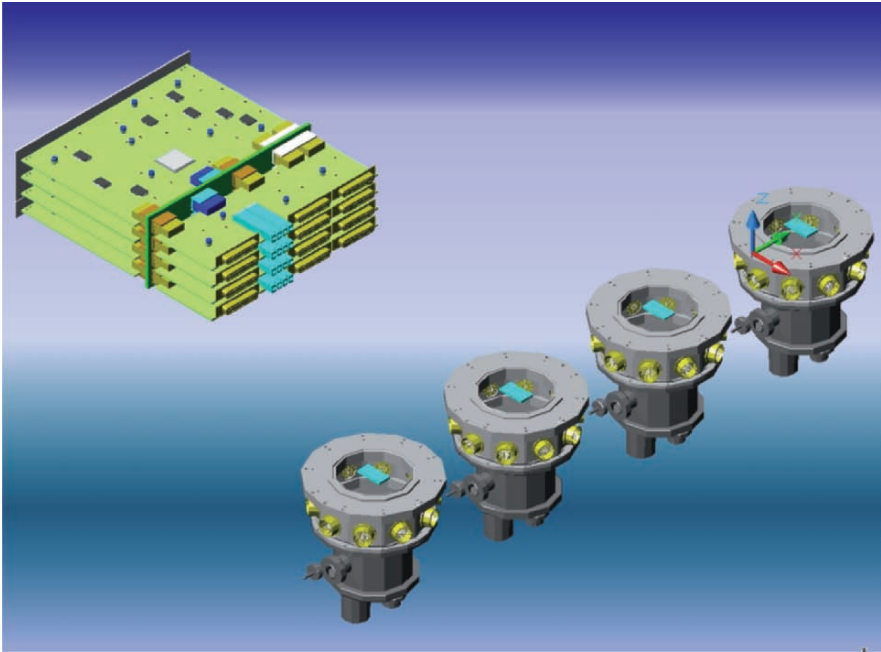
Figure 4. NGC configuration.

5.   CCD REQUIREMENTS

Table 1 shows the preliminary requirements for the most important CCD characteristics. Given the faintness of the science targets, the detector QE is of prime importance. Special attention is given to the redder ($\lambda > 0.6$ µm) part of the spectral range where the QE should be optimized. The 570 to 610 nm gap in QE requirements is given by a notch filter in the optical path that suppresses the scattered light of the Sodium Laser guide stars used for Adaptive Optics (AO).

Constraints on the chip flatness are due to the camera aperture (f/1.9) and expected image quality.

Table 1. Preliminary detector requirements.

Item	Value	Remarks
Detector format	4096×4096 or 2×2048×4096	
Detector dimensions	61.4 × 61.4 mm^2	
Pixel size	15 × 15 μm^2	
QE 465–570 nm	85% min; 90% goal	
QE 610–800 nm	85% min; 90% goal	
QE 800–930 nm	60% min; 70% goal	
PRNU	< 10%	Peak-to-peak
Fringing	< 10 %	Peak-to-peak of avg. sensitivity
Fringe stability	< 1%	Within 24 hours
Flat field stability	< 1%	Per night
Readout time	Goal:1 min; max: 3 min	4-port readout
Readout noise	< 4 e$^-$ RMS	@ 50 kpix/sec
Binning capability	4 × 4	Without increase of noise
Dark current	< 2 e-/pix/h	
Charge transfer efficiency	> 0.999995	
Linearity	< 1%	Up to 50,000 e$^-$
Full well	> 100,000 e$^-$	
Blooming full well	> 200,000 e$^-$	
Charge diffusion	< 0.1 pixel	FWHM equivalent gaussion convolution
Surface flatness	< 20 μm pp	
Cosmetics	Science grade	Number of defects TBD, no bright or dark columns.

6. REFERENCES

[1] Gerdes, R, Beletic J.W., and Duvarney, R.C., 1998, *Design concepts for a fast-readout low-noise CCD controller*, Optical Astronomical Instrumentation, Sandro D'Odorico (Editor), Proc. SPIE Vol. **3355**, p. 520-528.

[2] Meyer, M. et al, 2005, *ESO's next generation controller*, these proceedings.

ON-CHIP GUIDING WITH A MOSAIC OF HAWAII-2RG INFRARED DETECTORS

Martin Riopel[1], Douglas Teeple[2] and Jeff Ward[2]

[1]*Laboratoire d'Astrophysique Expérimentale, Université de Montréal,* [2]*Canada-France-Hawaii Telescope Corporation.*

Abstract: *This paper presents the guiding acquisition system for the CFHT WIRCam based on a mosaic of four HAWAII-2RG infrared detectors. This camera was designed and built by the Canada-France-Hawaii Telescope Corporation in collaboration with the Laboratoire d'Astrophysique Expérimentale of the Université de Montréal. The guiding system features four SDSU-3 boards modified to support dual optic fiber connections (master scientific and slave guiding) to allow simultaneous but independent guiding and scientific acquisitions. Stable and fast guiding at 50 Hz has been effectively achieved in infrared both in laboratory and on sky. The original SDSU software driver has been modified to support an interrupt-driven loop that automatically extracts one centroid from each of the four user-defined regions (one for each detector). The derived correction drives a PID closed loop Image Stabilization Unit (ISU) controller to effect guiding.*

Key words: *Infrared, controller, software, clocking, guiding, HAWAII-2RG.*

1. INTRODUCTION

CFHT WIRCam (Wide InfraRed Camera) is a shutterless camera that contains a mosaic of four 2048×2048 Rockwell HAWAII-2RG infrared detector arrays. The programmable window capability of the Rockwell multiplexer has been used to implement on-chip guiding. This paper describes the overall architecture of the system, explains the readout and guiding sequence and relates experiences on the sky with the guider in engineering runs.

2.   GENERAL DESIGN

The detector mosaic and its mount are shown in Fig. 1. Each pixel is sampled with a 16 bit ADC, producing a 32 megabyte scientific image size. For guiding, one small sub array of pixels (typically 8×8) containing a guide star is chosen for each of the four arrays of the science image. These pixels are blanked out in the science image and sent to the guide host.
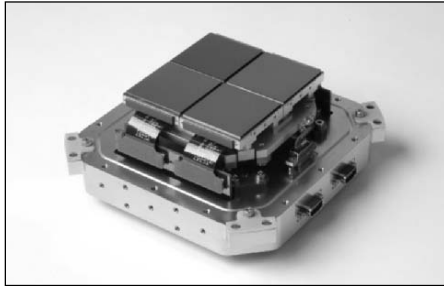
Figure 1. WIRCam detector arrays mounted on the GL Scientific module (photo by
        G. Luppino).

There are two separate host computers, one for guiding, which is mounted in the telescope cage, and another for science data, located in the control room. The science detector host runs Linux. It hosts 2 SDSU-3 PCI cards, with a split fiber connection. One is a two-way connection for scientific data transfer and the other only connects to the guide computer. Each SDSU-3 controller handles 2 arrays. The detector host runs CFHT Detcom to receive images and archive them with one chip per extension in MEF (Multi-Extension FITS) format. Focus and microdither sequences are saved as MEF cubes.

The guide host runs Linux based on kernel 2.4.20, built with RTAI real-time support. Two SDSU-3 cards are installed in the guide host, both in receive-only mode. The guide host also has a PowerDAQ A/D converter which supplies analog output, analog input, and digital control output and digital error status input from the ISU (Image Stabilization Unit). The SDSU-3 driver and the PowerDAQ A/D converter driver are installed as RTAI real time drivers. Figure 2 shows the connections of the two hosts to the detector arrays.

3.   READOUT AND GUIDING SEQUENCE

To achieve simultaneous but independent scientific and guiding acquisition, the pixels have been divided into blocks. Guiding images are sent to the host between each block of pixels. The guiding images are read fast enough not to interfere with acquisition. Guiding acquisition supports Fowler sampling and is done on a strictly regular basis to minimize the reset anomaly effect [1]. Data is sent through an optical fiber connection.

The guide driver is based on the Bob Leach [2] AstroPCI v1.7 driver and modified to support an interrupt-driven loop as shown in Fig. 3. In this loop, guider images are received from the fiber connection, processed into FITS images in shared memory and then 2D convoluted to extract one star in each of the four quadrants. The driver then uses a configurable weighting algorithm (based on FWHM, S/N, flux, etc.) to generate XY offsets which are processed through a Proportional Integral Differential (PID) transform to generate XY correction voltages for the tip/tilt control. The Image Stabilization Unit (ISU) controller has a range of ±1.5 arcsec with a resolution of 0.01 arcsec. The ISU receives guidance corrections at a rate of 1/20 ms. The driver typically takes about 0.15 ms to calculate centroids and send voltage corrections to the A/D converter and, since the duty cycle is 20 ms, the driver does not overrun and can support Fowler sampling.
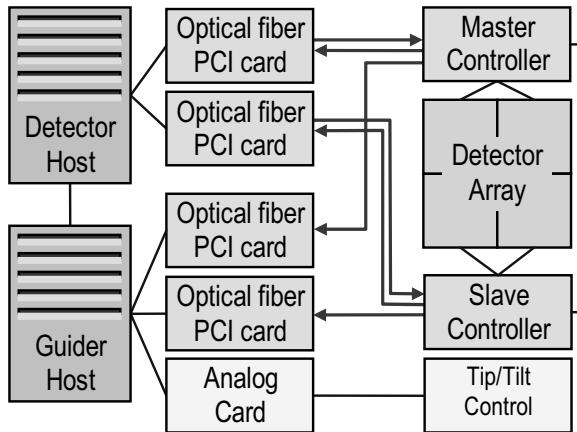
Figure 2. Host computer configuration.
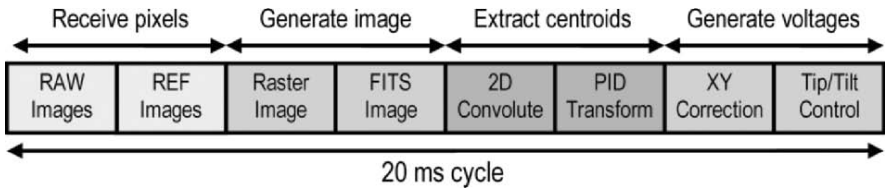
Figure 3. Guide image processing loop.

4.   PERFORMANCE

The on-chip guiding system has been tested successfully on sky during engineering runs of WIRCam in April and May 2005. Figure 4 shows the spatial frequency spectrum of the star guiding movement at full speed (50 Hz) open loop, closed loop and closed loop with TCS guiding. Low frequency movement is suppressed by about 30 dB. The crossover is between 6-8 Hz, which corresponds to the closed-loop tuning model used to set the PID parameters. Guide stars to the 14th magnitude were tested.
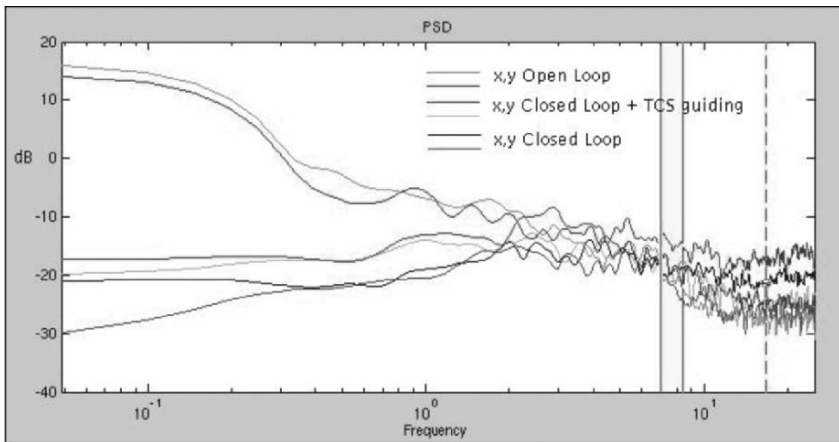
Figure 4. Spatial frequency spectrum of the guiding star movement.

5. CONCLUSION

In this paper, we have presented the WIRCam on-chip infrared guiding system that permits simultaneous scientific and guiding acquisitions with a mosaic of four HAWAII-2RG arrays. On-sky engineering tests have confirmed the effectiveness of the guiding system.

6. REFERENCES

[1] Riopel, M., Doyon, R., Nadeau, D. and Marois, C., 2004, *An Optimized Data Acquisition System Without Reset Anomaly for the HAWAII and HAWAII 2 Arrays*, Scientific Detectors for Astronomy, Paola Amico, James W. Beletic and Jenna E. Beletic (Eds), Dordrecht : Kluwer Academic Publishers, Astrophysics and Space Science Library, Vol. **300**, p. 453-457.

[2] Leach, R. W.; Low, F. J., 2000, CCD *and IR array controllers*, Optical and IR Telescope Instrumentation and Detectors, M, Iye & A. F. Moorwood (Eds), Proc. SPIE, Vol. **4008**, p. 337-343.

Martin Riopel and Louise Choquette thoroughly enjoyed the food
at the Hotel Naxos Beach.

The Istituto Nazionale di Astrofisica (INAF), the Italian National Astrophysical Institute, provided significant support to this workshop. Piero Benvenuti, the INAF president, welcomed the workshop participants.

THE BLUE CHANNEL OF THE LARGE BINOCULAR CAMERA
First test at LBT

Roberto Speziali [1], Fernando Pedichini [1], Andrea Di Paola [1], Emanuele Giallongo [1], Roberto Ragazzoni [2], Andrea Baruffolo[3], E. Diolaiti[4], C. De Santis[1], J. Farinato[2], Adriano Fontana[1], S. Gallozzi[1], F. Gasparo[5], F. Pasian[5], R. Smareglia[5], E. Vernet [2]

[1]*INAF – Osservatorio di Roma,* [2]*INAF – Osservatorio di Arcetri,* [3]*INAF – Osservatorio di Padova ,* [4]*INAF – Osservatorio di Bologna,* [5]*INAF – Osservatorio di Trieste.*

Abstract: *The Large Binocular Camera (LBC) is the optical imager that will operate at the prime foci of the Large Binocular Telescope (LBT). LBC is composed of two separated large field (27 arcmin) cameras, one optimized for the UBV bands (blue channel) and the second for the VRIZ bands (red channel). An optical corrector balances the aberrations induced by the fast (F#=1.14) parabolic 8.4 m primary mirrors of LBT, assuring that 80% of the PSF encircled energy falls within one pixel across more than the 90% of the field. The focal plane equipment consists of an array of four E2V-4290 chips (4.5K×2K) for the acquisition of science images, and by two E2V-4210 chips (2K×0.5K) placed at both lateral sides of the scientific array, dedicated to the guide and active optics systems. The blue channel was installed on LBT in late 2004, and it is in the commissioning phase now. The hardware has been fully tested and the camera software with the Telescope Control Software (TCS) will be integrated and commissioned in Summer 2005. The science validation phase is expected to begin in October 2005.*

Key words: *Large Binocular Telescope (LBT), Large Binocular Camera (LBC).*

1.   THE LARGE BINOCULAR CAMERA

As widely documented elsewhere [1,2,3], the Large Binocular Camera (LBC) cryostat is composed of three independent modules: a stainless steel rotator interface flange, a bimetallic (copper-nickel) nitrogen vessel and a

housing made of aluminium. The liquid nitrogen vessel has been designed with a spherical shape both to minimize the radiative thermal inlet and to make a compact instrument. The overall volume of the vessel is 16 liters and can be filled up to 8 liters even in the most unbefitting position (horizontal).

The rotator flange, made of a stainless steel (AISI 4130), holds the baseplate with the detectors and interfaces the cryostat with the rotator of the prime focus hub [4,5].

Due to the very fast focal ratio of the camera (F# =1.4), the co-planarity of the detectors in the rotator flange was a crucial issue. For an accurate measurement (± 1 μm) of this parameter we used a laser based measuring machine provided by Mitutoyo. With this machine it was possible to measure the height of the chips without any contact.

2.   LBC AT THE LBT LABORATORY

LBC blue was moved to the Large Binocular Telescope (LBT) in mid-2004. A small clean room has been prepared for the final assembly and tests (see Fig. 1). The camera window (Lens #6 of the corrector) was successfully installed, and we have performed some minor mechanical upgrades of the cryostat to fix some vacuum leaks (Torseal seals have finally been removed). We prepared the transportation and handling tools to move and mount the camera on the telescope. To allow more suitable handling, all 'external' electrical devices (shutter electronics, temperature telemetry, window heater) have been installed in a new case (see the black box in Fig. 1).
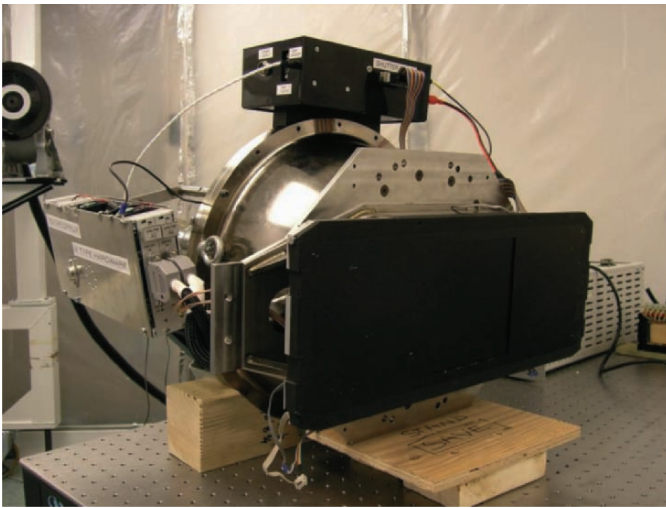
Figure 1. The LBC Blue Camera fully assembled in the clean room at LBT.

3. ON THE TELESCOPE

By 2005 all repairs had been performed, and the camera was mounted at the prime focus station of the left primary mirror of LBT (see Figures 2-4).
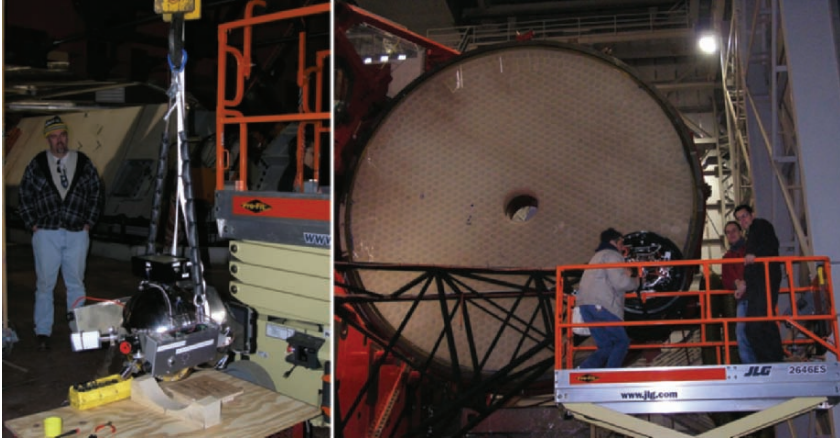
Figure 2. (left) The Blue Camera of LBC being raised. *(right)* The crew on the scissor lift mounting the camera at the prime focus station (the swing arm is in the 'out' position).
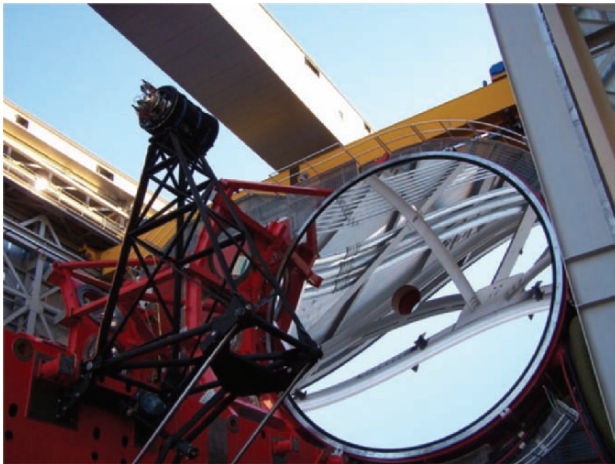
Figure 3. A recent picture of LBC Blue mounted on LBT.

All maintenance operations can be performed when the telescope is pointing toward the horizon and, possibly, with the swing arm in the 'out' position. By using a scissor lift we are able to carry out the pumping/ refilling/debugging operations.

The holding time of LN$_2$, when LBC is mounted on the telescope, ranges between 40 and 50 hours, depending on the ambient temperature. The cooling time is about 15-18 hours while the working temperature of the array is 198±5K.

The vacuum level inside the cryostat is kept constant at 1.4×10^{-5} mbar by the carbon getter inside, and was found to be independent of both the elevation angle of the telescope and the rotator angle.
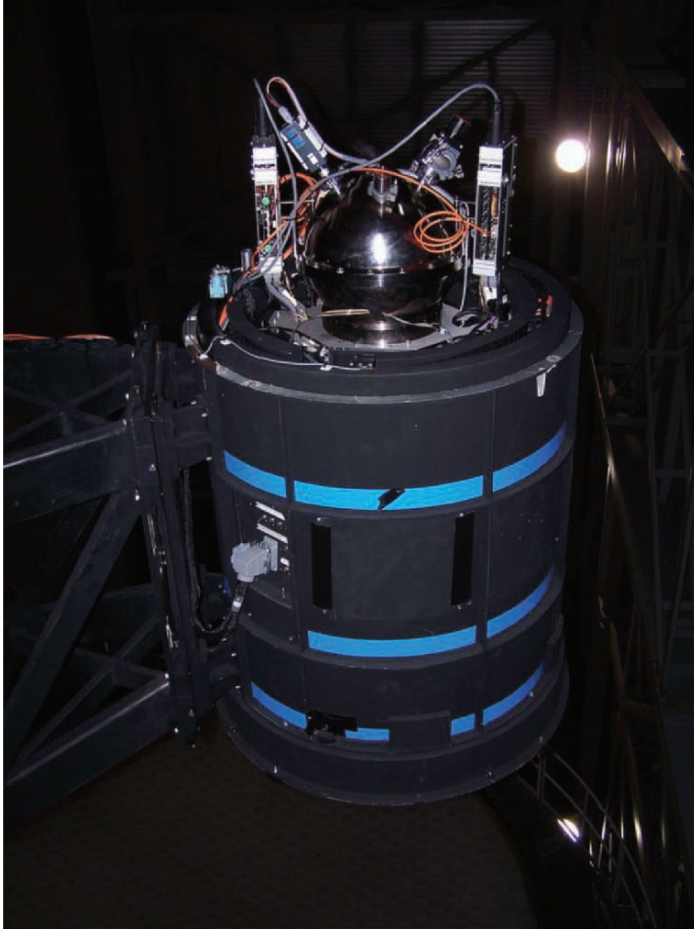
Figure 4. The blue channel of LBC.

4. FIRST TESTS ON THE SKY

The images of 10-15 point-like unsaturated sources have been extracted from the image of M51 (see Fig. 5). The average width at half maximum of the Point Spread Function (PSF) measured on this sample is FWHM = 5.4±0.2 pixel = 1.24±0.04 arcsec and the maximum percentage deviation with respect to the average is ±6%. This slight PSF variation may be due to the fact that, in this observing run, the active optics system was not working in closed loop, and so the control of the mirror shape and of the relative alignment between the primary mirror and the prime focus camera were performed by trial and error.
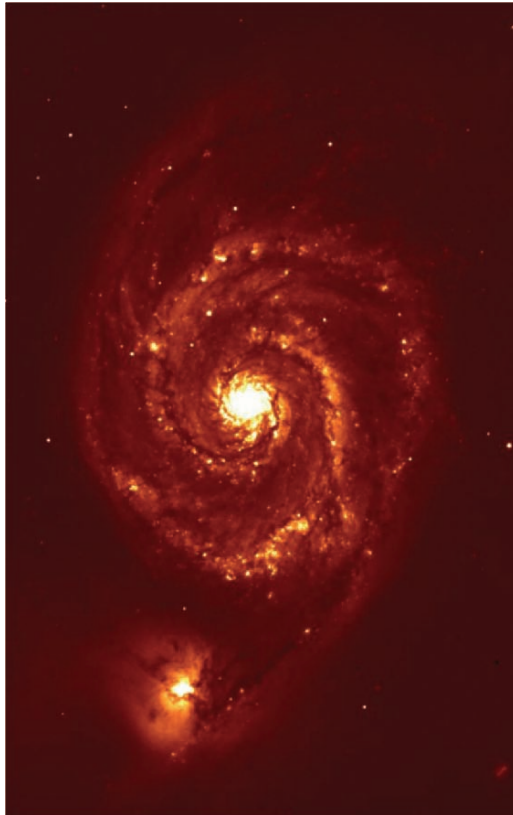
Figure 5. One of the first test images of LBC Blue: M51. (Chip #2, 60 sec, B filter, open loop).

By Summer 2005 the commissioning runs are concerned with the integration of the camera software and the Telescope Control Software

(TCS) to close the loop on the active optics and guiding systems with the aim to obtain sub arcseconds images.

5.   ACKNOWLEDGEMENTS

6.   REFERENCES

[1] Pedichini, F., et al,: 2003, *Instrument Design and Performance for Optical/Infrared Ground-based Telescopes*, Proceedings of the SPIE, Iye, Masanori, Moorwood, Alan F. M. (eds.), Volume **4841**, pp. 815-826.

[2] Pedichini, F. and Speziali, R., 2004, Scientific Detectors for Astronomy, The Beginning of a New Era, Amico, P.; Beletic, J. W.; Beletic, J. E. (eds.), Kluwer Academic Publishers, pp. 349-366.

[3] Speziali, R., Pedichini, F., Di paola, A., Fontana, A., Giallongo, E., 2004, *Ground-based Instrumentation for Astronomy,* Proceedings of the SPIE, , Iye, Masanori, Moorwood, Alan F. M. (eds.), Volume **5492**, pp. 900-908.

[4] Diolaiti, E., et al., 2003*, Instrument Design and Performance for Optical/Infrared Ground-based Telescopes,* Proceedings of the SPIE, , Iye, Masanori, Moorwood, Alan F. M. (eds.), Volume **4841**, pp. 552-563.

[5] Ragazzoni, R., et al., 2004, *Ground-based Instrumentation for Astronomy*, Proceedings of the SPIE, , Iye, Masanori, Moorwood, Alan F. M. (eds.), Volume **5492**, pp. 507-512.

RADIATION DAMAGE IN HST DETECTORS

Marco Sirianni[1,2] and Max Mutchler[2]
[1]European Space Agency, [2]Space Telescope Science Institute

Abstract: *We present an analysis of the radiation damage of CCDs on board the Hubble Space Telescope (HST). We describe the radiative environment of the HST and the impact seen in ACS, WFPC2 and STIS CCDs in terms of darkcurrent, hot pixels and charge transfer efficiency.*

Key words: *HST, radiation damage, CT E, hot pixels, annealing.*

1.   INTRODUCTION

The Hubble Space Telescope (HST) has been orbiting in a Low Earth Orbit (LEO) since April 1990. A large variety of scientific instruments have been installed on HST, each with a unique set of detectors (see Table 1).

2.   HST RADIATION ENVIRONMENT

HST orbits in a Low Earth Orbit, at about 580 km with an inclination of 28 degrees. Daily, HST completes approximately 15 orbits and on average crosses a portion of the South Atlantic Anomaly (SAA) region seven times/day.

The SAA is the region where the Earth's inner radiation belt makes its closest approach to the planet's surface. The inner belt contains mostly protons with energy between 10 and 50 Mev but also electrons, lower energy protons, cosmic ray ions. The population of trapped particles within the belts is not static. Increases in solar activity expand the atmospheres and increases

the losses of protons in LEO. Therefore, trapped radiation doses in LEO decrease during solar maximum and increase during solar minimum.

When HST tranverses the SAA, its detectors are exposed to several minutes of strong radiation. Although the radiative environment is constant, the unique properties of these devices pose different challenges to their functionality in space.

In this paper we will focus on the radiation impact seen in CCDs on board the HST. The amount of data available for this analysis varies among the instruments, with younger instruments being better monitored than older ones. We will, therefore, restrict our discussion to ACS, STIS and WFPC2 devices (see Table 2).

Two excellent reviews have been published in recent years. Pickel, et al. [1] and Srour, et al. [2] provide a summary of the evolution of radiation effect understanding in infrared detector technology, CCDs and active pixels sensors.

Table 1. Detector type and years on orbits for the main instruments of HST.

Detector type	Instrument	# of chips	Year on orbit
CCD	WFPC	8	3.5 (1990-1993)
	WFPC2	4	>12 (1993- present)
	STIS	1	>8 (1997-2004)
	ACS	3	>3 (2002- present)
	WFC3	2	0 (TBD)
Total		16 (+2)	
IR	NICMOS	3	>8 (1997- present)
	WFC3	1	0 (TBD)
Total		3 (+1)	
UV-MCP	SITS	2	>8 (1997-2004)
	ACS	1	>3 (2002- present)
	COS	1	0 (TBD)
Total		3 (+1)	

Radiation damage mechanisms in CCDs are divided into two general categories: Total Ionizing Dose (TID) and displacement damage effects [2,3]. Since all HST detectors are buried channel and are operated inverted they are principally subject to displacement damage and almost completely insensitive to charge generation and accumulation at the silicon-oxide interface, which is typical of TID damage. Displacement damage refers to the introduction of defects in the silicon lattice. Charged particles such as protons and neutrons can collide with silicon atoms and displace them from their lattice sites. This process results in vacancy-interstitial pairs, most of which immediately recombines. The vacancies that survive migrate in the lattice and form stable defects. Any defect gives rise to a new energetic level in the bandgap and alters electrical and optical performance of the device.

These defects degrade CCD performance by decreasing the Charge Transfer Efficiency (CTE), increasing the mean dark current and dark current non-uniformity by introducing individual pixels with very high dark current (also known as hot pixels or hot spikes).

Table 2. Basic HST/CCD specifications.

	ACS/WFC	**ACS/HRC**	**STIS**	**WFPC2**
	SITe	SITe	SITe	Loral
Qt. –Size (pixel)	2- 4096×2048	1- 1024×1024	1- 1024×1024	4- 800×800
Pixel size (µm)	15	21	21	15
Architecture	3-phase	3-phase	3-phase	3-phase
	thin- back ill.	thin- back ill.	thin-back ill.	thick-front ill.
Temperature (°C)	-77	-81	-83	-88
Readout	2 amp / MPP	1 amp /MPP	1 amp/MPP	1 amp /MPP
Parallel clock (Hz)	20	40	42	60
Minichannel	3 µm	3 µm	3 µm	-

3. ANALYSIS OF THE RADIATION DAMAGE

3.1 Dark Rate

In the depletion region of each pixel, energy levels near midgap are responsible for the generation of electron-hole pairs. Thermal excitation of a bound valence-band electron to the defect energy level can be followed by another excitation to the conduction band, thus generating a free electron-hole pair. Multi Pinned Phase (MPP) devices run into inversion and therefore the surface dark current is suppressed and the bulk dark current is the only contribution.

The average dark current increase correlates with the amount of displacement damage imparted by incoming protons. This behavior is seen on all HST CCDs as shown in Table 3. It is interesting to note that approximately five years after installation, the dark current for WFPC2 CCDs stopped increasing linearly. The reason for this behavior is still under investigation. It is known that the dark rate in WFPC2 is produced by two components. The first is the classical thermal generation of electron-hole pairs at the pixel level, the second is related to the fluorescence of the MgF_2 window, which correlates with the solar cycle.

3.2 Hot Pixels and Annealing

While the increase in mean dark rate with proton irradiation is important, the dark current non-uniformity (hot pixels) is generally a bigger concern for

astronomical applications. Some pixels show very high dark current up to several times the mean dark rate. Depending on the particular collision sequence, protons of the same energy may produce varying degrees displacement damage. Moreover, if a defect is created in a high electric field region, the contaminated pixel can show very large dark current as a result of field-enhanced emissions [4].

Hot pixels accumulate as a function orbit time. Figure 1 shows the evolution of the distribution of pixels over time at different dark rates for one ACS/WFC CCDs. As the proton-induced damage increases, the mean dark current (the peak of the distribution) and the hot pixels population (the tail of the histogram) increase. According to Hopkinson, et al. [5] a simple fit can be made assuming a Gaussian main peak whose half-width increases approximately as the square root of the fluence, and an exponential tail whose amplitude is proportional to fluence.

Table 3. Dark rate increase as a function of time for HST CCDs.

	WFC	HRC	STIS	WFPC2
e⁻/pix/hr/year	1.5 WFC1 2.0 WFC2	2.1	3.3 (side 1) 2.2 (side 2)	2.0 (1993- 1998) ~ 0 (>1998)
Temperature (ºC)	-77	-81	-83 (side 1) <-83 (side 2)	-88
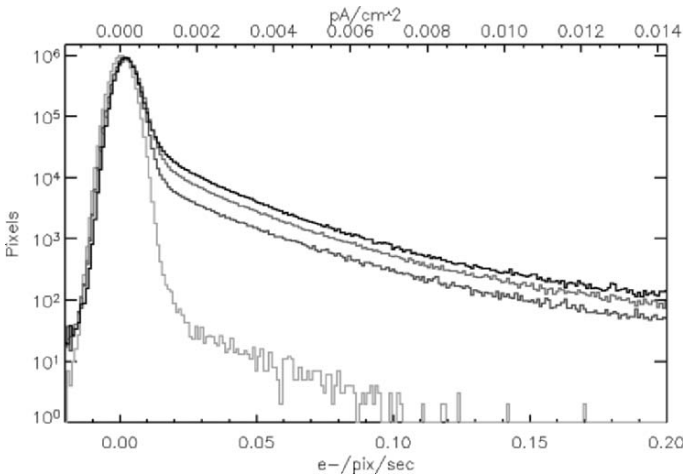
Figure 1. Distribution of dark pixels for *(bottom)* one WFC CCD at launch (2002), and after 1,2 and 3 years on orbit.

Sirianni, et al. [6] discussed the evolution of hot pixels in ACS CCDs and found that the number of new hot pixels with a dark current higher than the

mean dark current increases every day by few to several hundreds depending on the threshold used (see Table 4). In order to partially anneal the hot pixels, all HST instruments perform monthly anneal, by raising the CCD temperature to approximately +20 C for few hours. Although it is still not clear why significant annealing is observed at such low temperatures (the most common defects in silicon anneal at much higher temperatures), we can report a few interesting findings (see [7] for more details):

- The annealing rate strongly depends on the dark rate of the hot pixel. Very hot pixels show a higher anneal rate than warmer pixels and there is no impact on the average dark current level [6].
- The same anneal rate can be obtained at colder temperatures. In at least four instances, in occurrence of HST safing events, the temperature of ACS CCDs were raised to -10°C for periods ranging between 24 and 48 hours. After these periods the population of hot pixels decreased by the same amount as in a normal anneal cycle at +20°C.
- The anneal rate does not seem to be related to time. Since launch the anneal time for ACS CCDs have been reduced first from 24 to 12 hrs and more recently from 12 to 6 hr without impacting the annealing effectiveness.
- For any particular hot pixel, a complete anneal is a rare event. Most of the annealed hot pixels significantly reduce their dark current level but never rejoin the population of normal (Gaussian distribution) dark pixels.
- Several hot pixels show evidence of reverse annealing. While most of the hot pixels show some degree of healing in response to an annealing procedure, some of them may be activated to "hot" by the same procedure. This occurred to pixels that have been damaged by radiation and that, depending on the anneal cycle, they may lose or regain the status of "hot pixel". Figures 2 and 3 show examples of normal and reverse annealing respectively.

Table 4. Anneal rate for different HST CCDs.

	ACS/WFC		ACS/HRC		STIS		WFPC2	
Temp	-77	°C	-81	°C	-83	°C	-88	°C
Annealing Temp	-10 to + 20		-10 to + 20		+5		+30	
Annealing Duration	6 to 24 hr		6 to 24 hr		24 hr		24 hr	
Threshold	%	+/-	%	+/-	%	+/-	%	+/-
> 0.02	0.55	0.02	0.64	0.02			0.80	0.05
> 0.04	0.70	0.07	0.84	0.07				
> 0.06	0.78	0.04	0.84	0.04				
> 0.08	0.82	0.03	0.87	0.03				
> 0.10	0.84	0.02	0.85	0.02	0.77	0.05		
> 1.0	0.55	0.15	0.64	0.15				
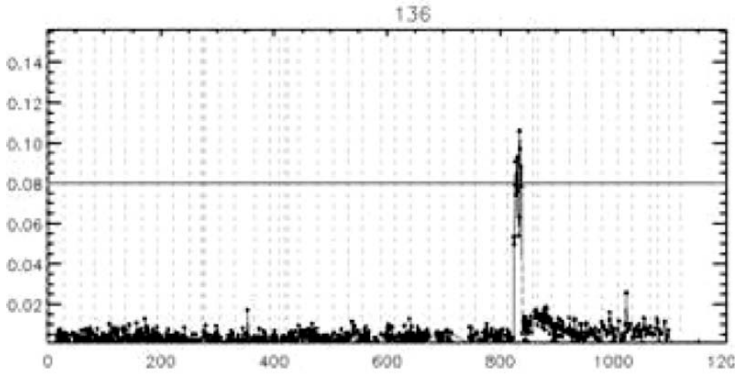
Figure 2. Signal level of hot pixel # 136 as a function of time (days). Vertical dashed lines mark the annealing dates. The horizontal line marks the threshold for hot pixel definition. The signal level is in e⁻/pix/sec at -77 C. The pixel is damaged just after
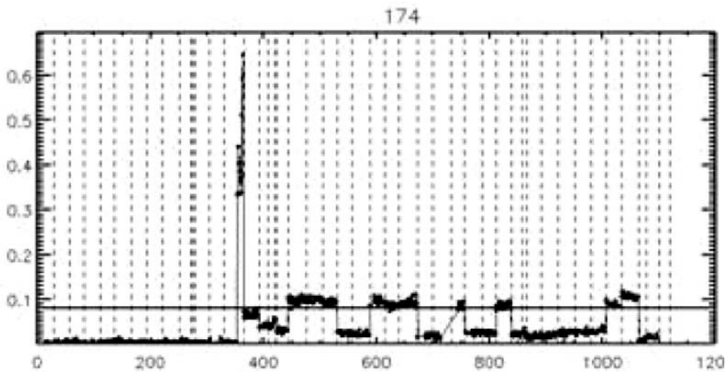
day 800 and it is fully healed after the first annealing cycle.

Figure 3. Signal level of hot pixel # 174 as a function of time (days). The pixel is damaged after day 350. Following anneal cycles partially heal the pixel whose dark current jumps between discrete levels in correspondence of anneal cycles.

3.3   Charge Transfer Efficiency

CTE degradation has the largest impact on the scientific application of CCDs in space. The trapping of charge during the readout causes errors in stellar photometry, stellar astrometry and the observed surface brightness of extended objects. There are many techniques to measure the CTE of a CCD. On HST only the flight software of ACS could enable Extended Pixel Edge Response (EPER) and First Pixel Response (FPR) tests during orbit. ACS

CTE is monitored monthly at the Fe^{55} signal level and twice a year over a wide range of signal levels (see Sirianni, et al. [6] and Mutchler, et al. [8] for more details). At each signal level the CTE is degrades linearly with time. For ACS and all the other HST CCD-based instruments a corrective formula applied to photometric measurements to remove the impact of CTE degradation has been derived by observing a star cluster (see for example Riess, et al. [9]). By positioning the same star in different positions across the CCD it is possible to measure the amount of charge lost due to CTE degradation. By using several stars with different brightness and different filters to simulate various background conditions it is possible to derive a formula that takes into account the signal in the PSF, the position in the chip, the background level and the time of the observation. These tests measure the "missing charge" and therefore can provide an absolute measurement of CTE. If Δmag is the missing flux (in magnitude) after the star has been transferred through n rows the classical CTE figure is:

CTE = 10^(Δmag/2.5n).

We compared CTE degradation for all HST CCDs in Fig. 4. For ACS/WFC the results from the EPER test and the photometric test are in perfect agreement. A corrective formula for ACS/HRC is still not available, so we show only the EPER results. The STIS and WFPC2 trends are derived from photometric tests. It is clear that the WFC CCD is degrading much less rapidly than WFPC2 CCDs. A fair comparison should take into account the operating temperature and the clocking rate, which are fundamental factors for CTE performance.
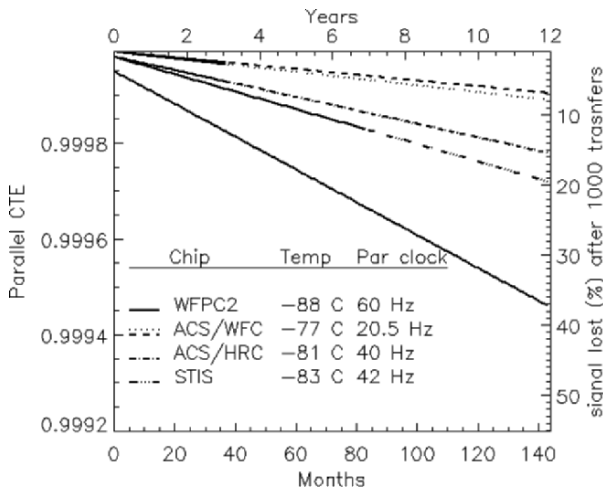
Figure 4. Evolution of parallel CTE as a function of time on orbit. Two lines are shown for ACS/WFC: the dotted line is the trend inferred from the star photometry test, the

dashed line is from the EPER test. The solid segment of each line shows the actual time spent on-orbit.

4.   REFERENCES

[1] Pickel, J.C., Kalma, A.H., Hopkinson, G.R., and Marshall, C.J., 2003, IEEE Trans. Nucl. Sci. vol **50**, 671.
[2] Srour, J.R., Marshall, C.J., and Marshall, P.W. 2003, IEEE Trans. Nucl. Sci. vol **50**, 653.
[3] Clampin, M., et al., 2005, these proceedings.
[4] Dale, C.J., Marshall, P.W., and Burke, E.A. 1990, IEEE Trans. Nucl. Sci. vol **37**, 1784.
[5] Hopkinson, G.R., Dale, C.J., and Marshall, P.W. 1996, IEEE Trans. Nucl. Sci. vol 43, 614
[6] Sirianni, M. Mutchler, M., Clampin, M., Ford, H., Illingworth, G., Hartig, G., van Orsow, D., and Wheeler, T. 2004, SPIE Vol **5499**, 173.
[7] Sirianni M. et al.. 2005, *The darkrate and hot pixels in ACS CCDs ACS-ISR* , STScI (Baltimore, MD), in preparation.
[8] Mutchler, M. and Sirianni, M. 2005, ACS –ISR 05-03, STScI (Baltimore, MD)
[9] Riess, A., and Mack, J. 2004, ACS –ISR 04-06, STScI (Baltimore, MD)

The workshop mug.

AN EUV IMAGE DETECTOR FOR THE SPACE SOLAR TELESCOPE

Qian Song, Binxun Ye and Zhaowang Zhao
National Astronomy Observatories, CAS

Abstract: *We have created an experimental model of the detectors for the EUV telescope, which will be on board the Space Solar Telescope as an important payload. A EUV detector, consisting of a EUV sensitive phosphor screen, an MCP image intensifier, a fiber optic taper and a CCD camera, was built and evaluated. Better than 26 Lp/mm resolution was achieved.*

Keywords: *EUV image detector, EUV phosphor, MCP intensifier.*

1.   INTRODUCTION

In an attempt to achieve a breakthrough in solar physics, the Solar Space Telescope (SST) expects to observe the transient and steady solar hydrodynamic and magneto-hydrodynamic processes and their continuous time evolution with 2-dimension real-time polarizing spectra, EUV and Hα images with high spatial and temporal resolution. The payloads will include: a Main Optical Telescope (MOT) with a 2-D polarizing spectrograph working in eight channels simultaneously, an EUV Telescope (EUT), an Hα and white light telescope, a wide band spectrometer investigating high energy flare processes at γ-ray and x-ray wavelengths, and a solar and interplanetary radio spectrometer working at 1-60GHz observing non-thermal electron populations [1].

EUT consists of four strictly parallel-aligned telescopes working at four EUV wavelengths simultaneously. The four normal incidence telescopes are mounted in a vacuum vessel and aligned with MOT to view the same target

area. To acquire EUV images of the quiet sun with a spatial resolution of
0.5", the detectors of EUT were designed as a system that includes an EUV
sensitive phosphor, fiber taper, MCP image intensifier, CCD, camera
electronics and cooling block. This not only improves sensitivity for low
intensity scenes, but as a bonus provides an electronic shutter with no
moving parts [1,2]. As the engineering study proceeded, we adjusted the 0.5"
resolution to 0.8" and also changed the focal length of the telescope. This
required adjusting the spatial resolution of the detector to 36.6 Lp/mm.
Based on this design an experimental detector was built and tested to
evaluate the feasibility of the architecture.

2.   DETECTOR DEVELOPMENT

The detector is designed as a synthesis of a phosphor screen, an MCP
image intensifier and a CCD with fiber optics to match the image format (see
Fig. 1).
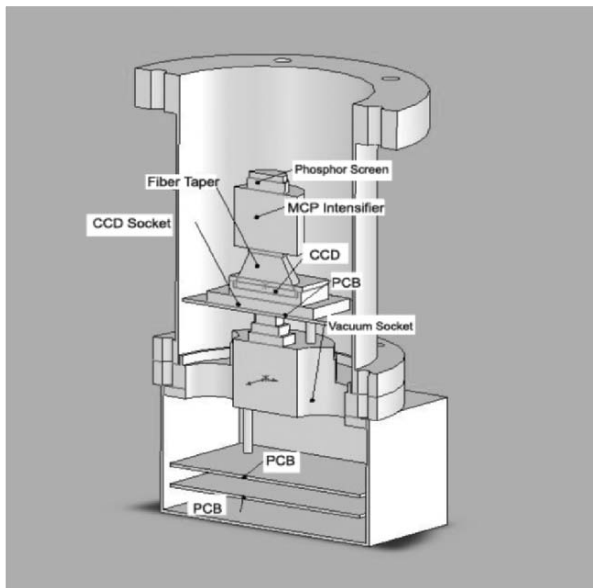
Figure 1. The structure of the EUV detector.

Other requirements are: 2048×2048 image format, a 12 bit dynamic
range between the CCD readout noise and full well capacity, and spatial
resolution that matches that of the telescope (0.8", 27.3 μm or 36.6 Lp/mm).

With the phosphor screen preceding the MCP intensifier, EUV photons become visible and are therefore able to penetrate the window of MCP intensifier. To verify the phosphor's response in the EUV band, the screen was tested at the Beijing Synchrotron Radiation Facility (BSRF). The phosphor screen was illuminated with EUV radiation and a photodiode was placed just behind the screen. The output current of the diode was measured as a function of incident radiation wavelength ranging from 6 nm to 27 nm (see Fig. 2).
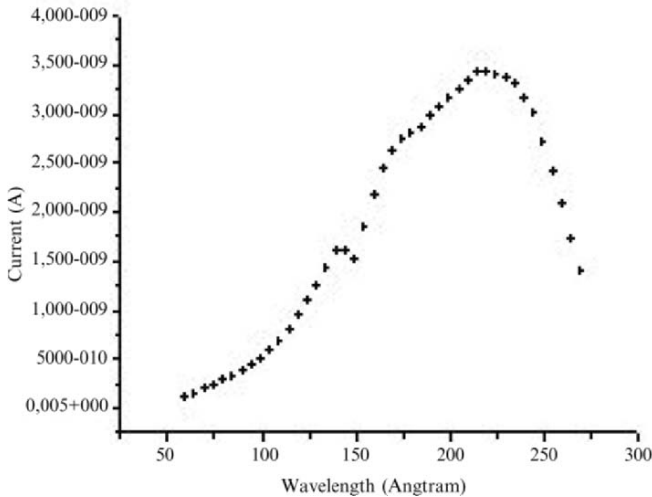
Figure 2. Response test of the EUV-converting phosphor screen.

Because the spectral intensity distribution over the tested EUV wave band was not calibrated, Fig. 2 does not exactly reflect the spectral response. The purpose of the experiment was to simply check if the phosphor is sensitive over the waveband concerned. Figure 3 shows the relationship of the photodiode's current generated by phosphor radiation and the current of the circulating electrons in the storage ring of the synchrotron radiation facility. Since the latter varies roughly linearly with respect to the intensity of the EUV radiation beam, Fig. 3 roughly reflects the linearity of the phosphor. The output of the diode did not increase after the current in the storage ring reached 90mA; this resulted from saturation of the phosphor.

The resolution of the MCP image intensifier is 57 Lp/mm. The gain is 8900 cd/m^2/Lx, which leads to an equivalent background irradiance 0.16 μLx. The resolution of the optic taper is better than 102Lp/mm. Figure 4 shows the integrated detector. The left panel shows the inside structure and the right panel shows the exterior.
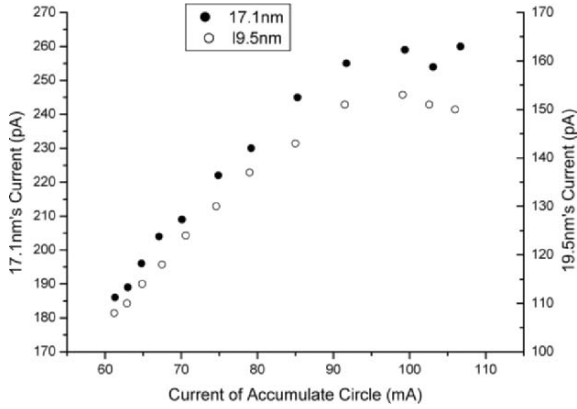
Figure 3. The relationship of the photodiode's current generated by phosphor radiation and
the current of the circulating electrons in the storage ring.
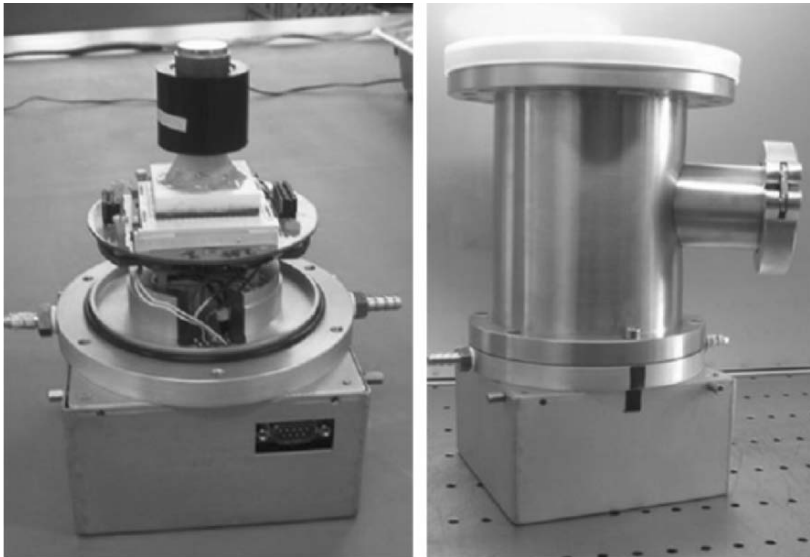
Figure 4. The integrated EUV detector.

3. TESTS AT THE OPERATING WAVELENGTH

The gain of the CCD camera, measured with the photon-transfer technique, was measured to be 3.95 e⁻/ADU. Figure 5 shows a 5 sec dark image of the integrated detector. The bright disk is the image of the MCP intensifier's background irradiance, which is an average of 800 ADU higher than the CCD.
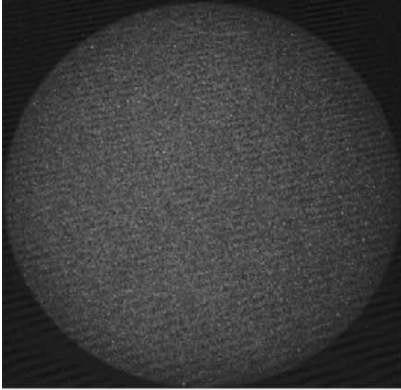
Figure 5. A 5 sec dark image.

Figure 6. Image of the beamed radiation at 17.1 nm

Figure 6 is an image of the 17.1 nm radiation of the beam used for the experiments. To evaluate the spatial resolution, a grid was used (see Fig. 7). The grid is divided into 4 areas with the opaque and void strips with widths of 9, 13, 19 and 23 μm respectively. Since the radiation beam was well collimated, the grid was installed directly in front of the phosphor screen of the detector with no additional optical devices to project the image of the grate on the detector. Figure 7 (right) shows the image of the grid acquired with the detector. The grid plate was not thick enough for the blocking strips to be completely EUV opaque and the darker area in the center results from a lack of thickness uniformity of the grid plate. In the image acquired, the 19 μm grid can be resolved. Therefore the detector resolution is better than 26 Lp/mm. Figure 8 is the intensity distribution of the 19 μm grid image.

The cross section of the EUV light beam is small enough to be confined within the sensitive area of the EUV photo-diode installed in the beam or within the bounds of the EUV detector. Therefore, the total photon flux F_{photon} of the radiation beam can be acquired with the diode by

$$F_{photon} = \frac{3.65}{E_{photon}} \cdot \frac{I}{q_e},\qquad(1)$$

where E_{photon} is the photon energy in eV, I is the current of the diode in amps and q_e is the charge of one electron in coulombs. We define the response of the detector as the ratio of output electrons in the CCD readout node to the number of the incident EUV photons. Figures 9 and 10 show this ratio at 17.1 nm and 19.5 nm. The response of the detector is measured to be 18 e⁻/photon and 21 e⁻/photon at wavelengths of 17.1 nm and 19.5 nm respectively.
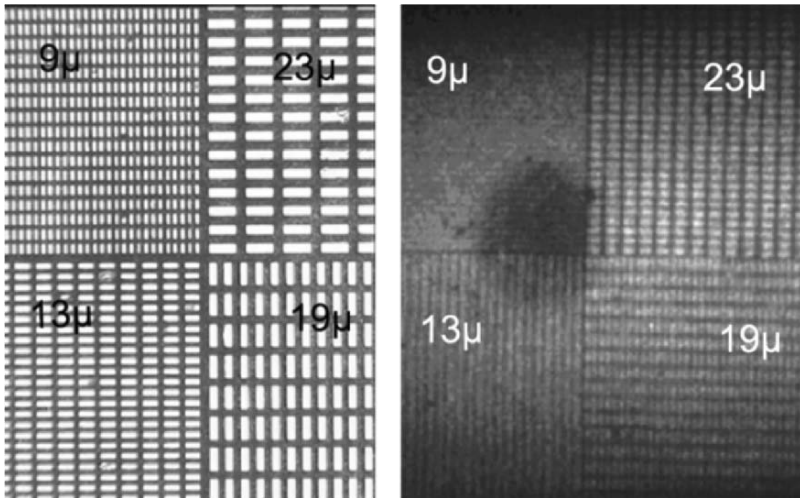
Figure 7. (left) Spatial resolution test grid and *(right)* its corresponding EUV image acquired with 17.1 nm wavelength illumination.
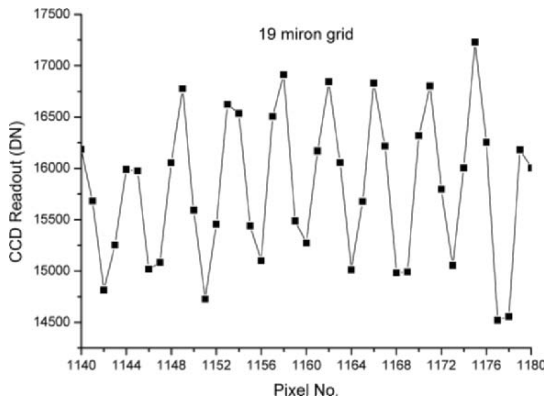
Figure 8. Intensity distribution of 19 μm grid image.
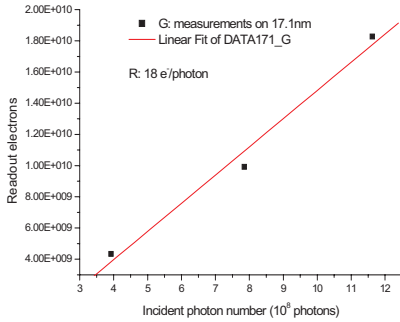
Figure 9. Response of the detector at a wavelength of 17.1nm.
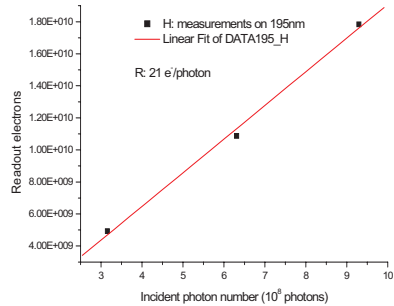
Figure 10. Response of the detector at a wavelength of 19.5nm.

4. DISCUSSION

From the data obtained we can conclude that the spatial resolution and response of the detector do not achieve the requirements of the project. The biggest constraint is the EUV sensitive phosphor.

A better phosphor is expected, which will improve performance without changing the architecture. However it will be difficult to find an appropriate replacement. Therefore, an open MCP intensifier with a CrI or KBr-coated photon cathode will replace the EUV phosphor and will drastically improve performances and hopefully meet requirements.

L3CCD technology is developing rapidly and is beginning to "shed light" on our endeavor of intensified EUV image detection. The combination of L3CCD technology and a 2K×2K EUV CCD is now feasible and may be the simplest solution to the problem.

5. ACKNOWLEDGEMENTS

6. REFERENCES

[1] Study Team of SST, 1997, *The Assessment Study Report of Space Solar Telescope.*

[2] Q. Song, B. Ye, J. Cao, B. Chen, W. Cao, 2001, Design concepts of EUV telescopes and the detectors boarded on the Solar-Space-Telescope, Proc. SPIE, **4498**, 335-342.

Qian Song and his wife Yimin Jiang enjoy the Festa Paesana
with the French Quarter looming behind.

THE CAMERA OF THE COROT SPACE EXPERIMENT: DESIGN, TESTS AND RESULTS

The CorotCam Team

Centre National d'Etudes Spatiales (CNES), Institut d'Astrophysique d'Orsay (I1S), Laboratoire d'Astrophysique de Marseille (LAM), Traverse du Siphon-Les trios Lucs, Laboratoire d'Etude Spatiales et d'Instrumentation en Astrophysique (LESIA), Observatoire de Paris-Meudon

Abstract: *The Corot project, developed in the framework of the CNES small satellite program with a widespread European cooperation, will be launched in 2006. It is dedicated to Astero-Seismology (AS) and Exo-Planet Finding (PF). It will perform relative photometry in visible light, during very long (150 days) observing runs. Both programs will run simultaneously and ~50,000 stars will be observed over 3 years of operation. The camera, test bench and testing are discussed.*

Key words: *Camera, space mission, instrumentation and calibration.*

1. INTRODUCTION

The Corot project, developed in the framework of the CNES small satellite program with a widespread European cooperation, will be launched in 2006. It is dedicated to Astero-Seismology (AS) and Exo-Planet Finding (PF). It will perform relative photometry in visible light, during very long (150 days) observing runs in the same direction [1]. Both programs will run simultaneously and ~50,000 stars will be observed over 3 years of operation.

The instrument is based on an off-axis telescope (27 cm pupil, 3° square field of view) using a dioptric objective that projects the stars onto the focal plane. The focal plane consists of four e2v back-illuminated, frame transfer, AIMO, 2K×4K pixels, CCD42-80 CCDs operated at -40°C. The focal

plane is arranged as two pairs of CCDs for each of the two camera systems. The AS and PF scientific programs each have dedicated cameras. Electronics boxes will perform the CCD readout, the thermal control and housekeeping, onboard software pre-processing, and data reduction [2].

The camera sub-system consists of a dioptric objective, focal plane array, front-end electronics boxes, mechanical parts (shielding) and thermal equipment (MLI, active thermal control).

The camera sub-systems were integrated and calibrated on a customized test bench. The qualification camera system has passed all the environmental tests (thermal balance and mechanical vibration). The flight camera system has been optically set-up with the telescope and calibrated, and is ready for delivery. The deliverables include the camera sub-system (constraints and design), test bench, and suite of test results consisting of focalplane integration, optical setup, thermal balance and camera calibration.

Teams from different French laboratories have worked on the cameras for over a year with support and funding from the French Space Agency.

2.   CAMERA DESCRIPTION

The following is a list of the different sub-systems that constitute the camera:

- The dioptric objective (OD), consisting of 6 lenses, projects the FOV onto the CCD. The OD is equipped with calibration LEDs and two active thermal controls (probes and heaters) controlled by the spacecraft.
- The focal-box (BF) contains the four CCDs, the prism and the active thermal control of the CCDs. The e2v CCD42-80 (2K×4K) CCDs (see Fig. 1) operate in AIMO and frame-transfer mode. Two CCDs are dedicated to each of the AS and the PF camera subsystems. The focal plane is divided into two parts with an offset of a few millimeters between each pair of CCD (for different PSF shaping).
- The front end electronics (EP) generate the clocks and biases for the CCDs, and performs processing on the video signal of pre-clamping and amplification. Connections to the CCDs are through flex cables.
- The thermal drains that cool the CCD and the front-end electronics (connected to dedicated radiators).
- The mechanical interface optimally focuses the CCDs . It consists of the BIF (interface mechanical piece) which contains all the mechanical parts including the shims (of different thickness) to optically align the CCD.
- The shield protects the CCDs against protons and cosmic rays and provides the mount for the EP boxes.

- Thermal components such as the MLI, thermal probes and heaters provide thermal regulation.

The manufacturers involved in the various design studies and realization of the project are:
- Sodern for the focal-box and dioptric objective.
- Soditech/Teuchos for the thermal and mechanical study.
- Alcatel Valence for the front-end electronics.
- e2v for the CCD42-80 CCDs.

The laboratories that provided management and performed some of the design studies are:
- CNES (Centre National d'Etudes Spatiales) for the thermal and mechanical studies.
- IAS (Institut d'Astrophysique d'Orsay) for the prism and optical studies.
- LAM (Laboratoire d'Astrophysique de Marseille) for the optical studies.
- LESIA (Laboratoire d'Etude Spatiales et d'Instrumentation en Astrophysique) for the management, system and electrical studies.
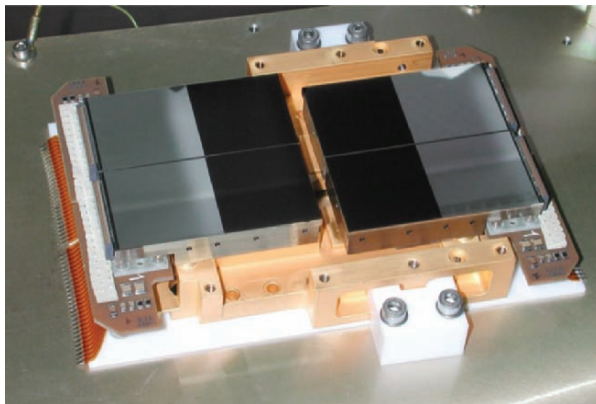
Figure 1. The focal plane with the four CCDs.

3.   THE CAMERA TEST BENCH

The test bench was developed at the Institut d'Astrophysique d'Orsay (IAS) where different facilities have been used.

The test bench has four separate parts:
- The vacuum chamber and the active thermal control (IAS facilities) cool and regulate various items including the focal plane which is stabilized to -55°C.
- The mechanical support for the camera and support electronics (IAS facilities) have X/Y axis motors that enables optical stimuli to be placed anywhere on the focal plane with an accuracy of 1µm.
- The optical bench has two test camera systems. One that measures the gap between the CCDs by simulating a star at a given "infinity" (the OD has a strong focal curvature). A wavefront analyzer allows control of the optical bench. The other for calibration that simulates a given field of view.
- The electrical test equipment and software that provides full control of the functions of the test bench and image acquisition. Some real time image processing (for quick-look) is available. All image data is stored on hard disk for later data analysis.

4.   THE TESTS PERFORMED

A variety of tests were performed on the camera. Their description follows:

Thermal tests:
- The internal and external interfaces were validated to determine that the absolute temperature of the CCD will remain under $-40°C$ during the life-time of the instrument.
- The active thermal control of the focal-box was analyzed to fine-tune (determine gain of the thermal control loops) the thermal control system.
- The passive thermal control of the electronics was validated.
- It was determined that external thermal probes can be used for the absolute calibration of the flight probes (used for house-keeping purposes).

Optical tests:
- The positioning of the CCDs inside the focal-box was measured to determine that the requirements of focus accuracy of $< \pm 20$ µm and lateral gap between CCDs of $< \pm 100$ µm were met.
- The effect of change in temperature of the DO on the shape of the PSF was determined. The focus of the OD was determined to have a temperature variation of 23 µm/K for a homogenous temperature and less than 5 µm/K for a spatial gradient.

- The dispersion of prism was measured and agreed with the expected value.
- The absolute transmission of the camera at different wavelengths was measured. The global "response" of the camera was in good agreement with the modeling (taking in account the response of the different sub-systems of the camera).

Electrical tests:

- Readout noise and cross-talk between the two CCD outputs was measured. At a pixel rate of 150 kHz, the global noise (including EMC) was 11 e⁻. Cross-talk was less than 0.1%.
- All flight electronics and flight chronograms were tested for electro-magnetic-compatibility. This showed predictable effects of about 1-3 ADU on the offset. In addition, the gains of different video chains were measured.

The qualification model passed the environment tests and the flight model has been integrated on the telescope for the final optical adjustment.

5.   REFERENCES

[1]   Auvergne, M, Boisnard, L, Buey, J.T., Epstein G., Hustaix H., Jouret, M., Levacher, P., Berrivin, S., Baglin, A., 2003, *COROT-high-precision stellar photometry on a low Earth orbit: solutions to minimize environmental perturbations*, Future EUV/UV and Visible Space Astrophysics Missions and Instrumentation. Blades, J. Chris, Siegmund, Oswald H. W. , (eds.), Proceedings of the SPIE, Volume **4854**, pp. 170-180.

[2]   Boisnard, L., Auvergne, M., COROT *System Requirements for Accurate Stellar Photometry*, 2001, 52nd International Astronautical Congress, Toulouse, France. IAF-01-Q.1.09.

Phillip MacQueen ponders reconstruction of the Greek temples in Agrigento.

Juliet Beletic and Ray DuVarney don't ponder, but get to work.

SECOND GENERATION IR DETECTORS FOR THE WIDE FIELD CAMERA 3

Massimo Robberto[1], Sylvia Baggett[1], Rebecca Blackmon[2], Tom Brown[1], Howard Bushouse[1], Gregory Delo[2], Donald Figer[1], Roger Foltz[2], George Hartig[1], Bryan Hilbert[1], Robert J. Hill[2], Scott D. Johnson[2], Randy A. Kimble[2], John W. Mackenty[1], Eliot M. Malumuth[2], Elizabeth Polidan[2], Sam Reed[2], Anne Marie Russell[2], Augustyn Waczynski[2], Yiting Wen[2]
[1]Space Telescope Science Institute, [2]NASA Goddard Space Flight Center

Abstract: *High-energy particles that induce a glow on the ZnCdTe substrate of the HgCdTe detectors of WFC3 may increase the background noise and reduce the scientific performance of the instrument. To eliminate this problem, a second generation of infrared detectors with substrate removed is under construction. Early tests indicate that the glow problem is eliminated and the quantum efficiency increases dramatically at shorter wavelengths, potentially providing a substantial improvement in the limiting sensitivity of the instrument.*

Key words: *Hubble Space Telescope (HST), Wide Field Camera 3 (WFC3), HgCdTe detectors, ZnCdTe substrate removal.*

1.   INTRODUCTION

The Wide Field Camera 3 (WFC3) is the latest imager built for the Hubble Space Telescope (HST) and is planned to replace the Wide Field Planetary Camera 2 (WFPC2) in the next servicing mission to the HST. WFC3 (see Fig. 1) is configured as a two-channel instrument [1]. The UVIS channel provides diffraction limited imaging from the 2000 Å to ~1 μm and uses two large format e2v CCD43 4K×2K CCD devices optimized for near-UV sensitivity. The IR channel is optimized for the 0.8-1.7 μm region. It

uses a HgCdTe focal plane from Rockwell Scientific Company (RSC) with long wavelength cutoff at 1.7 μm. The detector, operating at 150 K, is hybridized on a HAWAII-1R multiplexer providing 1024×1024 pixels of 18 μm pitch, including 5 outer rows and columns of reference pixels.
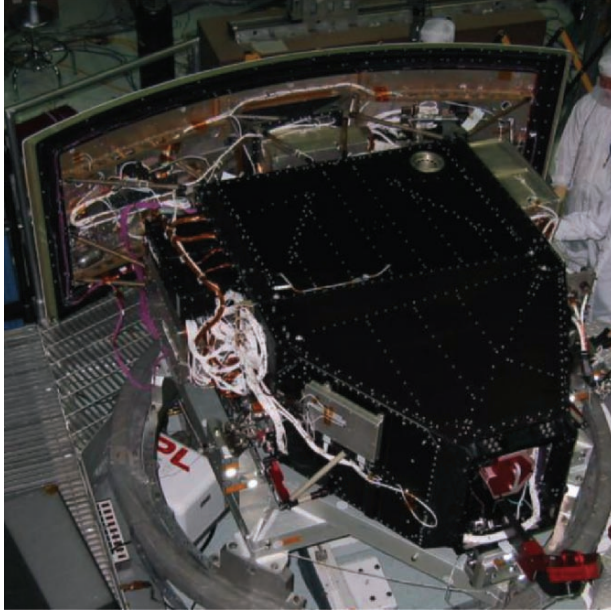
Figure 1.   Fully assembled WFC3 at the Goddard Space Flight Center prior to the installation of thermal blankets.

In September 2004 WFC3 successfully conducted a thermal vacuum performance characterization test at the Detector Characterization Laboratory (DCL) of the NASA Goddard Space Flight Center (GSFC). Its installation on the HST is contingent upon authorization of shuttle-based servicing of HST after a successful return-to-flight.

2.   CURRENT IR FLIGHT DEVICES: FPA64 AND FPA59

The production of the original flight detectors for WFC3-IR ended in Summer 2003 with the selection of two devices, FPA#64 as prime, and FPA59 as backup [2]. FPA#64 has been packaged in its flight assembly (see Fig. 2) and underwent extensive thermal vacuum testing. In parallel with the integration and system level tests done at Ball and at the GSFC, the WFC3 team has carried out further test activities to characterize the performance of

similar devices in the space environment. In particular, the effects of cosmic ray radiation have been evaluated in two runs at UC Davis, exposing the detectors to proton beams of different energy and flux while they were operated in standard data acquisition mode. A surprising result of these tests [3] was the appearance of an extra diffuse background between the pixels directly hit by the protons. Systematic investigation of the phenomenon vs. input proton energy demonstrates that the source is the deposition of proton energy in the thick (~ 0.8 mm) ZnCdTe substrate, while the morphological similarity of the background to the shape of short-wavelength flat fields suggests that the physical mechanism is likely luminescence near the short-wavelength cutoff of the ZnCdTe (near 800 nm).
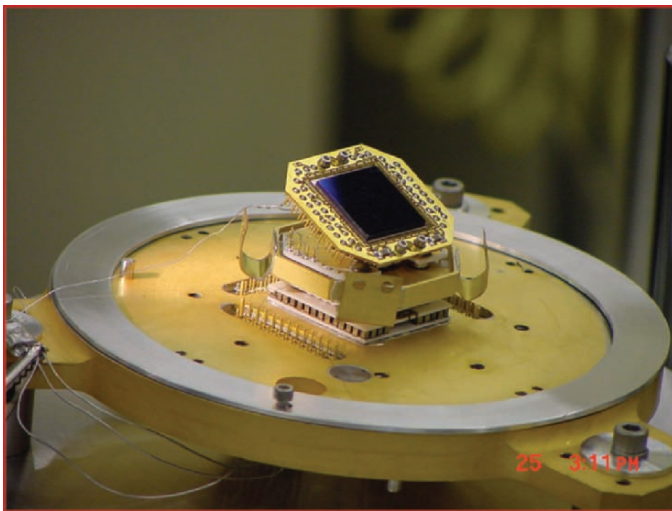
Figure 2. FPA64 packaged in its flight assembly.

Scaling of the laboratory results to the on-orbit high-energy particle fluxes suggests that this mechanism could add ~ 0.25 e$^-$/s/pixel to the diffuse background rate in the space environment, though in the absence of a detailed understanding of the physical mechanism, this estimate is highly uncertain. This level of background could lead to a significant degradation of the sensitivity of the instrument.

RSC suggested that removing the entire ZnCdTe substrate should eliminate the anomaly. Substrate removal also offers the advantage of increasing the quantum efficiency in the J-band and pushes the blue cut-off of the detector down to 0.4 μm.

3.   SECOND GENERATION DETECTORS WITH SUBSTRATE REMOVED

The substrate removal process has been carried out by RSC on two early WFC3 detectors. Radiation tests made at U.C. Davis have demonstrated that with these devices the extra background is now undetectable, with upper limits approximately three orders of magnitude lower than the previous substrate-induced background levels. Scaled to the orbital environment, these limits correspond to a negligible level of background signal compared with the intrinsic dark current of the devices. Two new lots of detectors have since been produced, and recent measurements at the GSFC Detector Characterization Laboratory confirm the expected increase of QE at shorter wavelengths (Fig.3).
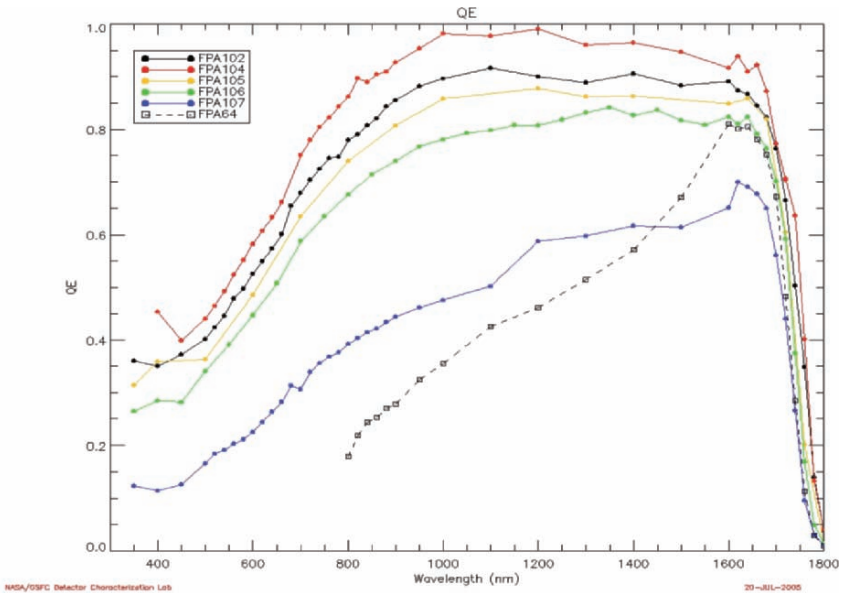
Figure 3. Comparison of the GSFC/DCL measured quantum efficiency of the current flight detector FPA#64 with a number of second generation, substrate removed, WFC3-IR FPAs. From top to bottom: FPA#104, FPA#102, FPA#105, FPA#106 (all substrate removed), FPA#107 (incomplete substrate removal), FPA#64. Detector gain was measured with photon transfer mode.

4. SCIENTIFIC PERFORMANCE

To illustrate the change in sensitivity, we compare the performance attained by WFC3 with FPA#64 vs. the new substrate removed FPAs in Fig. 4. We consider a few representative cases: 1) FPA#64 and WFC3 as-built; 2) FPA#64 with 1 e⁻/s/pixel of extra glow due to cosmic rays (worst case scenario); 3) FPA#64 with 0.25 e⁻/s/pixel extra glow (best guess scenario); 4) Second generation FPA with same RON of FPA#64 (24 e⁻/pixel DCS); 5) Second generation FPA with high RON (40 e⁻/pixel DCS); 6) Second generation FPA with low RON (15 e⁻/pixel DCS). We consider 4 filters, F110W and F160W (approximately the standard J and H passbands); F126N (a representative narrow-band filter) and F093M, roughly corresponding to the z-band often used with CCD detectors (e.g. ACS/HST).
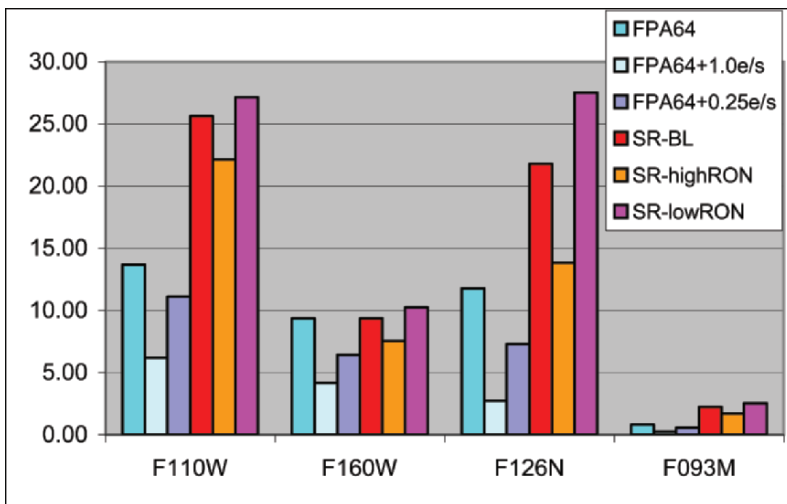
Figure 4. Discovery efficiency of WFC3 normalized to NICMOS Camera (F110W, F160W, F126N) and ACS/WFC (F093M).

Figure 4 shows the discovery efficiency (1/observing time needed to reach a given SNR on a faint point source × the detector area in square arcmin) normalized to the current NIC3 values (to ACS for F093M). The second generation detectors could nearly double the discovery efficiency at short wavelengths and also be competitive with ACS in the F850LP (note however the different pixel scale: 013" of WFC3-IR vs. 0.05 of ACS); for broad-band surveys the gain in blue QE easily offsets a potential increase of readout noise. On the other hand, a luminescence of 1 e⁻/s/pix would have a dramatic impact on the discovery efficiency with FPA#64.

5. CONCLUSION

ZnCdTe substrate removal on the WFC3 HgCdTe detectors eliminates proton-induced glow and significantly increases the detector QE at short wavelengths. Substrate removal therefore has two positive impacts on the limiting sensitivity of the instrument. Extensive tests are currently underway at GSFC/DCL to fully characterize the new devices. Early results are promising and suggest that WFC3 will significantly benefit from the inclusion of a substrate removed IR FPA.

6. REFERENCES

[1] Kimble, R.A., MacKenty, J.W., and O'Connell, R.W., and the WFC3 Team, 2004, Proc. SPIE, **5487**, p. 266.
[2] Robberto, M., Baggett, S.M., Hilbert, B., MacKenty, J.W., Kimble, R.A., Hill, R.J., Cottingham, D.A., Delo, G., Johnson, S.D., Landsman, W., Malumuth, E.M., Polidan, E., Russell, A.M., Waczynski, A., Wassell, E., Wen, Y., Haas, A., Montroy, J.T., Piquette, E.C., Vural, K., Cabelli, C., and Hall, D.B., 2004, Proc. SPIE **5499**, p. 15.
[3] Hill et al., 2005, these proceedings.

Massimo Robberto and his daughter Gloria enjoy the hike to the castle in Forza d'Agró. Olaf Iwert is on task in an intensive conversation in the background.

IMAGING TECHNIQUE OF THE DISR CAMERA ON THE HUYGENS LANDER

J. Rainer Kramm[1], Horst Uwe Keller[1], Richard Bredthauer[2] and Martin Tomasko[3]

[1]*Max-Planck-Institut für Sonnensystemforschung (MPS),* [2]*Semiconductor Technology Associates, Inc.,* [3]*Lunar and Planetary Laboratory (LPL), University of Arizona*

Abstract: *The Descent Imager/Spectral Radiometer (DISR) camera aboard the Huygens Probe to Saturn's moon Titan used a single frame transfer loral CCD to acquire image and radiometric data from nine individual optical sub-systems. The CCD was especially designed for DISR and was a German contribution to the DISR instrument established at the University of Arizona. Cassini/Huygens was launched in 1997, and the Huygens probe descended in 2005 through the atmosphere of Titan. DISR returned exciting pictures and spectra during descent and even after landing for more than 3 hours.*

Key words: *Charge-Coupled Devices (CCDs), Huygens probe, DISR.*

1.   INTRODUCTION

Cassini/Huygens originated as a joint NASA/ESA space mission to Saturn, with NASA responsible for the Cassini orbiter while ESA supplied the Huygens payload. Huygens descended through the tight atmosphere of Titan on January 14, 2005, and initiated 6 scientific instruments.

The building of the Descent Imager/Spectral Radiometer (DISR) instrument was led by the Lunar and Planetary Laboratory at the University of Arizona [1], applying detector techniques from Germany (CCD) and France (near-IR detectors). The instrument uses 13 optical apertures to acquire images and spectra from different directions. Nine of these optical paths were connected via a coherent fiber bundle to a single CCD imager to obtain a highly condensed experiment set-up with low power consumption.

2.   THE LORAL MAX-PLANCK CCD DETECTOR

The DISR CCD was designed and produced in the early nineties at Loral
[2] under contract from MPS, formerly the Max-Planck-Institut für
Aeronomie. The design was optimized for the DISR application in respect to
the rigid limitations in mass, power and data rate allocations provided by the
Huygens probe.

The CCD is a buried channel front side illuminated frame transfer device
with 256 active lines and 512 (+ 8 dark) columns. The detector is employed
2 phase MPP clocking and gated anti-blooming primarily used as an
electronic shutter, but also used to remove excessive charge from
overexposure. As shown in Table 1, the pixels are 17×23 μm^2 on 23 μm
centers leaving 6 μm for anti-blooming on the side of each pixel. The pixel
capacity of more than 150 000 e$^-$ is set to a full well of 125 000 e$^-$ by the
anti-blooming gate potential. The quantum efficiency is up to 50% at 600
and 800 nm.

Table 1. Summary of the Loral Max Planck chip specification.

Parameter	Specification
Device technology	Buried channel, Frame Transfer, FI
Clocking architecture	2 phase MPP clocking
No. of active pixels	256 lines, 512 (+8 dark) columns
Pixel size	17 $\mu m\times23$ μm; 23 μm pixel pitch
Pixel capacity	>150 000 e$^-$; 125 000 e$^-$ used
QE	up to 50% (600 and 800 nm)
CTE	0.999 999 (at the beginning)
Line transfer time	2 μs/line
Output amplifier	One single stage, 5-8 e$^-$ noise at 70 kHz
Anti-blooming	Gated anti-blooming incl. el. shutter function
Temperature sensor	2 AD590 dice on ceramic substrate

Fast line transfer of 2 μs/line allows rapid image shift into the memory
zone with minor image smear during the charge transfer. Highest shuttering
effect (up to 7% at the top of the images) occurred only in the early phase of
the observations with 7 ms exposure times, but can be effectively removed.

As shown in Fig. 1, the CCD die was bonded to a ceramic substrate,
which provides excellent electrical isolation to the metal package ground.
Such isolation allows the operation of the detector from up to several meters,
even in the noisy environment of a spacecraft. The DISR CCD imaging
system could therefore be suitably used for the Imager for Mars Pathfinder
(IMP, 1997) and further Mars camera applications [3].

A number of manufacturing lots were required to perfect the design. The
flight detector, CCD #093, received gold metallization on the back side of
the die substrate to establish reliable substrate grounding [4].
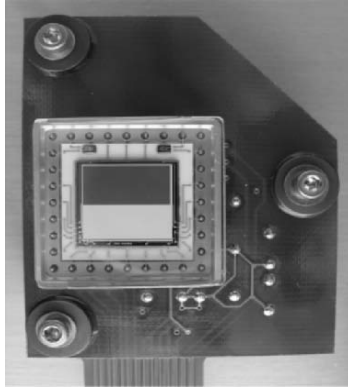
Figure 1. Front view to the DISR CCD on the top end of the Sensor Head Board (SHB). Two AD590 sensors visible on top of the CCD allow precise temperature measurements.

Figure 2 shows the arrangement of the optical channels on the imager as projected by the fiber bundle:

- HRI   High resolution down looking imager, 160×256 pixels
- SLI   Side looking imager 128×256 pixels
- MRI   Medium resolution imager 176×256 pixels
- ULVS   Upward looking visible spectrometer 8×200 pixels
- DLVS   Down. looking visible spectrometer 20×200 pixels
- SA1, SA2, SA3, SA4; Solar Aureole 1-4, $4 \times 6 \times 50$ pixels.

3.   CCD READOUT ELECTRONICS

The CCD is soldered to the top section of a Sensor Head Board (SHB) and mounted closely (20 μm) via 3 hard-points to the end of the fiber bundle. The upper end of the SHB is connected via a flexible 7.5 cm connection to the lower end that contains an OP16 JFET pre-amplifier and protection circuits. Both ends are widely thermally decoupled.

The readout electronics are concentrated about 60 cm away in the Electronics Assembly (EA) on a readout board containing the signal chain, the clock drivers and an A1020B FPGA based digital control and interface unit. Most electronic parts were selected according to a preferred parts list from NASA. We used OP16, an AD585 S/H and a 12 bit AD7672 ADC. With such limited converter resolution (30 e⁻/DU), the digitizing noise became the dominant noise source.

We finally achieved the following operation specifications:

- Total mass, Sensor Head Board: 95 g
- Total mass, Readout Board: 215 g

- Power consumption: 1.1 Watts
- Pixel readout timing: 16 μs/pixel
- Readout noise (CCD @ 193 K):   12.6 e⁻ r.m.s.

The data transmission capacity between Huygens and Cassini was limited to 8 kbit/s. As a consequence, a 15:1 compression was applied by using a DCT hardware compressor in addition to an adaptive pseudo-square rooting.
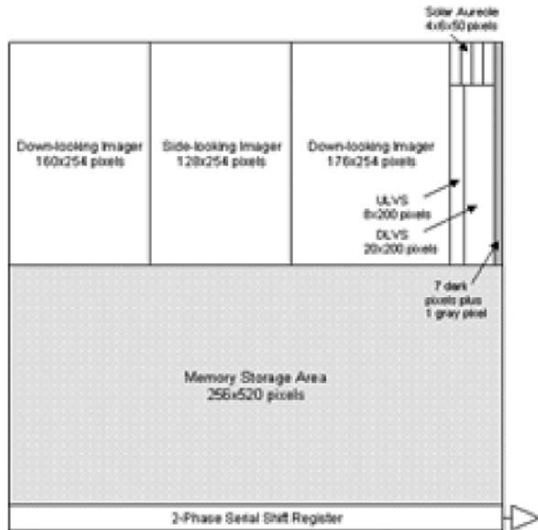
Figure 2. Distribution of optical channels projected to the imager plane.

4.   OPERATION RESULTS

The entire DISR instrument worked well during descent and even after landing, returning 600 images from the 3 camera channels. A number of dark frames were received between 260 K and 240 K. Early images from the haze can be profitably used to upgrade the flat field matrices.

Figure 3 (left) provides a plot of the CCD temperature throughout the operation. The CCD was passively cooled by a radiator that rapidly cools from 260 K to 170 K providing excellent operation conditions. The bulk of the images (and particularly the most interesting ones below 30 km where the cloud region was mostly passed) were taken with almost no dark charge components since the detector was cold enough and the exposure times were comparatively short (7-50 ms).

Flat fielding requires calibration of the hexagonal "chicken wire" pattern introduced by the fiber bundles along with singular deviations from fiber elements with degraded transmission. The resulting effect can be widely removed even though the pattern location varies slightly over temperature.
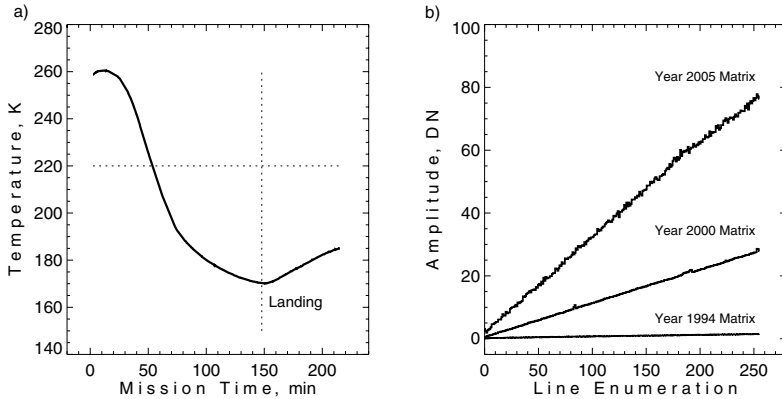
Figure 3. (left) CCD temperature and *(right)* column average dark charge at 260 K.

4.1 In-flight irradiation effects

During the mission, the CCD was continuously penetrated by proton irradiation from a nuclear heater located close to the camera head. The heater established a perfect thermal balance, but caused damages to the detector. During the flight of more than 7 years,

- the dark charge increased by a factor of 60 (see Fig. 3 (right)),
- the CTE decreased from 0.999 999 to ~ 0.999 750.

Both degradations, however, caused minor effects, because the temperature was low and the number of charge transfers is limited.

5. REFERENCES

[1] Tomasko, M.G., Doose, L.R., Smitt, P.H., West, R.A., Soderblom, L.A., Combes, M. et al., *The Descent Imager/Spectral Radiometer (DISR) aboard Huygens*, ESA SP-1177.

[2] Bredthauer, R.A., Keller, H.U. and Kramm, J.R., 2005, *A historical perspective, design, fabrication and performance of the Cassini/Huygen's probe DISR CCD imager*, IEEE Workshop on CCD and Adv. Image Sensors, Nagano, Japan, in press.

[3] Kramm, J.R., et al, 1998, *The CCD imager electronics of the Mars Pathfinder and Mars Surveyor cameras*, IEEE Tans. Instr. Meas., **47**(5).

[4] Kramm, J.R., Keller, H.U. and Behnke, T., 1994, *Performance degradations observed on scientific CCD imagers from Loral with erratic substrate grounding*, MPAE Report MPAE-W-472-03-02, MPI für Sonnensystemforschung, Katlenburg-Lindau, Germany.

6. APPENDIX

The following page provides a selection of 11 DISR images from the MRI, HRI and SLI channels. The SLI image was taken after landing showing details of Titan's surface.

Selection of DISR Images obtained from MRI, HRI and SLI imager channels

Titan's surface after landing
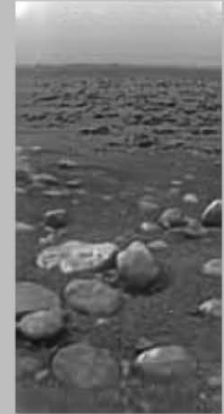
| V_0412 MRI | 16 km | V_0457 MRI | 14 km | V_0553 MRI | 8.9 km | V_0589 MRI | 7.1 km | V_0595 MRI | 6.9 km |

| V_0354 HRI | 22 km | V_0450 HRI | 14 km | V_0582 HRI | 7.3 km | V_0651 HRI | 2.8 km | V_0672 HRI | 2.1 km |
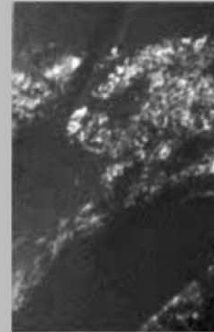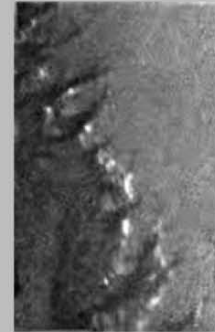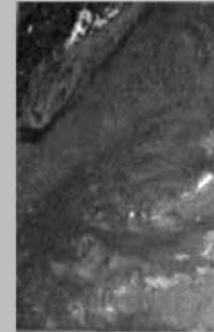
V_0724 SLI   0 km

Huygens probe:	
Begin	1990
Start (Cassini)	1997
Landing	2005

J. Rainer Kramm, et. al

SECTION II:

NON-ASTRONOMICAL APPLICATIONS

ADVANCED DETECTOR AND OPTICAL FABRICATION TECHNOLOGIES FOR IMPLEMENTING IMPROVED SPECTROSCOPIC INSTRUMENTATION

The Use of a CTIA Detector in Ion Mobility Spectrometry

M. Bonner Denton, Andrew K. Knight and Roger P. Sperline
Department of Chemistry, University of Arizona

Abstract: *The ability to detect ions is of foremost importance in a wide number of chemical instruments. Over the last five years we have made significant progress implementing mass spectrometer detector arrays using concepts adapted from CTIA preamplifier array technology. These detectors demonstrate all the desirable characteristics of Faraday type detectors, with sensitivities approaching those of multiplier detectors, but are easily fabricated into long linear arrays - providing an important multiplex advantage for focal plane geometry mass spectrometers. Optimized single channel detectors have been developed with the ultimate goal of direct detection of single ions. Extremely high impedance CTIA amplifiers have been integrated with low capacitance collection elements to produce a detection system capable of direct measurement of charge with very high sensitivity.*

Key words: *Capacitive Trans Impedance Amplifiers (CTIAs), ion.*

1.   INTRODUCTION

Adaptations of technology for astronomy are making dramatic impacts on many other areas of science and technology. This is probably most apparent in the field of modern chemical analysis. Low light level optical spectroscopies in the UV-visible and near IR regions (125 to 1100 nm) have advanced dramatically through the use of modern CCD and CID focal plane arrays. In atomic emission spectroscopy the venerable direct reader, using discrete photomultiplier tubes (PMTs), has been replaced by focal plane

arrays, often providing continuous wavelength coverage at higher resolution and improved sensitivity. Dispersive Raman spectroscopy has capitalized on the sensitivity and multiplex advantage of arrays, thus few scanning PMT based instruments are still employed. Although infrared focal plane arrays are gaining niche markets, total system costs have thus far limited their widespread adoption.

Capacitive Trans Impedance Amplifiers (CTIAs) are often employed as readout circuits in hybrid focal plane infrared arrays. This readout scheme has several desirable characteristics including a high degree of linearity and system gain determined by feedback capacitances, as well as the ability to provide high sensitivity for very small charge packets.

The ability to detect ions is of foremost importance in a wide number of chemical instruments. Mass spectrometers generally use a form of ion multiplier or, in cases where extreme accuracy is required (as in isotope ratio analysis), a Faraday cup or plate. Ion multipliers come in many configurations, but all utilize the principle of ion to electron conversion, which is accelerated onto a dynode to yield multiple secondary electrons. These secondary electron "packets" are subsequently accelerated into the next dynode (see Fig. 1). The process is repeated until a large, easily measured charge packet or steady state current is produced.
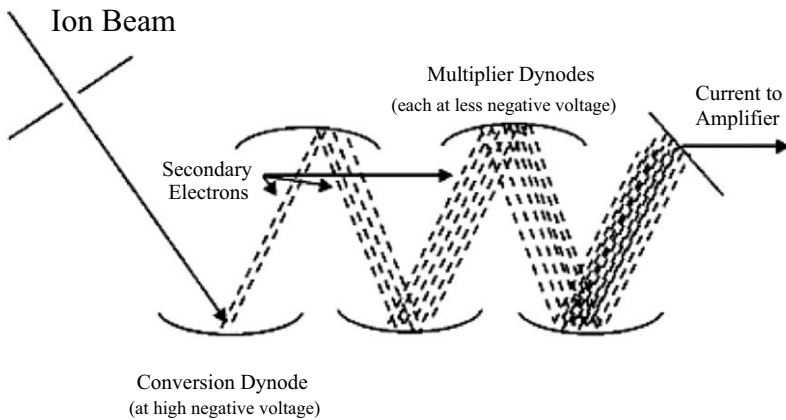
Figure 1.   Ion multipliers use avalanche electron multiplication to increase current measured by 10^6 or more. However, this technique does not work at atmospheric pressure.

Although this approach is successful in many applications, limitations exist which prevent the detection of extremely large ions (the ion lands on the conversion electrode without ejecting an electron capable of causing secondary emission). Another possible difficulty is that the process does not provide the required precision and stability because the efficiency of the

electron ejection process is influenced by ion mass and/or energy. Additionally, these charge multiplication techniques are not easily configured into large linear arrays suitable for focal plane mass spectrometers such as those using the Mattauch-Herzog geometry.

Over the last five years we have made significant progress implementing mass spectrometer detector arrays using concepts adapted from CTIA preamplifier array technology [1,2,3]. These detectors demonstrate all the desirable characteristics of Faraday type detectors, with sensitivities approaching those of multiplier detectors. However they are easily fabricated into long linear arrays - providing an important multiplex advantage for focal plane geometry mass spectrometers.

In this manuscript, similar detector technologies are evaluated for their compatibility with Ion Mobility Spectrometry (IMS). IMS is widely utilized for the detection of chemical warfare agents, hazardous chemicals explosives, and even for elucidation of large biological molecules (see Fig. 2).
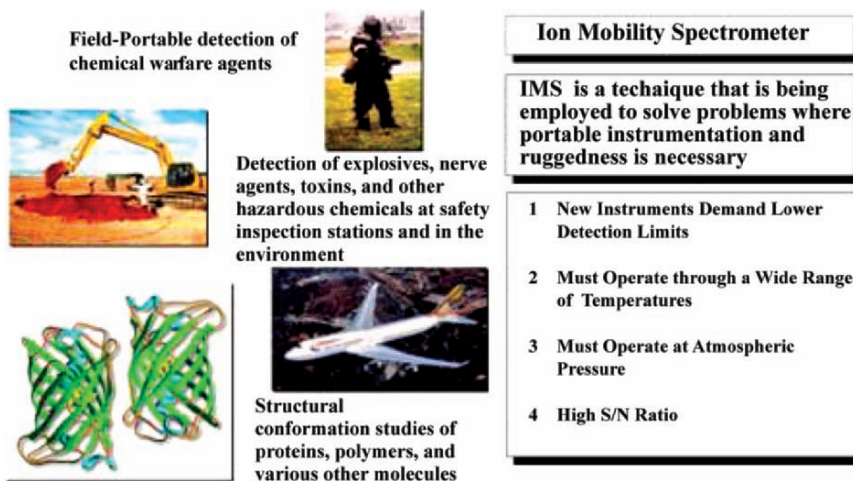
Figure 2. Ion mobility spectrometry is used today for a wide variety of ultra-trace field and laboratory analyses. One of the most common applications is screening for illicit explosives.

This technique, shown in Figures 3 and 4, involves ionizing the molecules of interest or a reagent gas, which subsequently transfers charge to analyte molecules. An ion shutter or gate pulses out a packet of ionized molecules accelerating them down a drift region over which a potential gradient is applied. The ions are collected as a function of arrival time at a Faraday plate or electrode.
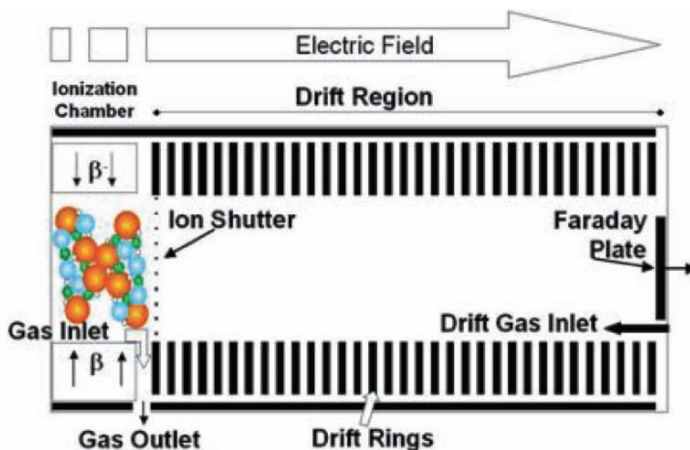
Figure 3. An ion mobility spectrometer consists of an ionization region where ions of analyte are generated, an ion shutter or gate to create a "pulse" of ions, a drift tube where different types of molecules are separated into discrete "packets," and a Faraday plate which collects the charge from individual ions.
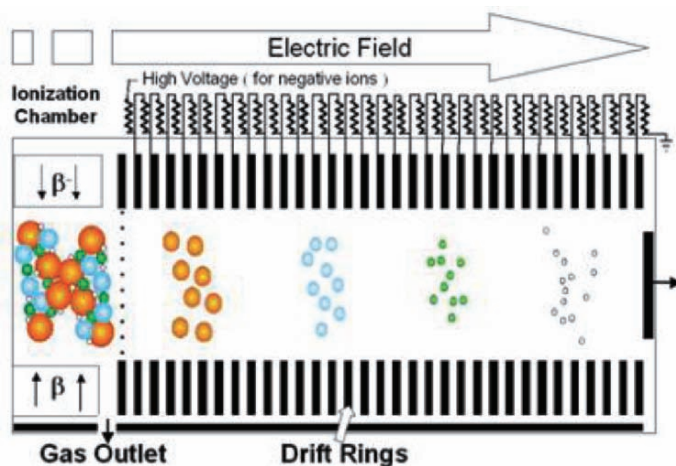
Figure 4. "Small" molecules migrate down the drift region faster than "big" molecules forming "packets" of ions of a single species.

Although this technique is similar to time of flight mass spectrometry, additional separation mechanisms are at work because the drift tube is usually operated at or near atmospheric pressure with a flow of drift gas (often air or nitrogen) from the detector end of the drift tube toward the ionization end. Hence the diffusion coefficient of the ion is also important. A more appropriate analogy of the process is atmospheric pressure ion

viscometry. The equation in Fig. 5 relates the ion mobility (K) to the other operational parameters.

Relationship of Ion Mobility to Molecular Terms

Drift Velocity: $v_d = KE$ Mobility: $K = \dfrac{d}{t_d E}$

$$K = \frac{3}{16}\frac{e}{N}\sqrt{\frac{1}{m}+\frac{1}{M}}\sqrt{\frac{2\ \pi}{k\ T}}\left(\frac{1+\Delta}{\pi r^2 \Omega}\right)$$

E	Electric Field Strength	D	Drift Path Length
t_d	Drift Time	e	Unit Charge
m	Ion Mass (analyte)	M	Molecular Mass (drift gas)
N	Number Density	k	Boltzmann-Constant
T	Temperature	r	Minimum in Potential Curve
Ω	Collision Integral	Δ	Correction Term
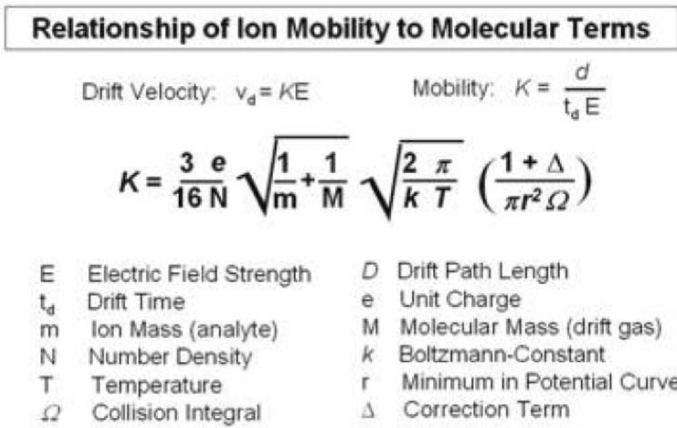
Figure 5. Relationship of ion mobility to molecular terms.

The use of ion multipliers is problematic at pressures near atmospheric due to secondary electrons colliding with drift gas. IMS researchers have thus been forced to utilize direct electrometer measurements on the very small signals produced by the ion packets. Electrometer measurements use amplifiers with high input impendence to measure the voltage resulting from the flow of current through high-precision, high-value resistors (typically 10^{10} to 10^{12} Ω, see Fig. 6) or from the accumulation of charge on a small input capacitor.
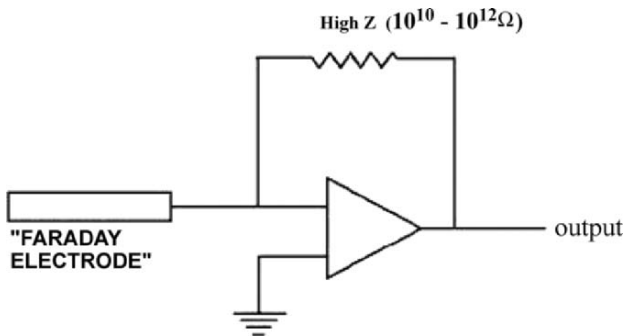
Figure 6.   Conventional instruments use a high input impedance operational amplifier in a current to voltage circuit.

Limitations on the smallest detectable current arise from noise effects in the amplifying feedback resistor, the variable capacitance of the ion

collector, the cables (inherent in the implementation of the discrete devices external to the operational amplifier), and from the amplifier itself. High-value feedback resistors are typically used to produce voltages from the small ion currents. For a $10^{12} \, \Omega$ feedback resistor, the thermal noise arising from thermally induced charge fluctuations amounts to about ± 1 femtoamp at room temperature. Additionally, the current commercially available operational amplifiers have a current noise of over 10 femtoamps at 10 KHZ bandwidths.

The other method for determination of charge is to measure the change stored on a capacitor. In conventional configurations, this approach suffers from the same noise fluctuations and detection limits as are obtained with a standard electrometer. Detection limits of several thousand ions have not yet been realized for portable ion mobility spectrometers which use this conventional technology. The CTIA approach, however, markedly reduces the detection limit.

2.   MATERIALS AND METHODS

The CTIA employed for IMS applications was designed by Eugene Atlas and associates at Imager Laboratories (San Marcos, CA), and fabricated using 0.35 micron technology. Feedback capacitors were measured to be approximately 10 femtofarad (high sensitivity/small full well mode) and 990 femtofarad (for a total of 1,000 femtofarad in low sensitivity/large full well mode, see Fig. 7).
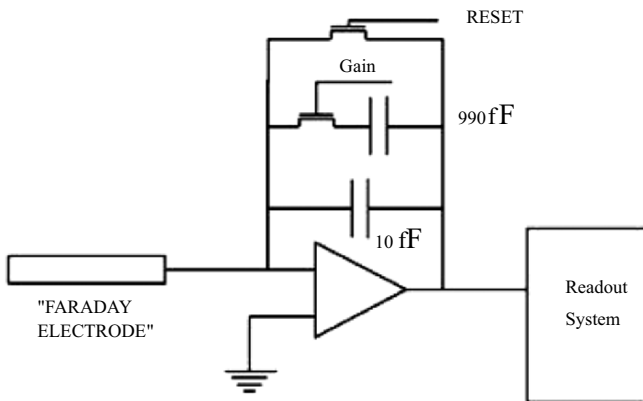
Figure 7.   The CMOS-CTIA is fabricated using the 0.35 micron process as a high input impedance amplifier with 10 fF and switch selectable 990 fF feedback capacitors. Read noise using multiple nondestructive readouts is below three electrons.

This manuscript evaluates the application of CMOS-CTIA technology in miniature portable IMS systems designed for detection of explosives in the field. The IMS ionizer/drift tube/high voltage power supply and gate circuitry fit in a volume 2"×1.56"×4" with a drift tube bore of 0.46" (Fig. 8). Miniaturization of the IMS causes a loss in sensitivity over systems with large volume ionizers and larger, longer drift tubes. This is obviously an application requiring improvements in sensitivity, and this need has been met by the CMOS-CTIA technology.
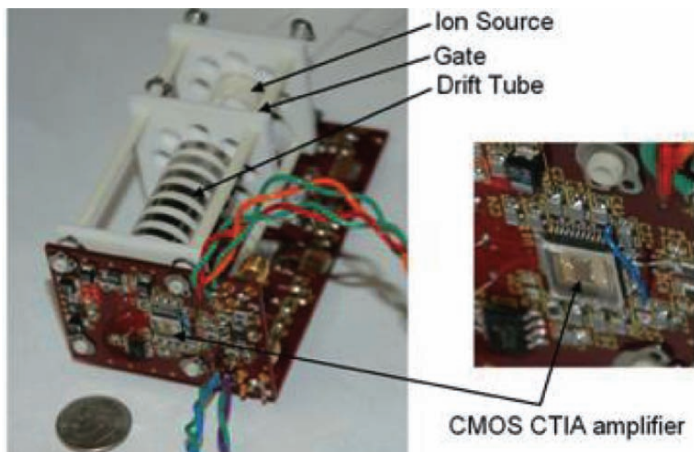
Figure 8. The miniature IMS system showing the motherboard containing the high voltage FET gating circuitry, divider string, and drift tube assembly. The detector and readout circuitry are mounted on a daughterboard at the detector end of the tube.

3. RESULTS AND DISCUSSION

Optimized single channel detectors have been developed with the ultimate goal of direct detection of single ions. Extremely high impedance CTIA amplifiers have been integrated with low capacitance collection elements to produce a detection system capable of direct measurement of charge with very high sensitivity. The small physical sizes of the collected elements and of the associated measurement circuitry resulted in a dramatic reduction in the input capacitance. Charge is accumulated on femtofarad-sized capacitors, whereas in a typical electrometer the input capacitance is tens of picofarads. The low relative capacitance produces a corresponding improvement in sensitivity. Read noise, using multiple nondestructive readouts [4,5], has been reduced to less than three electrons. Signals from a very low flux of ions can thus be reproducibly and quantitatively measured.

In addition to the high sensitivity, the ability to rapidly switch in additional feedback capacitance inherently gives the device a large dynamic range.

Detection sensitivity for explosives has been increased dramatically. Figure 9 shows a peak produced by 12.5 picogram of TNT. While the detection limit (signal $3\times$ the rms of the noise) in a similar miniature drift system, using a conventional operational amplifier for current to voltage conversion, was calculated to be 10 nanograms, the detection limit in this case is below 0.9 picograms.
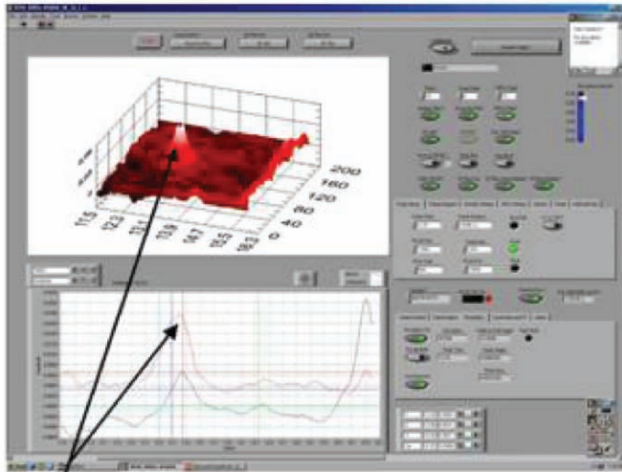
12.5pg TNT 96C, Filament, 1200 μs Pulse, B.C.

Figure 9. Showing the trace made by a 12.5 picogram sample of TNT. The detection limit is calculated to be approximately 0.9 pg. In the 3D trace, the left to right horizontal axis is drift time in milliseconds, and the front to rear horizontal axis is the scan number, with the sample being introduced at scan 82.

Unlike the operation of many focal plane arrays, integration times are very short (30-50 milliseconds), so dark current effects at room temperature are negligible. In fact, to evaluate operation in hostile desert environments, the detector was operated over a range of temperatures up to 80°C. The device operated properly and the read noise increased to < 6 electrons.

This initial application of a CMOS-CTIA device designed for IMS indicates that such devices may play a major roll in improving the sensitivity of IMS systems, which could have a dramatic impact on detecting improvised explosive devices.

4. ACKNOWLEDGEMENTS

5. REFERENCES

[1] Knight, A., Sperline, R., Hieftje, G., Young, E., Barinaga, C., Koppenaal, D., and Denton, M.B., 2002, *The Development Of A Micro-Faraday Array For Ion Detection*, Detectors And The Measurement Of Mass Spectra, Birkinshaw, K., (editor), Intl. J. Mass Spectrometry, **215**(1-3), 131-139.

[2] Knight, A.K., Denson, S.C., Sperline, R.P., Young, E.T., Barnes, J.H., Hieftje, G.M., Sinha, M., 2002, Wadsworth, M., Koppenaal, D.W., Barinaga, C.J. Gresham, C.A., and Denton, M.B., *The Impact Of Astronomy Technologies On Chemical Analysis*. Scientific Detectors in Astronomy Workshop, Amico, P., Beletic, J.W., Beletic, J.E. (editors).

[3] Hieftje, G.M., Barnes, J.H., Grøn, O.A., Leach, A.M., McClenathan, D.M., Ray, S.J., Solyom, D.A., Wetzel, W.C., Denton, M.B., and Koppenaal, D.W., 2001, *Evolution And Revolution In Instrumentation For Plasma-Source Mass Spectrometry*, Pure Appl. Chem, **73**(10), 1579-1588.

[4] Pomeroy, R.S., Sweedler, J.V., Denton, M.B., 1990, *Charge-Injection Device Detection for Improved Performance in Atomic Emission Spectroscopy,* Talanta, **37**(1), 15-21.

[5] Sims, G.R.; Denton, M.B., 1990, *Simultaneous Multielement Atomic Emission Spectrometry With A Charge-Injection Device Detector,* Talanta, **37**(1), 1-13.

Jason Henning, whose personal best solving the rubik's cube is 70 sec, helped tremendously with preparation of the workshop and finalization of the proceedings. Thanks Jason!

The internet is not just for e-mail anymore. Internet phone was very popular with workshop participants as demonstrated by Peter Moore (top) and Javier Reyes, Gustavo Rahmer, Marco Bonati and Klaus Reif (bottom, left to right).

CCD DETECTOR SYSTEMS FOR "SEMICONDUCTOR NANOSTRUCTURES" OPTICAL PROPERTIES RESEARCH

David, Darson, Pascal Morfin, Martial Nicolas, Guillaume Cassabois, Jérôme Tignon, Ivan Favero, Philippe Pace, Laurent Rea, Philippe Rossignol, Claude Delalande
Laboratoire Pierre Aigrain (LPA)

Abstract: *At LPA, we study, among other things, the physical properties of Semiconductor Nanostructures. Many of these properties are in the optical domain. Until 2002 we only used monochromator systems with Avalanche Photodiodes (APD) and a spectrometer. The performance of this kind of detector system is no longer efficient and so we began the development of CCD camera. As soon as the first system was installed, we were able to observe physical effects in these Nanostructures, as predicted by theory.*

Key words: *Detectors, CCD, semiconductor nanostructures.*

1. SPECTROSCOPY WITH THE OLD DETECTION SYSTEM

Until three years ago we only used monochromator systems with an APD coupled to a spectrometer for optical detection. For example, in our single Quantum Dot (QD) spectroscopy experimental set-up signal detection was performed, after spectral filtering by a 32 cm monochromator, by a low noise Si-based photon counting module with a sub-μeV spectral resolution [1]. But this kind of system takes too much time to record a complete spectrum. Indeed, there must be one acquisition for each wavelength of the spectrum. To keep a reasonable acquisition time, we must perform short

integrations or reduce the number of wavelength readings (low spectrum definition). On the other hand, if we want to increase signal-to-noise ratio we will have longer integrations and a readout spectrum time that is too long with the issue of experimental set-up stability (mechanical, thermal, etc.). It was time to change our method of detection.

To improve our installation we replaced the detector from "1 point" to at least 1D. In this manner we will be able to record a whole spectrum in only one acquisition.

The first system was built around a G9204-512S from Hamamatsu. It is an InGaAs linear sensor which consists of a photodiode array (512 elements) in the near infrared spectral range with one TE-cooling stage. It was mounted on experimental optical microcavities, which are structures that enable confinement of light to microscale volumes. We were able to directly record spectra; and thus able to increase integration times to obtain better S/N, or to make fast acquisitions to have high refresh rate.

However, a linear sensor must be perfectly aligned to coincide with the spectrum. That can create usage problems with frequent adjustment changes. Thus, for the next detection systems we will choose 2D detectors, and will thus not have delicate problems of spectrum positioning on a line.

2.   TWO NEW CCD SYSTEMS (SINCE 2002)

We chose 2D detector CCDs instead of CMOS image sensors. The main advantage of a CCD is its high quality. It is fabricated using a specialized process with optimized photodetectors, very low noise, and very good uniformity. The photodetectors have high QE (Quantum Efficiency) and low dark current. No noise is introduced during charge transfer. The drawback of CCDs include: they can not be integrated with other analog or digital circuits such as clocks generation, control and A/D conversion; they have high power consumption because the array is switching continuously at high speed; they have limited frame rate, especially for large sensors due to increased transfer speed while maintaining acceptable transfer efficiency. Note that CCD readout is destructive; the pixel charge signal can only be readout once. Reading discharges the capacitor and eliminates the data.

CMOS image sensors, however, generally suffer from lower dynamic range than CCDs due to their high read noise and non-uniformity. Moreover, as sensor design follows CMOS technology scaling, well capacity will continue to decrease, eventually resulting in unacceptably low S/N. However the most significant characteristics for us were low noise, high QE and low dark current. This consequently led to the choice of the CCD.

The first CCD system was built around an e2v CCD30-11 back illuminated device (1024×256) which was cooled in a liquid N_2 cryostat (see Fig. 1). It was a classical system with a CDS (Correlated Double Sampling) readout of 100 kHz (16 bits) and a readout noise under 10 e⁻. We saw the phonon effect for the decoherence in InAs/GaAs QD (Quantum Dot) for the first time with this system (see Fig. 2) [2]. In fact, the sidebands around the QD line are due to the recombination of one electron-hole pair with the lattice emission (for lower energy) and absorption (for higher energy) of acoustic phonons.
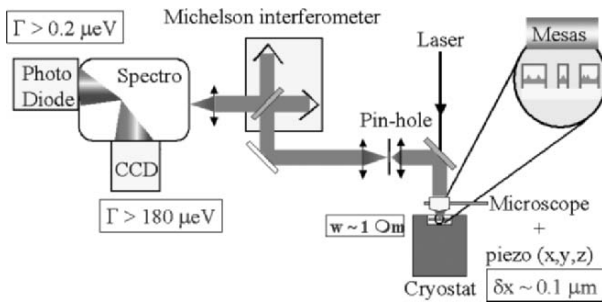
Figure 1. The experimental set up on which the CCD30-11 is assembled [1].
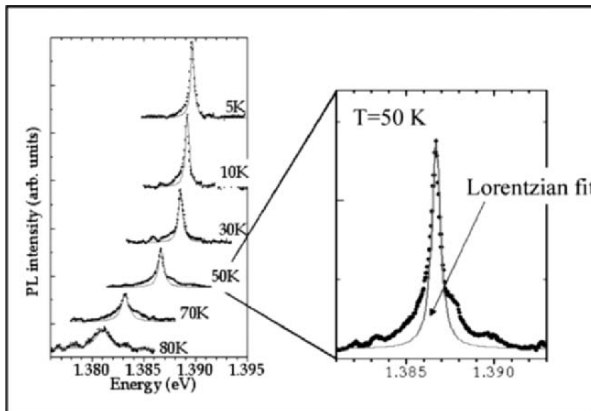
Figure 2. Photoluminescence spectra of a single QD spectra from the CCD30-11 system.

In 2005, we saw another effect owing once again to the improved S/N: a "giant optical anisotropy in a single InAs quantum dot " [3].

We made a second CCD "camera" to replace the Hamamatsu system (with linear InGaAs photodiodes array). It is used to detect the photons emitted from semiconductor microcavities. In semiconductor microcavities, a strong light-matter coupling regime can be reached, leading to new Eigenstates known as polaritons. Polaritons are hybrid quasi-particles, partly photonic and partly electronic. As such, they exhibit strong nonlinear behavior as well as strong coherent effects. This makes microcavities ideal candidates for the development of new integrated sources of twin or entangled photons, for quantum optics applications such as cryptography. Experimentally, the CCD is used for imaging the emission pattern on the surface of the microcavity structure. Alternatively, using a modified optical set-up, it acquires the emission diagram in the momentum space. Lastly, the CCD is also used to measure the spectrum of the emission.

This camera was built around an ICX285AL from Sony. It is a low cost interline CCD image sensor with excellent characteristics for its price: 1360(H)×1024(V) number of active pixels, horizontal drive frequency up to 28.64 MHz, high sensitivity, low smear, low dark current, excellent anti-blooming characteristics and continuous variable-speed shutter.

To have lower dark current the CCD for the moment is cooled by a single stage Peltier module at –20°C. In the future we will put a second TE cooling stage to reach –50°C for long exposures (>500s).

We continuously acquire the frames via an USB2 direct link connecting the camera and the computer with an average transfer rate up to 11 MB/s. So we can reach (in full resolution) a frame rate of about 4 fps (frames per second) at 14 bits, 8 fps at 8 bits, and up to 20 fps at 1360×256 resolution. The exposure time varies from 1/4000s to 1000s.

There is CDS readout and with this first version we have a readout noise of 30e$^-$ (for readout frequency at 2 MHz). In the second version we will improve it. Figure 3 gives a spectrum record taken during camera tests with our acquisition software.

3. FUTURE DEVELOPMENTS

We have just begun the development of a new system: a SWIR (Short Wave Infrared Red) system with a 256×256 InSb device from Raytheon. The SCA (Sensor Chip Assembly) consists of a hybrid structure of a CRC 744 silicon CMOS Read-Out Integrated Circuit (ROIC) interconnected, by indium bumps, to an InSb infrared photodetector array. This SCA is designed to work between 15 and 35 K, thus we will build our own He cryostat with a 15-35 K adjustable temperature.

We can perform, with this chip, a non destructive readout [4], so we will use non destructive oversampling ("Fowler" Sampling or MRDI: Multi Read During Integration [5]) to reduce readout noise and increase dynamic range.

4.　　CONCLUSION

During the last three years, we started to replace our detection optical systems (monochromator with APD and spectrometer) by CCD detector systems to largely increase the S/N ratio, reduce acquisition times, and have a better flexibility of use. With these systems of detection we began to see physical properties which had never been seen before in research on the optical properties of semiconductor nanostructures.
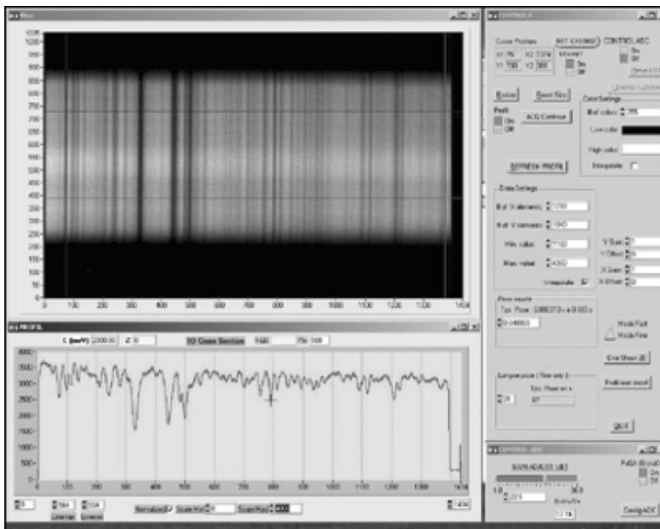
Figure 3. 3 magnesium absorption lines from the sun during camera tests.

5.　　REFERENCES

[1] Kammerer, C., Cassabois, G., Voisin, C., Perrin, M., Delalande, C., Roussignol, Ph., Gerard, J.M., 2002, Appl. Phys. Lett. **81**, 2737.
[2] Favero, I., et al., 2003, Phys. Review B**68**, 233301.
[3] Favero, I., et al., 2005, Appl. Phys. 86, 041904.
[4] Wu, J., Forest, W.J., Pipher, J.L., Lum, N., Hoffman, A., 1997, Rev. Sci. Instrum. **68**, 9.
[5] Fowler, A.M., & Gatley, I., 1990, ApJ, **353**, L33.

Manfred Meyer (top), and Christoph Geimer and Peter Sinclaire – No caption will suffice.

SECTION III:

CCDs

CCD TECHNOLOGY

Barry Burke[1], Paul Jorden[2], and Paul Vu[3]
[1]MIT Lincoln Laboratory, [2]e2v technologies, [3]Fairchild Imaging

Abstract: *Charge-coupled devices (CCDs) continue to reign supreme in the realm of imaging out to 1 μm, with the steady improvement of performance and the introduction of innovative features. This review is a survey of recent developments in the technology and the current limits on performance. Device packaging for large, tiled focal-plane arrays is also described. Comparisons between CCDs and the emerging CMOS imagers are highlighted in terms of process technology and performance.*

Key words: *Charge-coupled device, focal-plane array, modulation transfer function, point spread function, radiation tolerance, hybrid sensor, quantum efficiency, noise, dark current, packages, depletion, blooming, CMOS, electronic shutter, orthogonal-transfer array.*

1.   INTRODUCTION

In the 36 years since its first demonstration at Bell Laboratories, the charge-coupled device (CCD) has undergone remarkable growth and development. What began as a one-pixel demonstration of charge transfer between three metal gates on an oxidized silicon surface [1] has evolved to devices as large as 66 Mpixels filling a 150-mm silicon wafer [2]. Scientific CCDs are now the largest silicon integrated circuits (ICs), with die areas up to nearly 100 cm^2 compared to < 4 cm^2 for the largest digital ICs.

In this review we attempt to cover the highlights of current scientific CCD technology. Section 2 is a brief introduction to the structure and functioning of the CCD at the device level and a discussion of wafer processing issues. In Section 3 we survey the performance of current CCD technology in several key areas, including quantum efficiency (QE), noise,

charge point spread function (PSF), radiation tolerance, and blooming. In addition, the packaging technology for focal-plane mosaics is reviewed. Section 4 is devoted to a comparison between CCDs and the rapidly evolving CMOS technology, highlighting the differences between them and their comparative strengths and weaknesses. In Section 5 we examine some new concepts under development in CCD technology that are of potentially great interest in astronomy. These include the orthogonal-transfer CCD, electronic shuttering, curved CCDs, and an area of great promise just beginning to be explored, namely, the hybrid combination of CCD and CMOS technologies.

2.   CCD FUNDAMENTALS

2.1   Basic CCD Structure

Figure 1 depicts the basic elements of an n-channel, back-illuminated CCD; for p-channel CCDs, which have such advantages as greater resistance to space radiation, the labels "n-type" and "p-type" in Fig. 1 are interchanged. The starting material is a p-type wafer typically 600–700 μm thick. The n-doped buried channel region at the upper surface is typically no more than 0.1–0.2 μm thick. Photoelectrons are collected and transported to an output circuit within this layer. Its most important function is to ensure that the electrons are kept away from the Si/SiO_2 interface where they could otherwise be trapped by surface states. The wafer surface has a thin layer of SiO_2, and sometimes an additional layer of Si_3N_4, which serves as a gate dielectric, and on top of this layer is a set of electrodes or gates that control the collection and transport of the photoelectrons across the device.
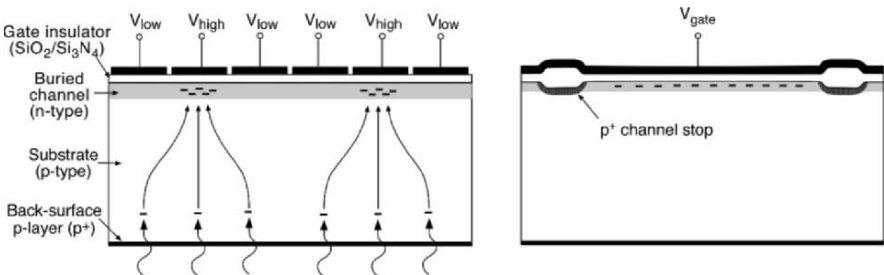
Figure 1. Depiction of the cross section of a three-phase CCD viewed *(left)* across the device gates and *(right)* parallel to the device gates.

After device fabrication the wafer must be thinned from the back surface to a final thickness typically 10 µm up to 300 µm to enable the CCD to be illuminated from the back. Such so-called back-illuminated devices offer the ultimate in high QE, as will be seen in Section 3, in contrast to conventional CCDs illuminated from the front or circuit side, which suffer from substantial reflection and absorption losses in the gates and dielectric layers. The back surface, however, must be carefully treated to avoid loss of photoelectrons to surface states or traps, and this usually means that a heavily doped p-layer (labeled p^+ in Fig. 1) is introduced into the back surface. An antireflection coating on this surface is also required for highest QE.

The process by which an image is formed is as follows. Photons incident on the back surface of the device create electron-hole pairs. The photoelectrons are collected by electric fields set up by the CCD gates in packets in the buried channel under the gates with high potentials (V_{high} in Fig. 1), and the neighboring gates at lower potentials (V_{low}) provide electrical isolation of the packets. For a three-phase device, each set of three gates defines a pixel along the direction of charge transport. Charge packets are transported from gate-to-gate by applying a set of time-varying waveforms to the gates.

In the cross-sectional view of a CCD taken in a direction perpendicular to the charge-transfer direction, shown in Fig. 1 (right), the important feature is the channel stops that define the left and right boundaries of a pixel or CCD channel. Typically, these are heavily doped p-type regions, and often the SiO_2 here is thicker than the gate dielectric. The channel stops terminate the edges of the channel. In later sections we will see how modifications of the channel stops are used in two advanced features of CCDs.

An important feature in understanding the image resolution of a CCD is the depletion layer. A depletion layer is depicted in Fig. 2 in the upper portion of the p-substrate and the n-buried channel. Here, the fields due to the CCD gates and the buried channel combine to remove the holes to a depth, called the depletion depth, that depends on the gate biases and the resistivity of the p-substrate. In this region the vertical component of the electric field is sufficiently strong to pull photoelectrons fairly quickly (a few ns) into the CCD channel. In the undepleted or neutral portion of the substrate near the back surface, photoelectrons may wander by thermal diffusion over substantial distances before they reach the depletion layer boundary and are swept into the channel. This process clearly degrades imaging resolution, and thus back-illuminated devices must be operated under nearly or fully depleted conditions.
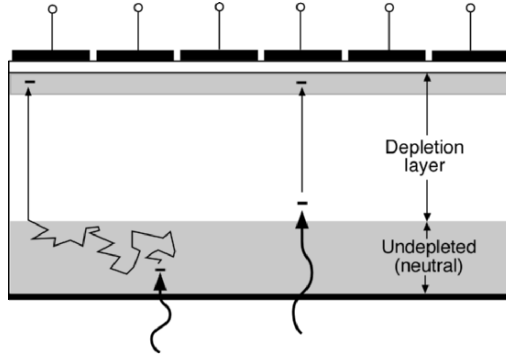
Figure 2. Cross section of a CCD depicting the depletion layer and the neutral undepleted layer at the back surface and its effects on photoelectron charge collection.

As we will see later in Section 3, it is extremely desirable to make CCDs as thick as possible in order to maximize QE in the near infrared (λ~700–1000 nm), where photon absorption depth becomes progressively greater and thicker devices are needed to absorb the photons. However, this makes fully depleted operation more difficult.

What are the factors that enable deep depletion depths in a CCD? Raising the gate biases increases the depletion depth, but this approach has its limitations because the higher fields across the device oxide layers lead to spurious charge generation and eventually to catastrophic dielectric breakdown. Another approach is to use lightly doped or high-resistivity substrate material, since depletion depths vary as $N_A^{1/2}$, where N_A is the doping concentration of the substrate (resistivity varies as $1/N_A$). Typical scientific CCDs are made on material having resistivities of the order of 100 Ω·cm or less, resulting in depletion depths of only about 15–20 μm. For better results, some CCDs are made on special material having resistivities of several thousand Ω·cm resulting in depletion depths of 60 μm or more.

The deepest depletion is obtained by combining high-resistivity substrates with a bias applied to the back surface. This approach has been used, for example, by the Lawrence Berkeley National Laboratory group to produce fully depleted p-channel CCDs that are more than 300 μm thick [3].

2.2   Processes

The basic process by which scientific CCDs are manufactured is essentially the same as it was 30 years ago. This process for a three-phase device, depicted in Fig. 3 together with a scanning electron micrograph (SEM) of a fabricated device, is based on the use of doped polycrystalline silicon, or polysilicon, films for the gate material. Beginning with a substrate

wafer, a thin gate dielectric layer(s) is grown on the surface, and a layer of polysilicon is deposited and lithographically defined to produce the first set of gates corresponding to one clocked phase. The wafers are then placed in a thermal oxidation furnace where the thin SiO_2 layer is grown over the polysilicon. For processes that employ a Si_3N_4 layer as part of the gate dielectric this oxidation step leaves the exposed dielectric unchanged, since Si_3N_4 is a barrier to O_2 and H_2O, and prevents the SiO_2 beneath it from becoming thicker. This is an advantage from the point of view of leaving the threshold voltages, and thus the clock drive voltages, the same for all three phases. For the second and third phases the process is repeated twice, but in each case the gates must slightly overlap the adjacent gates to ensure good control of the electrical potential in the CCD channel below.
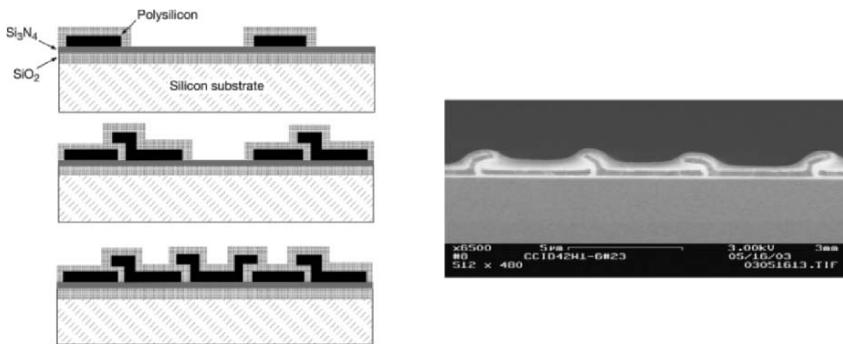
Figure 3. (left) Sequence of steps by which CCD gates are fabricated for a three-phase device and *(right)* SEM of a fabricated device.

2.3   CCD vs CMOS: Process Comparisons

As CMOS sensors begin to attract more attention, it is worthwhile comparing various aspects of the two technologies. Here, we examine the device processing differences, while later in Section 4 performance is compared.

To understand scientific CCD wafer processing, it is worth noting that for pixel sizes of interest in astronomy (~10–20 µm) the gate features have dimensions of several µm. In comparison to state-of-the-art silicon IC technology, where feature sizes of <0.1 µm are now the norm, these are extremely large geometries. On the other hand, CMOS sensors must have several field-effect transistors and other components placed inside the pixel, along with metal lines, to address, reset, and read out the pixel. This high

component density requires the tight sub-µm lithography characteristic of current CMOS wafer fabrication.

The simplicity of the CCD pixel and its readout circuit and its relatively generous design rules enable CCDs to be manufactured with fewer photomasks (typically 10–15) than CMOS (15–30 photomasks) and with less sophisticated (one might say "lagging edge") technology. In addition, CCDs have for the most part kept the relatively thick gate dielectrics (50–100 nm) and polysilicon oxide thicknesses (100–300 nm) from decades ago. By contrast, CMOS processes use gate dielectric thicknesses of the order of 5 nm or less. This, of course, has implications for device yields, since particulates of a size that may produce a fatal short in the gate oxide of a CMOS device may hardly affect a CCD. This fact, combined with the superb cleanliness and extremely low levels of contaminants in the process chemistry of modern wafer fabrication, have enabled high yields for the huge CCD die sizes alluded to in the introduction.

An important distinction between CCD and CMOS fabrication lies in the material requirements. CMOS requires thin epitaxial layers grown on heavily doped (low resistivity) substrates for proper circuit performance, whereas CCDs can be fabricated on almost any substrate, including the highly desirable high-resistivity material needed for deep-depletion depths. Conventional CMOS imagers, therefore, are fundamentally limited to extremely poor near-infrared response. For this reason the only inroads that CMOS can make into the astronomy market will be by hybrid devices, described in Section 5.2.1, in which a separate diode array, made on high-resistivity silicon, is bump bonded to a CMOS readout multiplexer (MUX) [4]. Whether this can be done in a cost-effective way remains to be seen.

CMOS has always appeared attractive for integrating on chip all of the support functions needed to drive a sensor, such as clock waveform timing and generation, biases, video processing, and analog-to-digital conversion. It is possible, and in fact has been demonstrated, that a CMOS process can be integrated into a CCD process, but the complications involved are significant and can involve performance compromises and extra costs. A more promising route is to combine CCD and CMOS, either as a bump-bonded hybrid or using newer approaches involving direct wafer bonding [5], to obtain an integrated device with all the support features in one compact sensor. Even a somewhat less integrated approach in which CCD and CMOS reside close to each other in a shared package is attractive in reducing the huge volume and power of the electronics needed to drive the coming generation of Gpixel focal planes. Custom CMOS, unconstrained by CCD process requirements, is now relatively inexpensive compared to large scientific CCDs, so that the case for hybridization is very compelling. Examples of this approach are described in Section 5.

3.   PERFORMANCE AREAS

3.1   Quantum Efficiency

A key performance parameter for an astronomical CCD is QE. CCDs are capable of detecting photons over a wide range, as shown in Fig. 4. The figure depicts direct silicon sensitivity, although wavelength-converting materials, e.g., phosphors, are also used. Several factors control silicon sensitivity: (1) High energies (X-rays) have a long absorption length, and sensitivity depends on the thickness of silicon. (2) Short-wavelength ultraviolet photons are absorbed close to the silicon surface and need back side illumination. (3) Photons of wavelength >100 nm are efficiently absorbed in a back side CCD with antireflection coating. (4) Photons of wavelength >400 nm can be detected by a front side illumination; electrodes limit response. (5) Photons of wavelength >700 nm have a long absorption length so thicker silicon helps; sensitivity is determined mainly by the thickness of silicon and partly by operating temperature (band gap shifts). (6) Photons of wavelength >1100 nm are not detected because of the silicon band gap limit, which also has a temperature dependence. Most of the following discussion will apply to the range 300–1100 nm, as used for "visible" astronomy.

Charge-coupled devices can be made as front side illuminated devices, but the spectral response is cut off at short wavelengths by absorption in the semitransparent polysilicon electrodes. Peak response is also normally limited to less than 50%. For astronomical use a back side illuminated CCD is the default. With careful processing and suitable antireflection coatings, spectral response can be obtained over a wide range with a peak approaching 100%. Figure 5 illustrates front side and back side illuminated CCD constructions.

A back side illuminated CCD offers high spectral response, but only if processed carefully. Devices are commonly thinned to a thickness of 10–20 μm, and require back surface treatment to ensure that photons absorbed near the surface are collected. Treatments that have been used include ion implantation followed by laser annealing [6], ion implantation followed by furnace annealing, chemisorption charging [7], and molecular-beam-epitaxy/delta doping.
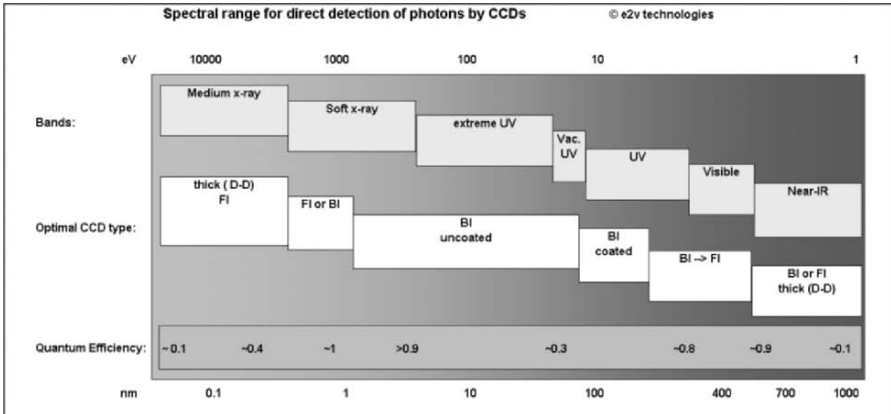
Figure 4. CCD electromagnetic spectral range. Courtesy of e2v technologies.
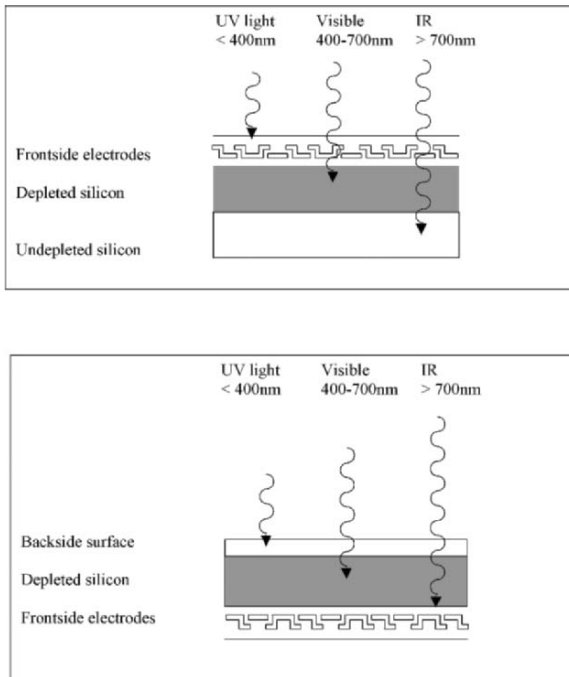
Figure 5. (top) Front side and *(bottom)* back side illumination.

An important requirement is the use of a suitable antireflection coating because silicon has a high refractive index (n~4). The usual material for a

single-layer λ/4 coating is hafnium oxide (n~2), which allows near-perfect photon collection especially at midband wavelengths. The curves in Fig. 6 illustrate typical spectral responses for different coatings.
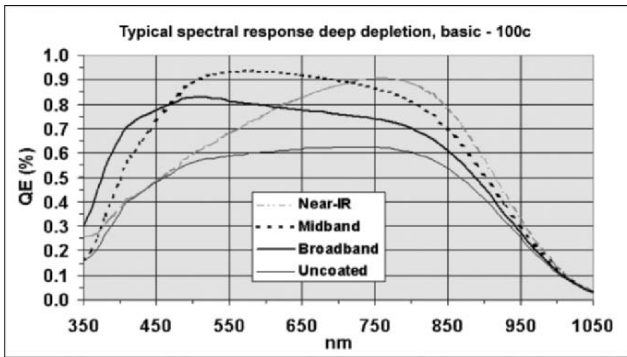
Figure 6. Example of CCD responses for different antireflection coating peak wavelengths.

For a device with a thickness of 40 µm, illustrated in Fig. 6, a common starting material is 20- or 100-Ω·cm resistivity silicon; after back-thinning and processing the final thickness is typically 10–16 µm. For long-wavelength (red) use, however, the absorption length of these photons exceeds the device thickness [3] so not all light is collected. To improve red response some manufacturers offer so-called deep-depletion CCDs; with higher-resistivity silicon, e.g., 1500 Ω·cm, the device may be made with a 40-µm thickness and consequent higher red response.

A possible further step is to make devices even thicker. In this case a so-called "high-rho" device can be made of very high resistivity bulk silicon, e.g., 10,000 Ω·cm. These devices generate larger depletion depths within the silicon and can also be operated with larger voltages to increase it further; a substrate voltage up to 50 V may be used in some cases. Such devices have been championed by the LBNL group [8] and also manufactured by e2v technologies and Lincoln Laboratory (originally for x-ray detection). Such devices can exhibit almost 100% QE at wavelengths around 900 nm, with an eventual reduction as the silicon band gap limit is reached. Figure 7 gives examples of spectral response for different thicknesses of silicon, and measurements [3] of LBNL 280-µm-thick samples.
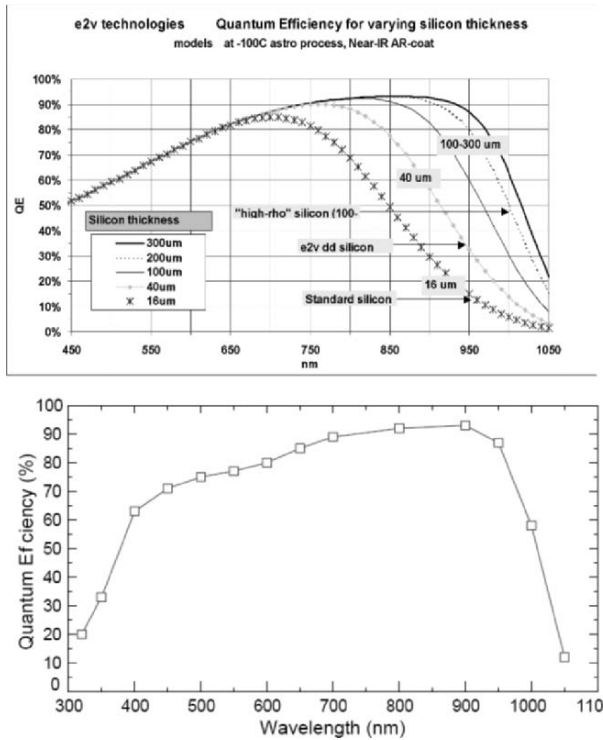
Figure 7. (*top*) Spectral response for different silicon thicknesses; (*bottom*) Lick/LBNL measurements. Courtesy of e2v technologies.

Another consideration is fringing. Back-thinned devices of "normal" thickness suffer from internal multipass fringes, which modulate the response at wavelengths longward of 700 nm, where the absorption depth is comparable or longer than the silicon thickness. Devices made of progressively thicker silicon suffer less from this effect [9]. The very thick silicon depth causes these devices to collect a significantly enhanced number of cosmic ray events. The devices can potentially have a poorer PSF, and so higher operating voltages are normal in order to maximize field strength and achieve good charge confinement.

3.2   Readout Noise

Noise is the second parameter that determines the signal-to-noise of recorded data, and a low value of readout noise is often considered essential for low-signal-level astronomical applications. A low noise floor is always important for use at low signal levels, often at low pixel rates. Low noise at

higher pixel rates makes the devices useful at higher frame rates, thereby reducing readout time and increasing observing efficiency.

Most scientific sensors utilize a two-stage on-chip output circuit. This allows a small first-stage transistor to couple to a small output node and provides a larger second-stage follower to provide reasonable output drive capability. Figure 8 shows an example of a two-stage (e2v technologies) output circuit. Note that an (optional) external junction field-effect transistor buffer is also shown, which is mainly beneficial for driving longer cables with appreciable capacitance.
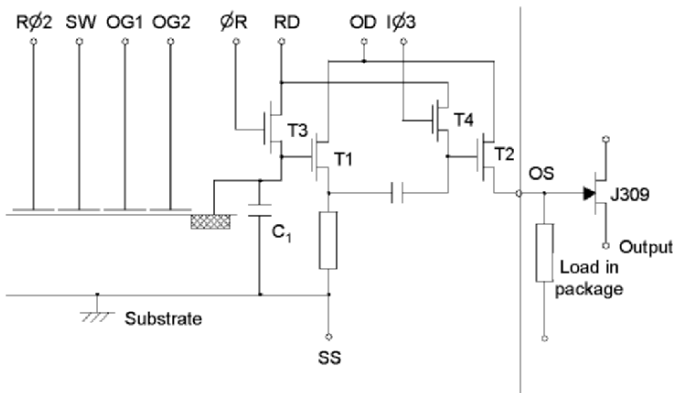
Figure 8. Two-stage CCD output circuit schematic.

It is usual to match the designs of the two stages, and one consequence is that very low noise levels need to be traded against the output drive requirements. Large-signal use and high-frequency operation, especially to capacitative loads, require large transistors with a higher noise floor. Figure 9 gives examples for different output amplifier designs.

For scientific use, CCDs are normally expected to have readout noise floors of $2–5$ e^- rms, although slightly higher levels are sometimes used. A recent development of avalanche gain technology (electron multiplication) within CCDs has made subelectron readout noise available. Figure 10 illustrates an example of such a device; applications are discussed in [10].
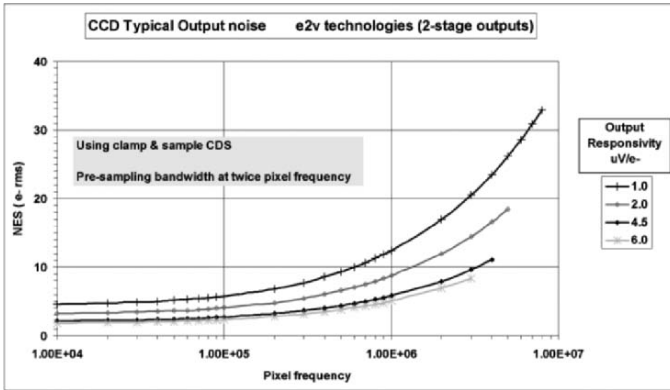
Figure 9. Readout noise vs frequency for different responsivity amplifiers. Courtesy of e2v technologies.
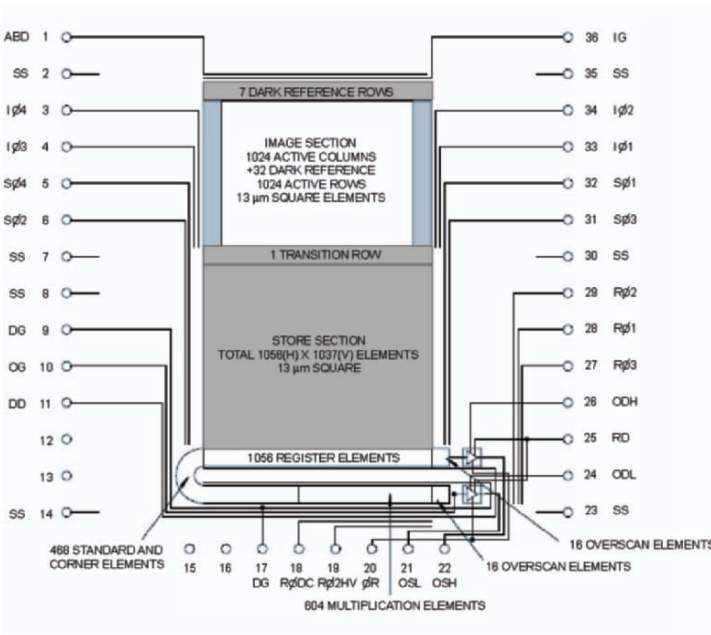
Figure 10. Example of avalanche multiplication structure. Courtesy of e2v technologies.

These devices have image areas and an initial serial register that are similar to normal CCDs. However, they utilize an extended serial register

with multiple stages (typically ~500), each of which allows a small probability of electron multiplication when operated with a high-voltage (up to 50 V) clock phase. The result is that the signal at the gain register may be amplified by a factor of 1000 or so before it feeds into the (standard) output stage. Thus, even an output amplifier with a high noise level can yield an input-referred readout noise in the subelectron region.

While these devices offer substantially reduced readout noise levels, appreciation of several factors is important for their full use. These include cooling to suppress dark current, control of operating temperature and high-voltage clock level for gain stability, different noise statistics resulting from the stochastic gain process, clock-induced charge at subelectron signal levels, and noise statistics different from the familiar (Gaussian) ones of traditional CCDs.

3.3   Dark Current

Charge-coupled devices collect dark current, which scales strongly with temperature. It has two main components—surface dark current and bulk dark current. The specific magnitude scales with pixel area and can depend on manufacturing process. Bulk dark current is typically 100 times lower than surface dark current. When multi-phase pinned (MPP) or inverted-mode operation (IMO) is used, devices should achieve bulk dark current levels, as seen in Fig. 11.
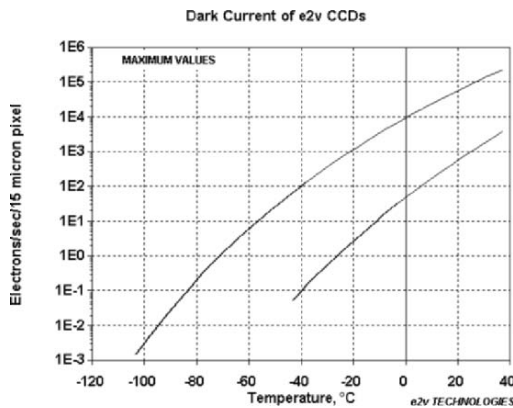
Figure 11. Curves showing *(upper)* surface and *(lower)* bulk dark current. Courtesy of e2v technologies.

When the device goes out of inversion, i.e., the clocks are raised above the inversion level, there is a characteristic time before the dark current

recovers from bulk to surface levels. This time constant can be appreciable for low temperatures. This means that dark current can be influenced by clocking dynamics. Surface dark current can be reduced by active clocking during integration, i.e., "dither" clocking, and can also be low immediately after a previous readout at low temperatures [11a, 11].

3.4   Modulation Transfer Function

The primary function of the image sensor is to produce an output that faithfully represents the scene being imaged. The sensor must accurately reproduce all the details in the image, which contains features of varying intensities and spatial frequencies. The resolving power of the sensor is determined by its modulation transfer function (MTF), defined as the response of the sensor to a sinusoidal signal of increasing frequency. The MTF describes the decrease in contrast in the reproduced image as the spatial frequency in the original scene increases. The reduction in modulation (contrast) of closely spaced line pairs results in image blur since the separation between the light and dark lines can no longer be observed. Different methods are used to measure MTF [12]. One is to directly measure the sensor response to a sinusoidal input source. Another is to perform the Fourier transform of the PSF, which yields the optical transfer function (OTF). The MTF is the magnitude of the real part of the complex OTF variable.

Modulation transfer function is defined as the ratio of modulation depth of the output signal to the input signal:

$$MTF = \frac{Modulation \ (Output)}{Modulation \ (Input)}, \quad where$$

$$Modulation = \frac{Signal_{MAX} - Signal_{MIN}}{Signal_{MAX} + Signal_{MIN}}.$$

The overall MTF of the instrument is the product of the MTF of each optical component of the system, including the lens, the sensor, the electronics, and the display; however, the MTF of the sensor is usually the limiting factor.

Since the sensor is essentially a spatial sampling device, the highest frequency that it can accurately reproduce is defined by the Nyquist frequency, $f_{Nyquist} = 1/2p$ where p is the pixel pitch. The finite sampling nature of the sensor is characterized by the sampling MTF, which is directly influenced by the pixel geometry. The MTF of the CCD is further limited by the charge-transfer inefficiency and carrier diffusion.

The overall MTF of a CCD is the product of three components: pixel geometry, charge-transfer inefficiency, and carrier lateral diffusion:

$$MTF_{CCD} = MTF_s \times MTF_t \times MTF_d.$$

The discrete spacing of the pixels in the CCD places a fundamental limitation on its performance. The CCD samples the image in spatially discrete steps, and the spatial MTF is given by

$$MTF_s = \sin(\pi f_s p)/(\pi f_s p) = \text{sinc}(f_s p),$$

where f_s is the spatial frequency and p is the pixel pitch. At the Nyquist frequency, MTF_s is limited to 0.637.

Imperfect charge-transfer efficiency (CTE) results in a reduction in the output signal, causing a loss in the response amplitude, and

$$MTF_t = \exp\{-n\varepsilon(1 - \cos 2\pi f/f_c)\},$$

where f is the spatial frequency of the signal transferred through the device at the f_c clock frequency, ε is the charge-transfer inefficiency per transfer, and n is the number of transfers in the CCD. Even with a large number of transfers, the MTF_t is usually a minor component in CCDs with high CTE.

Charge carriers that are generated inside the depleted region of the channel are driven by its electric field to the potential wells of the pixels directly above the location where they originated, but those charge carriers that are generated outside of the depleted region, in the field-free region, will diffuse randomly in the substrate and carry a high probability of being collected in the neighboring pixels instead. This effect represents the largest component of MTF degradation in the sensor. Since the photon absorption depth increases with wavelength, MTF_d is worse at longer wavelengths in a front-illuminated sensor, but in a back-illuminated sensor, the spatial resolution degradation occurs at the short wavelengths.

3.5 Point Spread Function

In a well-behaved optical system, a point source of light at the object plane will generate a corresponding spot image in the image plane. The shape of the image formed at the sensor by the point source, the PSF, ideally will have a circular shape and cover only a small region. The size of the PSF is due to spreading of charge carriers, by random diffusion in the field-free region below the pixels. The width of the PSF limits the spatial resolution of the sensor, and a common practice is to report the value at full width at half-maximum (FWHM), which is the diameter of the PSF where the signal intensity at the center of the image is reduced by half, as seen in Fig. 12.

Charge diffusion in the field-free region results in enlargement of the PSF, as shown in Fig. 13. To narrow the PSF the undesirable effects of charge diffusion must be controlled, either by reducing the size of the field-free region or by widening the depletion depth. The field-free region can be

minimized by reducing the thickness of the substrate, but this is an undesirable option since the QE at long wavelengths would suffer. A better approach is to fabricate the devices on high-resistivity material, which helps extend the depth of the depletion region.
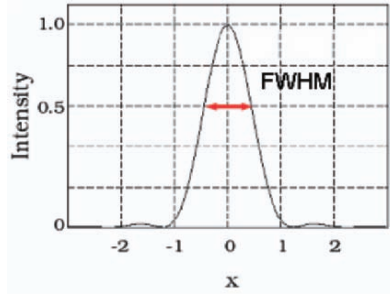
Figure 12. Diameter of PSF where signal intensity at the center of the image is reduced by half.
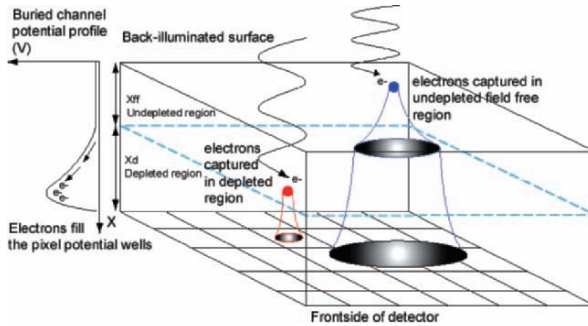
Figure 13. Enlargement of PSF resulting from charge diffusion in the field-free region.

3.6   Deep Depletion and Fully Depleted CCDs

To improve the QE response in the red and near infrared, deep-depletion CCDs are fabricated on high-resistivity silicon material, which helps to extend the depth of the depletion layer so that long-wavelength photons are effectively absorbed. Commercially available devices are produced on 50-μm-thick, high-resistivity material, achieving a depletion depth of about

30 µm under normal operating voltages. Both front-illuminated and back-illuminated devices are offered.

Fully depleted CCDs are fabricated on 200–300-µm-thick silicon material of very high resistivity (10–12 kΩ·cm). An independent bias is applied to the substrate to fully deplete the devices. The devices are back illuminated and yield exceptional QE in the near infrared, thanks to the thick substrate [3]. With the proper antireflection coating the QE at 1000 nm is about 60%, compared to a maximum of about 16% with a deep-depletion CCD.

The application of the substrate bias purges the mobile majority carriers from the substrate and generates an electric field that extends from the channel to the back side of the device. The electric field pushes the photogenerated carriers to the proper potential wells, inhibiting the lateral charge diffusion that lowers the MTF. The PSF of a 300-µm-thick fully depleted CCD at 400 nm measures 8–10 µm with 40-V substrate bias, and 6 µm when the substrate bias is increased to 77 V [13].

3.7   Radiation Tolerance

A CCD is normally capable of transferring charge with practically no loss after a very large number of transfers. This requires that the signal paths in the CCD be completely free of charge traps or other defects. When the devices operate in space, continued exposure to energetic particle radiation leads to degraded device performance. The main defect mechanisms are displacement damage and total ionizing dose effects [14]. In space applications, displacement damage effects have a stronger impact on CCD performance.

Radiation damage adds new energy levels in the band gap, facilitating the transition of electrons to the conduction band as seen in Fig. 14, and increases dark current. These defects can also trap charge and release them after some time constant, degrading the CTE. High-energy protons, neutrons, and electrons produce displacement damage when they collide with the silicon atoms, resulting in atomic defects, such as dislocations, in the crystal lattice, which cause an increase in dark current, generate hot pixels, and lower CTE because of the additional charge-trapping sites.
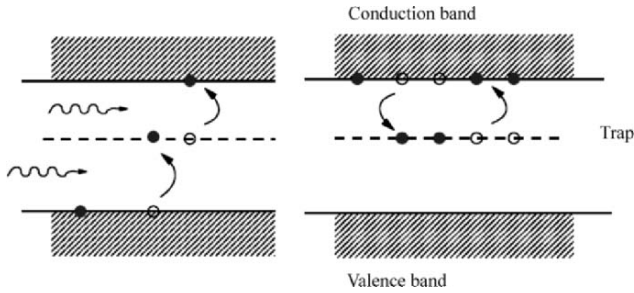
Figure 14. Illustration of effects of radiation damage, which facilitates transition of electrons to the conduction band.

Ionizing radiation damage results in the buildup of excess positive charge in the gate dielectric, which offsets the flatband voltage, effectively changing the effect of the applied bias and clock voltages. The generation of traps at the SiO_2 interface also results in an increase of dark current and a degradation of CTE.

A number of techniques have been developed to mitigate the effects of radiation damage, shown in Fig. 15, and accurate models have been developed to help predict the performance of CCDs following irradiation. Operating the CCD in inverted mode, so that the CCD surface is accumulated with holes, suppresses dark current and improves CTE, since the surface traps are filled and can no longer interact with the signal charge. This technique effectively improves the device resistance to total ionizing dose. The operating temperature and the clock frequencies can also influence the impact of radiation damage, since they affect the time constant of the charge traps and reduce their capture duty cycle. Adding a narrow notch in the CCD channel helps reduce the interaction between the signal charge packets and the trapping sites in the silicon. Introducing a sacrificial "fat zero" charge to all of the pixels in the CCD is another technique used to fill the traps and make them inactive, but this method increases the noise level.
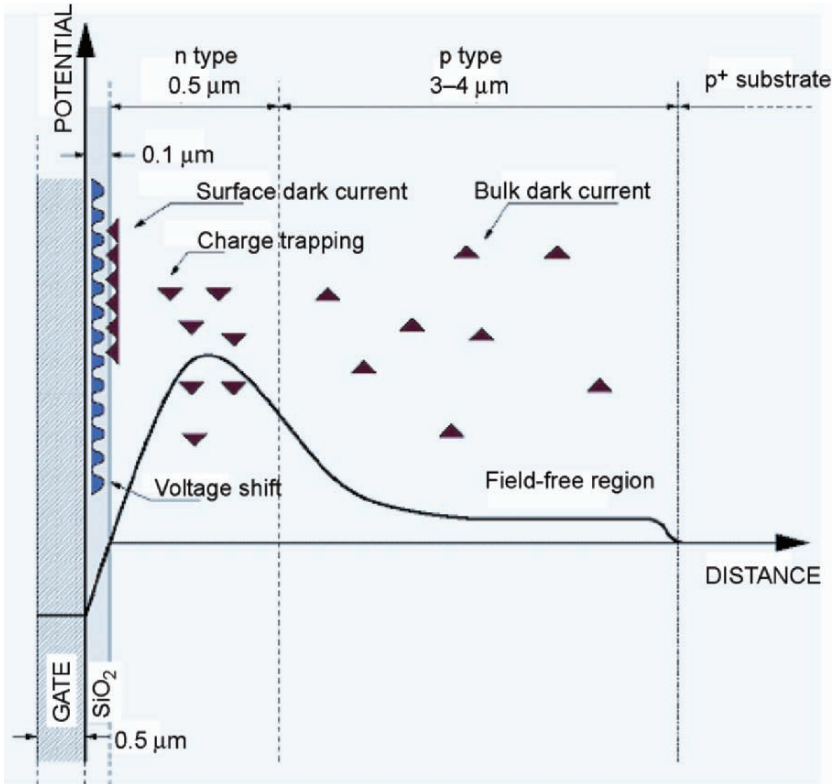
Figure 15.   Effects and defect locations from radiation damage due to ionizing and displacement damage. Courtesy of Niels Bassler, University of Aarhus.

Tests have shown that p-channel CCDs are more radiation tolerant than conventional n-channel devices. Proton irradiation tests performed on n-channel CCDs reveal the presence of traps with energy levels at 0.14, 0.23 and 0.41 eV below the conduction band. The 0.14-eV traps are due to A-centers (oxygen-vacancy complex), the 0.23-eV traps are caused by divacancies, and the 0.41-eV traps are believed to be caused by phosphorus vacancy (P-V) defects. Studies indicate that the P-V defects are responsible for the majority of the traps that degrade CTE performance in n-channel devices since their energy level is near the mid-gap level. These traps become much less effective when the device is cooled down below 180 K. The divacancies are considered to be the main defects that cause increase in bulk dark current. P-channel CCDs are not susceptible to the P-V defects and have demonstrated much greater radiation tolerance than conventional n-channel devices.

3.8   Packaging and Mosaics

Making CCDs is often easy compared to providing suitable packaging for specialized applications like astronomy. For commercial applications a simple ceramic (DIL) package can suffice and provide a cost-effective solution. For applications requiring good device flatness, metal packages are common with various connection schemes available. Large focal planes with high fill factors require the most compact buttable packages, in which a minimum footprint connector is also required. Six typical packages are shown in Fig. 16. Two large multichip applications are shown in Fig. 17.
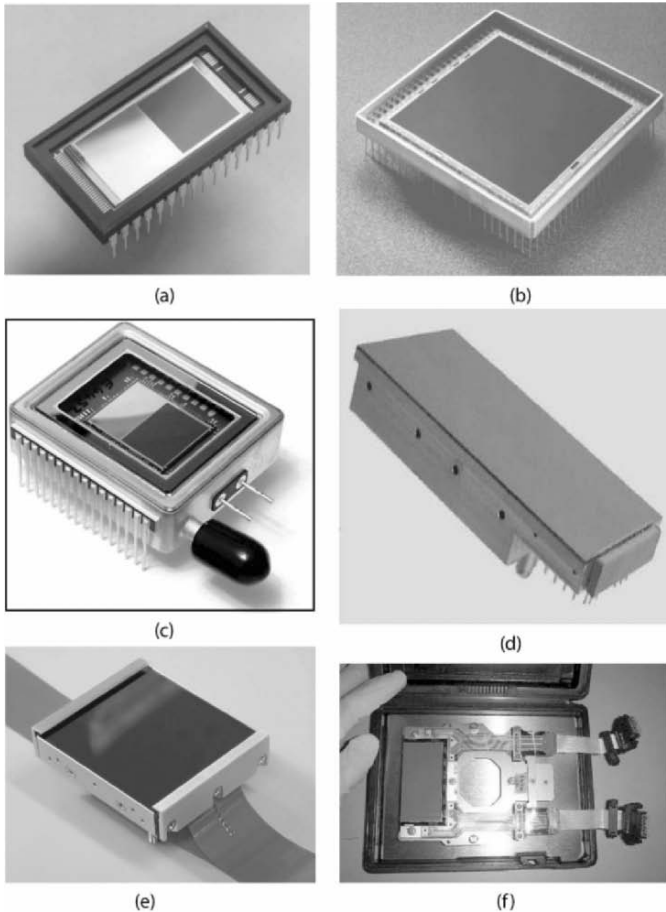
Figure 16. (a) Ceramic package (ccd47-20), *(b)* Kovar package (SITe), *(c)* sealed Peltier package, *(d)* three-side buttable metal package, *(e)* four-side buttable + flexis, *(f)* custom space package. *(a),(c),(d),(e),(f)* Courtesy of e2v technologies.
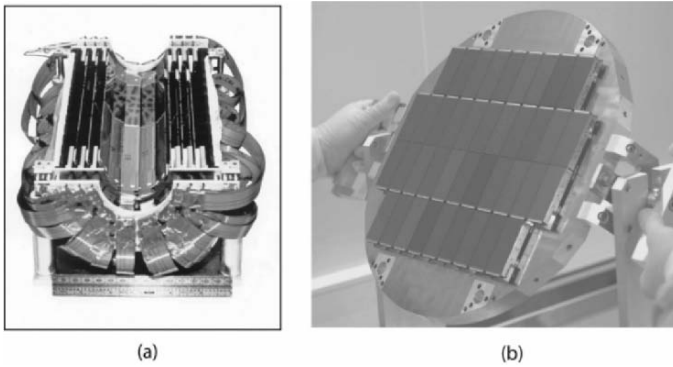
Figure 17. (a) Vertex vxd3 detector and *(b)* CFHT Megacam (377 megapix).

Many applications, especially single-chip, employ simpler packages. Development costs often preclude the use in ground-based astronomy of custom packages such as those utilized in space applications. For large focal planes or "extremely large" telescopes, however, more sophisticated packages become viable. Currently, several observatories have been constructing "megacam" arrays [15], and larger ones are planned such as for the Large-Synoptic Survey Telescope (LSST) Observatory. The routine manufacture of large-area sensors in quantity has made large mosaics feasible for astronomy, which has seen a considerable growth of these within the last decade or so, as illustrated in Fig. 18.
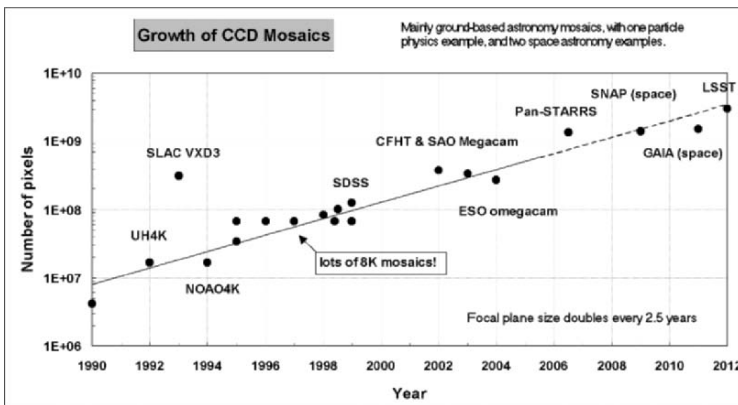
Figure 18. Illustration of large focal-plane sizes with Luppino/Burke "Moore's" law.

Along with the growth of mosaics using "standard" CCD packages, custom packages driven by the requirements of large mosaics have also been developed, as seen in Fig. 19.
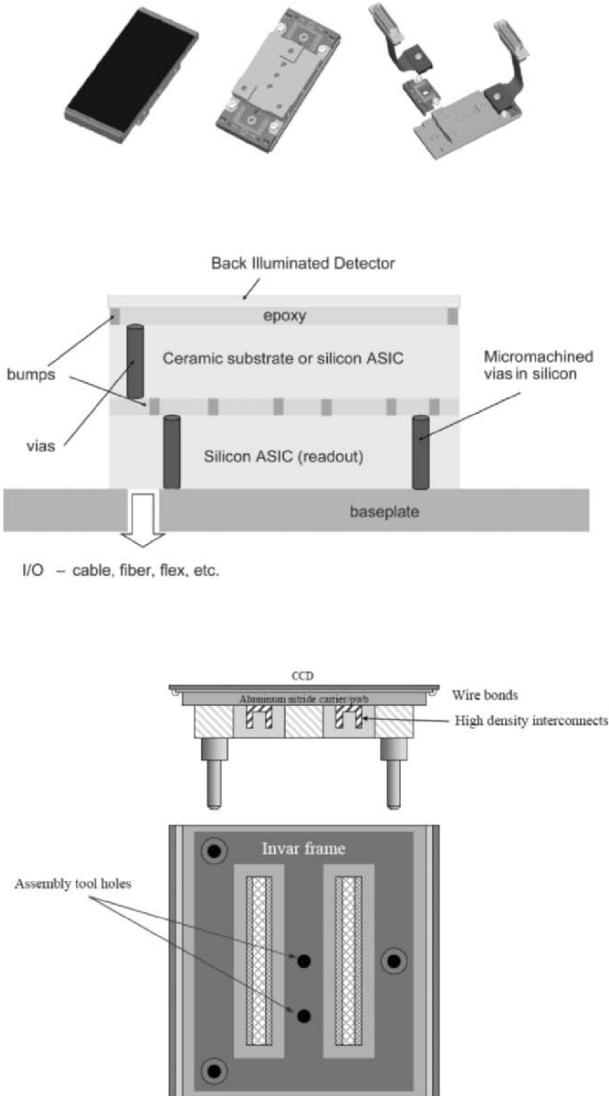
Figure 19. Examples of custom packages: *(top)* Luppino concept package; *(middle)* Lesser application-specific integrated circuit concept for LSST [16]; *(bottom)* LSST concept package.

3.9   Blooming Control

Because of the enormous range of object photon flux encountered in astronomy, the problem of pixel saturation, or blooming, inevitably arises in

direct sky imaging. In a typical scientific CCD the well saturation causes charge to overflow into adjacent pixels above and below the illuminated pixels and to a much lesser extent across the channel stops into adjacent columns, as illustrated in Fig. 20 (left). The reason for this is that the channel stops are at the substrate or ground potential while the CCD channel, even with its gates at the most negative potential, is always a volt or so positive. Thus, there is always a path for electrons into adjacent pixels within a column that is energetically more favorable than across the channel stops. However, when the illumination is so intense that photoelectron current cannot completely drain along this path, the excess electrons will diffuse into the substrate below and be collected by pixels in adjacent columns.
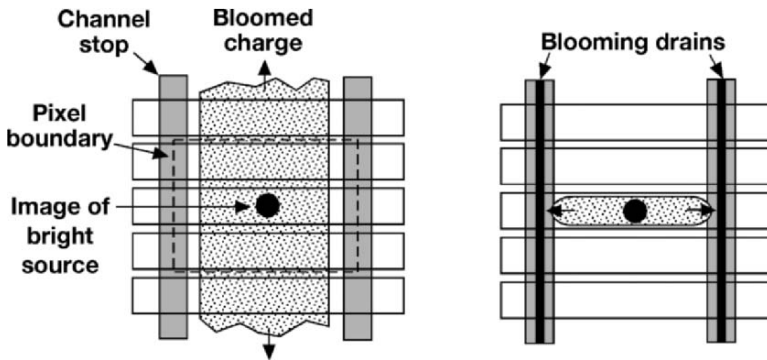
Figure 20. (left) Blooming in a three-phase CCD showing charge overflowing into adjacent pixels within the column, and *(right)* pixel with blooming drains embedded within the channel stops to absorb pixel overload.

A method of blooming suppression involving dithering of the clock waveforms, called clocked antiblooming (CAB), was described in 1983 [17] and can be applied to any buried-channel CCD, excluding those that have a built-in charge-transfer directionality, i.e., two-phase CCDs. The technique relies on a phenomenon called charge pumping, in which excess photoelectrons are made to recombine with holes via surface states before the blooming occurs. Charge packets must be transferred back and forth within the pixel, and each transfer results in the recombination, and therefore removal from the charge packet, of electrons equal in number to the surface states at the silicon/oxide interface.

To keep up with the build-up of excess charge, the integrated charge packet must be shifted repeatedly during image integration. The question that the required cycle rate raises is one of the limitations of this method, namely, that it depends on the surface state density of the device technology. Typical values of contemporary technology lie in the low 10^9 cm^{-2}, hence of

order 5000 states in a 15×15-µm pixel. Thus, for a device with a 200,000 e⁻ full well, each forward/backward shift can eliminate only 2.5 % of the pixel overload. At a 20-kHz back-and-forth shift rate this method can sink about 10 pA of bloomed charge per pixel. Of course, higher surface state densities would clearly be more attractive for this process, but manufacturers take great pains to reduce these states because they are a prime contributor to dark current.

A more attractive approach for the user is the kind of built-in blooming control first developed at what used to be RCA Laboratories (now Sarnoff Corporation) in the 1970s [18]. This feature is available from almost all the manufacturers of scientific CCDs, including e2v technologies, Fairchild Imaging, and Semiconductor Technology Associates. Figures 21(a) and 21(b) illustrate the pixel modifications used in this method. The standard p^+ channel stop is modified by placing an n^+ overflow or blooming drain flanked on both sides by n^- regions, whose doping level is carefully controlled to produce a potential barrier or charge "spillway" that allows charge to flow from the well into the blooming drain at some predetermined level. A p^+ photoelectron barrier is placed beneath these regions to deflect into the wells those photoelectrons that would otherwise be captured by the blooming drain. Figure 21(b) depicts electron potentials and charge flow when the blooming control is active. Clearly, the operation of this feature depends on the low level of the clock phases adjacent to the integrating phase in order to establish a blocking potential.
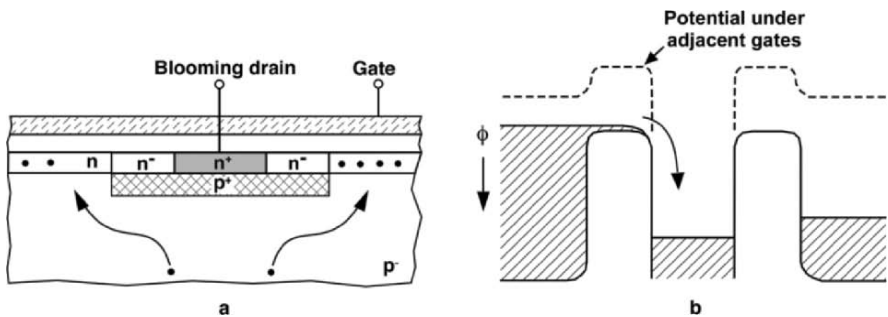
Figure 21. (a) Cross-sectional view of a channel stop modified for blooming control and (b) depiction of the potential profiles in the blooming-control structure.

The pixel modifications are not difficult from a process point of view, nor are they regarded as having a significant impact on device yield. The blooming control depicted here does occupy greater width than a standard channel stop and therefore results in some penalty to the full well. While standard channel stops have widths 1.5–3 µm (after lateral diffusion of the

p-dopants and the bird's beak encroachment), the blooming control as fabricated at Lincoln Laboratory [19] occupies about 4 μm. Data at Lincoln Laboratory on a 2K×4K, 15-μm-pixel device has shown that the blooming control can handle currents of at least 1 nA from a pixel before blooming sets in, or about 100× higher than charge pumping.

4.   CCD, CMOS, WHAT IS IT ALL ABOUT…?

4.1   CCD and CMOS Tradeoffs

We have all heard about the imminent doom of CCD technology, but it continues to thrive, and in many cases it is still the best approach when image quality is the most important criterion. The CCD is a straightforward device. The imaging section consists of an array of capacitors with overlying gate electrodes biased to create regions of high electrical potential in the pixels where charge carriers can be collected. Once the photogenerated charge has been accumulated in the potential wells, the signal is physically moved from one pixel to the next by alternating the bias voltage levels to shift the charge packets across the array. The pixels perform both the function of charge capture and of charge readout. To produce an image, the signal in the imaging region is shifted to the serial shift register—a single row of pixels dedicated to transfer the charge to the output amplifiers—a line at a time. Then the data are transferred, pixel-by-pixel, to a pre-charged output sense node that is connected to the output amplifier that finally converts the charge to a voltage signal.

The relatively simple structure of the CCD facilitates the fabrication of very large area sensors with very uniform pixel response. The CCD is capable of delivering exceptionally clean signals since the charge-transfer process is noise-free, and the design of the output amplifier can be optimized for low noise performance with little restriction in silicon real estate. On the other hand, CCD fabrication requires specific materials and processes that are not supported by high-volume silicon foundries that are geared for logic and memory devices. For example, the CCD multilayer overlapping polysilicon gate electrode arrangement is a unique requirement that involves special processes to avoid catastrophic electrical shorts.

The strengths of CMOS imagers include low power, high speed, and inclusion of more functionality on-chip [20]. With increasing demands on their imaging performance, however, the fabrication of high-quality CMOS sensors can no longer share the same recipes originally intended for standard

digital products. CMOS image sensors require processes tailored for analog and mixed-signal circuits that are more or less similar to the CCD fabrication process.

4.2   CCD vs CMOS: Imaging Performance Comparisons

Next, we compare CCD and CMOS sensors in terms of the following features: charge generation, charge collection, signal readout, signal measurement, and optical characteristics.

4.2.1   Charge Generation

Charge-coupled devices and CMOS sensors detect light by the photoelectric effect. Incident photons with energy greater than the band gap of silicon ($E_g = 1.12$ eV at 300 K) create electron-hole pairs as they penetrate the material. The absorption depth in silicon is proportional to $1/\alpha$. The absorption coefficient α is lower at longer wavelengths, so a larger volume of material is required to capture these photons. At 400 nm more than 80% of the photons will be absorbed within 0.2 μm of the silicon surface, while at 700 nm 10 μm of material is needed to absorb the same amount. CCDs are typically fabricated on 20-μm-thick epitaxial silicon, which is a custom thickness in a CMOS process. The higher doping concentration in the CMOS material, necessary to reduce short-channel effects, lowers the minority carrier diffusion length and reduces QE.

4.2.2   Charge Collection

In an ordinary slab of silicon, the mobile carrier concentration stays in equilibrium. As a result the photogenerated carriers recombine at the same rate that they are created, and no measurable signal can be produced unless the photogenerated electron-hole pairs can be separated and the resulting charge carriers collected in the potential wells. In CCD and CMOS sensors light detection is performed with a photodiode or a photogate. The electric field in the depletion region of the structures separates the electron-hole pairs and causes the charge carriers to drift to the potential wells, or regions with the highest electrostatic potential, where they accumulate. In a photogate CCD the fill factor of the pixel can be as high as 100%, but a CMOS pixel (photodiode or photogate) must include three or more opaque transistors, which reduces their sensitivity, and full-well capacity. The low-voltage operation of CMOS circuits combined with the low-resistivity epitaxial silicon results in shallow depletion depths, ~ 0.5 μm, which degrades QE. The effective collection volume in a CMOS sensor is small compared to a CCD, where the depletion depth is typically ~5 μm.

4.2.3 Signal Readout

Here lies the fundamental difference between CCD and CMOS imagers. In a CCD the signal charge in the pixel must be transferred across the entire array before it is converted to a voltage by one or a few amplifiers. CCDs are designed to transfer charge with practically no loss, routinely achieving 99.9999% CTE in scientific grade devices. The limited number of amplifiers yields very high output uniformity. To achieve high data rates, however, high-bandwidth amplifiers are required, and the amplifier noise may become a limiting factor. In a CMOS sensor the signal is converted to an output voltage in the pixel and is then read out directly by row and column selection. This architecture significantly reduces the amplifier bandwidth requirements, but the variations in threshold voltage and gain cause undesirable fixed-pattern noise, photoresponse nonuniformity, and temporal noise. Photogate and pinned photodiode CMOS sensors mimic CCD operation since the photocharge must be transferred to an output sense node to be converted to a voltage. In fact, the pixel design is identical to the final stage of a CCD register. Charge transfer is a difficult task to perform at low voltages, because of the weak fringing fields, and requires careful optimization of the doping profiles.

4.2.4 Signal Measurement

This is the final step where the photocharge in the pixel is converted to a voltage. In a CCD, when the signal charge is transferred to the sense node, its preset voltage level is reduced, and the voltage change is detected by the source-follower output amplifier, yielding an output voltage that is linearly proportional to the signal level. The noise source due to the uncertainty in the reset level of the sense node, due to the kTC noise of the reset FET, can be removed by performing correlated double sampling (CDS). The technique involves reporting the output signal as the difference between the video signal and the immediately preceding reset signal, so the reset noise is canceled out. In a CMOS sensor CDS requires additional sample-and-hold capacitors and extra switches in the pixel, impacting the fill factor, but without these components CMOS sensors will be limited by the kTC noise. To improve the fill factor, tighter design rules can be implemented, but the junction depths and voltage swings are also scaled down, lowering the dynamic range of the sensor.

4.2.5   Optical Characteristics

Differences between the architectures of CCD and CMOS sensors affect their optical performance. The entire area of a CCD pixel can be designed to be photosensitive, compared to a CMOS active pixel sensor, where every pixel must contain at least three transistors that are optically insensitive. The fill factor is the ratio of the sensitive area to the total pixel area, and the effective QE is reduced by the fill factor $QE_{eff} = FF \times QE$. In addition, the multilayer metallization process used in CMOS design results in the active area of the pixel being located inside of a deeply recessed opening in the metal layers, causing undesirable optical artifacts in fast optical systems such as light scattering and crosstalk.

4.2.6   CCD vs CMOS Summary

As summarized in Table 1, CCD technology and CMOS technology each has its strengths and drawbacks. While the CCD can approach near ideal imaging performance, CMOS can offer higher circuit integration, lower power, and higher-speed operation.

Table 1. Summary Comparison of CCD and CMOS Technologies.

CCD Technology	CMOS Technology
Highly optimized for optical detection, special fabrication requirements	Benefits from advances in manufacture of high-volume digital products
Very high signal-to-noise	Noise typically higher
Low photoresponse nonuniformity (PRNU), low fixed-pattern noise (FPN)	High PRNU, high FPN, improved by gain and offset correction
Low dark current	Dark current typically higher
High power dissipation	Low power consumption
Complex driver electronics, no on-chip logic and digitization	Single power supply operation, digital output
Serial readout, no windowing capability	Random addressing capability

5.   SPECIAL FEATURES AND NEW DEVICE CONCEPTS

5.1   Electronic Shuttering

Mechanical shutters are a perennial problem for astronomers, all the more so in this era of ever larger focal-plane arrays (FPAs). Thus, an electronic solution to this problem would seem to be enormously attractive. Interline-transfer devices have an effective shuttering capability but only for

front-illuminated formats where the charge can be shifted into the readout registers that have been covered with a thin-film light shield.

An electronic shuttering feature for back-illuminated CCDs has been demonstrated by Reich et al. [21] on small imagers intended for adaptive-optics applications but so far not demonstrated on large-scale devices. The modifications to the device needed to implement the shutter are depicted in Fig. 22.
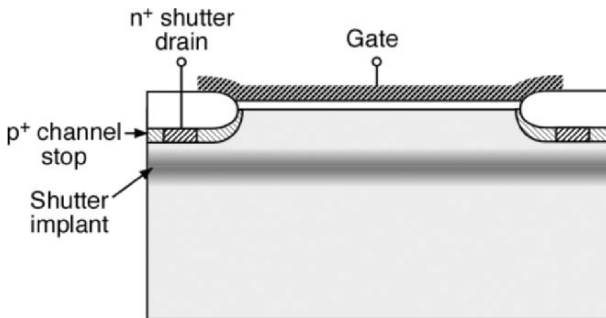
Figure 22. Cross-sectional view of a CCD with the principal features needed for the electronic shutter.

Two new features have been added to the pixel. The first is a deep p-type implant, called the shutter implant, which lies about 2.5 μm below the surface. This layer creates a potential barrier to photoelectron flow from the back surface, which can be modulated by the gate voltage. The second feature is an n^+ region within the channel stop whose function is to collect photoelectrons when the shutter is closed. The shutter operation is illustrated in Fig. 23.
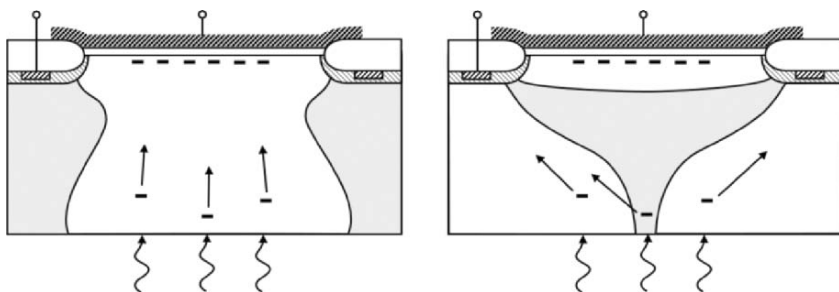
Figure 23. Operation of the shutter: *(left)* gate voltage is high and the shutter drain low, allowing photoelectrons to be collected; *(right)* gate voltage is at a lower setting for readout and the shutter drain high.

To open the shutter the imaging-array gates must be set to a relatively high potential, typically 18 V. The E-field set by the gate overcomes the potential barrier established by the shutter implant, and the depletion region is pushed all the way to the back surface. At the same time the shutter drain is biased to a relatively low potential. Under these circumstances all the photoelectrons are collected in the CCD wells. To close the shutter and read out the integrated charge the imaging gates are returned to lower levels, typically <8 V for the high state, in which case the depletion layer collapses to the depth of the shutter implant. To collect photoelectrons while the shutter is closed, the shutter-drain potential is raised to the point where it establishes its own depletion layer and collects photoelectrons.

An important performance metric for the electronic shutter is the extinction ratio, that is, the fraction of photoelectrons collected when the shutter is off. This is principally a problem in the near infrared, where deeply penetrating photons can be absorbed in the surface region above the shutter implant. Figure 24 shows the calculated extinction coefficient at −80˚C for back-illuminated devices of various thicknesses and a shutter depth of 1.3 µm. Clearly, a thick device is essential for good extinction out to 1000 nm.
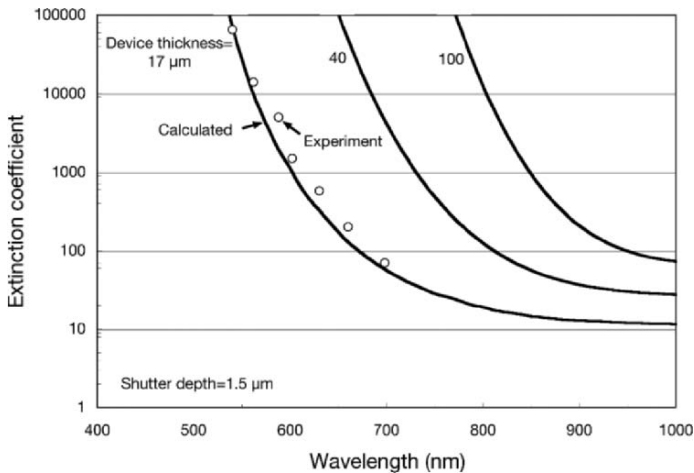
Figure 24. Measured and calculated extinction coefficients. Data and curve for 17-µm-thick device is for T = 20˚C, while the 40- and 100-µm calculated extinction is for T = −80°C.

5.2 Hybrid Detectors

Hybrid detector arrays exploit the benefits of a detector structure optimized for optical detection combined with a processing circuit to read out the signal. The detector array is dedicated to detecting the incident photons, while the readout circuit controls the operation and produces a suitable output. Infrared detectors are typically hybrid arrays consisting of a detector array fabricated in the proper material and mated to a multiplexer readout circuit. Hybrid detectors are somewhat more complex to build, but the technology effectively addresses some of the limitations of monolithic sensors, such as low fill factor and process incompatibilities between the detector array and the readout multiplexer. A variety of visible hybrid arrays have been developed with different technologies implemented in the detector array.

5.2.1 Silicon p-i-n Detector Arrays

The p-i-n detector array consists of a thick (~185 μm) active region of high-purity silicon sandwiched between regions doped p-type and n-type [4]. An example of this type of array is shown in Fig. 25. The illuminated side is implanted n-type, and the side bonded to the readout circuit is doped p-type. A high reverse bias is applied to the device, resulting in a strong electric field that separates the electron-hole pairs created by the photons absorbed in the high-resistivity region. The bulk of the detector array is nearly fully depleted, delivering excellent QE at long wavelengths and good MTF characteristics [22] since the diffusion crosstalk is negligible. The back-illuminated detector array is bump bonded to a CMOS multiplexer with a bump in each pixel. Noise levels comparable to CCD performance are achievable using Fowler's multiple sampling technique.

5.2.2 CCD/CMOS Hybrid FPAs

The CCD/CMOS hybrid FPA combines the imaging qualities of the CCD with the high-speed, low-power, and low-noise capabilities of a dedicated CMOS readout integrated circuit (ROIC). An example of this array is shown in Fig. 26. In a front-illuminated device, the FPA consists of two CMOS ROICs bump bonded to a CCD detector [23]. Each readout circuit is an array of capacitive transimpedance amplifiers (CTIAs) that are connected to each end of the CCD columns with indium bumps. A significant advantage of this configuration is that the fabrication process is simplified since fewer bump connections are required, and the design of the readout electronics is not restricted to the area contained within a pixel, which is the case in a

conventional hybrid detector. Without the conventional serial shift register and on-chip output amplifiers, the hybrid CCD operates with much lower power while maintaining excellent imaging performance. The column parallel readout architecture reduces the effective output bandwidth and provides sufficient silicon real estate in the ROIC to implement sophisticated amplifier circuit designs that dramatically reduce the readout noise. The CCD power consumption is also reduced, as a result of the elimination of high-speed serial clocking and high-current output amplifiers. This parallel readout arrangement dramatically improves the total frame rate and significantly reduces the noise floor, since the amplifier bandwidth is considerably lower than the level necessary for a conventional CCD with fewer output ports.
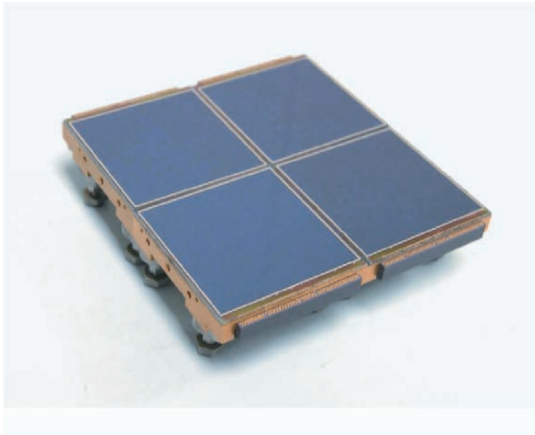
Figure 25.   Mosaic array of 2K×2K PIN hybrid FPAs. Courtesy of Yibin Bai, Rockwell Scientific.

5.2.3   CMOS/CMOS Hybrid FPAs

In CMOS/CMOS hybrid FPAs, a CMOS detector array fabricated for back illumination and biased for deep depletion is combined with a dedicated CMOS readout circuit [24]. A column-wise connection similar to the CCD/CMOS approach described above reduces the number of bump interconnects, lowers power dissipation, and increases speed.

5.2.4 SOI Arrays

Although relatively new, silicon-on-insulator (SOI) arrays show promising prospects. The devices are fabricated with two silicon layers separated by an insulating oxide layer. The readout circuitry is built in the top "device" layer and the photodiode in the bottom "handle" layer. Separate grounding for each layer eliminates substrate bounce and clock coupling. The resistivity of each layer can be tailored for best performance [25].
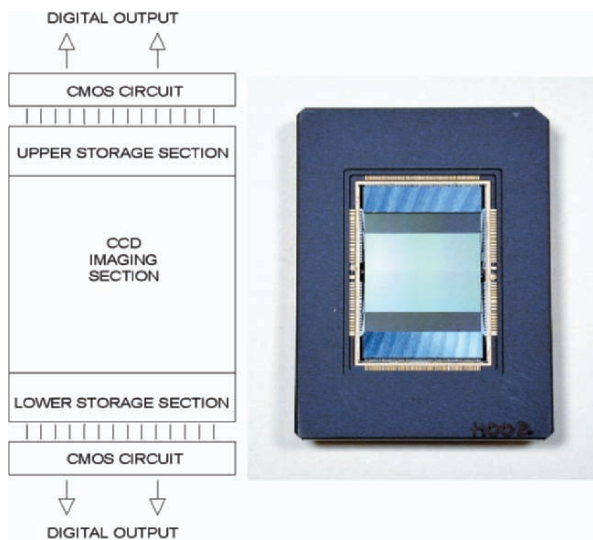
Figure 26. Prototype CCD/CMOS hybrid FPA. Courtesy of Fairchild Imaging.

5.3   Curved CCDs

It has always been tacitly assumed that image sensors must of necessity be flat, and that optical system designers must therefore take whatever pains and expense necessary to provide a flat image plane. This assumption is no longer valid, and in fact curved CCDs are now a reality, as evidenced by recent work at Sarnoff [26] and Lincoln Laboratory. Figure 27 is a simple demonstration of silicon deformability in which a 20-µm-thick silicon membrane is pressed down on a 175-mm-radius spherical section.
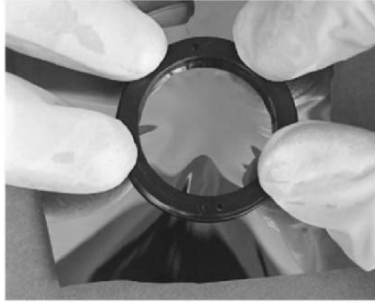
Figure 27. Deformation and buckling of a 20-µm Si membrane over a 175-mm-radius spherical section.

The mechanical limitations on deformability can be estimated from a simple formula. Consider a circular silicon membrane of radius r deformed to a spherical cap of radius R. The maximum strain is at the center of the cap and is given approximately by $(r/R)^2/6$, assuming the silicon thickness is much smaller than r. For a 60-mm CCD (e.g., a 4K×4K, 15-µm-pixel device) and a 1-meter radius of curvature, the maximum strain is $\sim 6\times 10^{-4}$, which is well below the mechanical limit of ~1% for silicon. The effects of strain on the performance of CCDs have not been thoroughly examined at this point, but preliminary results show the main effect to be an increase in dark current that arises from the decrease in band gap energy E_g. Measurements at Lincoln Laboratory show a dark-current increase that is consistent with a decrease in E_g of 80 meV/(% strain), compared to the theoretical value of 115 meV/(% strain). These numbers can be related to actual dark-current changes using well-known formulas for dark current in silicon [27].

5.4   Orthogonal-Transfer CCD

The orthogonal-transfer CCD (OTCCD) is a unique device in its ability to shift charge in all directions. Figure 28 illustrates a conventional three-phase pixel layout on the left and one of two OTCCD pixel layouts on the right. The unit cell of the OTCCD consists of four phases, and the layout shown here is a symmetrical arrangement of four triangular gates. With the phase-4 gates biased low, phases 1–3 can be clocked to shift charge vertically, while with either phase-1 or phase-3 blocking the remaining phases can shift charge horizontally.
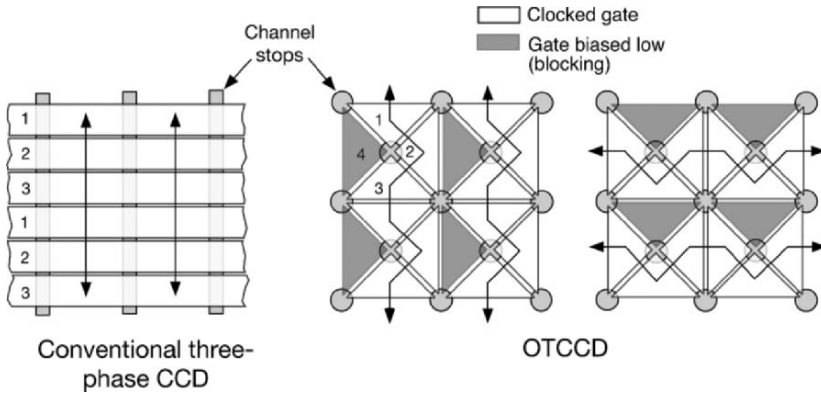
Figure 28. (left) Illustration of a conventional three-phase CCD and *(right)* one of two OTCCD pixel designs.

The obvious application of this device in astronomy is to perform electronically the tip-tilt correction to compensate for atmosphere-induced wavefront tilt and telescope shake. Results from a small prototype device (512×512 pixels) were reported at this conference in 1996 [28] and later in more detail [29].

The effectiveness of the device for correcting wavefront tilt is limited to angular distances on the sky of a few milliarcseconds. For wide-field imaging such a device would clearly lose its effectiveness, and a different approach with multiple OTCCDs is needed. Such a device, the orthogonal-transfer array (OTA) [30], is now under development for the Panoramic Survey Telescope and Rapid Response System (Pan-STARRS) program. Figure 29 illustrates the basic elements of the OTA under development. The device consists of an 8×8 array of OTCCDs or cells, each comprising about 500×500 pixels. The parallel clocks and the readout amplifier are under the control of a small block of NMOS logic that enables each cell to be controlled and read out independently. In this way each cell can be clocked in a manner that is optimum for the local image motion. Prototype devices have been demonstrated, and the first test results are described elsewhere in these proceedings [31].
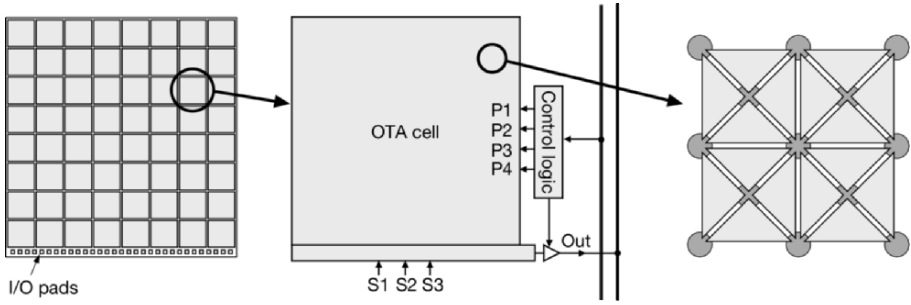
Figure 29. Principal elements of the OTA: *(left)* overall chip layout comprising an 8×8 array of OTCCD cells, *(center)* OTA cell with control logic, and *(right)* one of the OTCCD geometries.

5.5   Chip and Pixel Sizes

The size of a device is limited by wafer size (~6 in. is typical for specialist CCD manufacturers), lithography, and yield. Device size is increasing, with 4K×4K format becoming available from several manufacturers. For large cost-effective mosaics, special approaches can be adopted to increase yield, e.g., subdividing a device into functional units and integrating within the package, such as illustrated in Fig. 30. The requirement for a 5K×5K monolithic device is that there be no fatal defects across the whole area. It is possible to make 5K×1.25K (K = 1024) units on a wafer, select them by probing, and then use special packaging techniques to construct a 5K×5K unit device with minimal gaps between units. The unit components could be 1.25K, 2.5K, 3.75K, or 5K in height depending on the yield of each wafer.

The size of a pixel is limited by issues of lithography, process, and performance, e.g., full-well capacity. Pixel size is decreasing, with ~10 μm available from several manufacturers. In many cases, lithography and process developments allow smaller features to be made. Four-phase pixels may become more common in order to help maintain full-well capacity as pixels shrink in size.

6.   ACKNOWLEDGEMENT

We thank all who provided material directly or in publications, with apologies to those not mentioned or cited. We also wish to especially thank Karen Challberg of MIT Lincoln Laboratory for her excellent editorial assistance in assembling this paper.
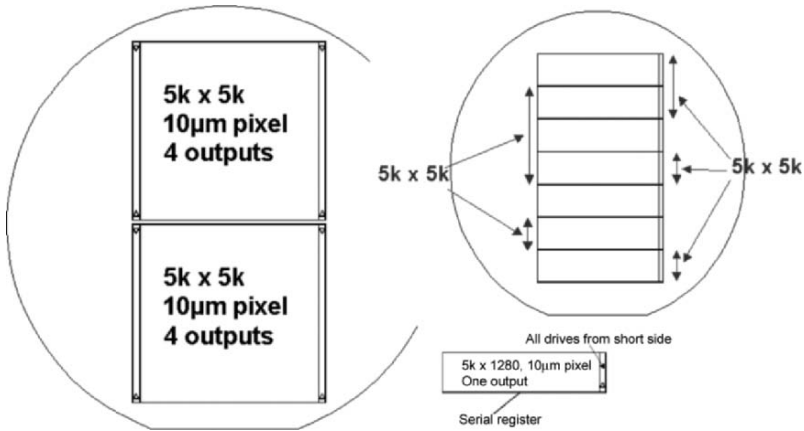
Figure 30. Example of concept for large device (5K×5K unit from 5K×1.25K components). Courtesy of e2v technologies.

7. REFERENCES

[1] G. F. Amelio, M. F. Tompsett, and G. E. Smith, 1970, *Experimental verification of the charge coupled device concept*, Bell Syst. Tech. J., vol. **49**, pp. 593-600.

[2] M. Lesser, 2004, *Very large format back illuminated CCDs*, Scientific Detectors for Astronomy, P. Amico, J. W. Beletic, and J. E. Beletic, eds., Kluwer, Dordrecht, pp. 137-143.

[3] S. E. Holland, D. E. Groom, N. P. Palaio, R. J. Stover, and M. Wei, 2003, *Fully depleted, back-illuminated charge-coupled devices fabricated on high-resistivity silicon*, IEEE Trans. Electron Devices, vol. **50**, pp. 225-238.

[4] Y. Bai, J. T. Montroy, J. D. Blackwell, M. C. Farris, L. J. Kozlowski, and K. Vural, 2000, *Development of hybrid CMOS visible focal plane arrays at Rockwell*, Proc. SPIE, vol. **4028**, pp. 174-182.

[5] V. Suntharalingam et al., 2005, *Megapixel CMOS Image Sensor Fabricated in Three-Dimensional Integrated Circuit Technology*, International Solid-State Circuits Conference, San Francisco.

[6] http://www.e2v.com

[7] M. P. Lesser and V. Iyer, 1998, *Enhancing back-illuminated performance of astronomical CCDs*, Proc. SPIE, vol. **3355**, pp. 446-456.

[8] Many LBNL papers available at http://www-ccd.lbl.gov/

[9] A. Kelt, A. Harris, P. Jorden, and S. Tulloch, 2005, *Optimised CCD anti-reflection coating*, SDW2005 Proceedings, Springer, Netherlands, these proceedings.

[10]   S. M. Tulloch, 2004, *Application of L3 technology to wavefront sensing*, Proc. SPIE vol. **5490**, pp. 1167-1176.

[11a] B.Burke and S. Gajar, 1991, *Dynamic suppression of interface-state dark current in buried-channel CCDs*, Trans IEEE ED-38, pp. 285-290.

[11]   P. Jorden, P. Pool, and S. Tulloch, 2003, *Secrets of e2v technologies CCDs*, Exp. Astron., vol. **14**, pp. 69-75.

[12]   T. E. Dutton, T. S. Lomheim, and M. D. Nelson, 2002, *Survey and comparison of focal plane MTF measurement techniques*, Proc. SPIE, vol. **4486**, pp. 219-246.

[13]   D. E. Groom, P. H. Eberhard, S. E. Holland, M. E. Levi, N. P. Palaio, S. Perlmutter, R. J. Stover, and M. Wei, 2000, *Point-spread function in depleted and partially depleted CCDs*, LBNL-45276, Proceedings of 4th ESO Workshop on Optical Detectors for Astronomy, Garching, Germany, pp. 205-216.

[14]   J. C. Pickel, A. H. Kalma, G. R. Hopkinson, and C. J. Marshall, 2003, *Radiation effects on photonic imagers—a historical perspective*, IEEE Trans. Nucl. Sci., vol. **50**, pp. 671-688.

[15]   P. R. Jorden, D. G. Morris, and P. J. Pool, 2004, *Technology of large focal planes of CCDs*, Proc. SPIE, vol. **5167**, pp. 72-82.

[16]   M. P. Lesser, and J. A. Tyson, 2002, *Focal plane technologies for LSST*, Proc. SPIE, vol. **4836**, pp. 240-246.

[17]   J. Hynecek, 1983, *Electron-hole recombination antiblooming for virtual-phase CCD imager*, IEEE Trans. Electron Devices, vol. **ED-30**, pp. 941-948.

[18]   D. J. Sauer, E. L. Hsueh, F. V. Shallcross, G. M. Meray, P.A. Levine, G. W. Hughes, and J. Pellegrino, 1990, *High fill-factor CCD imager with high frame-rate readout*, Proc. SPIE, vol. **1291**, pp. 174-184.

[19]   B. E. Burke, R. K. Reich, J. A. Gregory, W. H. McGonagle, A. M Waxman, E. D. Savoye, and B. B. Kosicki, 1998, *640×480 back-illuminated CCD imager with improved blooming control for night vision*, IEDM Technical Digest, pp. 33-36.

[20]   E. R. Fossum, 1997, *CMOS image sensors: electronic camera-on-a-chip*, *IEEE Trans. Electron Devices*, vol. **44**, pp. 1689-1698.

[21]   R. K. Reich, R. W. Mountain, W. H. McGonagle, J. C. Huang, J. C. Twichell, B. B. Kosicki, and E. D. Savoye, 1993, *Integrated electronic shutter for back-illuminated charge-coupled devices*, IEEE Trans. Electron Devices, vol. **40**, pp. 1231-1237.

[22]   L. J. Kozlowski, Y. Bai, M. Loose, A. B. Joshi, G. W. Hughes, and J. D. Garnett, 2002, *Large area visible arrays: performance of hybrid and monolithic alternatives*, Proc. SPIE, vol. **4836**, pp. 247-259.

[23]   X. Liu, B. A. Fowler, S. K. Onishi, P. Vu, D. D. Wen, H. Do, and S. Horn, 2005, *CCD/CMOS hybrid FPA for low light level imaging*, Proc. SPIE, vol. **5881**, pp. 79-87.

[24]   J. Janesick, 2003, *Charge coupled CMOS and hybrid detector arrays*, SPIE's Focal Plane Arrays for Space Telescopes, San Diego.

[25]   V. Suntharalingam, B. E. Burke, and M. J. Cooper, 2004, *Silicon-on-insulator-based single-chip image sensors—low-voltage scientific imaging*, Scientific Detectors for Astronomy, P. Amico, J. W. Beletic, and J. E. Beletic, eds., Kluwer, Dordrecht, pp. 155-162.

[26]   P. Swain, and D. Mark, 2004, Curved CCD detector devices and arrays for multi-spectral astrophysical applications and terrestrial stereo panoramic cameras, Proc. SPIE, vol. **5499**, pp.281-301.

[27]   J. Janesick, *Scientific Charge-Coupled Devices*, 2001, SPIE, Bellingham, WA..

[28]   J. Tonry, and B. E. Burke, 1998, *The orthogonal transfer CCD*, Optical Detectors for Astronomy, J. W. Beletic and P. Amico, eds., Kluwer, Dordrecht, pp. 281-291.

[29]   J. L. Tonry, B. E. Burke, and P. L. Schechter, 1997, *The orthogonal transfer CCD*, Publ. Astron. Soc. Pac., vol. **109**, pp. 1154-1164.

[30]   B. E. Burke, J. Tonry, M. Cooper, G. Luppino, G. Jacoby, R. Bredthauer, K. Boggs, M. Lesser, P. Onaka, D. Young, P. Doherty, and D. Craig, 2004, *The orthogonal-transfer array: a new CCD architecture for astronomy*, Proc. SPIE, vol. **5499**, pp. 185-192.

[31]   J. L. Tonry, B. E. Burke, P. Onaka, M. J. Cooper, and G. Luppino, 2005, *The orthogonal transfer array*, SDW2005 Proceedings, Springer, Netherlands, these proceedings.

Tres CCD amigos Paul Vu, Paul Jorden and Barry Burke (left to right) can't believe anyone would consider CMOS.

Rainer Kramm, Barry Burke and Mary Lou Burke
queue up for the opening reception.

Ray DuVarney, Leslie Beletic and Juliet Beletic enjoy the Festa Paesana.

SILICONUS MAXIMUS

Richard Bredthauer[1] and Michael Lesser[2]

[1]*Semiconductor Technology Associates, Inc.,* [2]*Steward Observatory, University of Arizona*

Abstract: *Recent discoveries reveal new promise for a technology formerly assumed to be extinct, CCDs. Silicon processing technology has made tremendous strides over the past 30 years enabling higher quality and ever larger CCDs. We will discuss prior and ongoing experience with large area CCD focal-plane arrays, which include innovative design and fabrication techniques that ensure performance and yield. Semiconductor Technology Associates (STA) will describe the development of an ultrahigh resolution large area CCD (up to the maximum limit of a 150 mm wafer) integrating high dynamic range and fast readout.*

Key words: *Ultrahigh resolution CCD, 4K×4K imager, VLSI.*

1.   INTRODUCTION

This paper summarizes rapid progress made in the past few years in the development of large area scientific imaging arrays. CCD imaging arrays from 3cm×3cm (2048×2048 pixels) to 9cm×9cm (10K×10K pixels) will be described. These devices show exciting promise in a variety of space-based, astronomical, and high resolution commercial imaging applications.

Bipolar transistors were fabricated on 1.5" silicon wafers in production during the late 60's. By the early 70's a stable MOS process had been established and wafers became 2" and 3" in diameter. Boyle and Smith of Bell Laboratories described and demonstrated working Charge Coupled Devices in 1970 [1,2]. They are elegantly simple devices which manipulate signals as small packets of charge from one area to another across the silicon surface. An array of MOS capacitors is fabricated over the silicon. The

discrete packets of charge are coupled from one capacitor to the next by alternately clocking voltages from one capacitor gate to the next. For scientific applications the signal packets are as small as only a few electrons. During the 70's the quality of the silicon starting material, process chemicals and laboratory cleanliness had not matured adequately to fabricate devices larger than several millimeters on a side. Imaging arrays of 380×488 pixels demonstrated good, high level performance, but showed significant signal trapping and fixed pattern noise at signal levels less than 1000 electrons. CCDs were proposed to fulfill a variety of functions ranging from analog memories, adaptive filters, radar signal processors, and imaging devices. The mainstream of silicon processing proceeded rapidly pushing the technology in digital CMOS and DRAMS.

Production wafers moved from 3" to 4" to 5" to 6" to 8". Presently Intel, Samsung and other major facilities are now utilizing 12" wafers for production. The cost of such facilities is several billion dollars and can only be sustained by very high volumes. Digital devices have taken over the potential CCD applications of signal processing and memory. Despite these changes CCDs still remain the dominant choice for very high end/resolution imaging applications.

Arrays as large as 4 centimeters on a side (4096×4096 pixels) were demonstrated in the late 80's [3]. Those imagers were designed with a pixel size of 15 μm sq. fitting a 4" (100mm) wafer (see Fig. 1). CCDs have one of the largest active gate areas of any semiconductor device. Creating a design which is tolerant to predominant process defects is key to yields.
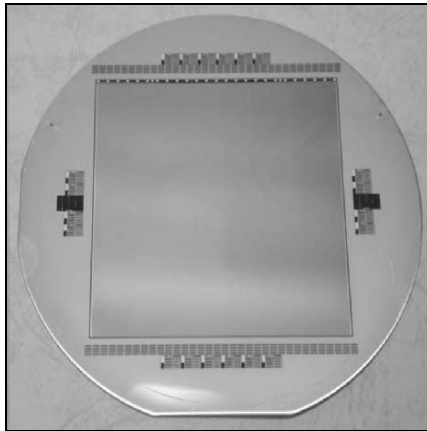
Figure 1. 4K×4K on a 4" wafer.

2. CCD IMAGER EVOLUTION

2.1 Guider Minimus

During the mid-80's fabricating a 2560×256 15 micron pixel array was a real challenge. Processing yield was on the order of 30% with many silicon defects and a very high noise level (>5 electrons rms). This John Geary designed CCD has been incorporated on recent fabrication runs. The results show remarkable improvement over the last 20 years. Yields exceed 95%, image quality is near perfect and noise levels are below 3 electrons rms. These imagers are used for telescope guiders at Carnegie telescopes in Chile and the Canada France Hawaii Telescopes in Hawaii.

2.2 Space Based Imagers

Mature silicon processing technology enabled the production of very high performance CCDs for space based applications. A space based planet finder for the NASA Kepler Discovery mission requires a 2200×1024 pixel imager with 27 micron pixels [4]. A large focal plane of 46 backside-illuminated imagers fills the requisite optical field. Figure 2 shows STA manufactured initial prototypes of the CCD.
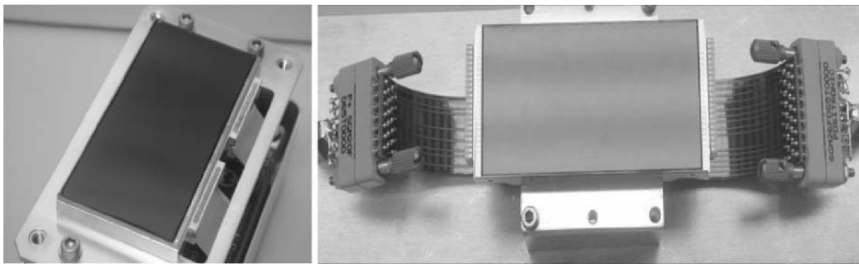
Figure 2. (left) Kepler 2K×1K and *(right)* FAME 2K×4K CCDs.

A somewhat larger 2048×4064 imager with a 15 micron pixel was produced for the Naval Observatories FAME program. This device incorporated a novel input serial register at the top of the CCD to allow for independent metered background charge to each column (see Fig. 2). This serves to mitigate radiation damage effects over long space missions by filling the radiation induced traps.

The excellent yield and performance of these devices demonstrates significant improvement in silicon material quality and processing cleanliness.

2.3   Orthogonal Transfer CCD

As silicon processing technology has improved, so has device capability. An example is the orthogonal transfer CCD [5]. This device requires 4 levels of polysilicon to achieve charge transfer in arbitrary directions. The additional complexity enables performance of astronomical tip-tilt correction directly within the CCD. In addition, on chip logic selects individual sub-arrays for readout.

Figure 3 shows the focal plane, whish consists of an 8×8 array of sub-arrays, each with 480×494 12 micron pixels. The CCD has 8 separate outputs. A column of 8 sub-arrays can be read out one by one through one of the outputs by setting the appropriate control lines. An important advantage of 64 separate sections for a large CCD is the inherent fault tolerance. If a section has a serious defect it can be deselected with a control signal. The benefit is a higher effective yield. A catastrophic defect in a normal 4K×4K CCD would disqualify the entire device. In an Orthogonal Transfer CCD this would mean only a single missing section of 64, and the device could still be utilized.

OTCCD Pixel   **OTCCD SubArray**   **8x8 Array of OTCCDs**
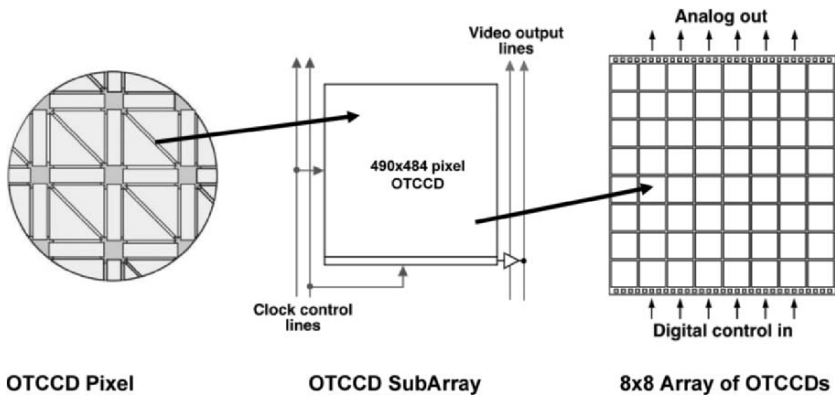
Figure 3. Orthogonal Transfer CCD configuration.

2.4   STA0500A 4k Imager

STA utilizes 150 mm wafers for CCD fabrication. There are significant advantages of these wafers. Our group originally fabricated 4K×4K imagers on 100 mm wafers at Ford Aerospace with only marginal yield of less than 10%. It is only possible to fit a single device on a wafer of this size (see Fig. 1). In conjunction with the Imaging Technology Laboratory (ITL) at the University of Arizona [6], we have designed a new 4K×4K imager

incorporating new process technology tools and an increased wafer size. Figure 4 demonstrates the advantages of such an approach.
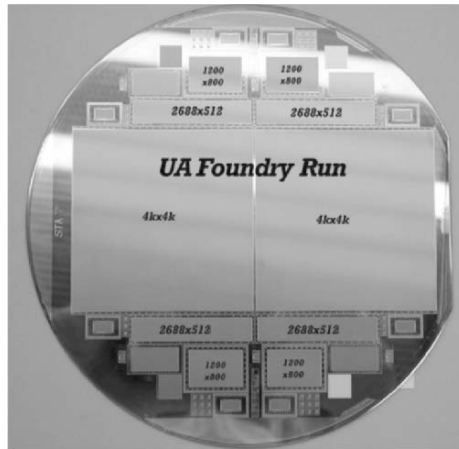
Figure 4. STA0500A wafer delineation.

The wafer mask was designed to include several different types of CCDs needed for various UA projects, including 800×1200 and 2688×512 spectroscopic format CCDs. These are updated designs of detectors produced many years ago and fabricated at Ford Aerospace by the author. The devices were designed by Dr. John Geary of the Smithsonian Astrophysical Observatory. A single wafer includes two 4K×4K CCDs, four 2688×512 CCDs, four 1200×800 CCDs, four 512×1024 frame transfer guider CCDs, eight 128×128 adaptive optics CCDs and several four side buttable demonstration CCDs. It is a significant cost benefit to fabricate a variety of CCDs on a single wafer. The cost of fabricating a 100 mm wafer is identical to the cost of a 150 mm wafer. Producing two 4K×4K devices on a single wafer results in one half the fabrication cost. It also reflects higher yields because the proportion of good silicon area to edge is higher. DC yields of 4Ks on 150 mm wafers routinely exceed 60%. Functional yield is also very high. A recent run yielded 15 astronomy grade (the highest) 4K CCDs out of 48, a 30% yield.

Once a fabrication run of 24 wafers is completed, STA performs DC parametric tests and nominal functional tests. The best wafers are selected and shipped to ITL for further low temperature testing and selection of candidates for thinning. Figure 5 shows a completed 4K in its dewar ready for mounting on the Magellan telescope. The results for 4K thinned devices have been excellent. Output noise is routinely ~2.8 electrons at 50kHz for the four outputs. HCTE and VCTE are >0.999998. For the multi-pinned

phase mode of operation full well charge capacity is >80,000 electrons. Dark current in non-MPP mode is ~10 e⁻/pixel/hour at -100C.
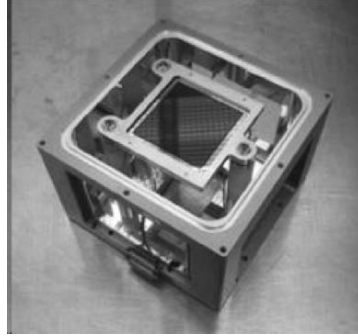
Figure 5. Backside thinned 4K CCD for Carnegie Magellan Telescope.

Maximum quantum efficiency is obtained by backside thinning and applying a suitable anti-reflection coating for the optical region of interest. Figure 6 shows the QE curve for a "blue" optimized 4K CCD.
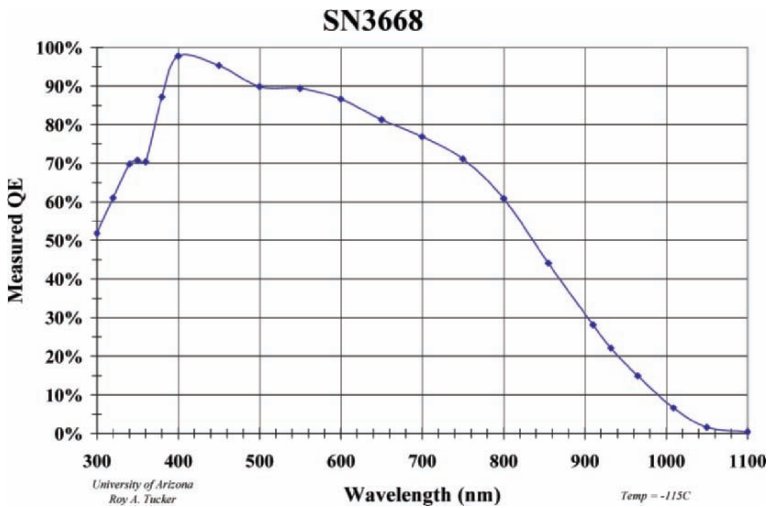
Figure 6. 4K QE at -115ºC optimized for blue response.

3. SILICONUS MAXIMUS

The next step in the evolution of large area CCDs is a single device, the maximum size for a 150 mm wafer. Such a device is now in development at STA for the Naval Observatory. We have completed a Phase I SBIR studying the various technology and design trades to produce such a device. The CCD will consist of 10,600×10,600 pixels. To read an image frame greater than 100 million pixels in 10 seconds will require a minimum of 16 outputs. A pixel size of 9 microns will provide a full 14 bit dynamic range with a readout noise <5 electrons rms. This size pixel also yields a 9.54×9.54 cm image area. For improved CTE and enhanced quantum efficiency the CCD will be fabricated on very high resistivity silicon wafers.

During Phase II of the program we will fabricate several runs of the CCDs. The best candidates will be thinned at ITL and backside AR coated to meet the QE requirements of the Navy. The devices will be packaged and mounted in a dewar with an Astronomical Research Cameras, Inc. Generation 3 CCD controller. The camera system will be mounted on a telescope for extensive evaluation and demonstration of the CCDs ability to provide accurate star positions for celestial navigation.

4. CONCLUSION

The present defacto standard CCD mosaic device is a 2K×4K 15 μm three side abuttable array. Astronomers are already contemplating mosaic arrays filling a field as large as 80,000×80,000 pixels. As silicon processing technology matures and wafer size increases it becomes possible to produce larger and larger individual CCD devices at reasonable prices. This 6.4 gigapixel hypothetical array would require 800 2K×4K CCDs. It would only need 400 4K×4Ks or 64 10K×10K CCDs. CCDs continue to be the only cost effective silicon imaging device for producing imagers of this size and resolution.

5. REFERENCES

[1] Boyle, W.S. and Smith, G.E., 1970, *Charge Coupled Semiconductor Devices,* Bell Systems Technical Journal, Vol. **49**, p. 587-593.
[2] Amelio, G.F. Tompsett, M.F. and Smith, G.E., 1970, *Experimental Verification of the Charge Coupled Concept*, Bell Systems Technical Journal, Vol. **49**, p. 593-600.
[3] Bredthauer, R.A., 1989, *Very Large Area 2048 and 4096 CCD Image Sensors*, SPIE Proceedings, Vol **1161**, p. 61-66.

[4] Philbrick, R., Geary, J., Dunham, E., Koch, D., 2004, *95 Million Pixel Focal Plane for use on the Kepler Discovery Mission*, Scientific Detectors for Astronomy, Amico, P., Beletic, J.W., Beletic, J.E. (eds.), Kluwer Academic Publishers, p 581.

[5] Tonry, J.L., Luppino, G.A., Kaiser, N., Burke, B., Jacoby, G.H., 2004, *Giga-Pixels and Sky Surveys*, Scientific Detectors for Astronomy, Amico, P., Beletic, J.W., Beletic, J.E. (eds.), Kluwer Academic Publishers, p. 395

[6] Lesser, M., Bredthauer, R., 1998, *Development of a 4096×4096 15 micron Pixel Scientific CCD*, The Proceedings of the International Conference on Scientific Optical Imaging, Georgetown, Grand Cayman.

[7] Lesser, M.P., 2004, *Very Large Format Back Illuminated CCDs*, Scientific Detectors for Astronomy, Amico, P., Beletic, J.W., Beletic, J.E. (eds.), Kluwer Academic Publishers, p. 137.

Joe Tufts, Dick Bredthauer, Virginia Bredthauer and Phillip MacQueen toast their workshop colleagues at the Murgo Winery.

CCD DEVELOPMENT PROGRESS AT LAWRENCE BERKELEY NATIONAL LABORATORY

William F. Kolbe, Steve E. Holland and Christopher J. Bebek
Lawrence Berkeley National Laboratory

Abstract: *P-channel CCD imagers, 200-300 μm thick, fully depleted, and back-illuminated are being developed for scientific applications including ground- and space-based astronomy and x-ray detection. These thick devices have extended IR response, good Point-Spread Function (PSF) and excellent radiation tolerance. Initially, these CCDs were made in-house at LBNL using 100 mm diameter wafers. Fabrication on high-resistivity 150 mm wafers is now proceeding according to a model in which the wafers are first processed at DALSA Semiconductor up to the Al contact mask step. They are then thinned and the remaining processing is done in small batches at LBNL. Alternative approaches are also discussed. In addition we have implemented designs that permit high-voltage biasing to further improve the PSF. With these designs, operation of 200 μm thick CCDs at 100 V or more bias with excellent PSF is practical.*

Key words: *Fully-depleted, back-illuminated, p-channel, IR response, high voltage, PSF.*

1. INTRODUCTION

We have developed fully depleted, back-illuminated CCD imagers fabricated on high-resistivity, n-type silicon for scientific applications (see Fig. 1, [1]). Since first described by Holland et al. [2], the virtues of such a CCD have been well established. The typical thickness of 200-300 μm results in good near-infrared Quantum Efficiency (QE) and greatly reduces fringing [3]. The Point Spread Function (PSF) is well defined and is determined by the transit time of photo-generated holes in an electric field that extends throughout the thickness of the device. Under full depletion conditions, the PSF is directly proportional to the thickness of the CCD and

inversely proportional to the square-root of the substrate bias used [1]. The PSF of a relatively thick, fully depleted CCD can be superior to that observed with a conventional thinned CCD if the latter has a significant field-free region at the backside of the device [4]. Since the CCD is p-channel, the radiation hardness due to bulk damage from protons in the space environment is improved significantly [5] when compared to conventional n-channel CCDs due to the lack of phosphorus-vacancy formation in the channels.
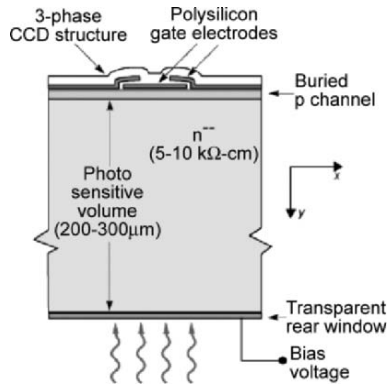
Figure 1. Schematic view of LBNL CCD showing the clock electrodes on the front surface and the bias voltage applied to the rear. These devices are operated fully depleted to achieve good PSF.

In this paper we describe efforts to fabricate fully depleted, back-illuminated CCDs on 150 mm diameter wafers. Three fabrication process flows that are under investigation to produce high performance CCDs are discussed. In addition, we report results to date on high-voltage compatible CCDs of particular interest to the proposed SuperNova/Acceleration Probe (SNAP) satellite [6].

2. CCD IMAGER DEVELOPMENT AT LBNL

2.1 Historical Development

In the early days of CCD development at LBNL, fabrication was done in-house in a Class 10 clean room using 100 mm diameter wafers. Figure 2 shows such a 100 mm wafer containing a 2K×4K, 15 μm pixel size CCD and other smaller devices. CCDs fabricated at this facility are currently in use at ground-based observatories.
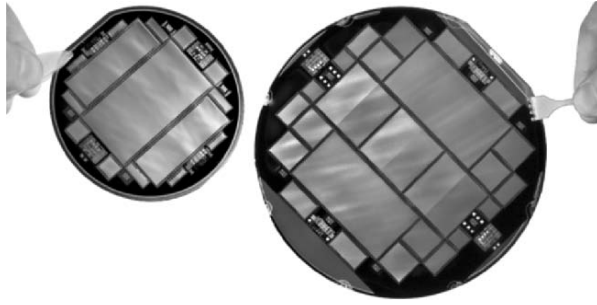
Figure 2. Photographs showing examples of CCD wafer layouts for *(left)* 100 mm wafer and *(right)* SNAP version-0 CCD on 150 mm wafer.

The processing steps critical to the fabrication of LBNL CCDs and the challenges in implementing them have been described in some detail in Holland, et al. [1] and Bebek, et al. [7]. In summary, they include completion at the full wafer thickness of all front-side processing up to the aluminum contact mask step. Then the wafers are ground and polished to final thickness of 200-300 μm. They are then back-side finished with an In-Situ Doped Polycrystalline silicon (ISDP) process at 650ºC making an extremely thin ohmic contact for biasing. The ISDP formation process temperature is too high for Al so the contacting and metallization is done afterwards.

2.2   Expansion and Outsourcing

With the advent of the proposed SNAP it became clear that the large number of devices required for this and other applications would require the services of an outside fabrication vendor. DALSA Semiconductor was selected. Since DALSA uses 150 mm wafers, new design formats were needed. Figure 2 shows a 150 mm wafer with three SNAP style version-0 CCDs and two 2K×4K, 15 μm CCDs. Two different pixel sizes 10.5 μm (2880^2) and 12 μm (2520^2) were chosen for the SNAP version-0 devices to accommodate early SNAP design requirements.

When the decision to outsource fabrication was made, the entire process was initially planned to be executed by DALSA. It was found, at an early stage, that significant process development would be required to work with the thinned 150 mm wafers. As a result, a business model was developed in which DALSA does front-side processing up to the contacting step. LBNL then finishes the processing using clean room equipment upgraded to 150 mm wafer capability using good quality used equipment. While a number of difficulties were encountered initially [7], recent results are very promising. A significant advantage of the business model is that the

processing necessary for back illumination is done at the wafer level, which results in a technology that is amenable to volume manufacturing.

In addition to the business model described above, two other approaches have been followed. These include the use of a refractory metal alloy (a Ti/TiN stack) instead of the standard aluminum interconnects. This material can withstand the ISDP process at 650ºC so the front-side can be fully completed at DALSA before thinning and back-side finishing. Although the TiN has higher resistivity than Al, good results have been obtained [7].

As a second alternative process we are collaborating with researchers at the Jet Propulsion Laboratory (JPL) to apply delta doping to p-channel CCDs. Molecular beam epitaxy is used to form the backside ohmic contact layer. This is a low-temperature process that grows a thin layer of Sb-doped silicon at temperatures not exceeding 450ºC, thereby permitting Al interconnects to be fabricated before thinning. This process is still under development [7] but continues to look promising, especially for UV-enhanced detectors.

2.3   Development of High Voltage CCDs

As the SNAP proposal evolved, further refinements in science requirements led to the specification of a pixel size of 10.5 µm together with a PSF of 4 µm rms. In addition, larger pixel counts were required. PSF measurements on the version-0 devices showed that this requirement could not be met without going to higher substrate voltages than version-0 was designed to accommodate. The version-0 devices were normally 250 µm thick and could safely withstand about 50 V of bias while PSF measurements and modeling predicted a need for 200 µm devices biased to 80 V. Figure 3 shows measured PSF data for 200 and 280 µm CCDs as a function of substrate voltage (Karcher, et al, [8] with additional measurements by J. Fairfield).

An analysis of breakdown conditions in the version-0 devices led to a number of design enhancements resulting in the version-1 CCDs. The wafer, shown in Fig. 4a, contains four version-1 devices, all with 3512×3512, 10.5 µm pixels and various design modifications together with other smaller test CCDs. More than 36 of the SNAP devices were fabricated (some un-thinned, some with the business model processing and some with TiN contacting), mounted and tested to determine performance. Most of the thinned CCDs with the high-voltage enhancements withstood voltages well in excess of 80 V. Some of the un-thinned devices withstood over 200 V of bias without any noticeable breakdown or "glow". There were some problems observed in some of the CCDs in which the signal baseline values

were unstable and tended to drift under certain bias voltage and exposure conditions.

A detailed analysis of the results was made and new simulation models were introduced to explain the observed behavior. Armed with these improved models, the current SNAP version-2 CCDs were designed. These were fabricated on the wafer shown in Fig. 4b, containing four devices of the same pixel count and size as the version-1.
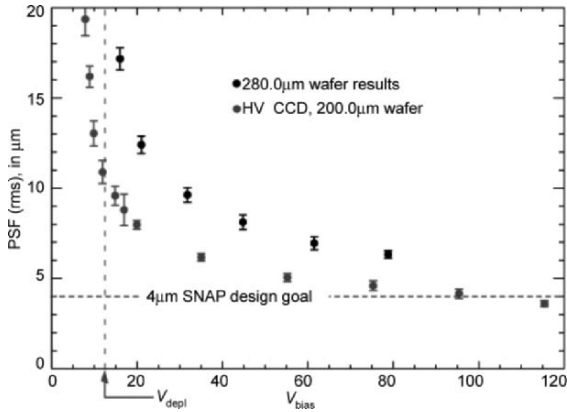
Figure 3. Graph showing measured PSF for a low-voltage CCD 280 μm thick and a high-voltage device 200 μm thick. The dashed line shows SNAP science requirement of 4 μm.
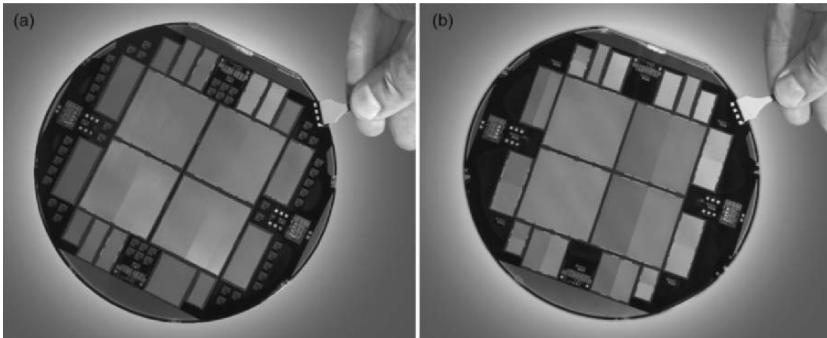
Figure 4. Wafer photographs showing *(a)* SNAP version-1 and *(b)* version-2 CCDs.

2.4   **Version-2 Device Test Results**

The version-2 design was submitted to DALSA in early 2005 and the first wafers were received in March. These were proof devices fully finished with Al metallization, ready to be tested un-thinned with front-illumination. All version-2 CCDs were wafer probed at -45ºC and tested for functionality prior to dicing. This was done at UC Lick with the help of Richard Stover and will soon be performed at LBNL when our own wafer prober commissioning is complete. Of 16 devices, about 80% were functional, and after mounting, most of those tested were found to perform well in our test dewar operated around 140 K.

An important goal of the version-2 design is to achieve reliable operation at the SNAP-required substrate voltage $V_{sub} = 80$ V. To test this, CCD performance was evaluated at voltages significantly higher than required. For example, Fig. 5 shows an 1800 second dark exposure of one of the un-thinned CCDs operated at $V_{sub} = 206$ V. At this voltage the CCD is fully depleted even though it is 650 μm thick. This can be seen by examining the cosmic ray tracks. Incomplete depletion leads to puffy track ends from diffusion in field-free regions. No evidence of "glow" or any other signs of breakdown were observed, and in fact, the dark current measured for this image was determined to be 0.63 e⁻/pixel/hour.
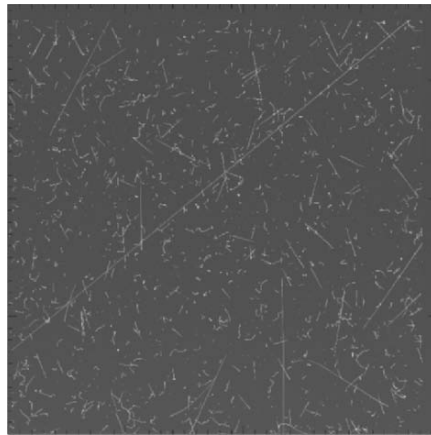
Figure 5. 1800 second dark exposure of a 650 μm thick front illuminated CCD operated fully depleted at $V_{sub} = 206$ V.

To measure gain and Charge Transfer Efficiency (CTE), x-rays from the radioactive source ^{55}Fe are used [9]. Figure 6a shows the x-ray histogram obtained from such a measurement of a different front-illuminated version-2 CCD operated at $V_{sub} = 107$ V. The well resolved K_α and K_β x-ray peaks

indicate good performance. The read noise for this CCD was 3.6 e⁻ rms (at 70k pixels/sec). In Fig. 6b is shown the parallel stacking plot for the same measurement. This and the corresponding serial plot yielded a serial CTE = 0.999 999 75 $\pm 1.4 \times 10^{-7}$ and a parallel CTE = 0.999 999 88 $\pm 1.2 \times 10^{-7}$.
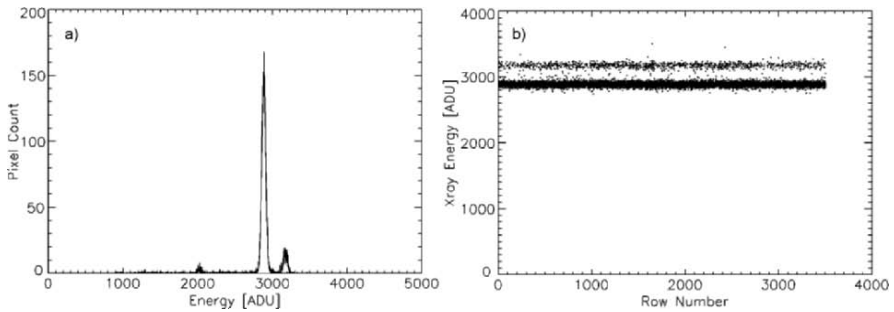
Figure 6. (a) ^{55}Fe x-ray histogram and *(b)* parallel stacking plot for front-illuminated SNAP version-2 CCD operated at V_{sub} = 107 V.

In addition to the full wafer thickness front-illuminated CCDs, a number of thinned and finished devices have been produced according to the business model and screened with wafer cold-probing (over 40, 200 μm thick CCDs to date). At the time of writing, only a couple of the SNAP version-2 CCDs have been tested. The promising results so far are illustrated in the projected test image shown in Fig. 7.
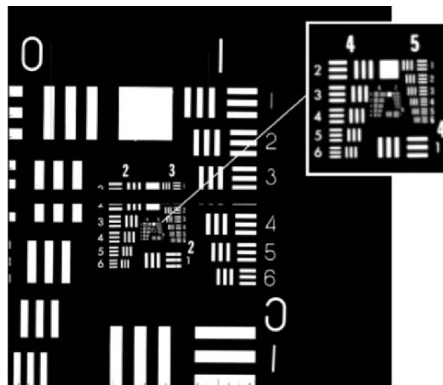
Figure 7. Image of USAF resolution test pattern projected on 200 μm thick finished CCD operated at V_{sub} = 206 V and read out via two amplifiers. Horizontal dark band along the center line is overscan. The inset shows a magnified view of central portion of image.

3.   ACKNOWLEDGEMENTS

4.   REFERENCES

[1]   Holland, S.E., et al., 2003, *Fully depleted, back-illuminated charge-coupled devices fabricated on high-resistivity silicon*, IEEE Trans. Elec. Dev., **50**, p. 225-238.

[2]   Holland, S.E., et al., 1996, *A 200×200 CCD image sensor fabricated on high-resistivity silicon, in IEDM-1996 Technical Digest*, pp. 911-914.

[3]   Groom, D.E., et al., 1999, Quantum efficiency of a back-illuminated CCD imager: an optical approach, Proc. SPIE, **3649**:80-90.

[4]   Bebek, C.J. et al., 2003, *Fully depleted back-illuminated p-channel CCD development,* Proc. SPIE **5167**, pp. 50-62.

[5]   Bebek, C.J. et al., 2002, *Proton radiation damage in p-channel CCDs fabricated on high-resistivity silicon,* IEEE Trans. on Nucl. Sci., **49**, pp. 1221-1225.

[6]   http://snap.lbl.gov

[7]   Bebek, C.J., et al., 2004, *Development of fully depleted back-illuminated charge coupled devices*, Proc. SPIE **5499**, pp. 140-150.

[8]   Karcher, A. et al., 2004, *Measurement of lateral charge diffusion in thick, fully depleted, back-illuminated CCDs,* IEEE Trans. on Nucl. Sci., **51**, p. 2231.

[9]   Janesick, J., 2001, Scientific Charge Coupled Devices, SPIE, Bellingham, WA.

ORTHOGONAL TRANSFER ARRAY

John L. Tonry[1], Barry Burke[2], Peter M. Onaka[1], Gerard A. Luppino[1], Michael J. Cooper[2]

[1]*Institute for Astronomy, University of Hawaii,* [2]*Lincoln Laboratory, Massachusetts Institute of Technology*

Abstract: *The Orthogonal Transfer Array (OTA) is a monolithic array of small CCDs that are 4-side buttable and can be mosaicked to make the 40K×40K focal plane required by Pan-STARRS.   These devices have other interesting properties such as a 'Deep Depletion' structure which enables 75 µm thick devices to be fully depleted with modest charge diffusion, while offering 35 % QE at 1 µm. Pan-STARRS has evaluated OTAs from a test lot, and is now fabricating the first two production lots. We expect to deploy the first of four cameras in June 2006.*

Key words: *Pan-STARRS, OTA, gigapixel.*

1.   INTRODUCTION

The biggest technological challenge for Pan-STARRS is the detectors [1,2]. We require in excess of 1 billion pixels in each of four focal planes, and exposures of 30 seconds or less, putting an extreme burden on the readout electronics to achieve a reasonable duty cycle. For example, at the 1 cent per pixel cost of many scientific CCDs, it would cost a 50 million dollars to equip all four focal planes. We therefore are striving to produce these cameras which comprise 10× as many pixels as have ever been deployed before using CCD devices at 1/10 the cost per pixel and at 10× the readout speed. We believe the key to this is the concept of a monolithic array of CCDs.

2.   THE OTA

The Orthogonal Transfer Array (OTA) is a device which consists of an 8×8 array of 600×600 pixel CCDs. Each CCD (known as a "cell") is equipped with logic which isolates it or connects it to the output circuitry. It subtends about 5K×5K pixels worth of sky, with inter-cell and inter-device gaps which reduce the fill factor to about 90%. This is a small loss of etendue compared to, for example, a 70% duty cycle of integration versus read time or a 40% fraction of time devoted to wide field imaging. The pixels are 10 micron and subtend 0.26 arcsec, so an entire cell is about 2.6 arcmin wide on the sky. The basic concept is described at length in Tonry, et al. [3,4].

There are many advantages to the division of the device into cells. Logic permits electrical isolation of a cell which has a catastrophic short circuit. This should improve the yield of these devices to better than 50% with a corresponding reduction in cost. Each cell comprises 1.6% of the area so the loss of one or two cells is not a significant reduction in filling factor. Bright stars are a nuisance for all wide field imagers. We will designate cells containing bright stars as "guide cells" and rapidly read out subarrays around the bright star for guiding, thereby mitigating charge pollution that would take place. We can read out cells in parallel, enabling us to shorten the readout time. The division of the focal plane into 2.6 arcmin wide tiles also permits us to remove image motion on that scale using the "orthogonal transfer" feature. We have created a rubber focal plane which can differentially correct for atmospherically induced image motion.

We have built a test lot of OTAs, comprising 24 wafers and 96 devices, implementing a large variety of design splits and pixel sizes. We did not expect to use any of these devices in a production focal plane, but rather wanted to explore design and parameter space before embarking on production runs. Since we will eventually require about 300 OTAs, and we will not have our first telescope until 2006, we thought this was a wise investment.

We have finished processing one-third of the wafers from Lot 1 and packaged and tested about 16 OTAs. All of our design splits have yielded at approximately the 50% level. In particular we have had equal success with 10 and 12 micron pixels, and we have had no loss of yield from two layers of metal and running metal lines directly over pixels. The remaining wafers have been slightly modified from the experience of the first half, and are just now proceeding to thinning and backside treatment. One of the most exciting splits is the "Deeper Depletion" implant which permits a substrate bias of up to -40 V. This appears to be successful, and two wafers were therefore thinned to 75 microns instead of the normal 45 microns. These demonstrate an enhanced QE at 1 micron, and with a -40 V substrate bias, exhibit decent charge diffusion.

We need to closely pack devices on four sides, so we have developed a custom package that uses a ceramic part to bring bond pads along one edge to a pin-grid array on the bottom. The ceramic also carries decoupling capacitors and JFET source followers for each video output. The silicon is glued to a molybdenum piece which has three legs to provide a quasi-kinematic mount for aligning the focal plane to an accurate figure. The pin-grid array plugs into a flexprint which connects below to a rigidflex board that carries the signals from four OTAs out of the cryostat to a pair of controller boards.

3.   OTA TESTING

We have tested these development Lot 1 devices quite extensively. We have performed all the usual CCD tests on the OTAs, and with the exception of noise and glow (discussed below) they function well.

We have built a powerful test facility to support the production of these devices (see Fig. 1). We have two cryostats, each of which carries four OTAs in loose-packed arrangements in mounts which allow easy and safe handling. The test facility uses an LCD screen imaged via an enlarger lens to put an arbitrary scene onto the devices. In addition to static optical tests, we can write a dynamic scene onto the LCD screen and image it, which permits us to shake down guide star tracking software on the test bench. The LCD screen is mounted on a swivel and a different screen can be swung into place instead. We have used this one for precision pinholes or other source of light.
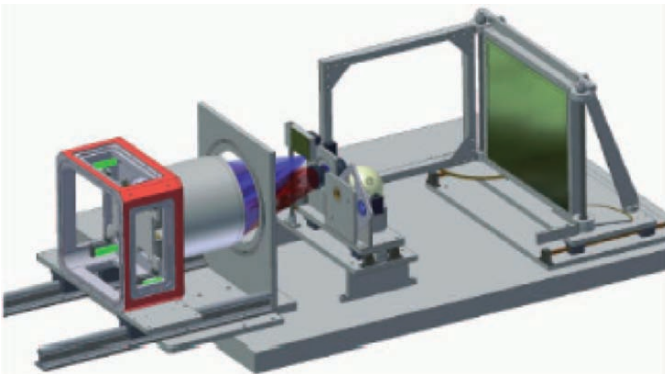
Figure 1. The OTA Test Bench is illustrated as a solid-body model for clarity. (The real image light source, monochromator, wires, fibers, and dark housing, electronics, etc., are more difficult to visualize.) The cryostat is in the device removal position; it is moved forward for operation.

The enlarger lens can be moved and an integrating sphere brought into place instead. This integrating sphere is fed by either a quartz halogen or mercury arc light source passed through a monochromator and a fiber bundle. In addition, there is a 1 mCi Fe55 source available to shine through a beryllium window onto the detectors when exposed by a shutter blade.

An important feature of this test facility is that it is completely automated. All motions are controlled by stepper or servo motors from a computer. LCD images, light sources, and monochromator settings are run by the computer. We measure light intensity using photodiodes at the focal plane read by a Keithley electrometer. We normally monitor 8 temperature diodes, and can regulate the temperature using a heater resistor. The Uniblitz shutter was built into a housing that has a Hall effect sensor so we can time the shutter duration to 0.1 msec accuracy.

We routinely run scripts to exhaustively search parameter space. No user intervention is required. Data are taken, analyzed, and summary tables produced automatically. The computer software which runs the test bench and the devices is configured as servers that accept simple text commands. It is therefore very easy to write scripts in any language to carry out almost any combination of device stimulation and device operation conceivable. Testing 300 OTAs required for Pan-STARRS is non-trivial, but we believe that we can easily cycle through a set of four devices in 24 hours: installation in the cryostat, evacuation, cooling, testing, analysis.

4.   NOVEL OTA FEATURES

Although OTAs have many interesting features, we concentrate this paper on a few quantitative results.

4.1   OTA Logic

Each cell of an OTA is equipped with logic and pass transistors which can be set to three states: active, standby, and floating. In active mode, a cell's parallel gates are connected to dynamic parallel clocking signals provided on bond pads, and the cell's video output can be connected to an output bus common to all cells in that column. In standby mode a cell's parallel gates are connected to static parallel clock levels appropriate to hold the charge quiescent in each pixel, and the cell's video output is isolated from the column bus. In floating or disconnect mode, the cell's parallel gates and video output are isolated from the external world. Once a cell's logic is set it stays in that state until reset.

We have examples of OTAs in which a cell or two have massive defects spewing so much charge that they badly degrade their immediate neighbors

and substantially degrade half of the device. A monolithic device with this problem could not be used in a focal plane. However, setting a bad cell to "disconnect" completely removes its noxious influence on its neighbors. It is unavailable for science, of course, but the remaining 98.4% of the OTA is uncontaminated.

We provide 8 row and 8 column select lines so any rectangular block of cells can have their state set simultaneously. To read out, therefore, all cells are set to standby, and then a row of cells are set to active. Application of the usual parallel and serial clocking signals brings the charge to the output amplifier and 8 channels worth of video appear. The output MOSFETs have a second stage follower on the cell prior to the pass transistor, and the column bus output is further buffered by the discrete JFET mounted on the package.

If a cell were designated for rapid readout of a subarray around a guide star, it would be the sole cell set to active and its readout would not affect any other cells. Distinct orthogonal transfer shifts can be applied to each cell by sequentially setting them to active, applying parallel clocks, and then returning them to standby. It should not take more than 10 μsec for the logic to change state so we can ripple through the 64 cells quite rapidly.

It is an obvious concern that we might encounter cross talk problems between different columns in an OTA. The columns share signals such as reset drain, although each video column has its own drain supply, current source voltage, and return. We do see crosstalk between columns, sometimes positive and sometimes negative, at the 10^{-4} level. This is negligible in comparison, for example, with the cross-talk between the two channels of an SDSU video board which appears at 3×10^{-4}.

4.2   Orthogonal Transfer

Orthogonal transfer pixels are symmetric under 90 degree rotations, and use gates to define both pixel dimensions rather than a channel stop implant. This permits parallel clocking to occur horizontally as well as vertically, which provides a fast, noiseless way to shift the charge of a developing image to follow the motion of the optical light producing it. This is much more effective than telescope guiding because it is much faster and accurate, and can be done differentially over a focal plane if the focal plane is divided into individually addressable cells. These pixels are discussed at length by Tonry, et al. [5,6] and Burke, et al. [7].

The choice of 2.6 arcmin for the OTA cell was driven partly by the desire for a large fill factor and rapid readout, but also by the fact that the isokinetic angle over which atmospheric image motion is coherent is generally somewhat larger than that on Mauna Kea.

Detailed experiments with CCID28 orthogonal transfer devices reveal that photometry is not impaired at all compared to 3-phase pixels, and astrometry is actually somewhat better, because astrometric residuals with standard 3-phase CCDs appear to be worse in the direction across the channel stops. Other advantages are that OT pixels do not bloom up a column when they receive too much charge, rather the charge puddles in a circular blot.

One might worry about parallel CTE effects causing a blurring which offsets the advantage of OT shifting to remove image motion, but quantitatively it is not a problem. At a 10 Hz rate of shifting (fast enough to remove virtually all telescope shake and almost all of power spectrum of atmospheric image motion) over a 100 sec exposure, we are only performing about 10^3 shifts. A typical CTI of 10^{-5} means that we are therefore taking 1% of the charge of a given pixel and putting it into a skirt of adjacent pixels. This is completely negligible blurring compared to a PSF which is well sampled.

4.3   Charge Transfer Efficiency

An operational challenge in testing OTAs is that the cells are so small (600 pixels) that it is very hard to see any CTE degradation from a simple readout. Even Fe55 xray events will only lose about 0.5% of their charge from single pixel events at the top of a cell compared to the bottom. We therefore resort to using the OT property to exaggerate the effects of CTE so that we can properly quantify it.

The first step is to take a picture of a scene. In this case it is a picture of text on the LCD screen which the OTB images onto the detectors. The next step is to take an identical image, but then perform OT shifting before reading it out. In this case we shift it around a 32×32 pixel square 100 times, for a total of 12,800 pixel shifts.

Subtracting the two images is then a very sensitive test of how well the charge has been transferred. The difference image in Fig. 2 has been stretched by 20 to show the features better. A hot pixel shows the 32×32 shift box. Charge that is shifted off the edge of the CCD is simply lost to the scupper. Charge transfer inefficiency appears as slight shifts of the characters creating small positive-negative signatures. Analysis of this suggests that the typical CTI is about 2×10^{-5}. Another way to quantify this is to ask how much worse the noise in this shifted pair of (bright) images is compared to a difference of unshifted images, and we typically see a noise which is 1.2 or 1.3 times worse than Poisson. Since this is approximately ~50 times more shifts than we would expect to perform during a 30 sec exposure, we regard this CTE performance as very good.
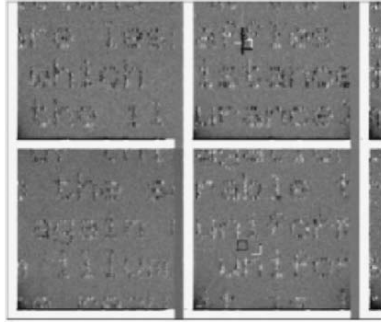
Figure 2. The difference between two LCD screen images shows very low level residuals. The pixelization evident is the result of the LCD screen pixels - each LCD screen pixel maps to about 13 CCD pixels.

4.4 OTA QE

The optical testbench focal plane uses Hamamatsu S1337 photodiodes to measure the absolute photon flux from monochromatic flatfields. These hermetic ceramic packages behave well under vacuum and at cold temperatures. We carefully calibrate them as a function of wavelength and temperature against the usual NIST-calibrated photodiodes. Figure 3 shows representative QE values for OTAs which are thinned to 45 micron (no substrate bias applied) and OTAs which are thinned to 75 micron (-20 V substrate bias applied to fully deplete the CCDs to reduce charge diffusion).
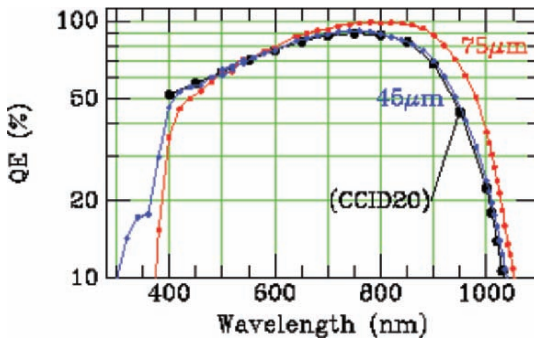
Figure 3. The quantum efficiency of 45 μm thick OTAs is the same as 45 μm thick CCID20s, tested by many people with many different setups. The QE of the 75 μm thick OTA is distinctly higher in the red, in accordance with its increased opacity to red photons.

The QE we measure from 45 micron thick OTAs is virtually identical to that of CCID20 devices whose QE has been determined by us and others with completely different apparatus. However, the 75 micron thick OTA has a markedly improved red response beginning at about 750 nm. By wavelengths of 1 micron, the 75 micron device has a 50% higher QE than the 45 micron thick OTA, as expected from the greater absorption depth for IR photons.

4.5   Substrate Bias

Figure 4 shows how the various components of an OTA cell are isolated. The result is that it is possible to run parallel clocking voltages below the ground of the NMOS transistors making up the logic without current flow between them. We therefore get better parallel clocking and transfer from pixels into the serial register. By applying a negative potential to the substrate connection, we bring the surface boron implant to a negative potential with respect to the buried channel where the electrons collect. This enhanced electric field fully depletes the silicon and decreases the charge diffusion.
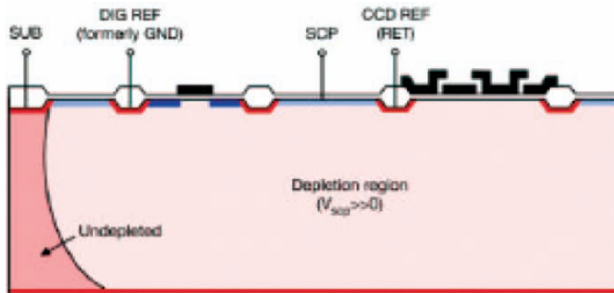
Figure 4.   There are three distinct reference potentials in the deep depletion OTA: the ground for the pixels and amplifier, the ground for the logic, and a substrate connection. Use of n-implants adjacent to the p-type implants for the channel stops create back-biased pn junctions which prevent current flow along the surface, and a high potential on the scupper connection depletes the bulk and prevents current there as well.

This feature permits us to trade off red QE against charge diffusion. The very red QE is essentially proportional to the thickness of the devices, whereas the charge diffusion is also roughly proportional to thickness and inversely proportional to the square root of substrate potential. Fe55 x-ray images immediately show that the substrate bias has a big effect. The number of single-pixel events increases dramatically as the substrate bias is increased.

We have found that x-rays are a very good quantitative measure of the extent of charge diffusion, and are much easier to provide than extremely small optical spots. We normally examine all x-ray events, decide which are K-alpha events, normalize them, and then assemble a distribution of pixel values found in the event. There are some very characteristic features visible in Fig. 5.
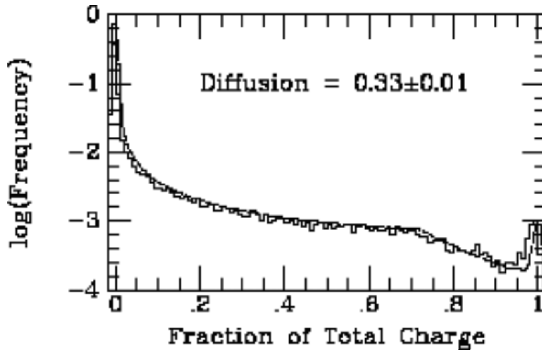
Figure 5. The histogram of pixel values around x-ray events can be matched in detail with a model which depends only on the surface charge diffusion length. The values are normalized to the full 1620 e⁻ of single pixel events.

Obviously there is a spike at 1, which is the single pixel events - all the charge found in a single pixel. The slope change at 0.7 corresponds to x-rays which convert at the surface of the device, in the center of a pixel. This discontinuity in the volume available for making events of a given fraction causes the discontinuity in slope. We find that we can fit the observed distribution accurately using a simple model which has an exponential absorption of x-rays, a constant electric field causing a diffusion size which scales as the square root of the height above the backside where photons are absorbed. The one free parameter of these models is the charge diffusion at the surface.

When we are confident that we understand the detailed distribution of x-ray pixel values, we can construct a simpler statistic which can be converted to physical charge diffusion length. The statistic, called "qdiff", is defined as the sum of the 8 adjacent pixels divided by the highest pixel of an x-ray event (and is therefore 0 for no diffusion at all and 8 for infinite diffusion.) We process x-ray images by identifying events, determine those which sum to K-alpha events (to avoid multiple x-ray photon events), stack the events by centering on the brightest pixel, and create the qdiff statistic. Application of the model above permits us to calculate a theoretical qdiff for arbitrary surface rms diffusion and we can thereby convert qdiff to surface rms in units of pixels and then microns.

As a function of substrate bias we find that the charge diffusion length scale gets smaller, as illustrated in Fig. 6. We obtain the same diffusion for different sized pixels, not surprisingly, and much greater diffusion at a given substrate bias for the 75 micron thick device compared to the 45 micron thick device. We regard a diffusion of 3.2 micron (rms) to be the limit of what we would like to have, since this corresponds to 0.2 arcsec FWHM degradation of images. We can achieve this amount of diffusion with the 45 micron devices and no substrate bias or application of a -40 V bias to the 75 micron devices. (Note the diverging diffusion for the 75 micron device as the substrate bias approaches 0; without a bias, this device is not fully depleted.)
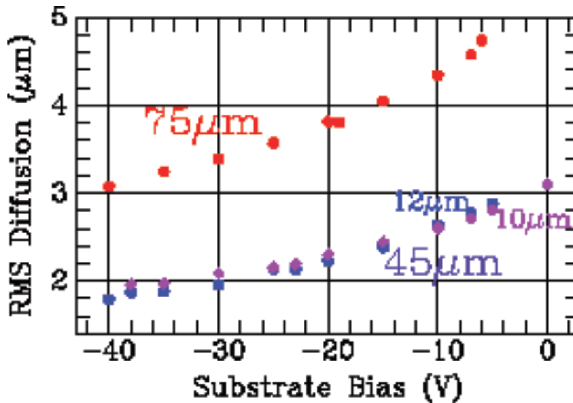
Figure 6. The charge diffusion can be measured from the x-ray histogram or qdiff statistic. We get identical results from devices with the same thickness but different pixel size. The diffusion depends on the thickness of the OTAs as well as the substrate bias voltage.

5.   LOT 1 SHORTCOMINGS

Although our development Lot 1 was extremely successful, it is not perfect. We find that the logic and the amplifier glow significantly, and we have an unpleasant tradeoff of glow versus not fully turning on the pass transistors. The glow is quite bright. The median across the images is about 10% of sky, and increases to greater than or equal to the sky in the corner of the cells. The amplifiers are quite noisy at ~20 e⁻, and their performance is completely dominated by 1/f noise. These devices are somewhat fussy about operating voltages of clock levels and scupper. Poor choices cause a variety of charge injection mechanisms we lump as "excess charge" (XSQ). The deep depletion design variant makes it much easier to mitigate the excess charge problems and allow for bigger parallel clock swings and so better parallel CTE.

However, we are quite confident that we understand all of the problems in the development lot. The noise originates from the use of surface channel MOSFETs in an attempt to lower the DC output level for the controller. It was a mistake, and we are now AC coupling the controller. The glow can be removed by lightly doping the drains of the logic inverters and pass transistors. We have two design improvements in Lot 2 which we can select by different metal masks, and the remaining wafers of Lot 1 have an effective LDD modification which we will soon be able to test.

The excess charge is primarily mitigated using the deep depletion and substrate bias. When the glow problem is solved it will also help the XSQ because we were deliberately choosing suboptimal voltages from the standpoint of XSQ to suppress the glow. Parallel CTE will be improved by better RC time constants, which can be improved by widening metal lines and poly gates. Since there is a vast area available by running metal over pixels this should no longer apply. We are also striving to reduce the pass transistor resistance. The two development lots comprise 192 devices, and if the yield from Lot 1 continues to hold, we should see ~100 OTAs by mid-2006.

6. CONCLUSION

The Pan-STARRS camera effort involves a large number of very talented and hard working people. There are more than ten people employed at the IfA on the camera project, and many people at MIT Lincoln Laboratory involved in detectors as well. We also have an ongoing and very fruitful collaboration with WIYN observatory who are building a pin-for-pin compatible OTA device through Bredthauer-Dalsa-Lesser. They are also building a "One Degree Imager" for WIYN which is virtually identical to the Pan-STARRS gigapixel cameras. The Scientific Detector Workshop was kind enough to award us the "Dream On" award in 2002 when we presented these ideas. At the time we were hoping for funding from an NSF proposal in collaboration with WIYN and MITLL, which was not realized. A year later, however, the AFRL funding for Pan-STARRS was realized and we embarked on this project. It is essential to recognize that Pan-STARRS is a science project and the timeliness of the science enabled by Moore's law is what makes this worth doing. We all believe that CMOS imagers and ASICs will foster wonderful detectors in the future, but Pan-STARRS must to walk a fine line between audacity and conservatism. We believe that we will achieve our three "orders of magnitude" improvement in wide field imaging and that we will do so on a timescale which will make Pan-STARRS unique for many years.

7. ACKNOWLEDGEMENTS

8. REFERENCES

[1] Kaiser, N., 2004, *Pan-STARRS: a wide-field optical survey telescope array*, Proceedings of the SPIE, Vol. **5489**, pp.11-22.

[2] Onaka, P.M., et al., *IOTA: the array controller for a gigapixel OTCCD camera for Pan-STARRS,* Proceedings of the SPIE, Vol. **5499**, p. 4990.

[3] Tonry, J.L., et al., 2002, *Giga-pixels and Sky Surveys*, Scientific Detectors for Astronomy, ASSL Vol. **300**, p. 395.

[4] Tonry, J.L., et al., 2002, *Rubber Focal Plane for Sky Surveys*, Proceedings of the SPIE, Vol. **4836**, p. 206.

[5] Tonry, J.L., et al., 1997, *The Orthogonal Transfer CCD*, PASP, Vol. **109**, p. 1154.

[6] Tonry, J.L., et al., 2002, *The Orthogonal Parallel Transfer Imaging Camera*, Scientific Detectors for Astronomy, ASSL Vol. **300**, p. 385.

[7] Burke, B.E., et al., 2004, *The orthogonal-transfer array: a new CCD architecture for astronomy*, Proceedings of the SPIE, Vol. **5499**, p. 185.

David Carter, Geoffrey Evans, Gregory Prigozhin, Ilya Prigozhin, Rob Philbrick, Ralph Holtom, David Morris and Reinhold Dorn queue up for the free 349 Megapixel detectors given away by Cyclops Imager Technologies, Inc.

A PNCCD DETECTOR SYSTEM FOR HIGH SPEED OPTICAL APPLICATIONS

Robert Hartmann[1], Hubert Gorke[2], Norbert Meidinger[3], Heike Soltau[1] and Lothar Strüder[3]

[1]PNsensor GmbH, [2]Forschungszentrum Jülich, Abteilung ZEL, [3]Max-Planck-Institut für extraterrestrische Physik

Abstract: *A novel type of backside illuminated pnCCDs has been fabricated and successfully tested. The devices with a pixel size of 51 μm and an imaging area of 264×264 pixel, corresponding to a sensitive area of 13.5×13.5 mm^2, feature a framestore region for both sides of the detector. By splitting the image into two framestore areas during readout, repetition rates of more than 1000 frames per second were achieved. The electronic noise contribution of the entire detector system is slightly higher than two electrons at an operating temperature of -55ºC. Along with fast detector readout, we will present a concept of data acquisition system able to handle pixel rates of more than 70 megapixel per second. Decentral data reduction and analysis units allow for real-time data processing. For example, it allows determination of the centroid of a great number of sub-images in a Shack-Hartmann wavefront sensor with a very low latency time. Due to the large sensitive volume of the detector and the development of an ultra-thin backside contact, near theoretical quantum efficiencies are achieved from the ultraviolet to the near-infrared. Detectors with optimized response in the visible and near-infrared regions were fabricated by implementing different types of anti-reflective coatings. The combination of very high speed, exceptionally low noise and high quantum efficiency makes these CCDs wavefront sensors in adaptive optics systems.*

Key words: *pnCCD, frame store, data reduction, astronomy, adaptive optics.*

1.   INTRODUCTION

Adaptive Optics (AO) has found widespread use in astronomical settings to compensate for atmospheric turbulences and telescopic aberrations. New generation AO systems will require wavefront sensors comprising large pixel arrays (256×256 up to 1024×1024 pixels). Future large telescopes will have deformable mirrors with several thousand actuators, requiring frame rates greater than a thousand frames per second to correct atmospheric turbulences, very low readout noise and high quantum efficiency in the optical and near-infrared regions [1]. Associated with the detector requirements are high demands of readout systems to process huge amounts of data within the allowed time.

In this paper, we will describe the concept and performance of a detector system, which fits the needs of a wavefront sensor for future AO systems. We will describe detector principles and optical properties. Afterwards we present the concept of our detector controller and data acquisition system, which is able to handle pixel rates of more than 70 megapixels per second. Finally, we describe results and performance data of the entire detector system.

2.   PNCCD AS AN OPTICAL DETECTOR

2.1   Detector Principles and Format

Differing from other CCD concepts, both sides of the pnCCD are depleted, thus forming a potential minimum for electrons within the detector substrate. Figure 1 shows a schematic cross-section of a pnCCD along a transfer channel. By increasing the voltage of the rear contact, the potential minimum is shifted close to the registers on the frontside of the device, forming well defined potential wells for collecting signal electrons in a depth of approximately 7 μm. Since there are no insensitive gaps between the registers, the device exhibits a fill factor of 100%. The unstructured and homogeneously implanted rear contact of the device acts as the radiation entrance window. The advantages of this concept of full wafer depletion are:
- sensitivity of the detector for ionizing radiation over its entire volume of 450 μm
- a very thin, uniform radiation entrance window with a high detection efficiency for short penetrating radiation, which provides a possibility for further coating of either light absorbing layers for X-ray applications or

appropriate Anti-Reflecting (AR) layers for applications in the Visible (VIS) and Near-Infrared (NIR) spectral regions

- an electric field distribution through the detector volume, which reaches its maximum value close to the radiation entrance window and thus reduces the spatial widening of charge clouds generated close to the detector entrance window.
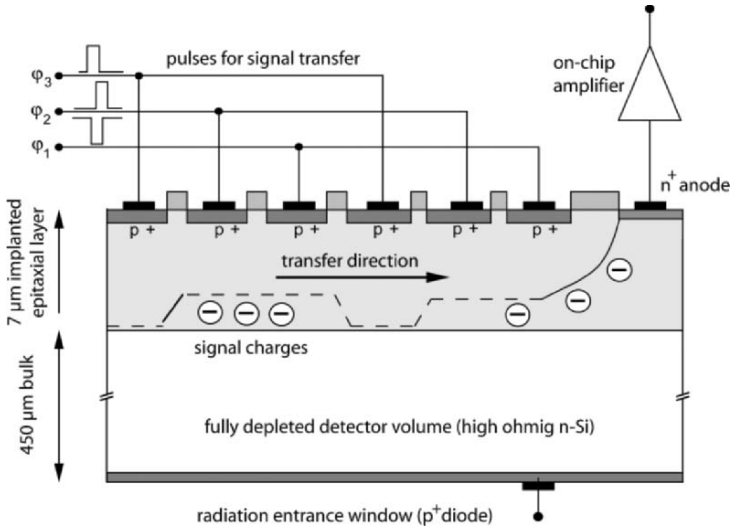
Figure 1. A schematic cross section of the fully depleted pnCCD along one transfer channel. The radiation entrance window and the transfer registers on opposite wafer sides are realized by p+ implantations in n-type silicon. After a signal charge packet is transferred to the readout anode, it is amplified by an on-chip JFET, which in turn is connected by wire bonds to an amplifying and shaping chip for further amplification.

Applying clocked periodic voltages to the registers transfers stored signal charges to the readout anode at the end of the transfer channel. Each anode is equipped with an integrated JFET transistor for on-chip amplification. JFETs inherently exhibit a very low 1/f noise and can be operated with low current for low noise applications [2]. The sources of each JFET are wire bonded to a multi-channel VLSI-chip for further amplification and signal filtering. A description of this readout chip is given in Sec. 2.3.

To allow high speed operations while maintaining imaging capabilities, the CCD is designed for operation in split-frame-transfer mode. Figure 2 shows the layout of the detector and the readout chips. The imaging area of 13.5×13.5 mm^2, comprising 264×264 pixels with a geometry of 51 µm², is divided in half for readout. Each half image is transferred to its storage section on opposite sides of the detector, which are shielded for incident

radiation. During the readout of both storage areas simultaneously, the entire imaging area is sensitive for incident photons. This way, the time resolution of the CCD is given by the time needed to readout and amplify the storage area, comprising half the pixels of the full imaging area. For a readout time of 7 μs per line, a frame repetition rate of nearly 1100 Hz was achieved with an electronic noise floor of less than 2.3 electrons ENC at an operating temperature of -55°C.
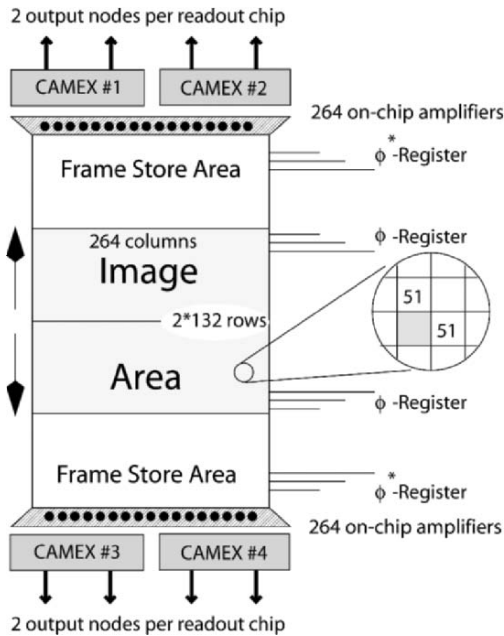
Figure 2. Schematic layout of a split frame-transfer pnCCD with an imaging area of 13.5×13.5 mm², containing 264×264 pixels with a size of 51 μm². Having up to four serial readout nodes on each side, thus totaling in eight readout nodes, a frame repetition rate of nearly 1100 Hz was achieved with an overall electronic noise contribution of slightly more than two electrons ENC at an operating temperature of -55°C.

    The probability of out-of-time events, which may lead to a smearing of the obtained image, is given by the ratio of the total transfer time of the image into the storage area relative to the total readout time of the storage areas. At 1100 frames per second, the entire readout time is approximately 900 μs whereas the transfer time for a half image into its storage area is in the order of 25 μs, resulting in an out-of-time probability of less than 3%. Due to a charge transfer efficiency of better than 0.99999 (i.e. a charge transfer inefficiency of less than 10^{-5}), the total loss of signal charge is less than 0.15% for rows most distant from the readout anode.

2.2 Optical Properties

The detection efficiency of back-illuminated CCDs for short penetrating radiation in the UV and soft X-ray region is mainly determined by the electric field properties close to the detector entrance window and the reflectivity of the detector surface. The radiation entrance window of pnCCDs is formed by a homogeneous, ultra-shallow p^+ implantation (see Fig. 1). The pn-junction is located at a depth of approximately 40 nm, which is also the location of the highest electrical field [3]. The internal quantum efficiency of a detector in the optical region describes the probability of the detection of generated signal charges, once an incident photon has passed the covering layers of the detector. Figure 3 shows the internal quantum efficiency from the vacuum UV to the near IR region. While the absorption length of silicon changes by more than four decades to values below 5 nm, the internal quantum efficiency remains at nearly one within the entire spectral region between 300 nm and 950 nm [4]. Below 300 nm the quantum efficiency increases due to the onset of secondary ionization processes by the primary generated photoelectron [5]. In the near IR region, a decrease is observed as expected when radiation transverses the 300 μm thick detector material.
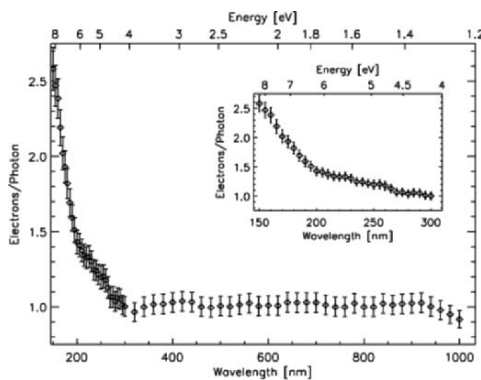
Figure 3. Internal quantum efficiency in the wavelength range from 150 nm to 1000 nm at room temperature. Below 300 nm a quantum yield is achieved. The large sensitive thickness of 300 μm allows for a high efficiency in the near IR region.

Based on detector internal quantum efficiency, one can calculate the expected external quantum efficiencies for various anti-reflecting coatings and tailor for the desired application. With an antireflection coating of SiO_2 and Si_3N_4 layers, an overall high optical respectively enhanced "red" and near IR responsivity can be achieved as shown in Fig. 4. In the first case, the efficiency remains greater than 80% within the entire optical region with

a maximum at the position of the sodium line at 580 nm. In the other case, the quantum efficiency remains higher than 90% from 750 nm up to 1000 nm. The calculations were confirmed by measurements, as indicated by the diamonds in Fig. 4. The entrance window of this detector was optimized for a CsI(Tl) scintillator readout at 548 nm. The calculations and measurements shown were made for room temperature, so figures at longer wavelengths will fall slightly due to energy band broadening of silicon at lower temperatures.
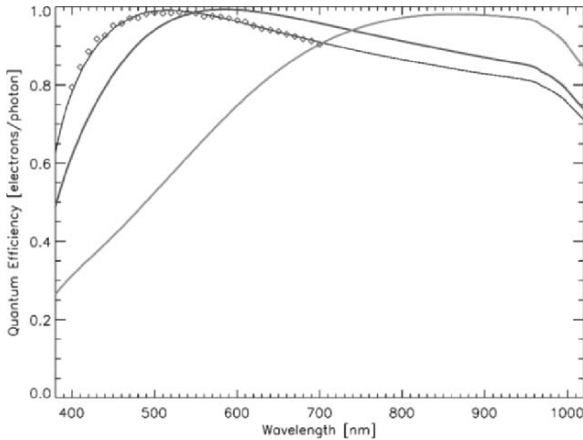
Figure 4.   Measured (diamonds) and calculated quantum efficiencies for a pnCCD with different kinds of AR coatings. The diamonds represent measurements of a detector, whose sensitivity was optimized for a CsI(Tl) scintillator readout at 548 nm. The calculation, based on the knowledge of internal quantum efficiency and the exact layer stack, represent the measurements very well. The other curves show calculations for entrance windows optimized for the 580 nm sodium line respectively to exhibit a very high QE in the NIR region.

2.3   Detector Readout

The pnCCD, as described in this paper, is a channel-parallel type of CCD [6], meaning all channels are read out in parallel thus omitting any serial transfer registers. For the readout of the CCD channels, a multi-channel readout ASIC is used. This CAMEX (CMOS Amplifier and MultiplEX) chip allows amplification and shaping of all of its 132 channels in parallel. For reading out the 2×264 channels of the CCD, two of these CAMEX chips are adjacently placed on each side of the detector and operated in parallel (see Fig. 2). Accompanying each of the 132 internal amplifiers of the CAMEX chips is a current source to operate the CCD on-chip FET of each channel in a source follower mode. The current source and the most sensitive first

amplification stage are realized with JFET technology; while all other sections of the CAMEX chip are build in standard CMOS technology. This means that the electronic noise contribution of the CAMEX chip is less than one electron.

Signal filtering is performed by Multi-Correlated Double Sampling (MCDS). By freely programmable internal registers, any value between 1-fold and 8-fold correlated sampling is selectable, allowing a tradeoff for either optimized noise behavior or high-speed performance. Different gain selections also allow for an optimum match of the dynamic range.

The pipelined signal processing path of the CAMEX chip enables an output multiplexing of amplified signals to the output nodes and, at the same time, the amplification and filtering of the following line of the CCD. Additionally, the CAMEX allows for operation by either multiplexing all 132 channels to one single readout node, or by multiplexing half of its channels (in our case 66 channels) onto two readout nodes in parallel to overcome speed limitations of subsequent analog electronic components. This highly parallelized signal processing allows for very short readout times.

3. CCD CONTROLLER AND DATA ACQUISITION SYSTEM

The CCD controller, containing the sequencer, ADC boards and DC-power supply units, is arranged in one double-height crate with an optical link to the data-acquisition computer. The internal bus system is the widely used compact-PCI (cPCI) bus. An optical interface allows for fast, bi-directional data transfer up to 200 meters and an electrically isolated connection. The DC-power supplies are fully controlled and parameters are determined by their control unit via software. The sequencer device is freely programmable with a time resolution of 10 ns, comprising of 64 LVDS-output lines. The program code is generated by dedicated software on a LINUX workstation and can be uploaded at any time to the processor, realized in a FPGA. The sequencer unit generates all digital control signals for the detector system such as the transfer pulses for the CCD, the timing for the CAMEX chip and the readout clock for the ADCs.

One ADC device holds two 105 MHz 14-bit flash ADCs, controlled and read out by the cPCI-bus. The entire system is scalable and can handle up to four ADC devices in the present stage. As shown in Fig. 2, the CCD readout requires up to eight ADCs. For the mentioned readout speeds of the detector of 1100 frames/second for an array of 264×264 pixel, the four ADC devices generate up to 140 MB of data per second. This constant data flow overloads

the connected PCI-bus. An option for data reduction is obtained through a fast FPGA within each ADC unit. Figure 5 shows the configuration of a DAQ-system able to operate a fast CCD detector system with eight analog output nodes.
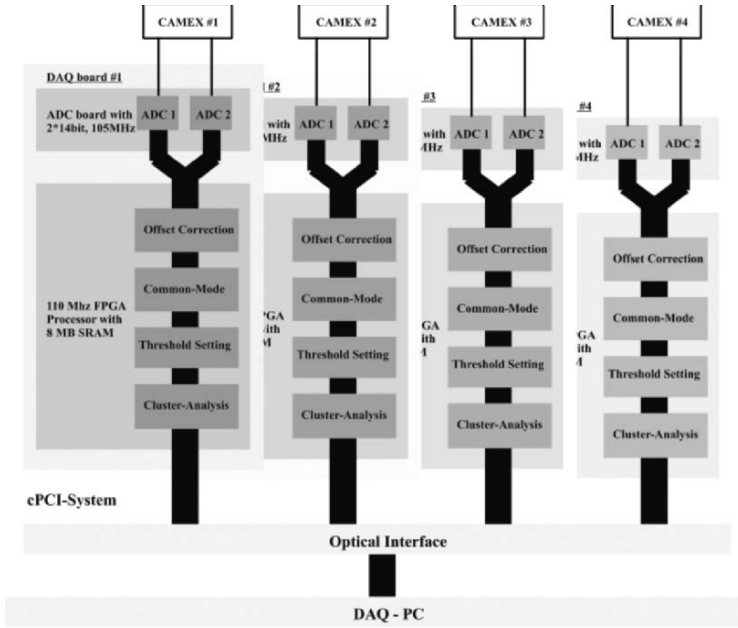
Figure 5. Configuration of a cPCI based DAQ-system for a fast CCD readout, comprising up to eight readout nodes. The configuration allows the operation of a 264×264 CCD at 1100 frames/sec, generating a constant data flow of 140 MB/sec.

To apply a threshold setting in the detector data, the data must be corrected for offset, gain and common-mode variations. As long as the data flow does not exceed the PCI-bus speed, data reduction could be done online by software. But for a high-speed detector setup, hardware data reduction is needed. The offset-, gain-, common-mode-corrections and the data reduction by threshold settings for both ADCs per ADC unit is done with a fast FPGA processor, equipped with a large, high-speed computer memory. The performance of the FPGA data processor also allows advanced computations of the data, e.g. cluster analysis. In the case of the CCD system in a Shack-Hartmann wavefront sensor, a centroid determination, including the determination of intensity and sigma of the distribution, of all dedicated sub-images will be performed with very short latency times. The software realization of this feature is under development.

4. MEASUREMENT RESULTS

Herein we will summarize some key results of performance measurements of a high-speed CCD detector system. All reported measurements were performed at an operating temperature of -55ºC and the CCD was CCD was operated in a framestore mode.

In standard operating mode, wherein the time for shaping and amplification of a pixel line is 15 μs, a readout noise of 1.8e⁻ ENC was achieved. The noise distribution is homogeneous over the entire CCD. For detector geometry, a pixel readout time of 15 μs corresponds to a frame rate of 500 frames/sec. In optimized high-speed timing mode, a frame rate of nearly 1100 frames/sec. was achieved at an electronic noise contribution of 2.3e⁻ ENC. The increase in electronic noise contribution was principally due to a necessary increase in bandwidth of the first charge sensitive amplifier of the CAMEX readout chip. It is shown that the same noise figures were obtained using slower readout timing but increasing the internal bandwidth in similar ways. Without going into the details of noise filtering, the obtained results indicated that further optimization of the noise performance is possible.

The spectroscopic performance was investigated by using soft X-ray lines. In particular, we studied the performance at the carbon K-line at 278eV (corresponding to a charge generation of 76 signal electrons per incident photon). A measured spectrum is shown in Fig. 6. The energy resolution regarding single events only comes up to 45 eV (FWHM) and increases slightly to 48 eV for all reconstructed events.

Considering the low and uniform noise performance of all pixels of the device, one may extrapolate from the obtained carbon spectrum, containing 76 electrons, that the detection limit in the optical region is in the order of eight photons.

5. CONCLUSION AND OUTLOOK

We have presented the setup and performance measurements of a CCD detector system, running at a speed of almost 1100 frames/sec with an electronic noise contribution of 2.3 electrons ENC. The operating temperature was -55ºC, so thermoelectric cooling could also be implanted. The uniform and temporal stable noise behavior allows for reliable threshold setting. The combination of exceptionally high quantum efficiency and low readout noise with high speed operating modes makes this detector superior to many other concepts used in wavefront sensors.

Parallel to the detector, we setup the entire DAQ-system to operate the detector system at frame rates of 1000 Hz and faster. Due to the described decentral data handling and data reduction, the system is able to handle pixel rates of more than 70 megapixel per second.
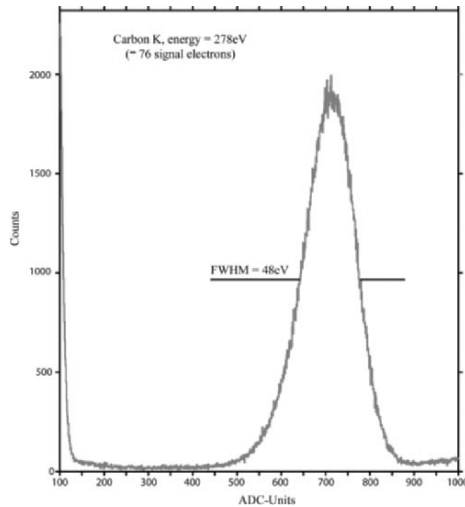
Figure 6.   Spectroscopic measurement of carbon K-line with an energy of 277 eV, corresponding to a generation of 76 signal electrons per photon. This is a spectrum of all reconstructed events. In case of regarding merely single events, the FWHM reduces to 45 eV from 48 eV. The operating temperature was -55ºC.

6.   ACKNOWLEDGEMENTS

7.   REFERENCES

[1] Hubin, N., 2004, Proc. SPIE 5490, p. 195.

[2] Bräuninger, H., Danner, R., Hauff, D., Lechner, P., Lutz, G., Meidinger, N., et al., 1993, Nucl. Instr. and Meth. A326, p. 129.

[3] Hartmann, R., Hauff, D., Lechner, P., Richter, R., Strüder, L., Kemmer, J., et al., 1996, Nucl. Instr. and Meth. A377, p. 191.

[4] Hartmann, R., Stephan, K.-H., and Strüder, L., 2000, Nucl. Instr. and Meth. A439, p. 216.

[5] Kolodinski, S., Queisser, H. J., Werner, J. H., and Wittchen, T., 1993, Appl. Phys. Lett. 63, p. 2405.

[6] Strüder, L., Briel, U., Dennerl, K., Hartmann, R., Kendziorra, E., Meidinger, N., et al., 2001, Astron. Astrophys. 365, p. 18.

L3 CCD WAVEFRONT SENSOR DEVELOPMENTS AT THE ING

Simon Tulloch

Isaac Newton Group of Telescopes (ING)

Abstract: *The current natural guide star (NGS) wavefront sensor at the ING is based around a conventional CCD39. The read noise of this detector limits the overall AO performance of the system. Simulations have shown that L3 technology could offer a 1-2 magnitude guide star limit improvement. We have constructed a new WFS head around an L3 CCD60 detector and integrated it into the NAOMI AO instrument on the William Herschel telescope. The head will eventually find application in the upcoming Rayleigh laser AO system (GLAS) where it will be used as a natural guide star tip-tilt sensor.*

Key words: *L3CCD, WFS, ING, NAOMI, GLAS, Rayleigh Laser Adaptive Optics.*

1.   INTRODUCTION TO L3 TECHNOLOGY

Conventional CCDs are limited by the intrinsic read noise of their output FET transistors in many applications. Reducing the noise bandwidth by slowing the readout is generally the only option if the system is read-noise limited. The engineer is then forced to make a compromise between speed and noise. L3 technology allows these two factors to be decoupled: making megahertz pixel rates possible with sub-electron read noise. This is achieved by the addition of a multi-stage avalanche gain register between the serial register and output transistor. Photo-electrons traversing this register during serial transfer emerge into the output node as a substantial charge packet that induces a voltage signal far in excess of the amplifier noise. The actual gain level can be tuned from unity up to $>10^3$ by varying the amplitude of the multiplication clock phase in the gain register. Clock amplitudes are typically 40-45V, larger than those available in most controllers, although still easily generated using custom clock generator boards based around

readily available DC:DC converters. e2v technologies [1] have, thus far, applied L3 architecture (see Fig. 1) to a number of small CCDs, although in principle it can be added to any chip design format.

The multiplication register can be thought of as the solid state analogue of a photomultiplier tube with a very low dynode gain of around 1%. For this reason the gain register contains 520 stages. This low probability of multiplication has the unfortunate side effect of introducing an additional statistical noise source that degrades the SNR by a factor of $\sqrt{2}$. The effect at lower signal levels is more than compensated for by a lack of read noise. Overall, the multiplication noise has the same mathematical effect as halving detector quantum efficiency (QE). L3 technology is valuable in certain read-noise limited, low flux niches, namely wavefront sensing and rapid spectroscopy. It is not a panacea, and in higher-flux applications a conventional CCD may still be the best choice.
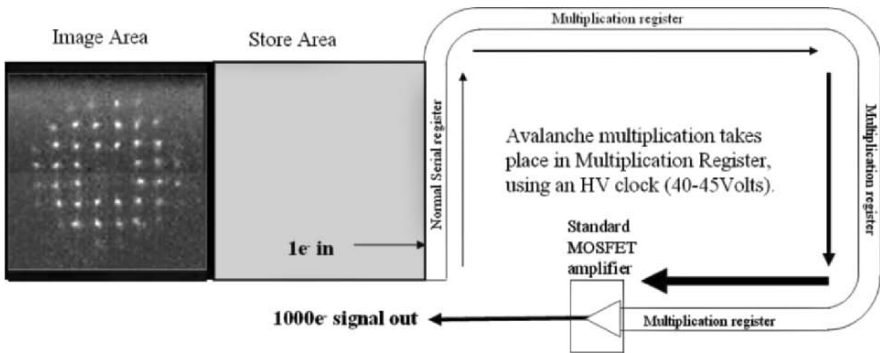
Figure 1. L3 CCD schematic.

All CCDs exhibit clock induced or 'spurious' charge (CIC); fast clock edges generate high electric fields that produce stray electrons within the silicon. If generated by the parallel clocks, these electrons are indistinguishable from photo-electrons and may be mistaken for dark current. If generated by the serial clocks they may be mistaken for increased amplifier read noise. The effect is small and may only be revealed in heavily binned images. For example, a poorly prepared CCD4280 had an observed read noise that increased approximately as the square root of the horizontal binning factor. Dropping serial clock amplitudes by a couple of volts eliminated the problem. For L3 CCDs a CIC of a fraction of an electron can limit the performance. Indeed, all L3 CCDs tested thus far have been CIC noise limited. Minimising CIC requires special attention to the clock edges and a minimisation of the on-time of the multiplication clock. If this is done carefully then approximately one pixel in 1000 contains a spurious electron.

Due to controller limitations we have been forced to use slower pixel rates and 1 pixel in 10 has been a more typical result.

It may seem remarkable to be able to measure such low levels of CIC. However, in an L3 image single electron events clearly stand out as discrete 'spikes'. The windowed frame in Fig. 2. shows the image area, serial overscan and parallel overscan of a CCD97 L3 CCD. The single electron events are obvious. Notice that there is a spread in brightness of the events. This is a consequence of multiplication noise. Also noteworthy is the relative absence of events in the broad overscan regions at the top and right of the image. These regions contain pixels that do not originate in the image area of the CCD (which is a frame transfer device) indicating that the image area clocks were still in need of some fine-tuning. Underlying the image is a faint Gaussian background with a hint of pattern noise, all well below the single electron event level.
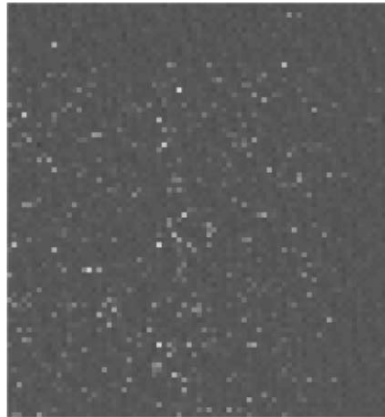
Figure 2. Windowed bias frame from an L3 CCD.

2. THE NAOMI AO SYSTEM AT ING

NAOMI is anNGS AO system that has been in operation at the William Herschel Telescope (WHT) since 2002. It can give near diffraction limited images in J,H and K with a Strehl of about 0.6 in K when coupled to the INGRID NIR camera. The NAOMI output is also available to the OASIS integral field spectrograph that has a CCD detector. In the R and I bands, partial correction is still obtained with typical halving of the seeing disc size. NAOMI is severely limited in its operation by the availability of suitably bright guide stars: an M_v15 guide star must be present within a few 10s of arc-seconds of the target object. This is only true for a few percent of the

sky. Guide stars are selected from the area around the target using a pickoff probe. Light from the guide star is then directed through a lenslet wheel that contains various formats of Shack Hartmann (SH) lenslets optimised for various seeing conditions as well as a plain lenslet for tip-tilt only correction when only very faint guide stars are available.

NAOMI (see Fig. 3) uses a 4-quadrant readout CCD39 Wavefront Sensor (WFS) with 80×80 pixels and a read noise of about 6 e[-]. The standard SH lenslet produces a 10×10 spot pattern on this CCD, the central 8×8 of which are illuminated by the telescope pupil. The SH spot images are individually centroided using an array of C40 DSP processors to yield the instantaneous shape of the seeing-distorted wavefront. Low order wavefront aberrations due to global tip-tilt terms in the atmosphere or telescope tracking errors are then offloaded to a fast steering mirror (FSM) and the telescope control system. Higher order wavefront errors are corrected by a 76 element segmented deformable mirror (DM) which is conjugate with the primary mirror. Each segment of this mirror can be independently adjusted in tip, tilt and piston and has a strain gauge feedback to eliminate hysteresis in its piezo actuators. There is a one-to-one mapping between each SH spot and an element of the DM. Each pair is in turn mapped to a specific region of the primary mirror measuring 0.5 m$\times$0.5 m. The deflection of the SH spot on the WFS allows the average wavefront gradient over that part of the primary to be determined, and the motion of the corresponding DM element corrects it. In practice it is slightly more complicated since each DM element piston setting also requires knowledge of the wavefront gradients in neighbouring regions. The loop speed of the system is typically 200 Hz, limited by the exposure time of the WFS. This bandwidth covers almost the entire atmospheric turbulence power spectrum. NAOMI also contains a second unutilised WFS head that can be illuminated simultaneously with the primary head via a half silvered mirror. The original plan was for one head to measure X centroids and the other Y centroids to gain speed. This secondary 'Slave' head, however, has never been utilised.

3.   THE 'GLAS' RAYLEIGH LASER UPGRADE

The poor sky coverage of NAOMI has limited its uptake in the astronomical community. Fortunately we have recently obtained funding from the NWO in the Netherlands to develop a Rayleigh laser guide star (LGS) beacon called GLAS (see Fig. 4). This system will use an artificial on-axis guide star anywhere in the sky permitting almost full-sky AO observations. GLAS is currently being designed at the ING, Durham AIG and ASTRON in the Netherlands.

The GLAS acronym stands for ground layer adaptive optics system. The system is so named because it only corrects for turbulence in the lower part of the atmosphere close to the telescope itself.
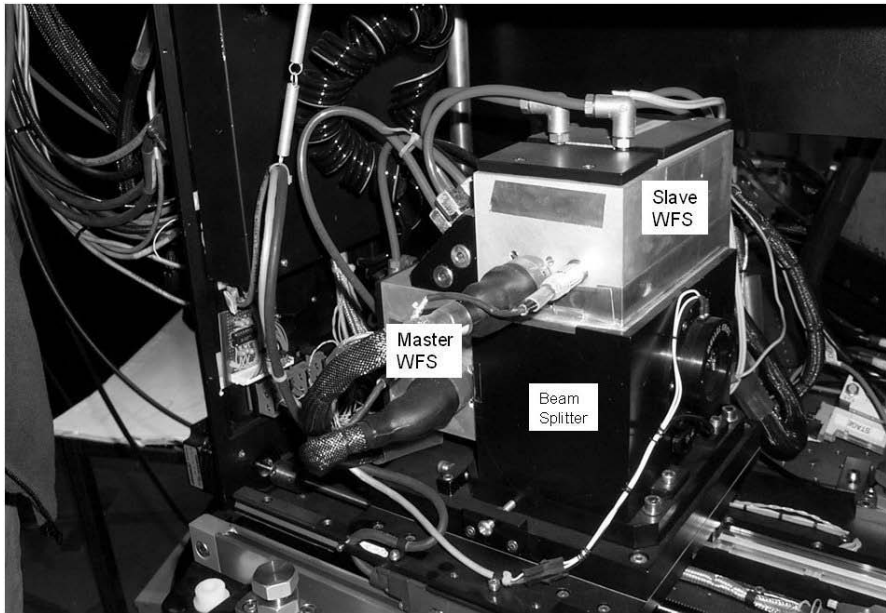
Figure 3. The original NAOMI WFS unit. The top slave unit has since been replaced with an L3 NGS WFS.

The laser beacon itself consists of a diode pumped Yb-YAG disk laser feeding into a frequency doubling crystal to yield a 30 W beam of 515 nm light. The laser is Q switched and emits a 7 KHz stream of 400 ns wide pulses. It will be mounted on the top-end ring where it will be coupled via an evacuated pipe to a 30 cm diameter refracting beam launch telescope (BLT) mounted behind the secondary mirror. These pulses are approximately 120 m long as they leave the BLT (see Fig. 5). 133 μs after the launch of each pulse a Pockels cell shutter briefly opens to allow laser light backscattered by the atmosphere to enter the wavefront sensor. The shutter acts as a range gate and effectively defines an artificial star within the atmosphere 20 km from the telescope. Since a Pockels cell must be used in combination with a polarising element it will at most have a 50% transmission. To overcome this loss, two cells will be used, one for each polarisation axis. The LGS light will be directed to each through a polarising beam-splitter. Light exiting the two shutters is then recombined using a second polarising beam-splitter before passing through the SH lenslet. The

SH spots produced on the WFS will be slightly elongated by 0.2" due to parallax effects from the finite laser beacon distance. Positioning the BLT above the secondary acts to minimise this elongation. Associated with the LGS WFS optics are a number of additional small diagnostic cameras to verify the position and intensity of the laser beacon. The LGS is brought to an intermediate focal plane containing a narrow 4" diameter field stop. The plane of this stop is conjugate to the 20 km distant beacon so any light scattered at lower altitudes will be so far out of focus at the pin-hole that only a small fraction of it will pass through - a neat 'lo-tech' solution to improving the shutter contrast ratio.
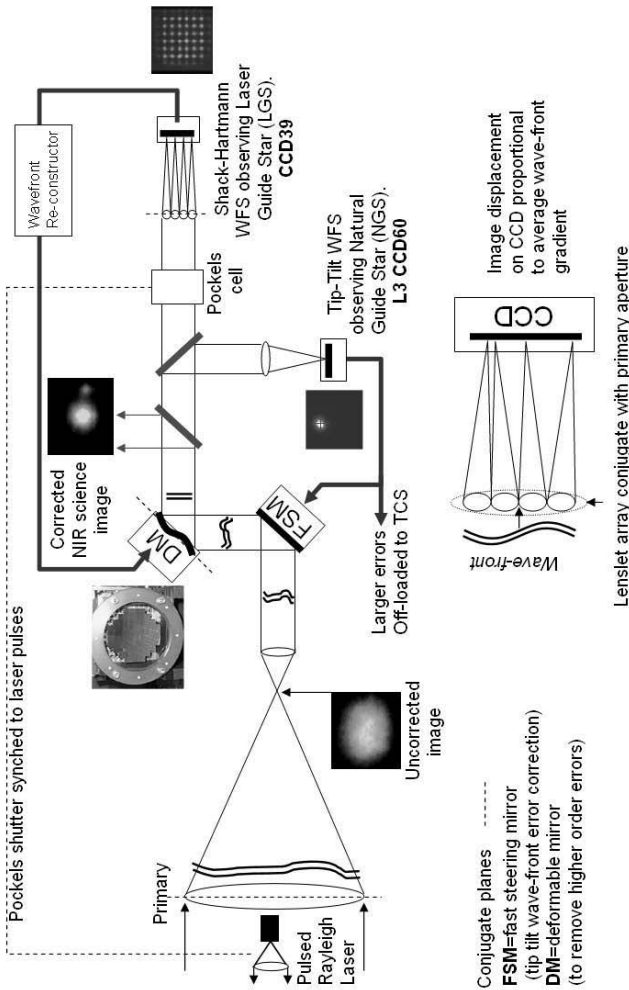
Figure 4. The Proposed GLAS AO system.

Whilst improving sky coverage almost 100%, using laser guide stars has certain disadvantages compared to natural guide stars. Firstly, there is the 'cone effect' where the volume of atmosphere through which the laser beacon light returns to the telescope is not the same volume as that traversed by light from the science object (see Fig. 6). The cone effect worsens as the distance of the beacon decreases and the aperture of the telescope increases. Secondly, any turbulence effects that cause a lateral displacement of the science object on the sky, i.e. 'global tip-tilt' terms, will not be detected by the laser beacon due to the double passage of the laser beam through any such turbulence layers. In these cases the lateral deflection of the laser beam in its upward passage will be cancelled by an equal but opposite deflection during its return journey to the telescope. Even when using the laser it is therefore still necessary to observe a natural guide star within 1-2' of the science object to remove these global tip-tilt distortions. This is not such a disadvantage because the tip-tilt guide star can be observed using the whole telescope aperture rather than just a small section as is the case with a Shack Hartmann sensor. Additionally the guide star can be selected from a wider area of sky with longer exposure times. Nevertheless, the availability of a natural guide star still limits sky coverage. If the NGS WFS can reach M_v18, the sky coverage at the Galactic Pole (the sparsest region) will still exceed 60%. The planned start of GLAS operations is October 2006. Until then NAOMI will still be available for observations using its NGS wavefront sensor.
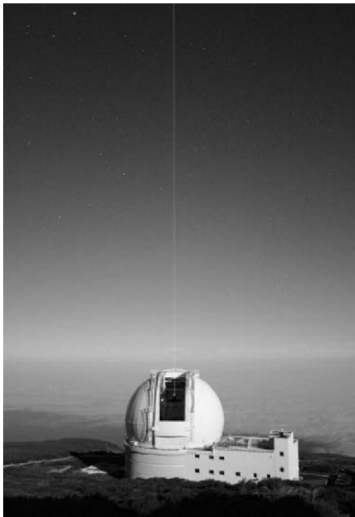
Figure 5. Rayleigh Laser launch at the WHT.   *Figure 6*. The cone effect.
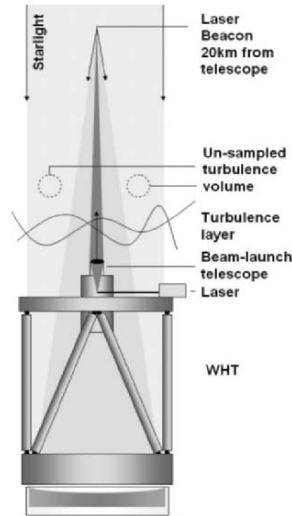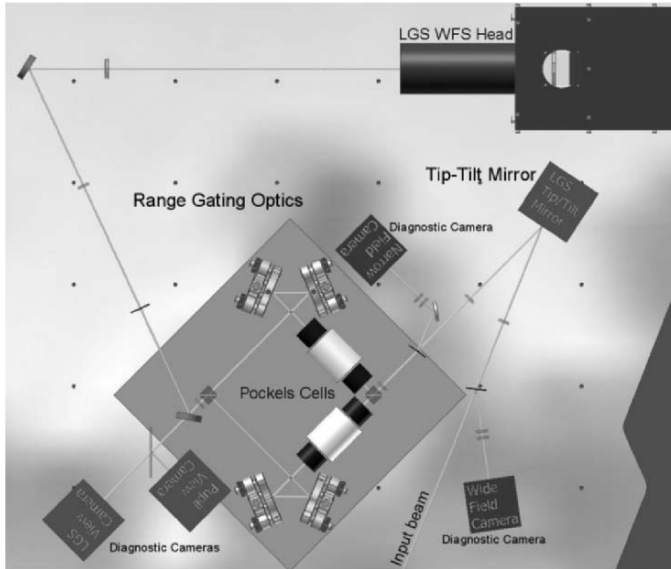
Figure 7. View of the additional GLAS LGS WFS optics fitted to the NAOMI optical bench.

4.   APPLICATION OF L3 TECHNOLOGY WITHIN GLAS

GLAS requires two wavefront sensor heads: one to observe the Natural Guide Star (NGS WFS, see Fig. 8) and one to observe the Laser Guide Star via a Shack Hartmann lenslet array (LGS WFS, see Fig. 9). The LGS will be quite bright (M_v9-10) and the current CCD39 WFS will serve well. It will, however, need to be physically moved and placed downstream of the Pockels shutter. Conveniently, the current NAOMI optical bench, which is located in a temperature controlled Nasmyth laboratory, has a spare corner where the LGS arm optics can be situated. The laser light is intercepted and redirected to this area of the bench using a narrowband notch filter tuned precisely to the laser. The wavelength range close to the laser line will not be available for science. The requirements of the second wavefront sensor needed by GLAS, the NGS WFS, are rather demanding and it seemed marginal that a conventional detector could reach the required M_v17 magnitude limit. A new head has therefore been built using a Peltier cooled L3 CCD60 and in May 2005 was mounted in the position previously occupied by the CCD39 destined to become the LGS WFS. This new head has already been tested on-sky in June 2005, not in its final role as a tip-tilt sensor but as a SH sensor, effectively emulating the behaviour of the original

CCD39. The SH image included in Fig. 1. was taken with this head It is hoped that, prior to the GLAS implementation, we can gain advantages from the L3 head in this role, and models predict a 1-2 magnitude improvement in guide star limit. The optics inside the WFS unit allow beam-switching between the master and slave WFS ports, so changing between the CCD39 and the CCD60 will take only a few minutes. This adds a useful level of redundancy if problems are encountered with the L3 head. The CCD60 only has a single output and this acts as a bottleneck preventing the full CCD39 (quadrant readout) pixel bandwidth being achieved. Using it with GLAS the CCD60 will be much faster since it only needs to read a single small window around the NGS. Three readout modes will be offered: 8×8, 16×16 and 32×32 pixel windows with a plate scale of 0.25" per pixel. The respective readout speeds through an SDSUII controller are 300, 200 and 100Hz. To achieve these speeds it was necessary to use the Modulo addressing mode of the controller DSP. Here, the waveform tables are first located at page boundaries. The DSP Rn register, which acts as a pointer to the next waveform-state word is then set to the start of the table and the corresponding Mn register set to the length of the table-1. When the post-incremented Rn pointer reaches the end of the waveform table it automatically loops back to the start to clock the next pixel. This gives a considerable time saving over the more conventional approach of JSR'ing to a subroutine for each pixel read or skipped.

A custom clock card has been designed and built as a PCB to generate the multiplication clock voltage. It fits into a vacant slot within the SDSU and connects via an edge connector to the standard SDSU clock and video cards. The clock amplitude can be programmed using one of the video board DACS for precise tuning of L3 gain.
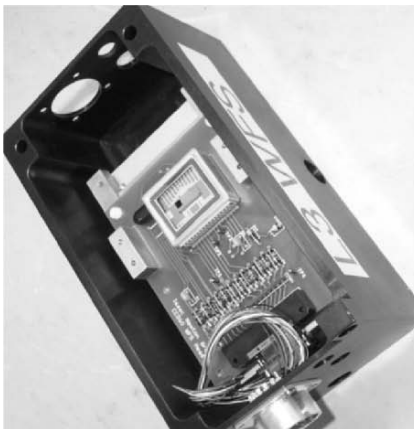
Figure 8. The new L3 NGS WFS head.

Figure 9. The slave head to be used as the LGS WFS.

5.   PREDICTED GLAS PERFORMANCE

Extensive measurements have been done of the turbulence characteristics on the sky above La Palma [2]. Both sodium and Rayleigh lasers have also been launched and their intensities have been measured [3]. Table 1 shows the predicted performance of GLAS on nights when ground layer turbulence dominates. These nights occur approximately 25% of the time. Higher level turbulence will not be well corrected due the previously mentioned cone-effect, i.e., incomplete sampling of the turbulent volume.

Table 1.   Median seeing, corrected versus uncorrected with Mv17 NGS and ground layer turbulence dominating.

	R	I	J	H
Uncorrected	0.61	0.58	0.53	0.51
Corrected	0.3	0.2	0.11	0.11

6.   PARALLEL DEVELOPMENTS: RAPID SPECTROSCOPY

Building on the experience obtained from using the CCD60 WFS, some larger format L3 CCDs have been purchased to test their suitability for rapid spectroscopy on the WHT's ISIS spectrograph. Two cryogenic cameras were built, containing a 512×512×16 mm pixel CCD97 and a 1024×1024×13 mm CCD201. These are shown in Fig. 10. They are both frame transfer devices. The CCD97 has already been used on sky to observe a short period eclipsing binary system (IP Pegasus). A full frame was read out in 500 ms, a 50×50 window in 60 ms. Sub-electron noise performance was demonstrated. In the future it is hoped to reduce the CIC to such a level that photon counting observations will be possible.

7.   ACKNOWLEDGEMENTS
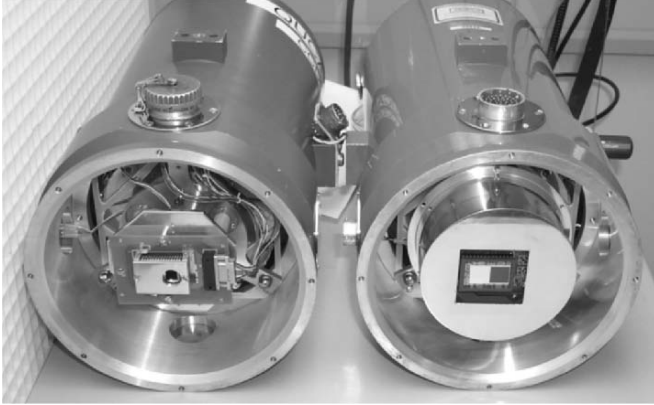
Figure 10. Cryogenic L3 Cameras (CCD97 and CCD201) for rapid spectroscopy on the WHT.

8. REFERENCES

[1] e2v L3 Technology web page http://e2vtechnologies.com/introduction/prod_l3vision.htm
[2] Wilson, R.N., 2002, *SLODAR: measuring optical turbulence altitude with a Shack-Hartmann sensor*, MNRAS **337**, 103.
[3] Clark, P., et al., 2003, *Rayleigh AO Demonstrator for the 4.2 m William Herschel Telescope*, Proc. SPIE **4839**, 516-523.

9. FURTHER BACKGROUND

Tulloch, S.M., 2004, *Application of L3 Technology to Wavefront Sensing*, SPIE **5490**, 34.
Tulloch, S.M., 2004, *Photon Counting and Fast Photometry with L3 CCDs*, SPIE **5492**, 173.

Maurizio Seracini, who gave a fascinating talk about using detectors to investigate
classical paintings, and his wife Marie-Louise Lodge
enjoy an evening in Forza d'Agró.
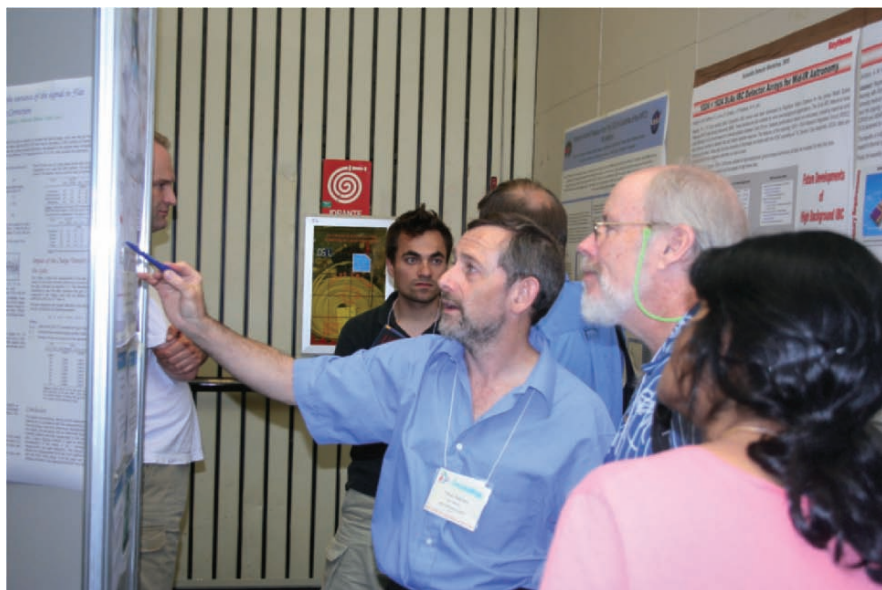
Paul Jorden proudly shows Bruce Atwood and Vyshi Suntharalingam another typo
he found in a poster paper, while Matthias Tecza (back left) tries to pretend it is
not his paper. Tim Goodsall (back middle) tries to comprehend it all.

ZERO NOISE WAVEFRONT SENSOR DEVELOPMENT WITHIN THE OPTICON EUROPEAN NETWORK

Philippe Feautrier[1], Thierry Fusco[2], Mark Downing[3], Norbert Hubin[3], Jean-Luc Gach[4], Philippe Balard[4], Christian Guillaume[5], Eric Stadler[1], Olivier Boissin[4], Paul Jorden[6] and José Javier Diaz[7]

[1]LAOG, Domaine Universitaire, [2]ONERA, [3]European Southern Observatory, [4]Laboratoire d'Astrophysique de Marseille, [5]Observatoire de Haute Provence, [6]e2v technologies, [7]Instituto de Astrofisica de Canaria

Abstract: *This activity, funded by ESO and the European Commission through the Opticon Network will attempt to define, fabricate and fully characterize the best possible detector working at visible wavelengths suitable for wavefront sensors in Adaptive Optics (AO) systems. The detector will be a split frame transfer array built by e2v technologies and called CCD220. The frame rate will be very fast (up to 1.2 kHz) while the readout noise will be kept extremely low (typically below 1 e⁻). The goal of this paper is to justify the choice of detector: an EMCCD with 240×240 pixels and 8 outputs that will provide sub-electron readout noise at 1-1.2 kHz frame rate. This paper shows that, despite the fact that EMCDDs have an excess noise factor of 1.4 due to the charge multiplication process; their virtually zero read noise should allow them to outperform the classical CCD. Such detectors do not yet exist and must be developed. Moreover, this paper explains how the OPTICON European network is organized.*

Key words: *Adaptive Optics (AO), electron multiplying CCD, readout noise, wavefront sensor, Strehl ratio.*

1.   THE NEED

The next generation of Adaptive Optics (AO) systems for 8-10 m class telescopes requires an increased number of degrees of freedom, which will increase the number of actuators required typically by a factor of 5 to 10 (>1k degrees of freedom).

This leads to very tight requirements on the detector. For example, a typical Shack Hartmann system with 6 pixels/sub-aperture and 40×40 sub-apertures will require a detector size of 57600 pixels (240×240). In addition, detectors with high frame rate (1-1.5 kframes/s) are mandatory. In order to reach the required limiting magnitudes, the detector must have a readout noise as low as possible (<1e$^-$) and a dark current adding negligible noise. Existing wavefront sensor detectors do not have the image area size, readout speed or low noise performance to meet these increased performance requirements. Therefore the need to develop a new generation of detectors is clearly established.

2.   DESCRIPTION AND INTEGRATION OF THIS ACTIVITY INSIDE THE OPTICON EUROPEAN NETWORK

OPTICON is a project which has been approved for funding by the European commission as part of its Sixth Framework Programme (FP6). The OPTical Infrared Coordination Network for astronomy (OPTICON) brings together all the international and national organizations which fund, operate and develop Europe's major optical and infrared astronomical infrastructures.

The OPTICON network is divided into 3 main activities:

- The Joint Research Activities (JRAs) are technical developments in the field of visible and infrared instrumentation for astronomy.
- The networking activities are promoting scientific and technical networks (adaptive optics, key technologies, interferometry, high time resolution astrophysics, etc.).
- The access program enables the sharing of telescope time from medium size telescopes (4 meters and less). This access program allows the access of such telescopes to all the astronomers from Europe.

The JRA described here is named "JRA2: Fast Detectors for Adaptive Optics".

3. CHOICE OF DETECTOR TECHNOLOGY AND FEATURES

The study presented hereafter was performed in the framework of the VLT Planet Finder concept study. The VLT Planet Finder is the next AO system for the ESO VLT. This system is mainly dedicated to the discovery of extra-solar planets and necessitates the use of a high contrast AO system. A preliminary study has shown that a visible wavefront sensor with 240×240 pixels is the best compromise for the wavefront correction of this AO system.

3.1 Choice of the Detector Technology: Classical CCD or EMCCD?

Two types of detectors were investigated. The first, called CCD1, is a classical back-thinned CCD having a high QE optimized in the red. The second CCD, called CCD2, is an EMCCD with an excess noise factor of 1.4. Because high-resistivity silicon is untried with EMCCDs, the red QE assumed for CCD2 is much poorer than that of CCD1, which has the red QE of the best-known classical CCD. Moreover, CCD2 suffers from the typical excess noise factor of 1.4 due to the electron multiplication gain of EMCCDs. This effect was taken into account in the simulations for CCD2.

3.2 AO System Assumptions for the Simulations

- 8 m diameter telescope at the ESO VLT at Paranal.
- Atmospheric conditions: 0.85 arscec of seeing, a wind speed of 12.5 m/s, i.e. a turbulence coherence time τ_0 of 3 ms.
- System assumptions: 40×40 sub-aperture Shack-Hartman wavefront sensor, 2 frames of delay, Weighted Centre of Gravity measurements (an optimized way to compute the centroid of a Shack-Hartman spot [1]), optimal modal integrator, wavefront sensor average wavelength: 0.65 μm, imaging wavelength of the science camera: 1.65 μm.

Different types of guide stars were considered: A0, G0, M0 and M5. The spectral types of these guide stars are different; A0 emits more in the blue and M5 more in the red.

3.3 Effect of the Detector Technology on a XAO System

Figures 1 and 2 show the Strehl Ratio (SR) evolution as a function of the visible magnitude of the guide star. The SR was optimized by varying the frame frequency for a given detector type, a given noise and a given

magnitude: between 250 and 2500 Hz for CCD1, 250 and 1500 Hz for the CCD2. Results for two types of guide stars are shown, a blue type A0 and a red type M5. These figures show that for the VLT-PF instrument and the typical conditions at Paranal, the EMCCD always gives higher SR, except for visible magnitude below 8.5 with an A0 type guide star and below 10.5 with a M5 type guide star. The gain of SR for a good classical CCD (CCD1 with 3e⁻ read noise) at low magnitude is just 1% whereas the value of an EMCCD (CCD2) is clear at high magnitudes (faint guide star). Moreover, building a classical CCD with < 3e⁻ of read noise at 1.5 kHz of frame rate is extremely challenging. These simulations lead to the following conclusions:

- An EMCCD (CCD1) with a read noise lower than 1e⁻ is the best option, especially if the QE can be improved in the red by using deep depletions devices.
- A classical CCD (CCD2) may be interesting (in particular because of its very good red QE) if a readout noise lower than 2e⁻ at high frame rate could be achieved.
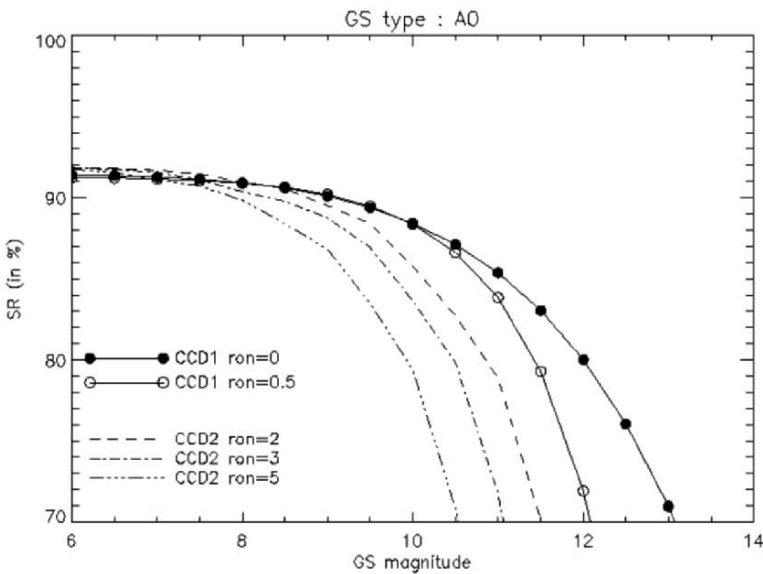
Figure 1.   Strehl Ratio comparison of CDD1 (classical) and CCD2 (EMCCD) for an A0 guide star type (blue guide star).

4. CONCLUSIONS

The results of these simulations show a strong interest in EMCCDs for AO wavefront sensors despite the fact they have lower red QE (because high resistivity silicon is yet untried) and an excess noise factor due to the electron multiplication process. In August 2004, a call for tenders was issued for the development and supply of 240×240 pixel, very low noise (1e⁻ or less), fast readout (1.2 kframes/s) CCD detectors that meet the set requirements (see Table 1). This culminated in a contract between e2v and ESO in April 2005 to start a detector development. Full details of this detector development and trade-offs are presented in [2]. The technical challenges of the detector controller are detailed in [3]. This new detector will be used for the next generation of ESO instruments requiring AO systems, and among them the ESO VLT Planet Finder, a high contrast AO system dedicated to the research of extra-solar planets. Figure 3 illustrates a Peltier cooled package similar to the one that will be used for the CCD220.

To conclude, this study clearly shows that for an AO wavefront sensor, a low readout noise is more important than high red QE.
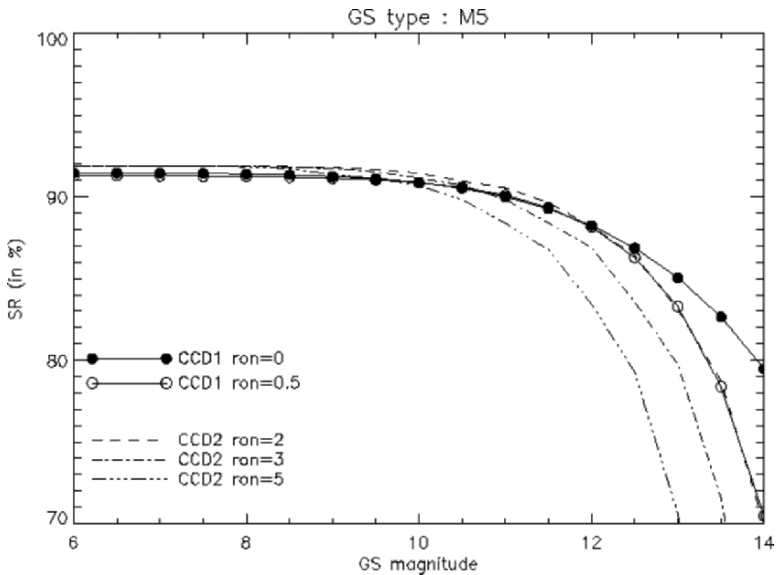
Figure 2. Strehl Ratio comparison of CDD1 (classical) and CCD2 (EMCCD) for a M5 type guide star (red guide star).

Table 1. AO wavefront sensor detector main characteristics.

Item	Specifications
Manufacturer	e2v technologies, UK
Name of the detector	CCD220
Detector format	240×240 pixels, split frame transfer
Technology	EMCCD, excess noise factor 1.4
Number of outputs	8
Frame rate	25 Hz – 1.2 kHz
Read noise	< 1e$^-$ at 1.2 kHz frame rate

Figure 3. CCD65 Peltier cooling package. The AO CCD220 detector will use a similar Peltier package.

5.   ACKNOWLEDGEMENTS

6.   REFERENCES

[1] Fusco, T., et al, 2004, *Optimisation of Shack-Hartman-based wavefront sensor for XAO system*, Proc. SPIE Int. Soc. Opt. Eng. **5490**, 1155.
[2] Downing, M., et al, *A Dedicated L3CCD for Adaptive Optics Applications*, these proceedings.
[3] Gach, J-L., et al, *A dedicated controller for Adaptive Optics L3CCD developments*, these proceedings.

A DEDICATED L3VISION CCD FOR ADAPTIVE OPTICS APPLICATIONS

Mark Downing[1], Norbert Hubin[1], Markus Kasper[1], Paul Jorden[2], Peter Pool[2], Sandy Denney[2], Wolfgang Suske[2], David Burt[2], Pat Wheeler[2], Kevin Hadfield[2], Philippe Feautrier[3], Jean-Luc Gach[4], Javier Reyes[1], Manfred Meyer[1], Dietrich Baade[1], Philippe Balard[4], Christian Guillaume[5], Eric Stadler[3], Olivier Boissin[4], Thierry Fusco[4], José Javier Diaz[6]

[1]European Southern Observatory, [2]e2v technologies, [3]LAOG, Domaine Universitaire, [4]Laboratoire d'Astrophysique de Marseille, [5]Observatoire de Haute Provence, [6]Instituto de Astrofísica de Canarias

Abstract: *ESO and JRA2 OPTICON have funded the development of a compact packaged Peltier cooled 24 µm square 240×240 pixel split frame transfer 8-output back illuminated L3Vision CCD, L3CCD, by e2v technologies. The device will achieve sub-electron (goal 0.1e⁻) read noise at frame rates from 25 Hz to 1.5 kHz and low dark current of 0.01 e⁻/pixel/frame. The development has many unique features. To obtain high frame rates, multi-output EMCCD gain registers and metal buttressing of parallel clocks will be used. To minimize risk, the baseline device will be built in standard silicon. In addition, a split wafer run will enable two speculative variants to be built; deep depletion silicon devices to improve red response and devices with an electronic shutter to extend use to Rayleigh Laser Guide Star (RLGS) applications. These are all unprecedented advancements for L3CCDs. This paper will describe requirements and outline the design established after careful consideration of the application, detector architecture, compact Peltier package, technology trade-offs, schedule and proposed test plan.*

Key words: *Adaptive Optics (AO), AO systems, Electron Multiplying CCD (EMCCD), L3Vision, L3CCD, readout noise, wavefront sensor.*

1. INTRODUCTION

The success of the next generation of instruments (e.g. VLT Planet Finder, MUSE, HAWK-I) for 8 to 10 m class telescopes will depend on the ability of Adaptive Optics (AO) systems to provide excellent image quality and stability. This will be achieved by increasing the sampling and correction of the wavefront error in both spatial and time domains. For example, future Shack Hartmann systems will require 40×40 subapertures at sampling rates of 1-1.5 kHz as opposed to 8×8 sub-apertures at 500 Hz of current systems. Detectors of 240×240 pixels will be required to provide spatial dynamics of 5-6 pixels per sub-aperture. Higher temporal-spatial sampling implies fewer photons per pixel. Therefore much lower read noise (<<1e⁻) and negligible dark current (<<1e⁻/pixel/frame) to detect and centroid on single or a small number of photons is required. Existing detectors do not have this combination of image area size, read out speed, and low noise performance. Since WFS detectors are critical in the development of future AO systems there is an urgency to develop better detectors.

Numerous European astronomy institutions, including ESO, have joined the OPTICON network [1], and obtained funds in the joint research activity JRA2, "Fast Detectors for Adaptive Optics", from the European Commission to support the massive R&D effort to develop a new detector. After extensive market research culminating in a Call For Tender, e2v was chosen to develop a custom-designed detector based on an extension of their L3Vision [2] EMCCD technology. Analysis [1,3] showed that the sub-electron read noise of L3Vision CCDs clearly outperformed classical CCDs even though L3Vision exhibits the excess noise factor of √2 typical of EMCCDs.

2. REQUIREMENTS

The OPTICON JRA2 science working group set the top level requirements after carefully considering the needs of AO systems for future instruments and their science programs. The following detailed requirements were established:

1. Big pixels, square 24 μm (goal), to ease the optical system design, but not too large to produce excessive Dark Current (DC) or CTE problems.
2. Versatility of a 100% fill factor and 240×240 square grid array of pixels that can be used by any WFS systems: SH, curvature, or

pyramid, with or without gaps (guard bands) between subapertures.

3. Format size of 240 pixels being a number that is divisible by the number of output nodes, 8, and binning factors and aperture sizes of 1, 2, 3, 4, 5, 6 and meets the minimum pixel requirement of 40 subapertures × 6 pixels/subapertures.

4. Low read noise of <1 e$^-$/pixel and goal of 0.1 e$^-$/pixel.

5. Range of operating frame rates from 25 frames/s (fps) for use when photon starved with faint-NGS (Natural Guide Star) to highest sampling rate of 1,200 fps for use with bright-NGS and LGS (Laser Guide Star).

6. Easy to use; eight output nodes each operating at maximum pixel rate of 15 Mpixel/s, that provide a good compromise between the number of connections between the detector and the outside world and operational practicalities such as power dissipation, pixel rates and clocking rates.

7. Low image smearing (<5%) when transferring from the image to store area; an undesirable effect that can be corrected.

8. Cosmetic defect free, as every defect will either complicate the centroiding or make it impossible to centroid a subaperture.

9. Good spatial characteristics, PSF <0.9 pixel FWHM over 460 to 950 nm, to accurately determine where the photons are detected.

10. Very low DC, of <0.01 e$^-$/pixel/frame at 1,200 fps and <0.04 e$^-$/ pixel/frame at 25 fps to minimize large errors introduced by the quantum nature of DC; as the electron is the smallest unit. A single electron of DC creates a large error when centroiding on a small number or single photon event. DC includes contributions from the clock induced charge (fixed amount per frame readout), the image area during exposure ($\propto$ exposure time), the frame store and the serial register during readout ($\propto$ frame read out time).

11. Peltier cooled package for small compact size, maintenance free, and minimal support equipment so that the final assembled camera system can fit in the small volumes usually reserved for AO systems.

12. Detection signal limit of 5 ke$^-$. In normal operation, the system will be photon starved without too many bright NGS and LGS will be operated at as low a power as possible. Well depth and output amplifier dynamic range can be traded to improve other parameters such as higher gain of output amplifier and lower clock amplitudes to transfer charge.

13. Linearity of <2%. Analysis shows that this level of nonlinearity introduces insignificant errors. Nonlinearity can be corrected by a look-up table.

3.   DESIGN

The design (see Fig. 1) is a 24 µm square 240×240 pixels split frame transfer 8-output back illuminated L3CCD, designated as the CCD220. The shuttered variant is designated as the CCD219.
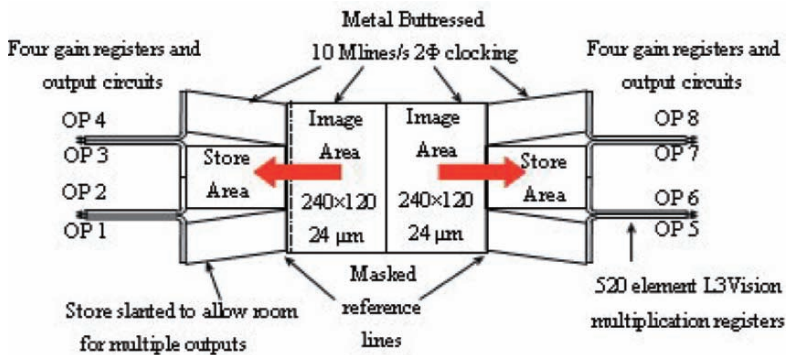
Figure 1. Schematic of CCD220.

The image and store area are built with metal-buttressed parallel clock structures to enable line shifts of 10 Mlines/s for a total transfer time of 12 µs from image to store, and low smearing of under 1.5% at 1,200 fps. Two phase clocking was chosen for simplicity, lower power dissipation, and symmetry of drive. See Gach et al. [4] for a discussion of the benefits of a symmetric drive for the CCD controller.

The store area is slanted to make room for the standard serial registers (three phase clocking) to curve around (see Fig. 2) and provide space for the output circuitry. Each output will have a 520 element 16 µm standard L3Vision gain register whose gain is controlled by the voltage of the multiplication phase. The output amplifier will be single stage (see Table 1) and of similar design to that employed on recent L3V CCDs. The gain register and output amplifier will be optimized for a gain of 1000, a value typically expected for AO applications, to provide an overall effective read noise of under 0.1e$^-$. The serial registers, gain registers, and output amplifiers are designed to operate up to 15 Mpixel/s to achieve a full goal frame rate of over 1,500 fps.
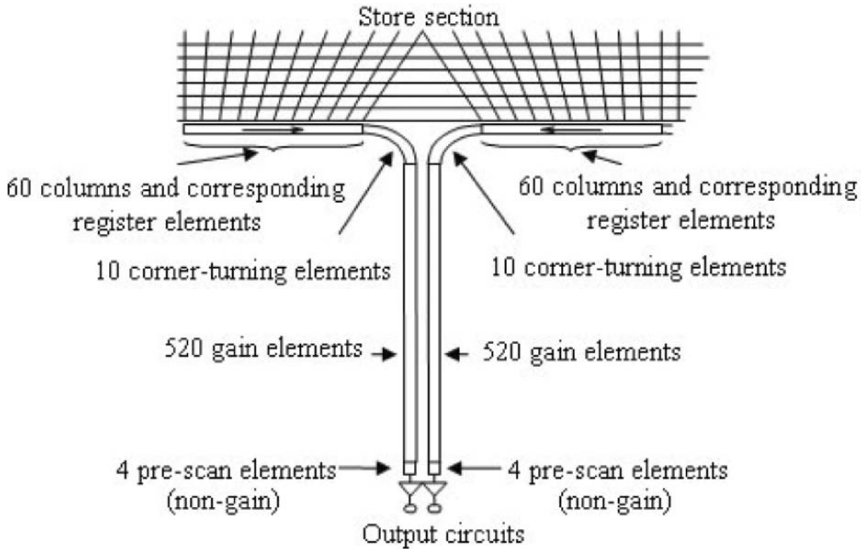
Figure 2. Details of serial and gain register.

Table 1. Specifications of output amplifier.

Feature	CCD220
Overall responsivity	1.7 µV/electron
Node capacitance	57 fF
Noise (rms with CDS ~ 15 MHz)	45 electrons
Reset rms noise (dominates without CDS)	100 electrons
Saturation (3V swing at node)	1.0M electrons
Output impedance	350 Ohms
Maximum frequency (settling to 1%)[1]	15 MHz
Maximum frequency (settling to 5%)	25 MHz

The baseline device will be built in standard silicon and is low risk with guaranteed delivery of devices that meet minimum requirements. This meets the risk profile of both JRA2, who must produce a design report to the EU on a 2-3 year timescale, and ESO, who require working detectors for their next generation of instruments. A split wafer run will enable the production of two speculative variants. The first will build devices in deep depletion silicon offering much improved red response. High red response is important for applications that rely on natural GS such as VLT Planet Finder. The second is to build devices with an electronic shutter to extend the use of the detector to applications such asRayleigh Laser Guide Star (RLGS), which require very short shutter times of µs. These short shutter times are not

---

[1] Load capacitance (external and package) <10 pF

possible by mechanical means. RLGS systems can offer substantial savings in costs and development efforts in that they can use commercially available pulsed lasers as opposed to specialized sodium lasers.

No dump gate was included in the design as it was doubtful whether its response time to dump charge would be faster than simply clocking the serial register. It was also a concern if it would add excessive capacitance to neighboring registers and add pins to the package resulting in a larger package size and more heat load. Additionally, for deep depletion devices a much wider dump gate would be required to avoid parasitic effects resulting in an even slower dump time.

As well reducing pin count, summing wells were not included because with low read noise of $0.1e^-$ binning could easily be performed off chip.

4.   PACKAGE

The devices will be mounted in a compact Peltier cooled package similar to that shown in Fig. 3. Peltier cooler and package will be custom designed and able to cool the CCD sufficiently to meet DC requirements over the full operating frame rates. The estimated power dissipation of the CCD at 1,200 fps (worst case scenario) is shown in Table 2. The Peltier cooler, ceramic chip carrier and CCD will be glued by a thermally conductive epoxy adhesive. The package will be sealed and filled with 0.9 bar of Krypton gas to minimize heat transfer to the outside.

Table 2. Estimated total and on-chip power dissipation of CCD220 at 1,200 fps.

Section	Load	Delta V	Mean f	W_{total}	$W_{on-chip}$
Image	4.2 nF	10 V	185 kHz	78 mW	23 mW
Store	3.6 nF	10 V	370 kHz	133 mW	40 mW
Register	1.5 nF	10 V	13.2 MHz	2.0 W	800 mW
HV	0.4 nF	45 V	13.6 MHz	11.0 W	220 mW
Amplifiers				8×50 mW	400 mW
Total					~1.5 W

The CCD220 die will have four fiducial crosses situated with two on either side of the device image area, in the region of the bond pads. These will be clearly visible through the package window for alignment purposes such as when attaching lenslet arrays. An AD590 temperature sensor will be glued to the ceramic chip carrier to provide sensor for temperature regulation. The sapphire entrance window will be of a high optical quality (double path wavefront error of <50 nm rms), good surface quality (defects

meet 5/2×0,05 DIN3140), and AR coated with transmission >98% over range 400-950nm.
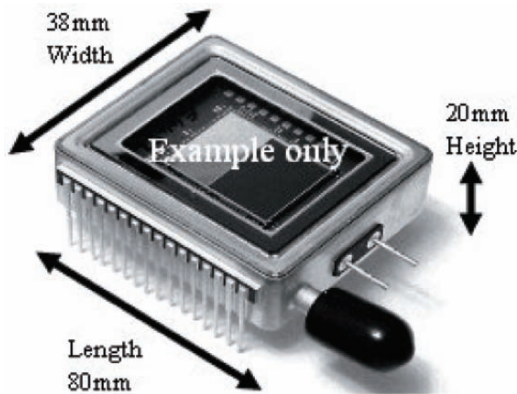
Figure 3. Photograph of CCD65 Peltier cooling package. The AO CCD220 detector will use a similar Peltier package. Dimensions shown are the requirements on the maximum package size.

5. SCHEDULE

The major milestones (see Table 3) are CDR in Q3 2005, package review by 2005, and final device delivery in Q2 2007. Test equipment and camera electronics is being developed by Gach, et al. [3] and will be loaned to e2v for testing. The same test equipment will be used by the IAC (JJD) for acceptance testing. ESO is developing the New General detector Controller, NGC, [5,6,7] to support the CCD220 for deployment on the VLT.

The test plan is for e2v to do parametric and functional tests and measure standard parameters such as noise, gain, cosmetics, dark current, smearing, and CTE and for IAC (Canary Islands) and ESO to do full acceptance tests plus measure the more exotic parameters such as crosstalk, PRNU, fringing, and PSF.

Table 3. Major milestones of CCD220 development.

Milestone	Date
Kick-off meeting	March 2005
CCD220 and Test Equipment Critical Design Review (CDR)	Q3 2005
Package Design Review	End 2005
Mechanical samples delivery	Mid 2006
ESO supplied test equipment delivery	Q3 2006
Devices delivery	Q2 2007

6.   CONCLUSION

Several European institutions under the umbrella of OPTICON have formed a successful relationship with e2v to develop a new 240×240 pixel wavefront sensor detector. This detector, CCD220, will have subelectron read noise at 1,200 fps that will enable future AO systems to provide the image quality and stability to guarantee the success of next generation of instruments on 8 to 10 m class telescope. Baseline development is low risk by extending existing e2v L3Vision technology to multiple outputs and metal buttressing parallel clock structures. In addition higher risk (more speculative) but higher performance devices in deep depletion silicon and with electronic shutter will be developed in parallel. For compactness and low maintenance the CCD is mounted in an optimized Peltier cooled package.

7.   REFERENCES

[1] Feautrier, P., et al., 2005, *Zero noise wavefront sensor development within the Opticon European network*, these proceedings.
[2] Jerram, P., et al., 2001, *The LLCCD: low-light imaging without the need for an intensifier*, Proc. SPIE, Vol. **4306**, pp. 178-186.
[3] Fusco, T., et al., 2004, *Optimisation of Shack-Hartman based wavefront sensor for XAO systems*, Proc. SPIE Int. Soc. Opt. Eng. **5490**, p. 1155.
[4] Gach, J-L., et al., *A dedicated controller for Adaptive Optics L3CCD developments*, these proceedings.
[5] Reyes, J., et al., *NGC Front-end for CCDs and AO application*, these proceedings.
[6] Cumani, C., et al., *Software for the New General detector Controller*, these proceedings.
[7] Meyer, M., et al., *NGC Detector Array Controller Based on High Speed Serial*, these proceedings.

THE ULTIMATE CCD FOR LASER GUIDE STAR WAVEFRONT SENSING ON EXTREMELY LARGE TELESCOPES

James W. Beletic[1], Sean Adkins[2], Barry Burke[3], Robert Reich[3], Bernie Kosicki[3], Vyshnavi Suntharalingham[3], Charlie Bleau[4], Ray DuVarney[4], Richard Stover[5], Jerry Nelson[6], Francois Rigaut[7]

[1]*Rockwell Scientific Company,* [2]*W.M. Keck Observatory,* [3]*MIT Lincoln Laboratory,* [4]*SciMeasure Analytical Systems,* [5]*Lick Observatory,* [6]*University of California, Santa Cruz,* [7]*Gemini Observatory*

Abstract: *All of the extremely large telescopes (ELTs) will utilize sodium laser guide star (LGS) adaptive optics (AO) systems. Most of these telescopes plan to use the Shack-Hartmann approach for wavefront sensing. In these AO systems, the laser spots in subapertures at the edge of the pupil will suffer from spot elongation due to the 10 km extent of the sodium layer and the large separation from the projection laser. This spot elongation will severely degrade the performance of standard geometry wavefront sensing systems. In this paper, we present a CCD with custom pixel morphology that aligns the pixels of each subaperture with the radial extension of the LGS spot. This CCD design will give better performance than a standard geometry CCDs for continuous wave lasers. In addition, this CCD design is optimal for a pulsed sodium laser. The pixel geometry enables each subaperture to follow a laser pulse traversing the sodium layer, providing optimal sampling of a limited number of detected photons. In addition to novel pixel layout, this CCD will also incorporate experimental JFET sense amplifiers and use CMOS design approaches to simplify the routing of biases, clocks and video output. This CCD will attain photon-noise limited performance at high frame rates, and is being incorporated in the plans for the Thirty Meter Telescope (TMT).*

Key words: *CCD, sodium laser guide star, Shack-Hartmann wavefront sensing, ELT, CMOS design concepts.*

1.   A CCD OPTIMIZED FOR PULSED LASER GUIDE STAR WAVEFRONT SENSING

Our project team is developing a CCD that is optimized for the detection of short laser pulses that illuminate the sodium layer for wavefront sensing. The combination of this CCD and a pulsed sodium laser can overcome the problem of spot elongation that limits standard LGS AO systems. The spot elongation problem is shown graphically in Fig. 1. The LGS return is stretched in one dimension, due to the viewpoint of the subaperture. The laser guide star spot elongation is proportional to the distance that a subaperture is off-axis.   Since the error of the tip/tilt measurement is proportional to the width of the LGS spot, the quality of wavefront measurement is significantly degraded for large off-axis distances.
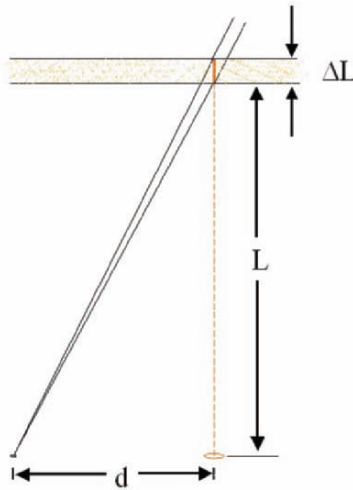
Figure 1.   Geometry of laser spot elongation, where L is the lower altitude of the sodium layer, ΔL is the thickness of the sodium layer, and d is the lateral separation between the laser and the subaperture. The horizontal scale is greatly exaggerated to demonstrate the geometry. The sodium layer is approximately 10 km thick, centered at 90 km altitude above sea level. An observatory is typically located 3-5 km above sea level. A laser guide star is generated by a thin cylinder of excited sodium atoms: ~50 cm diameter and ~10 km long. The extension of the sodium guide star return is ~2.5 arc sec for every 10 m that a subaperture is separated from the axis of laser projection.

Deanna Pennington and her colleagues at the Lawrence Livermore National Laboratory have been funded to develop a pulsed sodium laser with 1-3 μsec pulse length. Other groups are also pursuing development of

pulsed sodium laser guide stars. While the pulse travels through the sodium layer at the speed of light, it can easily be tracked on a CCD since the two-way path through a 10 km layer will take 60 µsec at the wavefront sensor. The combination of a pulsed laser and a specially designed CCD will eliminate the laser spot elongation problem as shown in Fig. 2.

To track the laser pulse in the focal plane of the subaperture of a Shack-Hartmann wavefront sensor, we will use rectangular arrays of square pixels, but will align the orientation of the pixel array within each subaperture so that charge transfer follows the direction of spot travel (see Fig. 3).
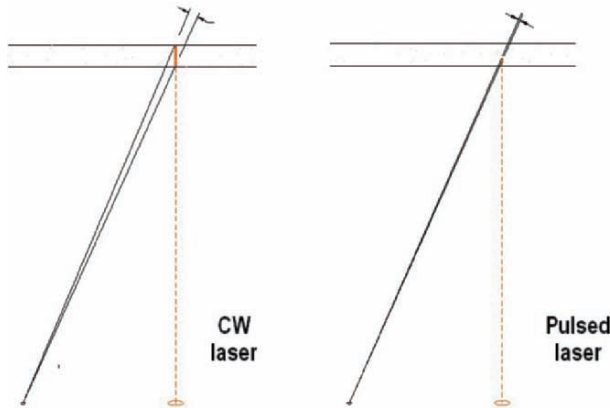
Figure 2. A pulsed laser will significantly reduce laser guide star spot elongation. The diagram on the left shows the effect of perspective elongation on a continuous wave (CW) laser return, while the diagram on the right shows the tenfold reduction in spot elongation achieved by using a short (1-3 µsec) pulse of laser light.
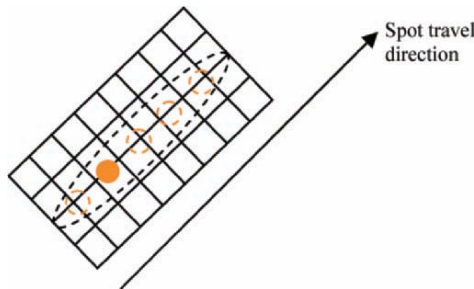
Figure 3. The image array pixels for one subaperture of a pulsed laser guide star Shack-Hartmann wavefront sensor. Pixels within a subaperture are aligned with the orientation of the laser pulse travel. The laser pulse will travel in a radial direction away from the location of laser projection. Thus, the pixels of each subaperture will need to be aligned to different directions. An image array of 4 by 8 pixels are shown as an example, but most likely we will use 4×16 pixels per subaperture to accommodate variations in the sodium layer that can be up to 20 km thick. The size of each pixel is not finalized, but a possible scale is 0.5 arc sec square, in which case the image area per subaperture will be 2×8 arc sec.

1.1   Top Level Requirements

In this project, we are designing test CCDs to verify the performance of a new JFET charge-sense amplifier and to prototype the CCD that will be used on an ELT. We have defined the CCD requirements in conjunction with the staff of the Thirty Meter Telescope (TMT) project. The requirements of any sodium LGS wavefront sensor are:

- High quantum efficiency at 589 nm
- Less than 3 electrons readout noise at all frame rates

The TMT has specified three additional system level requirements, listed in priority order:

1. Ensure the design can expand to 100×100 subapertures. There are about 8000 subapertures within the TMT telescope pupil. We will prototype the TMT device with a much smaller number of subapertures.
2. While a pulsed laser, with our CCD, is the ultimate solution to spot elongation, we should not base our entire design on the development of a pulsed laser. Our CCD design should be able to work with a CW laser.
3. The CCD should operate at frame rates up to 1500 Hz.

1.2   Detailed Requirements

Taking into account the optics of the TMT, the physics of the sodium layer and atmospheric seeing, and the practical aspects of CCD design, we have developed the following detailed requirements:

- The CCD should work with sodium layers that are up to 20 km thick. Assuming projection from behind the secondary of the TMT, the subapertures should be able to sense elongations of up to 7.5 arc sec at the edge of the 30 m telescope.
- To work with CW lasers, each subaperture should have a frame transfer region that is the same size as the image region.
- The CCD should have 0.5 arc sec pixels, so that there are 1.5 pixels for the typical FWHM expected at the TMT (0.7 arc sec).
- The width of the image area, orthogonal to the spot elongation, should be 2 arc sec.

- It is easiest to design every subaperture to be the same, so each subaperture should have 4×16 pixels in both the image and frame storage areas.

1.3   Recent Technology Developments Simplify Design

Our design benefits from new developments in CCD technology at MIT Lincoln Laboratory (MIT/LL):

- We will use a two-level-metal process based on MIT/LL's SOI (silicon-on-insulator) CMOS process. This will allow us to run clock and video lines over each other.
- We will add a second stage amplifier to the low noise first stage amplifier to allow the chip to read out at 1 MHz per port and faster, if so desired.
- We will place the two-stage amplifier within each subaperture region and multiplex the output signals on a video "column bus" to a column amplifier that will drive the signal off-chip.

These design features are similar to those used in CMOS sensors. These features will greatly simplify the CCD design and significantly improve sensor performance.

1.4   Subaperture Design

The requirements above are further detailed in the subaperture design:

- Each subaperture will have image and frame transfer areas.
- Each aperture will have a dump drain for rapid flushing of the image and frame storage areas.
- Both image and frame storage areas will have 3-phase clocks that are independently programmable as a function of annulus (distance of the subaperture from the laser).
- Two-stage amplifiers will be placed at each subaperture. The second stage has the drive capacity to run at 1 MHz and faster readout rates, and can be turned off when not in use to save power.
- The center of the image area in each subaperture lies on a square 2-D grid.
- The orientation of the pixels in each subaperture lies along a radial vector from the center of the pupil.

- All image array pixels in the entire chip are square and of the same size – corresponding to 0.5 arc sec on the sky.
- A summing well will be provided to allow noiseless binning.
- An output select amplifier will be used to multiplex the signal on the video out "column bus".

Combining these requirements, we have developed the subaperture design shown in Fig. 3.
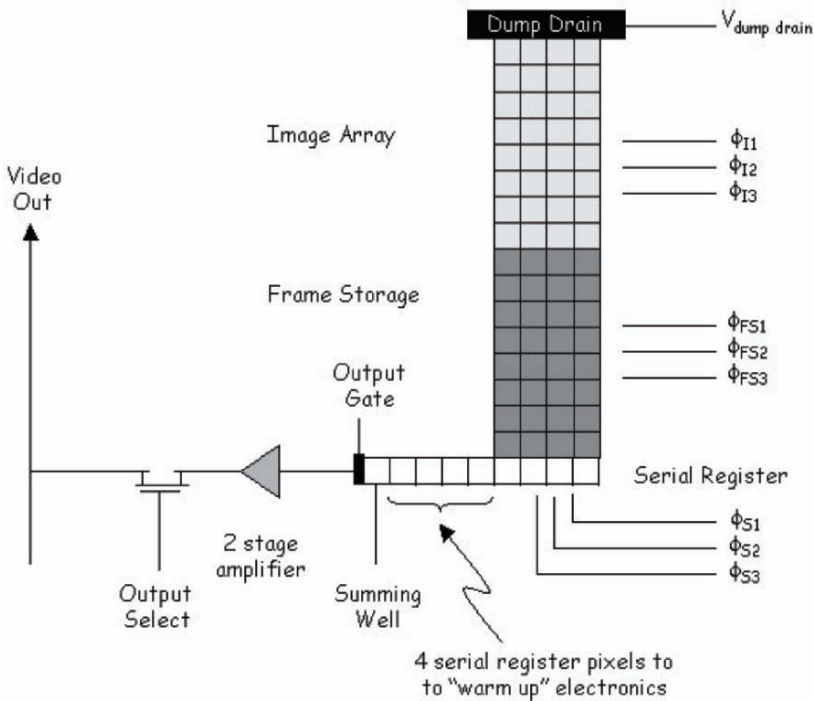
Figure 4. The subaperture design of the CCD we are developing to sense pulsed sodium laser guide stars on an ELT. Not shown in this schematic is the orientation of the pixels of each subaperture. Each subaperture will align the image array pixels with the direction of laser spot elongation, i.e. along the radial direction from the center of the telescope pupil (assuming laser projection from behind the secondary). The center of the image array of each subaperture will lie on a square 2-D grid. We expect that there will be 4×16 pixels in the image and frame storage arrays; only 4×8 pixels are shown in this figure. A computer simulation has been developed to model the performance of the wavefront sensor as a function of atmospheric seeing, pixel size, readout speed, readout noise and light level. This simulation is being used to optimize the number of pixels per subaperture and size of pixels projected on the sky (arc sec per pixel).

2.   NEXT STEPS IN THIS PROJECT

The first phase of this project is a test of a new type of readout amplifier that has been recently developed by MIT/LL. This amplifier is a planar JFET design with lower 1/f noise than achieved by standard buried-channel MOSFET amplifiers and higher conversion gain (responsivity). To test the planar JFET, MIT/LL has developed a standard AO pixel geometry CCD with 160×160 pixels in the image area, split frame transfer and 10 readout ports on each side of the array. These CCDs are being fabricated during calendar 2005, and based on the results of the phase 1 test chip, we will decide on the amplifier to use for the radial geometry LGS CCD.

In addition to being a test chip for the experimental planar JFET amplifier, the first phase CCD will provide greatly improved performance in the adaptive optics systems at the Keck Observatory. These CCDs are planned for a wavefront controller upgrade that is being funded by the Keck Foundation. The performance improvement is provided by:

- greatly enhanced sampling (8×8 pixels per subaperture, instead of the 2×2 pixels in the present system) which can be used for larger field of view and/or better sampling of the PSF,
- much lower noise (2-3e⁻ at 1 kHz frame rate) due to more and better readout amplifiers (20 advanced MOSFET or JFET amplifiers, instead of the 1995 era chip with four older generation MOSFET amplifiers),
- higher frame rate (2000 Hz by binning to 2×2 pixels per subaperture, or 1500 Hz with 4×4 pixels per subaperture – binned or central 4×4).

The design and layout of the phase 2 radial CCD will take place during late 2005 and early 2006, with the first CCDs fabricated in 2006. The major design challenge of the radial CCD will be the layout of the clock and video signal paths to clock the charge in the image areas as a function of annulus, since the laser spots will move at different rates as a function of distance from the projection axis. Complicated coding may also be required in the controller developed by SciMeasure Analytical Systems.

Testing of the LGS CCDs will be done by our project partners (SciMeasure, Lick Observatory), as well as the TMT project and the Laboratory for Adaptive Optics at the University of California, Santa Cruz.

After the test chip is validated, and the TMT is fully funded, we expect this technology will be used to make a full-scale wavefront sensor device for the TMT and other extremely large telescopes. For the final chip design, we expect that the signal wiring will be implemented differently. The best solution may be hybridization of the CCD to a CMOS readout circuit that routes clock lines and biases to each subaperture and multiplexes the video

signals off-chip. Ideally, correlated double sampling would be done within each subaperture so that each subaperture could operate at a relatively slow readout rates, almost guaranteeing less than 2 electrons noise at 2 kHz frame rate. This performance could be achieved with today's MOSFET amplifiers. With the improvements foreseen in the JFET amplifiers, single electron and possibly sub-electron noise is "just around the corner".

3.   SUMMARY

This project is developing a CCD that has a high probability of providing photon-noise limited performance of sodium laser guide star wavefront sensing for extremely large telescopes. To have this critical aspect of technology development be so well-developed nearly a decade before first light of the next generation telescope is remarkable.

This project has been able to combine the best of the technologies of CCDs and CMOS - utilizing the charge transfer and low noise single read features of CCDs and the multiplexing capabilities of CMOS design.

4.   ACKNOWLEDGEMENTS

THE MMT MEGACAM

Focal Plane Design and Performance

Brian McLeod, John Geary, Mark Ordway, Steven Amato, Maureen Conroy, and Thomas Gauron
Harvard-Smithsonian Center for Astrophysics

Abstract: *The MMT Megacam is a mosaic camera with 36 2048×4608 pixel CCDs, covering a 25'×25' field of view and mounted at the f/5 Cassegrain focus of the 6.5 m MMT. Megacam was commissioned in November 2003 and has been conducting scientific observations since then. In this paper we describe some of the design and performance characteristics of the Megacam focal plane.*

Key words: *MMT Megacam, mosaic cameras.*

1.   INTRODUCTION

The MMT Megacam is a mosaic camera that resides at the f/5 Cassegrain focus of the converted MMT telescope on Mt. Hopkins, Arizona, USA. The science focal plane is comprised of 36 2048×4608 pixel CCDs, model CCD42-90, manufactured by e2v technologies. An additional two CCDs of the same type are used for guiding and focus corrections. A three-element refractive corrector plus a field-flattener that serves as the entrance to the Megacam dewar provide a flat focal plane which is 35 arcmin in diameter. The Megacam science field of view is 25'×25' square. Megacam was commissioned in November 2003, and has been scientifically productive since then [1]. In this paper we describe some of the features relating to the focal plane and CCD operation. Further description of the shutter, filter assemblies, and electronics can be found in McLeod, et al. [2], and Geary & Amato [3]. An up-to-date comprehensive description of the instrument is in preparation.

2.   CCD MOUNTING

One of the challenges in building a large CCD mosaic is focusing the detectors simultaneously when cooled. The CCD42-90 package is ideally suited for this purpose. The CCD is epoxied to an Invar block. Three precision shims are attached to the bottom of this block, lapped by the manufacturer so they define a plane 14 mm from the CCD surface. We then faced the task of providing a flat surface on which to bolt them. We chose to mount them on a 6 mm thick Invar plate, suspended around the edge by six titanium flexures from a warm support ring (see Fig. 1). These flexures provide the necessary thermal isolation. The tilt and axial position of the cold plate was set by adjusting the location of the warm ring with a set of spring loaded screws. Once the location was set, precision spacers were machined and bolted into place. The mounted plate was measured to be flat to ~10μm P-V before any CCDs were installed. Note that our original design used a molybdenum plate, which provides much better thermal conductivity. However, this plate arrived from the vendor broken in two pieces, so we chose to replace it with the less brittle material.
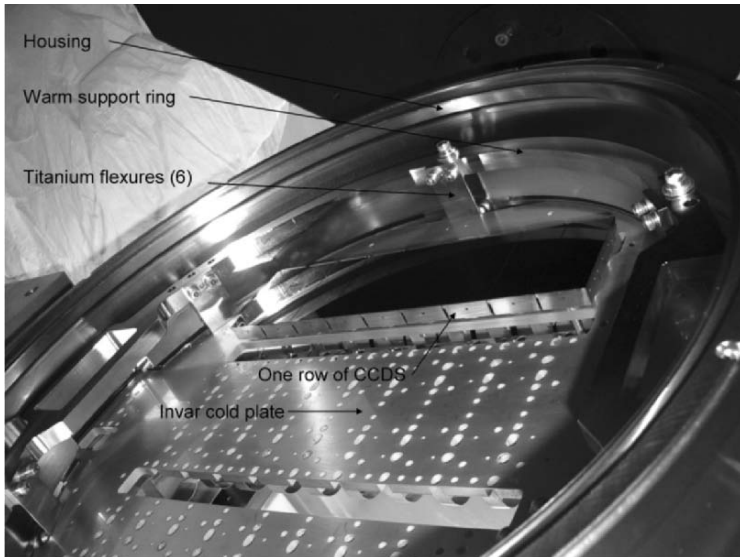
Figure 1. The Megacam cryostat.

To verify the focal plane flatness we relied on focus measurements on the sky. Our current measurements indicate that that there is roughly 100 μm P-V of deviation from the best focus across the plate. This is larger than expected, but has a completely negligible effect on the image quality. An

image taken in 0.4 arcsec seeing shows essentially no variation in FWHM across the entire Megacam field. There are no discontinuities from one CCD to the next, showing that the CCD packages were manufactured well.

3. THERMAL DESIGN

The thermal layout is shown in Fig. 2. The cooling path from the CCDs travels through the CCD42-90 package's precision shims to the Invar mounting plate. Copper straps connect the Invar plate to a set of four cold copper bars. These copper bars are connected to two IRLabs ND-14 dewars mounted on opposite sides of the central dewar. The copper straps were trimmed once after the initial cool down and the CCDs vary in temperature from -130ºC to -115ºC across the focal plane. A more uniform distribution could have been obtained with further iterations of trimming. The temperature of the CCDs can be stabilized using a set of heater resistors mounted on the back side of the Invar plate. The heaters are all wired in a single zone.

The total LN2 consumption of the Megacam is 40 W or 20 liter/day. The ND-14 dewars are filled from the bottom and thus contain a tube that extends inside the tank to prevent the liquid from running back out. We have chosen to make this tube extend 60% the height of the tank. This means we can only fill the tank 60% full, but are not concerned with the dumping of large quantities of LN2 when the telescope tips over. The hold time in this configuration is roughly 36 hours. The thermal load is dominated by radiation coupling from the dewar window to the CCDs. Several features minimize other sources of thermal loading. We have gold-plated the Invar plate, and copper straps and bars. The flex circuits connecting to the CCDs have two ground layers to provide electrical isolation between the AC and DC signals. Instead of a solid plane, these layers are laid out in a serpentine path to minimize the thermal conductivity. Titanium was chosen for the flexures because of its high stiffness and low thermal conductivity. The flexures contribute only 5 W of the 40 W load. Finally, we put radiation shields between the flex circuits and the Invar cold plate.
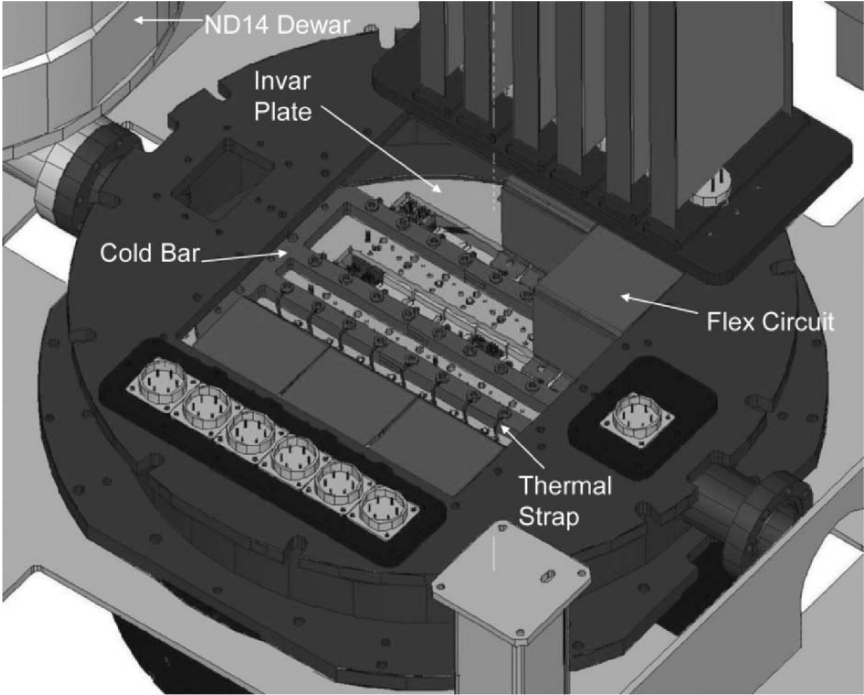
Figure 2. Megacam thermal connections. Note that thermal straps are actually 0.005" thick copper sheet rather than the wires shown. Radiation shields (not shown) are located under the horizontal part of the flex circuit.

4.   ELECTRONICS

4.1   Electronics Design

Herein we describe the CCD electronics. The data acquisition computer is currently a Sun Workstation running Solaris, but will soon be replaced with a rack mounted Linux server. The computer contains an EDT PCI-FOI interface card, which is connected to the CCD electronics via optical fiber. There are two electronics racks, dubbed master and slave, each of which drives one half of the focal plane. Each rack contains its own power supplies. The CCD electronics, which are 6U format, have the following cards: 1) one I/O card in the master rack which contains the EDT fiber interface, 2) one timing generator in the master rack, 3) 9 A/D cards in each rack, 4) 6 driver cards in each rack, and 5) one driver/receiver card in each

rack, which drives command and data signals between the two racks. These boards are connected together via a VME-style backplane. From the driver and A/D cards, connections to the CCDs pass via connectors on the backplane to preamplifier cards which are then connected to hermetic connectors via discrete wiring (see Fig. 3). These connections are the only discrete wiring in the system.
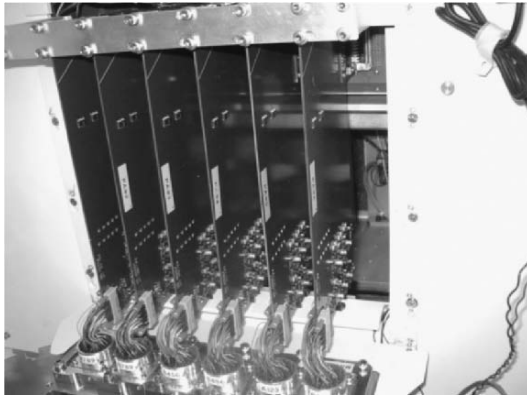
Figure 3. Preamp cards. The upper end of each card connects to the electronics rack backplane. The bottom end connects to the hermetic connectors. Each preamp card serves 3 CCDs.

Inside the cryostat, signals travel on custom flex circuits, 3 CCDs per flex (see Fig. 4). Each CCD electronics driver board drives three CCDs. To reduce the number of wires going into the cryostat, we generate the following signals in common for the three CCDs and split them on the flex circuit in the cryostat: S1L, S1R, S2L, S2R, S3, SW, DG, and OG1. The following are generated per CCD: P1, P2, P3, and RD. The following are generated per amplifier: OD, OG2, RG, and, obviously, OS. A thermistor on one of every three CCDs is wired out. The connection from the flex circuit to the CCDs is made by a ZIF connector (Tactic Electronics, model 40-H). Initially we had some continuity problems between the ZIF and the CCD because we did not solder the flex circuit to the ZIF with the two parts flush against each other. This allowed the pins inside the ZIF to move and not lock properly. This problem was completely resolved by resoldering all the ZIFs with the flex circuits flush against the connector body and each pin pulled fully out from the connector as it was soldered.

Figure 4.   Flex circuits inside the cryostat. In this figure one of the outer rows of CCDs is
              already installed and connected. Zener diodes are soldered onto the flex circuit to
              provide ESD protection.

4.2   Electronics Testing

Before we installed the CCDs we verified every signal at the ZIF
connector. To do this, we manufactured a set of dummy CCD packages that
we installed in the focal plane. Instead of a CCD on the top, they had a
circuit board which contained capacitors to mimic the CCD capacitance,
and a D-connector. These D-connectors were mated in turn to a test box
(see Fig. 5) which allowed us to dial up each of a CCD's signals onto an
oscilloscope in quick succession.   The test box also contained a video
generator circuit that fed the dummy CCD with an artificial signal which
then made its way up the signal chain. This testing system proved itself very
valuable and efficient in tracking down problems before any CCDs were
installed.

4.3   Electronics Performance

We experimented with operating the output amplifier of the CCD42-90 in
a state which lowers the gain by a factor of 5 and increases the full-well
capacity by a similar factor. This is accomplished by raising OG2 to roughly
12 V above the substrate voltage (see the manufacturer's data sheet).
Unfortunately, limitations in our electronics only permitted us to reach 10 V
above substrate. With this value of OG2 we realized a factor of 3 reduction
in gain, but also observed a noticeable amount of non-linearity. We are not
currently supporting this mode for observers.
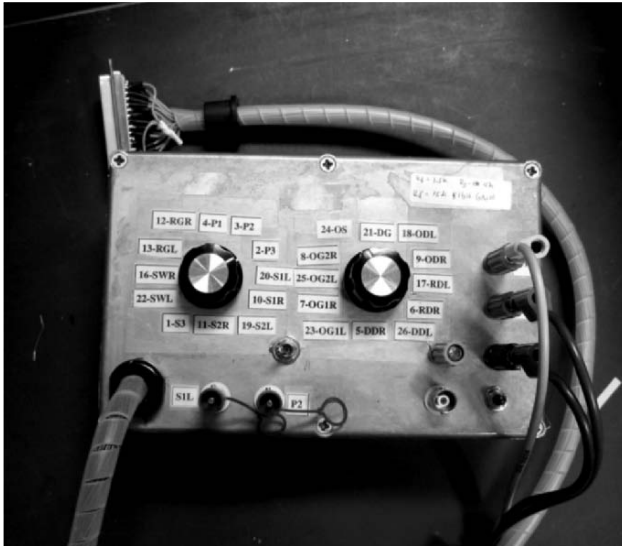
Figure 5. CCD test box.

In normal operation we use a gain of 3.5e⁻/ADU, and a 200kHz pixel clock. In this mode, we measure a read noise of 4-5e⁻. The output amplifier of the CCD saturates around 60,000 ADU, giving us nearly optimal dynamic range. We have measured no channel-to-channel crosstalk down to the 10^{-5} level.

5.   REFERENCES

[1] Hartman, J. D., Stanek, K. Z., Gaudi, B. S, Holman, M. J., and McLeod, B. A. 2005, AJ, in press.
[2] McLeod. B. A., Conroy, M., Gauron, T. M, Geary, J. C., and Ordway, M. 2000, Further Developments in Scientific Optical Imaging, M. B Denton (ed.), Royal Soc. Of Chemistry, p. 11.
[3] Geary, J. C. and Amato, S. 1998, SPIE, **3355**, 539.

Molly McLeod steers her father Brian to the right using an old motion control technology - pulling on Dad's ear.

Roger Smith (left), 2002 and 2005 Most Loquacious award winner, expands on the features of his sandals vis-à-vis Gert Finger.

THE OMEGACAM 16K×16K CCD DETECTOR SYSTEM FOR THE ESO VLT SURVEY TELESCOPE (VST)

Olaf Iwert[1], Dietrich Baade[1], Andrea Balestra[1], Andrea Baruffolo[2], Alessandro Bortolussi[1], Fabrice Christen[3], Claudio Cumani[1], Sebastian Deiries[1], Mark Downing[1], Christoph Geimer[1], Guy Hess[1], Joachim Hess[4], Koen Kuijken[5], Jean Louis Lizon[1], Harald Nicklas[6], Roland Reiss[1], Javier Reyes[1], Armin Silber[1]

[1]European Southern Observatory, [2]INAF – Astronomical Observatory of Padova, [3]Kapteyn Institut Groningen, [4]Universität-Sternwarte München, [5]Leiden Observatory, [6]Universität-Sternwarte Göttingen

Abstract: *A broad account of the main characteristics of the OmegaCAM 16K×16K detector system is given. Requirements and additional constraints, design strategy, implementation, and first laboratory results are described for the detector head, cooling system, temperature and shutter control. Synchronization of multiple controllers, and careful safety provisions are explained. The system has already passed most acceptance tests and will soon be ready for shipment. Commissioning in Chile is foreseen in 2006.*

Key words: *Mosaic, multiple controllers, synchronization, contamination, plasma cleaning, stray light, coating, cooling, Pt100, safety.*

1.   INTRODUCTION

A 16K×16K detector system was developed for the OmegaCAM instrument at the newly constructed ESO 2.5 m VLT Survey Telescope (VST, [1]), featuring a 1 degree × 1 degree field. While the OmegaCAM instrument was built by a multinational consortium [2], the 16K×16K OmegaCAM detector system was developed by ESO, but funded by the

consortium. The focal plane consists of an 8×4 mosaic of 2K×4K e2v CCDs with 15 μm pixels, accompanied by four 2K×4K CCDs on the periphery for the opto-mechanical control of the telescope.

2.   INTERFACES & MAIN REQUIREMENTS

Compared to the ESO 8K×8K Wide Field Imager on the ESO 2.2 m telescope, the 16K×16K OmegaCAM detector system is not a fourfold replica. The basically identical 2K×4K unit detectors must be butted on four sides. This leads to considerable complexity of the mechanics and electronics within the cryostat head. In spite of this, the two instruments and telescopes have comparable size, so the overall filling factor at the Cassegrain focus is very much larger, and the instrument reaches the weight and momentum limits of the VST. The very small back-focal distance forces the cryostat to be deeply imbedded in the instrument while the optical design requires, as an additional constraint, that the last field flattener element be the cryostat entrance window. Lack of space eliminates all possibilities of mounting the cooling system around the cryostat head and a customized CCD controller with the shortest cable length below.

The cryostat had to be equipped with a fully self-contained vibration-free cooling system providing about 65 W of cooling power to the CCD mosaic, while having a high degree of autonomy. Following standardization requirements, FIERA controllers had to be used in multiple synchronized configurations within the hierarchical VLT computer control system. Whereas the CCD mosaic was challenging in terms of data volume, the auxiliary CCDs presented additional challenges in the numerical functions to be accommodated in the design and implemented in coordinated real-time operation. The need for differential guiding required two fixed large field guider CCDs in the same focal plane, whereas for the telescope active optics control two large field CCDs were offset against the focal plane by +/-2 mm. As OmegaCAM is the only instrument on the VST, a maximum downtime of 1% has to be satisfied by the OmegaCAM detector system because switching to an alternative instrument is impossible.

In response to these challenges, the OmegaCAM system incorporates several novel ideas customized to the VST and OmegaCAM, but are nevertheless compliant with VLT standards.

3.   THE CCD DETECTORS

The unit detectors are e2v CCD44-82 devices, whose UV sensitivity was vital to this project. They have been further enhanced by means of an integrated Pt100 temperature sensor, which helped to homogenize e2v and ESO test data, as well as permitting direct control loops of the CCD temperature. A revised package has been designed in connection with a custom-made ZIF socket especially for the enhanced four side buttability and space constraints of the underlying flexrigid connector boards. All detectors have been tested and qualified individually on the ESO test bench against the contractual specifications. As the CCDs in each quadrant of the cryostat are partially sharing parallel and serial clocks, they have been selected by quadrant according to their channel potential. The cosmetic defects are well below the specified global defect budget. CCD flatness and accurate package metrology by e2v eased the integration into the mosaic without further space adaptations. More details about the individual testing procedures for these detectors can be found in Christen, et al. [3].

4.   THE DETECTOR HEAD

The cryostat head is the nexus of all interfaces of the detector system. Conflicting requirements from different domains had to be accommodated since the instrument was not developed within ESO. The outside space limitations from the surrounding instrument together with the circular field flattener imposed a high filling factor and several form factors onto the cryostat. Following the symmetrical focal plane layout with 'left, left, right, right' CCD output register location (per mosaic column), the mechanics of the detector head was designed with square housing. But the instrument housing (above) and the cooling system (below) are both circular. Symmetrical mechanical design, wherever possible, helped the modularity, the thermal properties of the CCD mosaic table, as well as the space, flexure and earthquake safety constraints.

Due to the limited access to all parts inside the cryostat and the fact that all mechanical and electronics parts had to be mounted without prior prototypes, the system was integrated without ultra-cleaning. After a few minor modifications the final cleaning was applied with strategies suitable to the types of materials in question. Owing to the sheer size of the parts conventional cleaning methods could not always be applied. Therefore, amongst others, plasma cleaning was employed in-situ in the cryostat vessel. [4]. Thereafter the clean cryostat head was integrated inside the clean room with the other cleaned component groups. Over some months, it was

gradually put into cryogenic and electrical operation. The CCD mosaic was stepwise populated and tested with different numbers and different grades (mechanical, engineering, science) of detectors to reduce the possible impact of mechanical and chemical risks, and electrical damage.

Key design drivers of the cryostat detector head were therefore symmetry, modularity, and easy access to all parts during all phases of assembly, integration, and testing. On the outside this principally concerned an easily separable but precisely tilt-aligned and centered optical field flattener with integrated defogging system at the top and the cooling system at the bottom with a special interface for the easy lift-off of the detector head. Inside the detector head, cryogenic connections and electronic boards had to be designed to ensure that they functioned independently and that each part inside the detector head can be integrated or disassembled at any time without removing others. Despite an external diameter of 70 cm, the overall alignment error budget required all critical parts to be machined with a precision of a few microns.

To ensure effective cooling of the CCD mosaic, all intermediate levels of cooling were largely abandoned. The aluminum-based CCD mosaic table was based on previous experience and the ability to distribute thermal energy quickly and uniformly. Following detailed calculations, this base plate was designed as a light-weight yet stiff 3D structure by integrating it into the outer frame. On the top it resembles Swiss cheese with mounting openings for CCDs and ZIF sockets, the bottom side interfaces with its cold fingers directly to the clamps that connect it both mechanically and thermally to the cooling system. After application of different machining technologies and many thermal cycles to release mechanical stress, a flatness of a few μm was achieved. It is held and thermally isolated by fiberglass parts which are dimensioned according to the flexure budget and earthquake safety. All fiberglass parts have been Parylene coated to reduce outgassing in the vacuum.

The integrated electronics have approximately 1400 contacts to the outside world and are designed to have low thermal conductivity, high modularity, and good signal separation. A 'four-in-one bus board' was developed to optimize both manufacturing cost and routing space. It is mounted in the bottom cavities of the mosaic table. Per quadrant (see Fig. 1), two of these boards support eight CCDs and interface with one flexrigid interface board per signal group to a total of three vacuum connectors with 128 pins each. The connections for each of the four auxiliary CCDs are fed through this board set to the nearest quadrant. The symmetry of the focal plane in connection with the symmetry of the mechanics permits the electronics of two quadrants to be identical. All quadrants link to identical outside cabling for testability and ease of cabling. A total of 28 flexrigid

boards have been designed and hand routed in complex 3 D shapes for the cryostat system. The use of glue-free materials was mandatory to avoid contamination. Figure 2 shows a bottom view of the cryostat head, while Fig. 3 shows the 16K×16K mosaic.
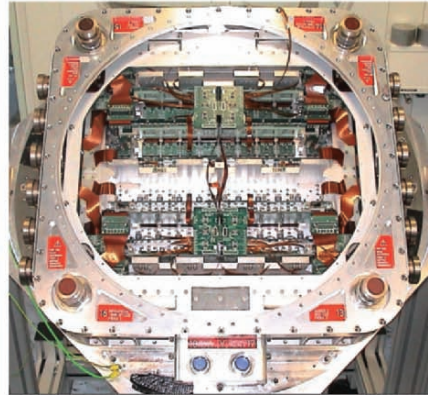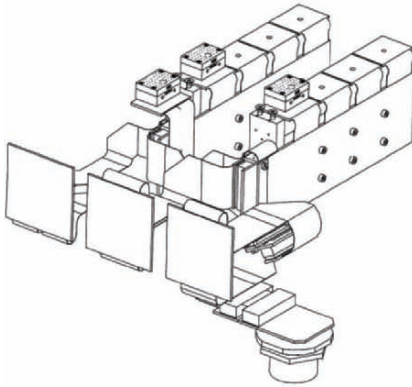
Figure 1. One quadrant of cryostat electronics.   *Figure 2.* Bottom view of cryostat head.

All parts in the light entrance between auxiliary CCDs and the CCD mosaic were blackened with Keplacoating to avoid contamination and straylight (see Fig. 4). An actively cooled shield acts as an ice barrier. The shiny bond wires of the CCDs were masked with both cold and warm shields. After stepwise qualification of all alignment-critical parts, the CCD mosaic was laser-triangulated at -120 C (and through a special dewar entrance window without optical power); a flatness value of 25 μ (pp) had been achieved.
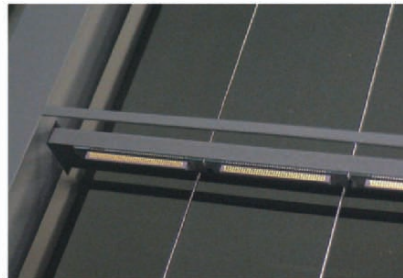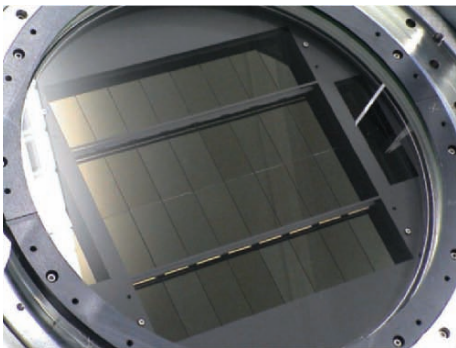
Figure 3. The 16K×16K mosaic.   *Figure 4.* Close-up of baffling.

5.   COOLING AND TEMPERATURE CONTROL

According to model calculations a heat load of 65 W had to be accommodated by the cooling system, which is mounted below the CCD detector head. As no options for external compressors or cooling lines through the telescope cable wrap existed, a self contained LN2-based system was developed (see Figures 5 and 6). It utilizes the maximum cooling power of liquid nitrogen through the combination of an integrated 40 liter LN2 tank, combined with the main top heat exchanger operated in continuous flow mode by the cryostat cooling controller. The top heat exchanger is coupled by means of electrically isolated silver foils to cooling clamps which link directly to the bottom cooling fingers of the CCD mosaic table in the CCD detector head. This way the weight of the cooling system (about 120 kg) could be decoupled from the flexure of the mosaic table. This also minimized vibration and allowed us to overcome position-angle dependence of conventional bath cryostat systems at Cassegrain focus. As the cooling clamps can be opened and closed through the vacuum vessel, the cooling connections are easily separable before the detector head is mounted or dismounted.

Figure 5. Cooling system top interface.   *Figure 6.* Detector head bottom interface.
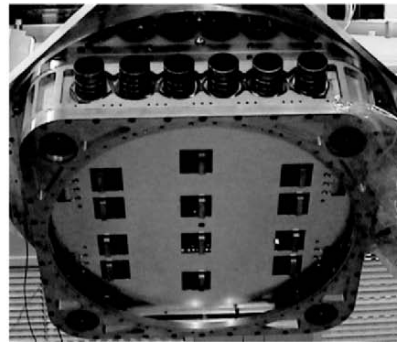
During laboratory operation, very good margins have been obtained to reach the necessary CCD operating temperature of -120 ºC and a hold time of about 40 hrs. For the cryogenic and vacuum system control, the cooling system has integrated (heated) sensors for level sensing at top and bottom, a heat-able charcoal sorption pump, and two fully redundant sets of temperature and vacuum sensors. Further details about the cooling system can be found in Lizon, et al. [5].

100 temperature sensors with optional permanent logging were integrated into the cryostat at intermediate levels. These were implemented as

diagnostics of the new construction of both the detector head and the cooling system (considering all integrated electronics). They will prove very useful for checking the cooling clamp interface after reintegrating the detector head and cooling system in Chile.

Pt100 boards with standardized glue-free mechanical mounting interface have been developed for universal use. They interface by means of an interconnection kit in different lengths to four multiplexers within the head. Heat dissipation and wiring are minimized.

The Pt100 boards are connected to PULPO2 [6], responsible for reading, logging and alarm signaling of up to 125 temperature and vacuum sensors. Furthermore PULPO2 operates four independent PID heater control loops with freely programmable control sensor assignments. In full CCD mosaic operation a homogeneity of 2 K (pp) was achieved across the focal plane.

6. COORDINATION AND SYNCHRONIZATION OF MULTIPLE CCD CONTROLLERS

Three FIERA CCD controllers are used to satisfy all operational needs. Two identical FIERA systems were assigned to the mosaic and half of each supports the maximum number of 4×4 video channels. Together with their associated UltraSparc control computers, they form two nearly independent systems. However, due to the sharing of parallel and serial clocks, they had to be synchronized in soft- and hardware for wipe, integrate, and read functions of the mosaic CCDs. A jitter of one sequencer tick (25 ns) would already lead to a jump in bias level of several ADUs. With the exception of the individual CCD voltages, the software on these two controllers is identical (also with respect to image assembly). FIERA1 operates as the master controller, which triggers the slave controller FIERA2 and also communicates via PULPO2 with the shutter controller [7].

FIERA3 is defined as software camera #1 for the two guider CCDs and as software camera #2 for the two image analyzers. Synchronization to the master controller is only needed for the shutter opening and the full-frame acquisition images of each auxiliary CCD. After the automatic or interactive selection of the guide stars and the setting of the respective readout windows and exposure times on the auxiliary CCDs, the operation sequence for a scientific exposure is as follows: Wipe both mosaic halves synchronously (FIERA ##1 & 2), set to synchronized integration, open shutter. Start staggered continuous rapid readout loops with the two guiders (software camera #1 on FIERA #3). The same is true for the image analyzer CCDs but somewhat longer exposure times (software camera #2 on FIERA #3). When camera #2 on FIERA3 requires readout, operation of camera #1 is suspended. Both loops stop when the integration time on the mosaic is

finished, the shutter is closed, and the subsequent synchronized readout of the two mosaic halves takes place. The data of the two half images are assembled, sent to the instrument workstation, combined, displayed, archived, and made available for automatic (pipeline) or interactive analysis. The full mosaic is read out in 30s with a read noise of 5e⁻. The overhead for file merging and storage adds 15s.

7.   SAFETY & EMERGENCY FEATURES

During the daily nitrogen refilling operation, the cryostat cooling controller is responsible for a number of automatic, safety relevant actions, such as triggering the interlock of the telescope motion and to open and close the relevant valves for the tanking process. Likewise PULPO2 takes preventive actions for the safety of the detector mosaic. For example, it heats to a preset temperature to avoid uncontrolled warm-up and subsequent contamination in the case of operational errors or problems with the cooling or vacuum systems. In the case of vacuum loss an on-board emergency pump with associated electromagnetic valve is activated. Both subsystems have user definable parameters in their firmware for their respective alarms and emergency actions. They link to the Central Alarm System (CAS), which notifies maintenance personnel via wireless pagers. Power cuts and overheating of the FIERA controllers are signaled in the same way. Furthermore, the instrument control software can be configured for each of these parameters to issue a software warning on the instrument control before the value of a hardware CAS alarm is triggered. Continuous logging of all essential parameters on the instrument workstation level permits trend monitoring and fault analysis.

8.   REFERENCES

[1] Cappacioli, M., et al., 2005, The ESO Messenger, No. 120, p. 10.
[2] Kuijken, K., et al., 2004, Proc. SPIE, vol. **5492**, p. 484.
[3] Christen, F., et al., 2004, Kluwer, ASSL, vol. **300**, p. 485.
[4] Deiries, S., et al., 2005, *Plasma Cleaning, A New Method of Ultra-Cleaning Detector Cryostats,* these proceedings.
[5] Lizon, J-L., Silber, A., 2005, these proceedings.
[6] Geimer, C., et al., 2005, *Keeping Control: PULPO 2*, these proceedings.
[7] Reif, K., et al., 2005, *Bonn Shutters for the Largest Mosaic Cameras*, these proceedings.

CCD MOSAICS AT CTIO AND SOAR

Ricardo E. Schmidt
Cerro Tololo Inter-American Observatory (CTIO)

Abstract: *Four Mosaics based on different 2K×4K CCDs with 2 output amplifiers and 15 μm pixels are briefly reviewed. An 8K×8K mosaic is in use on the 4 m Blanco telescope. Two 4K×4K mini-mosaics are included in instruments for the SOAR 4.1 m telescope. A 62 CCD mosaic will be used by the Dark Energy Camera project, which should be available at the 4 m Blanco telescope by 2009.*

Key words: *CCD mosaic, p-channel CCD, high resistivity CCD.*

1.   THE INSTRUMENTS

1.1   4 m BLANCO Telescope: 8K×8K Mosaic-2 Imager

8 three-side buttable SITe002A CCDs are used by Mosaic-2 at the prime focus to cover a FOV of 36'×36' at a scale of 0.27 arcseconds per pixel. Both the shutter and 14-filter track, which runs in a loop over the dewar top, are pneumatically actuated. Mosaic-2 has been in regular use for the past 6 years and is typically scheduled 120 nights per year. Mosaic-2, a copy of KPNO's Mosaic-1, is read out through 16 channels (Mosaic-1 uses 8 channels to read out), 4 per each of four Arcon controllers. One Mosaic image represents 140 MB of data.

1.2   SOAR IMAGER (SOI): 4K×4K Mini-Mosaic of e2v CCDs

On the SOAR 4.1 m telescope a mini-mosaic of two rectangular CCD44-82 detectors has a FOV of 5.5'×5.5', covering the isokinetic patch for the telescope, at a scale of 0.08"/pixel. SOI [1] includes twin filter wheels, with five 4-inch filter positions each, and a fast linear shutter. This imager began operating in 2004 and has been used as the commissioning instrument for the telescope. A LabVIEW based GUI called ArcVIEW plus a SDSU-2 controller are used with SOI.

1.3   SOAR Goodman Spectrograph (P.I.: Chris Clemens, UNC)

The SOAR Goodman Spectrograph has long-slit & multi-slit capabilities, with a 4K×4K mini-mosaic that covers an effective 7.2' in diameter FOV at a scale of 0.15"/pix. The instrument is being commissioned, and observing is foreseen in 2005. The Goodman Spectrograph [2] has an articulated camera to optimize the use of virtual phase holographic gratings. The camera can move in an angle of $0°$ to $90°$ with respect to the collimator. This movement requires a 1.2 m cable to the SDSU-2 controller. This system is optimized for the UV/Blue.

1.4   The Dark Energy Camera (DECam) on the 4 m Blanco Telescope

The Dark Energy Camera (DECam) [3] is a collaboration led by Fermilab to build a 62 CCD Imager. DECam observing is scheduled to start in 2009. Entirely replacing the existing PF assembly of the 4 m Blanco telescope, this 62 CCD Imager (see Fig. 1) spans a FOV which is 2.2 degrees or 448 mm in diameter, at a scale of 0.27"/pix . DECam will be used for a 5000 sq. deg. survey to constrain the dark energy parameter *w* to within 5%. Dark energy will be probed by way of galaxy cluster counting, weak gravitational lensing, spatial clustering of galaxies and type Ia Supernovae distances.
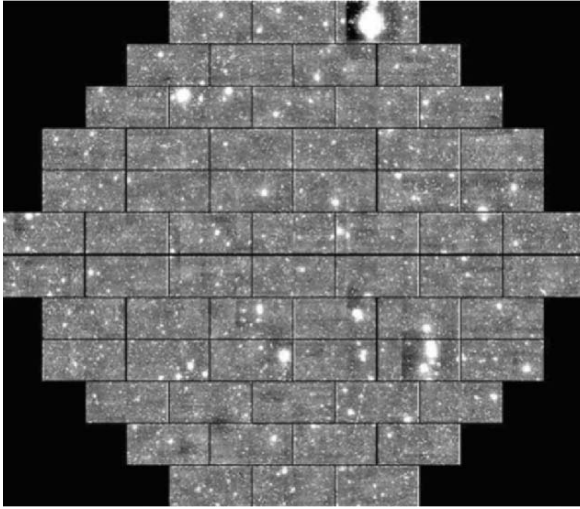
Figure 1. A simulated image of the 62 CCDs in the DECam focal plane.

2. THE FOCAL PLANES

2.1 The 4K×4K Mini-Mosaics for the 4.1 m SOAR Telescope

2.1.1 e2v CCD44-82s in the 4K×4K SOAR Imager (SOI)

CCD44-82s (see Fig. 2) are 3-edge buttable and have an extra FET output buffer, hence 2 output drain voltages are used: V_JD and V_OD. This CCD has two output gates and also a dump drain. A 4×4 binned image is read out in 6 sec (@ RON of $3.8e^-$). At the telescope, images show fringing of < 2% in the I band. No after- images are seen.

2.1.2 MIT/LL CCID20s in the 4K×4K Mosaic for the Goodman Spectrograph

The CCID20 (see Fig. 2) uses high-resistivity bulk silicon thinned to 40 μm with an associated red QE boost and less fringing due to a greater thickness. This 3-side buttable CCD is back-illuminated but not MPP. For

the CCID20 we get a lowest noise of 1.9e⁻ at a conversion gain of 0.4e⁻ /ADU. We have treated the CCID20 with dry air and heat to solve cosmetic problems and attempt to increase QE.

The CCID20 requires sequencing of reset and drain voltages on power up and power down. The output drain should be the last to be turned on and the first to be turned off.
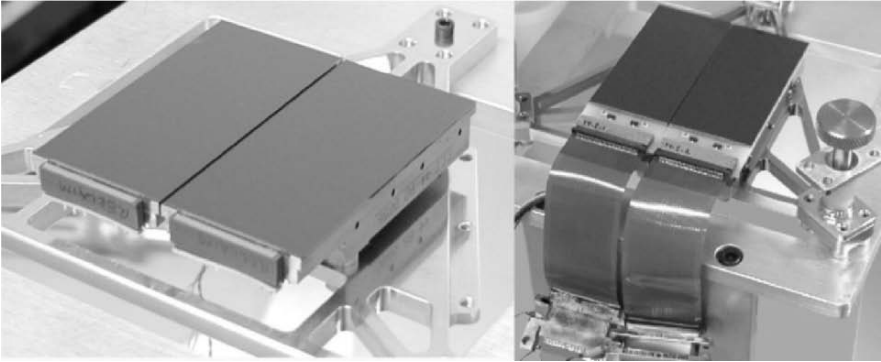
Figure 2. Two SOAR mini-mosaics, *(left)* 2 CCD44-82s and at *(right)* 2 CCID20s.

2.2   Mosaics at the 4 m Blanco Telescope Prime Focus

2.2.1   SITe002A Detectors in Mosaic-2

The peak QE for SITe002As is 85% at 600 nm and the CCDs run at -95°C. Fringing is less than 5% in the I band. There is some low level crosstalk, which is successfully removed. There are no after-images. A Mosaic-2 image is shown in Fig. 3.

2.2.2   LBNL 2K × 4K CCDs for DECam

To achieve the requisite depth in the redder passbands within the available survey time, LBNL high-resistivity, back illuminated CCDs [4] with a QE >50% at 1000 nm will be used. Using a buried p-channel, these chips use clock and bias voltages that are reversed in sign from conventional CCDs. These CCDs use a backside bias voltage to fully deplete the substrate and to control the PSF. Fermilab will package the CCDs.

Monsoon will control the 62 science CCDs. The plan is to share the same clock rails between groups of 3 CCDs. The CCD temperature will be read for each CCD and used for QE corrections.
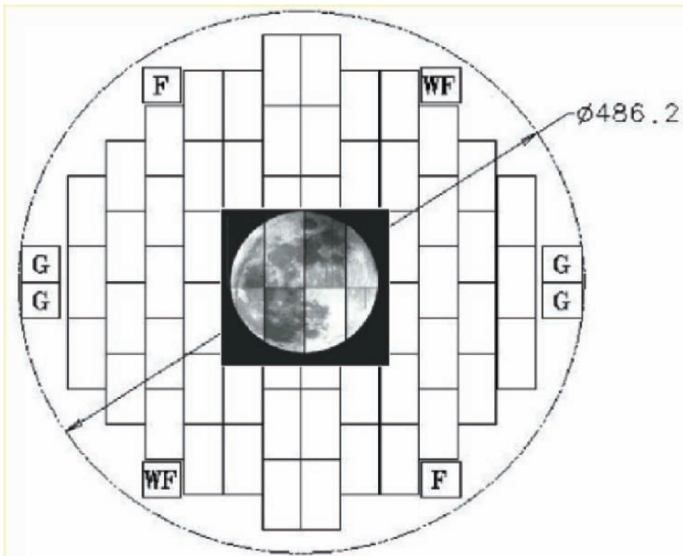
Figure 3. A Mosaic-2 image shown at the center of the DECam field. At the edges special CCDs for Guiding (G), Focus (F) and Wavefront Sensing (WF) are shown.

3. SYSTEM SIMILARITIES AND DIFFERENCES

3.1 Detectors

SITe002A and CCD44-82 are thinned, n-channel CCDs. The CCID20 uses an n-channel high-resistivity CCD (40 microns thick). The LBNL 2K×4K CCD is a p-channel, high-resistivity device (250 microns thick). Their responsivities and typical readout noises (RON) for gains in the 2.0 e$^-$/ADU to 2.4 e$^-$/ADU range are given in Table 1. The LBNL readout noise quoted is the minimal requirement.

Table 1. Responsivities and RON values.

	SIT002A	CCD44-82	CCID20	LBNL 2K×4K
responsivity	1.8 μV / e$^-$	5 μV /e$^-$	10 μV /e$^-$	3 μV /e$^-$
RON	5.9 e$^-$	3.8 e$^-$	3.1 e$^-$	< 10 e$^-$

3.2   Controllers, Controller Cooling, Dewar Connections and Front Ends

SDSU-2s are used for the SOI and the Goodman Spectrograph. These SDSU-2s use a liquid coolant and are connected via cables to the dewar (0.5 m for SOI, 1.2 m for Goodman). Each SDSU-2 uses 2 video boards, with 2 channels per board. Mosaic-2 uses 4 Arcon controllers and DECam will use 4 Monsoon controllers. Arcon uses passive cooling, whereas Monsoon will reside inside cooled racks. Arcon connects directly to the dewar, while Monsoon requires a 0.7 m cable. Each Arcon includes a 4 channel video board. Monsoons for DECam will use three 12-channel video boards each. Mosaic-2 is the only system that uses DC-coupled input signals (Arcon).

3.3   Inside the Dewar (wiring, electronics, cooling, mounts, heaters)

For CCD connections all systems except DECam use discrete Teflon insulated wires (typically 0.003" to 0.010" Cu and Constantan wires). DECam will require flex cables. Thus far none of our CCD systems have ever used electronics inside the dewar, however, DECam may require preamplifiers inside the dewar. Mosaic-2 and SOI use classical LN2 cooling for their CCDs whereas the Goodman Spectrograph uses a Cryotiger and DECam will use a cryocooler. All systems except SOI, which uses Al, use Invar for their chip mount baseplate. For heaters, Mosaic-2 uses power resistors embedded in the Invar chip mount, SOI uses a Nickel-Chromium wire embedded via a groove in the Al chip mount and Goodman uses 8 FETs on a PCB attached to the Invar chip mount. DECam will use power resistors for heaters.

3.4   Typical Times for each System

Typical dwell, pixel and frame readout times are given in Table 2.

Table 2. Typical times for the different systems.

	Mosaic-2	SOI	Goodman	DECam
Dwell time [us]	3.6	1	1	1
Pixel time [us]	14	3.7	3.7	4
Frame time [s]	100	20	20	20

3.5 Typical Bias Voltages for each CCD Type

Typical values for output drain, reset drain and output gates are shown in Table 3. The CCD44-82 is a special case; it has a second ouput gate running one volt more than the V_OG shown in the table. The CCD44-82 also needs a bias of 26V for the FET output drain.

Table 3. Examples of typical bias voltages.

	SITe002A	CCD44-82	CCID20	LBNL 2K×4K
V_OD	25 V	23.2 V	18.5 V	-22 V
V_RD	14.3 V	10V	12.7 V	-12.5 V
V_OG	2 V	-4.7V	-1 V	2.2. V

3.6 Signal Sharing per System

Mosaic-2 shares the rails for all horizontal clocks and SW per horizontal register half, while LG_A and LG_B are tied together. SOI per each CCD44-82 has RG_L and RG_R tied together, and also ties the dump drain to one of the two Reset Drains (=RD_L). The Goodman Spectrograph connected both reset gates on each CCD. The respective phases for upper and lower parallel clocks are also tied together. DECam plans to share clock rails per groups of 3 CCDs for the LBNL.

3.7 Some Issues with the CCDs

The long readout time for Mosaic-2 is principally a result of slow parallel clocking required by the SITe002A CCDs. The CCD44-82 can experience output amplifier glow if V_OD is driven too high. With the 18.5 V in use we see the onset of this glow. Our CCID20s required special treatment with dry air plus heat to improve their QE and cosmetics. The current maximum QE is 68% at 500 nm and we are working to improve it. To obtain good PSF LBNL CCDs require a backside bias, which can be as high as +80 V. A special erasure procedure is needed to solve image persistence problems.

4. REFERENCES

[1] Schmidt, R., 2002, Scientific Detectors for Astronomy, Kluwer A.P., p. 247.
[2] Clemens, C., Crain, A., Anderson R., 2004, SPIE Volume **5492**, Glasgow, p. 331.
[3] http://www.darkenergysurvey.org
[4] Holland, S., 2002, Scientific Detectors for Astronomy, Kluwer A.P., p. 95.

Ricardo Schmidt and his wife Isabel Mujica celebrate the arrival of their lost luggage by wearing their favorite striped shirts.

The CCD-CMOS "Spaghetti Western" roundtable. (left to right) James Beletic, Peter Pool, Paul Jorden, John Philips, Peter Love, Paul Vu, Alan Hoffman, Markus Loose, Vyshi Suntharalingam, Morley Blouke, Dick Bredthauer and Barry Burke. The newest member of the manufacturer circle appears to not have fully integrated.

FOCAL PLANE DETECTORS FOR THE DARK ENERGY SURVEY

Juan Estrada and Ricardo E. Schmidt
1Fermi National Accelerator Laboratory, 2 Cerro Tololo Inter-American Observatory (CTIO)

Abstract: *The scientific requirements of the focal plane array for the Dark Energy Survey (DES) are reviewed. The status and plans for CCD testing and characterization for this project are presented.*

Key words: *Dark Energy Survey (DES), CCD, mosaic.*

1. INTRODUCTION TO DARK ENERGY SURVEY (DES)

The DES collaboration [1] was established with the objective of developing a new instrument for the Blanco 4 m telescope at Cerro Tololo Inter-American Observatory (CTIO) [2] in partnership with NOAO. The project consists of building a 520 megapixel CCD camera (DECam) and wide field optical corrector for the prime focus. The DES collaboration will utilize this instrument for surveying, but the new camera will be available to other Blanco users for their own objectives. A schematic drawing of DECam is shown in Fig. 1.

The principal scientific goal for DES is the measurement of *w,* the dark energy equation of state, to a precision of order $\delta w \leq 5\%$ using four separate techniques: cluster survey, weak lensing, galaxy angular power spectra and supernovae.

1.1   Cluster Survey

In this method we measure the cluster redshift distribution and cluster power spectrum. Cluster mass estimates are measured indirectly using the bias of the cluster power spectrum, and also directly from SZE, weak lensing, and cluster galaxy observables. To accomplish our goals, we must be able to locate and measure the redshift of clusters of galaxies to $z \approx 1$, because this is the expected extent of the coordinated South Pole Telescope [3] SZE (Sunyaev-Zel'dovich Effect) cluster survey.
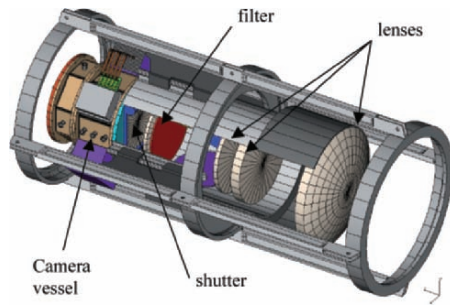
Figure 1. Proposed layout of the prime focus cage with the 2.1 degree corrector. Light comes in from the right. Camera vessel and 2 data acquisition electronics are shown at left.

1.2   Weak Lensing

The weak lensing of background galaxies by foreground mass sheets, correlated with itself (shear-shear correlations) or with foreground galaxies (sheargalaxy correlations) is sensitive to dark energy as a standard ruler and growth function probes. The DES instrument must be able to measure the weak lensing signal from large scale structure in several redshift bins with small and stable instrumental point spread functions. Large solid angle is required to probe the shear field over the largest possible range in physical scales.

1.3   Galaxy Angular Power Spectra

Measurement of the angular power spectra of galaxies in several redshift bins can also put constraints on w, because it is a standard ruler probe. To accomplish this measurement, we must have a stable photometric

calibration, cover a large solid angle to probe a wide range of physical scales, and have faint limiting magnitudes to increase our sample size and probe to redshifts beyond $z\sim1$.

1.4 Supernovae

The apparent magnitude of Type Ia supernovae provides a standard candle luminosity distance measurement. The DES Instrument will be used to measure light curves of more than 1900 supernovae out to $z = 0.8$. The observations must cover a moderately large solid angle repeatedly to obtain lightcurves of the SN. These SN observations must be taken in multiple (at least three) bandpasses to provide object colors, both for reddening measurements and color-based SN-type discrimination. Excellent red response is necessary to obtain adequate signal for higher redshift SN lightcurves. Detailed knowledge of the system passbands as a function of wavelength is required for accurate k correction calculations.

2. THE DES FOCAL PLANE

Our survey goals require that we have high Quantum Efficiency (QE) at the near infrared wavelength of ~1000 nm. Standard astronomical CCDs typically have a QE at this wavelength of 5-10% because the charge collection region is 10-20 μm thick and the total device thickness is often less than 50 μm. The absorption length in silicon is 205 μm at a wavelength of 1000 nm, and thus thick sensors are required for a better QE at that wavelength. Photons at near infrared wavelengths will simply pass through 50 μm of silicon. LBNL has developed thick, fully depleted, back illuminated CCDs 200-300 μm thick [4,5]. For DES, we will use 250 μm LBNL CCDs. The QE of LBNL CCDs is shown in Fig. 2 compared with a standard thinned astronomical CCD and a deep-depleted CCD. Table I includes a list of the requirements for the DES CCDs compared with the performance of the thick LBNL devices. Figure 3 shows our reference design for the focal plane layout with the 2K×4K 4-side buttable LBNL CCDs. It contains 62 CCDs and a total tile active area of 3.0 deg^2.
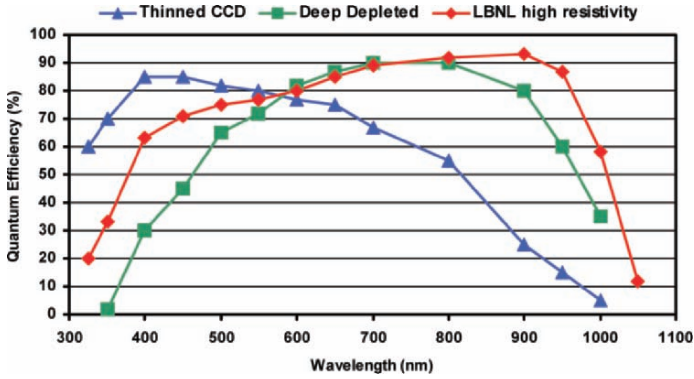
Figure 2. Quantum efficiency as a function of wavelength for different types of CCDs
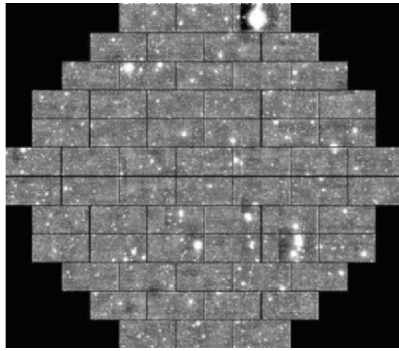
Figure 3. A simulated image of the 62 CCDs in the DECam focal plane. Each CCD is a
2K×4K device and the total focal plane has a diameter of 50 cm.

Table I. CCD requirements for DECam compared with the performance for LBNL devices.

	LBNL CCD	**DECam requirements**
Pixel array	2048 × 4096 pixels	2048 × 4096 pixels
Pixel size	15 µm × 15 µm	15 µm × 15 µm (nominal)
<QE (400-700 nm)>	~70%	>60%
<QE (700-900 nm)>	~90%	>80%
<QE (900-1000 nm)>	~60%	>50% at 1000 nm
Full well capacity	170,000 e$^-$	>130,000 e$^-$
Dark current	2 e$^-$/hr/pixel at −150ºC	<~25 e$^-$/hr/pixel
Persistence	Erase mechanism	Erase mechanism
Read noise	7 e$^-$ at 250 kpixel/s	<10 e$^-$
ChargeTransfer Inefficiency	<10^{-6}	<10^{-5}
Charge diffusion	8 µm	<10 µm
Linearity	Better than 1%	1%

3. CCD TESTING AND CHARACTERIZATION AT FERMILAB

Every device to be installed in the DES focal plane will first be characterized in the CCD testing facility being built at Fermi National Accelerator Laboratory (Fermilab). Testing and grading includes an initial phase in which CCDs are exercised and characterized, and a production phase in which the production devices will be characterized to determine which should populate the focal plane. This initial phase is important to develop the infrastructure and experience so that the production phase may begin when devices first become available. The production phase will be designed to test up to 20 devices per month, with some capacity to absorb bursts of higher delivery rates. Packaging of the devices for the focal plane will also be performed at Fermilab.

The testing and grading task is required to make a comparison of the test results against the device requirements to insure that each CCD device installed meets the minimum requirements for use in DES. This is also required to determine grade, so that the highest quality devices will be used.

The electronics chosen for the readout of the focal plane devices in DES will be based on the Monsoon standard [6]. These readout electronics will also be used for CCD testing and characterization. DES is currently adapting the Monsoon readout system to accommodate LBNL devices. The electronics engineering group at DES is designing a 12-channel acquisition board for Monsoon that is required for the number of channels in the DES focal plane.

A prototype test stand exists at Fermilab, and has successfully operated LBNL CCDs. This testing station provides a variety of measurement conditions. CCDs are installed in a dewar (see Fig. 5) that is cooled to -100ºC, and controlled by a PID temperature controller (temperature fluctuations are below 0.2 K). An automated mechanical shutter is used for the control of the exposure time. A broadband light source is used for illuminating CCDs inside the dewar, and a flat field is obtained by using an 6' integrating sphere. A calibrated photo-diode provides an absolute intensity measurement of the light. Exposure of the CCD to Fe^{55} can be used for charge transfer efficiency and gain measurements. Narrow band (10 nm) filters are used to select a wavelength for illumination onto the device to measure quantum efficiency. The production testing facility will also include the monochromator for greater wavelength selecting capabilities. The existing testing station is shown in Fig. 4. The testing facility is located in a humidity controlled room equipped with ESD safety tools to reduce the risk of damaging a CCD. In the production phase we expect to have three of these testing stations.
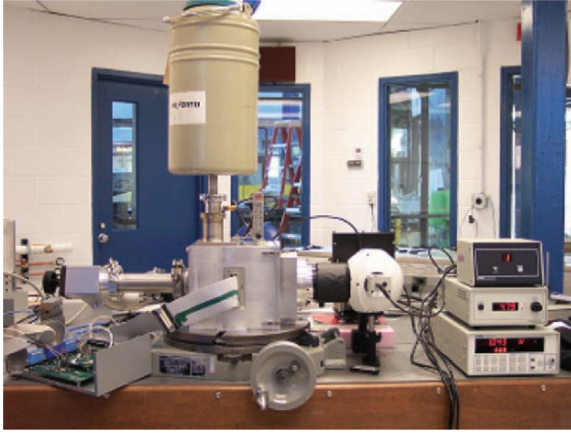
Figure 4. Existing prototype CCD testing station at Fermilab. The aluminum dewar is mounted on a rotating table for easy access to the removable front cover and the CCD. A 6' integrating sphere is used for illumination, and the light level is controlled in another output of the same sphere using a photodiode. Mechanical shutter and filter wheel allow for controlling exposure time and wavelength of the illumination. The container mounted in the chimney of the dewar is filled with LN2 and allows 15 hours of stable operation for 15 hours.
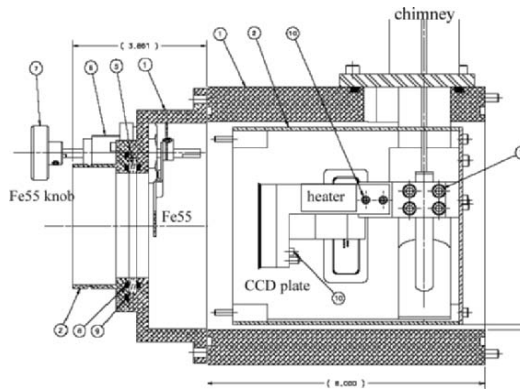
Figure 5. CCD testing dewar. This dewar is cooled with LN2 from the chimney. A fused silica window in the front (see left side of figure) allows for the illumination of the device. To avoid condensation in the CCD, vacuum is pumped inside the dewar. A 10 watt heater is installed in the cold finger connecting the chimney (fill tube) to the CCD to provide the heat needed for CCD temperature stability. An Fe55 source is mounted on the inside of the from cover of the dewar, to allow for X-ray exposures of the CCD. The source can be moved out of the way (Fe55 knob) and parked in a shielded garage when not in use.
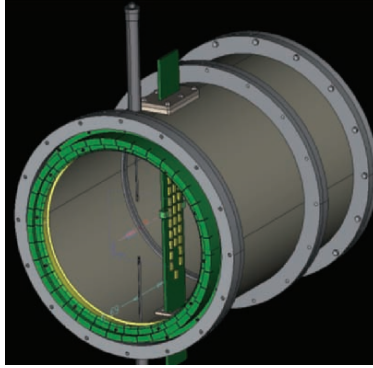
Figure 6. Full size CCD testing vessel. It will have a focal plane that can hold up to 6 CCDs and will be a test bench for many of the mechanical design ideas for the DES camera vessel. It will be equipped with a movable Fe55 source to produce X-ray exposures of the devices in the focal plane.

Also programmed as part of the CCD testing at Fermilab is a full size camera vessel prototype (see Fig. 6), with a focal plane of 6 CCDs and operated with Monsoon electronics. This will become a test for the readout electronics (10% of the full DES focal plane) and will contribute significant information for the final mechanical design of DECam.

4.   REFERENCES

[1] http://www.darkenergysurvey.org
[2] http://www.ctio.noao.edu/
[3] http://astro.uchicago.edu/spt/
[4] Bebek, C.J., at al., 2004, SPIE **5499**, 10.
[5] Holland, S.E., Groom, D.E., Palaio, N.P., Stover, R.J., and Wei, M., 2003, LBNL-49992, IEEE Trans. Electron Dev. **50** (3), 225-238.
[6] http://www.noao.edu/ets/monsoon/

Ben Karcher is thrilled over the sand toys given to
the youngest guests of the detector workshop.

OPTIMISED CCD ANTIREFLECTION COATING
Graded Thickness AR Coating (for Fixed-Format Spectroscopy)

Andrew Kelt[1], Andrew Harris[1], Paul Jorden[1], Simon Tulloch[2]
[1]*e2vtechnologies,* [2]*Isaac Newton Group*

Abstract: *Backthinned CCDs normally use an Anti-Reflection (AR) coating in order to maximise quantum efficiency; such a coating is often optimised for a single wavelength peak. e2v has designed a custom evaporation technique to allow a graded AR coating to be deposited with good uniformity across a large-area scientific CCD. Test results show that the technique provides an excellent coating with optimised response from 300-1000 nm along the 60 mm length of the sensor. An important secondary benefit is the strong reduction of red wavelength fringes when the minimum reflection corresponds with the illuminated wavelength.*

Key words: *Graded thickness anti-reflection coating, fringes, quantum efficiency.*

1. INTRODUCTION

Although most CCDs are used for multi-band imaging or variable dispersion spectrographs, there are some fixed-format spectrographs where it can be useful to match the CCD peak response to the wavelength being measured. The performance of CCDs in such instruments can be improved by adjusting the AR coating thickness across the device to match the wavelength projected by the spectrograph [1]. This paper describes the results of depositing a graded thickness coating of hafnium oxide on large format detectors.

A graded-AR coating has been previously been supplied on CCD25-20 sensors for the MERIS/ENVISAT ESA satellite. The Meris coating was of tungsten oxide and was deposited on each individual packaged device. This material has some losses at UV wavelengths.

The preferred material for single layer AR coatings on CCDs operating from ultraviolet to infrared wavelengths is hafnium oxide. The deposition conditions (higher temperature) and the available deposition geometry (whole wafers) make the production of graded thickness coatings more difficult to realise. Development work has been carried out at e2vtechnologies to allow a graded thickness of hafnium oxide to be deposited onto large format CCDs.

2. AR-COATING DEPOSITION

After preliminary trials, full-sized 5" wafers were coated with a graded thickness, and used to manufacture CCD44-82 devices (2K×4K) for evaluation. A proprietary coating process was used to achieve the graded thickness deposition. The deposited coating was designed to provide minimum reflectivity (maximum QE) ranging from 300 nm to 1000 nm at the two extremes of the CCD length (61 mm). The coating was applied to standard silicon wafers (backthinned to 16 µm) and to deep depletion ones (thinned to 40 µm). An image of the chip is shown in Fig. 1.
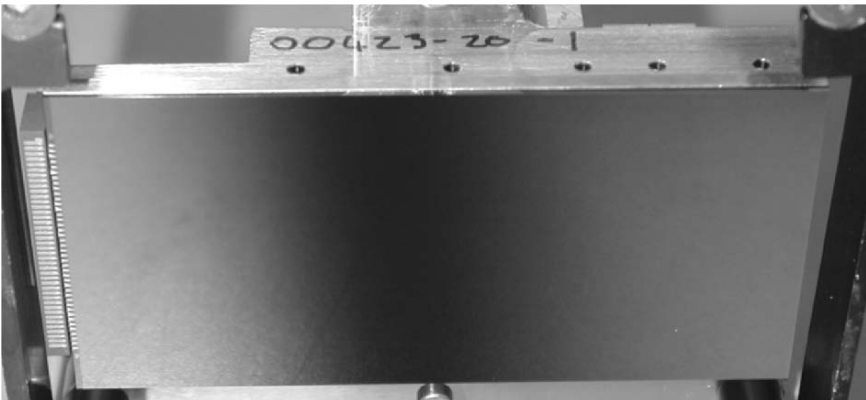
Figure 1. Backside surface of CCD44-82 showing graded coating along the major axis.
Note. See colour section of proceedings for colour copy of figure.

The coating thickness was measured by ellipsometry (Geartner Scientific Corp., model-L117). The coating was slightly thinner than target, but the gradient was very close to the intended design. Note that the thickness varies non-linearly, since refractive index is non-linear, especially at blue wavelengths. We anticipate that with our improved understanding of the coating process, we will be able to achieve coatings very close to the design intention.

The following sections describe performance measurements, some measurements were taken before the device was sawn from the wafer, and others taken on the completed device.

3. NARROW BAND FLAT FIELDS AND QE

Figure 2 shows predicted spectral response (at –100ºC) for such an optimised CCD, compared to that expected for a device with a single layer coating. Note that this data applies to a deep depletion CCD.
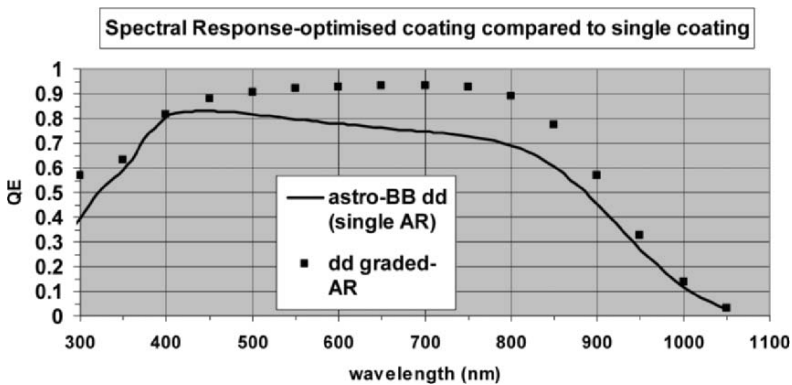
Figure 2. Predicted spectral response for optimized coating, compared to single coating.

For the standard silicon device narrow band (10 nm bandwidth) flat field frames were recorded at -100ºC for three wavelengths. The 300 nm and 650 nm plots include some row-averaging to improve signal/noise. Figure 3 shows spectral response at different chip locations. As expected, peak quantum efficiency varies along the long axis of the chip, where the reflection has been minimised. At 300 nm a second smaller maximum occurs at ~3× (lambda/4).
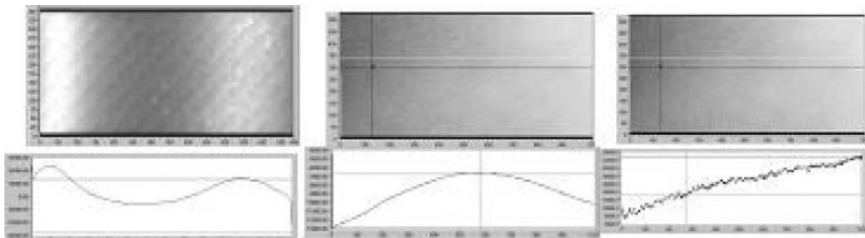
Figure 3. 300nm, 650nm, 900nm flat fields and column (long-axis) profiles.

4.   REFLECTIVITY AND FRINGE AMPLITUDE

The specular reflectivity of the device has been measured at normal incidence and room temperature. Figure 4 shows reflectivity as a function of wavelength, measured at five selected positions along the graded length of the CCD.

Reflectivity at different positions along CCD
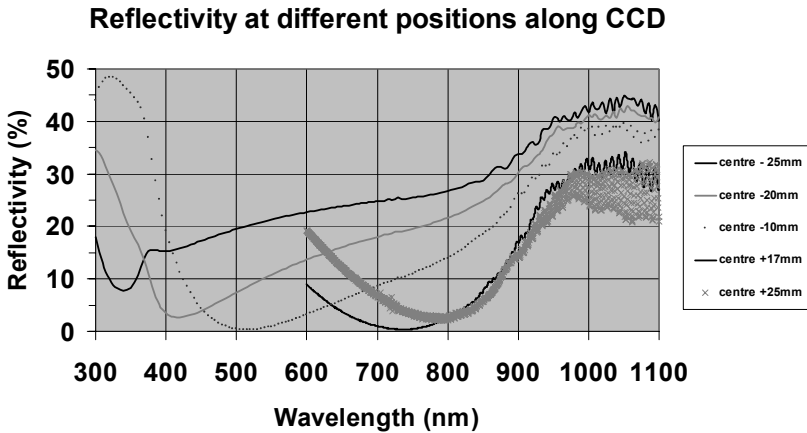
Figure 4. Variation of total reflectivity across the wafer.

Reflectivity at blue optimisation (minus centre) was measured with 10 nm bandwidth and 5×1 mm spot which suppresses fringe amplitude in the IR compared to reflectivity measured at red optimisation (plus centre), which was measured with a 1 nm bandwidth and 1 mm spot. With these differing measurement conditions absolute magnitude of fringing cannot be directly interpreted between different measured positions.

Reflectivity was also determined by dividing with a running average to give a normalised value; this emphasises changes in reflectivity and fringing effects. Figure 5 shows plots at the red (C+25 mm) and blue (C−20 mm) ends of the device.

The red end data (C+25) shows that the fringe amplitude is minimised at ~870 nm although the total reflection minimum is at ~800 nm. This is because fringes are minimum at the AR coating optimised wavelength (870 nm), which gives minimum *backsurface* reflectivity. However *total* reflectivity minimum (and QE maximum) can differ slightly due to the multi-layer structure of the device (Some reflection occurs from the frontside of the chip after double pass through the device at long wavelengths).

The blue end of the device shows fringe amplitudes that increase progressively with wavelength, as expected, since there is no reflectivity suppression for red wavelengths.
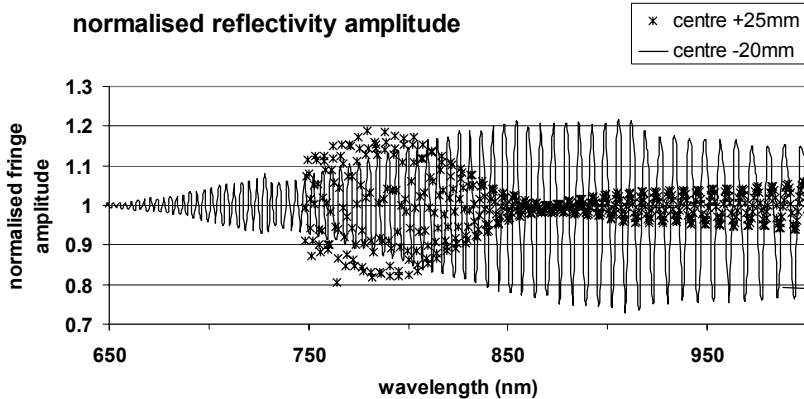
Figure 5. Normalised reflectivity, measured at blue and red ends of the CCD.

5. RESULTS FROM THE ISIS SPECTROGRAPH

Sample 44-82 devices on standard (16 µm) and deep depleted (40 µm) silicon were measured on the ISIS spectrograph at ING. The sensors were built into cameras at ING and tested on the red arm of ISIS on the William Herschel Telescope.

The first sample chip was a standard, thin CCD44-82 (non-deep depletion 2K×4K, 15µm pixels) with a graded Anti-Reflection (AR) coating. The coating varied along the length of the chip and was designed to match the low dispersion R158 ISIS red grating; dispersion was 0.12 nm/pixel. With the centre wavelength of this grating set to 600 nm, the spectrum incident on the chip was then exactly matched to the AR coat at every pixel. This chip was tested to show the importance of the AR coat for minimisation of fringing since this is crucial to allow good data extraction. The second sample was a deep-depletion CCD44-82 also with a similar graded AR coat.

Firstly, arc spectra were taken for alignment and wavelength calibration. For subsequent fringe measurements a tungsten spectrum was taken. The spectra were block averaged in the spatial (short-axis) direction (×4) to reduce the noise. A single image column was then extracted. The fringe amplitude was measured after a bias subtraction followed by flat-

field division. This flat field was obtained by block averaging the tungsten spectra by a factor sufficiently large to smooth out any fringes.

Two spectra were taken with the graded-AR chip. The first was with the grating angle set to give a perfect match between illumination wavelength and AR coat optimisation, across the whole chip area. The second was taken with the grating tilted so as to project a negative-order reversed-spectrum for comparison. The difference in the fringing between these two spectra showed the importance of a good AR coat (see Fig. 6). The optimally illuminated spectra showed very low fringing even though this was a thinned non-deep-depleted CCD.
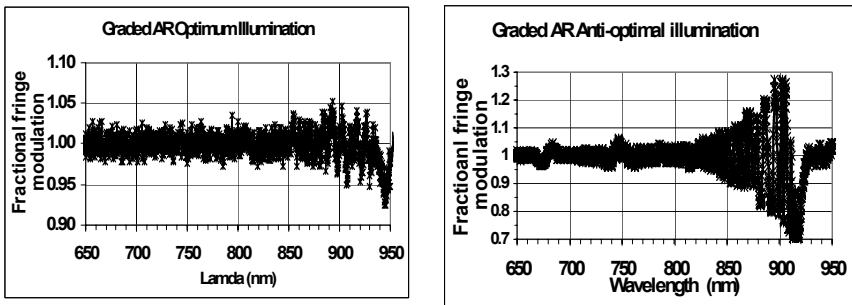
Figure 6. Fringes in graded-AR standard silicon CCD *(a)* optimum, *(b)* anti-optimum. Note that the abscissa scale varies between the two plots.

6.   CONCLUSIONS

A variable thickness AR coating can be designed and deposited across large-area CCDs with good accuracy. The measured reflectivity matches expected values, and the spectral response peaks correspond to reflectivity minima. At red wavelengths fringes are drastically reduced if reflectivity is a minimum at the projected wavelength. A graded-AR coating is ideal for use on fixed format spectrographs and can allow maximum QE and minimum fringing. The coating gradient can be tuned by design to match the application.

7.   REFERENCE

[1]   Andersen, M.J., 2000, *Optimising CCDs for Spectrographs,* Optical Detectors for Astronomy II, Amico, P. and Beletic, J.W., Editors, ASSL Vol. **252** p. 279.

SECTION IV:

CMOS-BASED SENSORS

CMOS DETECTOR TECHNOLOGY

Alan Hoffman[1], Markus Loose[2], and Vyshnavi Suntharalingam[3]
[1]Raytheon Vision Systems, [2]Rockwell Scientific Company, [3]MIT Lincoln Laboratory

Abstract: *An entry level overview of state-of-the-art CMOS detector technology is presented. Operating principles and system architecture are explained in comparison to the well-established CCD technology, followed by a discussion of important benefits of modern CMOS-based detector arrays. A number of unique CMOS features including different shutter modes and scanning concepts are described. In addition, sub-field stitching is presented as a technique for producing very large imagers. After a brief introduction to the concept of monolithic CMOS sensors, hybrid detectors technology is introduced. A comparison of noise reduction methods for CMOS hybrids is presented. The final sections review CMOS fabrication processes for monolithic and vertically integrated image sensors.*

Key words: *CMOS, image sensor, APS, active pixel sensor, focal plane array, hybrid, HgCdTe, InSb, CCD, three-dimensionally stacked circuits, vertical integration.*

1.   INTRODUCTION

The idea of using complementary metal oxide semiconductor (CMOS) technology to build two-dimensional arrays of photosensitive pixels is over 20 years old. However, the first CMOS arrays were designed exclusively for use in hybrid infrared detector arrays and were therefore too exotic and too expensive for the general public to notice. In the mid 1980s, the sensor domain for visible light had just been taken over by the newly developed charge-coupled device (CCD) technology, and CMOS with its large design rules was not a serious alternative. CMOS technology was superior for the infrared where silicon is not sensitive, and where the pixels were big and the

large feature size of CMOS did not matter. As a consequence, large hybrid arrays of up to 1K×1K resolution became available by the mid 1990s.

At about the same time, CMOS process technology had advanced to sufficiently small dimensions to enable building monolithic CMOS sensors with small pixels and good performance. It took many more years, however, before CMOS sensors became capable of achieving the high performance level of CCDs. Today, CMOS image sensors make up a significant share of the commercial sensor market and can be found in a variety of consumer devices. In addition, CMOS hybrid technology has progressed further into multimegapixel arrays for both infrared and visible applications.

2.   GENERAL CMOS SENSOR CONCEPT

CMOS image sensors use the same highly integrated circuit technology as microprocessors and memory chips. For that reason, any desired circuit can be implemented, and there are virtually no limits to the functionality and complexity of CMOS sensors. On the other hand, most of the imagers follow the same basic concept and have a similar architecture. The following sections introduce common principles applicable to the majority of today's CMOS sensors.

2.1   Basic Principle

The goal of any image sensor is to detect light as efficiently as possible. CCDs and CMOS-based imagers use the photoelectric effect of a semiconductor to convert photons into electrical charges. Unlike CCDs, however, CMOS sensors are not limited to silicon as the detector material. Instead, a number of different materials can be hybridized to a CMOS readout integrated circuit (ROIC) to provide sensitivity for ultraviolet, visible, or infrared light, as discussed in Section 4. The following description of the basic CMOS concept is applicable to both monolithic CMOS detectors and hybrid CMOS detectors.

Figure 1 compares the principle of CMOS sensors to that of CCDs. Both detector technologies use a photodiode to generate and separate the charges in the pixel. Beyond that, however, the two sensor schemes differ significantly. During readout, CCDs shift the collected charge from pixel to pixel all the way to the perimeter. Eventually, all charges are sequentially pushed to one common location (floating diffusion), and a single amplifier generates the corresponding output voltages. On the other hand, CMOS detectors have an independent amplifier in each pixel, also called an active pixel sensor (APS). The amplifier converts the integrated charge into a

voltage and thus eliminates the need to transfer charge from pixel to pixel. Instead, the voltages are multiplexed onto a common bus line using integrated CMOS switches. Analog and digital sensor outputs are possible by implementing either a video output amplifier or an analog-to-digital (A/D) converter on the chip.
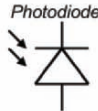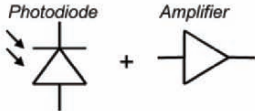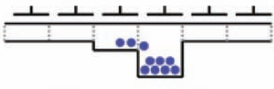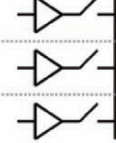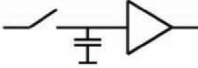
Figure 1. Comparison between the CCD-based and the CMOS-based image sensor approach.

2.2 Architecture of CMOS Image Sensors

In addition to the basic concept of active pixels, a number of common features can be found in most CMOS-based imagers. As shown in Fig. 2, two different scanners surround the actual pixel array: a vertical scanner to control the row selection, and a horizontal scanner to amplify and multiplex the analog pixel signals. While most CMOS imagers include comparable vertical scanners, they differ quite substantially in the architecture of the horizontal scanner. Low-speed astronomy detectors typically use a row of analog switches controlled by a simple digital shift register. Faster image sensors require additional circuitry in each column like sample/hold stages or column buffers. In some cases, even the A/D conversion is integrated into the horizontal scanner as a part of the column structure.
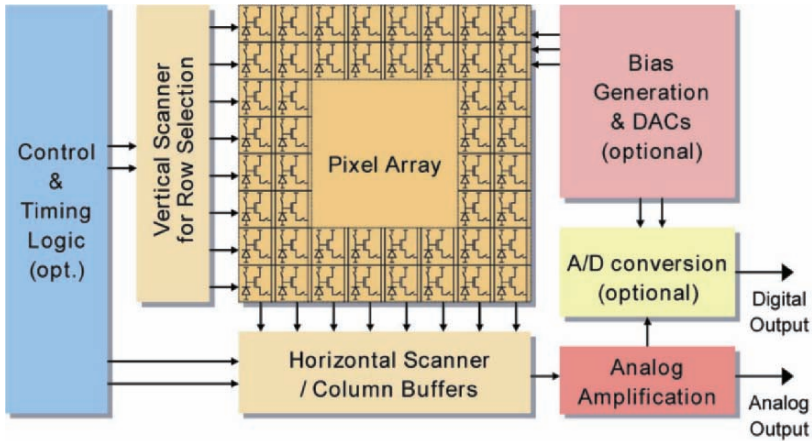
Figure 2. Block diagram of a generic CMOS sensor.

Most CMOS sensors include additional circuitry for bias generation, timing control, and A/D conversion. The latter can be found more and more in modern sensors that use deep submicron process technologies. By integrating all the support electronics into the same silicon as the pixel array, complete cameras can be built on a single chip. This approach is very attractive to the commercial image sensor market because of size and cost constraints. On the other hand, high-performance scientific sensors typically do not push towards the highest integration level. Here, very high resolutions at very low power levels require a simpler detector architecture, and most of the support circuitry is provided by external electronics.

2.3   Common CMOS Properties

A high level of flexibility and a number of unique features characterize CMOS detector technology. This section summarizes some of the important aspects, in particular the properties that set CMOS detectors apart from CCD sensors.

In terms of manufacturing, CMOS imagers in general benefit from the large availability of foundries worldwide. Using the same foundry resources as microchips guarantees cost-efficient production and highly mature process technology. Design rules as advanced as 0.13 µm are being used for the latest generation of image sensors.

A significant advantage of CMOS sensor technology is its high level of flexibility. Small and simple pixels with three or four transistors are being used to achieve basic light detection at high resolutions. Larger and more complicated pixels with hundreds of transistors provide A/D conversion or

other image processing capabilities directly at the pixel level. Furthermore, additional on-chip circuitry can support many analog and digital signal processing functions to reduce the requirements on system power or transmission bandwidth. Fortunately, CMOS imagers operate at very low power levels and therefore can tolerate the increased power consumption of most on-chip functions.

Typically, CMOS-based detectors do not need a mechanical shutter. Instead, integration time is controlled electronically. Two of the main electronic shutter concepts, the snapshot shutter and the rolling shutter, are explained in Section 2.4. An interesting feature is that pixels can be read out without destroying the integrated detector signal (nondestructive read). This allows, each pixel can be read multiple times, thereby reducing read noise by averaging multiple reads. Unlike CCDs, the detector array can be scanned in a number of different ways, including random access to any pixel at any time. Section 2.3.1 illustrates some of the special scanning techniques.

Because every pixel includes active components, the matching of device properties from pixel to pixel is important. Any mismatch can lead to pixel-to-pixel nonuniformities, called fixed pattern noise (FPN) or photoresponse nonuniformity (PRNU). Many sensors resolve the issue by providing on-chip correlated double sampling (CDS). This reduces the FPN and, at the same time, eliminates the temporal kTC noise. However, in some cases, the correction for the nonidealities has to be performed outside the sensor, thus adding complexity to the system.

2.3.1 Scan Modes

Similar to a memory chip, CMOS sensors are capable of accessing pixels in random order. It is merely a matter of the surrounding scanner logic to define the available scanning methods. Figure 3 shows four examples of common scanning schemes beyond the standard full frame read mode. Because of a reduced number of effective pixels, all special scanning modes provide the advantage of faster frame rates compared to the full frame mode.

The first example is the window mode, in which a rectangular shaped subsection is being read out. The location and the size of the window are usually programmable parameters. If the window can be reset and read without disturbing the other pixels in the detector array, the window mode can be used for simultaneous full field science exposure and fast guide window operation for telescopes. The second special scanning technique is called subsampling. In this method pixels are skipped during the frame readout. As a result, the complete scene is captured at a faster frame rate, yet at a reduced resolution. The third possible readout or reset scheme is random access. Every pixel is read when desired, and no predefined sequence has to

exist. This can be helpful in selectively resetting saturated pixels. Fourth, CMOS sensors can combine multiple pixels into one larger pixel. This process is similar to the binning technique known from CCDs. However, CMOS devices typically do not achieve the same improvements in signal-to-noise ratio from binning as do CCD devices, and the scheme is therefore not as commonly used.

window / guide mode　　　subsampling　　　random access　　　binning
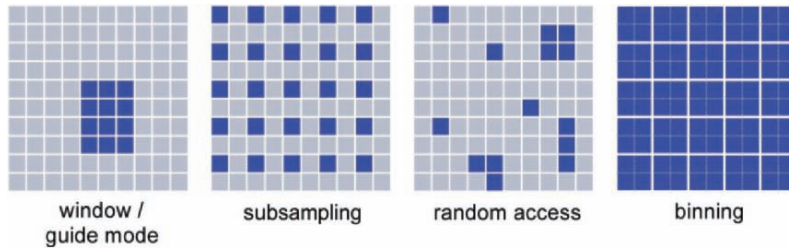
Figure 3. Different scanning schemes available in CMOS sensors.

2.4　　　Snapshot vs. Rolling Shutter

Two main concepts of electronic shutters have been established for CMOS image sensors: the snapshot shutter and the rolling shutter. Neither requires a mechanical shutter, but they differ with respect to their specific implications. Figure 4 illustrates both shutter concepts by means of a timing diagram of five consecutive rows. In the case of the snapshot shutter (left side), all rows start and stop integrating at the same time. Consequently, a complete picture is captured simultaneously by the whole array, a fact that is very important for fast moving objects. Depending on the design and the complexity of the pixel, the next exposure has to wait until all pixels are read (integrate, then read), or the next exposure can start while the previous values are being read (integrate while read).

The rolling shutter approach, on the other hand, does not globally start and stop the exposure. Instead, the start and the stop time of the actual integration is shifted every row by one row time with respect to the previous row. This can be seen on the right side of Fig. 4. Basically, as soon as the exposure of one row has finished, the row is read out and then prepared for the next integration period. Thus, the pixel does not require any sample and hold circuit. This results in smaller pixels and typically higher performance. The rolling shutter is beneficial for all applications that observe static or slow moving objects.
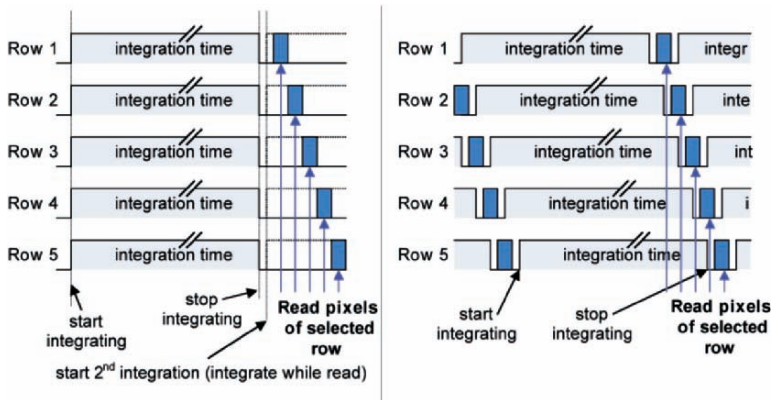
Figure 4. (left) Snapshot shutter vs. *(right)* rolling shutter.

2.5   CMOS-Based Detector Systems

As described in Section 2.2, CMOS image sensors require additional support electronics for controlling and biasing the detector system and for digitizing the analog signals. Three main approaches are used for implementation of the support electronics, as shown in Fig. 5, (a) a single chip solution like in Kozlowski et al. [1], (b) a system with analog image sensor and discrete external electronics, (c) a dual chip approach with analog image sensor and application specific integrated circuit (ASIC).

The single chip system is the most integrated concept since all required electronics are part of the sensor chip itself. Single chip camera systems can be very small and do not consume much power. However, they are difficult and expensive to design. Also, they can show undesired side effects like transistor glow or higher power consumption close to the pixel. Both effects potentially increase the detector dark current. Therefore, single chip solutions are typically not being used for high-performance scientific applications in order to maintain lowest dark current and highest sensitivity.

Conventionally, scientific detectors, and in particular astronomy camera systems, have been using the second approach comprising of an analog sensor chip and discrete external electronics. Some of the advantages include modularity, i.e., one controller can be used with many different detectors, and a less expensive detector design. On the negative side, discrete systems dissipate more power and are much larger.

To combine the benefits of the two concepts, a third approach is being pursued. Here, the detector system is composed of two separate chips. The first one is an analog image sensor, like the one used with discrete

electronics controllers. The second chip is a programmable mixed-signal ASIC that effectively combines all functions of the discrete controller in a single chip [2]. The two chips together form a small and lightweight, yet flexible and high-performance, camera system.
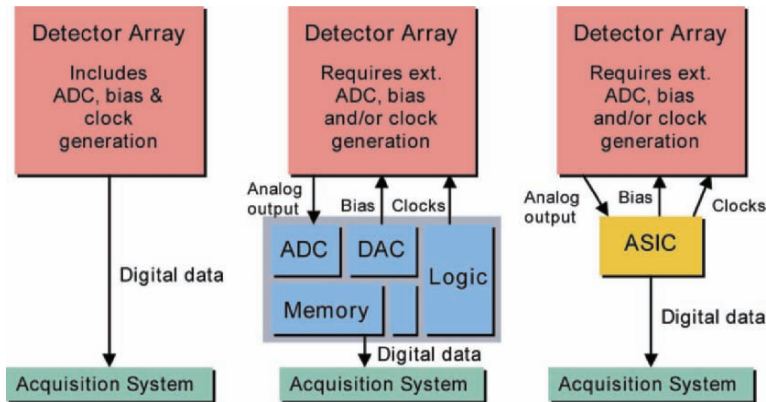
Figure 5.   Three concepts for implementing support electronics in CMOS-based detector systems: *(left)* single chip, *(center)* discrete electronics, and *(right)* dual chip.

2.6   Stitching

The maximum size of a CMOS chip in modern deep submicron technology is limited to about 22 mm × 22 mm. This is the maximum reticle size that can be exposed in a single step. To build larger sensor arrays, a special process called *stitching* has to be applied. To do this, the large CMOS sensor is divided into smaller subblocks. These blocks have to be small enough that they all fit into the limited reticle space. Later, during the production of the CMOS wafers, the complete sensor chips are being stitched together from the building blocks in the reticle. Each block can be exposed multiple times within the same sensor, thus creating arrays much larger than the reticle itself.

An example of a stitched FPA is shown in Fig. 6. The left part of the picture includes the reticle with six independent subblocks. The right half illustrates a completely assembled CMOS readout chip, built from the individual subblocks in the reticle. The ultimate limit for this approach is only the wafer size itself, i.e., 15 to 30 cm depending on the process technology. However, yield limitations will make it nearly impossible to manufacture wafer-scale arrays, and mosaics of smaller independent detectors are typically used to build very large focal plane arrays (FPAs).
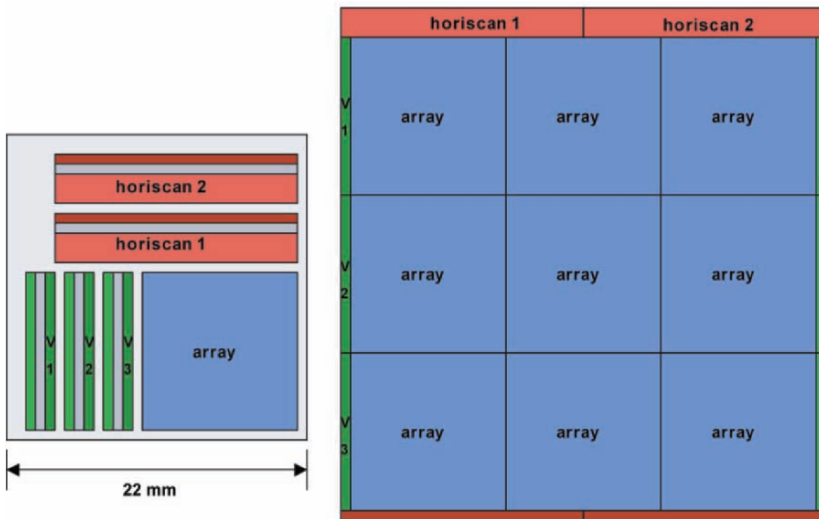
Figure 6. (left) Mask reticle and *(right)* stitched CMOS readout array.

3. MONOLITHIC CMOS SENSORS

Monolithic CMOS sensors are image sensor chips that combine the photodetectors and the readout circuitry on the same piece of silicon. Compared to hybrid FPAs, monolithic arrays are less expensive to manufacture, but the sensitivity is limited to the visible and near infrared wavelength range. Over the course of the last decade, monolithic CMOS technology has made significant improvements. In recent years, a large number of consumer products, including cell phones, digital cameras, and camcorders, have been replacing CCDs with CMOS sensors for the sake of smaller, cheaper, and lower-power systems. A monolithic CMOS sensor is also called an APS.

Although a wide variety of pixel designs exist, most sensors use one of the two circuits shown in Fig. 7. The circuit on the left side consists of three transistors (3T): a reset field-effect transistor (FET), a selection switch, and a source follower for driving the signal onto the column bus. The right side of Fig. 7 displays a pixel with four transistors (4T) and a pinned photodiode. Three of the FETs have the same function as in the 3T pixel. The fourth transistor works as a transfer gate that moves charge from the photodiode to a floating diffusion. Usually, both pixels operate in rolling shutter mode. The 4T pixel is capable of performing CDS to eliminate the reset noise (kTC noise) and the pixel offsets. The 3T pixel can only be used with

noncorrelated double sampling (DS), which is sufficient to reduce the pixel-to-pixel offsets but does not eliminate the temporal noise. However, temporal noise can be addressed by other methods like soft reset or tapered reset.
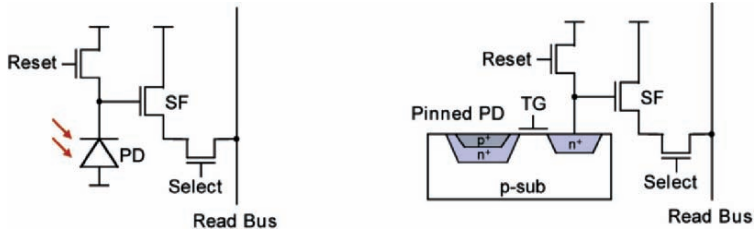
Figure 7.   Diagram of two common monolithic CMOS pixel circuits: *(left)* three transistors with regular photodiode and *(right)* four transistors with pinned photodiode.

In a monolithic CMOS sensor, the photodiodes share the pixel area with the transistors. For that reason, the fill factor is always less than 100%. In addition, most CMOS imagers are front side illuminated. This limits the sensitivity in the red because of a relatively shallow absorption material. A typical quantum efficiency (QE) plot for a monolithic CMOS sensor with microlenses can be seen in Fig. 8 [3]. The curve corresponds to a 3T pixel with roughly 50% fill factor. For comparison, the same figure shows two QE plots of silicon PIN detectors. Because they are hybrid FPAs with a dedicated detector layer, the thicker material and 100% fill factor result in much improved red response.

4.   HYBRID CMOS TECHNOLOGY

The hybrid CMOS revolution began in the mid 1970s when the indium bump interconnect technology was invented. By 1990, CMOS processing of silicon was standard for the commercial analog and digital integrated circuit industry. The CMOS process has continuously improved because of demands of the computer industry, allowing higher-density circuits and large array formats. At the same time, indium bump hybridization has also improved to the point where 16 million pixels per array can be reliably connected.

The hybrid CMOS approach separates the problems of (1) converting electromagnetic radiation into an electronic signal and (2) amplifying the electronic signal, processing it, and multiplexing the signals from many detector elements onto a single output line. In a hybrid CMOS device, the first function is performed by a detector array that is typically electrically

connected to a CMOS integrated circuit chip using an array of indium bumps, one per detector element. The CMOS chip, often called a ROIC (readout integrated circuit), performs the second function. A detector hybridized to a CMOS ROIC may be called a hybrid array, a sensor chip assembly (SCA), or a focal plane (FPA).

Because the detection and electronics functions are separated in a hybrid CMOS SCA, the design and processing of detectors and ROICs can each be optimized for its own function. In addition, detectors and ROICs can often be interchanged, that is, a given ROIC design might be hybridized to different detector arrays depending on the wavelength of interest. Similarly, a given detector array might be hybridized to different ROICs depending on the desired frame rate, well capacity, or other signal processing functions.
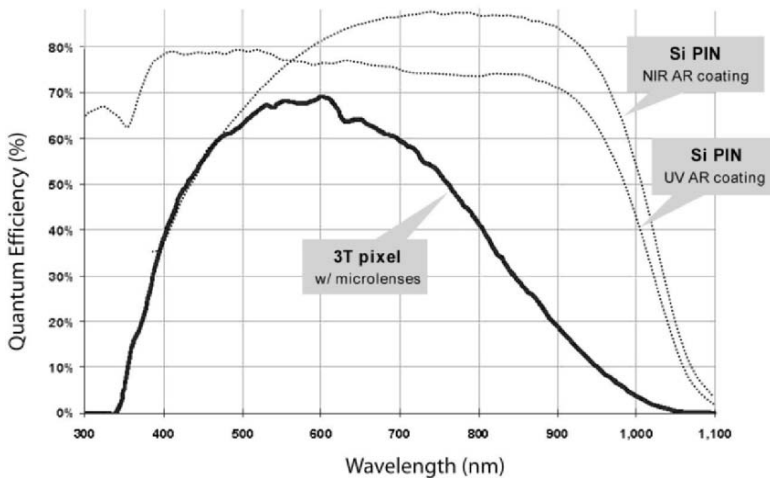
Figure 8. Spectral QE of a monolithic CMOS image sensor with three transistors per pixel.

4.1 Detectors

Some of the detector materials available in large array formats and compatible with the CMOS hybrid approach are shown in Table 1. The spectral range of each material is listed along with the approximate operating temperature to achieve much less than 1-electron/second dark current. All of these detector materials have been demonstrated in formats of 1K × 1K or greater, all have essentially 100% fill factor, and all have very nearly 100% internal QE if the detector is properly designed and fabricated. All of these

detectors, with the exception of Si:As, are generally produced as p-on-n diode structures and are interchangeable with regard to ROIC hybridization.

Table 1. Detector Materials Available for Large-Format CMOS Hybrids (SCAs).

Detector Material	Spectral Range[a] (µm)	Operating Temperature[b] (K)
Si PIN	0.4–1.0	~200
InGaAs[c]	0.9[d]–1.7	~130
HgCdTe[c]		
1.7 µm	0.9[d]–1.7	~140
2.5 µm	0.9[d]–2.5	~90
5.2 µm	0.9[d]–5.2	~50
10.0 µm	5.0–10.0	~25
InSb	0.4–5.2	~35
Si:As IBC (BIB)	5.0–28.0	~7

(a) Long wave cutoff is defined as 50% QE point.
(b) Approximate detector temperatures for dark currents <<1 electron/second.
(c) Requires special packaging due to thermal contraction mismatch between detector and ROIC.
(d) Spectral range can be extended into visible range by removing substrate.

One of the design issues facing the hybrid CMOS structure has been how to deal with differences in thermal contraction of the detector and ROIC as the SCA is cooled. For example, if the detector contracts much more than the ROIC, the indium bump connections could be torn apart upon cooling. The problem becomes more severe for larger arrays and for lower operating temperatures. Fortunately, for a thinned detector such as InSb, the membrane-like detector (10 µm thick) is able to stretch to match the contraction of the ROIC. For thick detectors, such as HgCdTe and InGaAs, detector manufacturers have devised mechanical structures to force the ROIC to contract the same amount as the detector material, thus nearly eliminating stress at the indium bump interface. For silicon-based detectors, such as Si PIN and Si:As, there is little differential contraction compared to a silicon CMOS ROIC, and thermal cycle reliability is not a concern.

4.2   ROICs

CMOS technology allows complex input amplifier circuits to be designed to temporally integrate the detector signal. Figure 9 depicts schematic examples of the three most widely used, and simplest, input circuits—the source follower per detector (SFD), the capacitive transimpedance amplifier (CTIA), and the direct injection (DI).
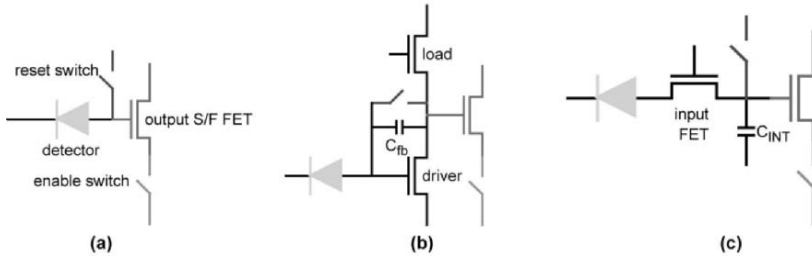
Figure 9. Circuit schematics for the three most commonly used input circuits for CMOS ROICs: *(a)* the SFD, *(b)* the CTIA, and *(c)* the DI.

Table 2 provides a description of the advantages and disadvantages of each circuit. The SFD is most commonly used in large-format hybrid astronomy arrays as well as commercial monolithic CMOS cameras. It is simple, has low noise, low power, and low FET glow. The CTIA is more complex and higher power but is extremely linear. The DI circuit is used in higher-flux situations and has the same low power and FET glow as an SFD. The gain (volts out / charge in) of the input circuits are determined by charge integration capacitors: for an SFD, it is the detector capacitance; for CTIA and DI, charge is integrated on ROIC capacitors. ROIC capacitors are determined by the layout of the ROIC and can be varied according to the application.

4.3   Noise Reduction Techniques for CMOS Hybrids

There are three general types of noise in CMOS hybrids: temporal, fixed pattern, and random telegraph signal (RTS). Temporal noise may be divided into white or uncorrelated noise and 1/f noise. This noise may be from the detector and/or ROIC, depending on the design. Fixed pattern noise is caused by residual nonuniformity after calibration, which in turn may be caused by 1/f noise or drift in key system parameters such as focal plane temperature. RTS is randomly occurring charge trapping/detrapping events and is highly dependent on CMOS process and design parameters.

White temporal noise has usually been the dominant type of noise in CMOS devices used astronomy. A common technique to reduce this noise is to sample each detector element multiple times during a long integration time, as illustrated in Fig. 10.

There are two common methods of analyzing multiply sampled data. One is Fowler sampling, where the first N samples and the last N samples are each averaged and the two averages are then subtracted. Noise is reduced by root N if sample-to-sample noise is uncorrelated. This technique also

performs a CDS function, reducing noise introduced by resetting the integration capacitor (kTC and other noise sources). The second technique is to perform a least squares fit of all samples to a straight line or polynomial.

Table 2. Comparison of Attributes of the Three Most Common Input Circuits.

Circuit	Advantages	Disadvantages	Comments
Source follower per detector (SFD), …"self-integrator"	Simple Low noise Low FET glow Low power	Gain fixed by detector and ROIC input capacitance Detector bias changes during integration Some nonlinearity	Most common circuit in IR astronomy
Capacitance transimpedance amplifier (CTIA)	Very linear Gain determined by ROIC design (C_{fb}) Detector bias remains constant	More complex circuit FET glow Higher power	Very high gains demonstrated
Direct injection (DI)	Large well capacity Gain determined by ROIC design (C_{INT}) Detector bias remains constant Low FET glow Low power	Poor performance at low flux	Standard circuit for high flux
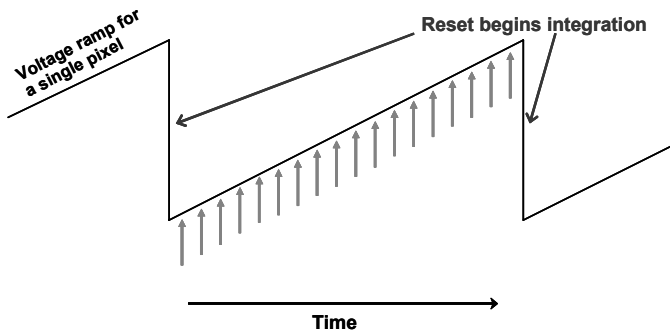
Figure 10. Illustration of multiple sampling of a detector during a long integration. The sawtooth line represents the voltage on the output of a detector input circuit as a function of time. The upwardly rising ramp represents the integration of photocurrent; the sudden downward voltage is the reset that begins the next integration. Arrows show regularly spaced points in time where the integrated signal is sampled.

Figure 11 compares the signal-to-noise ratio (SNR) for Fowler sampling with the sample-up-the-ramp (SUTR) noise reduction technique for the theoretical case where all samples are uncorrelated. This example uses a total of 64 samples scaled so that Fowler-1 (CDS) SNR is set to 1. The SNR

of the Fowler sampling is a function of sample pairs with 32 being the maximum in this case. A peak in SNR where the number of Fowler pairs is one third of the total number of samples (take the last third of the samples and subtract from the first third while ignoring the middle third) and is a general result. The Fowler SNR peak is 6% below the SUTR peak. Detector dark current and photocurrent are integrated, and therefore later samples are correlated to earlier ones. In the limit of background-limited performance (BLIP), Fowler-1 (simple CDS) yields the best SNR, which is 9% better than SUTR [4]. Noise as low as 2 electrons rms has been achieved with cryogenic (30 K) CMOS ROICs in a Fowler-16 mode [5].
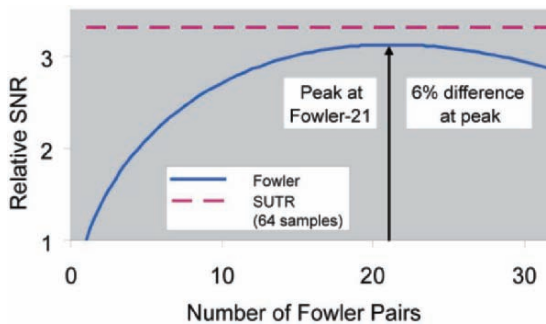
Figure 11.   Example of SNR improvement with multiple uncorrelated samples. SNR as a function of Fowler sample pairs is shown in comparison to SUTR. In this example, there are a total of 64 samples spaced over equal time intervals. SNR is scaled for SNR=1 for Fowler-1 (CDS). The peak in Fowler sampling occurs when the number of Fowler pairs is one third of the total number of samples and the middle third of the samples are ignored. This peak is 6% below the SUTR SNR value.

5.   CMOS FABRICATION PROCESSES

The attraction of CMOS-based process technologies for imaging applications is that they can bring control electronics and a sophisticated range of signal processing tools in very close proximity to the focal plane. Still, CCD fabrication methods have been steadily optimized over the past 35 years to produce large-format devices with broad spectral response, low noise readout, and good yield. In this section we compare the process technologies used for CCD- and CMOS-based imagers and describe why the newest advancements in CMOS processes offer some attractions for high-performance imaging.

5.1   CCD vs. CMOS Fabrication Process Comparison

CCD imagers are generally fabricated on 125-mm silicon substrates in facilities that are "trailing" in feature-size advancements relative to the most aggressive CMOS foundries. The circuits fabricated in CMOS-based process technologies benefit from improvements encouraged by a wide-scale demand for fast, compact, low-power electronics. The concurrent economics of scaling wafer size up and feature size down propel frequent migrations to new technology "nodes," which correspond to logic speed improvements. Many CMOS foundries are routinely processing 200-mm wafers, with the newest facilities now handling 300-mm wafers, and most research laboratories using 150-mm wafers. Commercial ventures benefit from wafer size increase because the cost per chip generally goes down, but even research efforts are eventually forced to migrate up in wafer size because of the availability of high-quality substrates and advanced deposition, etch, and lithography tools.

Manufacturers of CCDs may eventually feel this pull as well, though presently the very high resistivity float-zone silicon substrates (5000–7000 Ω-cm) required for deep depletion and good spectroscopic performance at long wavelengths are only available up to 200-mm diameter, and the commonly used full-wafer lithography tools are not yet available for the larger wafer sizes. Since float-zone silicon is vulnerable to the generation of plastic slip and dislocations and requires special processing techniques that limit thermally induced stresses during high-temperature processes [6], migrating a science-grade CCD process technology to an even larger wafer size would require reassessment of all thermal processing as well as design/layout methods to minimize stresses induced by multiple layers of patterned polysilicon crossing channel stops.

In its highly evolved present state, the common implementation of a CCD imager structure does produce a satisfactory yield of millions of active elements in a single device. The buried-channel structure, multiple oxidation cycles, and composite gate dielectric are all engineered to have superior charge transfer efficiency, noiseless operation (until readout), and resistance to interpoly and substrate shorts. However, CCDs generally require clocks of at least 10 V to maintain sufficient charge capacity in the well. These 10-V clocks are incompatible with the 1- to 5-V levels necessary for low-power on-chip circuitry. Shallower CCD buried channels and thinner gate dielectrics can produce imagers that operate at lower voltages [7], and such improvements have the greatest benefit if accompanied by on-chip access to digital logic gates as well.

Most mixed-signal CMOS technologies easily support implementation of single chip designs with multiple operating voltages, for example, to manage

dynamic range and power. A further aid to the circuit designer is the presence of several levels of interconnect metal (typically five to seven), which permits great flexibility in routing methodology. The highly nonplanar structure of a CCD hampers reliable patterning and isolation of even one or two levels of metal interconnect. An extreme case of this is seen in Fig. 12, which presents an early optical micrographic view of the four-poly pixel array and a scanning electron cross section through the pile-up of layers that cross the channel stop. Each reentrant edge seen is a vulnerable spot for interpoly shorts and a trap for hidden metal shorts.
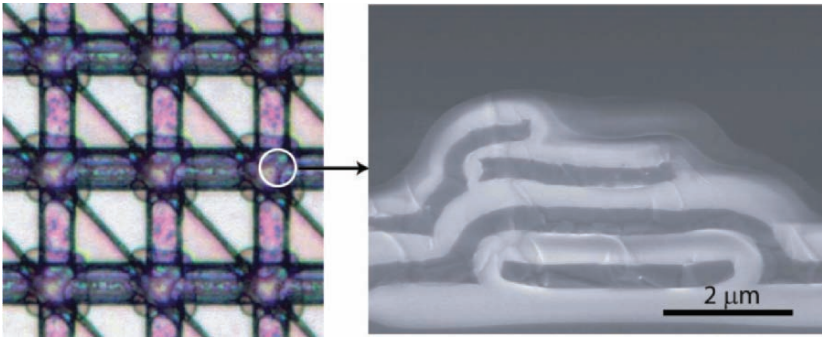
Figure 12. Optical photomicrograph and cross section through channel stop region of four-poly orthogonal-transfer CCD (OTCCD).

The structure of CMOS devices can be appreciated in the scanning electron micrographs of Fig. 13, which provide a detailed view of a five-transistor SRAM cell and a cross section through three interconnect metal layers with planarized interlevel dielectrics.

Manufacturers of CCDs are choosing to implement some of these CMOS-developed processes when appropriate, but one remaining comparison is architecturally, rather than process, driven—the repetitive transfer of charge packets through the silicon lattice in a CCD causes the device to be vulnerable to space-radiation-induced traps. CMOS-based active pixel imagers require few to no charge transfers and can readily adopt a number of design and process hardening methods to yield science-grade imaging sensors that are suitable for long-term space-based applications.

5.2 CMOS Technology Features and General Limitations of Monolithic Imagers

CMOS device size and voltage scaling are driven by logic applications that demand ever-faster computation with reduced power dissipation. In each generation of fabrication technologies a number of process features change,

as detailed in Table 3. For example, the local oxidation process (LOCOS) used for device isolation in both CCD and larger-geometry CMOS technologies is replaced by a more compact shallow trench isolation (STI) process that permits much higher circuit layout densities and better junction isolation.

To produce the same transistor channel inversion charge the lower operating voltage requires higher gate capacitance, and so the gate dielectric is made thinner and nitrogen may be introduced to inhibit dopant penetration from the gate into the silicon channel. For high transistor on-state current with well-behaved off-state current, the shallow device junctions have sharply defined doping profiles fixed by rapid thermal activation of the extension and source/drain implants.

However, many of the process modules that become standard for highly scaled CMOS, such as STI, thin gate dielectric, and silicided junctions, introduce additional sources of device and junction leakage, and the optically opaque silicides can block photoabsorption in the silicon. While anisotropic physical profiles are obtained with now-common plasma (dry) etch processes, the surface damage created may not be repaired within the strict thermal budget. Even low levels of surface damage or stress-induced stacking faults like those seen in Fig. 14 can create leakage that contributes to dark current.
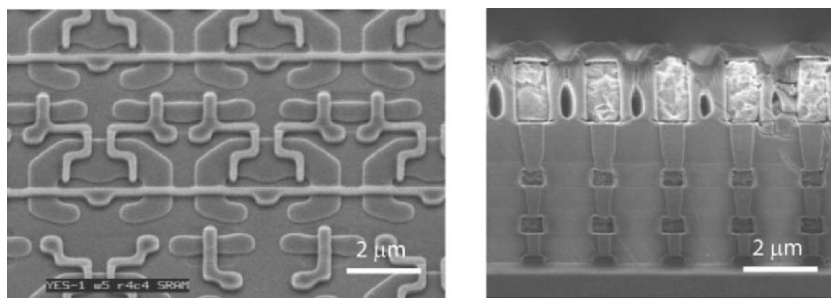
Figure 13.   *(left)* Silicon-on-insulator (CMOS) 180-nm SRAM cell and *(right)* three levels of metal stacked with vias to poly.

To support the fabrication of low-cost CMOS image sensors for consumer applications, many CMOS logic foundries now offer special steps that protect the sensitive pixel transistors from some of the most damaging exposures. The process flow shown in Fig. 15 [8] illustrates how pixel transistors are coated with an additional oxide layer, which is etched back and patterned to permit silicide formation only on the gate polysilicon and on the source/drain regions of peripheral devices.

Table 3. Summary of CMOS Process Technology Features.

Feature	0.35–0.60-μm Gate Length Technology	0.18–0.25-μm Gate Length Technology
Operating voltage	3.3–5 V	1.8–2.5 V
Field isolation	LOCOS	Shallow trench isolation
Gate oxide	70–125 Å	32–50 Å
Gate dielectric	Silicon dioxide	Nitrided silicon dioxides
Junction profile	Graded junction	Shallow junction
Thermal budget	Furnace anneal	Rapid thermal processing
Spacer etch	Oxide spacer	Silicon nitride spacer
Device	Polycide/poly	Self-aligned silicide
Planarization	Spin-on-glass and reflow	Chemical mechanical planarization
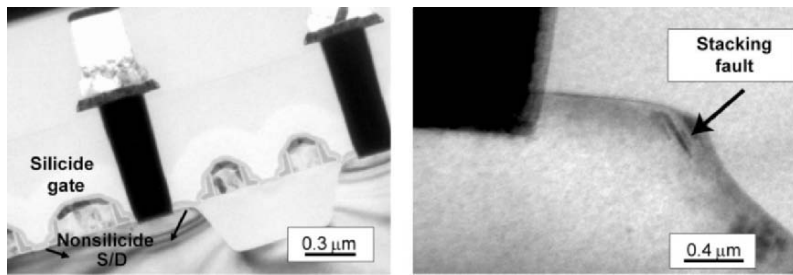
Figure 14. Cross-sectional transmission electron micrograph of pixel. From Wuu et al. [8].

6. EMERGING TECHNOLOGIES

For monolithic active pixel architectures the pixel area must be shared between the photodiode and the access and amplification transistors, as seen in the plan view and schematic cross-sectional view of Fig. 16. The photo-collection junction is typically formed at the drain-substrate or well-substrate interface. It is clearly seen in these views not only that the fill factor of the pixel is less than 100% but also that the fabrication of the photojunction and access transistors must be co-optimized, with some necessary compromises on layout density, absorption layer thickness, and device isolation. Foundries targeting consumer applications typically apply microlenses to compensate for the loss of optical fill factor.
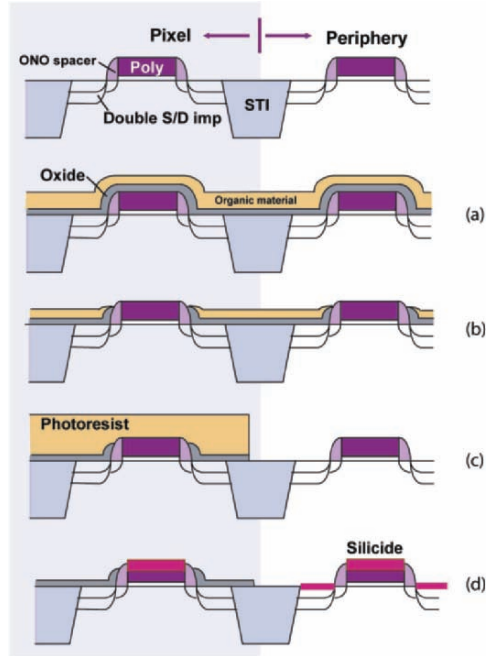
Figure 15. CMOS pixel process flow: *(a)* deposit oxide and spin coat organic material, *(b)* etch back and remove oxide, *(c)* remove organic material and pattern oxide (photo/etch), and *(d)* form silicide on peripheral devices. Adapted from Wuu et al. [8].

6.1   Vertically Integrated Active Pixel Imager

Without further limiting the pixel fill factor, monolithic architectures also require that addressing and signal processing circuitry be placed at the periphery of the array. In contrast, a three-dimensionally (3-D) stacked circuit construct, such as shown in Fig. 17, relieves many of the limitations inherent to monolithic structures. Active-pixel focal plane architectures are well suited for 3-D interconnection because signal integration, amplification, and readout can be in close proximity to the photodetection elements while still achieving 100% optical fill factor. The further capability to perform complex signal processing behind every pixel can dramatically reduce total image sensor power and bandwidth requirements.
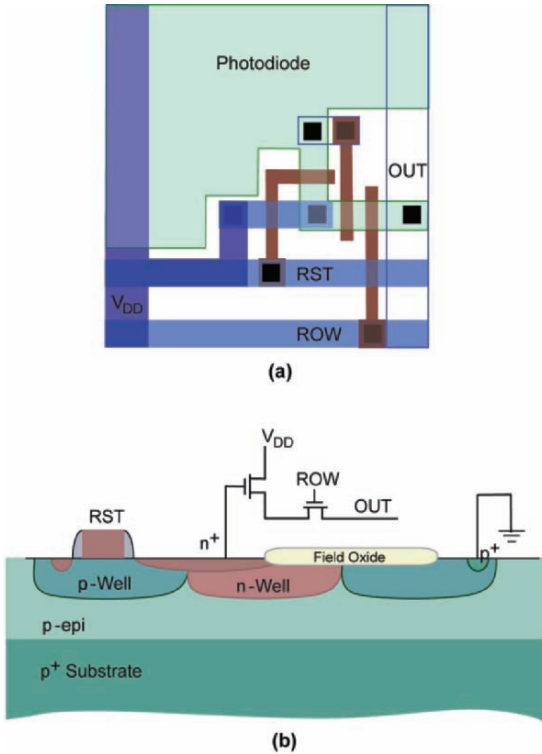
Figure 16. Example of three-transistor pixel layout *(a)* in plan view and *(b)* in cross-section.
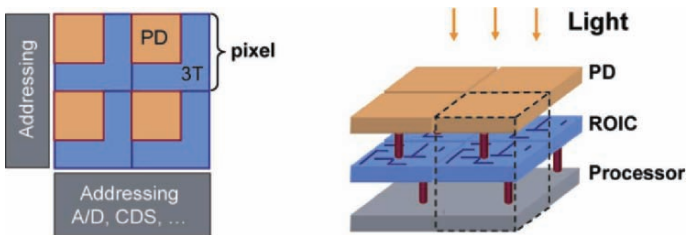
Figure 17. Advantages of vertical integration: *(left)* conventional monolithic APS compared with *(right)* 3-D pixel.

Vertically hybridized flip-chip imagers already offer independently optimized photodetector and readout multiplexer designs that can achieve scientific-grade image sensor performance [9]. However, these bump-bonded approaches are limited to two circuit layers, to large pixel sizes (≥ 18 µm), and do not permit post-integration hydrogen-passivation anneals, which are critical for dark current suppression. In Fig. 18 a feature-size

comparison is made among three methods to vertically interconnect circuit layers: (a) bump bond, (b) insulated through-silicon vias, and (c) Lincoln Laboratory's SOI based via. The Lincoln integration method is extendable to three or more circuit layers and is capable of achieving far smaller pixel sizes than possible with bump bonding.

The process technology for the method in Fig. 18(c) has recently been used to demonstrate a four-side abuttable 3-D integrated 1024×1024, 8-μm pixel visible image sensor fabricated with oxide-to-oxide wafer bonding and 2-μm-square 3-D vias in every pixel. The 150-mm wafer technology integrates a low-leakage, deep-depletion, 100% fill factor photodiode layer to a 3.3-V, 0.35-μm gate length fully depleted (FD) SOI CMOS readout circuit layer [10].
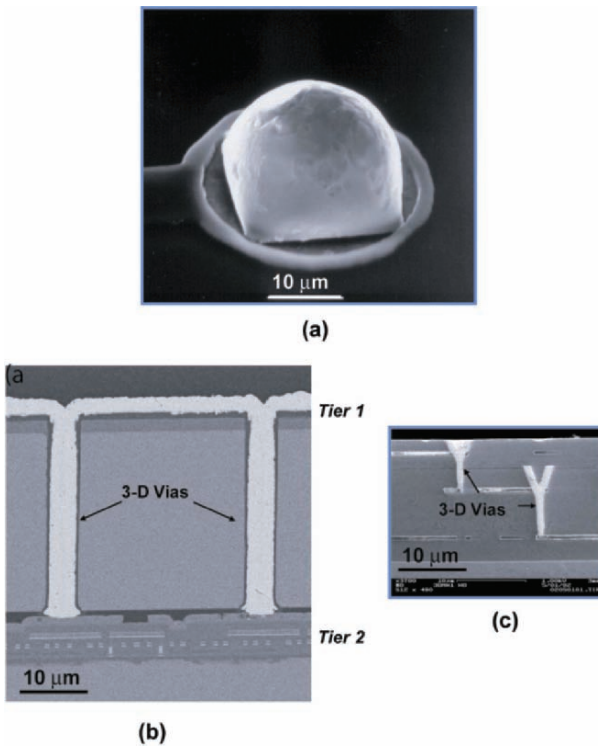
Figure 18. Approaches to 3-D integration: *(a)* Bump bond used to flip-chip interconnect two circuit layers, *(b)* two-layer stack with insulated vias through thinned bulk Si, and *(c)* two-layer stack using Lincoln Laboratory's SOI-based vias. Illustrations are to scale. Photo in (b) courtesy of RTI.

A cross-sectional scanning electron micrograph (SEM) through several 8-μm pixels of a functional active pixel imager is shown in Fig. 19. The

oxide-oxide bond between the two tiers is imperceptible. A 3-D via connects tier-2 FDSOI CMOS metal 3 to tier-1 (diode) metal 1, and a metal cap (back metal 1) covers the 3-D via plug. The 50-nm-thick SOI transistor features can be seen near the top of the SEM. The dominant misalignment (~1 µm) is created by the wafer-to-wafer bonding step; newer tools and methods in development are expected to further reduce this misalignment.

Each sensor contained over 3.8 million transistors and over one million 3-D vias. We measured pixel operability in excess of 99.9% with the principal yield detractor arising from column or row dropouts, i.e., not 3-D vias. The devices have successfully been processed through diode wafer thinning for back-illumination operation.
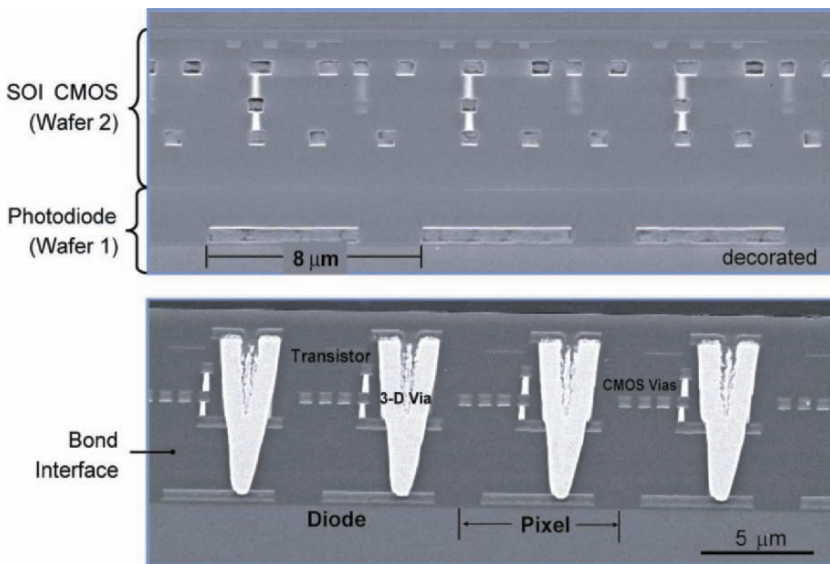
Figure 19. Cross sections through 3-D imager.

The high degree of pixel functionality can be seen in Fig. 20, which presents an image acquired by projecting a 35-mm slide onto either front-illuminated or back-illuminated processed imaging devices (different chips).

6.2 Digital focal plane architectures

Conventional analog focal plane architectures reach a readout bottleneck when the system implementation demands wide-area coverage, high frame rates, and high bit precision. By digitizing the signal while the photoelectrons are being collected, rather than after charge accumulation, the need for large charge storage capacitors and highly linear analog electronics

can be eliminated. Additionally, the power dissipation and noise problems, which result from communicating analog signals across an imager at high data rates, are greatly reduced.

Using hybridization methods, Lincoln Laboratory has demonstrated 32×32-pixel focal planes based on Geiger-mode avalanche photodiodes (APDs), which can detect a single photon and produce a digital logic pulse directly from the detector [11]. As shown in Fig. 21, the detector is connected directly to a CMOS inverter, the output of which serves as a stop signal to a digital timing circuit, or in the case of intensity imaging as an increment signal to a counter. This digital-domain design yields power savings, noiseless readout, and quantum-limited sensitivity. Multiple operating voltages for arming the APD and operating the low-power digital circuitry can be readily accommodated. By using the SOI-based, oxide-bonded, micron-scale 3-D interconnection technology previously described, the pixel pitch of the array can be further reduced and the timing resolution improved, to produce a scalable architecture.
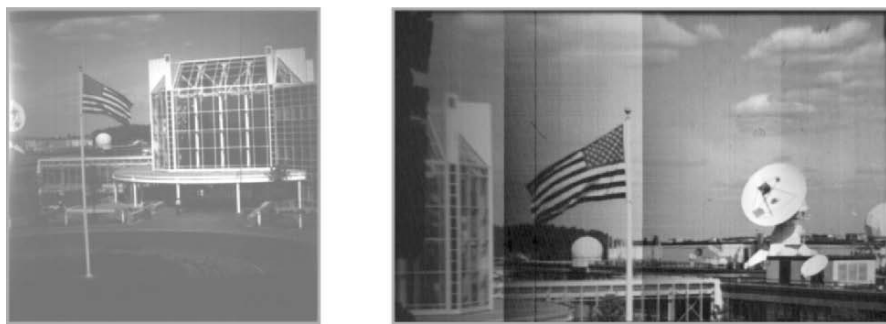
Figure 20.   Four-side abuttable vertically integrated imaging tile: *(left)* front illuminated and *(right)* back illuminated (partial frame of top 700 rows).

7.   ACKNOWLEDGEMENTS
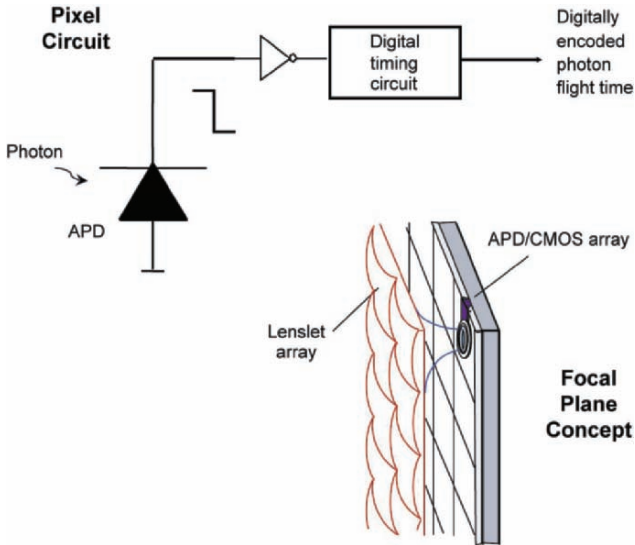
Figure 21. Geiger-mode imager illustrating photon-to-digital conversion.

8. REFERENCES

[1] L. Kozlowski, G. Rossi, L. Blanquart, R. Marchesini, Y. Huang, G. Chow, and J. Richardson, 2005, *A progressive 1920×1080 imaging system-on-chip for HDTV cameras*, IEEE International Solid-State Circuits Conference, Digest of Technical Papers, pp. 358-359.

[2] M. Loose, L. Lewyn, H. Durmus, J. D. Garnett, D. N. Hall, A. B. Joshi, L. J. Kozlowski, and I. Ovsiannikov, 2003, *SIDECAR low-power control ASIC for focal plane arrays including A/D conversion and bias generation*, Proc. SPIE, vol. **4841**, pp. 782-794.

[3] A. Joshi, D. Chiaverini, K. Jung, V. Douence, G. Wijeratne, G. M. Williams, and M. Loose, 2005, *Scalable architecture for high-resolution video-rate CMOS imaging system on chip*, IEEE Workshop on Charge-Coupled Devices and Advanced Image Sensors, pp. 181-184.

[4] J. D. Garnett and W. J. Forrest, 1993, *Multiply sampled read limited and background limited noise performance*, Proc. SPIE, vol. **1946**, pp. 395-404.

[5] C. W. McMurtry, University of Rochester, private communication. Data shown in A. Hoffman et al., 2005, *1024×1024 Si:As IBC detector arrays for mid-infrared astronomy*, SDW 2005 Proceedings, Springer, Netherlands, pp. ?.

[6] J. A. Gregory, B. E. Burke, M. J. Cooper, R. W. Mountain, and B. B. Kosicki, 1996, *Fabrication of large-area CCD detectors on high-purity float zone silicon*, Nucl. Instrum. Methods Phys. Res. A, vol. **377**, pp. 325-333.

[7] V. Suntharalingam, B. Burke, M. Cooper, D. Yost, P. Gouker, M. Anthony, H. Whittingham, J. Sage, S. Rabe, C. Chen, J. Knecht, S. Cann, P. Wyatt, and

C. Keast, 2000, *Monolithic 3.3 V CCD/SOI-CMOS imager technology*, International Electron Devices Meeting Technical Digest, pp. 697-700.

[8]   S. G. Wuu, D. N. Yaung, C. H. Tseng, H. C. Chien, C. S. Wang, T. K. Fang, C. C. Wang, C. G. Sodini, Y. K. Hsiao, C. K. Chang, and B. J. Chang, 2000, *High performance 0.25-μm CMOS color imager technology with nonsilicide source/drain pixel*, International Electron Devices Meeting Technical Digest, pp. 705-708.

[9]   Y. Bai, S. G. Bernd, J. R. Hosack, M. C. Farris, J. T. Montroy, and J. Bajaj, 2004, *Hybrid CMOS focal plane array with extended UV and NIR response for space applications*, Proc. SPIE, vol. **5167**, pp. 83-93.

[10]   V. Suntharalingam, R. Berger, J. A. Burns, C. K. Chen, C. L. Keast, J. M. Knecht, R. D. Lambert, K. L. Newcomb, D. M. O'Mara, D. D. Rathman, D. C. Shaver, A. M. Soares, C. N. Stevenson, B. M. Tyrrell, K. Warner, B. D. Wheeler, D. R. W. Yost, and D. J. Young, 2005, *Megapixel CMOS image sensor fabricated in three-dimensional integrated circuit technology*, IEEE International Solid-State Circuits Conference, Digest of Technical Papers, pp. 356-357.

[11]   B. F. Aull, A. H. Loomis, D. J. Young, A. Stern, B. J. Felton, P. J. Daniels, D. J. Landers, L. Retherford, D. D. Rathman, R. M. Heinrichs, R. M. Marino, D. G. Fouche, M. A. Albota, R. E. Hatch, G. S. Rowe, D. G. Kocher, J. G. Mooney, M. E. O'Brien, B. E. Player, B. C. Willard, Z.-L. Liau, and J. J. Zayhowski, 2004, *Three-dimensional imaging with arrays of Geiger-mode avalanche photodiodes*, Proc. SPIE, vol. **5353**, pp. 105-116.

On their free day, the participants paid an emotional visit to the burial place of deceased astronomical detectors. (Courtesy: Sandro D'Odorico).

OVERVIEW OF ROCKWELL SCIENTIFIC IMAGING TECHNOLOGIES

Michael H. MacDougal, Yibin Bai, Markus Loose, James W. Beletic
Rockwell Scientific Company

Abstract: *Rockwell Scientific Company (RSC) is a leading provider of CMOS-based Sensor Chip Arrays (SCAs) to the astronomy community. The most advanced astronomy product is the 2K×2K HAWAII-2RG (H2RG) Readout Integrated Circuit (ROIC) that offers a large number of advanced features to the astronomer including embedded reference pixels, guide window, and sub-frame integration. The H2RG ROIC is most often hybridized with HgCdTe detector material for infrared light detection. RSC is delivering a large number of H2RG HgCdTe arrays to several large telescopes; with a 3-side buttable package, the H2RG is being integrated into at least six 4K×4K mosaics for ground and space telescopes. The H2RG ROIC is also used for visible light sensing by mating it to silicon PIN diodes that have high quantum efficiency and high operability – this product is called HyViSI. The integration of HAWAII-1RG and HAWAII-2RG SCAs into instruments is now made easier by the SIDECAR ASIC that provides interface electronics on a single silicon chip. The SIDECAR ASIC enables a hundredfold reduction in the size, power, and weight of the external electronics system. RSC is now developing the next generation astronomy arrays, 4K×4K and 6K×6K SCAs, that further extend the scientific reach of astronomers.*

Key words: *HAWAII-2RG, mosaic, SIDECAR, ASIC, HgCdTe, silicon, HyViSI.*

1. LARGE FORMAT FOCAL PLANE ARRAYS

Rockwell Scientific Company (RSC) produces a wide variety of Sensor Chip Arrays (SCAs) for demanding astronomical imaging and spectroscopy applications. These devices achieve high quantum efficiency, low readout

noise and extremely low dark current. Presently, RSC array formats range from 256×256 (PICNIC) to 2K×2K (HAWAII-2RG). The HAWAII-2RG [1] is the fifth generation RSC astronomy Readout Integrated Circuit (ROIC) and contains many desirable features including:

- reference pixels (row and column plus reference output)
- independent readout of a guide window of adjustable size
- complete glow suppression from output buffer and clock drivers
- radiation single event upset error-detection and correction
- Schmidt triggering of the clock signals
- selectable number of outputs (1, 4 or 32)
- low power output amplifiers
- three-side close buttability
- three reset options (frame, line and pixel)
- full ROIC programmability via 3-line digital interface
- 100-500 kHz "slow" output mode
- 1-10 MHz "fast" output mode
- 1× to 16× gain

As shown in Fig. 1, the ROIC can be hybridized to both infrared and visible RSC detector technologies. Typical infrared astronomy applications require spectral response out to 1.7 μm (NIR), 2.5 μm (SWIR) and 5 μm (MWIR), however RSC has also fabricated a Long-Wave Infrared (LWIR) 10 μm cutoff 512×512 SCA using the HAWAII-1RG as the ROIC. RSC has two technologies for fabricating infrared detector material:

- PACE-1 Liquid Phase Epitaxy (LPE) for SWIR,
- Molecular Beam Epitaxy (MBE) for NIR through LWIR applications.

PACE-1 HgCdTe is grown on sapphire substrate and MBE HgCdTe is grown on lattice matched CdZnTe substrate. While the cost of sapphire substrates is lower than CdZnTe, the CdZnTe crystal structure is better matched to HgCdTe and produces higher quality detectors. Consequently PACE is relatively more economical while MBE provides higher performance; the user can choose which IR detector material is most appropriate for the application.

   For visible spectral sensitivity, RSC has two detector technologies:

- substrate-removed MBE HgCdTe (discussed in Section 1.1),
- Si PIN detector - named HyViSI™ for Hybrid Visible Silicon Imager (discussed in Section 1.2).

While substrate removed MBE HgCdTe provides continuous visible through infrared spectral coverage, HyViSI offers lower cost and higher operating temperature at visible wavelengths.

	NICMOS 1987	PICNIC 1990		HAWAII-1 1994	HAWAII-2 1998	HAWAII-1R 2000
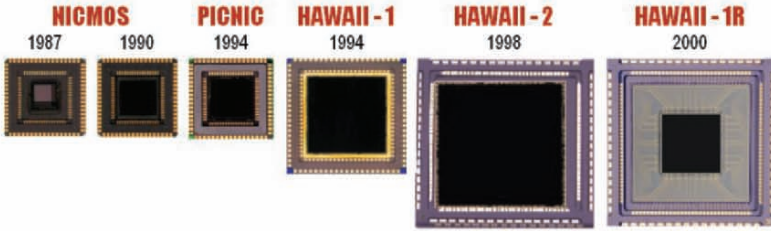
# of Pixels	128 x 128	256 x 256		1K x 1K	2K x 2K	1K x 1K
Pixel size		40 μm		18.5 μm	18 μm	
CMOS gen.			0.8 μm			0.5 μm
Read Speed		up to 500 kHz (out of each port)			up to 250 kHz (out of each port)	
# of Ports		4			4 or 32	
Reset mode	Line and Pixel reset			Line reset only		
Integration			Full frame integration only			
Features						Reference pixels

HAWAII	1RG 2001	2RG 2002	4RG-10 2006	6RG-10 and 4RG-15 2006	

# of Pixels	1K x 1K	2K x 2K	4K x 4K	6K x 6K	4K x 4K
Pixel size	18 μm		10 μm	10 μm	15 μm
CMOS gen.			0.25 μm		
Read speed	up to 500 kHz (slow mode) and up to 10 MHz (fast mode) - out of each port				
# of Ports	1, 2 or 16	1, 4 or 32	1, 4, 16, 32 or 64	1, 6, 24, 48 or 96	
Reset mode	Global (frame), Line and Pixel reset options				
Integration	Full frame or sub-frame integration options				
Features	Reference output, reference pixels Guide window Interfaces directly to SIDECAR ASIC		Reference output, reference pixels Guide window, Anti-blooming drain in each pixel Interfaces directly to SIDECAR ASIC		

Detector Material Options (each of these can be hybridized to any of the readout circuits)				
Bandpass	**Technology**	**QE**	**Comments**	
SWIR	PACE-1 LPE (liquid phase epitaxy) HgCdTe on Sapphire substrate	50 - 80 %	Dark current < 0.05 e⁻/pix/sec	
NIR, SWIR MWIR, LWIR	MBE (molecular beam epitaxy) HgCdTe on CdZnTe substrate	65 - 95 %	Dark current < 0.005 e⁻/pix/sec Low persistence	
VIS - LWIR	Substrate-removed MBE HgCdTe	70 - 95 %	Visible through IR response Eliminates substrate cosmic ray issues	
VIS	HyViSI Silicon	80 - 90 %	QE vs. λ optimized by AR coating Thick detector gives good QE to 1.05 μm	

Figure 1. The RSC astronomy array family, an industry leader for 20 years.

1.1   Mosaic Focal Plane Arrays (FPAs)

Mosaic FPAs using several RSC SCAs are now in use at ground-based observatories, and are being designed and assembled for space telescopes. These arrays are enabling astronomers to continue to push the boundaries of astronomical science. Figure 2 shows an image taken at the UKIRT by the WFCAM imager, which employs a mosaic of four HAWAII-2 SWIR SCAs. While this paper was written, Canada-France-Hawaii Telescope was commissioning a mosaic of four HAWAII-2RG SCAs in its WIRCAM instrument (see Fig. 3). The University of Hawaii has an operating 4K×4K HAWAII-2RG mosaic and the Gemini and European Southern observatories are also commissioning mosaics of four HAWAII-2RG SWIR SCAs.

Figure 2. Image taken by a mosaic of four HAWAII-2 SCAs in the WFCAM instrument on the UKIRT telescope (image courtesy of JAC).
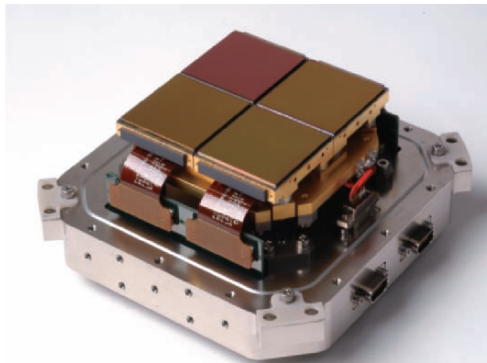
Figure 3. Packaged mosaic of HAWAII-2RG SCAs for the WIRCAM instrument on the CFHT telescope (image courtesy of GL Scientific and CFHT)

The development of high performance detectors with the feature-rich HAWAII-2RG ROIC convinced the JWST team at NASA to use RSC's substrate-removed SWIR and MWIR SCAs in the Near Infrared Camera (NIRCam) and Near Infrared Spectrometer (NIRSpec), both instruments include mosaics of HAWAII-2RG SCAs [2].

1.2   Silicon PIN HyViSI™ Visible Sensors

In addition to the infrared arrays, RSC also produces SCAs based on silicon technology that is sensitive to the visible spectrum. RSC's HyViSI™ utilizes Si PIN detectors mated to the several RSC ROICs to attain low noise images in the visible range [3].

Figure 4 shows the quantum efficiency of a HyViSI SCA. The quantum efficiency is greater than 80% for the 500-900 nm range, and achieves greater than 50% QE in the deep red, between 900 and 1000 nm, due to the thickness of the silicon detector layer. The detector material has a bias voltage so that it is fully depleted which minimizes charge diffusion – point spread functions of less than 7.5 µm FWHM have been demonstrated. These arrays consistently show high operability (>99.99%), single CDS read noise of <13 electrons at 100 kHz clock rate, dark current of less than 0.001 electrons/pixel/sec at 140 K, and response non-uniformity less than 4%.
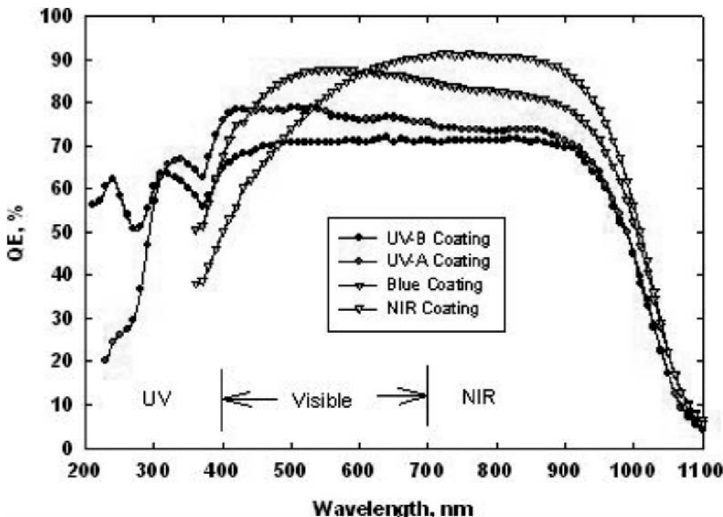
Figure 4. Quantum efficiency of Rockwell Scientific's HyViSI Si PIN arrays. The QE at each wavelength is a function of the AR coating.

2.   THE SIDECAR ASIC

Most contemporary astronomy SCA designs, including visible CCDs and infrared SCAs, are analog devices that require external electronics for operating the SCA. Support electronics tend to be bulky and power hungry, with a complex interface to the SCA. To dramatically improve SCA integration by reducing size, weight, and power, and to greatly improve overall system performance, RSC has developed an Application Specific Integrated Circuit (ASIC) called SIDECAR (System for Image Digitization, Enhancement, Control And Retrieval) [4]. SIDECAR is a SCA interface chip that provides clocks and biases to the SCA, and performs amplification and analog-to-digital conversion of the SCA analog outputs. SIDECAR has 36 analog input channels, and digitization can be done with 12 or 16 bit resolution. SIDECAR presents an all-digital interface to the external world, providing the following advantages to system design:

- Simplifies the overall system architecture and reduces the number of wires within the system
- Eliminates the risks and problems of transmitting low-noise analog signals over long distances
- Reduces the risk of integrating one or more SCAs into mosaics
- Offers high flexibility and redundancy due to broad programmability
- Digitizes 16-bit data at 500 kHz (per port) or 12-bit data at up to 10 MHz (per port) for a maximum total 12-bit pixel rate of 160 MHz

Figure 5 shows a schematic diagram of the SIDECAR ASIC and interfaces with SCA (multiplexer) and the host (external) electronics. For more detail, see the paper by Loose, et al. in these proceedings [4].
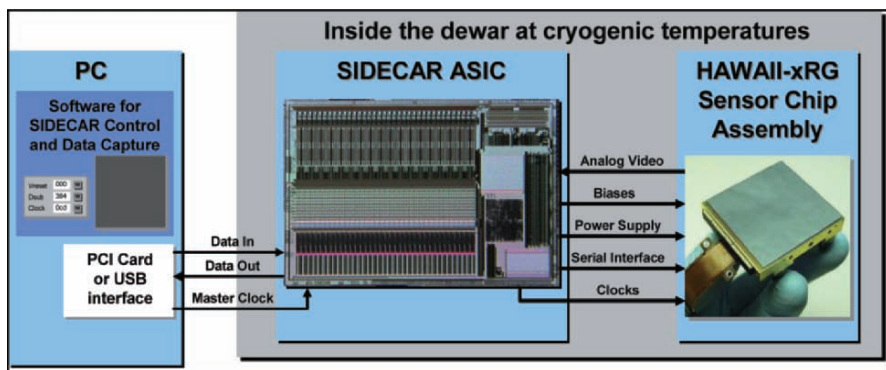
Figure 5. Schematic diagram of a system using the SIDECAR ASIC

Testing of the 2nd version of the ASIC is completed and all major functional blocks have been demonstrated. When configured for low power

astronomy applications, the total power consumption is 8.4 mW for a 2K×2K H2RG SCA and SIDECAR (four 16 bit ports at 100 kHz).

The Analog-to-Digital Converters (ADCs) have demonstrated excellent performance. The 12 bit ADCs have excellent linearity (DNL < ± 0.3 LSB, INL < ± 0.8 LSB) and noise is less than 0.3 LSB. The 16 bit ADCs also have excellent characteristics: DNL < ± 0.3 LSB, INL < ± 0.7 LSB. When the SIDECAR is used in conjunction with a HAWAII-2RG SCA, the total noise in a 1000 sec exposure has been measured to be less than 6 electrons (after averaging multiple reads). The first shipments of SIDECAR ASICs to astronomers will be in the fourth quarter of 2005.

3.   4K × 4K, 6K × 6K AND BEYOND

RSC is currently completing the design of a new readout circuit, a design that will be completed and in fabrication by the time that these proceedings are published. This design, which we have named the "HxRG", incorporates all the excellent features of the H2RG and also includes an improved amplifier design for lower noise and anti-blooming circuitry in every pixel. We can use the ROIC design to fabricate very large arrays, up to 16K in one dimension, with the largest ROIC only limited by the size of a silicon wafer, the maximum size of detector arrays, and the economics of yield of large hybrid sensors. In 2006, this ROIC will be used to make 4K×4K visible and IR imagers with 15 μm pixels, and 4K×4K and 6K×6K HyViSI visible imagers with 10 μm pixels. These developments along with ongoing process improvements will provide higher performance, lower cost SCAs for next generation instruments and the coming generation of extremely large telescopes.

4.   REFERENCES

[1] Loose, M., Farris, M., Garnett, J.D., Hall, D.N.B., Kozlowski, L.J., 2002, *HAWAII-2RG: A 2K×2K CMOS Multiplexer for Low and High Background Astronomy Applications*, SPIE Astronomical Telescope and Instrumentation Symposium.

[2] Garnett, J., Farris, M., Wong, S., Zandian, M., Hall, D.N.B, Jacobson, S., Luppino, G., Parker, S., Dorn, D., Franka, S., Freymiller, E., McMuldroch., S., 2004, *2K×2K Molecular Beam Epitaxy HgCdTe Detectors for the James Webb Space Telescope NIRCam Instrument*, SPIE Astronomical Telescope and Instrumentation Symposium.

[3] Bai, Y., Bernd, S.G., Hosack, J.R., Farris, M.C., Montroy, J.T., Bajaj, J., 2003, *Hybrid CMOS Focal Plane Array with Extended UV and NIR Response for Space Applications*, SPIE Annual conference.

[4] Loose, M., 2005, *SIDECAR ASIC - Control Electronics on a Chip*, these proceedings.

Jim Beletic expediting the pizza service in Forza d'Agró.

Martin Roth enjoying the beautiful coast of Sicily during
the Wednesday free afternoon.

2K×2K NIR HGCDTE DETECTOR ARRAYS FOR VISTA AND OTHER APPLICATIONS

Peter J. Love, Alan W. Hoffman, Ken J. Ando, Elizabeth Corrales, William D. Ritchie, Neil J. Therrien, Joe P. Rosbeck, Roger S. Holcombe
Raytheon Vision Systems

Abstract: *The demand for large-format NIR arrays has grown for both ground-based and space-based applications. These arrays are required for maintaining high resolution over very large fields of view for survey work. We describe results of the development of a 2048×2048 HgCdTe/CdZnTe array with 20 micron pixels that responds with high Quantum Efficiency (QE) over the wavelength range of 0.85 to 2.5 microns. With a single-layer antireflection coating, the responsive QE is greater than 70% from 0.9 micron to 2.4 microns. Dark current is typically less than $1e^-$/sec at 80 K. The modular package for this array, dubbed the VIRGO array, allows three-side butting to form larger mosaic arrays of 4K×2nK format. The VIRGO ROIC utilizes a PMOS Source Follower per Detector (SFD) input circuit with a well capacity of about 3×10^5 electrons and with a read noise of less than 20 e^- rms with off-chip Correlated Double Sampling (CDS). Other features of the VIRGO array include 4 or 16 outputs (programmable), and a frame rate of up to 1.5 Hz in 16-output mode. Power dissipation is about 7 mW at a 1 Hz frame rate. Reset modes include both global reset and reset by row (ripple mode). Reference pixels are built-in to the output data stream. The first major application of the VIRGO array will be for VISTA, the UK's Visible and Infrared Survey Telescope for Astronomy. Raytheon Vision Systems has completed delivery of 16 Science Grade arrays and four Engineering arrays to VISTA. The VISTA FPA will operate at near 80 K. The cutoff wavelength of the HgCdTe detector can be adjusted for other applications. Space applications include SNAP, the Supernova/Acceleration Probe, which requires a shorter detector cutoff wavelength of 1.7 microns. For applications which require both visible and NIR response, the detector CdZnTe substrate can be removed after hybridization, allowing the thinned detector to respond to visible wavelengths as short as 0.4 microns.*

Key words: *VIRGO, VISTA, NIR, HgCdTe, SFD, large-format, mosaic FPA, SCA.*

1.   INTRODUCTION

The demand for large-format NIR arrays has grown for both ground-based and space-based applications. These arrays are required for maintaining high resolution over very large fields of view for survey work. RVS has developed a Readout Integrated Circuit (ROIC) that can be fabricated in integer m×n multiples of a basic 512×1024 format building block using Reticle Image Composition Lithography (RICL). The ROIC, referred as the VIRGO array [1], and the module package housing the 2K×2K Sensor Chip Assembly (SCA) have been designed to be 3-side buttable for fabrication of large mosaic arrays of 4K×2nK format. The first major application of this array will be for VISTA, the UK's Visible and Infrared Survey Telescope for Astronomy, which requires 16 Science-Grade 2K×2K modules. VISTA is designed to operate in the Z, J, H, and K_s bands between about 1 micron and 2.5 microns. The SWIR HgCdTe detectors will operate near 80 K. The following sections will briefly describe the module package and a summary of the performance of the 16 delivered Science Grade modules. Additional details on the detectors, VIRGO ROIC and module package may be found in a previous publications [2,3,4]. Finally, detailed data will be shown for one science grade module, Module 39.

2.   2K × 2K MODULE PACKAGE

The 2K×2K module package for VISTA is a reliable, robust 3-side buttable package which allows the fabrication of large mosaic arrays of 4K×2nK format (see Fig. 1). Since each module is designed to be identical, all the modules are interchangeable. The module consists of an SCA mounted to a metal pedestal on which a thermal flex cable is mounted. A multilayer ceramic motherboard provides electrical connections between the SCA and the cable and also supports surface mount components including heaters, temperature sensors, resistors and capacitors.   The module is designed to be easily integrated onto a platform with "plug-and-play" operation. This is accomplished with three simple interfaces: a mechanical interface which allows automatic alignment in x, y, and z through precision datums on the module pedestal; an electrical interface through a thermal flex cable with a 51-pin MDM connector; and a thermal interface which consists of a cold strap attachment to the back of the module pedestal. For VISTA, 16 modules are mounted in a 4×4 configuration on a "plate" to form the mosaic focal plane array. VISTA doesn't require butting of adjacent modules.

- **3-side buttable**
- **45-trace cable**
- **51-pin micro-D MDM connector**

Cover

Sensor Chip Assembly (SCA)

Pedestal

Motherboard

45 Trace Cable

Cable Clamp

Flatness requirement:
  Each detector (2K × 2K module) shall be flat to 12 µm
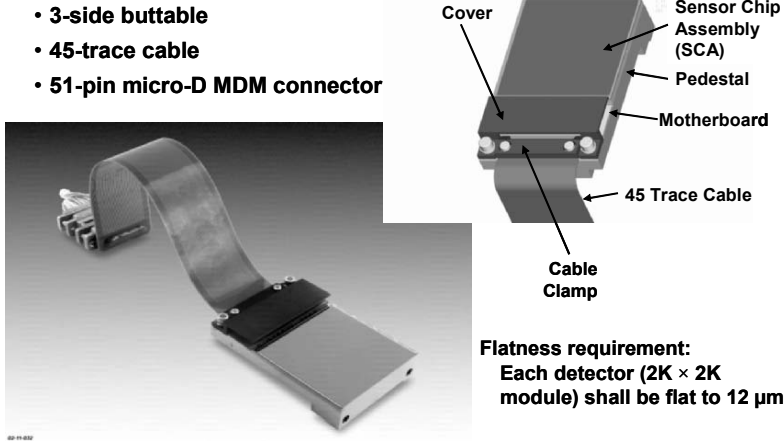
Figure 1. VISTA 2K×2K module package.

3.   PERFORMANCE SUMMARY FOR 16 SCIENCE GRADE VISTA MODULES

Figures 2, 3 and 4 provide a summary of the performance of the 16 science grade VISTA modules. Figure 2 shows array-average QE for the J, H, and K bands. These values reflect the average of all 2048×2048 active pixels on each array. In Figure 3, the QE uniformity is shown for the same modules (sigma/mean in %). All modules meet the VISTA QE requirements in all three spectral bands (J-band: >38%; H- and K-bands: >47%). In addition, all modules meet the QE uniformity requirement of <10% sigma/mean with the exception of the J band on two modules (see Fig. 3). Similar results are shown for dark current in Figure 4. Dark current was measured at 78 K with 500 mV of applied detector bias. Array-average dark currents were generally less than 1e$^-$/sec at 78 K. Other institutions have measured significantly lower dark currents than measured at RVS. For example, Roger Smith [5] at Caltech measured 0.025e$^-$/sec at 79 K on module 19 compared to the RVS value of 0.92e$^-$/sec and Craig McMurtry [6] at the University of Rochester measured a mean dark current of 0.019e$^-$/sec (median dark current was 0.029e$^-$/sec) on module 27 compared to the RVS value of 0.45e$^-$/sec. Roger Smith also measured a MUX glow of 0.04e$^-$/read for the VIRGO MUX.
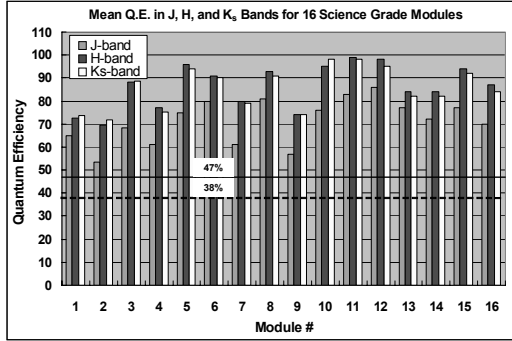
Figure 2.   QE performance summary for the 16 science grade VISTA modules. The VISTA requirement is >38% for the J-band and > 7% for the H- and K-bands.
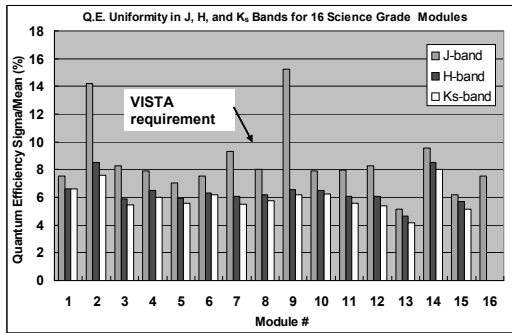
Figure 3. QE sigma/mean performance summary for the 16 science grade VISTA modules. The VISTA requirement is sigma/mean <10% for all three spectral bands.
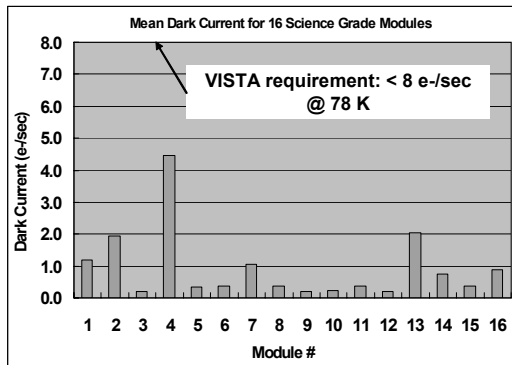
Figure 4. Dark current performance summary at 78K for the 16 science grade VISTA modules. The VISTA requirement is <8e⁻/sec at 77K.

4.   VISTA MODULE 39 PERFORMANCE

This section provides sample data for delivered science grade Module 39. Data for Module 22 were reported in a previous paper [3] and data for Module 45 are reported in another paper in these proceedings [7].   As described above, this module received a single-layer AR coating with a minimum in reflectance at a wavelength of 1.4 microns. Figure 5 shows a map of QE in the J band for the entire 2048 × 2048 active array together with the associated QE histogram.
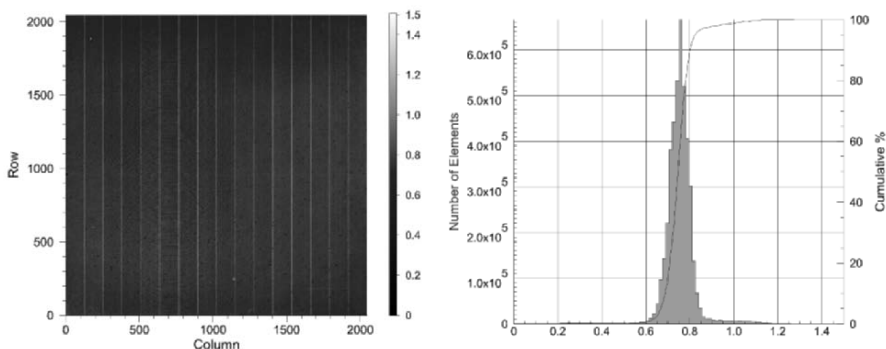
Figure 5. QE: J-Band Array-Mean = 76.0% with sigma/mean = 7.9%. Pixel operability is 99.74% (entire 2048 × 2048 array).

The mean QE in the J band is 76.0% with uniformity (sigma/mean) of 7.9%. QE operability for the entire 2048×2048 array in the J band is 99.74%. Figures 6 and 7 display similar data for the H and K bands. For the H band, the mean QE is 95.0% with uniformity (sigma/mean) of 6.5%. QE operability for the entire 2048×2048 array in the H band is 99.76%. For the K band, the mean QE is 98.0% with uniformity (sigma/mean) of 6.2%. QE operability for the entire 2048×2048 array in the H band is 99.84%.

Figure 8 shows dark current performance and Fig. 9 shows detector relative spectral response. Figure 10 displays an interferogram illustrating the flatness of the detector, which shows a peak-to-valley flatness of 3.1 μm as measured over 20 points on the detector.
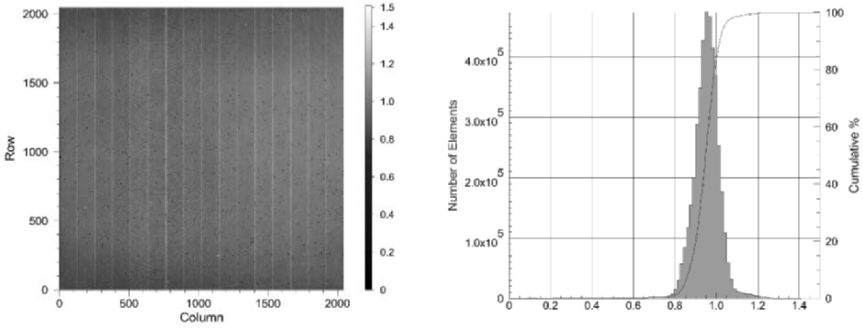
Figure 6.   QE: H-Band Array-Mean = 95.0% with sigma/mean = 6.5%. Pixel operability is
99.76% (entire 2048×2048 array).
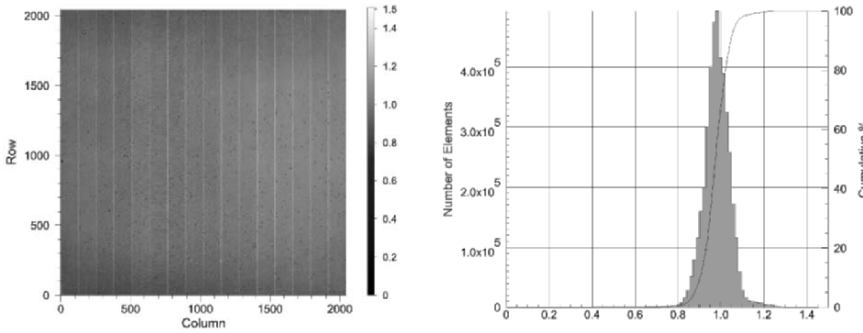
Figure 7.   QE: K-Band Array-Mean = 98.0% with sigma/mean = 6.2%. Pixel operability is
99.84% (entire 2042048 array).
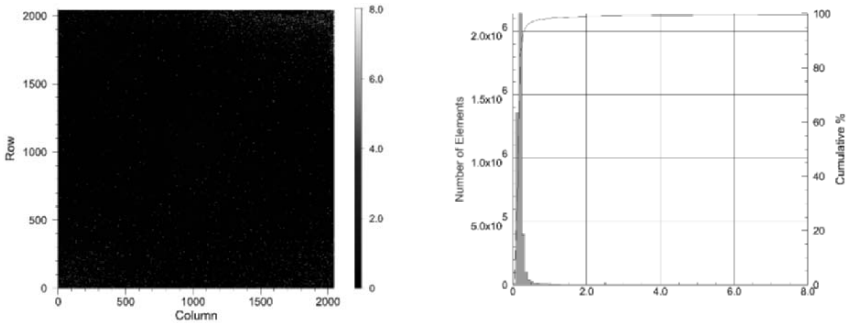
Figure 8.   Dark current: Array-Mean = 0.23 e⁻/sec with a pixel operability of 99.47% (entire
204×2048 array).
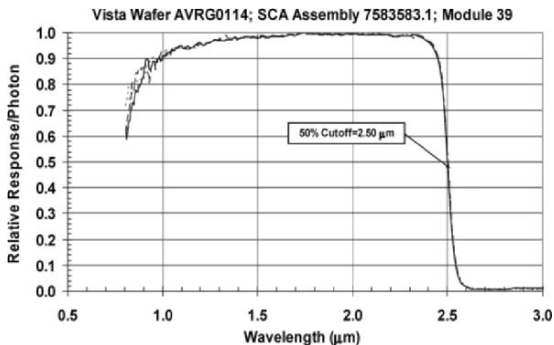
Figure 9. Detector relative spectral response. The cutoff wavelength is 2.50 μm (50% relative response per photon). The cuton wavelength of ~0.8 μm is determined by the CdZnTe substrate.
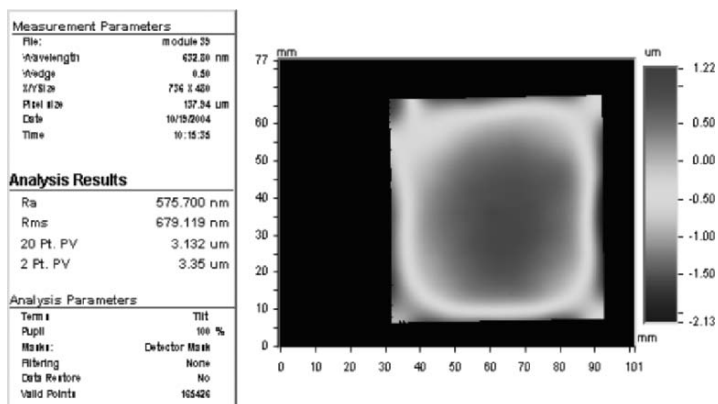
Figure 10. SCA Flatness: 3.1 μm Peak-to-Valley (20 points).

5. SUMMARY

Raytheon Vision Systems has completed delivery of 16 science grade 2K×2K/20 μm modules to VISTA. The modules meet all VISTA requirements with the exception of QE uniformity in the J band on two modules. Although designed specifically for VISTA, which utilizes SWIR HgCdTe detectors with a cutoff wavelength of 2.5 microns operating at ~80 K, the VIRGO ROIC is compatible with a variety of detectors, including HgCdTe with other cutoff wavelengths, InSb and Si PIN detectors [8]. The HgCdTe detectors have high QE and flat response over the wave-band of interest. With a suitable AR coating, QE in excess of 90% can be achieved

over a wide wavelength range. A robust and reliable 3-side buttable module package has been developed for the 2K×2K SCA which provides a simple "plug-and-play" interface. Thermal cycle reliability is excellent, with more than 200 thermal cycles between ambient and 80 K demonstrated to date with no loss in pixel operability. The module package designed for VISTA is now available for other astronomy programs, which may require different detector cutoff wavelengths. For example, the Supernova/Acceleration Probe (SNAP) will require a detector with a cutoff wavelength of 1.7 microns. Significant progress has been made in optimizing 1.7 micron HgCdTe detectors at 140 K: Roger Smith has measured 80% QE with "flat" response and CDS read noise of 16e⁻ rms with no observable RTS noise in the VIRGO MUX [9]. RVS has measured a dark current of 0.25 e⁻/sec at 140 K for a 1.8 micron cutoff detector. Further reduction in the dark current is expected by reducing the cutoff wavelength to 1.7 microns.

6.   REFERENCES

[1] Gulbransen, D. J., Love, P. J., Murray, M. P. , Lum, N. A., Fletcher, C. L., Corrales, E. Mills, R.E., Hoffman, A. W., Ando, K. J., 2002, *Megapixel and Larger Readouts and FPAs for Visible and Infrared Astronomy*, Proc. SPIE, Instrument Design and Performance for Optical/Infrared Ground-based Telescopes, M. Iye and A. F. M. Moorwood, (eds), **4841**, pp. 395-404.

[2] P. J. Love, A. W. Hoffman, D. J. Gulbransen, M. P. Murray, K. J. Ando, N. J. Therrien, J. P. Rosbeck, R. S. Holcombe, 2003, *Large-Format 0.85 - 2.5 Micron HgCdTe Detector Arrays for Low-Background Applications*, Proc. SPIE, Focal Plane Arrays for Space Telescopes, T. J. Grycewicz and C. R. McCreight (eds), **5167**, pp. 134-143.

[3] N. Bezawada, D. Ives, G. Woodhouse, 2004, *Characterization of VISTA IR Detectors*, Proc. SPIE, Optical and Infrared Detectors for Astronomy, J. W. Beletic and J. D. Garnett (editors), **5499**.

[4] P. J. Love, A. W. Hoffman, K, J. Ando, E. Corrales, W. D. Ritchie, N. J. Therrien, J. P. Rosbeck, R. S. Holcombe, and D. J. Gulbransen, 2004, *2K × 2K HgCdTe Detector Arrays for VISTA and Other Applications*, Proc. SPIE, Optical and Infrared Detectors for Astronomy, J. D. Garnett and J. W. Beletic (editors), **5499**, pp. 68-77.

[5] R. Smith, private communication.

[6] C. W. McMurtry, T. Allen, W.J. Forrest, J. L. Pipher, 2005, *Characterization of 2.5 Micron HgCdTe VIRGO/VISTA Detector Array*, Proc. SPIE, Focal Plane Arrays for Space Telescopes II, T. J. Grycewicz and C. J. Marshall (editors), **5902**, in press.

[7] N. Bezawada and D. Ives, 2005, *Performance Overview of VISTA IR Detectors*, these proceedings.

[8] A. W. Hoffman, P. J. Love, and J. P. Rosbeck, 2003, *Mega-Pixel Detector Arrays: Visible to 28 μm*, Proc. SPIE, Focal Plane Arrays for Space Telescopes, T. J. Grycewicz and C. R. McCreight (editors), **5167**, pp. 194-203.

[9] R. Smith, 2005, *Characterization of 1.7 μm cutoff detectors for SNAP*, these proceedings.

1024 × 1024 SI:AS IBC DETECTOR ARRAYS FOR MID-IR ASTRONOMY

Alan Hoffman, Peter J. Love, Elizabeth Corrales, Nancy A. Lum
Raytheon Vision Systems

Abstract: *1K×1K Si:As Impurity Band Conduction (IBC) arrays have been developed by Raytheon Vision Systems for the James Webb Space Telescope (JWST) Mid-Infrared Instrument (MIRI). The Si:As IBC detectors have dimensions of 25 µm pixels and respond to infrared radiation from 5 to 28 µm. Detector performance results are discussed, including dark current and relative spectral response. ROIC noise is 10e⁻ (Fowler-8) at 7 K as measured by the University of Rochester. Sensor Chip Assembly (SCA) data from NASA Ames show low dark current and uniform response. Design details of a companion 1024×1024 array suitable for high-background, ground-based astronomy are also revealed for the first time. This array will have a large well capacity and high frame rate capability.*

Key words: *Aquarius, astronomy, Si:As IBC, JWST, MIRI, ROIC, SCA*

1. INTRODUCTION

The MIRI on the JWST requires detectors that sense infrared over a wavelength band of 5 to 28 µm. The obvious (and perhaps only) choice of detector material that can achieve low dark current in this band is Si:As IBC. This paper describes 1024×1024 element arrays with 25 µm pixels for MIRI that are in development. A summary of MIRI's focal plane requirements derived by JPL, which has primary responsibility for MIRI, is shown in Table I. The requirements are similar to those for the IRAC instrument on the Spitzer Space Telescope, the predecessor to JWST.

Table I. MIRI primary focal plane requirements.

Parameter		Requirement	Measured
Noise (Fowler-8 sampling)		< 19 e- @ 7.1K	10 e- @ 7.1K
Dark Current		< 0.1 e-/sec @ 7.1K	< 0.1 e-/sec @ 7.1K (Test Limit)
QE:	5 - 6 µm	> 40%	> 50%*
	6 - 12 µm	> 60%	> 60%*
	12 - 26 µm	> 70%	> 70%* (12 - 24 µm) > 30%* (24 - 26 µm)
	26 - 28.2 µm	> 5% (Goal)	> 5%

2.   SI:AS IBC DETECTORS

The most difficult requirement for the MIRI detectors is high Quantum Efficiency (QE) over the full spectral range and low dark currents. The relative response per photon as a function of wavelength is shown in Fig. 1 for three Si:As IBC detector material types.
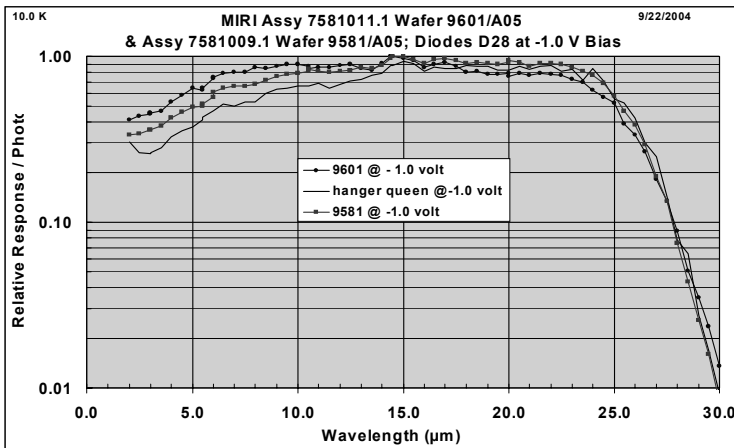
Figure 1. Relative spectral response measurements for three Si:As IBC detector materials: MIRI baseline (top curve), MIRI contingency (middle curve), and material similar to that used on Spitzer/IRAC (bottom curve). The MIRI material has higher response in the 5 to 10 µm spectral region than Spitzer/IRAC.

All these materials have nearly 100% internal QE at ~15 µm; thus these relative response curves are nearly the same as responsive QE (gain=1) if the detector has perfect Anti-Reflection (AR) coating. The material used as the baseline for MIRI exhibits the highest response. The middle curve is a material with a thinner detecting layer, processed as a "contingency" in case

the more difficult-to-produce baseline wafer failed to yield. The bottom response curve is a material similar to that flown on Spitzer/IRAC. Notice that response of the MIRI baseline material is approximately 60% higher than the Spitzer material at 5 µm. Since bare silicon reflects approximately 30% of the incident light, AR coatings have been developed for MIRI to reduce reflection losses. One coating has a minimum reflectance at 6 µm and the second has its minimum at 16 µm. Low dark current has also been achieved with MIR detectors, but due to the difficulty in measuring such low currents, the measurements must be made at the SCA level. The results are described in Section 4.

3. READOUTS (ROIC)

The primary technical challenge for the MIRI 1024×1024 readouts is functionality and low noise at the detector operating temperature of 7.1 K. Two types of starting material were used in the readout wafers: "standard" material which had been used previously for low-temperature CMOS ROICs, and "alternate" material, which was untried but was believed, for theoretical reasons, that it could be lower noise at 7 K.

Noise measurements confirmed that the "alternate" material did produce readouts that were lower noise, possibly the lowest noise ever at the 7 K operating temperature. Figure 2 shows ROIC noise as a function of the number of Fowler samples for the alternate material. These measurements, which were performed by Craig McMurtry at the University of Rochester, show that the noise is 10 electrons (Fowler-8), approximately 50% lower than the comparable noise achieved on Spitzer/IRAC.

4. 1024×1024 SENSOR CHIP ASSEMBLIES (SCAS)

Hybridization of 1024×1024 Si:As IBC detector arrays to MIRI readouts has resulted in several excellent SCAs. With 25 µm pixels, the detecting area is approximately 1 inch by 1 inch. Nearly all SCAs fabricated to date have >99.5% of the 1048576 indium bumps making electrical contact between the detector and ROIC and no degradation has been observed with repeated thermal cycling.

NASA Ames Research Center has made several key measurements of the MIRI SCAs. Figure 3 shows dark current spatial uniformity of a 1024×1024 SCA and an Arrhenius plot of log(dark current) as a function of 1000/Temperature as measured by NASA Ames. The dark current follows the expected straight line on the Arrhenius plot to 8K, indicating a thermally-

generated current. The dark current bottoms out at 0.2 e⁻/sec and appears to be uniform. The uniformity may be too good to be limited by the detector array and thus due to other effects such as dewar light leaks or hot spots. Since the detectors are sensitive to 28 μm, areas inside the dewar slightly above 10 K can contribute to the measured "dark" current. Therefore, 0.2 e⁻/sec at 7 K may be an upper limit on the detector dark current.
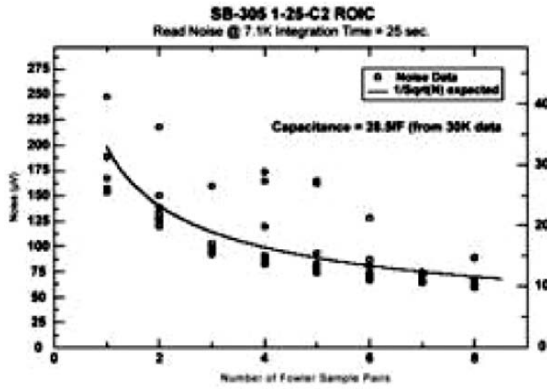
Figure 2. Noise as a function of number of Fowler samples for an "alternate" MIRI ROIC. Smooth curve represents expected 1/sqrt(N) noise reduction. While the majority of the data follow the curve, several points are above the line due to cosmic rays and excess noise in the first 80 rows.
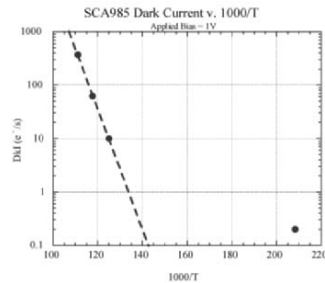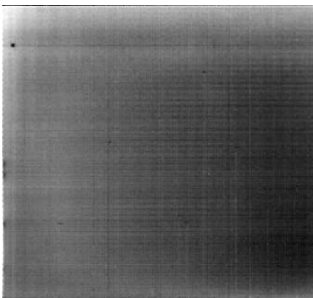
Figure 3. Preliminary dark current measurement on SCA985 by NASA Ames. *(left)* The spatial plot shows the uniformity of the dark current over the 1024×1024 array. *(right)* An Arrhenius plot of log(dark current) vs. 1000/Temperature. The dark current decreases along a straight line on this plot down to approximately 8 K, as expected for a thermally generated current. An upper limit of 0.2 e⁻/sec was measured at approximately 4.8 K.

The response uniformity of the same SCA, SCA985, was also measured by NASA Ames. Figure 4 shows spatial response uniformity and relative response as a function of detector bias. Although these data are preliminary, the SCA appears to perform well.
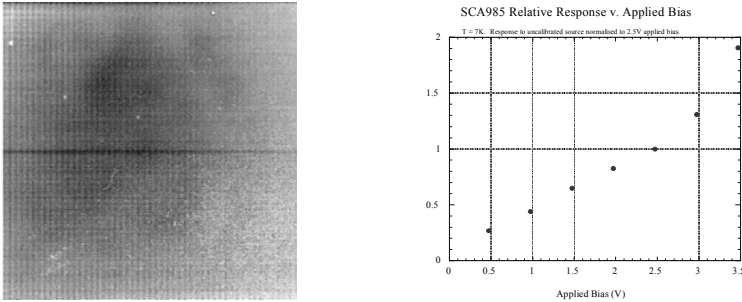
Figure 4. Preliminary response measurement of SCA 985 by NASA Ames. *(left)* The spatial plot shows the uniformity of the response to infrared radiation over the 1024×1024 array. *(right)* The relative response as a function of detector bias. All measurements were made at 7 K.

5. CURRENT STATUS FOR MIRI

Detectors and readout have both been successfully fabricated in the 1024×1024 (25 µm pixel) format required by MIRI. Compared to Spitzer/IRAC, the detector QE is approximately 60% higher between 5 and 10 µm and the ROIC noise is approximately 50% lower. SCAs have also been successfully fabricated with good indium bump interconnect yield and good thermal cycle reliability. Preliminary SCA data show low dark current and good array uniformity. Prototype SCAs are complete and the project is ready for the flight build.

6. AQUARIUS: A 1024×1024 SI:AS IBC ARRAY FOR GROUND-BASED ASTRONOMY

Based on the success of MIRI, a large-format Si:As IBC array is proposed for higher background applications, such as ground-based astronomy. This array has the same high QE and broad 5 – 28 µm spectral response as MIRI, but with much larger ROIC well capacities and higher frame rates. The pixel size is tentatively set for 30 µm, with the understanding that larger is better for MIR instruments. The gain is

selectable for high gain (1 Me⁻ well capacity) and low gain (15 Me⁻). The number of outputs is also selectable as 16 or 64. With 64 outputs, the frame rate is 100 Hz. A windowing capability, where only a selected number of rows are read out, is available for even higher frame rates. The Aquarius SCA has the capability of being read out in either snapshot mode, with externally controlled integration times, or rolling integration mode, where the integration time is the same as the frame time.

Figure 5 shows the proposed Aquarius readout layout. The unit cells are organized into blocks (shown here in 16 output mode). Each output line reads one block 128 columns wide (32 columns wide in 64 output mode) by 512 rows tall. Bond pads are located only on the top and bottom of the SCA for close-butting of arrays from end-to-end. If sufficient interest is expressed by the astronomy community, SCA design will begin in Fall 2005.
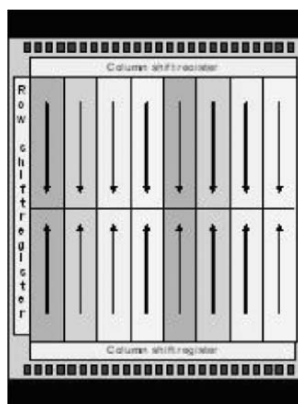
Figure 5. Layout of Aquarius 1024×1024 readout. Bond pads are located at the top and bottom with half of the outputs (selectable as 16 or 64 total) on each end of the chip. Each output reads one block of pixels 128 (32) columns wide by 512 rows tall in 16 (64) output mode. SCAs can be close-butted and stacked end-to-end to produce larger focal planes.

7. ACKNOWLEDGEMENTS

THE JAMES WEBB SPACE TELESCOPE AND ITS INFRARED DETECTORS

Bernard J. Rauscher[1] and Michael E. Ressler[2]
[1]NASA Goddard Space Flight Center, [2]Jet Propulsion Laboratory

Abstract: *The James Webb Space Telescope (JWST) was conceived as the scientific successor to the Hubble Space Telescope (HST) and Spitzer Space Telescope. The instrument suite provides broad wavelength coverage and capabilities aimed at four key science themes: 1) The end of the dark ages: first light and reionization, 2) The assembly of galaxies, 3) The birth of stars and protoplanetary systems, and 4) Planetary systems and the origins of life. To accomplish these ambitious goals, JWST's detectors provide state-of-the-art performance spanning the $\lambda = 0.6 - 28$ μm wavelength range. In this paper, we describe JWST with an emphasis on its infrared detectors.*

Key words: *James Webb Space Telescope, infrared, detector.*

1.   INTRODUCTION

The James Webb Space Telescope (JWST) was conceived as the scientific successor to the Hubble Space Telescope (HST), and to the Spitzer Space Telescope.[1] Answering scientific questions beyond the grasp of these previous missions requires a large and flexible infrared observatory. In turn, these considerations motivated the selection of a deployable, segmented primary mirror, and an L2 orbit far from the earth.

JWST has four Scientific Instruments (SIs). These are as follows: Near-Infrared Camera (NIRCam), Near-Infrared Spectrograph (NIRSpec), Mid-

---

[1]JWST was named in honor of James E. Webb, the administrator who directed NASA during the Apollo era.

Infrared Instrument (MIRI), and Fine Guidance Sensor with Tunable Imager (FGS/TI). The four SIs are located in the Integrated Science Instruments Module (ISIM), which is located behind the primary mirror in Fig. 1. In total, the SIs incorporate 16 Rockwell HAWAII-2RG mercury-cadmium-telluride (HgCdTe) Sensor Chip Assemblies (SCAs), and 3 Raytheon SB-305 Si:As SCAs (see Fig. 2).
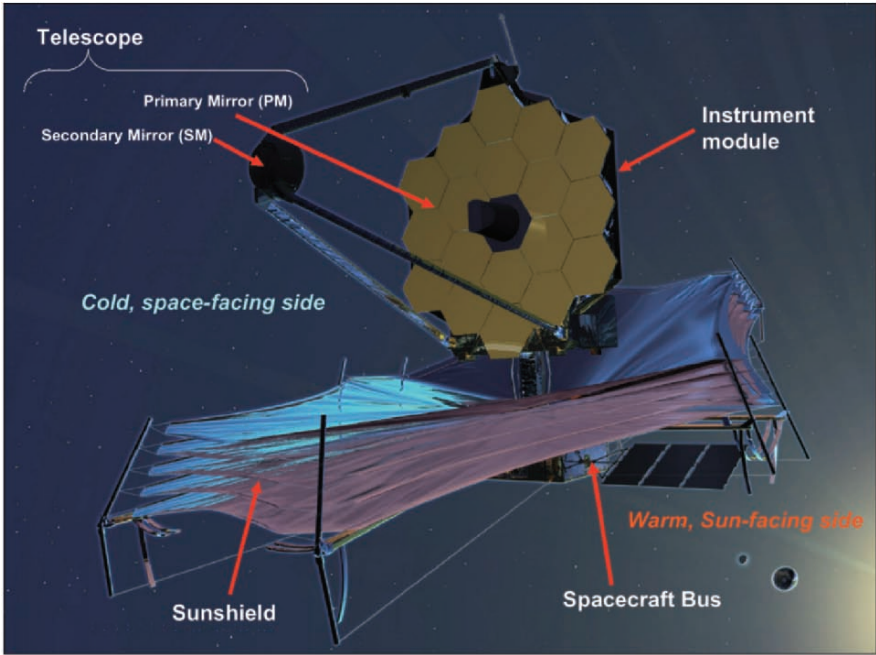
Figure 1. Fully deployed JWST showing major components.

In this paper, we briefly summarize JWST's science goals to provide context, and then discuss the mission and each of the SIs with an emphasis on detectors. Readers who are more interested in JWST's science goals may wish to see one of the more recent articles on the subject [1].

2.   SCIENCE THEMES

1) First Light: JWST's top science goal is finding the light from the first objects to coalesce after the Universe cooled following the Big Bang (see Fig. 3). The potential of JWST for studying distant sources has prompted a number of theoretical studies predicting the properties of the first stars,

which are thought to be quite different from stars forming today because of the lack of any elements heavier than helium.

- Rockwell Scientific selected for NIRCam, NIRSpec and possibly FGS
  - Total of 19 Hawaii-2RG sensor chip assemblies (SCAs) for flight and flight spare
- Raytheon Vision Systems selected for MIRI
  - Total of 6 SB-305 SCAs for flight and flight spare
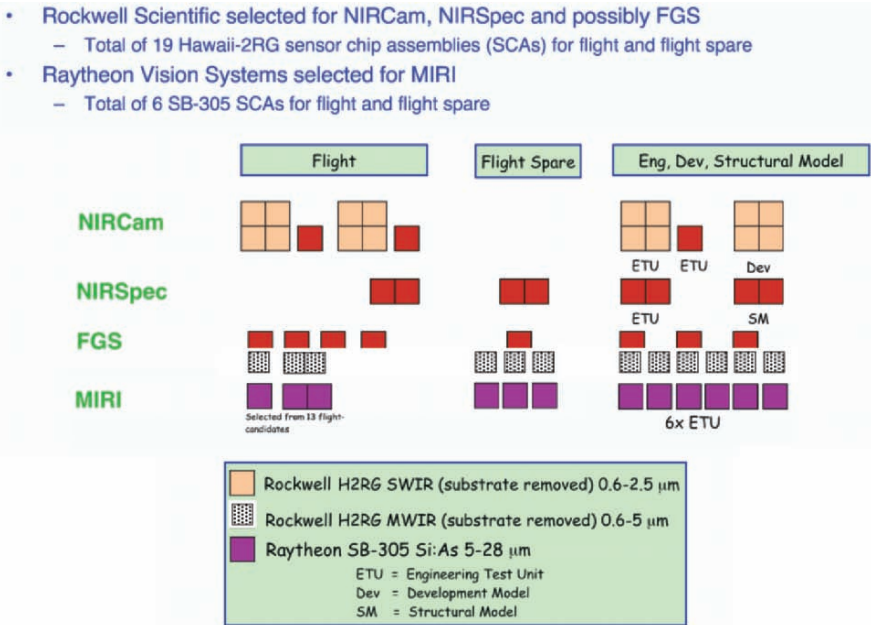
Figure 2. JWST detector summary.

Ultra-deep imaging and spectroscopic surveys using JWST are expected to detect the first super star clusters, or proto-galactic objects, to form at redshifts as high as $z = 15$-20. Appropriate timing of the observations may enable the detection of individual supernovae of super-massive population III stars. These surveys, along with spectroscopy of the highest redshift quasars, will trace the evolution of the first light objects through the epoch of reionization.

2) Assembly of Galaxies: The same observational drivers that define the search for first light also support detailed study galaxy assembly. Specifically, how do galaxies evolve from small, sub-galaxy sized fragments into the suite of morphologies and galaxy types (the Hubble Sequence) that we see today? For example, there is a significant body of literature describing how smaller mass condensations might hierarchically cluster (and evolve) to build clusters of galaxies, and eventually individual galaxies that we see today (see Fig. 4). Areas requiring additional work include the details of how the mass condensations predicted by Cold Dark Matter (CDM) models form stars and become luminous. This, of course, relates to the first

light theme, although the full history of star formation is of interest from the perspective of the assembly of galaxies.
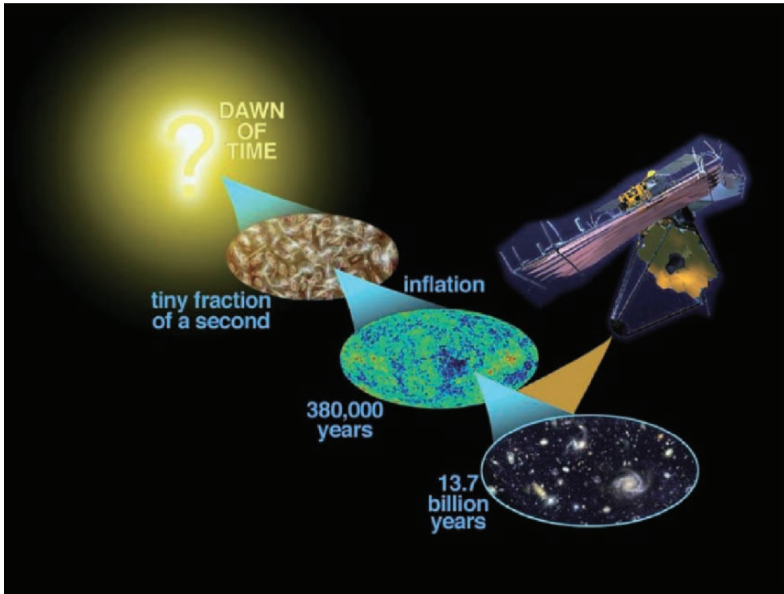
Figure 3. JWST will explore the dark ages.
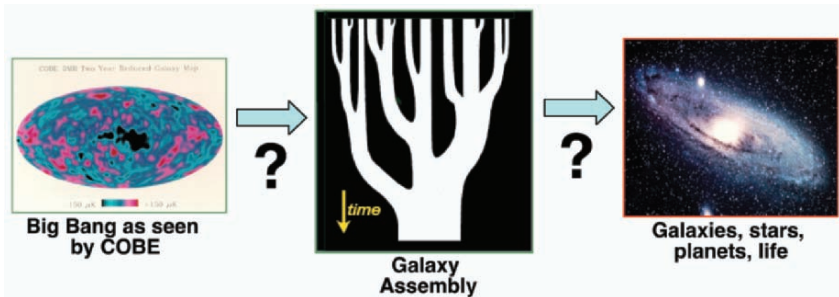
Figure 4. Hierarchical clustering models suggest that structure in the Universe begins to form on small scales, which then aggregate to build the superclusters and clusters of galaxies that we see today. The middle pane illustrates the merger process. Although hierarchical clustering has had considerable success in building up mass aggregations, work is still needed, particularly with regard to how the first stars form in low-metalicity mass aggregations.

Understanding how today's galaxies evolved from first light objects requires more knowledge than can be provided by imaging alone. Multi-object spectroscopy is required for a statistically significant sample of

galaxies spanning the redshift range over which galaxies formed. A spectral resolution, R~1000, is needed to separate diagnostic spectral lines and for estimating heavy element content and star formation rates. Moreover, NIRSpec's Integral Field Unit (IFU) will provide R~3000, 3-dimensional spectra of individual galaxies at moderate and high redshift. The IFU will provide important dynamical information on targets including active and merging galaxies.

For studying galaxies, JWST's MIRI, which also incorporates an IFU, will provide a more complete picture of galaxy structure and evolution than is possible using only near-IR wavelengths (see Fig. 5). By looking through dust (see Fig. 6) that can obscure our view of star forming regions, and imaging warm and hot dust in dense, star forming cores, MIRI will facilitate mapping the regions of galaxies that are undergoing the most intense star formation. Moreover, MIRI IFU spectroscopy will be used to diagnose the role of active galactic nuclei in the evolution of galaxies.

Figure 5. JWST's near-IR and mid-IR instruments, working together, provide essential and complementary astrophysical information. This is illustrated by the above near-IR and mid-IR composite view of the spiral galaxy M81. The 3.6 μm (left; near-IR) image is dominated by older, evolved stars. The 8 μm (middle; mid-IR) image emphasizes warm dust in the spiral arms. Finally, the 24 μm (right; mid-IR) image highlights the hot dust associated with deeply embedded star forming regions. The composite image, at bottom, clearly shows where the older, well established stars that dominate the mass are found, as well as fine structure in the spiral arms and a relatively un-obstructed view of the regions of active star formation. Credit: NASA/JPL-Caltech/K. Gordon (U. Arizona), S. Willner (Harvard/CfA), & N.A. Sharp (NOAO/AURA/NSF).

3) The Birth of Stars and Protoplanetary Systems: A good framework is in place for understanding how stars form and how they may form

planetary systems, but a number of key steps in the process are not yet understood. JWST will work to unravel the birth and early evolution of stars, from infall onto dust-enshrouded protostars to the genesis of planetary systems. JWST needs to provide high sensitivity and high spatial resolution over a span of wavelengths that can penetrate the clouds enveloping the early stages of star formation and that can penetrate large column densities along the lines of sight through our galaxy.
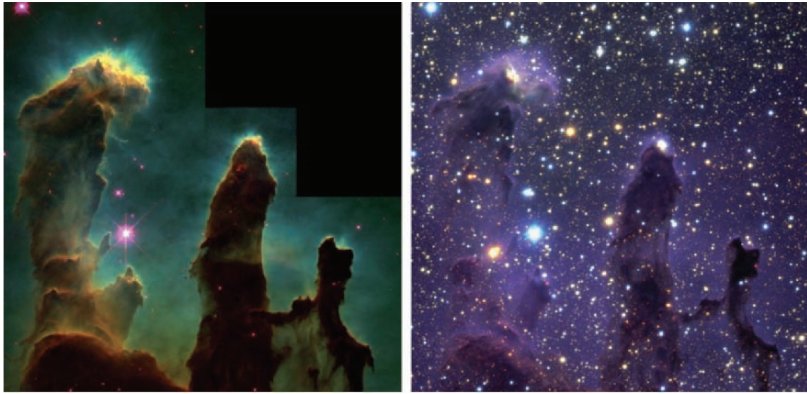
Figure 6. Infrared wavelengths cut through dust that obscures our view of the visible Universe. *(left)* An optical wavelength image of the Eagle Nebula, M16, taken by HST. *(right)* A composite near-IR image (J, H, and K_{short} bands) taken using the ISAAC camera on the ESO VLT ANTU telescope. Credit: *(left)* NASA, ESA, STScI, J. Hester & P. Scowen (Arizona State University) & *(right)* Mark McCaughrean & Morton Andersen, Astrophysical Institute Potsdam (AIP), and the European Southern Observatory (ESO).

4) Planetary Systems and the Origins of Life: Recent discoveries of many exosolar planets lends impetus to programs designed to characterize them. Equally important is developing an understanding of how planetary systems form, and what determines the numbers and arrangements of planets in a system. Spitzer Space Telescope discoveries of how debris disks, the likely remnants from planetary system formation, decay with time are a good illustration of how the observation of these disks tie in to the solar system and hence to planetary systems in general. JWST will be an excellent platform for studying these low surface brightness objects with high sensitivity MIRI coronagraphy. JWST will also provide a wealth of information on the surface compositions and albedos for Kuiper Belt Objects in the solar system, which will facilitate comparing what happens in debris disks with what is seen very locally. NIRCam imaging and NIRSpec spectroscopy are needed to measure absorption features from a variety of ices, while MIRI observations are needed to image the disks.

2.1 Launch and Deployment

JWST will be launched using an Ariane V rocket provided by the European Space Agency. Prior to launch, the primary mirror and other deployable elements (incl. sunshade & secondary mirror) are folded into a shroud. After launch, JWST and its sunshield will be deployed while the spacecraft is still relatively warm (see Fig. 7 for the deployment sequence). During the cruise phase to L2, the telescope and instruments will cool to reach their eventual operating temperature of ~35 K. The detectors, apart from MIRI's λ_{co}=27 µm Si:As SCAs, are cold-biased to operate a few degrees K above the temperature of the SI.

Figure 7. JWST deployment. The time sequence is from left to right and from top to bottom. Deployment steps are as follows: (1) fully deployed observatory showing partner logos, (2) JWST leaving earth following Ariane V launch, (3) beginning of deployment, (4) solar panels deploy, (5-8) sunshade deploys, (9) mast deployment, (10) secondary mirror deployment, and (11-12) primary mirror deployment. For scale, the primary mirror is about 6.5-meters in diameter and the sunshade is about the size of a tennis court.

2.2   Instruments & Detectors

The high-level instrument capabilities are summarized in Fig. 8. In the following paragraphs, we describe the instruments and their detectors. For more detailed technical information and test results, interested readers should see, for example, Figer et al. [2] for NIRCam, NIRSpec, and FGS/TI. For MIRI's Si:As SCAs, Hoffman, et al. [3] presents some more recent information.

Instrument Overview

Fine Guidance Sensor (FGS)
· Ensures guide star availability with >95% probability at any point in the sky
· Includes Narrowband Imaging Tunable Filter Module
· CSA/EMS provided
· 2 (2048x2048) 68mas pixels
· John Hutchings, lead

Near Infra-Red Camera (NIRCam)
· Detects first light galaxies and observes galaxy assembly sequence
· 0.6 to 5 microns, 2 (4096x4096) 31mas pixels & 2 (2048x2048) 62mas pixels
· Supports Wavefront Sensing & Control
· Univ. of AZ - LMATC instrument; Marcia Rieke, PI

Mid-Infra-Red Instrument (MIRI)
· Distinguishes first light objects; studies galaxy evolution; explores protostars & their environs
· Imaging 1 (1024x1024) 110mas pixels
· Spectroscopy (R~3000) 2 (1024x1024) 200-470mas pixels
· 5 to 27 microns; Cooled to 7K by cryocooler
· ESA/JPL, George Rieke, Gillian Wright leads

Former location of dewar

Near Infra-Red Spectrograph (NIRSpec)
· Measures redshift, metallicity, star formation rate in first light galaxies
· 0.6 to 5 microns
· Simultaneous spectra of >100 objects
· 2 (2048x2048) 100mas pixels
· Resolving powers of ~100, ~1000, ~3000
· ESA/Astrium provided, with NASA Detectors & Microshutter

Figure 8. JWST's science instruments are housed in the Integrated Science Instruments Module (ISIM). These instruments are as follows: (1) Near-Infrared Camera, (2) Near-Infrared Spectrograph, (3) Mid-Infrared Instrument, and (4) Fine Guidance Sensors with tunable filters. During an earlier phase of the JWST project, MIRI used a dewar to cool its detectors. Although the dewar has since been replaced by a cryocooler located in the spacecraft, the former dewar location can still be seen in this figure.

With the exception of MIRI's three actively cooled λ_{co}=27 µm Si:As SCAs, which are operated at T < 7 K, all of JWST's near-IR SCAs will be operated a few degrees Kelvin warmer than the SI optical benches, T~37.5-39 K. At these temperatures, we have found the dark current from the most recent Rockwell/JWST HAWAII-2RG SCAs to be ~0.001-0.005 e⁻/s/pixel.

In the case of a few non-flight NIRCam parts, dark currents <0.001 e⁻/s/pixel were measured [4].

One interesting phenomena seen in the near-IR JWST detectors is popcorn noise (see Fig. 9), or "popcorn mesa noise" [5,6]. The popcorn mesa noise appears as an almost digital toggling between states as charge integrates up during long, dark exposures. It is thought that popcorn mesa noise is associated with single charge trapping effects in sensitive regions of the multiplexer. Individual popcorn events can happen on timescales shorter than one frame (12 seconds), as well as on scales longer than 1000 seconds. We anticipate doing more detailed statistical analysis on popcorn mesa noise when Engineering Test Unit (ETU) SCAs begin to arrive in late 2005.


```
x = 1250          lob = stsci
y = 129           Filename = dark_37K_250_min_1_04.fits
hitType = 3       FINDHITS_PRO version 2.4
hitIndex (#) = 47 sthresh (sigma) = 10
```
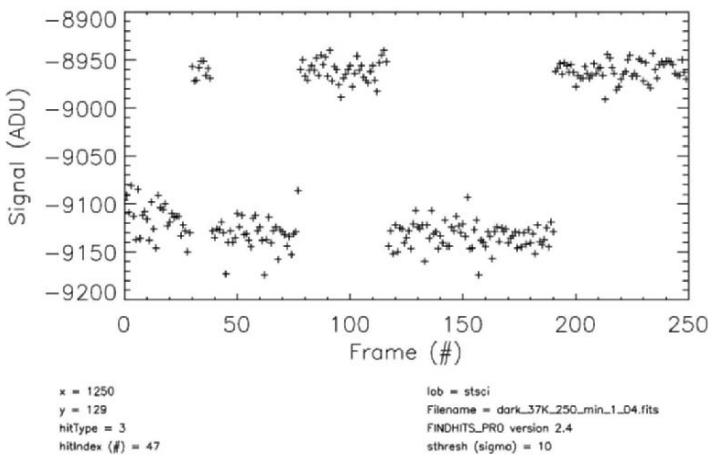
Figure 9. Popcorn mesa noise is occasionally seen in individual pixels as charge integrates during exposures. In this particular figure, popcorn events endure for several frames (100s of seconds). In other pixels, popcorn is sometimes detected on timescales shorter than 12 seconds [5,6]. Conversion gain for this figure is about g=1.3 e⁻/ADU and the frame rate is about 10.7 seconds per frame.

NIRCam: The NIRCam (see Fig. 10) is a $\lambda = 0.6$-5 µm imager provided by the University of Arizona with Marcia Rieke as the Principal Investigator. NIRCam also performs an observatory function to support wavefront sensing [1]. NIRCam uses refractive optics and beam splitters to create two wavelength channels and ther are two fully redundant modules. Each channel uses 4 $\lambda_{co} = 2.5$ µm Rockwell HgCdTe HAWAII-2RG SCAs for λ=0.6-2.5 µm, and 1 $\lambda_{co} = 5$ µm SCA for λ =2.5-5 µm. In total, NIRCam uses 10 SCAs, with 5 in each channel. Each SCA is controlled using one Rockwell SIDECAR ASIC, which is described in more detail in Section 2.3. SIDECAR stands for System for Image Digitization, Enhancement, Control And Retrieval, and ASIC is an Application Specific Integrated Circuit.
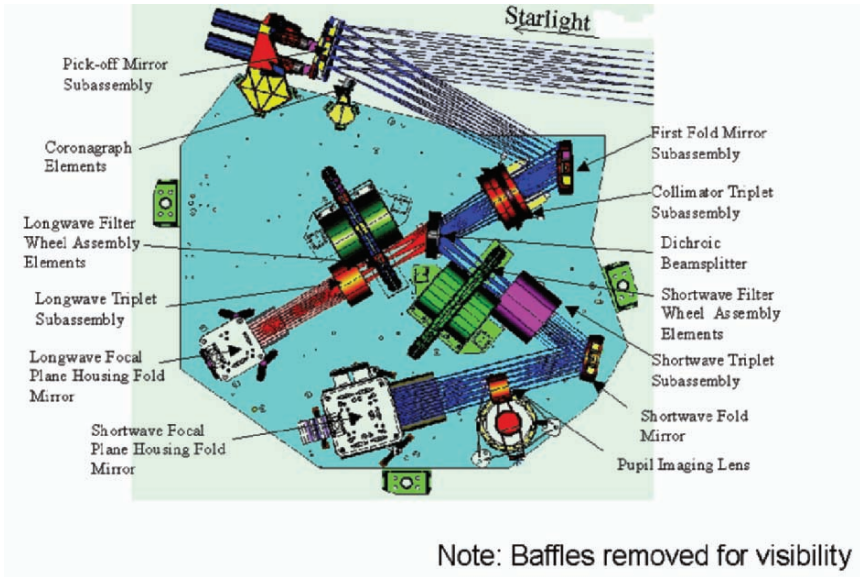
Figure 10. Optical layout of NIRCam. The instrument consists of two of these assemblies
bolted together.

NIRSpec: The NIRSpec is a $\lambda = 0.6 - 5$ μm multi-object spectrograph
provided by ESA. NIRSpec incorporates two NASA-provided components.
These are: (1) the detector subsystem and (2) a Micro-Machined Silicon
(MEMS) Micro-Shutter Array (MSA). NIRSpec's modes are broadly
summarized in Fig. 8. Figure 11 shows the instrument layout that has been
conceived by EADS Astrium, ESA's Prime Contractor for the instrument.
The FPA is being designed by ITT Industries, under sub-contract to the
NIRSpec FPA provider, Rockwell Scientific.

NIRSpec's FPA consists of two, $\lambda = 0.6 - 5$ μm Rockwell HgCdTe
HAWAII-2RG SCAs. Each SCA will be controlled using one SIDECAR
ASIC. ITT has used an elliptical footprint for the FPA structure (see Fig.
11). According to their analysis, this geometry helps them to meet cryogenic
FPA flatness requirements.

FGS/TI: The Fine Guidance Sensor/Tunable Imager (FGS/TI; see
Fig. 12) is provided by the Canadian Space Agency. Because JWST is a
large and relatively flexible telescope structure, tracking targets to the
required accuracy cannot be accomplished by steering the bulk telescope
structure. The telescope is therefore configured as a three-mirror anistigmat,

with a fine steering mirror located at a pupil. Tracking is achieved by imaging a guide star with the FGS on an array identical to the ones used in NIRCam and NIRSpec. A centroid is measured, and an error signal is generated and fed to the fine steering mirror. The spacecraft's body pointing is updated as needed to keep the mirror within its range of travel.

The FGS/TF incorporates a tunable filter module. This portion of the instrument has the same field of view as one half of NIRCam. A dichroic is used to view this field by using short wavelength and long wavelength tunable filters simultaneously. These filters have R~100 and also include a coronagraphic capability. In total, the FGS/TF incorporates 4 Rockwell HAWAII-2RG SCAs. One SIDECAR ASIC will be used to control each SCA.
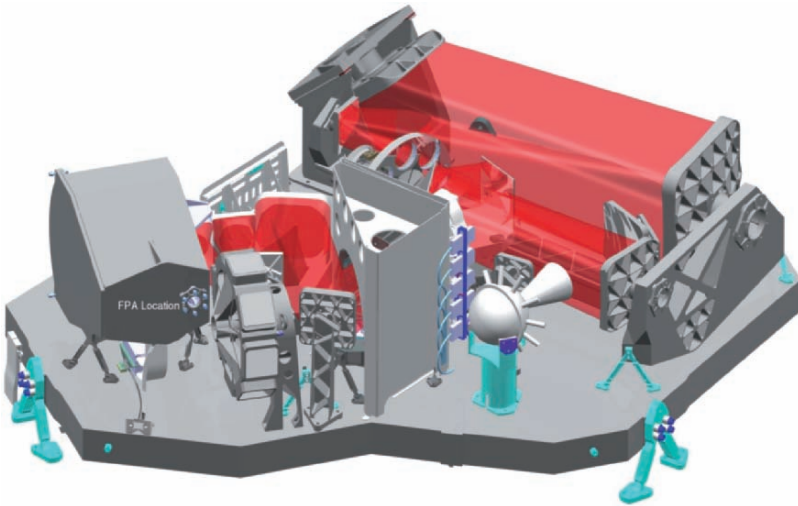
Figure 11. JWST NIRSpec. Major instrument structure is entirely silicon carbine (SiC). Notable exceptions include the FPA, micro-shutter array, and filter wheels. Credit: Overall instrument design is by EADS Astrium and FPA assembly design is by ITT Industries.

MIRI: Mid-infrared imaging and spectroscopy are provided for JWST by MIRI (see Fig. 13). MIRI is being developed jointly by a consortium of European astronomical institutes, led by the United Kingdom Astronomy Technology Center, which has responsibility for the optical bench, and by the Jet Propulsion Laboratory, which has responsibility for the focal plane system, cooler, and flight software. MIRI's detectors need to operate near 7K so more cooling is needed than can be achieved with a passive radiator system, and the extra cooling will be supplied by a cryocooler.
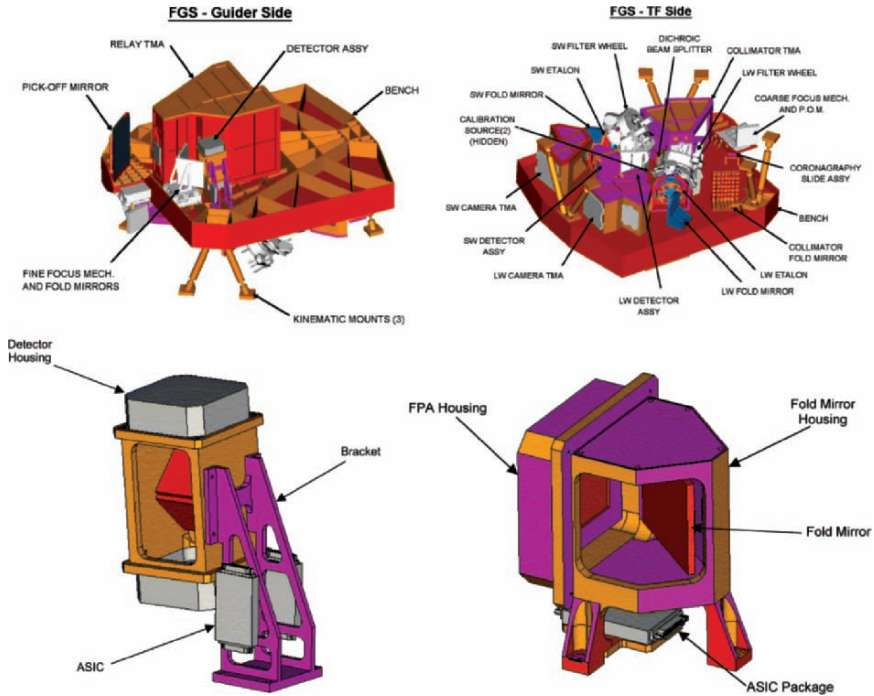
Figure 12. JWST Fine Guidance Sensor / Tunable Imager.

Figure 13 shows the layout of MIRI with its imager on one side of its deck and the spectrometer modules on the other. The imager has a 1.9×1.4 arcminute field-of-view and 9 filters to cover 5.6 to 25.5 μm. MIRI's spectrometer is configured as four integral field units to cover the spectral range from 5 to 28 μm with a spectral resolution of order 3000. The field of view scales from 3.5"×3.5" at the short wavelength end to 7"×7" at the long wavelength end.

Planet detection is an important science program for MIRI and it will be equipped with two types of coronagraph, a traditional focal plane mask and a phase mask. The coronagraphs share a detector with the imager. The phase mask has the advantage of being able to observe closer to the central source in the region where the traditional mask is opaque. It has the drawback of working over only a limited spectral range so MIRI will have three phase masks to provide a wavelength choice.
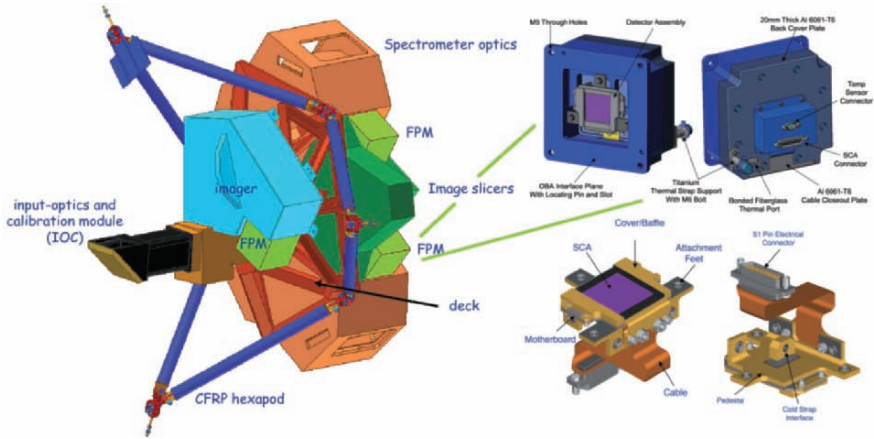
Figure 13. (left) MIRI with mounting struts to ISIM and *(right)* detail of a MIRI FPM.

2.3   SIDECAR ASIC

JWST's near-IR SCAs will be controlled using Rockwell's SIDECAR ASIC (see Fig. 14). The SIDECAR generates all clocks and low-noise biases needed by the SCA, performs pre-amplification and 16-bit ADC conversion, and executes data conditioning and transmission to ISIM data systems. Prior to selecting the SIDECAR, the JWST project reviewed all aspects of the ASIC design. During this review, the SIDECAR demonstrated outstanding performance, exceeding JWST specification in important areas including total noise for NIRSpec (see Fig. 15).
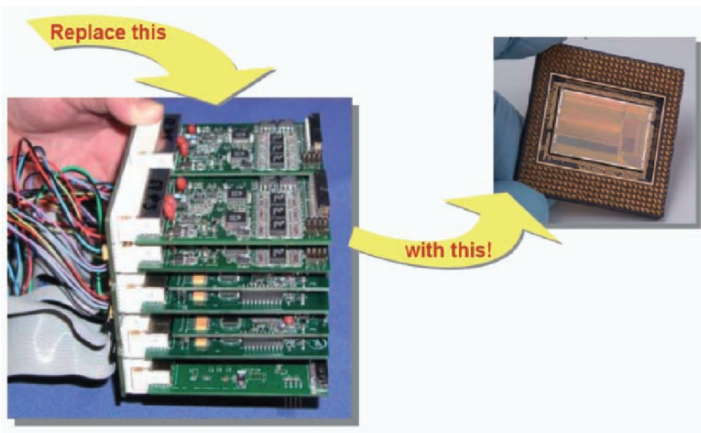
Figure 14. Rockwell's SIDECAR ASIC will be used for near-IR FPA control and readout.

Rockwell Scientific Self-reported Measurements	Noise at low bias[1]	Noise at medium bias[1]	JWST Requirement
ASIC by itself (NIRSpec 4-22 multiaccum)	2.0 e-	1.8 e-	2.4 e - (NIRSpec)
ASIC + HAWAII-2RG CDS	16.5 e-	16.2 e-[3]	24 e- (extrapolated)
ASIC + HAWAII-2RG Fowler 8-8	6.8 e-	6.7 e-	9 e- (NIRCAM)
ASIC + HAWAII-2RG (4 –22 multiaccum)	5.3 e-	5.2 e-[2,3]	6 e- (NIRSpec)

[1]100 kHz pixel rate

[2] MULTIACCUM-22x4 calculated using 4 out of 6 measured ramps due to larger frame-to-frame pedestal in remaining 2 ramps.

[3]Analysis of test data independently confirmed by NASA/GSFC

Figure 15. Prior to baselining the SIDECAR ASIC, the JWST Project reviewed its readiness. Rockwell's self-reported measurements met JWST requirements for parameters, including noise. Independent analysis of the data by GSFC confirmed important results including total noise <6 e⁻ rms in the NIRSpec readout mode.

3.   SUMMARY

In this paper we present a general introduction to JWST, with an emphasis on detectors. Readers who are interested in detailed JWST SCA test results should see, for example, Figer, et al. [2] for early test results related to NIRCam, NIRSpec, and FGS/TI. For MIRI's Si:As SCAs, Hoffman, et al. [3] presented some recent test results. Others attending this conference discussed detectors similar to those that will be used by JWST. Finger [7] discusses effects due to capacitive coupling in Rockwell HAWAII-2RG SCA pixels that potentially affect noise and quantum efficiency measurements by most test labs at the 10-30% level. Moore, et al. [8] discussed capacitive coupling effects from a theoretical perspective.

4.   REFERENCES

[1] Rieke, M.J., 2005, *NIRCam/JWST mission overview*, Proc. SPIE, Vol. **5904**, in press.
[2] Figer, D.F., et al., 2004, *Independent Testing of JWST Detector Prototypes*, Proc. SPIE, Vol. **5167**, 270.
[3] Hoffman, A., Love, P.J., Corrales, E., & Lum, N.A., 2005, *1024x1024 Si:As IBC Detector Arrays for Mid-IR Astronomy*, these proceedings.
[4] Hall, D.H. 2004, Personal communication.
[5] Rauscher, B.J. et al. 2004, *Detectors for the James Webb Space Telescope Near-Infrared Spectrograph*, Proc. SPIE, Vol. **5487**, 710.
[6] Bacon, C.M., McMurtry, C.W., Pipher, J.L., Forrest, W.J., & Garnett, J.D., 2005, *Burst Noise in the HAWAII-1RG Multiplexer*, Proc. SPIE, Vol. **5902**, in press.
[7] Finger, G., et al., these proceedings.
[8] Moore, A.C., Ninkov, Z. & Forrest, W.J. 2004, *Interpixel capacitance in non-destructive focal plane array*, Proc. SPIE, Vol. **5167**, 204.

ACTIVE PIXEL SENSOR DEVELOPMENTS FOR FUTURE ESA (EUROPEAN SPACE AGENCY) SPACE SCIENCE MISSIONS

Ludovic Duvet and Didier Martin
ESA/ESTEC, Science Payload and Advanced Concepts Office

Abstract: *Optical imaging sensors in space science payloads were, until now, exclusively based on CCDs due to their superior optical performance and existing successful heritage. However recent technological improvements within the CMOS world as well as the commercial market have led to Active Pixel Sensor (APS) designs offering an advantageous alternative to CCDs. Their high suitability as a detector for virtually every wavelength range of sensors promises a very significant gain in complexity, power and integration. They also offer the possibility of high radiation hardness and high-speed readout. These points have motivated the choice of APS technology for the imaging payloads of the ESA BepiColombo MPO (Mercury Planetary Orbiter). Other missions, such as Solar Orbiter, follow the same trend. This paper gives an overview of the foreseen developments by ESA in that respect.*

Key words: *Active Pixel Sensor (APS), CMOS sensor, BepiColombo, Solar orbiter.*

1. BACKGROUND

Until now, the use of APS on ESA missions has been mainly limited to infrared wavelengths. Numerous scientific grade infrared APS (mainly manufactured in US) have been flown on missions such as Rosetta [1], Mars Express [2] or on those that are about to take-off, such as Venus Express [3].

In the optical range, VMC (Visual Monitoring Camera) or Star Tracker [4] have been the dominant applications. It was indeed in the last field that

CMOS technology could provide numerous advantages over competing technologies such as CCDs:

- Integration: mixed-analog CMOS designs allow the possibility of integrating processing features within the detector, such as centroid calculations, data packet formatting for direct spacecraft interfacing and many others [5].
- Power consumption: inherently low in CMOS, a crucial aspect for space applications.
- Radiation hardness: design techniques and genuine tolerance is definitely an interesting aspect of CMOS technology (particularly for submicron applications). As far as SEE (Single Event Effect) is concerned, mitigation techniques are now widely known and directly inherited from the high energy physics domain.

Successful chips like the STAR1000 [6] have been developed under ESA contracts. The imminent insertion of these parts in the EPPL (ESA Preferred Parts List) adds a very important dimension, namely reliability. However, to our knowledge, no scientific grade optical APS has used aboard a European mission thus far. Indeed electro-optical properties of existing devices could still not compete with the CCD's excellence. Two parameters may soon alter this state of fact:

- Recent improvements of APS electro-optical performances [7].
- Mission constraints and orbits: indeed, mission scenarios lead to more and more constraints in terms of mass and power. Besides, these scenarios bring the spacecraft and its payload in ever harsher environments for longer durations. Close-up solar observations like Solar Orbiter (see Sec. 2.3), or atmosphere free planets like Mercury for the Bepi Colombo mission (see Sec. 2.2), tend to expose the detectors to challenging radiation environments.

In the UV or EUV domain, instruments have been based on MCP (Micro-Channel Plate) or phosphor intensified CCDs thus far. APS may soon offer advantageous alternatives. Indeed, processes like back thinning have been used (based on CCDs heritage) to provide improved blue response [8]. Hybridization of CMOS readout circuitry to GaN or AlGaN substrates is another possible technical path in that wavelength range with the possibility to achieve solar blindness [9].

In order to further develop APS technology for space applications in Europe, ESA, through the Science Payload and Advanced Concept Office[1],

---

[1] The Science Payload and Advanced Concepts Office (SCI-A) at ESTEC is responsible for the assessment studies of future science missions, the identification of the corresponding technology development needs as well as instrument developments.

has decided to initiate several scientific grade APS developments within the frame of two major upcoming missions, Bepi Colombo and Solar Orbiter.

2. DEVELOPMENT SPECIFICATIONS

2.1 Space-based Observation Constraints

Space-based observation constraints are quite different from their ground-based counter part. This may seem obvious, but it is important to briefly recall some basic facts to fully appreciate the challenging task that is ahead of us as well as the choices that have been made.

Scientific requirements are the prime drivers for the definition of an instrument with parameters such as wavelength coverage, surface resolution, field of view, time resolution, etc. The mission scenario leads to constraints for the instrument in terms of mass, volume, power, telemetry and environment. Mass and volume will orientate the instrument towards a certain optical/mechanical topology. Power will determine the amount of cooling available for the detector or the amount of processing which can be achieved on board. Telemetry will have a direct influence on the time resolution, frame size, and compression. The environment will dictate the amount of thermal protection needed, as well as if radiation tolerant or radiation hard optical and electronic parts are needed. The overall definition process is of course very complex and necessitates a dichotomist approach where trade-off is the master word.

For remote surface observations, pixel size is a significant system parameter. Indeed, for a given altitude and a given ground resolution, smaller pixels lead to shorter focal lengths, and consequently a more compact instrument, with direct impact on mass and volume. The radiation hardness of the detector limits the risks and offers a very cost effective solution in terms of mass. The operating temperature of the detector also has a strong impact at system level: "the higher the better". Indeed, cooling a detector in space is always complicated since it requires extra power, extra mechanical design and risks (with moving parts), spacecraft attitude constraints, etc. These three parameters, pixel size, radiation hardness and operating temperature have strongly influenced the overall requirements of the Bepi Colombo and Solar Orbiter.

2.2   **Bepi Colombo Developments**

The Bepi Colombo[2] spacecrafts are scheduled to take-off in 2012 on a journey lasting up to 4 years and 2 months [10]. A very complete payload, distributed over two spacecraft, will scrutinize Mercury's surface as well as its exosphere and magnetosphere. This multidisciplinary mission, managed in cooperation with the Japanese Space Agency (ISAS/JAXA), will answer some of the numerous unanswered questions on the least explored planet of the inner solar system. SYMBIO-SYS is the Remote Sensing Imaging consortium on board MPO. It consists of:

- HRIC (High Resolution Imaging Channel): 5 m/pxl, 400-900 nm
- STC (Stereo imaging Channel): 100 m/pxl, 500-900 nm
- VIHI (Visual and Infrared Hyperspectral Imager channel): 100 m/pixel, 400-2200 nm

Table 1 shows the main specifications for the optical APS. The targeted technology is still undecided: back-thinned back-illuminated or silicon on silicon hybrids are being investigated. The strong emphasis put on the pixel size will very likely orient the design towards the former technology since sub-10 µm bump bonding pitch is an extremely challenging task from the technical and cost aspects in itself.

Table 1. Main specifications for the optical APS foreseen for the BepiColombo mission (all parameters are end of life).

Parameter	Unit	Goal
Pixel size	µm	10
Number of pixels	N/A	2048×2048
Wavelength range	nm	400-900
Readout speed	Mpixel/s	8
Full well capacity	electrons	150k
External quantum efficiency	%	>80 (400-800 nm) and >50 (800-900 nm)
Readout Noise	electrons	<15 (rms)
Dark current	$e^-.pix^{-1}.s^{-1}$	< 1000
PRNU	%	<0.5 (rms)
DSNU	%	<1 (rms)
On chip AD conversion	bits	12
Operating temperature	Celsius	-20/+30
Power dissipation	mW	<500
Radiation hardness	N/A	100 krad, SEE immune

Table 2 displays the foreseen performances for the optical/SWIR detector. Constraints in terms of operating temperature and dark current as well as wavelength range naturally lead to HgCdTe with substrate removal

---

2   Named after Giuseppe Bepi Colombo (1920-1984), who was an Italian mathematician, engineer and scientist, and contributed to space science exploration.

to extend the quantum efficiency towards the optical range. Very high quality MBE (Molecular Beam Epitaxy) grown substrates will have to be produced to reach the very stringent dark current levels. This technology is available in Europe but still requires improvement.

Table 2. Main specifications for the optical-SWIR APS foreseen for the BepiColombo mission (all parameters are end of life).

Parameter	Unit	Goal
Pixel size	(µm)	20
Number of pixels	NA	512×512
Wavelength range	nm	400-2500
Readout speed	Mpixel/s	3
Full well capacity	electrons	10^7
External quantum efficiency	%	>50
Readout Noise	electrons	<150 (rms)
Dark current	$e^-.pix^{-1}.s^{-1}$	<3.5×105at 200 K for λc = 2.5 mm typical
		<3.5×106at 220 K for λc = 2.5 mm typical
PRNU	%	<5
DSNU	%	<5
Operating temperature	Celsius	-70/-40
Power dissipation	mW	100
Radiation hardness	NA	100 krad, SEE immune

The developments will begin by autumn 2005. For the optical APS, CCDs are kept as reserve, with the known direct impact on mass, power and radiation impact on performance.

2.3 Solar Orbiter APS developments

To be launched in Oct 2013 for a maximum of 8 years extended mission, the solar orbiter spacecraft will have an elliptical orbit around the Sun with increasing inclination up to 35 degrees with respect to the solar equator, and approaching as close as 45 solar radii. This will give unprecedented resolution images and the closest measurements yet [11]. The preliminary remote sensing payload consists of:
- VIM (Visible Light Imager and Magnetograph): 400-700 nm
- EUS (Extreme Ultraviolet Spectrometer): 17-100 nm
- EUI (Extreme Ultraviolet Imager): 13.3 nm, 17.4 nm, 30.4 nm
- COR (Coronograph): 450-600 nm (121.6 and 30.4 nm optional)

Two dedicated developments are foreseen (Q1 2006), they will focus on:
- Radiation hardness improvements
- Increased UV and EUV sensitivity
- Solar blindness
- Pixel size: 8 to 5 µm

At this stage, monolithic and hybrid technologies are in competition. However, we think that hybridization offers much more flexibility and possibilities in the long term.

3.   CONCLUSION

We have briefly reviewed the potential advantages of APS imagers and how they can respond to pending ESA planetary and solar observation missions, namely Bepi Colombo and Solar Orbiter. Some challenging developments are foreseen in Europe by autumn 2005 in the optical, NIR and UV range. The novelty lies essentially in the choice of APS technology in the optical and UV range, breaking the long domination of the CCD technology.

4.   REFERENCES

[1] Coradini, A. et al, 1999, *Virtis: an imaging spectrometer for the ROSETTA mission*, American Astronomival Society, DPS meeting #31, #29.07.
[2] Bellucci, G. et al, 2004, *The OMEGA Instrument on board Mars Express: First results*, Memorie della Societa Astronomica Italiana Supplement, Vol. **5**, p. 27.
[3] Drossart, P. et al, *The VIRTIS Infrared Imaging Spectrometer on the ESA/Venus Express Mission*, American Astronomical Society, DPS meeting #35, #41.02.
[4] Bogaerts, J., 2002, *Star 250 Radiation tolerant APS for Star Tracker Application*, CNES atelier.
[5] Van Hoof, C., 2003, *A CMOS APS single-chip radiation-tolerant imaging system*, presented at: 4th Round table on Micro/Nano Technologies for Space. (20-22 May 2003; Noordwijk, The Netherlands.)
[6] Star 1000 datasheet, www.fillfactory.com/htm/ products/htm/star1000/star1000.htm
[7] Dierickx, B., 2004, *Advanced developments in CMOS imaging*, presented at Fraunhofer IMS workshop, Duisburg, May 25th 2004.
[8] Prydederch, M. et al, 2004, *A Large Area CMOS Monolithic Active Pixel Sensor for Extreme Ultra Violet Spectroscopy and Imaging*, Sensors and Camera Systems for Scientific, Industrial, and Digital Photography Applications, Proc. of SPIE, Vol. **5301**, p. 175-185.
[9] E. Munoz, E. Monroy, F. Calle, E. Calleja, F. Omnes, B. Beaumont, P. Gibart, 2000, *AlGaN-based UV detectors and Applications*, Optoelectronics Review **8**, 43-55.
[10] Grad, R. et al., *Bepi Colombo*, ESA bulletin 2000, Vol. **103**, page 11-19.
[11] Marsh, E, 2004, *Solar Orbiter-mains goals and present status*, p.1681, 35th COSPAR Scientific Assembly, 18-25th July 2004, Paris, France.

ENERGY: A PROPOSAL FOR A MULTI-BAND CMOS IMAGING PHOTOMETER

Fernando Pedichini, Andrea Di Paola and Roberto Speziali
INAF-Osservatorio Astronomico di Roma

Abstract: *Multi-color photometry of an astronomical field in the Johnson's bands is a common task performed daily in modern observatories using CCD imagers and optical filters. The main drawback of this approach is the lack of simultaneous data on the same target in different bands, due to the use of a single detector camera with a filter wheel. Especially in the case of fast variable targets, with time scales of the order of a second or less, the time needed for the filter change and the detector readout can mask important features in the multi-band light vs. time plot. Multi-detector cameras using dichroic filters are the standard but bulky solution to this problem. Alternatively, one can use Bayer type color detectors, but this reduces the global QE and introduces Moire effects in the images, which are not well accepted in the astronomical community. The advent of CMOS detectors using Foveon technology brings a new solution to this problem. Foveon detectors have pixels that output 3 voltages proportional to the amount of blue, green and red photons collected during integration. We discuss the Foveon technology from an astronomical point of view, showing its predicted performance at an 8 meter telescope compared to a standard CCD imager and at a small 60cm Schmidt telescope.*

Key words: *Imaging, CMOS, Foveon, photometry, optical filters, dichroic, optical bands.*

1. MULTI-CHANNEL PHOTOMETRY

Multi-channel photometry is one of the most used tools in astronomy. Photometry requires "standard" systems for comparing data from different instruments. The most used photometric systems for photoelectric detectors are the UBVRI or Johnson/Cousin/Bessel systems [1-4].

Several empirical formulae help the astronomer to convert data between the various photometric systems and to calibrate instruments. Effective temperature, metallicity, red-shift, mass and other interesting physical parameters are commonly derived from multi-band photometry of stars and star systems, but very often data from different bands are acquired at different times. Especially in the case of time series or light-curves, this introduces artefacts that can mask interesting features in the data. This is the case, for instance, for fast transient stars with no periodic behaviour, GRB optical counterparts, novae flashes or supernovae bursts. Instruments dedicated to light curves photometry either, (1) sample the requested bands at different frequencies in different times; or (2) sample "all" the bands each time at a specific frequency. Independently of the relative merits of each technique, it is important to note that simultaneous band sampling, provided that it reaches the required sensitivities, saves telescope time and is therefore less expensive.

Colored glass filters installed in front of any kind of detector are simple devices used in astronomy to select optical bands. The time needed to change a filter in a modern instrument can be as low as one second, typically less than integration time or the readout time of the detector. Wide and large band filters have peak transmission of 90% and do not significantly degrade the overall excellent QE performances of modern CCDs. Assuming that the exposure time (E_{time}) is the same for all the filters and that the shutter-reload-cycle and the filter-changing time are lower than the detector readout time (R_{time}), the astronomer needs to cycle all the filters (N_{filt}), one exposure after another. This increases the minimum sampling time (T_{min}) needed to complete the multi-band observations to:

$$T_{min} = N_{filt} \times (E_{time} + R_{time}) \qquad\qquad (1)$$

The use of mosaic filter detectors is an alternative to the use of filters [5]. A Bayer filter usually gets 3 optical bands in one shot, but it has some drawbacks that limit its use to amateur astronomy and security video markets fields. First of all, it is mandatory to apply the Bayer filter in perfect phase with the pixel pitch. Therefore, it is not possible to apply it on the back side of a detector, because on this side of the CCD the exact pixel location is unknown. This limits the peak QE of Bayer type detectors to about 40-50%. Secondly, the 3 bands are not user-selectable; finally, since the rendered image is obtained extrapolating the color in each pixel by means of a matrix convolution which uses data from the neighbouring pixels (see Fig. 1), color artefacts are introduced along the sharp edges of the images (this is known as the Moire effect).

The use of several dichroic filters to split the focal plane light beam into different bands is a common solution for multi-band imaging. Despite its mechanical complexity and the needs of a slow optical beam, this solution is used in several astronomical instruments, like EMMI at the ESO NTT, the NIR camera on the REM telescope [6] or the BUSCA camera on the 2.2 m at Calar Alto [7]. The cost of such a camera is typically 3 to 4 times the cost of a single imager, because several standard CCD cameras are needed to fill the multiple focal planes. Dichroics also have the drawback of introducing partial polarization of the reflected and transmitted light beams. Despite these limitations, dichroic cameras can reach on average 80% Q.E. on all detectors and allow simultaneous observation in several bands. When costs or mechanical constraints are not an issue, a dichroic-camera approach to multi-color imaging is best.

| RGBRGBRGB |
| BRGBRGBRG |
| GBRGBRGBR |

| GRGBGRGBG |
| BGRGBGRGB |
| GRGBGRGBG |

Figure 1. Two types of Bayer filters: the letters R,G and B (Red, Green and Blue) filtered pixels. The left matrix has a perfect balance of R, G and B pixels. The right one, which is used mainly for photography and TV applications, has 50% of the pixels filtered in green to increase the luminosity information of the images.

2. THE FOVEON DETECTOR

A new approach to multi-band imaging is provided by FOVEON Inc., which produces two large format detectors, 3.3 and 10 Mpix, that feature a novel technology: each pixel is a stack of three electron collection areas, sensitive to blue, green and red photons. Figure 2 shows a comparison between the architectures of a standard mosaic detector and the Foveon [8].

To better understand how a Foveon detector works, we refer to the silicon photon absorption plot of Fig. 3. The mean distance travelled by a photon inside silicon, before it generates a photoelectron, depends on its wavelength: the blue photoelectrons will be generated near the silicon surface while the red ones in deeper regions. The Foveon pixel is built by means of peculiar ion implants and dopings, which define three depletion regions located progressively deeper in the silicon and therefore suited to collect electrons from blue, green and red light. Three amplifiers and a CMOS multiplexer enable the readout and resetting of this detector with the features of CMOS arrays, such as windowing, rolling shutter and high frame rate live video.
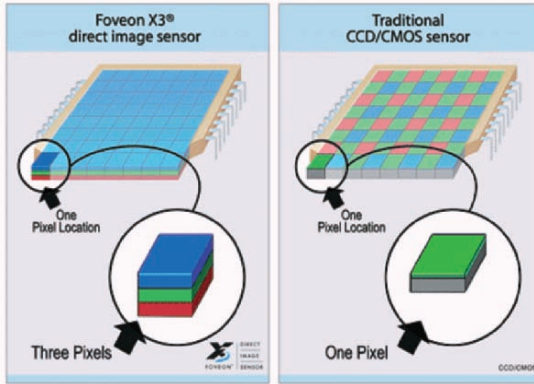
Figure 2. Comparison of a Foveon detector and a Bayer type detector. In the Foveon direct image sensor there are three layers of pixels. Each pixel detects 1 color sample.
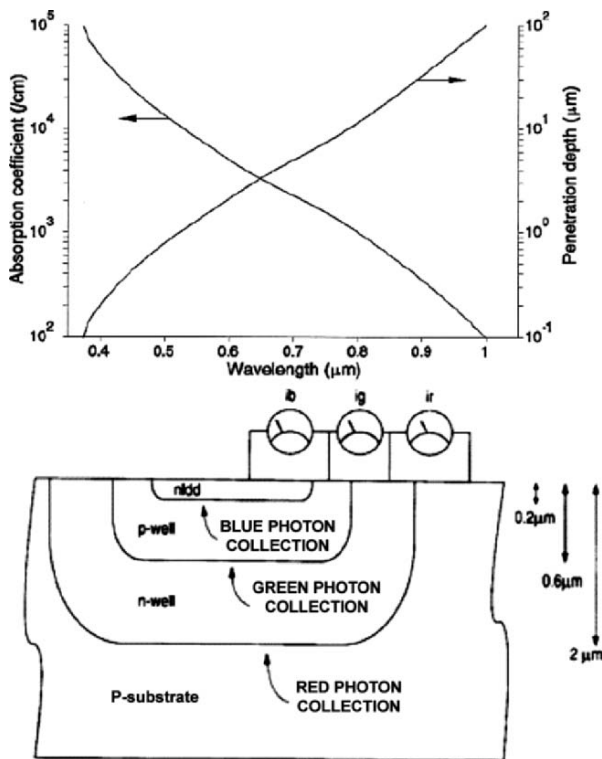
*Figure 3. (top)*The absorption coefficient and the penetration depth of photons inside silicon at different wavelengths. *(bottom)* The schematic structure of a Foveon pixel with the 3 different electrons collecting regions.

The peculiar photon absorption and charge collection processes of the Foveon result in three photoelectrical optical bands with peak QE of 35% as shown in Fig. 4. Hereafter, we name these bands red (R_f,), visual (V_f) and blue (B_f). With large bandpass overlap, the Foveon bands form what is commonly called an "over-sampled colorimetric system", which makes this kind of detector one of the best to render colors in photography [9-10]. Moreover, the stacked structure of independent pixel arrays does not produce "color aliased" images when imaging high contrast regions with sharp edges.
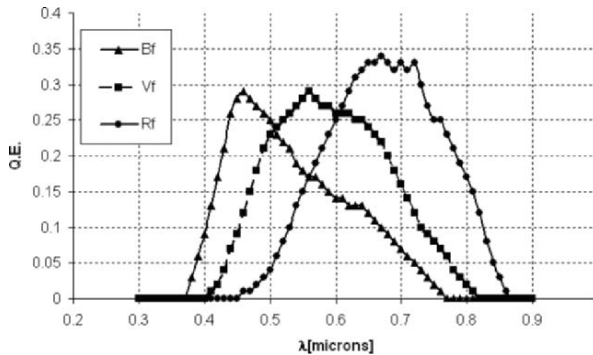
Figure 4. The Foveon optical bands as reported by the manufacturer.

2.1 Performance

The manufacture lists the Foveon M10 detector performance as:
- 3 layers of 2200×1500 pixels, square 9.12 microns pixels.
- Readout time <0.25 sec. (rolling shutter), RON <30 e⁻ at 15 MHz.
- Binning, windowing and live video (30 fps at VGA resolution).
- CMOS 3.3V single supply, 3×12 bit ADC on detector.

3. ASTRONOMY USES OF FOVEON DETECTORS

3.1 Reduction to the Johnson Bands

The reduction of "proprietary instrumental optical bands" to a standard photometric system is not mandatory when using an astronomical imager, but it is required for comparison with measurements taken by other instruments. To understand the usefulness of the Foveon detector for astronomical studies, it is therefore important to find out if the Foveon bands R_f, V_f and B_f can be compared to the standard Johnson bands. We convolved

the Foveon bands of Fig. 4 with the flux of seven blackbody spectra in the range 2000-20,000 K and compared the results to the Johnson's magnitudes obtained from the same spectra. The Johnson minus Foveon magnitudes differences are a simple monotonically increasing function with respect to the color index (V_f-R_f), therefore we could use second order polynomials to convert the data between the two systems (see Fig. 5).
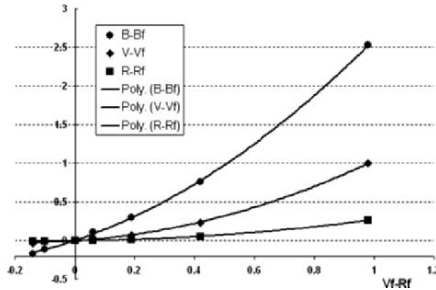
Figure 5. Residuals of Johnson minus Foveon magnitudes as a function of the Foveon color index (V_f-R_f) for blackbody spectra. The lines are second order polynomial interpolations.

The rms errors are less than a few percent when using relations like the following, derived for the V band:

$$(V-V_f) = 0.7818 \cdot (V_f - R_f)^2 + 0.2571 \cdot (V_f - R_f) - 0.0051 \qquad (2)$$

Similar formulae can be derived for the other Foveon bands with comparable errors. Our simulations therefore show that the Foveon magnitudes can be converted into astronomical standard magnitudes with a precision comparable to the one given by classic CCD imagers with filters.

3.2   Foveon vs. CCD on a Large Telescope (8.4 m)

We compare the performance of a hypothetical Foveon camera, which we name "Energy", and a state-of-the-art traditional CCD imager with filters (see Table 1). Our test science application aims at detecting fast transient phenomena in B, V and R bands by means of fast recursive imaging of a star field. The pixel size of both imagers is set to 9 microns.

Figure 6 shows the computed ratio of the CCD and Foveon exposure times needed to reach a S/N of 100 in all three bands for a given magnitude. It is evident that Energy is better than the CCD, because the bands are sampled simultaneously and faster. This is especially true for brighter magnitudes, despite Energy's larger noise and lower QE. Above 19th

magnitude, both cameras are comparable, except for the simultaneous sampling of Energy.

Table 1. Comparison of hypothetical Foveon camera and traditional CCD imager performance.

Parameter	CCD	Energy
Detector size [Mpix]	4	4
RON [e⁻]	5	30
Read Out Time [sec]	1	0.25
Gain [e⁻/ADU]	2	5
Filter change time [sec]	1	Not needed
Scale ["/pix]	0.15	0.15
f-number	1.4	1.4
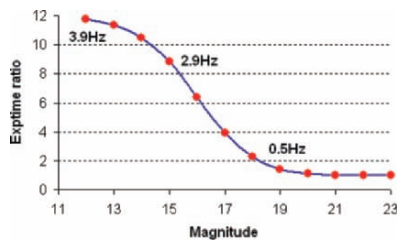
Figure 6. Exposure time ratio of CCD and Energy cameras on an 8.4-meter telescope as function of target magnitude at S/N=100. The dots represent the sampling frequency of the target using the Foveon detector.

3.3 Foveon GRB hunter on a small telescope (0.6 m)

The performance of the Energy camera can be also evaluated for small Schmidt telescopes that search for GRB optical counterparts of "X-ray satellite alerts", a specific but popular astronomical application. In this case, the pixel scale is 1″ and the imaged field is 1/3 deg squared. Optical counterparts are sometimes as bright as magnitude V=5. If the real-time data reduction pipeline is smart enough to detect the fast optical transient then it can be monitored in all three bands with the frequencies reported in Fig. 7. Table 2 compares the Foveon detector to standard technology imagers.

The Foveon detector looks promising and it could become the leader of a new family of optical detectors for photometric studies, especially if the manufacturer could:

1. reduce the RON,
2. increase the QE (e.g., with thinning and back illumination),
3. extend the UV and IR response, with more Foveon bands per pixel.
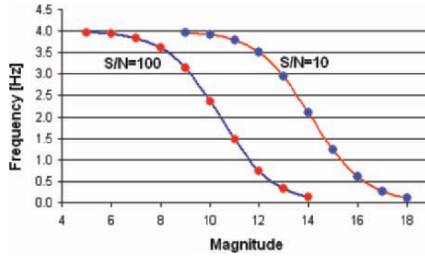
Figure 7. Sampling frequency vs. target magnitude at a 60 cm Schmidt telescope for S/N=100 and S/N=10 using the Energy camera.

Table 2. Comparison of a Foveon detector to standard technology imagers.

Detector	Q.E. %	Sampling	Simultaneous	Complexity
Filter Wheel	90	Good	No	Standard
Mosaic (Bayer)	20-30	Bad (Moire)	Yes	Low
Dichroic	80-90	Good	Yes	High
Foveon	30	Good	Yes	Low

4.   ACKNOWLEDGEMENTS

5.   REFERENCES

[1] Johnson and Morgan, 1953, ApJ **117**, 313.
[2] Cousins, 1974, MNRAS **166**, 711.
[3] Cousins, MNASSA **33**, 149.
[4] Bessell, 1979, PASP **91**, 589.
[5] Bayer B. E., 1976, *Color Imaging Array*, US Patent 3,971,065.
[6] Vitali F., F.M. Zerbi, G. Chincarini, G. et al., 2003, *The REM-IR camera: High quality near infrared imaging with a small robotic telescope*, SPIE **4841**, 627.
[7] Reif K., Poschmann H., Bagschik , Cordes O., Harbeck D., Muller P., 2000, *Optical Detectors for Astronomy II,* Kluwer Academic, Amico P. and Beletic J. (Editors).
[8] Lyon F., Hubel M., 2003, http://www.foveon.com/files/CIC10_Lyon_Hubel_FINAL.pdf.
[9] Hubel M., Liu J., Gottosch R.J., 2003,
      http://www.foveon.com/files/FrequencyResponse.pdf
[10] Gottosch R.J., 2003,
      http://www.foveon.com/files/Color_Alias_White_Paper_FinalHiRes.pdf

SECTION V:

AVALANCHE PHOTODIODES

SPADA: AN ARRAY OF SPAD DETECTORS FOR ASTROPHYSICAL APPLICATIONS

Giovanni Bonanno[1], Massimiliano Belluso[1], Franco Zappa[2], Simone Tisa[2], Sergio Cova[2], Piera Maccagnani[3], Domenico Bonaccini Calia[4], Roberto Saletti[5], Roberto Roncella[5], Sergio Billotta[1]

[1]INAF, Catania Astrophysical Observatory, [2]Dept. of Electronics, Politecnico di Milano, [3]LAMEL, IMM-CNR, [4]European Southern Observatory, [5]Dept. of Information Engineering, University of Pisa

Abstract: *Astrophysical studies require accurate, sensitive and fast detectors to detect faint sources with high variability. Recently an array of Single Photon Avalanche Diodes (SPAD), SPADA, has been developed. This array is suitable for competitive adaptive optics operations and fast transient image acquisition at a fraction of the current cost of imaging arrays. The fabricated solid-state photon counters are rugged, easily integrated with the optics, free from readout noise, and have very fast frame rates (>10kHz, for visible corrections) with nanosecond electronic gating. In this paper, the following are described: the development of silicon monolithic arrays of 60 photon-counters, the detection electronics (based on integrated active quenching circuits for each pixel of the array), the real-time data-processing board implemented into FPGA and some aspects of the mechanical housing.*

Key words: *Single photon avalanche photodiode, photodetector array, photon counter, adaptive optics, fast transient phenomena.*

1.   INTRODUCTION

In astrophysical observations CCDs are the most utilized detectors for many applications, but they fail in cases where the photon shortage becomes severe and images must be obtained in short acquisition times.

CCDs are integrating devices with relatively slow readout (even with multi-port architectures) and show readout noise. Techniques of signal intensifying "on-chip" (L3 CCD) or off-chip (MCP coupling) are good only for the observation of faint sources. Different detectors are needed to observe faint and rapidly varying photon sources. Furthermore, if these detectors are capable of fast timing and gating without a complex controller, they can also be useful in adaptive optics.

Recently at LAMEL IMM-CNR (Bologna, Italy) an array of Single Photon Avalanche Diodes (SPAD) named SPADA has been manufactured suitable for competitive adaptive optics operations and fast transient image acquisitions. The advantage of solid state photon counters is that they are intrinsically digital devices, giving out a TTL pulse for each photon detected. They have no readout noise and combine good sensitivity with a large dynamic range.

2. SPADA ELEMENTS AND OPERATING MODE

Basically, a SPAD detector is a semiconductor junction diode that can sustain an avalanche multiplication process when reverse biased (see Fig. 1). As opposed to a standard avalanche photodiode (APD), which is operated below the breakdown voltage in the analog multiplication regime, a SPAD is biased above its breakdown voltage and forced to operate in Geiger mode.
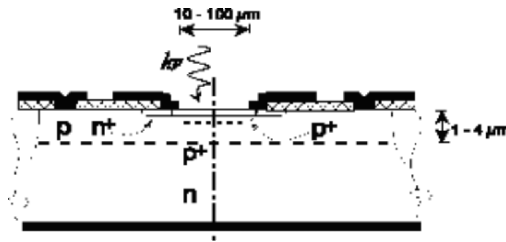
Figure 1. Typical SPAD planar structure with thin depletion for fast timing response.

At such overvoltage, the electric field within the depleted region of the device is so high that a single carrier generated in that region is highly accelerated and collides with a bound electron to create an electron-hole pair. These electrons are then accelerated to generate additional electron-hole pairs leading to an exponential increase of current.

3.   SPADA DETECTOR

The SPADA sensor is made of 60 SPAD elements placed at the focus of small sphere lenslet arrays, and each element is arranged to correspond to each sphere as shown in Fig. 2 (left). The overall SPADA chip is squared, with dimensions of 18 mm ×18 mm. Each element consists of four SPADs, with diameters of 20 μm, 35 μm, 50 μm, and 75 μm (see Fig. 2 (right)).
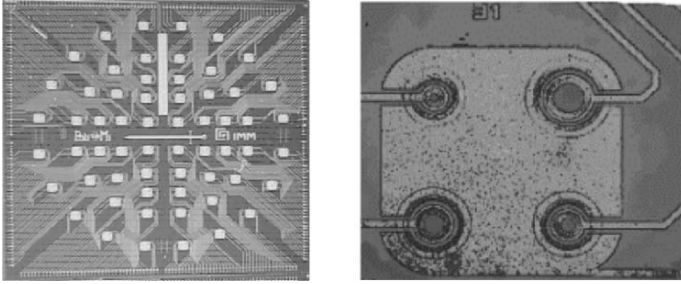
Figure 2. (left) The SPADA chip. Each element has four independent SPADs of different diameters. *(right)* Only one set of 60 SPADs is finely connected to the detection electronics.

The SPADA chip is assembled on a ceramic holder over a Peltier cooler and then mounted on the central plate of the housing as shown in Fig. 3. The focusing opto-mechanics are aligned on top of the SPADA through alignment marks patterned on the SPADA chip, on the SPADA holder, and on the metal plate.
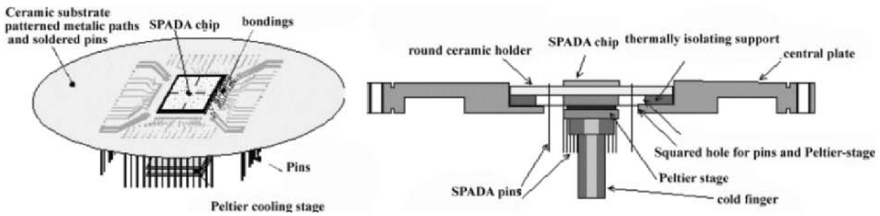
Figure 3. (left) A SPADA chip assembled on a ceramic holder and on the Peltier stage. *(right)* Cross-section of the mounting of the on the central plate of the housing.

To reduce dark counts to a few counts per second, it is mandatory to operate the SPAD at temperatures below 0°C. However temperatures lower than -30°C must be avoided because spurious counts increase due to the afterpulsing effect [1,2]. The cooling system based on a Peltier thermoelectric cooler has been designed in collaboration with ESO and finalized via industrial contracts. The housing is filled with dry nitrogen to avoid fogging and condensation.

4.   DETECTION AND CONTROL ELECTRONICS

Each SPAD is biased and driven by appropriate detection and control electronics. The core of the detection electronics are the integrated Active-Quenching Circuits (iAQC), one for each SPAD. Each iAQC is able to bias the corresponding SPAD above the breakdown voltage, generate a digital pulse each time a photon is detected and quickly quench the SPAD (by lowering its bias below breakdown). At the end of the cycle, the SPAD is ready to detect a new photon. Figure 4 shows the block diagram of each iAQC. The iAQCs are packaged with a possible five on one chip.
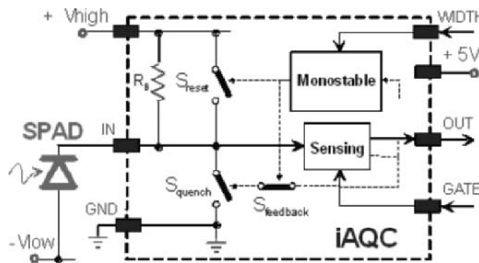
Figure 4. Block diagram of each one of the 60 integrated iAQC needed to bias the SPADA.

The entire detection board provides not only the 12 chips containing a total of 60 iAQCs , but also 15 quad output drivers that output 60 differential lines through two SCSI connectors (requested by ESO for backward compatibility with the existing MACAO systems).
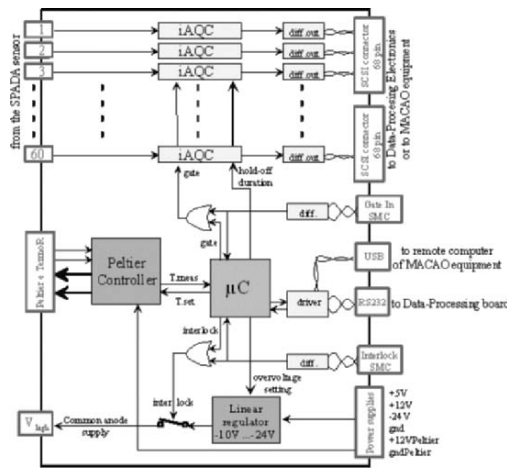
Figure 5. Schematic block diagram of the detection board.

Moreover, an 8-bit micro-controller manages all settings, diagnostics, and signal communication. Commands and telemetry (temperature, over voltage, hold-off duration) will be transferred through an USB interface. Figure 5 shows the block diagram of the detection board.

5.   SPADA SYSTEM: A CURVATURE WAVEFRONT SENSOR FOR MACAO

The optomechanical and electronic design of the SPADA wavefront sensor is driven by the requirement to be compatible with the ESO MACAO systems, replacing the lenslet-fibre-APD module section of the wavefront sensor. SPADA is also designed to be applied to the CALDO pulse laser LGS-AO experiments, foreseen by ESO in collaboration with the Durham University. Moreover on board processing has been added to use the SPADA in standalone mode as curvature sensor analyzer and as a Fast Transient (FT) phenomena detector. The readout is in parallel for all pixels and takes few tens of nanoseconds per photon; hence, the upper limit of the dynamic range can attain several million of counts per second.
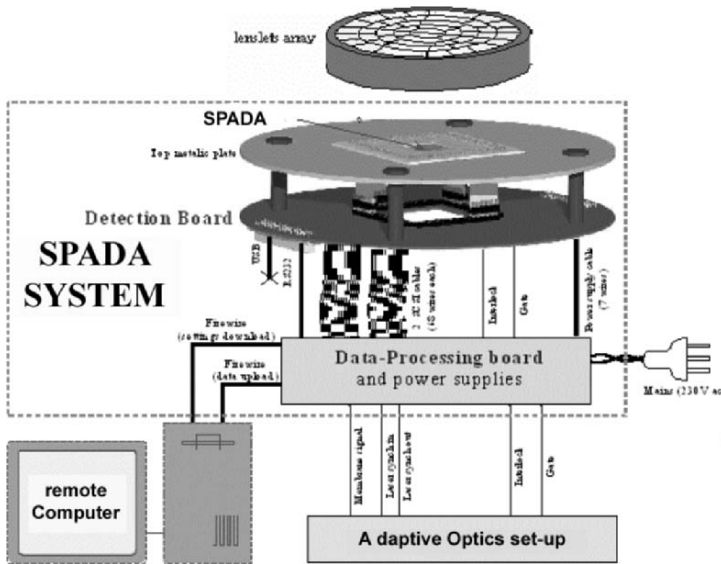
Figure 6. Block diagram of the entire SPADA system.

The whole system consists of a "Detection Board" for detecting the ignition of each element and a "Data Processing Board" based on FPGA and DSP able to acquire all the pixel signals and perform the photon-counting

and real-time processing. A remote computer with appropriate software procedures is used to provide the system control, data uploading and post-processing. The block diagram of the entire SPADA system is shown in Figure 6.

At the moment the lenslets array (already available at ESO for the MACAO instrument), the SPADA chip, the detection board, the data processing board and the data acquisition software are completed and some operational tests have been carried out in laboratory. Only the mechanical housing is under construction and we expect to assemble the entire system at the end of this year.

6.   ASTROPHYSICAL APPLICATIONS

The system has been designed for two different applications, in adaptive optics and in FT phenomena observations.

6.1   Adaptive Optics

The system acts as a Curvature Wave Front System (CWFS). By means of a moving membrane, the conjugated plane is moved with sinusoidal oscillations "before" (detected counts A) and "after" (detected counts B) the SPADA focal plane. The curvature signal is then evaluated as the ratio of the two quantities: (A-B) and (A+B). The acquisition is repeated in free running.

6.2   Fast Transient Phenomena

In this operational mode, data corresponding to the 60-pixels SPADA detector are acquired every integration time window (programmable in the range 100 μs/100 ms). This allows time-tagging of incoming photons, with enough resolution for astronomical applications where fast timing is required, for example, fast events due to gamma rays burst, or sources with low luminous flux and high temporal variation, such as pulsars. Another interesting field where this kind of system can be used is the asteroseismology.

7.   REFERENCES

[1] Belluso, M., et al., *Electro-Optical Characteristics of the Single Photon Avalanche Diode (SPAD)*, these proceedings.
[2] Belluso, M, et al., *Characterization of SPAD Arrays: First Results*, these proceedings.

ELECTRO-OPTICAL CHARACTERISTICS OF THE SINGLE PHOTON AVALANCHE DIODE (SPAD)

Massimiliano Belluso[1], Giovanni Bonanno[1], Sergio Billotta[1], Antonio Calì[1], Salvo Scuderi[1], Massimo Cataldo Mazzillo[2], Piergiorgio G. Fallica[2], Delfo Sanfilippo[2], Emilio Sciacca[3], Salvatore Lombardo[3]
[1]INAF, Catania Astrophysical Observatory, [2]ST Microelectronics of Catania, [3] CNR, IMM of Catania

Abstract: *Observation of faint sources is affected by a chronic lack of photons. This problem becomes critical when very short integration times are required (from micro to milliseconds). An example is observations of transient phenomena and when using adaptive optics to correct atmospheric turbulence in real time. To detect weak and fast transients CCDs are inadequate because of readout noise and read technique. SPAD detectors, which benefit from photon counting operating mode, can perform much better. SPAD detectors are very innovative and can offer opportunities in astrophysical observations. Electro-optical characterization of these devices is very important to prove their potential and to test the range of their applicability to astrophysical observational programs. Dark rate and quantum efficiency measurements of various SPADs in different operating conditions have been made by using a "reflection objective" that focuses a beam with a FWHM of about 10 µm diameter on the detector surface. Non-uniformity of the SPAD was also investigated. Here we discuss the equipment used and the results obtained.*

Key words: *Single Photon Avalanche Photodiode (SPAD), photon counter, detector characterization.*

1.   INTRODUCTION

Recently, ST Microelectronics has planned to investigate how to improve the characteristics of their SPAD devices. In this context they have

manufactured SPADs using different technologies with varying sensitive areas. In the framework of a collaboration between our institute and the STM undertaken few years ago we have characterized some devices.

Using recently available instrumentation based on a reflective objective capable of measuring sub-pixel non-uniformity, we investigated SPAD surface non-uniformity.

2.   MECHANICAL HOUSING AND INSTRUMENTAL APPARATUS

To reduce the dark counts to a few counts per second it is mandatory to operate the SPAD at temperatures below 0°C.

The mechanical housing able to host the packaged detector has been designed to work under vacuum conditions. To cool the SPAD, a two stage Peltier module has been used as well as hydrophilic material (Zeolite) to adsorb contaminating molecules and preserve vacuum integrity. Figure 1 shows the mechanical housing hosting the SPAD detector.
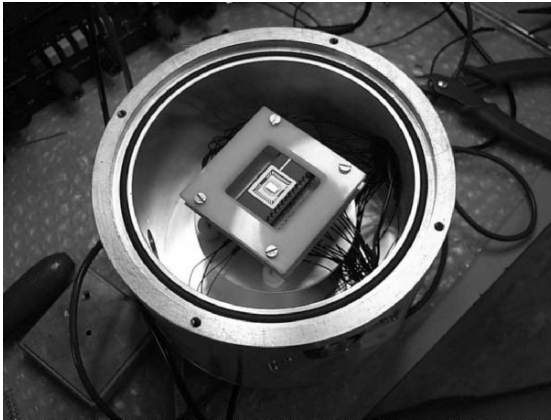
Figure 1. Mechanical housing hosting the SPAD packaged detector.

3.   DARK COUNTS AND AFTER-PULSING

Basically, a SPAD detector is a semiconductor junction diode that is biased over its breakdown voltage. Thus in dark conditions it can sustain an avalanche multiplication due to the thermally generated carriers. Another effect to take into account is the so called "after-pulsing" that may affect the dark rate due to the presence of traps in silicon that release charge at a different time. We measured the dark count rate for a 20 µm diameter SPAD

by varying the hold-off time (time in which the devices are switched off) from 0.6 to 6 μs. The measurements have been obtained by biasing the SPAD at voltages of 10%, 20%, and 30 % over the breakdown (BV=25,6 Volt). Figure 2 shows the measured dark rate versus the hold-off time.
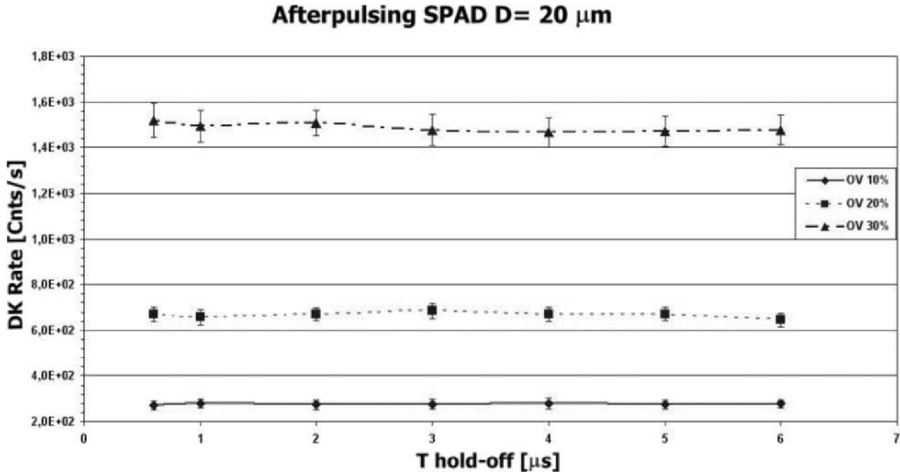
Figure 2. Dark rate versus the hold-off time.

It can be noted that for hold-off time greater than 0.6 μs the device does not show after-pulsing. Also, at room temperature the dark rate ranges from 300 to 1500 counts/s.

4.   QUANTUM EFFICIENCY

The quantum efficiency measurements have been performed in our lab using the facility developed many years ago [1] and modified to allow simultaneous measurements through an integrating sphere that guarantees uniform illumination on both the detectors: SPAD and calibrated diode. Figure 3 shows the block diagram of the QE measurement apparatus. In this way the photon flux is simply obtained by scaling for the detector area.

ST Microelectronics adopted a standard DIP 32 pin package to bond the various SPADs. Devices with different sensitive areas are available for measurements. We selected SPADs with 10, 20 and 50 μm diameter and operated them at voltages of 10%, 20% and 30% above the breakdown voltage. The results for a 20 and 50 μm diameter are plotted in Figure 4.

For all the SPADs we find a QE typical of silicon devices, peaking at 550-600 nm. We may note QE dependence not only from the SPAD diameter but also from the overvoltage. This last effect is under study, and

one possible cause is the electric field generated by the SPAD biasing voltage.
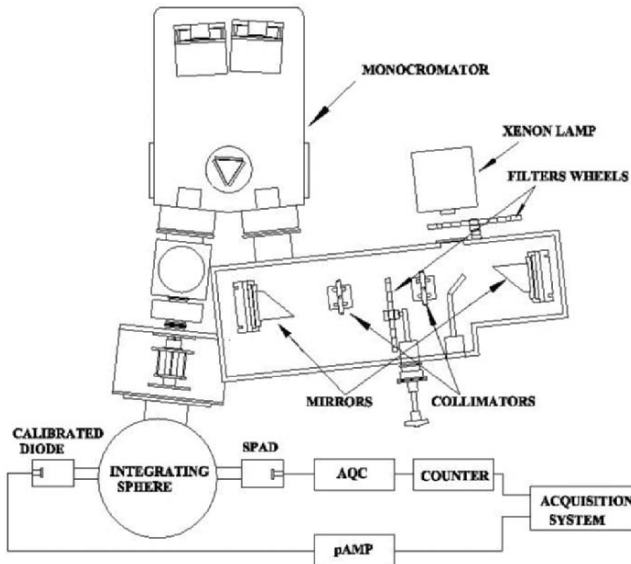
Figure 3. Quantum efficiency measurements apparatus
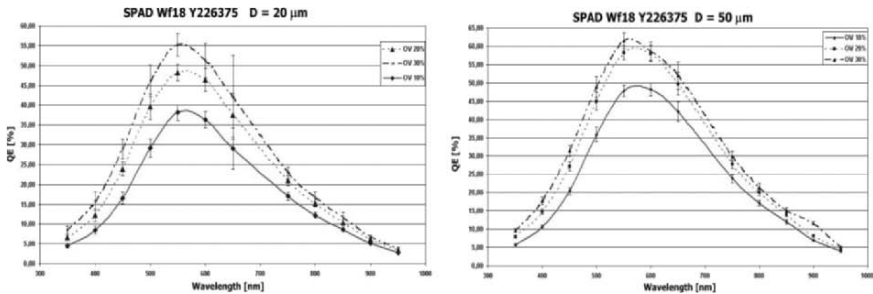
Figure 4. QE plot at three different overvoltages (10%, 20% and 30% above the breakdown voltage) for *(left)* a 20 μm diameter and for *(right)* a 50 μm diameter.

5.   RESPONSE UNIFORMITY MEASUREMENTS

The response uniformity has been measured using a recently available facility. This facility consists of a three axis translator mounted on a reflective objective and housed in a light tight box. Figure 5 shows the opened black box on the left and a detail of the reflective objective on the right.
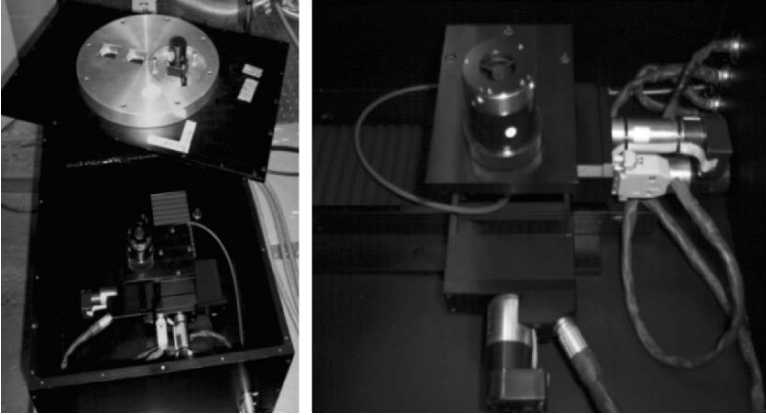
Figure 5. (left) Black box containing the reflective objective and *(right)* a detail of it.

The motorized translators are able to move the reflective objective in the X (150 mm) and Y (30 mm) directions with resolution and repeatability of 1 μm and in the Z (12 mm) direction with a better resolution to allow the beam focusing. The reflective objective is illuminated through a 10 μm pinhole by a fiber optic fed by monochromatic radiation produced by the characterization system. In this way we can obtain a monochromatic spot with a size smaller than 10 μm FWHM at the focal plane of the reflective objective to evaluate the pixel-to-pixel non-uniformity as a function of wavelength. Figure 6 shows a sketch of the system.
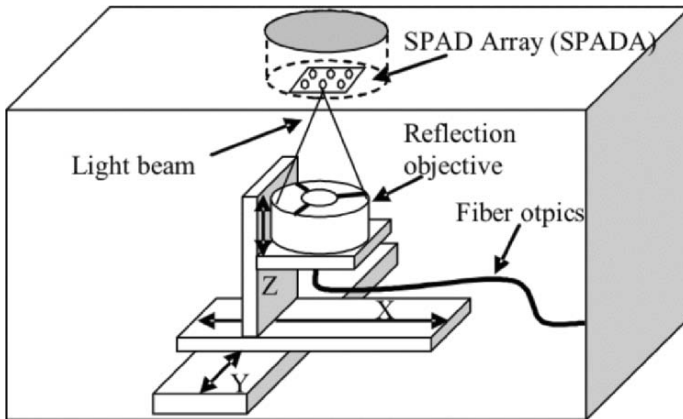
Figure 6. Schematic sketch of the motorized reflective objective.

To find the best condition in terms of focus and position we developed an automated procedure that operates a scanning procedure. The procedure,

shown in Fig. 7, begins with the objective not illuminating the SPAD (a), and moves along the X direction of a given ΔX (b). Having reached the end X position, the procedure moves the objective at the initial X position and moves along the Y direction of a given ΔY (c) starting a new X direction scan.
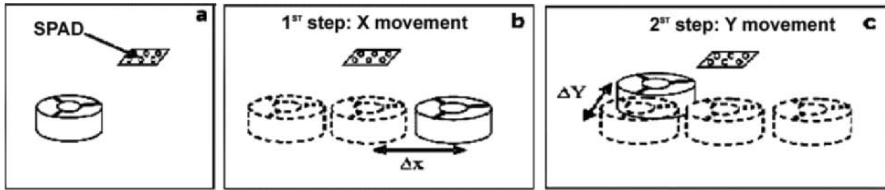
Figure 7. Schematic sketch of the scanning procedure.

With each movement the corresponding count rate is acquired and stored in a file. Simultaneously, an IDL procedure reads the file and produces a 3D plot of the currently acquired data. Examples of 3D plots are showed in Figure 8. The left plot was obtained by setting ΔX and ΔY to 150 μm and the right plot by setting ΔX and ΔY to 20 μm.

Figure 9 shows a 3D plot of 50×50 μm scan with 5 μm resolution. It is evident that the 5×5 μm central area presents a flat response corresponding to ~5000 counts/s. Thus we can confirm SPAD uniformity in that area. The shape of the 3D plot can be explained by considering the convolution of the SPAD sensitive area (20 μm) and the luminous spot (FWHM 10 μm). To better study the SPAD uniformity we will use a smaller spot and a scan resolution of 2 μm.
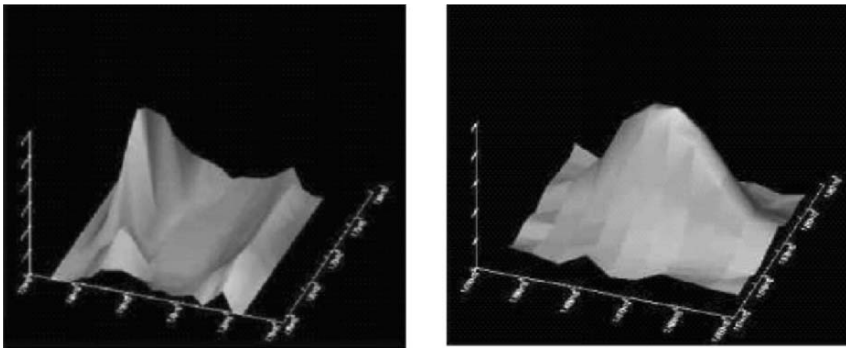
Figure 8. 3D plots obtained by scanning the SPAD at different resolutions: *(left)* 150 μm and *(right)* 20 μm. It is evident in the left plot that the beam is unfocused while in the right the beam is near the focus position.
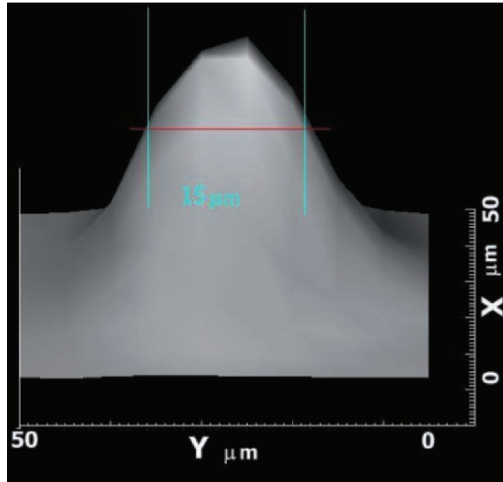
Figure 9. 3D plot of 50×50 μm scan with 5 μm resolution.

6. FUTURE MEASUREMENTS

The method described above used to measure QE suffers from uncertainties depending on the size of the sensitive area of both SPAD and calibrated photodiode, and on the illumination uniformity. Using a monochromatic spot smaller than 10 μm FWHM could overcome the problem. By using the described apparatus and replacing the SPAD with a calibrated detector able to detect a faint signal (a CCD or a photomultiplier can be used instead of a calibrated photodiode) and measuring the flux (on a pixel sub-area) we can evaluate the SPAD QE while avoiding the uncertainties due to the luminous spot diameter, the calibrated photodiode area and the effective SPAD sensitive area.

7. REFERENCES

[1] Bonanno, G., Bruno, P., Cali A., Cosentino, R., Di Benedetto R., Puleo M., Scuderi S., 1996, SPIE Proc., Vol. **2808**, p. 242.

Sebastian Deiries climbed Mt. Etna solo in the days preceding the workshop.

The view of the Teatro Greco (Greek Theater) seen by participants during the Monday tour of Taormina. The theater was being prepared for a fashion show (we were not invited).

CHARACTERIZATION OF SPAD ARRAYS: FIRST RESULTS

Massimiliano Belluso[1], Giovanni Bonanno[1], Sergio Billotta[1], Antonio Calì[1], Salvatore Scuderi[1], Massimo Cataldo Mazzillo[2], Piergiorgio G. Fallica[2], Delfo Sanfilippo[2], Giovanni Condorelli[2], Emilio Sciacca[3], Salvatore Lombardo[3]

[1]INAF – Catania Astrophysical Observatory, [2]ST Microelectronics of Catania, [3]CNR – IMM of Catania

Abstract: *SPAD detectors are very promising for astrophysical applications. Large arrays are crucial to cover as much of the focal plane as possible. ST-Microelectronics has developed various monolithic arrays of SPAD. At present, the manufacturing of 5×5 arrays (each with an active area of 40 μm and pitch between adjacent pixels of 240 μm) is completed and improvements in terms of pixels and technology are under study and development. An appropriate cryogenic system to host the packaged SPAD arrays and detection electronics to drive them have been designed and realized. Electro-optical characteristics of various arrays in different operating conditions have been measured and the obtained results are presented herein.*

Key words: *Single Photon Avalanche Photodiode (SPAD), SPAD Arrays, photon counter, detector characterization.*

1.   INTRODUCTION

In accordance with ST Microelectronics' manufacturing program, we have characterized some recently produced SPAD arrays. For these detectors an appropriate AQC board and a new mechanical housing capable to host both chip and AQC boards have been developed.

2.   MECHANICAL HOUSING AND INSTRUMENTAL APPARATUS

To test the SPAD arrays, a mechanical housing working under vacuum conditions while hosting the packaged detector and AQC boards has been deigned and built. Figure 1 shows the housing for the SPAD array detector and the AQC boards. To cool the detector a two stage Peltier module is used and a particularly long cold finger has been manufactured to allow the stacked assembly of four aligned AQC boards. The cryogenic system is able to operate the array detector at temperatures from -30 to 30°C.
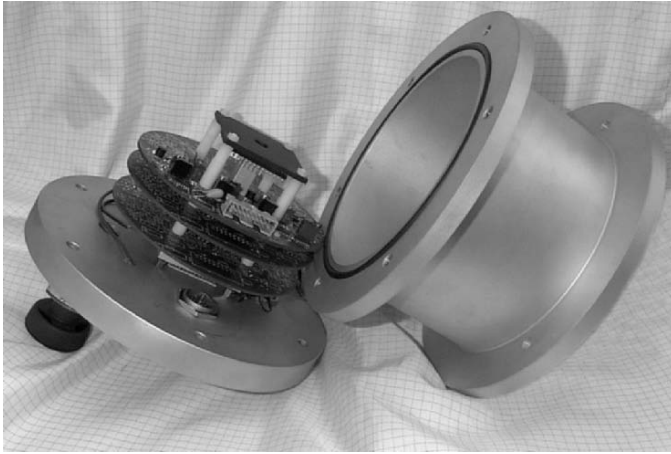
Figure 1. Mechanical housing hosting the SPAD array detector and the AQC boards.

On the bottom are electrical connectors and the vacuum valve, while a quartz window allows photons to enter through the top. The mechanical interface has easy mounting on the three axis translator light tight box.

3.   AQC BOADRS

Each AQC board is able to drive up to four elements of the SPAD array. The main characteristics of each AQC are listed in Table 1.

Due to mechanical constraints we can accommodate up to 4 AQC boards inside the cryostat. Thus we can drive up to 16 SPADs simultaneously. The 16 outputs are TTL standard and can be read either by specialized counter boards or off-the-shelf USB data acquisition systems.

The AQC boards are mounted inside the cryostat to reduce the wiring connections as much as possible and prevent detector biasing from noise sources. Figure 2 shows a 4-AQC board mounted under the SPADA chip.

Table 1. Main characteristics of each AQC.

Break Down Voltage	20 V - 35 V
Over Voltage	5 V - 12 V
Quenching Time	< 30 ns
Hold-off Time	100 ns - 6 μs
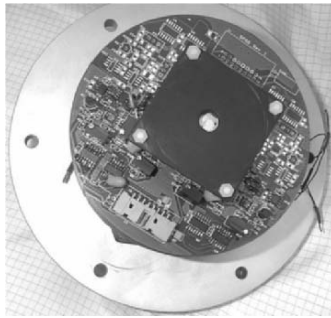
Figure 2. Board hosting four AQCs connected to the SPAD array. A black plate has been used to cover the device to avoid reflections due to the detector package.

4. CHIP LAYOUT

Three years ago ST Microelectronics began manufacturing SPAD arrays with different architectures. Currently 5×5 arrays (with each SPAD having active area of 40 μm and pitch between adjacent pixels of 240 μm) are produced. Furthermore, technology improvements in terms of quality, QE and cross-talk reduction are under study and development. Figure 3 shows the mask of a 5×5 40 μm SPAD array and the SEM image.
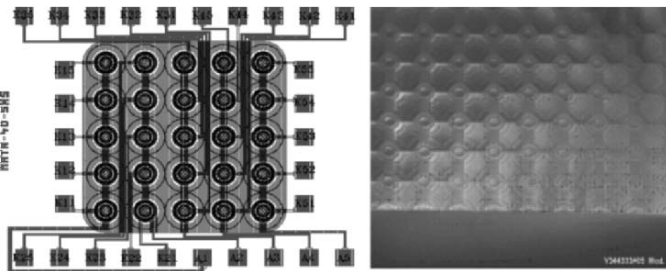
*Figure 3. (left)*Mask of a 5×5 40 μm SPAD array, and *(right)* a SEM image.

5.   DETECTOR OPERATING CONDITIONS

Due to the most recent adoption of array production technology and the consequent late availability of SPAD arrays for testing, we only operated the detectors at room temperature. Each single array element has been biased with a voltage of 10% and 20% above the breakdown voltage (about 25,6 V) and the hold-off time (time in which the devices are switched off) has varied from 0.4 to 6 µs.

6.   DARK COUNT RATE MAP

The measured dark count rate for each array element, obtained by using a bias voltage of 20% above the breakdown and a 6 µs hold-off time, is mapped in Fig. 4. At room temperature only two elements are outside the 3-sigma limits of the mean value of about 3000 counts/s, and thus measures show that the dark rate is quite uniform over the array.
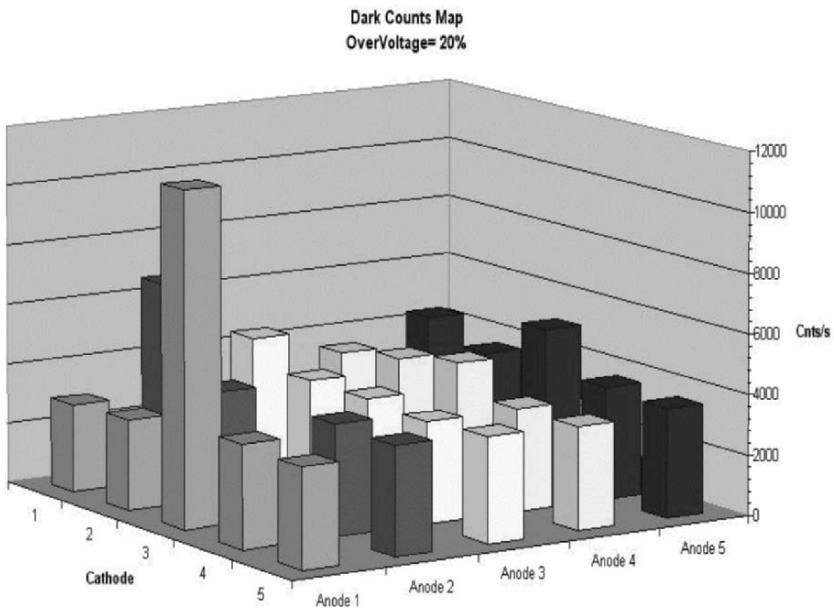
Figure 4. Dark count rate map of a 5×5 SPAD array, obtained at room temperature, by setting the bias voltage to 20% above the breakdown and the hold-off time to 6 µs.

7. QUANTUM EFFICIENCY

The Quantum Efficiency (QE) of the array at 600 nm is mapped in Fig. 5. The QE has been measured for each element by setting an overvoltage of 20% above the breakdown, and a hold-off time of 6 µs. The mean value is about 57% and it is evident, at this wavelength, that there is uniform sensitivity over the array. QE curves of anode 5, cathode 4 elements obtained by biasing with three different overvoltage levels are shown in Fig. 6. As expected, QE increases with the applied bias, and this increase is due to the electric field generated on the SPAD sensitive area.
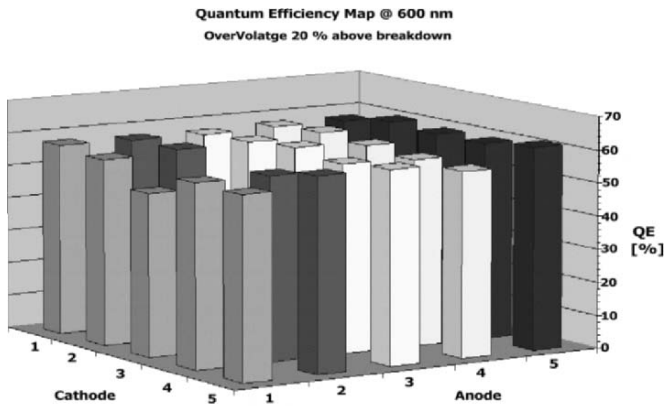
Figure 5. QE map of all the array at 600 nm, obtained by setting the hold-off time to 6 µs.
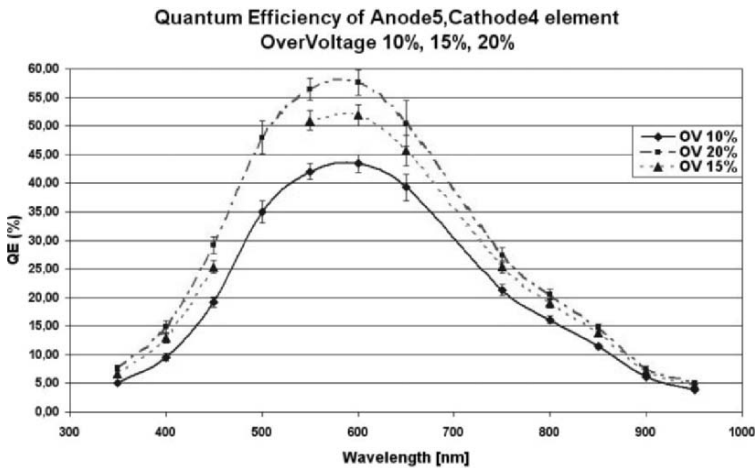
Figure 6. QE curves of the SPAD corresponding to anode 5, cathode 4 obtained by biasing at three overvoltage levels.

In Fig. 7 the QE values at 400, 600 and 800 nm are plotted versus biasing voltage (breakdown voltage plus overvoltage).
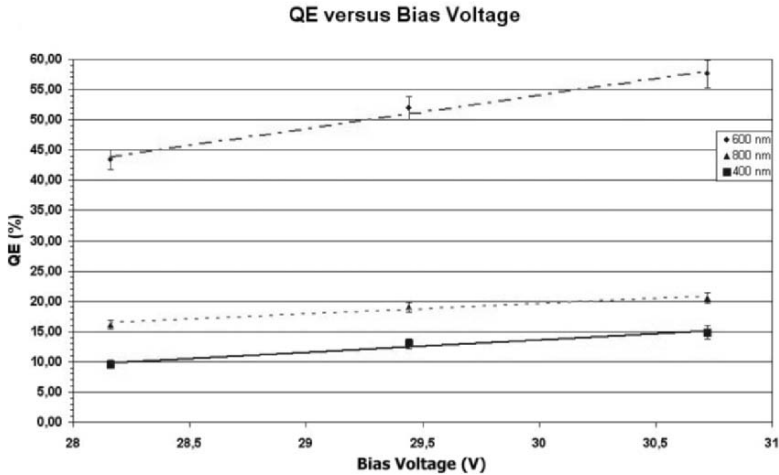
Figure 7. Plot of QE values at 400, 600 and 800 nm with respect to bias voltage (breakdown voltage plus overvoltage).

The QE value at a given wavelength increases with the SPAD bias voltage. It is evident from these plots that, in the selected range of voltages, we can simply derive the QE value (within an error of 5%) through a linear regression. Thus, by setting a bias voltage in a range of 28-31 V, we can predict the QE value with an uncertainty less than 5%.

8.   FUTURE DEVELOPMENTS

First results show that STM SPAD arrays function even at room temperature for certain applications. This encourages us to continue performing measurements and STM to improve fabricating technology to obtain better and larger arrays.

To better characterize these SPAD arrays, measurements of the principal electro-optical parameters at temperatures below 25°C are necessary. Thus we have planned future measurements operating the detector at various temperatures ranging from +25°C to -30°C. The cryogenic system will allow us to set, monitor and stabalize the cold finger temperature.

Furthermore by simultaneously biasing more elements, the optical and electric cross-talk will be measured. STM announced that SPAD arrays with optical trenches have been produced and are awaiting characterization.

SECTION VI:

DETECTOR TESTING & CHARACTERIZATION

CONVERSION GAIN AND INTERPIXEL CAPACITANCE OF CMOS HYBRID FOCAL PLANE ARRAYS

Nodal capacitance measurement by a capacitance comparison technique

Gert Finger[1], James W. Beletic[2], Reinhold Dorn[1], Manfred Meyer[1], Leander Mehrgan[1], Alan F.M. Moorwood[1], Joerg Stegmeier[1]
[1]European Southern Observatory, [2]Rockwell Scientific Company

Abstract: *The conversion gain of optical and infrared focal plane CMOS hybrid arrays is a fundamental parameter, whose value computes into the derivation of other parameters characterizing the performance of a detector. The widespread "noise squared versus signal" method used to obtain the conversion gain can overestimate the nodal capacitance of the detector pixel by more than 20% for infrared arrays and by more than 100% for Si-PIN diode arrays. This is because this method does not take account of the capacitive coupling between neighboring pixels. A simple technique has been developed to measure the nodal capacitance directly by comparing the voltage change of an external calibrated capacitor with the voltage change on the nodal capacitor of the detector pixel. The method is elaborated in detail and has been verified with a Si-PIN diode array hybridized to a Hawaii-2RG multiplexer using an Fe^{55} X-ray source. It is also in good agreement with a stochastic method based on 2D autocorrelation.*

Key words: *conversion gain, interpixel capacitance, CMOS hybrid, quantum efficiency, HgCdTe, Hawaii-2RG, Si-PIN.*

1.   INTRODUCTION

The measurement of the Quantum Efficiency (QE) of CMOS hybrid arrays recently produced implausible efficiencies exceeding 100%. Many factors such as radiation geometry, blackbody calibration, temperature

dependence of the filter transmission, and filter leaks may contribute to this problem [1]. During the characterization of infrared arrays, we have tried to reduce the errors of each factors listed above without succeeding in obtaining a quantum efficiency in K-band of a λ_c=2.5µm HgCdTe Hawaii-2RG array below 105%.

The remaining major uncertainty in our QE measurements was the conversion gain, C_0/e, measured in units of electrons per millivolt. The nodal capacitance C_0, which is the capacitance of the integrating node, is composed of the voltage dependent diode capacitance of the detector pixel and the fixed gate capacitance of the unit cell source follower gate. The nodal capacitance of CMOS hybrids has, until now, usually been determined by the widely used shot noise method that assumes photon shot noise limited performance of the detector. Photons are governed by Bose-Einstein statistics. If the photon energy is small compared to kT (k is the Boltzmann constant and T is the absolute temperature of the radiation source), the variance of the integrated number of photons is equal to the mean number of photons. In this case, the nodal capacitance C_0 can be calculated from the slope of the plot of noise squared signal versus mean signal according to Eq. (1). However, this equation only holds true if the signals of neighboring pixels are uncorrelated as explained in Sec. 3.

$$C_0 = e \frac{\langle V \rangle}{\langle V^2 \rangle} \tag{1}$$

2.   CAPACITANCE COMPARISON METHOD

To obtain the nodal capacitance C_0 by a direct measurement that does not rely on statistical methods, a simple technique has been developed. This technique compares the voltage change of a large calibrated external capacitor to that of the unknown nodal capacitance C_0, which is many orders of magnitudes smaller.

During normal operation the reset voltage, V_{reset}, is connected to an external bias voltage of the detector control electronics and the bias provides the charge required to reset the integrating node capacitor. The hardware setup for the capacitance comparison simply entails adding a switch (relay) between the bias and V_{reset} and adding a calibrated capacitor, C_{ext}, between V_{reset} and detector substrate voltage D_{sub} as shown in Fig. 1. The external capacitor is charged to the nominal reset voltage and disconnected (using the relay) from the external bias. The charge to reset the nodal capacitor C_0 of

each pixel slowly discharges the external capacitor, C_{ext}. If the 2K×2K pixels of the detector are exposed to a high photon flux and several frames are read out and reset, the charge to repeatedly reset the complete array will discharge C_{ext}, generating a voltage drop across C_{ext} large enough to be accurately measured. Since the voltage drop ΔV_{ext} on C_{ext} and the signals of each pixel $V_{i,j}$ are known, the nodal capacitance C_0 and thus the conversion gain C_0/e can be calculated as shown in Eq. (2).

$$\Delta V_{ext} C_{ext} = \sum_{n=1}^{n_{frames}} \sum_{i=1}^{2048} \sum_{j=1}^{2048} V_{n,i,j} C_0 \qquad (2)$$
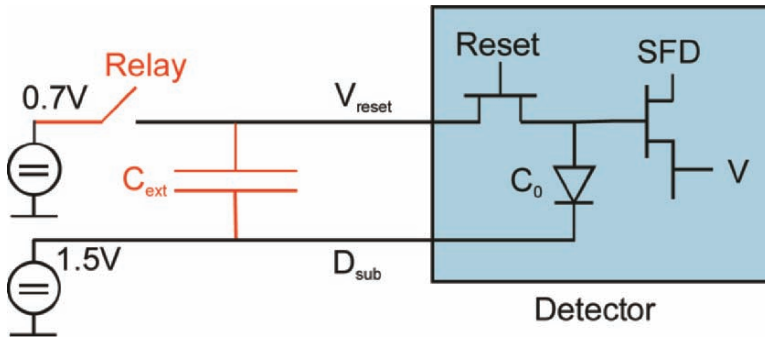
Figure 1. Hardware setup for capacitance comparison method for the measurement of the conversion gain.

A capacitance of 9.26 µF was used for C_{ext}. It is much larger than the sum of the capacitance of all the cables and other stray capacitances. The capacitances of these components may, therefore, be neglected. Low leakage current capacitors such as foil should be used for C_{ext}. Ceramic capacitors should be avoided. Filtering, antistatic and protection circuitry on V_{reset} should be removed or modified if they have large leakage currents. For example, the antistatic protection Zener diode on our preamplifier board next to the focal plane was removed because of its large leakage current. In addition, the ceramic capacitor of the lowpass filter for V_{reset} was replaced by a foil capacitor. No modification is needed for D_{sub}. Leakage currents do not affect D_{sub} as it remains connected to the bias voltage.

An example of the detector signal is shown in the oscilloscope traces in Fig. 2. The detector is operated in read-reset-read mode using line reset. In the left image of Figure 2, the detector signal $V_{n,i,j}$, the nth frame of pixel (i,j),

is the difference between the voltages at the end of the integration ramp and the beginning of the next ramp immediately after applying the reset voltage, which recharges the nodal capacitor of the detector pixel C_0. After charging the external capacitor C_{ext} and opening the relay, the charge to reset C_0 is provided by C_{ext}. Consequently, the DC level of the detector signal slowly decreases (see the right side trace of Fig. 2) as the external capacitor C_{ext} is discharged. With increasing photon flux the discharge rate of C_{ext} increases.

500μs/div   10s/div
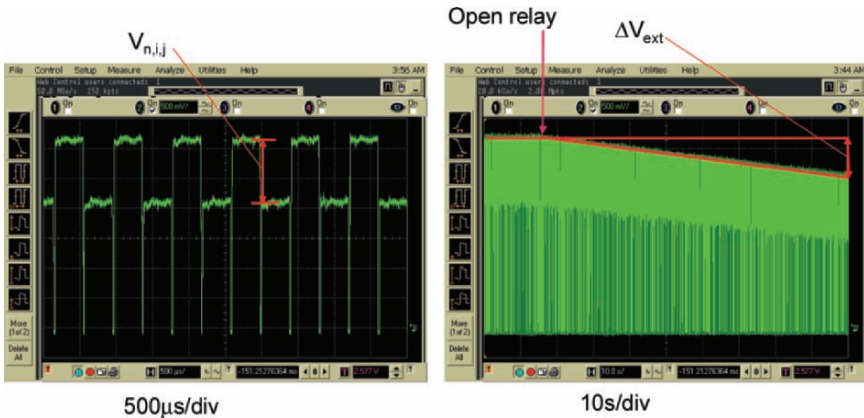
Figure 2.   Oscilloscope traces of the detector signal while applying the capacitance comparison method. *(left)* Detector signal in read-reset-read mode using line reset. Time resolution is 500 μs/division. All 64 pixels of a detector row are read at the end of the integration ramp, the row is reset and read again at the beginning of the next integration ramp. $V_{n,i,j}$ is the detector signal of the nth frame of pixel (i,j). *(right)* The same detector signal taken with time resolution of 10 s/division covering 50 frames. After the relay opens the DC level of the detector signal decreases due to the discharge of the external capacitor C_{ext}.

The detector signal and its change in DC level can be observed by using the normal data acquisition chain operating the detector in the read-reset-read mode. By simply recording the raw data values before and after reset rather than the differences, as is normally done in double correlated sampling, both the pixel intensities and the DC level of the detector signal can be calculated. This is illustrated in Fig. 3, which shows a small part of the array. The bright stripes are the pixels of the row read at the end of the detector integration. The dark stripes are pixels read immediately after reset and are the voltage V_{ext} on the external capacitor C_{ext}. The difference is the detector signal.
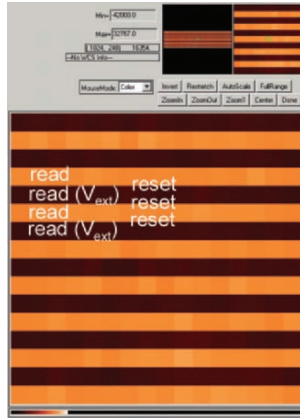
Figure 3.   Read-Reset-Read: Bright stripes are pixels of a row read at the end of the integration. Dark stripes are pixels read immediately after reset and are the voltage V_{ext} on the external capacitor C_{ext}.
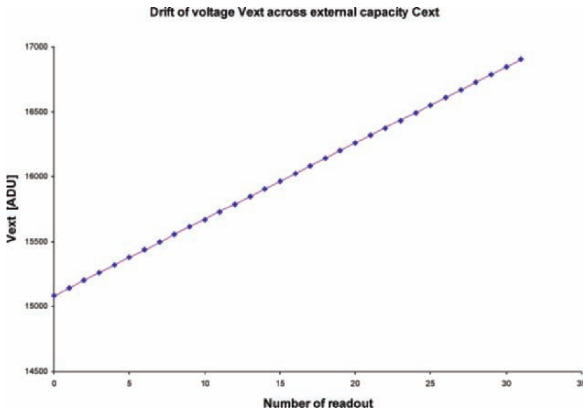
Figure 4. Drift of voltage V_{ext} across the external capacitor C_{ext} versus the number of detector integration. ΔV_{ext}=58.6 ADU/frame.

Depending on the photon flux to which the detector is exposed, the DC level of the detector signal drops at a proportional rate ΔV_{ext} /frame in ADU's per frame as shown in Fig. 4. The number of frames can be selected to be sufficiently large to measure the voltage drop per frame ΔV_{ext} with the desired accuracy. This voltage drop is measured at different photon flux levels and plotted in Fig. 5 versus the sum of the detector signal for the corresponding flux level. (Note that each datum in Fig. 5 comes from one slope of the measurements shown in Fig. 4.)

Voltage drop V$_{ext}$ versus total detector signal
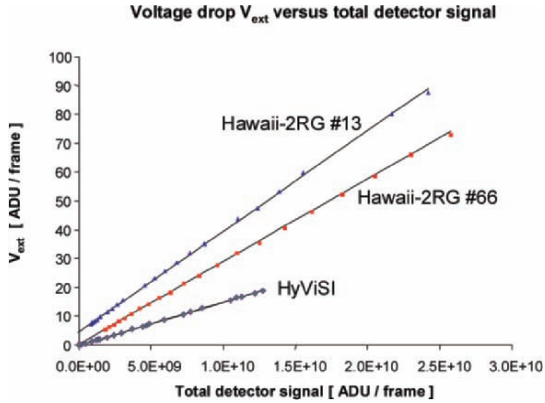
Figure 5. Voltage drop across the external capacitor V$_{ext}$ versus the sum of the voltages of all detector pixels (total detector signal) for the corresponding flux level. The total detector signal is changed by increasing the photon flux on the detector. The slope of the least square fit is the ratio of the nodal capacitance and the external capacitance C$_0$/C$_{ext}$.
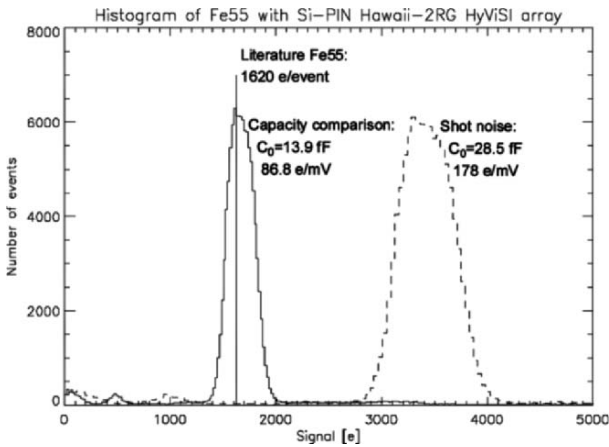
Figure 6. Histogram of HAWAII-2RG Si-PIN HyViSI array exposed to Fe55 X-ray source. The same data set is plotted with nodal capacitances derived from capacitance comparison method (solid histogram) and the shot noise method (dashed histogram). Literature value is indicated as a vertical line.

As shown by Eq. (2), the slope of ΔV_{ext} plotted versus the total detector signal $\sum V_{i,j}$ is equal to the ratio of the nodal capacitance and the external capacitance, C_0/C_{ext}. The external capacitor is 9.26 µF. Using the slopes from Fig. 5, the nodal capacitances of two different $\lambda_c=2.5$ µm HgCdTe arrays (HAWAII-2RG #13, HAWAII-2RG #66) and one Si-PIN array (HyViSI) hybridized to HAWAII-2RG multiplexers can be calculated.

The discrepancy of nodal capacitances C_0 determined by the capacitance comparison and the shot noise method is substantial (> 20% for HgCdTe and more than a factor of two for Si-PIN arrays) as can be seen in Table 1.

Table 1. Comparison of nodal capacitances of CMOS hybrid arrays determined by capacitance comparison and shot noise method.

Device	Conversion gain capacitance comparison [e⁻/mV]	C_0 capacitance comparison [fF]	C_0 shot noise [fF]
$\lambda_c=2.5$ µm HgCdTe HAWAII -2RG #13	201	33.5	40.9
$\lambda_c=2.5$ µm HgCdTe HAWAII -2RG #66	164	27.4	38.1
Si-PIN HyViSI HAWAII-2RG	86.8	13.9	28.5

Nodal capacitances obtained with the capacitance comparison method (Table 1) yields quantum efficiency for the HgCdTe HAWAII-2RG array #13 in K-band of 86% instead of 105%, the value derived with the shot noise method. The shot noise method does not achieve plausible quantum efficiency using conversion gains derived from the standard "noise squared versus signal" technique.

In an effort to compare and validate the two methods of deriving conversion gain we used the K_α line of Fe^{55} which generates a well known number of electrons per absorbed x-ray photon and has been in use for many years to calibrate the conversion gain of optical CCDs [2]. Unfortunately, the Fe^{55} method cannot be applied to the HgCdTe double layer planar heterostructures of infrared arrays. The HgCdTe diode arrays of infrared detectors are grown by molecular beam epitaxy on a CdZnTe substrate which absorbs the x-ray rays of the Fe^{55} source and blocks them before they reach the depletion region of the infrared diodes. The CdZnTe substrates of HgCdTe arrays can be removed by chemical etching. For this type of HgCdTe arrays the Fe^{55} method can be applied, but ESO does not yet have such a device. For the Si-PIN diode array, however, Fe^{55} calibration is applicable. A histogram showing the number of electrons generated by the absorption of one x-ray photon is shown in Fig. 6. The solid curve represents

the histogram generated using the nodal capacitance C_0 determined by the capacitance comparison method; the dashed curve shows the histogram of the same data set but using the nodal capacitance determined by the standard photon transfer curve technique. The accepted value [1] used in calibrating CCDs is shown as a vertical line in Fig. 6. (K_α x-rays generate an average of 1620 electrons in silicon). It is evident that the capacitance comparison method is consistent with the Fe^{55} value cited in literature. The limitations of the applicability of the shot noise method using "noise squared versus signal" have to be investigated and a more thorough interpretation of the method is required.
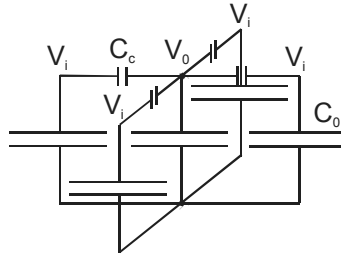
Figure 7. Interpixel coupling capacitance.

The Fe^{55} method can also be applied to InSb detectors which do not have a detector substrate. First measurements yield a value of 2500 electrons per absorbed K_α x-ray photon. Possibly, the Fe^{55} method will also be applicable to HgCdTe arrays, if their substrate is removed. Further investigation in this area is needed.

3.   INTERPIXEL CAPACITANCE

The nodal capacitance C_0 derived by the shot noise method appears to be too large. Since Eq. (1) shows that C_0 is inversely proportional to the variance, the measured variance of the detector signal $\langle V^2 \rangle$ should be larger to obtain a smaller but more plausible nodal capacitance. The discrepancy cannot be explained by excess noise of the data acquisition chain as more noise would only make the variance larger not smaller. On the contrary, a mechanism has to be introduced which does not store signal charge but reduces the photon shot noise of a single pixel. The larger capacitance seen by the shot noise may be explained by coupling capacitance between neighboring pixels. As a consequence of interpixel capacitance the signal of a pixel is spread by capacitive coupling to adjacent pixels, which reduces the apparent photon shot noise. The photon shot noise method does not yield the pixel capacitance C_0, but the provides a measure of the sum of C_0 and all

the coupling capacitors in series with the nodal capacitors of the neighboring pixels as shown in Fig. 7.
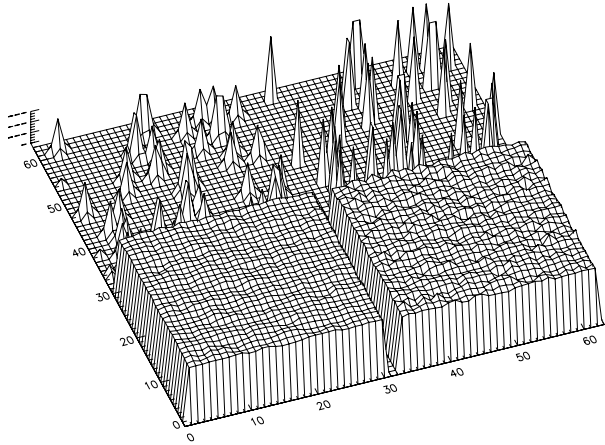
Figure 8. A surface plot of numerical simulation illustrating the effect of interpixel capacitance. In this example, the interpixel capacitance is made relatively large, x = 0.3, to dramatically demonstrate the effect. Upper half: short time exposure showing signal of individual, Poisson distributed photons. Lower half: long time integration with reduced intensity scale. Right half: no interpixel capacitance. Left half: interpixel capacitance, signal of single photon is spread to closest neighbors. Long exposures show a smoother surface.

Using the coupling capacitance C_c and the ratio of coupling capacitance and nodal capacitance x = C_c/C_0, a simple model of the apparent capacitance seen by the shot noise is $C = C_0(5x+1)/(x+1)$. For simplicity, only coupling to the 4 closest neighbors is considered here. By applying Kirchhoff's law it can also be shown that the total signal with coupling V_0+4V_i is equal to the total signal V without coupling, i.e., $V_0+4V_i = V$ with V being the signal for $C_c=0$. This implies that the interpixel capacitive coupling conserves photometry. For uniform illumination of the array no signal charge is stored on the coupling capacitors. The coupling capacitors reduce the photon shot noise because the voltage response of a photon-generated electron is not confined to a single pixel, but spread over all neighboring pixels. This nominal reduction of noise is accompanied by reduced image contrast and degraded detector MTF.

The effect of interpixel capacitance has been simulated numerically by generating random Poisson distributed short time exposures as shown in the upper halves of Fig. 8 as surface plots, and in the upper halves of Fig. 9 as images. The right sides of Figures 8 and 9 represent a detector without interpixel coupling whereas the left sides introduce an interpixel capacitive

coupling of x = 0.3. The crosstalk can be clearly seen in the upper left quarter of both the surface plot of Fig. 8 and the image of Fig. 9. The lower half of Fig. 8 and Fig. 9 show the images with and without interpixel coupling for a much longer integration time with a larger intensity scale.
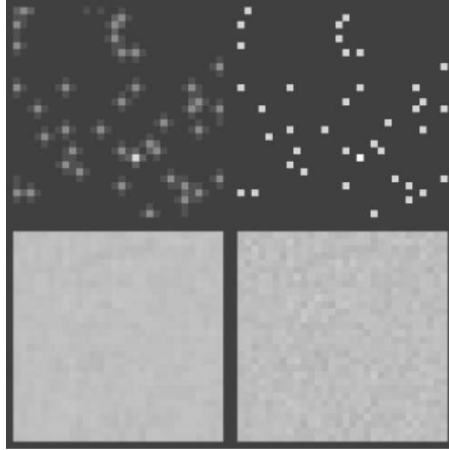
Figure 9. Image of numerical simulation illustrating the effect of interpixel capacitance.
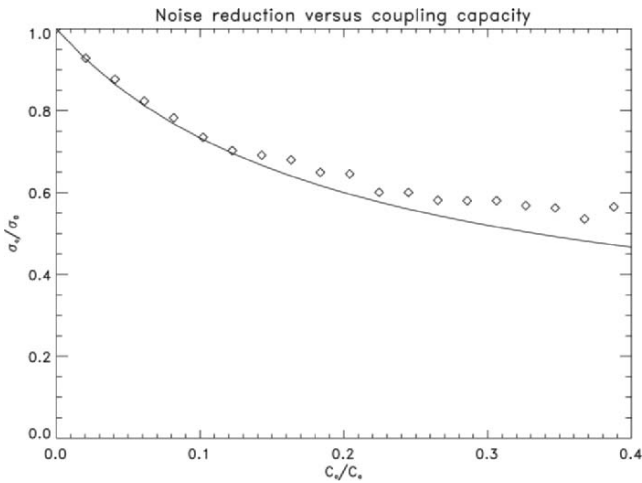
Figure 10. Ratio of standard deviation with interpixel capacitive coupling σ_c and without interpixel capacitive coupling σ_0 as function of coupling C_c/C_0. Diamonds: simulation of random Poisson distributed short time exposures. Solid line: ratio of total capacitance C and nodal capacitance C_0 taking into account the four closest neighbors $C/C_0 = (5x+1)/(x+1)$.

The pixel to pixel variance without coupling on the right side is equal to the average number of integrated photons in agreement with Poisson statistics. The variance with capacitive interpixel coupling is smaller as shown by the smoother surface and image in the lower left quadrants of Figures 8 and 9. The ratio of the standard deviation with capacitive interpixel coupling σ_c and the standard deviation without coupling σ_0 as derived from the numerical simulation using Poison statistics is shown by diamonds in Fig. 9. For small coupling ratios C_c/C_0 , the ratio σ_c/σ_0 follows the ratio of the total capacitance C and the nodal capacitance C_0 which is represented by the solid line in Fig. 9. This ratio is given by the expression $C/C_0=(5x+1)/(x+1)$ only taking into account the coupling to the four closest neighbors.

4.   AUTOCORRELATION

Moore, et al. [2] have examined the detector edge spread and MTF; they were the first to introduce interpixel coupling as one mechanism to degrade the image sharpness of CMOS hybrid detectors. They devised a stochastic method of measuring the interpixel coupling using 2-D autocorrelation and arrived at the same conclusion regarding the overestimation of the nodal capacitance by the shot noise method. We have applied their autocorrelation method to both HgCdTe and Si-PIN diode arrays hybridized to the HAWAII-2RG multiplexer. If the difference of two uniformly illuminated shot noise limited images have pixel intensities $V_{i,j}$, and $R_{m,n}$ is the autocorrelation function, the factor φ by which the nodal capacitance is overestimated by the shot noise method using "noise squared versus signal", is given in Eq. (3)

$$\varphi = \sum_{m,n} R_{m,n} \qquad with \qquad R_{m,n} = \frac{\sum_{i,j} V_{i,j} V_{i+m,j+n}}{\sum_{i,j} V^2{}_{i,j}} \qquad (3)$$

If all the cross products $V_{i,j}V_{i+m,j+n}$ with $m \neq 0$ and $n \neq 0$ are 0, the signals of neighboring pixels are not correlated, since the interpixel capacitance is negligible. For this case φ is 1 and the "noise squared versus signal" method yields the correct nodal capacitance. If there is a correlation between neighboring pixels due to coupling capacitances, the correct nodal capacitance can still be derived from the shot noise of difference images by

properly taking the correlation between pixels into account which is expressed by the correction factor φ given in Eq. (3).

We determined the correction factors φ for the nodal capacitance of CMOS hybrids with the 2D autocorrelation method of A. Moore. The measured values are φ_{HgCdTe}=1.20 for the HgCdTe array and φ_{Si-PIN}=2.03 for the HyViSI Si-PIN array (see Fig. 10). Both arrays are hybridized to the same type of HAWAII-2RG multiplexers. The correction factors are in good agreement with the results given in Table 1 and further support the results obtained with the capacitance comparison method described in this paper.
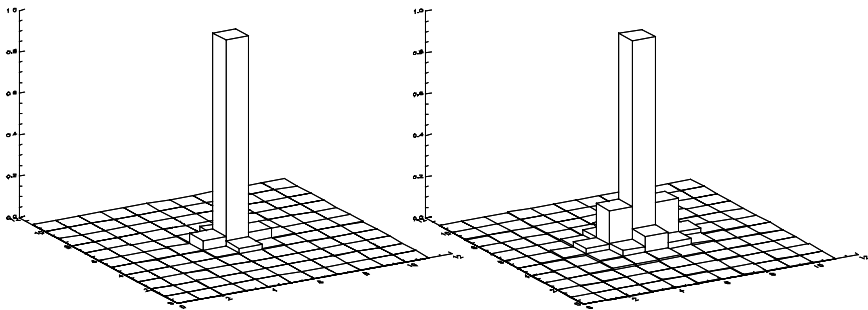
Figure 11. Autocorrelation of CMOS HAWAII-2RG hybrid arrays. *(left)* λ_c=2.5 μm HgCdTe array, φ=1.23. *(right)* Si-PIN HyViSI array, φ=2.03.

5.   CONCLUSIONS

Modern CMOS hybrid focal plane arrays have small pixels. Hence, the coupling capacitances between neighboring pixels, even if they are only a few percent of the nodal capacitance of the detector pixel, must be accounted for when the conversion gain is determined with stochastic methods. The usual "noise squared versus signal" method can lead to an overestimation of the nodal capacitance of more than 20% for infrared arrays and more than 100% for Si-PIN diode arrays. An alternative method of measuring the nodal capacitance, the capacitance comparison technique, is the most direct method which is also simple to implement. It delivers nodal capacitances which yield plausible quantum efficiencies well below 100%. Furthermore, it is consistent with the 1620 electrons generated in silicon PIN diodes by the absorption of K_α x-ray photons emitted by Fe[55]. Additional confirmation for

the capacitance comparison method comes from a stochastic method based on 2D autocorrelation to determine the nodal capacitance.

The high spatial resolution of extremely large telescopes will require focal planes of several Gigapixels. This future demand entices detector manufactures to increase the detector format by shrinking the pixel size, because available detector substrates are limited in size. This trend, however, should not be pursued without carefully addressing all issues of interpixel coupling. For smaller pixel sizes, designs and techniques must be developed to minimize the capacitive coupling between neighboring pixels. The spacing between indium bumps can be increased by using smaller indium bumps. Epoxy glues with high dielectric constants between the indium bumps should be avoided if possible; however, epoxy "backfill" may be necessary for substrate removal. Investigation into designs and fabrication techniques to reduce interpixel capacitance has already commenced at the Rockwell Scientific Company.

The authors received data from the VISTA [4] project, which has infrared hybrid arrays with slightly larger pixel sizes of 20 μm. The arrays have no epoxy backfill between the indium bumps. Data have been analyzed with the 2D autocorrelation method. A correction factor of φ=1.03 has been calculated, a result reported independently by McMurty, et al. [5].

The Si-PIN diode array is hybridized to the same HAWAII-2RG multiplexer as the HgCdTe infrared array, but has much larger interpixel coupling capacitances. In this case, the main contribution to the interpixel capacitance is not located in the multiplexer or between the indium bumps, but within the Si-PIN diode arrays itself. It will be a challenge to substantially reduce this coupling.

Capacitive coupling between detector pixels is a deterministic process that conserves photometry and can be accounted for, if properly calibrated. In the photon noise limited regime both the signal and the noise are attenuated by the same factor. However, for point sources in the read noise limited regime the spreading of the signal response to neighboring pixels seriously affects the signal to noise ratio and degrades the detector MTF and image sharpness. This will degrade the performance of high order adaptive optics systems. For these reasons the advantages and disadvantages of reducing the pixel size to provide larger detector formats have to be carefully weighed.

6. ACKNOWLEDGEMENTS

7. REFERENCES

[1] Beletic, J., Figer, D., Finger, G., Love, P. and Smith, R., 2005, *Detector Testing and Characterization, Workshop on Scientific Detectors for Astronomy*, these proceedings.

[2] Janesik, J.R., 2001, *Scientific Charge-Coupled Devices*, SPIE Press, p. 134.

[3] Moore, A.C., Ninkov, Z. and Forrest, W.J., 2003, *Interpixel Capacitance in Non destructive Read-out Focal Plane Arrays,* Proc. SPIE **5167**, 204-215.

[4] Bezawada, M., 2005, private communication.

[5] McMurty, C. W., Allen, T. S., Moore, A.C., Forrest, W.J., and Pipher, J. L., 2005, *Characterization of 2.5 micron HgCdTe VIRGO/VISTA Detector Array*, SPIE, in press.

Extreme last minute presentation preparation.
Gert Finger, James Beletic, Peter Love, Roger Smith (left to right) and Don Figer (not shown) were finalizing slides on three computers until five minutes before their presentation on Sensor Test and Characterization. Most of this presentation was dedicated to the recently discovered phenomenon of interpixel capacitance.

MBE MCT ARRAYS FOR JWST
Ultra Low Background Characterization and Temperature Drift Compensation

Donald N. B. Hall
University of Hawaii, Institute for Astronomy

Abstract: *2K×2K arrays developed by the collaborative efforts of University of Hawaii (UH) and Rockwell Scientific Company were selected for all three near infrared instruments on the James Webb Space Telescope (JWST). We report improvements in the UH test system and procedures that have led to temperature control to <1mK rms over days, determination of dark current to a few e⁻/hour and characterization of total noise. Current JWST λ_c ~2.5 µm arrays consistently achieve dark current <2 e⁻/Ksec and total 1,000 second noise <4 rms e⁻. Results obtained using spatial and temporal averaging are in good agreement. For JWST, control of the focal plane temperature to <1 mK rms is challenging, even in the laboratory. We report measurements of the temperature coefficient of array output voltage, $\delta V/\delta T$. It is constant for each pixel with an average value of 3.25 µV/K corresponding to ~0.75 e⁻/K. However, within the array, individual pixel values vary over the range from 0 - 6.5 µV/K. An algorithm utilizing the measured frame temperature to scale a template and allowance for a time lag, correct slow (<10 mK/min) temperature drifts to a precision of ± 1 - 2 e⁻ over a range of at least ± 50 mK about 37.000K.*

Key words: *HAWAII-2RG, MBE HgCdTe arrays, dark current, total noise, temperature drift compensation.*

1.   INTRODUCTION

A University of Hawaii (UH)-Rockwell Scientific Company (RSC) team developed the MBE HgCdTe based HAWAII-2RG arrays eventually selected for all three James Webb Space Telescope (JWST) Near Infrared (NIR) instruments. The UH test lab has developed techniques for evaluation

of key noise characteristics, notably dark current and total noise, under JWST conditions. Initially spatial averaging was used for computational simplicity. This is particularly valuable in initial screening arrays, Near Infrared (NIR) instruments on the JWST will require a total of sixteen 2K×2K flight detector arrays with flight spare and engineering detectors – a total in excess of 100 Mpxl. However, the science goals for the NIR instruments, particularly the Near Infrared Spectrometer (NIRSpec), place very stringent requirements on detector performance and require detailed characterization of individual pixels. For this we have used a data cube approach to provide temporal averaging.

Characterization of the full ultra low background performance of H2RG arrays has required thermal control of the array temperature to <1mK rms throughout the tests. In order to relax this requirement, we have measured the sensitivity of output voltage to temperature and have demonstrated temperature drift compensation techniques, which relax the temperature control requirement to > ± 50 mK.

2. CHARACTERIZATION OF HAWAII-2RG ARRAYS FOR JWST

2.1 Test Conditions Matched to JWST

Operation of 2K×2K arrays and larger mosaic focal planes within the power, control and data handling constraints of JWST has resulted in the adoption of a parallel read out of four 512×2048 pixel "stripes" at a 100 Kpxl/sec rate for a <12 second frame rate. Characterization data is taken with noise bandwidth 3 DB filtered at 160 KHz (10 τ or >14 bit settling) and resets are pixel by pixel, also at 100 Kpxl/sec. For optimum temperature stability, the array is always clocked at 100 Kpxl/sec in either readout or reset mode. The data reported here are for an early JWST array produced for the Near Infrared Camera (NIRCam), part number JWST-002, operated at 37K with detector bias of 250 mV achieved with a substrate voltage of 350 mV and reset voltage of 100 mV.

2.2 Dark Current and Total Noise Measured by Spatial Averaging

This technique, reported by Hall, et al.[1], utilizes a set of identical ramps, each consisting of resets followed by a fixed number of frames. The standard UH data set consists of five ramps, each made up of 2 pixel by

pixel resets followed by 145 frames resulting in a 6.1 Gbyte data set. The DC dark current for each ramp is determined by subtracting the average of the upper and lower reference pixels for each stripe and fitting each pixel in the corrected frames up the ramp. The total noise for each stripe is determined by subtracting corresponding frames in adjacent ramps, masking out anomalous pixels, determining the variance of the difference frame and normalizing by two.

2.3   Dark Current and Total Noise Measured by Temporal Averaging

The temporal averaging technique requires a data set of enough identical ramps to significantly determine the properties of individual pixels. The standard UH data set consists of thirty six ramps, each made up of 2 resets followed by 145 frames. The raw, four dimensional (36 ramps×145 frames× 2048×2048) data approaches 44 Gbytes and takes 18 hours to accumulate. After flagging pixels affected by cosmic ray hits in individual ramps, the data set is used to generate a ramp by ramp data cube of dimensions 2048× 2048×36 for the required parameter. This typically accumulates charge and its sigma for each pixel, over a specified time interval using either CDS samples (which may be averaged) or slope fitting. These are then converted into dark current and total noise.

The dark current in the NIRCam arrays is so low (<0.002 e$^-$/sec) that over ½ hour ramps its determination for individual pixels is dominated by read noise. For Fowler CDS averaging, we divide frames 9–144 of each ramp into four blocks of 32 frames each and then derive the dark current and total noise for CDS averages of 1-1, 2-2, 4-4, 8-8, 16-16 and 32-32 frames centered in the blocks separated by 384, 768 and 1152 seconds. Typical dark current and total noise histograms are presented in Fig. 1 and total read noise is summarized in Figures 2 and 3. Note that the 768 second values closely match the optimum signal to noise for CDS averaging over the nominal JWST 1,000 second exposure limit and that for all three time intervals, the 8-8 total noise is below the NIRSpec requirement of 6 rms e$^-$.
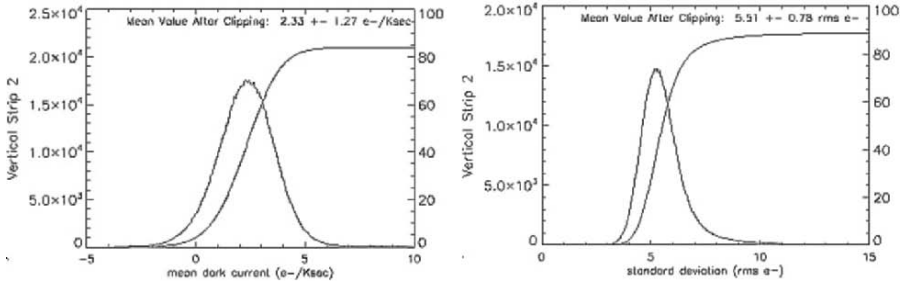
Figure 1. Dark current and total noise histograms for 8-8 CDS at 768 seconds.
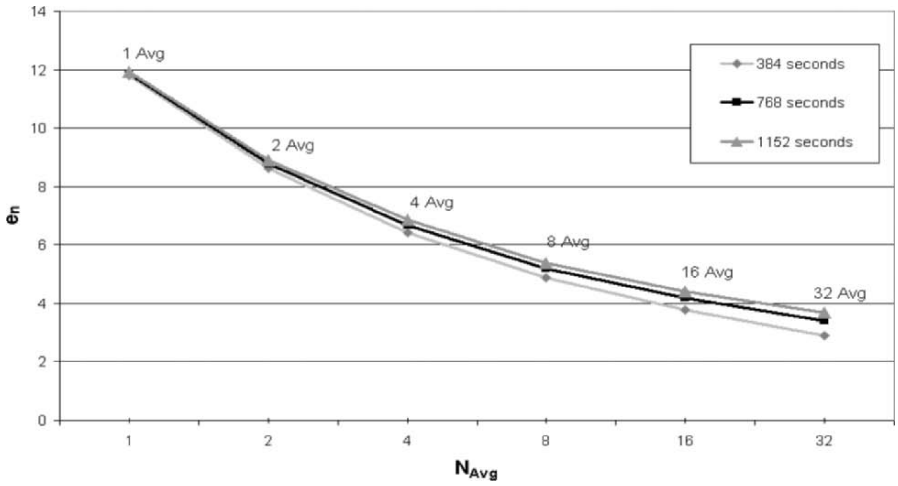
Figure 2. Standard deviation for JWST-002 at 384 sec, 768 sec, and 1152 sec.
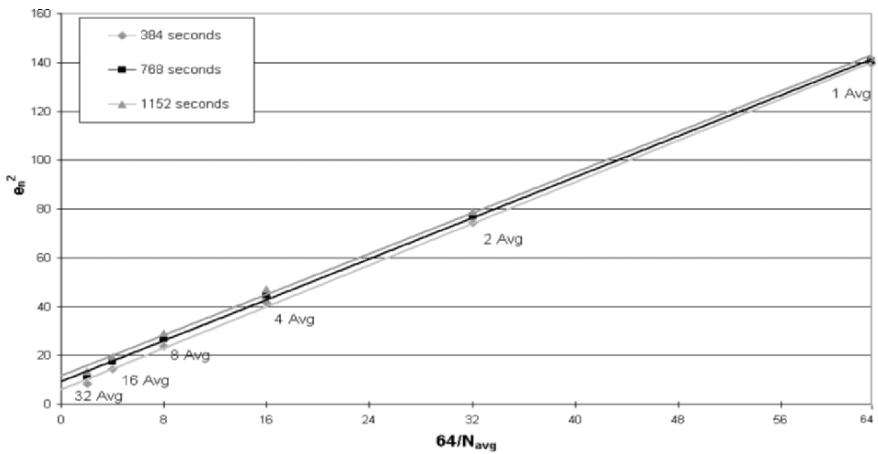
Figure 3. Variance noise power for JWST-002 at 384 sec, 768 sec, and 1152 sec.

2.4 Spatial versus Temporal Averaging – Consistency of Results and Relative Merits

Measured CDS 1-1 and 8-8 total noise values for JWST-002 are listed in Table 1 for the two averaging techniques (note that the uncertainties are for a stripe average in the spatial case and for individual pixels in the temporal case). The consistency between the two techniques validates the use of the simpler spatial averaging for screening purposes.

Table 1. Measured CDS noise (in ADU – 1 ADU is 4.33 µV or ~ 1e⁻) for JWST-002.

	Stripe 1	Stripe 2	Stripe 3	Stripe 4
CDS 1-1				
Spatial	12.50 ± 0.15	12.50 ± 0.05	12.60 ± 0.09	12.70 ± 0.10
Temporal	11.74 ± 1.69	11.77 ± 1.71	11.99 ± 1.75	11.91 ± 1.73
CDS 8-8				
Spatial	5.51 ± 0.03	5.65 ± 0.09	5.70 ± 0.07	5.96 ± 0.07
Temporal	5.03 ± 0.73	5.04 ± 0.73	5.37 ± 0.77	5.30 ± 0.78

The advantage of the spatial averaging technique is that it requires only a modest data set and computationally simple reduction to provide reliable estimates of stripe (or sub-array) total noise along with accurate estimates of individual pixel dark current. It is thus valuable for initial evaluation and screening of arrays. The primary disadvantage is that because dark current is so low it is a negligible factor in total noise, it provides no information on total noise in individual pixels. At the expense of increased time for acquisition and reduction of test data along with greatly expanded data storage requirements, the temporal averaging technique has been demonstrated to yield reliable estimates of total noise in each pixel.

3. TEMPERATURE DRIFT IN HAWAII-2RG ARRAYS

For all UH tests the detector temperature is held constant to <1mK rms, approximately a nominal temperature (37 K for JWST tests) throughout data taking. This level of control may be difficult to achieve even in ground based instruments and will increase complexity, weight and the potential for EMI in space applications. We have therefore characterized the shift in output signal with temperature ($\delta V/\delta T$) in 9.12 mK/min ramps of ± 50 mK and ± 600 mK about 37K and find significant effects not compensated by the

reference pixels. We have subsequently developed a technique to correct such drifts to the 1ADU (~ 1 e-) level in post processing of the data.

3.1   Characterization of Temperature Drift

Without active thermal control, temperature drifts in the JWST NIR focal planes may have amplitudes of up to ± 50 mK at rates up to 10 mK/min. We have evaluated output temperature drift under such conditions by running a series of standard 145 frame ramps in which the temperature is held constant at 36.950K for the two resets and the first part of the ramp, then ramped up 100 mK at 9.12 mK/min (55 frames) and finally held constant at 37.050K for the remainder of the ramp. This is followed by a similar sequence ramping back down 100 mK. The entire process is repeated five times to produce a set of five "up" ramps and another of five "down" ramps. The detector output for the five "up" ramps, corrected using the horizontal reference arrays (see Fig. 4) along with a histogram of the change over 100 mK for each pixel. From more detailed analysis we conclude that over 100 mk $\delta V/\delta T$ is constant for each pixel with an array average value of 0.75 ADU/K or 3.25 µV/K although values range from 0 – 1.5 ADU/K (0 – 6.5 µV/K) for individual pixels. In order to meet JWST requirements without correction the focal plane temperature must be held constant to a few mK.
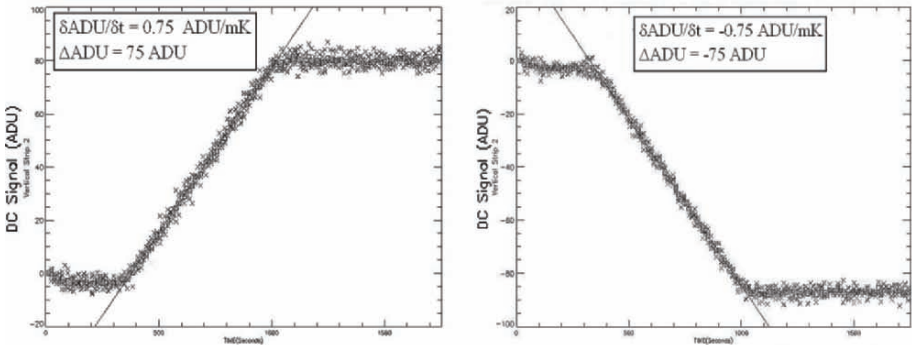
Figure 4. The detector output for the five "up" ramps and five "down" ramps, corrected using the horizontal reference arrays.

By ramping JWST-002 between 36.4 and 37.6K at 9.12 mK/min and taking full 145 frame ramps at each temperature, we have established linearity over this range and a template frame of $\delta V/\delta T$ for each pixel. Subtraction of the scaled template to form individual frames of the 5 "up" and 5 "down" ramps eliminates drift between the plateau frames at each side of the ramp (see Fig. 5), but leaves an offset ~ 8.5 ADU (37 µV) during the ramp. We interpret this as a time lag between the temperature of the

mounting plate and that of the array. Delaying the temperature used for correction by 5 frames (60 seconds) relative to the plate temperature corrects this effect to within the noise as evident in Fig. 6.
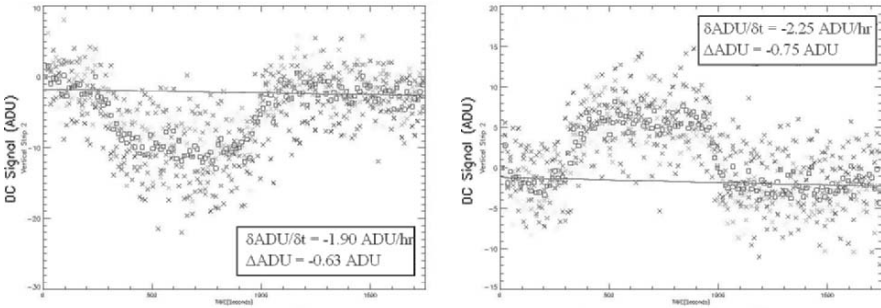
Figure 5. Time lag between the temperature of the mounting plate and that of the array limits correction during the temperature ramp.
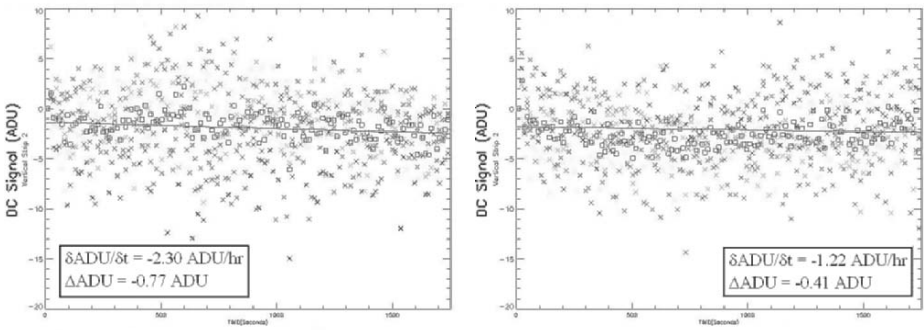
Figure 6. After inclusion of a 60 second time lag between the temperature of the mounting plate and that of the array, correction is within the noise.

We conclude that the $\delta V/\delta T$ template technique combined with an optimized lag time will fully correct temperature excursions of at least ± 50 mK at rates up to 10 mK/min. This holds promise of allowing the JWST NIR instrument focal planes to meet requirements without active temperature control.

4.   ACKNOWLEDGEMENTS

5.   REFERENCES

[1] Hall, D. N.B., et al., 2000, Optical and Infrared Instrumentation and Detectors, Iye, M., and Moorwood, A.F.M., (ed) , Proceedings of SPIE, Vol. **4008**, p. 1268.

Paola Amico and Don Hall trade Hawaiian secrets in Forza d'Agró.

PERFORMANCE OVERVIEW OF THE VISTA IR DETECTORS

Nagaraja Bezawada and Derek Ives
UK Astronomy Technology Centre (ATC)

Abstract: *The IR camera for the Visible and Infrared Survey Telescope for Astronomy (VISTA) will have a sparse mosaic of 16 Raytheon VIRGO 2K×2K HgCdTe detectors in its focal plane. All the 16 detectors have been individually tested in a custom built test facility at the UK ATC to confirm that their performance meets our specifications. This paper summarises the overall performance of all the detectors but also presents a detailed characterisation of a science detector in depth. In particular, we present important characteristics such as quantum efficiency, dark generation, read noise, well capacity and linearity, persistence, pixel operability and long term stability. We also discuss the precise estimation of the system gain and noise using both pixel-to-pixel (spatial) and temporal methods, read noise performance with multiple sampling, the apparent increase in the dark generation followed by reset, behaviour of reference pixels and our attempts to use these pixels to reduce low frequency noise.*

Key words: *VISTA IR detectors, VIRGO detectors, performance overview.*

1. INTRODUCTION

The Visible and Infrared Survey Telescope for Astronomy (VISTA) is a 4 m class telescope dedicated for survey in the visible and near infrared regions of the spectrum. During its initial operations VISTA will be equipped with the world's largest infrared camera (IR Camera) which will have 16 2K×2K Raytheon VIRGO detectors in a sparse mosaic of 4×4 arranged at 90%×42.5% of active width of a detector. The full field (1.65º with 0.34 arc sec pixel) will be sampled and reconstructed by a set of offset

frames with suitable overlaps in X and Y directions. Raytheon Vision Systems (RVS) has supplied over 20 detectors and these are individually tested in a custom built test cryostat at the UK ATC to confirm that their performance meets IR camera requirements. This paper presents an overview of the performance of the 16 detectors selected for the IR camera.

2.   VIRGO DETECTORS AND TEST SETUP

VIRGO detectors or Sensor Chip Assembly (SCA), are p-on-n type HgCdTe detectors grown by liquid phase epitaxy on a lattice matched CdZnTe substrate and hybridized to VIRGO readout integrated circuit. These are 2K×2K pixel format detectors with 20 µm square pixels and a cut-off wavelength of 2.5 µm. The readout can be organized into vertical strips of either 512/128×2048 pixels and are accessible through 4/16 outputs respectively. The design allows up to a 400 kHz pixel rate in each channel which equates to a 0.68s frame readout time in 16-channel mode. The detector requires 15 bias supplies, 3 control lines and only two clocks to operate. All other clocks that operate row and column shift registers are generated on-chip and some of the bias supplies are used as upper and lower rails for the internally generated clocks. The control lines allow the selection of output mode, reset enable and reset type (row or global reset).

The test facility includes a custom built low background closed cycle cooled cryostat and ESO's standard Infrared Array Control Electronics (IRACE). The cryostat consists of a temperature controlled detector mount stage, a 16-channel pre-amplifier board close to the detector, which works reliably at temperatures below 77K with a manually controlled cold filter wheel with J, H, K filters for responsivity tests and a cold blank for dark generation measurements. The detector and light path are surrounded by low background baffles to reduce the light scatter and stray light reaching the detector. The IRACE detector control software allows complete control of electronics, data acquisition and provides real-time display of data.

3.   PERFORMANCE OF VIRGO DETECTORS

The operation and performance of the VIRGO multiplexer and the test results from the first science detector were reported by Bezawada, et al. [1]. Over 20 detectors have been individually tested since then and the performance of the 16 science detectors is summarized in the following sections whilst a few specific characteristics from SCA-45 are detailed.

3.1 Conversion Gain

The gain is determined from the spatial photon transfer using several pairs of identical flats obtained by varying integration time whilst the input flux is kept constant. A sample box of 50×50 pixels is moved over the frame and a histogram is obtained from all samples corresponding to signal levels ranging from 20 to 70% of full well. The full well is determined from the noise roll-over point from the signal vs. variance plot (see Fig. 1). The detector transimpedance conversion gain showed a strong dependence with the signal level and varies up to about 14% with SCA-45 (see Fig. 1). A similar dependency is also observed with photon transfer from pairs of flats obtained at various flux levels with fixed integration time. This dependence can be attributed to the increase of the detector junction capacitance (hence the decrease of the node sensitivity) as the input node integrates towards saturation. For the purpose of estimating the full well, the average conversion gain obtained from the signal levels of 20 to 70% of the full well is used. For the purpose of estimating dark, read noise, persistence etc. a conversion gain estimated from low signal level (up to 20% of the full well) is used. The conversion gain is also estimated using the temporal method where the variance is calculated for each pixel in the frame from a sequence of 100 Correlated Double Sample (CDS) frames at a given signal level. The gain estimated from the spatial method agrees very closely with the values obtained from the temporal method at any given signal level. However, the effect of the inter-pixel capacitance on the conversion gain (hence the node capacitance) is being investigated and reported by Finger, et al. [2].
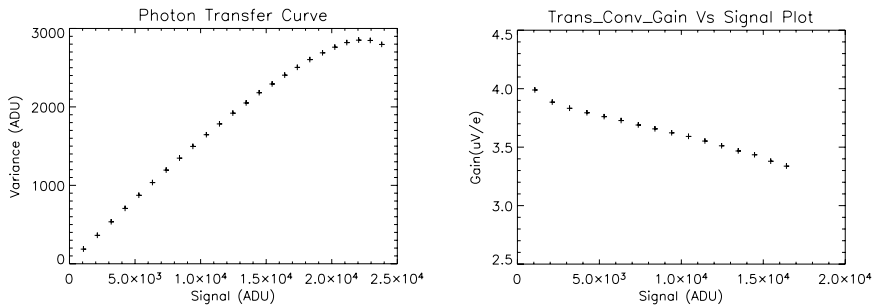
Figure 1. Conversion gain depends on signal level. *(left)* Photon transfer curve. *(right)* Transimpedance conversion gain dependency with signal level.

Both the conversion gain and the full well are proportional to the applied detector bias (see Fig. 2). The higher detector bias results in a slight increase in the mean dark generation as well as the non-linearity. The non-linearity is

measured from 10 to 80% of a full well and is about 3 to 5% for most of the detectors.
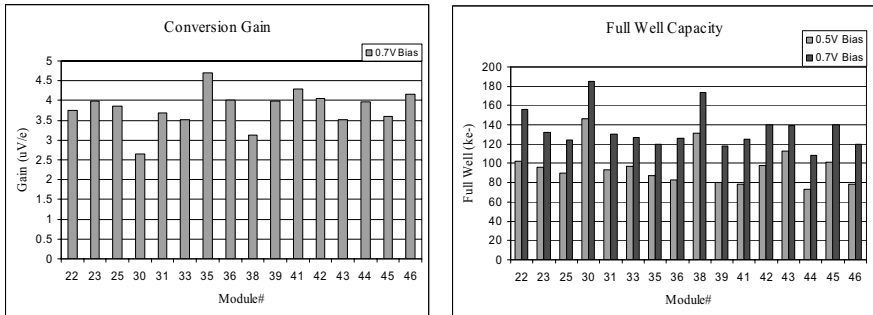
Figure 2.   *(left)* Conversion gain at 0.7V detector bias. *(right)* Full well capacity at 0.5 V and 0.7 V detector bias for all modules.

3.2   Quantum Efficiency

Quantum Efficiencies (QE) are measured in J, H and K pass bands using blackbody radiometry. The uncertainties in QE measurements are up to 12% and are mainly due to the uncertainties in the blackbody temperature, emmissivity of the emitting surface, filter pass-bands and the estimation of conversion gain. The systematic error due to inter-pixel capacitance is being investigated. Another uncertainty that is difficult to estimate is the internal reflections within the test cryostat. Fig. 3 shows a QE histogram in K band from SCA-45 and a QE bar chart for all the 16 science detectors. QE in Z and Y bands has been measured on SCA-46 and the values are 70.7% and 81.0% respectively.
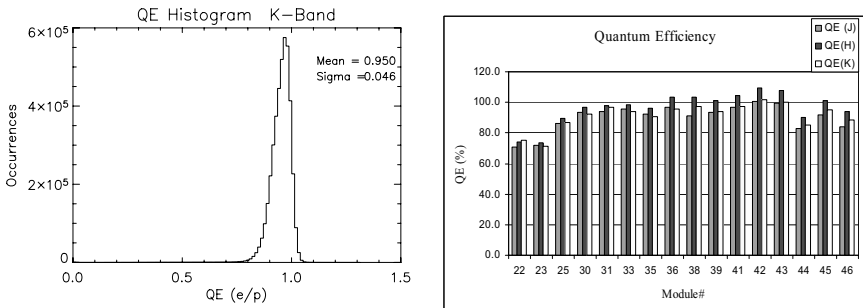
Figure 3.   *(left)* QE histogram for SCA-45 through K-band and *(right)* QE bar chart for all modules in J, H and K bands.

3.3   Dark Generation

The dark generation is measured from a set of 240s CDS frames and it includes the reset transient. The detector shows slightly higher rate of dark generation immediately after the reset and reduces exponentially to its final value. The good pixels show negligible transient whilst the hot pixels show a large transient following the reset. As the test setup is not optimized for measuring low dark generation, it is possible that the reset transient is dominated by the background signal for good pixels. Figure 4 shows the dark histogram for SCA-45 and dark performance for the other detectors.
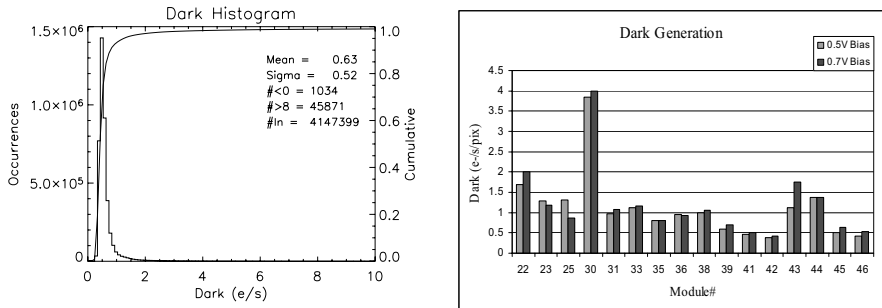
Figure 4.   (left) Dark generation histogram from SCA-45 and *(right)* Dark generation for all the 16 detectors.

3.4   Read Noise

Figure 5 shows the read noise measured from both pixel-to-pixel (spatial) and temporal methods. The spatial method involves subtraction of two CDS frames obtained with minimum detector integration time and the resulted frame is divided by $\sqrt{2}$. The hot pixels ($>8e^-$/s/pix) and defects are eliminated from the measurement. The temporal read noise is obtained by estimating the noise for every pixel in the frame from a series of CDS frames. The mean of the resultant noise histogram agrees very closely with the sigma from pixel-to-pixel method indicating that the noise and the gain variations from pixel to pixel are small. The temporal noise with 32 Fowler pairs reduced under $6e^-$ whilst it is $\sim 10e^-$ with 64 non-destruct samples.

3.5   Persistence

The persistence signal decay is measured from a sequence of CDS frames of 10s dark integrations following the saturation with 200ke$^-$ fluence (10sec

exposure). The persistence signal decays below read noise in ~40s for most of the detectors. It has been found that it is the time that the persistence signal has to decay after the first reset that is important and the subsequent resets had little or negligible effect.
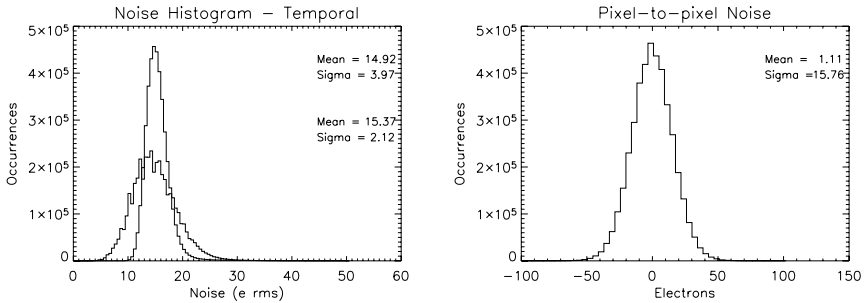
Figure 5.   Read noise histograms obtained from (*left*) temporal method using a stack of 10 (broad) and 100 CDS (narrow) frames and (*right*) pixel-to-pixel method.

3.6   Reference Pixels and DC Drift

The VIRGO multiplexer has two types of reference pixels. There is a row of reference pixels in the beginning of the array and there are 6 column reference pixels in every readout channel. The reference pixels have similar DC drift with temperature as active pixels (~830e⁻/K with SCA-22), but have different DC offsets. We tried to use the reference pixels to correct the low frequency banding, but little improvement could be achieved as the low frequency banding was only about +/-1.5ADUs (p-v) and the read noise in a CDS frame is ~15e⁻ (rms).

4.   PERFORMANCE SUMMARY

From the field of 20 detectors, the best 16 detectors are selected for the IR camera focal plane leaving 3 potential spares and a true engineering detector. Figure 6 shows the bitmaps of these 16 detectors through K-band. The numbers identify the each module by its serial number. These bitmaps are stretched between the same limits, so it is apparent that a couple of earlier modules (22 and 23) have relatively low QE around 70%. Most of the detectors showed high QE over 90% and some showed near and above unity (100% QE). Modules 22 and 23 have unstable, hygroscopic Anti-Reflection (AR) coatings and are needed to be stored in a dry environment. All modules

from #25 onwards have received robust AR coating and also exhibit high QE. The other features in these bitmaps are the large area cluster defects on module#35 (up to 1.8% pixels), excess hot pixels on modules#30 and #43 and a column defect on #43. Most of the detectors achieved pixel operability over 98% with few exceeding 99% operability and met specifications with sufficient margin. Modules#30 and #43 possess excess hot pixels but the mean dark generation is well within the specifications. Cosmetically, the distinguished feature of these detectors is the numerous defective spots across the array, but some detectors have not shown such spots. Cluster defects ~20 pixels in diameter are present in most of the detectors. The read noise is ~17e$^-$ in most of the detectors and could be reduced under 6e$^-$ with multiple sampling. Table 1 summarises the performance of the module SCA-45. More performance data on these detectors is also presented by Love, et al. [3].
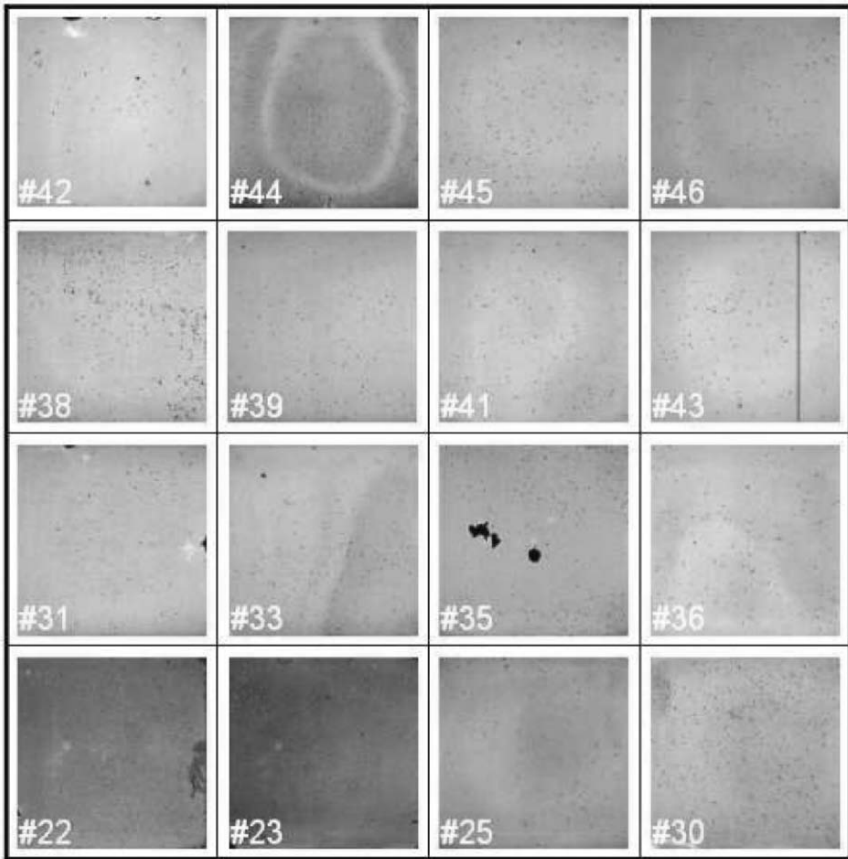
Figure 6. K-band bitmaps of the 16 VIRGO detectors (the numbers identify the modules by the manufacturers serial numbers).

Some of the detectors showed cosmic events throughout the tests. The events are quire irregular: some are tiny blobs, some spread over tens of pixels and few are like comet tails. As these events are not seen in few other detectors, the source of these events is unknown.

Table 1. Performance summary for SCA-45.

Parameter	SCA-45 (72K)	Notes
Quantum Efficiency	92% (J), 101%(H), 95%(K)	Radiometry uncertainty ~12%
Well capacity	140ke$^-$	Measured at 0.7V bias
Dark Generation	0.63e$^-$/s/pix	From operable pixels
Read-noise	15.4e$^-$ (rms)	Temporal noise method
Non-linearity	3.5%	From 10 – 80% full well
Persistence signal	11e$^-$	in a 10s dark after 1min
Pixel Operability	98.54%	

5.   ACKNOWLEDGEMENTS

6.   REFERENCES

[1] Bezawada, N., Ives, D. and Woodhouse, G., 2004, Optical Infrared Detectors for Astronomy, J. D. Garnett, J. W. Beletic (ed.), SPIE Vol. **5499**, p. 23.
[2] Finger, G., Beletic, J., Dorn, R. J., Mayer, M., Mehrgan, L., Moorwood, A. F. M., Stegmeier, J., 2005, these proceedings.
[3] Love, P. J., Hoffman, A. W., Ando, K. J., Corrales, E., Therrien, N. J., Rosbeck, J. P., Ritchie, W. D., Holcombe, R. S., 2005, these proceedings.

THE EFFECTS OF CHARGE PERSISTENCE IN ALADDIN III INSB DETECTORS ON SCIENTIFIC OBSERVATIONS

Randall D. Campbell[1] and David J. Thompson[2]
[1]W.M. Keck Observatory, [2]California Institute of Technology

Abstract: *Charge persistence is defined as the signal that remains on a detector array after the illumination source has been removed. It is characteristic of many types of photo detectors, but is particularly prominent in near-infrared arrays that utilize Indium Antimonide (InSb) as their photosensitive material. Persistence can be a significant issue for scientific observation due to the potential reduction of data quality. We have studied the properties of persistence in an Aladdin III array from Raytheon which is installed in Keck Observatory's adaptive optics camera, NIRC2. In this paper we discuss the types of observations that are at risk from persistence effects. We present data on the characteristics, which include the following results: 1) the level of persistence is more strongly influenced by incident flux than that of fluence (flux × integration time), 2) the persistence is wavelength independent, 3) the persistence level is not reduced by continuous reset-reads of the array or "flushing", 4) the determination that the persistence decay scales with a power law and is proportional to 1/t.*

Key words: *Persistence, charge trapping, image latency, Indium Antimonide, InSb, Aladdin.*

1.   INTRODUCTION

Charge persistence of photo-detectors, sometimes referred to as latency or memory, is defined as the signal that persists on the array after the illumination source has been removed from the field of view [1]. The residual charge decays with time and can result in significant amounts of

unwanted signal in subsequent images. Many types of detectors have this characteristic, but near infrared detectors with indium antimonide, InSb, as their photo-sensitive material are particularly susceptible to this phenomenon. Solomon concluded that the cause of persistence is impurity sites in the passivation layer that can trap holes, which then tunnel back into the InSb layer [2]. In this paper we explore the characteristics of charge persistence, some of its effects on ground based astronomy, and strategies to minimize the difficulties that persistence can present to astronomers.

2.   DIFFICULTIES OF PERSISTENCE

NIRC2 is an imager and spectrometer for Keck II's adaptive optics system that uses an Aladdin-3 array, a 1024×1024 InSb developed by Ratheyon Vision Systems, RVS [3]. NIRC2 is both an imager and a spectrometer, and since there is no slit viewing camera the images of the science target must be used to align the spectrometer slit. The difficulties of persistence in NIRC2 can be significant because the higher fluxes from direct imaging create persistence effects that are a problem for the subsequent spectroscopic integrations. Since persistence is a current source that gradually leaks out, longer spectroscopic integrations are particularly susceptible to this effect. The problem is illustrated in Fig. 1, which is a 1200 second exposure of a crowded field near the galactic center. The image in Fig. 1 contains many features, including horizontal continuum spectra from several stellar sources, emission features from hot gases, residual absorption and emission telluric features from materials in the earth's atmosphere, and artifacts from bad pixels, hot pixels, and cosmic rays. However, the source of the largest signal in this 1200 second integration is charge persistence from the previous image. This is in spite of care taken to protect the array from bright sources which could create the trapped charge. The region of interest on the array where the spectra were scientifically interesting was protected as observers went to extraordinary lengths to keep the array quiet prior to obtaining the spectra. This included observing blank-sky spectra prior to the science field, shuttering the camera when slewing, pre-imaging at very short exposure times with a narrow band filter to not saturate, and using nod patterns that moved the spectra of interest away from regions that are contaminated with persistence. Even with these precautions one can see that data quality can easily be degraded if a careful observing plan is not followed. Persistence is a major problem for imaging spectrographs (like NIRC2), when using the instrument as an imager prior to spectroscopic observations. However, observing bright sources like standard stars or the

high flux background in the thermal infrared will still cause problems for subsequent faint-object spectroscopy in pure spectrographs.
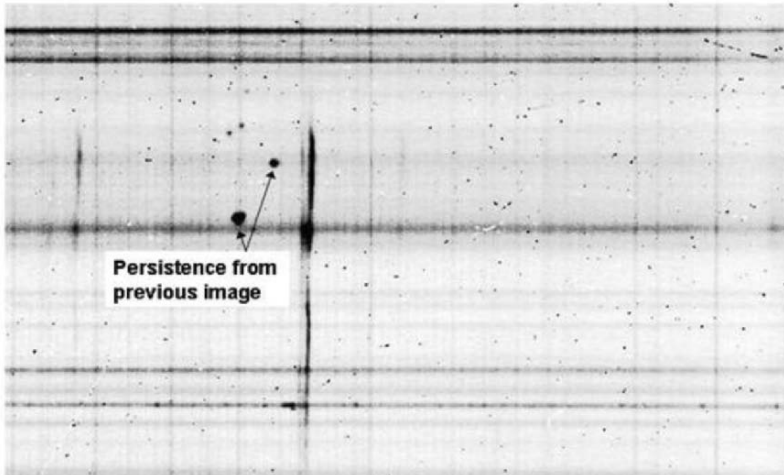
Figure 1. An example of persistence contamination: NIRC2 K-band (2.0-2.5μm) long-slit spectra from a crowded region near the Galactic Center (photo credit A. M. Ghez). The image includes continuum spectra from several point sources and emission features from hot ionized gases. There are persistence features from a previous direct image evident in the array. These features have a strong signal and can easily contaminate the data if not carefully accounted for. These data were acquired with a 1200 second integration. Since charge persistence is effectively a current source, longer integrations used for acquiring spectra are very susceptible to persistence effects.

3.   CHARACTERIZATION OF PERSISTENCE

To help avoid the troubles associated with persistence, we collected experimental data in an effort to better understand the character of this phenomenon. In the case of NIRC2, persistence was analyzed while the instrument was being developed in the Caltech laboratories and additional measurements were conducted after the instrument was delivered to the Keck II telescope. Several experiments were setup to quantify the characteristics, including decay time, various source inputs that can create persistence, and whether or not amelioration techniques would help remove the unwanted signal.

3.1   Decay Time

Persistence is often quantified in terms of the percentage of charge present at period of time after the source is removed. However, since persistence is actually a current source, the percentage measurement is dependent on the integration time of the latency image. Thus all of our measurements are divided by the integration time and quoted in terms of current with a unit of electrons per second. Persistence can be thought of as "virtual dark current" and can be compared to a minimum amount of unwanted current, the lower limit being the amount of true dark current.

We performed several experiments where the detector was exposed to high flux sources of various wavelengths and the amount of persistence signal was measured as function of time after the illuminating source was removed. The amount of trapped charge has an upper limit [4], so increasing the flux beyond a certain point does not increase the persistence effect. We also found that the wavelength of the incoming flux has no measurable effect on the persistence characteristics over the wavelength range tested, which was 1.1 μm to 4.1 μm. This independent wavelength result is consistent with tests on other types of InSb arrays [5]. The decay time measurements are summarized in Tables 1 and 2. The decay time data are plotted in Fig. 2, which includes a fit to the data and the true dark current limit measured after the detector was maintained in a dark environment for greater than 72 hours.

Tables 1 and 2. Decay time measurements for persistence current.

Persistence Current Decay Data Set 1		
Integration Time (sec)	Time from Illumination Removal (sec)	Persistence Current (e⁻s/sec)
100	54	19.680
100	270	2.480
100	486	1.360
100	702	0.920
100	918	0.640
128	2994	0.250
256	3258	0.250
512	3778	0.211
1024	4810	0.160
1024	6874	0.121
1024	7906	0.113

Persistence Current Decay Data Set 2		
Integration Time (sec)	Time from Illumination Removal (sec)	Persistence Current (e⁻s / sec)
1	6	92.000
2	16	38.000
4	28	19.000
8	44	13.000
16	68	9.500
32	108	6.375
64	180	3.938
128	316	2.500
256	580	1.406
512	1100	0.773
1024	2132	0.398
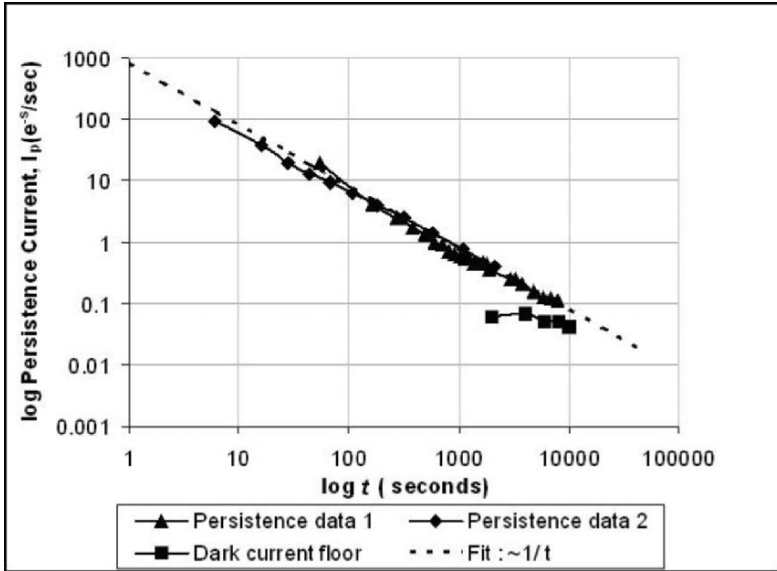
Figure 2. Persistence current, *Ip*, decay rate. Charge persistence leaks into the measured signal of the detector at a rate that is proportional to the time after the illuminating source has been removed. The persistence current appears as a nearly straight line when plotted with log(*t*) vs log(*Ip*). The decay rate of current is proportional to $1/t$. The dark current limit is overlaid on this plot, which was measured after 72 hours of no light on the detector. These data indicate that a waiting period of greater than 10,000 seconds is required to allow the persistence to reach an acceptable level.

3.2 Source Flux and Fluence

Persistence can result in saturation of the array with too long of an exposure time or from high levels of incident flux on the array, independent of integration times. We compared the level persistence from both types of sources in order to determine which of these are more important to avoid. Fluence is defined as flux multiplied by integration time. Figure 3 plots a comparison of the persistence current verses source intensity in units of full-well percentage. The saturation full-well capacity of the Aladdin-3 array is approximately ~25,000 e^{-s}. The data points plotted using the square symbols were a result of keeping the integration time constant while increasing the incident flux. The data plotted with the circle shaped symbols resulted from a relatively low incident flux while letting the detector saturate with increasing integration times. In both plots the persistence was measured immediately after the illumination was removed using an integration time of 10 sec. This comparison shows that incident flux is a more significant factor

in generating latent charge than letting the array saturate from longer integrations. The data presented in Fig. 3 was acquired at 2.20 μm (K-band) and data acquired at 1.25 μm (J-band) was virtually the same. Longer wavelength versions of this test were not performed due to the difficulty of achieving a low incident flux environment at thermal infrared wavelengths.
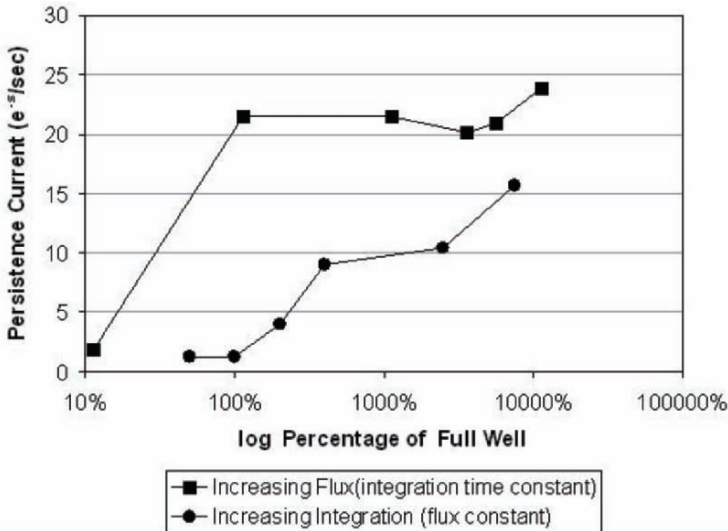
Figure 3.   Comparison of incident flux and fluence (flux×integration time) effects on persistence current. With integration time held constant (1 sec) a light source was adjusted with varying ND filters to increase the flux incident on the array to beyond saturations levels (square symbols). Another test was performed by keeping the flux source constant and increasing integration times to beyond the saturation point (circular symbols). The residual current was measured in each case and plotted above. The plot shows that flux alone is a stronger source of persistence than fluence.

3.3   Removing the Trapped Charge with Continuous Resets

There is anecdotal evidence that with certain types of arrays, the persistence can be removed or the decay time can be improved if the array is flushed, which is defined as series of reset-reads. We tested this technique by comparing decay times with and without flushing applied. After illuminating the array with the identical source, the persistence level was measured every hour, except in one set of data in which the array was reset and readout continuously in the period between samples. Figure 4 plots this comparison and shows that this type of attempt at ameliorating the charge not only failed

but seemed to make things worse, presumably by raising the dark current level through internal heating of the array.
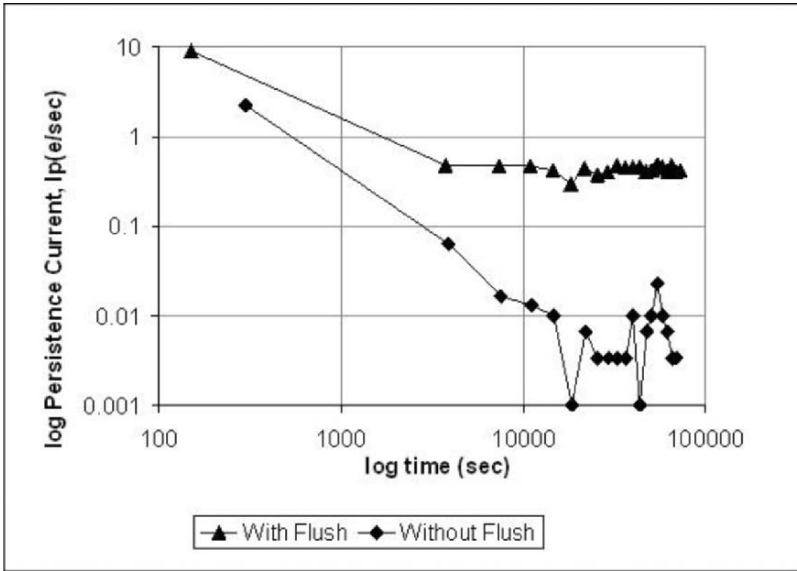
Figure 4. Effects of flushing (continuous reset/reads) on persistence decay. This plot not only indicates that continuous reset-reads fail to improve persistence decay, but actually make things worse. Images were saved each hour with continuous reads occurring between data sets in one series, and no reads or resets in the other. The decay rate was not significantly different between the two but the dark current floor became worse when flushing. This may be due to local heating effects on the detector. The Aladdin-3 was maintained at 29.0 K during these tests.

4.   CONCLUSIONS

Persistence is a significant characteristic of detectors used for astronomy, particularly in infrared hybrid arrays with InSb as the photo-sensitive material. Observing plans must account for this effect in order to keep the area where faint object scientific data will be gathered on the array protected from high flux sources. Saturation levels in this region of the array should also be avoided. Persistence can require up to 3 hours to return to acceptable levels of charge leakage near the normal dark current lower limit. Persistence is a current source and thus longer integrations are more susceptible to the negative consequences of its effects. The persistence current decay time is proportional to t^{-1}. High flux sources are more

significant than high fluence sources and flushing the array with continuous reset-reads is not effective at ameliorating the trapped charge.

5.   REFERENCES

[1] Solomon, S. L., Garnett, J. D., Chen, H,, 1993, Infrared Detectors and Instrumentation, Albert M. Fowler (editor), Proc. SPIE Vol. **1946**, p. 33-45.

[2] Solomon, S. L., 1999, *Charge Trapping in InSb Photodiode Arrays*, Ph.D. Dissertation, University of Rochester, Rochester, N.Y.

[3] Fowler, A. M., Gatley, I., McIntyre, P., Vrba, F. J., Hoffman, A. W., 1996, Infrared Detectors for Remote Sensing: Physics, Materials, and Devices, Longshore, R. E., Baars, J. W., (editors), Proc. SPIE Vol. **2816**, p. 150-160.

[4] Benson, R. G., Forrest, W. J., Pipher, J. L., Glaccum, W. J., Solomon, S. L., 2000, in Infrared Spaceborne Remote Sensing VIII, Strojnik, M., Andresen, B. F., (editors), Proc. SPIE Vol. **4131**, p. 171-184.

[5] Figer, D. F., et al., 2004, Focal Plane Arrays for Space Telescopes, Grycewicz, T. J., McCreight, C. R. (editors), Proc. SPIE, Vol. **5167**, p. 270-301.

Randy Campbell was an intimidating presence as session chairman, and no one ran over their allotted time.

AN ULTRA LOW PHOTON BACKGROUND 1 TO 5 MICRON DETECTOR MOSAIC TEST FACILITY

Reinhold J. Dorn, Siegfried Eschbaumer, Gert Finger, Jean-Paul Kirchbauer, Leander Mehrgan, Manfred Meyer, Armin Silber and Joerg Stegmeier
European Southern Observatory

Abstract: *This paper presents the design of a new ultra low background detector mosaic test facility for IR detectors with cutoff wavelengths up to 5.3 µm and operating temperatures down to 20 Kelvin. In instruments with high spectral resolution such as ESO CRIRES, dark current and readout noise of the detector system is often the limiting performance factor. This test facility allows us to develop, optimize, test and assess the functionality and performance of IR detector mosaics for low flux applications prior to the integration in the instrument. Therefore detector tests must be performed under extremely low photon backgrounds of << 0.1 photons/sec/pixels. No cryostat window is used and the blackbody is contained inside the hermetically sealed radiation tight cold structure.*

Key words: *IR Detectors, FPA, mosaics, detector testing, low background.*

1. INTRODUCTION

Many contemporary and pending infrared instruments at ESO use large IR mosaics in their focal planes. Usually these detectors cannot be properly tested within the instrument due to time restraints and the testing of other instrument components. To enable the testing of large detector mosaics for future ESO IR instruments, the IR detector group developed a new ultra low background mosaic test facility. Almost all performance parameters and calibration measurements as well as optimization procedures can be carried

out with fast cooldown capability and easy handling of the detectors. Key issues are:

- Functionality and cryogenic performance of the detector system
- Optimization of feedtroughs and radiation shielding
- Darkcurrent and readnoise for very low flux applications
- Development of new readout modes
- Optimization of readout parameters to get maximum signal to noise ratio
- Cosmetic quality, uniformity and electroluminescence
- Quantum efficiency in J, H, K, L and M
- Analog bandwidth of the video output
- Photon transfer curve and calibration

2.   CRYOGENICS REQUIREMENTS

In order to maintain simplicity, no image quality tests are performed and therefore no optics are installed on the instrument. However it is possible to put a pinhole grid mask in front of the detector mosaic to illuminate selected areas on the detector for crosstalk tests. Extremely low background radiation was the major goal of the facility and instead of a window, a cryogenic blackbody has been implemented. To determine the cryogenic requirements, the thermal flux seen by the detector from 2π steradian was calculated as a function of instrument temperature for detectors with a cutoff wavelength of 5.3 microns. To obtain a photon flux <0.1 electrons/sec/pixel assuming a pixel size of 27 micron, the warmest part of the testfacility needed to be less than 77 Kelvin. Figure 1 shows this curve for the CRIRES Aladdin mosaic [1].
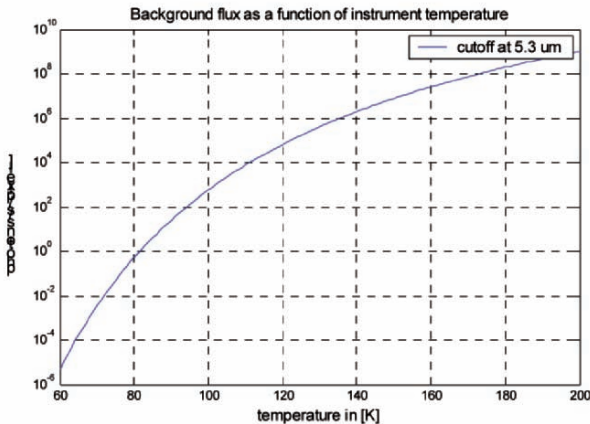
Figure 1. Background flux from 2π steradian as a function of instrument temperature.

The thermal flux observed by the detector from the cryogenic blackbody can also be calculated with Planks law of photon emittance by including the geometric properties and the detector mosaic to be tested. Figure 2 shows the flux in electrons/sec/pixels in the case of the CRIRES mosaic. To calculate flux for QE measurements the filtercuves must be included.
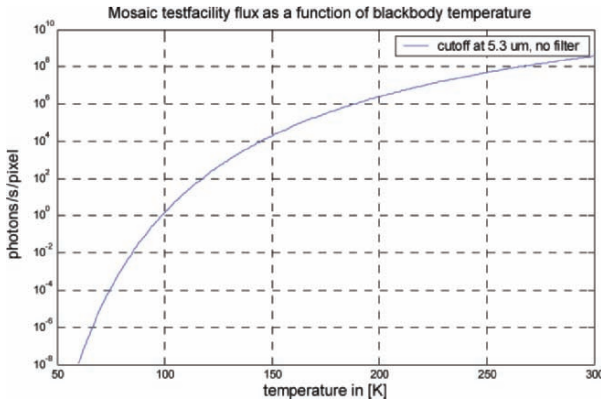
Figure 2. Flux seen by the detectors as a function of blackbody temperature.

3. DESIGN OF THE TEST FACILITY
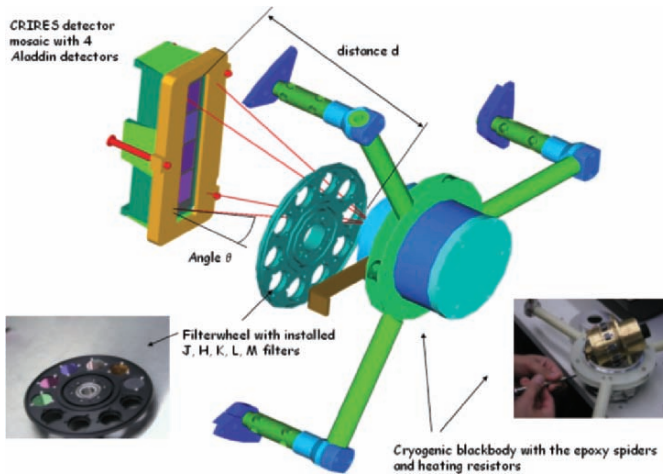
Figure 3. 3-D model of the test facility design.

A 3-D model of the CRIRES facility is shown in Fig. 3. The blackbody is supported by epoxy spiders at a distance of 20 cm from the focal plane with an aperture of 20 mm. A filter wheel hosting 1 inch filters which are heat sinked to 60 Kelvin is mounted in front of the blackbody. The blackbody temperature can be changed from 80 to 380 Kelvin without changing the temperature of the focal plane by more than 10 mK. A background level of <0.2 electrons/sec/pixel was obtained with the Aladdin mosaic. A picture of the testfacility is shown in Fig. 4.

Inner cold structure of the testfacility

View from the top with the detector mosaic facing down looking inside the structure. The cryogenic preamplifiers and the cold braid connection are shown.

Picture of the Leybold closed cycle cooler attached to the backside of the testunit
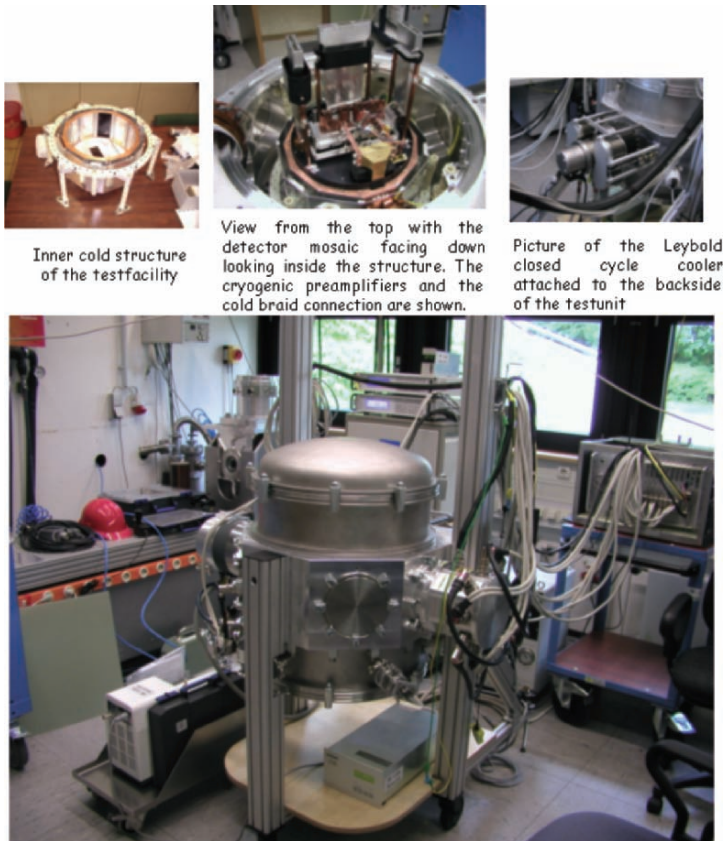
Figure 4. Moasic test facility in the ESO infrared laboratory. The blackbody and detectors are temperature controlled by two Lakeshore 340 controllers. The closed cycle cooler is mounted on the backside. On the right the cable connectors and the 128-channel IRACE controller can be seen. On the left the pre-vacuum and the turbo vacuum pump are shown (turbomolecular pump directly attached to the vessel).

3.1 Illumination distribution

As there are no optics within the cryostat, the angle θ (maximum 18 degrees in the case of CRIRES) defines the intensity of illumination across the detector array. The illumination for off axis points on the detector mosaic falls off. For Ω as the solid angle on axis, the solid angle off the axis at an angle of θ will be $\Omega \cos^3\theta$. Since the illumination falls obliquely at an angle of θ, there is a further factor of cos θ. Therefore the off axis illumination falls by $\cos^4\theta$. Figure 5 shows a diagram used for the correction of the CRIRES mosaic together with an image of the four detectors masked by the pinhole grid mask. Hence it is possible to calculate the exact flux on the detectors to obtain the quantum efficiency.
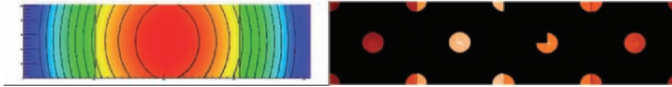
Figure 5. Illumination distribution and map of efficiency for the CRIRES mosaic.

4. THE CRIRES AND HAWK-I MOSAICS

The first application of the test facility was the CRIRES 512×4096 pixel Aladdin InSb focal plane array mosaic mounted on the newly developed 3-side buttable package shown in Fig. 6 (left). The second application is the Hawk-I detector mosaic [2] with four 2K×2K Rockwell HgCdTe MBE buttable arrays with 2.5µm cut-off. GL Scientific provided the packaging and mount as seen in Fig. 6 (right).
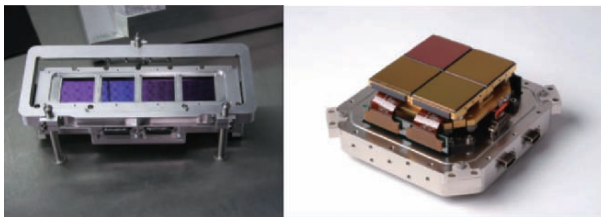
Figure 6. (*left*) The CRIRES and (*right*) HAWK-I detector mosaics.

5.   EXAMPLES OF RESULTS

Some results obtained with the CRIRES detectors are shown in Fig. 7. Figure 7 (left) is a photon transfer curve and (right) is the relative efficiency of the four Aladdin detectors tested. For further information see [3].
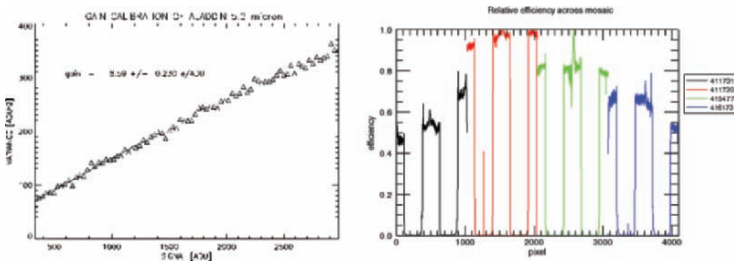
Figure 7. Gain calibration curve for an Aladdin array and comparison of efficiency corrected for $\cos^4$ dependence of illumination.

6.   CONCLUSIONS

The new ESO IR detector mosaic test facility allows us to develop, optimize, test and assess functionality and performance very efficiently. It also shows that many detector parameters can be evaluated without a cryostat window, which aids in the achievement of ultra-low background flux levels.

7.   REFERENCES

[1] Dorn, R. J. et al., 2004, *The CRIRES InSb megapixel focal plane array detector mosaic*, Proceedings of the SPIE's International Symposium on Astronomical Telescopes and Instrumentation.
[2] Pirard, J., et al., 2004, *HAWK-I: A new "wide field" 1-2.5 μm imager for the VLT*, Proceedings of the SPIE's International Symposium on Astronomical Telescopes and Instrumentation.
[3] Finger, G., et al., 2005, *Conversion gain and interpixel capacitance of CMOS hybrid focal plane arrays*, these proceedings.

ON SKY EXPERIENCE WITH THE HAWAII-I DETECTOR AT THE CAMERA/SPECTROGRAPH LIRIS

José A. Acosta-Pulido, Rafael Barrena Delgado, Cristina Ramos Almeida, Arturo Manchado-Torres
Instituto de Astrofísica de Canarias

Abstract: *We report about the relevant parameters of the LIRIS HAWAII-I detector such as linearity range, gain, readout noise and about peculiarities detected in the different observing modes. We also discuss the effects of operating the detector at different temperatures.*

Key words: *HAWAII-I, near infrared, reset anomaly.*

1.   INTRODUCTION

1.1   The Instrument

LIRIS is a near-infrared imager and spectrograph built by the Instituto de Astrofísica de Canarias [1]. It is operated as a common user instrument (see Fig. 1) on the 4.2 m William Herschel Telescope at the Observatorio del Roque de Los Muchachos (ORM-La Palma) since August 2004. The detector is a HAWAII-I array operating at 70 K. Currently, LIRIS includes imaging and spectroscopic observing modes. Spectroscopy is performed with long-slit and a number (~8) of multi-object masks. Grisms are used as dispersion elements providing a resolution of 650. In the future it will also include R~3000.

Figure 1. LIRIS attached to the Cassegrain platform at the 4.2 m William Herschel Telescope.

1.2   Main Characteristics of the Detector

The detector is controlled by an SDSU controller unit with 4 parallel outputs. The operating temperature is 71K. The measured gain is 5 e⁻/ADU. The linearity range is up to 60000 e⁻ for deviation below 1%, and full well depth is 150000 e⁻. The available readout modes are Multiple Non-Destructive Readouts (MNDR). For imaging purposes a double correlated mode is used, whereas for spectroscopy the use of MNDR is recommended. The detector can also be read using 4 non-overlapping windows.

2.   DETECTOR COSMETICS

The scientific grade detector of LIRIS has relatively good cosmetics. The most noticeable detector flaws are (see Fig. 2):

- A shallow, fan-like feature in the lower right quadrant, detectable at low signal levels. It is not a flat-field effect but is washed out after sky subtraction.
- A bright spot (lower left quad.) plus two small scratches (outer edge of the upper left quad). They should be masked in the data reduction.
- A number of extended darker spots in the two left quadrants. This is a pure flat-field effect and is easily corrected.
- A picture frame effect, which appears as a border frame of ~15 pixels width showing an enhanced response relative to the mean illumination.
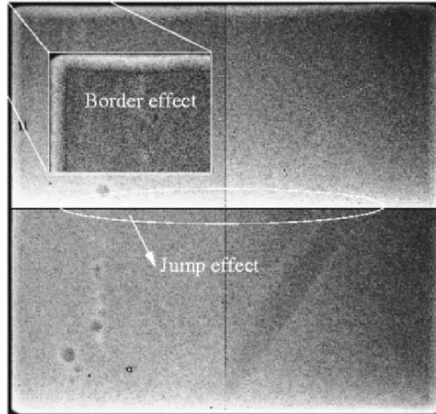
Figure 2. A flat-field image in which several detector flaws can be noticed.

3.   THE JUMP EFFECT OR THE RESET ANOMALY

Most of LIRIS images present a vertical gradient across the quadrants, which produce an abrupt jump at their intersection. This effect has been described as a consequence of the reset anomaly by Finger, et al [2]. This effect introduces some difficulties in the correction of flat-field in imaging mode, and also when performing spectroscopy of extended objects. The value of the signal jump varies with the exposure time and with the flux level. In some cases it can reach 10-20% value of the average signal. In addition the signal jump changes from the first one to the following ones, becoming more pronounced when taking consecutive exposures to perform signal co-addition (see Fig 3). Some techniques have been introduced in other instruments to alleviate the effects [3].

4.   THE DENSITY OF HOT PIXELS

Hot pixels appear as bright spots on the detector and are easily identified in dark exposures. It has been noticed that their number increases with the exposure time (see Fig. 4). For the most common values used in imaging mode the density of hot pixels remains ~0.1%. It begins to increase rapidly for exposures times longer than 40s, reaching values of ~0.5% at 600s.
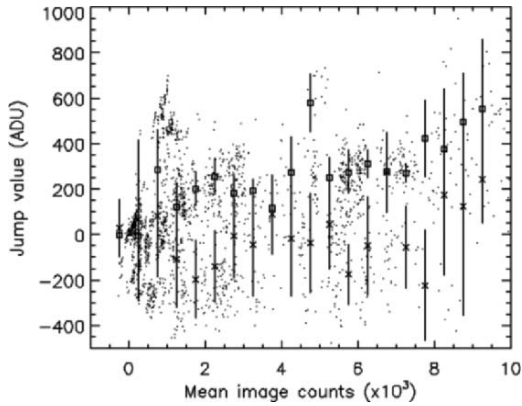
Figure 3. The signal jump across quadrants as a function of the mean signal value.
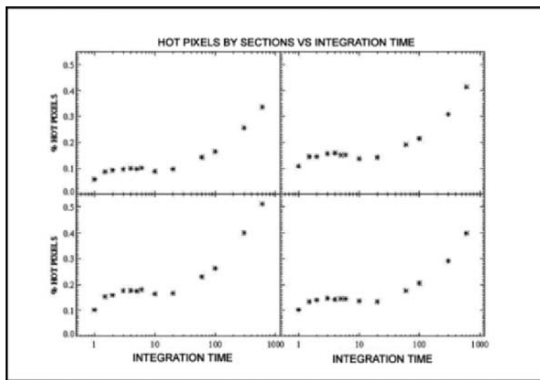
Figure 4. Density of hot pixels as function of exposure time. Each panel represents a detector quadrant, which behave similarly to each other.

5.   DARK SIGNAL AND READOUT NOISE

The readout noise measured in double correlated mode shows a variation between 9 and 16 e⁻ depending on the observing period. The reasons for such variations are under investigation. With usual exposures times the detector always operates in the background limited case for imaging mode.

The variation of the dark signal as a function of exposure time seems to reflect two different regimes. Below 20 s dark measurements likely reflect readout effects related to the reset anomaly [2]. The true dark current

becomes evident only for exposures times beyond 30-40s, in such case the dark current is ~0.03 e⁻/s.

6. THE QUANTUM EFFICIENCY AS A FUNCTION OF THE DETECTOR TEMPERATURE

We have studied the variation of detector characteristics as a function of temperature. Constant illumination was guaranteed by the use of a blackbody source. Detector temperature was controlled using a Lakeshore 340 ($\Delta T < 0.01K$) in the range 65-80 K. We found that the QE increases differently with temperature depending on the wavelength. Thus for wavelengths of ~1 μm QE increases up to 30% from 65K to 80K, whereas at wavelengths around 2.2 μm the increment is only of 15%. However, an unwanted effect at 80K is a very large number of hot pixels. We adopted a temperature of 70K to avoid this effect.

7. PERSISTENCY OR NON EFFICIENT RESET

Often during observations of faint sources a bright source appears in the field of view. In these cases and when the dithern pattern is performed, a trace marking the movement of the bright source becomes evident. However the data acquisition system guarantees that the telescope is not moving when the exposure begins. This behavior results from the fact that the detector is continuously receiving sky light (there is no shutter) while the telescope is slewing, despite it is being reset. Thus the detector reset does not efficiently remove accumulated charges. Further investigation revealed that the only efficient way to eliminate the effect was to introduce a set of clean reads before beginning the exposure. The number of wasted reads should be approximately three or more to keep the memory of a previous bright source below 1%.

8. FRINGING

A fringing pattern becomes evident when observing with a narrow pass-band filter centered on 2.16 μm (see Fig. 5). It also appears at low levels in K band observations. This pattern is usually removed after sky subtraction.
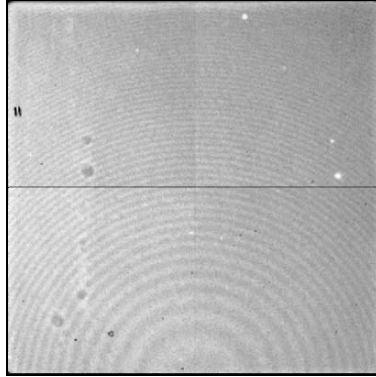
Figure 5. An image taken through the narrow band filter centered on Brα (2.12 µm).

9.   REFERENCES

[1]   Manchado, et al., 2004, *Ground-based Instrumentation for Astronomy*, Moorwood, A.F.M., and Masanori, I., (Eds.), Proceedings of the SPIE, Vol. **5492,** p. 1094.

[2]   Finger, G., Mehrgan H., Meyer M., Morwood A.F., Nicolini G., and Stegmeier J., 2000, *Optical and IR Telescope Instrumentation and Detectors*, Iye, M., and Moorwood, A.F.M., (Eds.), Proc SPIE Vol. **4008**, p. 1280.

[3]   Riopel, M., Doyon R., Nadeau, D., and Marois C., 2004, Scientific Detectors for Astronomy, The Beginning of a New Era, Amico, P., Beletic, J. W., Beletic, J. E., (Eds.), Kluwer Academic Publishers, p. 453.

The hotel garden was a lovely site for the Wednesday evening reception.

EMIR DETECTOR CHARACTERIZATION

José Javier Díaz[1], Fernando Gago[1], Carlos González-Fernández[1], Francis Beigbeder[2], Francisco Garzón[1,3], Jesús Patrón[1]
[1]Instituto de Astrofísica de Canarias (IAC), [2]Observatoire Midi-Pyrénées (OMP), [3]France Departamento de Astrofísica, Universidad de La Laguna

Abstract: *EMIR is a multiobject intermediate resolution near infrared (1.0-2.5 microns) spectrograph with image capabilities to be mounted on the 10 m Gran Telescopio Canarias (GTC), located on the Spanish island of La Palma. The instrument uses a HAWAII-2 infrared detector. In this paper, results of the detector characterization are presented. Apart from tests to obtain the typical figures of merit, such as readout noise, well depth, dark current, quantum efficiency or maximum pixel rate, some detailed studies have been performed to characterize the detector persistence, crosstalk between channels and the disturbing effects that appear in these detectors just after reset or after a certain time without being read. These effects and the techniques we have tried to minimize them are also presented*

Key words: *Detector characterization, HAWAII-2.*

1.   HARDWARE CONFIGURATION

Detector characterization was performed using 4-channel architecture. To reduce noise in the signal chain amplification, cryogenic circuitry was introduced at an early stage. A Leach controller and an acquisition and data handling system based on a PC were used (see Fig. 1).
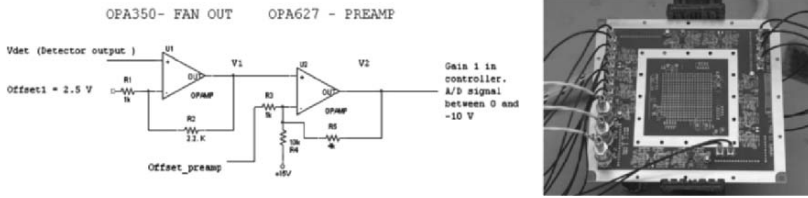
Figure 1. Hardware configuration.

2. DARK CURRENT AND NOISE MEASUREMENTS

To obtain dark current and noise data, an image sequence was performed following this scheme:

- 10 consecutive reset cycles of the whole detector
- Acquisition of 6 consecutive images
- Wait for 10 minutes
- Acquisition of 6 consecutive images
- Repeat wait & acquisition multiple times
- The data was processed and the results indicate that the mean dark current for the whole detector is around 0.12 e$^-$/sec.

A remarkable effect was noticed. The initial pixels show a transient response after long periods of integration with output amplifier inactivity. Figure 2 shows the result of subtracting two consecutive frames obtained immediately after a long period of inactivity with the detector in dark conditions. This effect has been identified as a characteristic variation of the amplifier during temperature stabilization. The tests show that this phenomenon is observable after 20 seconds of detector inactivity. Once the thermal transient of the outputs of the detector has finished, a much more stable output is appreciated.
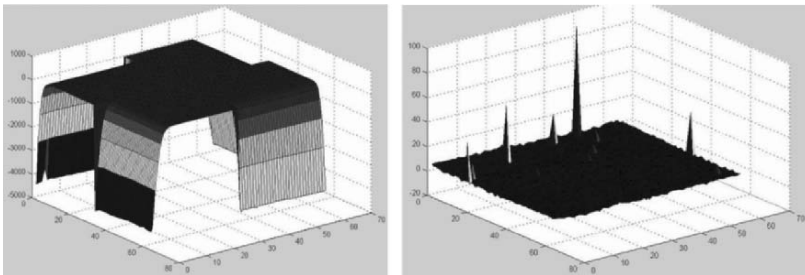
Figure 2. Transient effect due to thermal stabilization in the detector output stage.

The reset value depends on the previous saturation state of the detector. This is the case illustrated Fig. 3, showing the result of a persistency effect especially remarkable in one of the corners of the graph.
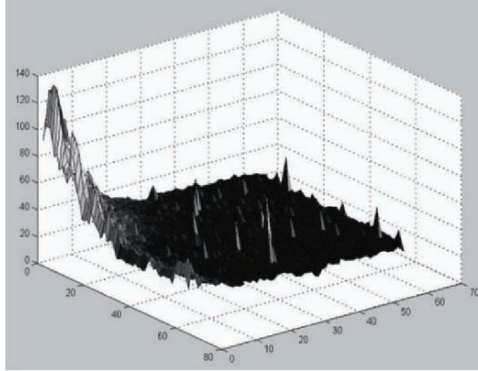
Figure 3. Persistency effect due to previous saturation.

A variation of the dark current versus time has been observed. Figure 4 illustrates the evolution of the dark current versus time. Different profiles correspond to different values of signal. The higher the charge before the reset, especially if the detector enters the saturation regime, the higher the initial dark current.
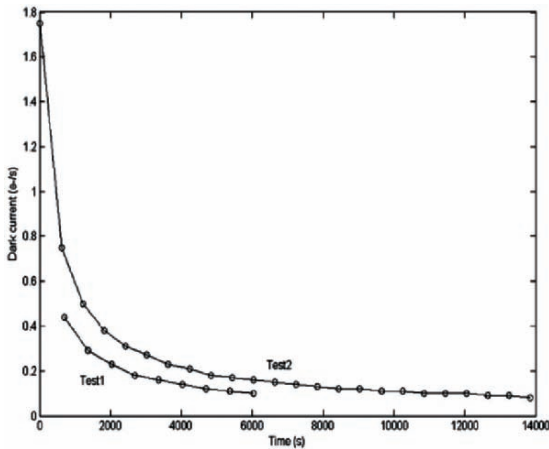
Figure 4. Dark current variation vs. time.

The dark files have been used to compute the detector noise. The mean readout noise value is 11 electrons.

3.   SYSTEM GAIN

The system gain (e⁻/ADU) was computed independently in 4 sections corresponding to different quadrants (see Table 1, Fig. 5). As the electronic chain is identical for every channel the result is used to search for unbalanced gain in different areas of the detector.

Table 1. Detector gain computed for each channel independently.

Quadrant 1	2.35 e⁻/ADU
Quadrant 2	2.33 e⁻/ADU
Quadrant 3	2.43 e⁻/ADU
Quadrant 4	2.44 e⁻/ADU
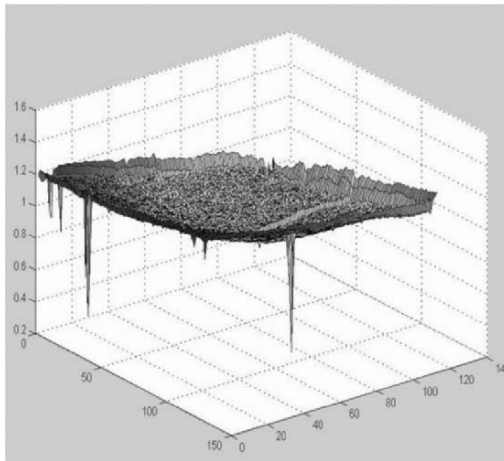
Figure 5. 3-D representation of normalized system gain.

4.   RELATIVE QE MEASUREMENTS

The detector was illuminated with a blackbody. The flux received on the detector for several filters has been measured and compared with the theoretical flux to calculate the relative quantum efficiencies at different wavelengths. The test is performed at 2 different temperatures (800ºC and 980 ºC) to validate the results (see Table 2).

Table 2. Relative QE measurements.

Paschen Beta/H2	0.63
H/H2	0.94

5. DETECTOR COSMETICS

Pixels have been grouped in different categories according to their response to illumination. Table 3 shows the criteria and the number of pixels in each category and Fig. 6 shows the detector defects.

Table 3. Detector cosmetics.

	Quadrant #1	Quadrant #2	Quadrant #3	Quadrant #4
(μ - 4σ)	18272	16417	19134	16536
(μ + 4σ)	45858	36660	50181	43358
Cold pixels	524 (0.05%)	633 (0.06%)	291 (0.03%)	225 (0.02%)
Hot pixels	0	57 (0.005%)	0	11 (0.001%)
Dead_0_0	483 (0.05%)	65 (0.006%)	527 (0.05%)	122 (0.01%)
Dead_65535_65535	161 (0.02%)	435 (0.04%)	0	0
Other_dead	6 (0.0006%)	14 (0.001%)	0	2 (0.0002%)
Total bad pixels	1174 (0.11%)	1204 (0.11%)	818 (0.08%)	360 (0.03%)
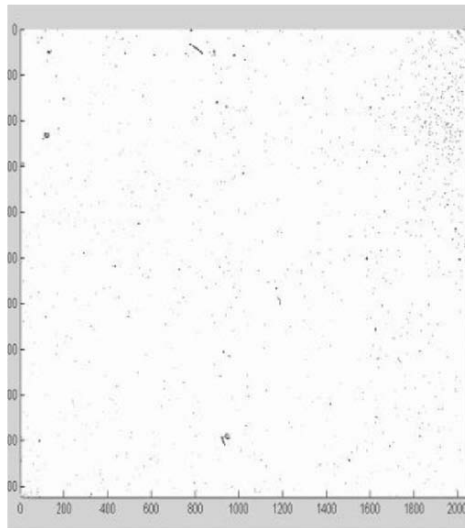
Figure 6. Detector defects.

6. WELL DEPTH AND WELL CAPACITY

The detector was illuminated with a stable black body uniformly over its surface. The contribution in the linear regime was obtained using a 2% and 5% linearity criteria. The full well was also computed and the total charge

while considering the signal saturation zone. The results are summarized in the Table 4.

Table 4. Well depth and full well capacity.

	Linearity 2% considering 1st pixel in ramp	Linearity 2% not considering 1st pixel in ramp	Linearity 5% considering 1st pixel in ramp	Linearity 5% not considering 1st pixel in ramp	Full well
Quadrant 1	115000	121500	121500	121500	127500
Quadrant 2	115000	119000	119000	119000	127500
Quadrant 3	117667	127000	127000	127000	133500
Quadrant 4	115000	124000	124000	124000	131750

7.   PERSISTENCY

To perform persistency tests the detector is initially saturated. It is exposed to laboratory radiation for 1 minute with no filter placed and then is covered with a cool blank before proceeding to acquire data.

The conclusion is that it is necessary to repeat the reset cycle to remove the effect produced by initial saturation. Also, a dark current increase is associated to the previous saturation of the detector (see Fig. 7).
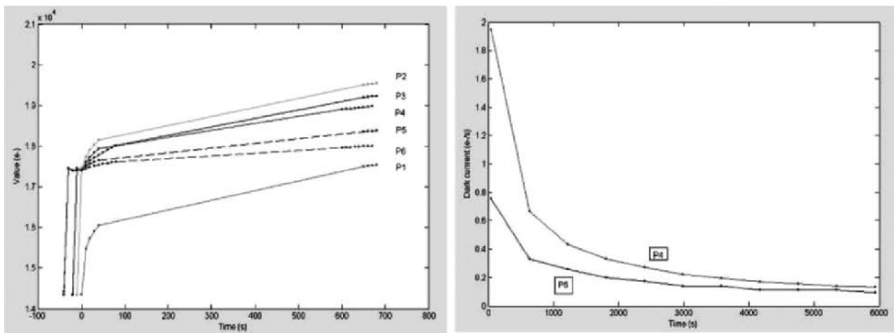
Figure 7. Persistency, dark current increase vs. saturation.

INTRA-PIXEL RESPONSE OF A HAWAII-1RG MULTIPLEXER

Tim Hardy, Marc R. Baril, and James S. Stilburn
National Research Council, Herzberg Institute of Astrophysics

Abstract: *The Fine Guidance Sensor (FGS) is an infrared guide camera for the James Webb Space Telescope. The current design specifies 5 μm cutoff HAWAII-2RG detectors for the focal plane array. The FGS optics will produce a slightly under-sampled point spread function of the guide stars. Thus, we plan to investigate the response of a HAWAII-1RG at sub-pixel resolution to determine whether variations on this scale would affect the guiding accuracy of the camera. Using a simple experimental setup we were able to obtain measurements of a H1RG multiplexer with a resolution of ~4 μm.*

Key words: *Intra-pixel response, HAWAII-1RG, Fine Guidance Sensor (FGS).*

1. INTRODUCTION

The Fine Guidance Sensor (FGS) camera will provide fine pointing data to the James Webb Space Telescope (JWST) [1]. The optical design of the FGS was driven by the need for a large field of view to ensure availability of guide stars, balanced by the need for sufficient resolution to provide the required guiding precision. The result is a camera with a slightly under-sampled point spread function and a concern that guiding performance may be adversely affected by sub-pixel scale variations in the response of the detectors. The HAWAII-2RG infrared detector arrays have been selected for the baseline design of the FGS. However there are some characteristics of these devices that are not well known, including the uniformity of the response at scales smaller than a pixel.

We have designed an experiment to provide more information on the response of these detectors at these scales. Due to long delays in obtaining test devices, by the time of writing this paper we have only obtained results for a bare multiplexer. These results are described in the following sections.

The multiplexer, or ROIC, is the silicon integrated circuit that routes the electrical signals from the array of infrared photodiodes in the detector layer to the output amplifiers of the device. The silicon responds to visible light and therefore an un-hybridized multiplexer can be used for basic imaging. We exploited this fact in our experimental setup.

The detector we tested is a HAWAII-1RG multiplexer from a technology development program for JWST [2]. The 1024×1024 array has 18 µm square pixels. The manufacturer (Rockwell Scientific) cautioned that it was not representative of the quality of their production devices.

2.   EXPERIMENTAL SETUP

A schematic diagram of the experimental setup is shown in Fig. 1.
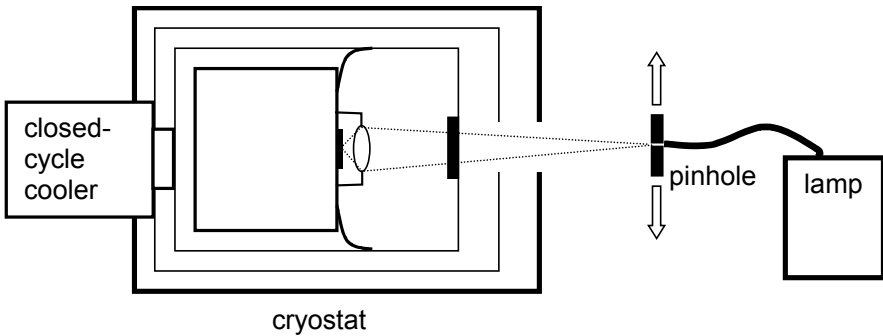
Figure 1. Experimental setup.

The source is a pinhole illuminated by a regulated lamp through an optical fibre bundle. Narrow-band filters could be added to verify wavelength dependence. There is a PK50 IR cut filter (cutoff at 2.5 µm) mounted in the face plate of the inner radiation shield to reduce the background. Mounted 4 mm in front of the detector is a small plano-convex lens (6.1 mm focal length, 2.2 mm aperture). Initial tests with a 160 µm pinhole at a distance of ~180 mm from the lens and white light show what appears to be reasonable sub-pixel resolution (~4µm).

The pinhole is mounted on a two-axis motorized micrometer stage. The actuators have an accuracy of 0.1 μm, which is more than adequate given the demagnification of the optics.

3.   PROCEDURE

A software program was written that will automatically obtain a series of small (10×10 pixel) images while stepping the pinhole image across the array by moving the source. We used a step size corresponding to 0.1 pixel and scanned the pinhole image over a 3×3 pixel region of the detector, for a total of 30×30 (=900) images. The resulting images then were combined into a pixel response map. To create the response map one pixel is chosen, and its value in each image is plotted versus the position of the source for that image. The plot gives the relative response of the pixel as a function of sub-pixel position.

4.   RESULTS

The pixel map from our initial tests with the multiplexer at room temperature is shown in Fig. 2. A grid showing the assumed pixel boundaries has been overlaid on the map. Although we know the scale of the pixel grid, we have no way of determining the actual position of the boundaries, so we have made an estimate based on the assumption that the highest response will be within the pixel. For our purposes, the offset from the actual boundaries is not important because we are interested in relative motions. The map shown in Fig. 2 has been expanded to a 5×5 pixel region by concatenating the response maps from adjacent pixels. This is why there is a small discontinuity visible in the fifth column.

The bare multiplexer, unsurprisingly, shows a fair amount of structure in its response. This is presumably due to the transistors which consume parts of the pixel area and reduce the fill factor. There is also a large amount of cross-talk between adjacent pixels, especially from the pixel directly below in the map. Initially we saw a greater degree of cross-talk along the rows in the direction of the readout scan. We suspected that this was electrical cross-talk due to the finite bandwidth of the detector output amplifier. By reducing the readout rate to the recommended 100 kHz, this extra cross-talk was eliminated.

5.   CONCLUSION

These results give us confidence that our experimental setup works. Beginning with the multiplexer was advantageous because the visible structure in the pixel response gave clear indications that the resolution of our system was significantly finer than a single pixel. Unfortunately, when we cooled the system to perform measurements at the FGS operating temperature (40K), the device failed. It appears that thermal stress caused the multiplexer to fracture. We plan to repeat our measurements (without the failure!) on a hybridized HAWAII-1RG with a 5 μm cutoff HgCdTe detector layer.
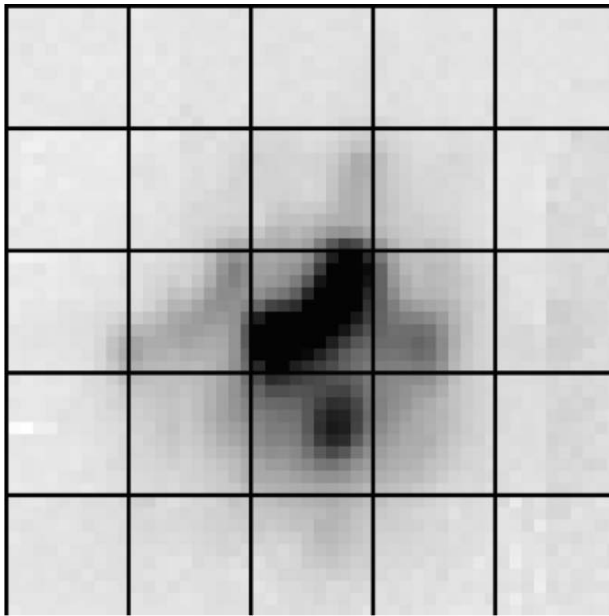
Figure 2. Bare multiplexer response map.

6.   REFERENCES

[1] Rowlands, N. et al., 2004, *Proceedings of SPIE,* Vol. **5487**, pp. 664-675.
[2] Garnett, J.D. et al., 2004, *Scientific Detectors for Astronomy*, Amico, P., Beletic, J.W., and Beletic, J.E. (eds.), Kluwer Academic Publishers, Dordrecht, The Netherlands, p. 59.

FAST CONVERSION FACTOR (GAIN) MEASUREMENT OF A CCD USING IMAGES WITH VERTICAL GRADIENT

Fabrice Christen[1], Konrad Kuijken[1,2], Dietrich Baade[3], Cyril Cavadore[4], Sebastian Deiries[3], Olaf Iwert[3]

[1]*Kapteyn Astronomical Institute,* [2]*Sterrewacht Leiden,* [3]*European Southern Observatory,* [4]*Thales*

Abstract: *This paper describes a fast technique for estimating the conversion factor of a CCD. It is based on the adjustment of the standard photon transfer curve technique to 2 TDI (Time Delay Integration) images. The data used to test the procedure are recorded with the ESO test bench, in the context of characterizing the OmegaCAM CCDs. No modifications of the test bench are needed to use this technique. For five CCDs, results from the standard photon transfer method (also called variance method) and with the technique developed in this paper were compared. Results are compliant. This technique proved reliable even if it is still under development with possible future improvements. It can be used for simple and efficient gain measurements of CCDs.*

Key words: *CCD characterization, conversion factor, gain*

1. INTRODUCTION

During tests of the OmegaCAM[1] CCDs [1], TDI images have been acquired using the ESO test bench [2] to check the linearity of the chips. This paper will describe how to use these data to measure the conversion factor. This parameter reported in electrons per analog digital unit (ADU),

---

[1] OmegaCAM is a one square degree wide field imager which will be mounted on the VST telescope in Paranal, Chile [3,4].

relates the pixel value to the number of electrons and will be extracted from the photon transfer curve derived from two TDI images.

After a description of the procedure in Section 2, the first results will be presented in Section 3. Conclusions are reported in Section 4.

2.   PHOTON TRANSFER CURVE FROM TWO TDI IMAGES

This section will describe how TDI images[2] can be used to measure conversion factor. To acquire two TDI images, the test bench is set at the setting used to record flats. There is one particular condition; the test bench must be able to open the shutter during the reading of the CCD. The monochromators are set to a wavelength of 630 nm and 10 nm bandwidth. In this condition, the photon response nonuniformities of 44-82 e2v CCDs are negligible (~1%). Most of the noise is photon noise. Equally important, the illumination of the CCD has to be homogeneous all across the surface (the ESO test bench achieved this criteria. it produces a flat illumination with fluctuations which are less than 1%). Under these conditions, it is not necessary to flat field out the TDI images. Otherwise, the method described in this paper is still usable, but it would involve more computation process stages.

The principle and the mathematical tools are the same as in the standard photon transfer curve technique [5]. The variance in Analog Digital Units is related to the signal (ADU) by the following linear equation,
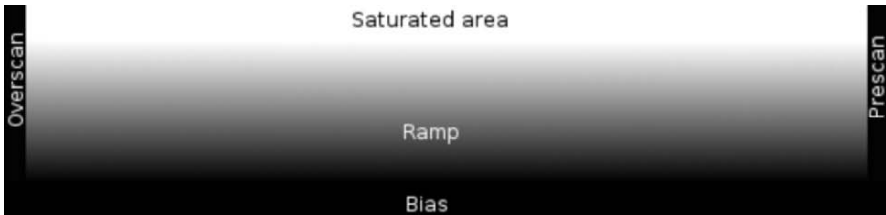
Figure 1.   Example of a TDI image recorded using the ESO test bench. Here is a 2148×512 pixel image. A legend has been added. The area where the ramp shows up is also called in this paper "sensitive area".

---

[2]   A TDI acquisition consists in collecting light and continuously reading out the detector one row of pixels at a time from the bottom (where the output register is located) of a detector chip. Under constant illumination, this reading out mode will create an image (see Fig. 1) with the required response.
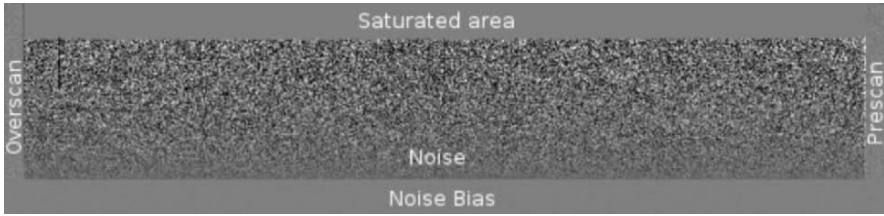
Figure 2. Example of noise pattern after the subtraction of two TDI images.

Digital Units is related to the signal (ADU) by the following linear equation,

$$\sigma_a^2 = \frac{1}{g}\overline{S_a} + \frac{1}{g^2}\sigma_{ron}^2 \tag{1}$$

g : Conversion factor (e⁻/ADU)
$\overline{S_a}$: Average pixel value (ADU)
σ_a : Total rms noise (ADU)
σ_{ron} : read out rms noise (e⁻)

The variance of the signal will be plotted versus the mean signal. To extract these parameters the following manipulations must be carried out.

To measure the mean signal, the two TDI images are averaged. In the sensitive area, the mean of each row, $\overline{S_a}$, is measured and the bias subtracted.

To measure the variance one TDI image is subtracted from the other (see Fig. 2). For each row of the sensitive area, the variance, σ^2, is measured ($\sigma_a^2 = \sigma^2/2$. The variance is divided by two to obtain the variance of the line in a single frame).

The plot of the $\left(\overline{S_a}, \sigma_a^2\right)$ pairs will provide the photon transfer curve and the linear fit of this plot, the slope which is the inverse of the conversion factor.

3. RESULTS

To test the gain measurement with two TDI images, sets of data from five CCDs are used. Based on the procedure developed above, the photon transfer curve for each CCD is plotted (see for example Fig. 3) and the conversion factor calculated. The results are in Table I. The gain measured with one (see Appendix B in this paper) and two TDI images are in accordance with the variance method (see Appendix A in this paper) used in

the OmegaCAM test procedure. The maximum difference in this set is 1.5%. These results are very promising.
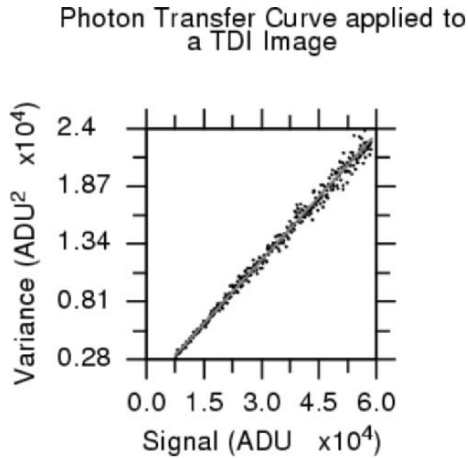
Figure 3. Example of a photon transfer curve realized with two TDI images.

The variance method used to measure the gain in the OmegaCAM procedure has been compared to the measurements of the gain made with the ^{55}Fe method. The results show that both techniques are in accordance. Further confidence to the method is related to non linearity. When this defect is observed in the standard photon curve, the photon curve from TDI images shows the defect too.

Table 1. Gain measured for five CCDs with three different methods.

CCD serial number	Gain (e^-/ADU) obtained from		
	One TDI Image	Two TDI Images	Variance method
02263-07-02	2.60 ± 0.01	2.58 ± 0.01	2.59 ± 0.02
02111-01-02	2.51 ± 0.01	2.50 ± 0.01	2.52 ± 0.02
00152-01-02	2.64 ± 0.01	2.62 ± 0.01	2.58 ± 0.01
02111-05-02	2.50 ± 0.01	2.50 ± 0.01	2.51 ± 0.01
02111-13-01	2.62 ± 0.01	2.60 ± 0.01	2.62 ± 0.01

In column one are the serial number of the CCDs. In column two is the gain measured with one TDI image. In column three is the gain from two TDI images and in column four, the gain measured with the photon transfer technique.

4. CONCLUSION

This paper described a fast technique to estimate the conversion factor (gain) of a CCD. It is based on the photon transfer curve adjusted to two TDI images. It has been tested on data taken at ESO Garching by the Optical Detector Team (ODT) team to characterize the OmegaCAM CCDs. The TDI images are taken during the ESO CCD test procedure to measure the linearity of the chips. The preliminary results to measure the gain with these data are very promising. They are in agreement with the standard gain measurement method.

This technique is advantageous because it could use the ESO Test bench without any modification, providing many more points for the photon transfer curve (here in our test about 400 points per plot compare to ~20 usually) and is very quick. Only two TDI images are required to measure the conversion factor. If a set of flat fields is considered to correct the photon response non uniformity, the linearity and residual-non-linearity can also be calculated.

Due to the fact that the gain measurement with this method is faster than the standard one, it turns out to be appropriate to use it during the tuning of CCDs (i.e. voltage adjustment). This technique, even if further work is needed to improve it, already proved reliable and can be used for simple and efficient gain measurements of CCDs.

5. ACKNOWLEDGMENTS

6. APPENDIX A, THE VARIANCE METHOD

The standard method used to measure the conversion factor with the ESO test bench is based on the photon transfer method (or variance method). Two flat fields and two bias exposures are acquired. The bias frames are subtracted from the flat frames. These bias corrected images are divided, one by the other, and the result is multiplied by the mean value of one of the images. To get the final result, 100 sub-windows are selected and in each of

them the mean signal and variance are measured. Then the gain, G, is measured. The median gain is calculated over all the sub windows. The gain's error is the standard deviation of the 100 conversion factors measured.

7.   APPENDIX B, PHOTON TRANSFER CURVE FROM ONE TDI IMAGE

The major problem with measuring the gain of TDI images is the precise repetition of data acquisition. It can be difficult to start the integration at the same line index if the shutter suffers from random delay when opening. To circumvent this problem, the photon transfer curve with one TDI image can be used [5]. The mean and the variance of the ramp are calculated for each line and the pair of points (intensity, variance) plotted.

In normal circumstances, in a flat field for example, the variance measured will not provide you the shot noise but instead, the shot noise plus the pixel to pixel non uniformity variation.

In the case of a TDI image, the quantity of electrons in a pixel is the sum of all the elementary flux it received during its complete transfer until the output register. The pixel intensity in the output image is thus barely affected by the pixel to pixel non uniformity, except in the first few lines read out.

That's why in this paper, utilizing this technique which uses only one TDI image, the twenty first rows (minimum) of the sensitive area must be discarded to measure the gain. In these first lines, pixel to pixel non-uniformities bias the measurements of the variance, and, because of the propagation of the errors, the estimation of the gain.

8.   REFERENCES

[1] Christen, F., et al, 2002, Scientific Detectors for Astronomy, The Beginning of a New Era, Kluwer Academic Publishers, Dordrecht, Holland, pp. 485-488.
[2] Amico, P., and Böhm, T., 1996, Optical Detectors for Astronomy, Kluwer Academic Publishers, Dordrecht, Holland, pp. 95-105.
[3] Kuijken, K,. et al, 2004, Proceedings of the SPIE, Volume **5492**, pp. 484-493.
[4] Iwert O., 2005, *The OmegaCAM 16K×16K CCD Detector System for the ESO VLT*, these proceedings.
[5] Janesick J. R., 2001, Scientific Charge-Coupled Devices, SPIE press monograph, Bellingham Washington.

CCD CHARGE TRANSFER EFFICIENCY (CTE) DERIVED FROM SIGNAL VARIANCE IN FLAT FIELD IMAGES
The CVF method

Fabrice Christen[1], Konrad Kuijken[1,2], Dietrich Baade[3], Cyril Cavadore[4], Sebastian Deiries[3], Olaf Iwert[3]

[1]*Kapteyn Astronomical Institute,* [2]*Sterrewacht Leiden,* [3]*European Southern Observatory,* [4]*Thales*

Abstract: *This paper describes a novel technique for estimating the CTE of a CCD. It is based on the change in variance with CCD rows or columns in simple flat field images, and uses the fact that imperfect charge transfer during readout has a smoothing effect on the final image. The data used to test this procedure is acquired using the ESO test bench, in the context of characterizing OmegaCAM CCDs. Nine CCDs' results from the CTE measurements by e2v and with the variance based technique developed in this paper were compared. Results are promising. This technique, still under development, proved reliable and can be used for simple and efficient CTE measurements.*

Key words: *Charge-Coupled-Device (CCD) characterization, charge transfer efficiency.*

1.   INTRODUCTION

During testing of the OmegaCAM[1] CCDs [1], flat images have been acquired using the ESO test bench [2] to check cosmetics of the chips. This paper will describe how to use these data also to measure charge transfer efficiency. This parameter, reported in units of percent, characterizes the efficiency to correctly transfer charges from one pixel to its neighbor. It will be extracted from the study of the variance of the signal measured in them.

---

[1]   OmegaCAM is a one square degree wide field imager which will be mounted on the VST telescope in Paranal, Chile [3,4].

After a description of the Change in Variance in Flat field (CVF) method in Section 2, first results will be presented in Section 3. Preliminary conclusions are described in Section 4.

2.   CHANGE IN VARIANCE IN FLAT FIELD (CVF) METHOD

Instead of studying the loss of signal as in the EPER method [5], the loss of variance across flat field images will be analyzed. During the transfer of charges, flat field images will be smoothed due to the charge loss. The signal in the flat field remains constant during the transfer but the variance from one line (column) to the other will decrease when the CCD is read. In Eq. (1) the effect of an imperfect transfer on the variance is shown:

$$\sigma_e^2(i) = a^{2i} N_e + \binom{i}{1}^2 a^{2i-2} b^2 N_e + \cdots + \binom{i}{i-1}^2 a^2 b^{2i-2} N_e \qquad (1)$$

$$\sigma_e^2(i) = a^{2i} N_e + O(b^2) \qquad (2)$$

$\sigma_e^2(i)$: Variance of the signal in e⁻ of the line i
N_e : Number of electrons
a : Charge Transfer Efficiency, CTE
b : Charge Transfer Inefficiency, CTI, $(b = 1 - a)$
$O(b^2)$: Residual, $O(b^2) \ll a^{2i} N_e$

By using the CTI $b = 1 - a$, and considering that $b \ll 1$, the term $(1 - b)^{2i}$ becomes $1 - 2ib + O(b^2)$ and Eq. (2) can be written as follows:

$$\sigma_e^2(i) = N_e - 2ibN_e + O(b^2) \qquad (3)$$

Equation (3) can be expressed in Analog Digital Unit (ADU) instead of electrons. The signal and the variance, measured in electrons, are related to the signal and variance respectively in ADU by:

$$N_e = gN_a \text{ and } \sigma_e = g\sigma_a \qquad (4)$$

g : Gain in electrons per ADU
N_a : Number of ADU
σ_a : rms noise in ADU

Equation (3) becomes:

$$\sigma_a^2(i) = \sigma_{a0}^2 - 2b\sigma_{a0}^2 i + O(b^2) \tag{5}$$

σ_{a0} : rms noise in ADU before any charge shift

Eq. (5) shows a linear dependence between the variance of the signal in line (column) i and the line number i. To estimate this equation, we will use the best fit line of the set of points $(i, \sigma_a^2(i))$.

To measure the variance of each line, two flats (same level) and two biases are taken. The bias images are subtracted from the flats and these two new images are divided, one by the other. The result is multiplied by the mean of one of the images. The final result will give an image (R) with fixed pattern noise (Photon Response Non Uniformity, PRNU) flat fielded out. The total noise (in pixel units, ADU) in this image R will be composed of photon noise and read out noise essentially. To measure the photon noise, the read out noise[2] is subtracted from the total noise.

To create the plot variance of lines (columns) versus lines (columns), we measure the variance for each line (column) of R. This value is divided by 2 to obtain the variance of one line and the point $(i, \sigma_a^2(i))$ is plotted (see Fig. 1). During the calculation of the variance, bad pixels are eliminating by using the sigma clipping method.

The best fit line will give us:

$$\sigma_a^2(i) = \mu - \nu i \tag{6}$$

μ : y-axis intercept (in ADU^2)
ν : slope of the streak

The constant term μ will give us the variance of the signal before being affected by the charge transfer inefficiency and the slope, ν, divided by 2μ, the charge transfer inefficiency. The charge transfer efficiency, a, is then:

---

[2] This parameter is measured by subtracting two bias images. The variance of the pixels in the difference image is equal to two times the read out noise squared. The variance from this image can be directly subtracted from the variance measured in the image R to have only two times the photon noise squared in ADU.

$$a = 1 - \frac{v}{2\mu} \tag{7}$$

Variance of lines versus lines   Variance of lines versus lines
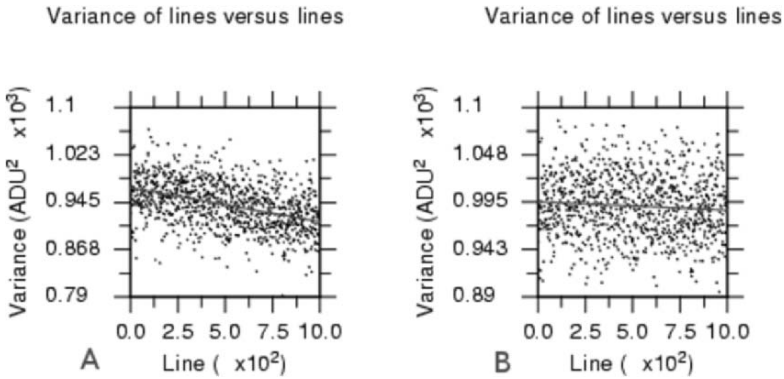
Figure 1. Image A and B show the plot $\left(i, \sigma_a^2(i)\right)$ at different CTEs with the best fit line cutting through. In A, the CTE is 0.999970 and in B, 0.999996. These plots have been made with simulated data. The dimensions of the images are 1K×1K. The number of electrons in the images is 1000 plus a Poisson noise. The CTE is applied after. Similar pattern are observed with real data. In the x-axis, the line count increases away from the readout register.

3.   RESULTS

3.1   Simulated Data

The CVF method has been tested on simulated data. Two images (1K×1K) with a mean intensity of 1000 e⁻ and a photon noise of $\sqrt{1000}$ have been created. For each set of images different CTEs have been applied (see column one and four of Table I). The procedure, based on the study of the variance and developed Section 2 is used to extract the horizontal and vertical CTE.

The first tests with these simulated data show, (see Table I), that the CVF method approximates CTE extremely well. The measurements are in accordance with the original values of the CTE.

Table 1. CTE measured with the CVF method applied to simulated data.

CTE	CVF		CTE	CVF	
H & V CTE	H-CTE	V-CTE	H & V CTE	H-CTE	V-CTE
	0.9999.. ± 0.000001		0.999992	92	92
1.	1.	99	0.999990	90	90
0.999998	98	98	0.999985	85	85
0.999996	95	95	0.999980	80	81
0.999994	93	94	0.999970	71	71

The first and fourth columns are the theoretical CTE in the simulated data. Columns two, three, five and six are the horizontal and vertical CTE measured with the CVF method.

3.2 Real Data

The CVF method has been tested on the data of 9 different CCDs. For each CCD two bias and two flat field images have been recorded. For 5 CCDs, data is acquired with a read out speed of 225kpix/s and a gain of $\sim$0.55 e^-/ADU. For 4 CCDs, data is taken with the same read out speed and a gain of $\sim$2.5e^-/ADU. The operating temperature is -120ºC.

The CTE from the e2v data sheet are included in our table of results for comparison. e2v uses the [55]Fe method [5]. The working temperature is -100ºC and the read out speed, 250kpix/s.

The results, reported in Table IIA and Table IIB are encouraging. Almost all the measurements carried out with the CVF method are consistent with the measurements from e2v.

While producing similar results, the differences between the devices 02111-01-02 and 02111-05-02 should not be overlooked. For these two CCDs, the CVF method is not in accordance with the e2v results. This difference may be due to traps. In flat fields, the traps are full and do not catch charges during the transfer which is not the case with images taken with the [55]Fe setup. In that case the traps catch more charges and reduce CTE.

4. CONCLUSION

This paper described an interesting alternative technique to estimate the charge transfer efficiency of a CCD. This method is based on the study of the change in variance with CCD row or column in simple flat field images, and uses the fact that imperfect charge transfer during readout has a smoothing effect on the final image.

The data used to test the CVF method are simulated data (an ideal 1K×1K CCD with only charge transfer inefficiency) and real data from the OmegaCAM CCDs. The results are very promising. The measurements done

with simulated data are in accordance with the theoretical CTE. We observe the same results with almost all the measurements achieved with real data. In that case the CVF method is compared with the measurements done with a [55]Fe set up. Additionally, this method overcomes the use of a dangerous radioactive material, such as [55]Fe, that needs special tooling and entrance windows to perform the measurements.

This technique is still at its preliminary development however, convinced by these first results, the procedure will be intensively tested and improved.

Table 2. Horizontal and Vertical CTE measured with the CVF and [55]Fe method.

CCD	H-CTE		V-CTE	
	CVF	[55]Fe	CVF	[55]Fe
A	0.9999.. ± 0.000001			
09253-13-01	99	99	98	98
00152-16-01	98	98	98	98
00152-13-02	98	97	98	97
00152-05-01	96	97	99	98
00152-12-02	98	99	97	97
B				
02111-01-02	97	93	99	99
02111-05-02	98	95	98	99
02111-13-01	97	97	98	98
02263-20-02	95	96	99	98

In part A, the data is taken with a readout speed of 225kpix/s and with a gain set at ~0.55 e/ADU. In part B, the readout speed is the same but the gain is set at ~2.55e[-]/ADU.

5.   ACKNOWLEDGEMENTS

6.   REFERENCES

[1] Christen F. et al, 2002, Scientific Detectors for Astronomy, The beginning of a New Era, Kluwer Academic Publishers, Dordrecht, Holland, pp. 485-488.
[2] Amico P. and Böhm T., 1996, Optical Detectors for Astronomy, Kluwer Academic Publishers, Dordrecht, Holland, pp. 95-105.
[3] Kuijken K. et al, 2004, Proceedings of the SPIE, Volume 5492, pp. 484-493.
[4] Iwert O., 2005, these proceedings.
[5] Janesick J. R., 2001, Scientific Charge-Coupled Devices, SPIE press monograph, Bellingham Washington.

DC CHARACTERIZATION OF CCD-BASED DETECTORS FOR USE IN SPACE-BASED APPLICATIONS

Robert Philbrick and Morley Blouke
Ball Aerospace & Technologies Corporation

Abstract: *The cost to replace individual CCD-based detectors or associated electronics in multi-chip focal plane arrays increases significantly as the instrument assembly schedule progresses. Thus, it is imperative that all detectors considered for use exhibit well-understood and tightly controlled performance characteristics. In some applications, full functional (AC) characterization of incoming CCD detectors can only be performed after expensive package assembly steps have been completed. In such situations a quick and thorough method of evaluating incoming CCDs using only DC measurements is highly desirable. In this paper several DC characterization measurement techniques are discussed, which have proven invaluable in evaluating CCD sensors for use in space-based applications.*

Key words: *DC test, CCD, Focal Plane Array (FPA).*

1. INTRODUCTION

A common problem when building up complex focal plane array assemblies is how to quickly and accurately qualify scientific grade CCD-based detectors prior to their integration into complex packages and/or multi-chip focal plane arrays. Full functional Electro-Optical (EO) characterization of incoming CCD detectors can sometimes be performed only after expensive package assembly steps have been completed. And discovering CCD tolerance issues after complex packaging steps is expensive and can significantly impact development schedules. Furthermore, EO testing, while imperative for the proper assessment of

detector performance, does not adequately reveal all potential problems that can arise when dealing with CCD image sensors. Augmenting EO testing by performing thorough DC characterization is a speedy and effective way to accurately qualify CCD-based detectors [1]. The DC tests of most interest in detector screening are Continuity, Leakage Current, Diode Breakdown, Diodes/Opens, Channel Potential, and DC Gain. However due to limited space, this paper will briefly discuss only the Leakage Current, Channel Potential, and DC Gain tests.

2.   LEAKAGE CURRENT

The leakage current measurement typically involves applying a fixed voltage across two groups of detector pins (e.g. serial clock phase 1 at +15 volts and substrate at zero volts) and then recording the resulting DC current flow. While the test is quite simple to perform, it yields invaluable information regarding the health of the detector if the current resolution is sufficiently high. For example, the typical leakage current into the reset gate on most CCD detectors is approximately 5 nA, and most of this is frequently due to parasitic loads. If the leakage current were to rise to 100 nA, say as a result of an ESD event occurring during a critical packaging step, the detector would most likely continue to function within specification. However, the rise in leakage current is a likely indicator of a fatigued gate which could potentially result in an early-life failure. Electro-Optical testing typically does not discover such fatigue and, hence, the detector would continue to be treated as a flight candidate. It is therefore recommended that leakage current testing be performed after each significant handling step in the FPA assembly process.

Using an automated DC test system, with a programmable matrix and precision voltage/current sources, several hundred leakage current tests can be performed in a matter of minutes and the results can be easily tracked over time. As an added precaution during testing, each stimulus source connected to the CCD should have compliance limiting capability. That is, every voltage source should have a programmable current compliance limit, as should every current source. Most modern Semiconductor DC Parameter Analyzers and Programmable Stimulus Measurement Units incorporate compliance limiting and, hence, using such instrumentation is highly recommended during all types of DC testing.

3. CHANNEL POTENTIAL

The channel potential test measures the electro-static potential under each electrode of interest on a CCD detector. To perform the test, the gate of interest must be surrounded by two diodes, with one diode statically biased and the other, the measurement node, setup to source a very small current (e.g. 20 nA). All other gates between the diodes must be biased 'on' and to ensure that the correct measurements are obtained other gates may need to be biased 'off'. Figure 1 depicts the measurement of Summing Well 'A' (SWA) on a hypothetical detector. Note that in Fig. 1 all gates, excluding SWA, within the serial register are biased 'on' and the parallel register clocks are biased 'off'.
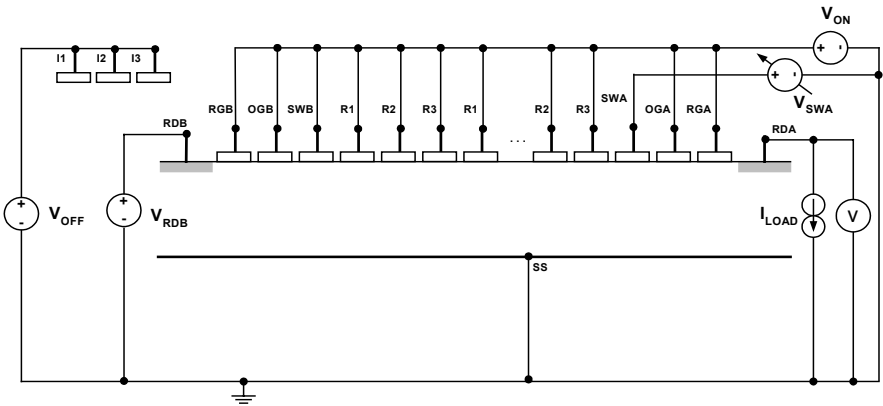
Figure 1. Schematic diagram of channel potential setup on a typical CCD.

The measurement proceeds as follows. Once the static voltage and current biases are applied, the voltage on the gate of interest is swept from negative to positive and the resultant voltage on the measurement node, which floats to the electro-static potential under the gate of interest, is recorded. The potential measured at the zero gate voltage is defined as the threshold potential and the voltage corresponding to the breakpoint under negative bias is defined as the inversion voltage. The slope of the channel potential curve is also a critical parameter as it represents the effective gain between external applied gate voltage and the resultant electro-static potential within the silicon detector.

The fundamental configuration of a basic MOSFET and a typical resultant channel potential curve are shown in Fig. 2. The clipping of the curve at the negative gate voltages less than V_{IN} is a result of the Si-SiO$_2$ interface operating in inversion, assuming an n-type buried channel in a p-type epi substrate. The clipping of the curve at positive gate voltages occurs when

the potential under the gate of interest exceeds the potential under the statically biased diode.
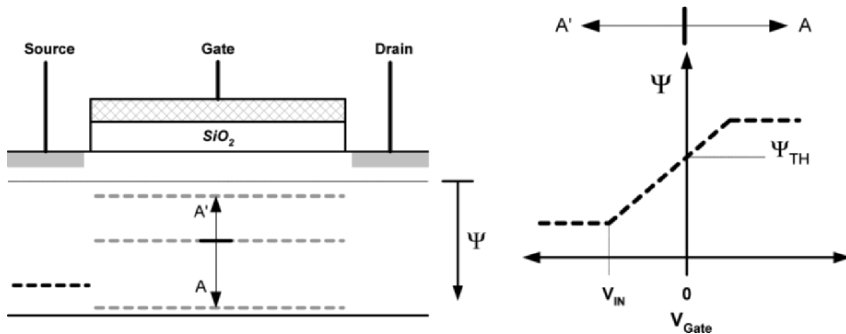
Figure 2. (left) Basic MOSFET *(right)* and a typical measurement result.

Like all the DC tests described herein, the channel potential measurements can be efficiently performed using an automated DC test setup. With the threshold potential and inversion voltages in hand, a complete Channel Potential (CP) diagram can be drawn showing the entire serial register or parallel register. Including instrument design, measured part-to-part tolerances and post radiation CP shifts, the channel potential diagrams provide an easy way of verifying correct operation of the CCD detector throughout the life of the instrument.

4.   DC GAIN

The DC gain test measures the low frequency, small-signal gain on each on-chip charge-to-voltage amplifier. Each amplifier is, in turn, biased up and the reset drain input is swept from 0.0 to the Output Drain (OD) bias (see Fig. 3). The CCD output can be biased using either a passive (resistive) load or a constant current source, with the latter being preferred on most automated test stations.

The small signal gain, i.e. Gain = $\Delta V_{OS}/\Delta V_{RD}$, is calculated at each reset drain setting and then the resultant gain curve is graphed, an example of which is shown in Fig. 4. The features of most interest on the gain curve are the recommended operating points for reset drain with respect to the reset gate cutoff point, $V_{RG\text{-}CUT}$ in Fig. 4, and the general flatness of the gain curve over the voltage operating range of the CCD output.
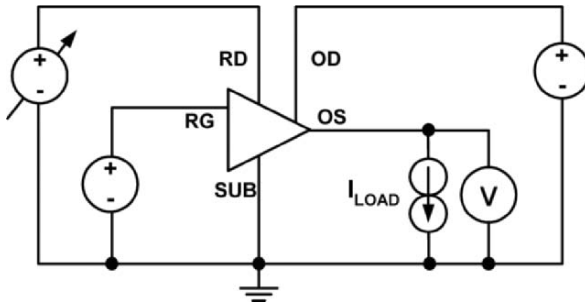
Figure 3. Schematic diagram of DC gain test setup.
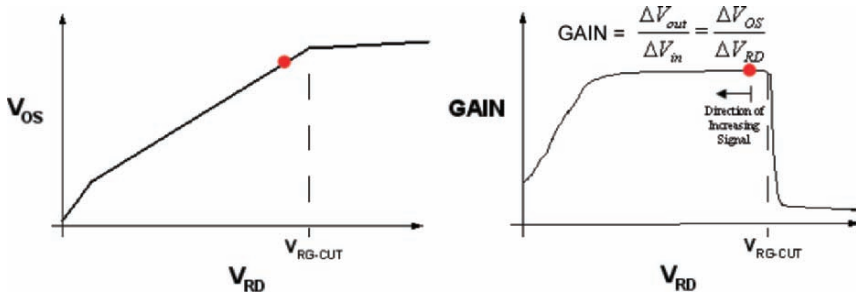
Figure 4. (left) Typical DC response curve *(right)* and DC gain response.

5.   CONCLUSIONS

DC characterization provides a fast, accurate, and thorough means for evaluating incoming CCD-based detectors. Though DC characterization does not replace full EO testing it does allow the build up of complex and expensive multi-detector FPA to proceed with high confidence that all CCD detectors are "healthy" and have the necessary clock and bias tolerance ranges. DC characterization on CCD detectors early in a program can identify processing and design problems undetectable by some detector vendors and most EO camera systems. Furthermore, DC testing is extremely useful, if not mandatory, when performing burn-in, accelerated life, and radiation tolerance testing on CCD detectors for use in space-based applications. The DC tests discussed herein are easily implemented on an automated DC test station, which allows for hundreds of measurements to be taken in only a few minutes. This, in turn, enables the DC testing to be performed at multiple points in the build up process of complex focal plane assemblies – yielding a high confidence in the reliability of the resultant focal plane assembly.

Some recent examples of the usefulness of DC testing are presented below. Figure 5 shows two examples where the DC gain measurements showed non-optimal performance. In Fig. 5 (left) the vendor-recommended operating point for reset drain is clearly too close to the reset gate cutoff point and in Fig 5. (right) the curve shows the recommended output drain bias is too low. Fig. 6 is an example of channel potential curves for two parallel register phases yielding significantly different inversion voltages, which would have resulted in one phase not running into inversion during integration.
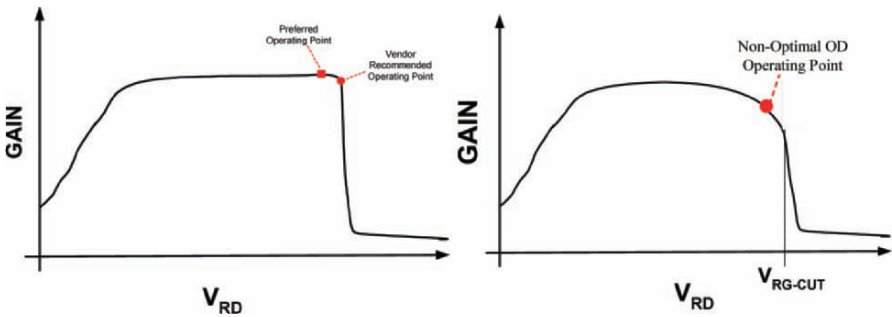
Figure 5. *(left)* Example of non-optimal RD and *(right)* OD operating point.
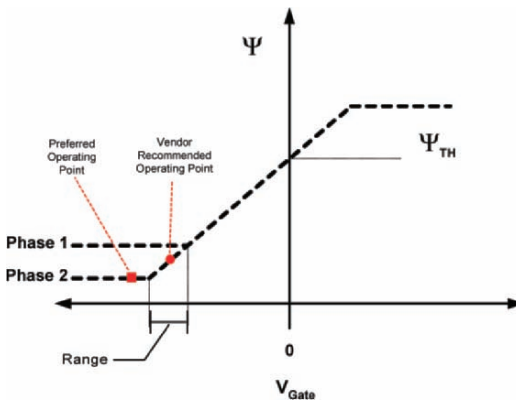
Figure 6. Example of non-optimal clock-low voltage for a parallel clock.

6.   REFERENCES

[1] Philbrick, R. H., 2003, *DC Characterization of CCD-Based Detectors for use in Multi-Chip Focal Plane Arrays,* Fifth International Conference on Scientific Optical Imaging (ICSOI – 5), Cozumel, Mexico.

DETECTOR TESTING METHODOLOGIES FOR LARGE FOCAL PLANES

Peter Moore[1] and Gustavo Rahmer[2]
[1]National Optical Astronomy Observatory, [2]Cerro Tololo International Observatory

Abstract: *The use of large detector mosaics to support future instrumentation poses new demands on the timeliness and rigor of detector testing procedures. Ideally, the characterization and selection of detectors for any particular new instrument should not appear as a critical path in the project. Committing to a large lot run of devices is expensive and deserves deep analysis of the factors that affect scientific tradeoff, developmental risk, and delivery schedules. We propose a methodology that involves incorporation of the elements of detector testing at the very beginning of the instrument requirement definition process: In this way the selection of detectors to provide the maximum science potential can be assured and audited.*

Key words: *Detector testing, large focal planes, testing methodologies.*

1.   INTRODUCTION

It is a familiar saying that in science, asking a question usually provides more questions than answers. In this way, the questions we asked yesterday have led us to ask new questions today that require ever increasing contributions of social, political, and capital investment to answer. In this regard, a subtle change of paradigm is in process with regard to the methodology of developing astronomical instrumentation. Historically instrumentation was designed specifically for an institutional telescope, or a small group of telescopes, and with a relatively wide range of application for general application to astronomy. With relevance to this paper, this often meant designing or adapting an instrument to utilize a new or enhanced detector technology within the current focus of a national group of scientists.

Today we see a trend towards large collaborations to supply the scientific, engineering, and capital investment required to provide the instrumentation needed to supply an answer to perhaps just one or two specific questions. In this new paradigm, the science objectives have clear priority; the instrument is designed specifically for these requirements, and often, a telescope built to accommodate the instrument. To assure that these strict science objectives can be met, detector testing has to be involved at the very beginning of the instrument requirements definition and continue throughout the development so as to achieve these specific objectives. We present a methodology of detector test analysis that convolves specific detector characteristics into performance metrics that are specific to the scientific objectives.

2.   FIRST ORDER INTER-RELATIONSHIP OF DETECTOR PROPERTIES TO INSTRUMENT SCIENCE OBJECTIVES

By analyzing the science tradeoffs that will occur when detector performance is less than (or better than) the instrument specification, a figure of merit can be established for each tested detector. This will allow an unambiguous comparison of different detectors and detector technologies to be made and will reflect the degree of suitability of any particular detector to the instrument science objectives. To derive the figure of merit for each detector, metrics are obtained from direct measurements of a detectors' performance, which are then normalized to a typical operational model of an instrument observational unit. In this paper, five metrics are considered in the figure of merit for a detector. These are cadence (i.e. Observed sky / time), observed optical quality, observational depth, photometric accuracy, and observatory efficiency. The metrics for each tested detector are then presented as a three-axis histogram to aid in the visual identification of areas of merit or deficiency for a particular detector. The X axis of the histogram represents the five different metrics, the Y axis is the calculated metric score and the Z axis is the wavelength dependence of each metric. A figure of merit value is then derived from the five metrics according to a weighted product that reflects the priorities of each one towards the science objectives of the instrument. In this way detector type suitability to a particular objective is presented by using either measured, published, or projected performance values. When delivery of the chosen detectors begins, each detector is tested and the individual suitability is determined using the same criteria. In this way, the suitability of different detector technologies, individual detector test results, and detector testing results from different laboratories can be directly compared.

2.1 Normalization of Metrics

To provide fair weighting of each metric to the overall figure of merit value obtained for a detector, the conditions for calculating them are normalized to a 'standard' observation on a 'standard' sky using a 'standard' telescope. Nominal values for these standards are derived from expected performance figures of the instrument and telescope in the wavelength regions of interest. For the purpose of this paper, the standards are derived with respect to the LSST mission and the nominal values for these taken from the LSST Exposure Time Calculator. Detector performance parameters that are measured but not included within the calculation of metrics must be proven to be at a value that does not interfere with the figure of merit i.e. they must be 'in the noise' or not limit the measurements used to derive the metric.

2.1.1 Standards

Standard Observation
Five 10 second integrations, one each using the UBVRI band pass filters, on a standard sky through a standard telescope. Seeing for the standard observation is set to 0.8 arcsec rms. Table I defines these properties.

Table I - Standard Observation

Defined quantities	Symbol	Units
Integration time	T	seconds
Seeing	S	arc sec rms
Required SNR for observation	Snr	ratio

Standard Sky
A standard sky is described as a plane peppered with 10th and 24th mag stars at all wavelengths and with representative sky brightness in bands. Table II define these properties.

Table II - Standard Sky

Defined quantities	Symbol	Units
Bloom star	Bm	Vmag
Object star	Om	Vmag
Sky brightness	Sm	Vmag
Bloomstars in each arcminute^2	Bn	stars

Standard Telescope
A standard telescope is established as a 7 meter diameter effective aperture telescope with a nominal throughput of 85% at all wavelengths. The plate scale is set to 20 arcsec / mm and a three degree^2 field of view is available. Table III defines these properties.

Table III - Standard Telescope

Defined quantities	Symbol	Units
Free aperture	A	meters
Plate scale	Pm	arcs / mm
Throughput	E	%
Field of view	Fov	arc degrees^2

2.1.2   Metrics

Due to space limitations of this paper, only two metrics, <u>Cadence</u> and <u>Optical depth</u>, of the five total will be described here. The missing metric calculations are performed in a similar manner to those described here.

<u>Cadence</u> (MUc, MBc, MVc, MRc, MIc)

Cadence is the ratio of time between that required for a standard observation using the instrument detector specifications and the time calculated to achieve the same observation in detector testing. The cadence metric is shown in Table V and is derived using the parameters defined in Table IV.

Table IV - Cadence Metric Parameters

Measured quantities	Symbol	Units
Pixel size	Ps	microns
Bright pixels	Pb	% of pixel count
Dark pixels	Pd	% of pixel count
Traps	Pt	rows and columns
Readout noise	Nrd	e- rms.
Quantum efficiency	Qλ	% efficient at λ
Readout time	Tr	seconds
Fill factor	F	% of detector area active
Dark current generation	Di	e- / pixel / sec
Full well	Fw	e-
Blooming control	Bc	% Fw before bloom occurs
Seeing correction	Sc	% reduction of seeing disk

<u>Observation depth</u> (MUd, MBd, MVd, MRd, MId)

The difference in observed magnitude between the calculated magnitude achieved in a standard observation using the instrument detector specifications and that calculated using measured detector parameters. This metric does not consider field coverage. The observational depth metric is shown in Table VII and is derived using the parameters defined in Table VI.

Table V - Cadence Performance Metric (Mc) Development
Using the quadratic of form: Results in:

$$x = \frac{-b \pm \sqrt{b^2 - 4ac}}{2a}$$

where :

$a = Q\lambda^2 Of^2$

$b = -Snr^2 Q\lambda (OfSf)$

$c = -Snr^2 + PnNt^2$

$x = T$

$$M\lambda c = \frac{T + Tr}{Ed}$$

Table VI - Observational Depth Metric Parameters

Measured quantities	Symbol	Units
Pixel size	Ps	microns
Quantum efficiency	Qλ	% efficient @ λ
Readout noise	Nrd	e- rms
Fringing	Frλ	% rms mean signal @ λ
Image latency	Li	e-
Dark current generation	Di	e- / sec / pixel
Seeing correction	Sc	% reduction of seeing disk

Table VII - Observational Depth Metric (Md) Development
Using the quadratic of form: Results in:

$$x = \frac{-b \pm \sqrt{b^2 - 4ac}}{2a}$$

where :

$a = Q\lambda^2$

$b = -Snr^2 Q\lambda$

$c = -Snr^2 (Q\lambda SfPn + (PnNt)^2)$

$x = Of$

$$M\lambda d = -2.5 \log\left(\frac{x}{1.51^7 J\lambda_0 \, \Delta\lambda/\lambda}\right)$$

2.1.3   Derived Values

These values are derived from the predicted first order performance metrics of the instrument plus telescope and used to define the operational conditions of the detectors under review.

Table VIII. Derived Performance Parameters

$$Seeing\,Pixels\,(Pn) = \frac{\left(\dfrac{S^2}{4}\pi\right)}{Pm^{10^{-6}}\,Ps_x\,Ps_y} \tag{1}$$

$$Object\,Flux\,(Of\,)(photons\,/\,pix\,/\,sec) = \frac{10^{(-0.4Omt)}\,J\lambda_0 1.51^7\,\Delta\lambda\big/_\lambda\,AE\,\lambda}{Pn} \tag{2}$$

$$Bloom\,Flux\,(Bf\,)(photons\,/\,pix\,/\,sec) = \frac{10^{(-0.4Bm)}\,J\lambda_0 1.51^7\,\Delta\lambda\big/_\lambda\,AE\,\lambda}{Pn} \tag{3}$$

$$Sky\,Flux\,(Sf\,)(photons\,/\,pix\,/\,sec) = 10^{(-0.4Sm)}\,J\lambda_0 1.51^7\,\Delta\lambda\big/_\lambda\,AE\,\lambda\,Ps_x\,Ps_y \tag{4}$$

$$Snr = \frac{Q\lambda Of\,T}{\sqrt{Q\lambda(Sf+Of\,)T+(Pn\,Nrd)^2}} \tag{5}$$

$$Nt(e-rms)(Total\,Noise) = \sqrt{Nrd^2 + TDi^2 + \left((Fr\lambda + Li)(Q\lambda(Of\,Sf\,T))\right)^2} \tag{6}$$

$$Effective\,Detector\,Area\,(Ed) = \left(Pt - \left(\frac{(Bf\,Pn\,Dfov\,Bn)}{Fw\,Bc} + Pb + Pd + (100\,Pt\,/\,F)\right)\right)Pa \tag{7}$$

2.1.4   Metric Calculation Methods

The calculations for deriving the various metrics are performed with an Excel spreadsheet. Graphics are used to display the results and enable a rapid and decisive estimation of science performance based on detector performance.

CALIBRATION OF FLIGHT MODEL CCDS FOR THE COROT MISSION

Vincent Lapeyrere, Pernelle Bernardi, Jean Tristan Buey
Laboratoire d'Etudes Spatiales et d'Instrumentation en Astrophysique (LESIA)

Abstract: *Corot is a mission of high accuracy photometry with two scientific programs: asteroseismology and planet finding. The focal plane is composed of four CCDs. Ten 2K×4K e2v CCD42-80s have been calibrated on a test bench to choose the best for flight. Very high instrument stability is required. Taking environmental perturbations into account (temperature, ACS jitter, radiations, etc.) we have studied the sensitivity of CCD gain and quantum efficiency to temperature and sensitivity of the output signal to bias voltages. Attention is paid to pixel capacity and noise sources coming from dark current and pixel response non uniformity.*

Key words: *CCD, calibration, photometry, CoRoT.*

1.   INTRODUCTION

The CoRoT (Convection Rotation and Transit) small satellite is a space mission dedicated to stellar seismology and the search for extra-solar planets as primary goals. The Astero-Seismology channel (AS channel) should be able to detect periodic variations of luminosity between 2 and 10 ppm with a typical lifetime of five days and periods between one minute and three hours. Fifty to sixty stars will be continously monitored over 150 days [1].

The Planet Finder channel (PF channel) method is based on the detection of fortuitous transits of planets in front of their parent star. The amplitude of a typical transit is between 7.10^5 for telluric planets and 2.10^{-2} for Jupiter-like planets, and its duration is between 3 to 12 hours [2]. A maximum number of 60 000 stars will be measured during five 150 days runs.

To detect such small variations a high instrumental stability is required (see [3] for a description of the main environmental perturbations). The goal is to keep each white noise contributor at less than one tenth of the photon noise for a $m_V = 6$ star and to keep each periodic perturbation of the orbital motion at less than 2 ppm.

The focal plane of the Corot instrument is composed by 4 CCDs covering a surface of 2.66×3 degrees on the sky. Ten CCDs, e2v42-80, were purchased from e2v with Corot specifications. All CCDs were characterised with two objectives: select the best four CCDs for flight, and determine parameters which will be used for data corrections.

This paper presents results obtained during the sorting and calibration process. The number of CCDs tested (nine were fully characterised) give us a good idea of typical characteristic of this kind of CCD. Sec. 562 gives a short description of Corot, the mission and the instrument. Sec. 563. presents the test bench. In Sec. 564 we describe the measurements made on the CCDs.

2.   COROT DESCRIPTION

2.1   Corot Mission

Corot is a mission managed by CNES (Centre National d'Etude Spatiale) in association with three major French laboratories and several European countries contributing to the payload and to the ground segment. Corot is the third mission on the multi-mission platform PROTEUS designed for low earth orbits. PROTEUS development is carried out under the partnership of the French space agency (CNES) and Alcatel Space Industries.

2.2   The Payload

The optics have been designed to minimize scattered light at the focal plane level. An off axis afocal telescope and a dioptric objective allow efficient baffling. To avoid saturation on bright targets, images of the AS field are slightly defocused and cover approximately 300 to 400 pixels. In front of the PF CCDs a prism gives a low resolution spectrum (100 nm. pixel^{-1}) for each target.

The focal box is cooled by a radiator via a passive thermal link at a temperature of approximately –40°C. The orbital temperature variations of the radiator are filtered by an active control system which maintains the temperature with a stability of ±0.005 K.

The front end electronic boxes for signal amplification and bias voltage generation surround the focal box and their temperature stability surpasses 0.014 K. The video electronics are on the upper side of the equipment bay which has a passive regulation with two radiators on each side of the satellite, maintaining temperatures of approximately 16 ±0.2°C. The expected whole gain sensitivity to temperature is less than 20 ppm.K^{-1}.

2.3 The CCDs

The four CCDs are e2v42-80s. They are frame transfer CCDs with an image area of 2048×2048 pixels and a memory area of 2048×2054 pixels. They are thinned, back illuminated and use Advanced Inverted Mode Operation (AIMO) to limit the interface dark current.The line transfer time is 100 μsec for AS CCDs and 150 μsec on PF channel. The memory zone is read on two outputs during the integration of the following exposure. The whole memory zone is read for PF once per 32s while ten 50×50 pixel windows are read on AS CCDs once per second. Quantum efficiency has been measured by e2v. The mean quantum efficiency on the bandwidth 300-950 nm varies from 60% to 64.5%.

3. THE TEST BENCH

The heart of the experiment consists of the CCD mounted in a cryostat. The CCD is linked to a large metal bar cooled by a cryogenic device. This bar increases the thermal stability of the CCD. A temperature of –45°C is reached with fluctuations less than 0.01 °C.

The CCD is illuminated with light from three LEDs or from a monochromator. Wavelengths are 470 nm (Δλ = 35 nm), 640 nm (Δλ = 17 nm) and 880 nm (Δλ = 80 nm). In the monochromator the halogen lamp is stabilized with a current regulation and the bandwidth is adjustable between 10 to 50 nm.

The two light sources are also used to illuminate an integrating sphere to obtain a flat illumination of the entire CCD. The intensity of illumination across the field is uniform to within approximately 5%. To mimic star image, a mask consisting of a metal plate drilled with holes can be placed in front of the integrating sphere output. The mask is imaged onto the CCD with an objective. The F/4 aperture of this objective reproduces the same photon incidence as that of Corot on the CCD.

The standard readout of the CCD is in video mode. The exposure time is therefore controlled by the time between two image transfers in the memory area. The acquisition frequency is 1 image per 32 s. The transfer of the

image in the memory area takes 0.2 s (150 µs per line), so that the exposure time is 31.8 s. The flux received by CCDs is defined by illuminating the experiment by flashing LED with a controlled duration during exposure.

4. CCD CALIBRATION

4.1 Dark Current

The dark current law has the standard form in Eq. (1):

$$D(T) = D(T_0) \alpha T^3 e^{\frac{-\beta}{T}} \tag{1}$$

$D(T_0)$ is the dark current at 280 K and is equal to 250 e⁻.pix⁻¹.s⁻¹ for AIMO mode and to 10^4 e⁻.pix⁻¹.s⁻¹ for non AIMO mode. The α and β values are respectively (1.14 10^6, 122) and (9080, 6400). The AIMO mode is only active when all phases are at 0 V, i.e. when charges are immobile.

The dark current was measured at a temperature of –40°C on series of 30 dark images with 60 s exposures. On these images the mean time spent by charges in the CCD is 71 s (integration plus readout) with 99.2 % of this time in MPP mode. In this condition and according to Eq. (1) the expected dark current is about 0.18 e⁻.pix⁻¹.s⁻¹. The mean values measured are between 0.07 and 0.14 e⁻.pix⁻¹.s⁻¹. On the 9 CCDs, a total of 7 columns with dark current greater than 1 e⁻.pix⁻¹.s⁻¹ are detected among which 4 columns are in the range 5 to 15 e⁻.pix⁻¹.s⁻¹.

4.2 Pixel Response Non-Uniformity (PRNU)

The intrapixel non uniformity [4,5] was not measured because we believe that its impact is marginal. It has been shown that when a pixel is illuminated by a spot smaller than the pixel area and moving in the x or y direction, the flux measured by the illuminated pixel can vary by several tens of %, but the flux summed over the nine adjacent pixels remains constant to within about 1% and this variation cannot be distinguished from the pixel to pixel non-uniformity. This is true only for thinned back-side illuminated CCDs. This diffusion process is negligible for our photometric application, the total flux being measured in a large aperture (300 pixels for AS channel and 80 pixels for PF channel).

The CCD was illuminated with the integrating sphere. 30 images are summed to reduce readout and photon noise. The measurement accuracy on

the relative quantum efficiency is estimated to be less than 0.07%. To reduce the contribution of non uniform illumination, the local PRNU is computed in windows of 32×32 pixels. Figure 1 shows the evolution of the local PRNU with wavelength measured with a bandwidth of 10 nm.

For all CCDs the PRNU is lower than 0.6% except for wavelengths greater than 800 nm because of fringing. When the bandwidth is larger, e.g. with LED (Light-Emitting Diode) images, the fringing disappears entirely as can be seen Fig. 1 with measurments made with LEDS. The led at 880 nm has bandwidth of 80 nm.

We note on flat field images (on all CCDs) the presence of rows with lower or greater value than the mean value by a few percent. These rows are # 512, 1024 and 1536, and correspond to junctions between masks of 512 rows used to manufacture CCDs. At these junctions pixels can have a different size which implies a different collecting surface. The quantum efficiency does not differ strongly on these rows, but the difference of collecting surface changes the collecting efficiency.
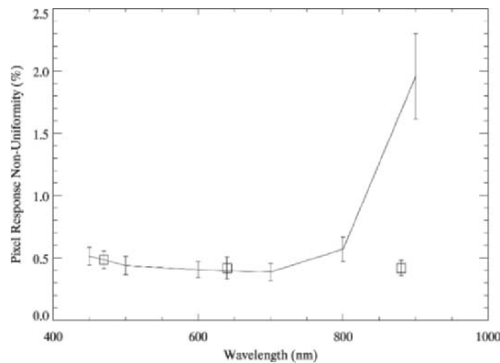
Figure 1. Evolution of local PRNU with wavelength. Measurements made with a bandwidth of 10 nm. Error bars represent the dispersion on all CCDs (for wavelength greater than 800 nm, PRNU is dominated by fringing). The three square points represent measurements with led.

4.3 Gain of CCD

The CCD gain (G_{CCD}) is deduced from the camera (g) gain measured on the photon transfer curve. The slope of the curve variance versus the mean is equal to $1/g$ [6]. This is true only if the quantum efficiency is perfectly uniform. To avoid the PRNU contribution to the variance, the variance was

computed on the difference of 2 images with the same mean illumination level. In this case the slope of the relationship $n_{adu} = f(\sigma_{adu})$ is equal to $2/g$.

The CCD gain mean value for all CCD is 4.28 μV.e^{-1} with a dispersion of 0.12 μV.e^{-1} and the difference between left and right output is lower than 5% for all CCD. The precision on the gain measurement is 1%. The gain is measured for different temperatures to determine relative sensitivity to CCD temperature a_G expressed in ppm.K^{-1}. The mean value for all CCDs is –900 ppm.K^{-1} with a dispersion of 100 ppm.K^{-1}. The measurement precision is about 15%.

4.4   Pixel Capacity

To characterise the entire surface of the CCD we need a criterion to determine the pixel capacity on flat field images. Two quantities can be used: the evolution of intensity (ADU) versus flux and the evolution of variance. The first shows the break on the linearity curve and the second identifies the case where the poisson statistic (average equals variance) is no longer respected. We use the variance to determine pixel capacity because it is more sensitive.

Flat field images are taken with white LED illumination and with different flash durations. For each flash time we compute the variance and the average on a difference of two images and on boxes of 40 by 40 pixels at different positions. For each position we plot the variance and average versus flash duration. On this plot the pixel capacity is the average of the image about which the variance is decreasing.
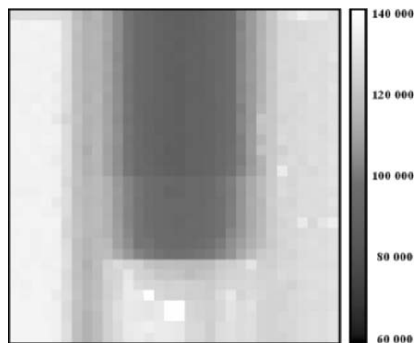
Figure 2. Pixel capacity map (e$^-$/pixel).

The result on the entire surface of a CCD is presented in Fig. 2. Each square represents the pixel capacity of that position. This capacity map shows a difference between the center and the edges of the CCD. This difference is observed on five of the ten CCDs tested. The saturation in the

center of the CCD occurs during charge transfer because charges spread upward. This non-uniformity is explained by the difference between the well shape during transfer at the edges of the CCD (where phases are injected) and the shape in the center far from the injection point. This difference is due to the resistivity and capacity encountered by phases to reach the center of the CCD.

4.5 CCD Response Sensitivity to Temperature

The CCD response is sensitive to temperature due to CCD gain variation, but also due to quantum efficiency variation. Quantum efficiency sensitivity $\alpha_{Qe}(T,\lambda)$ depends on wavelength.

$$\alpha_{CCD}(T_0) = \alpha_g(T_0) + A_{Qe}(T_0)$$

(2)

Where $A_{Qe}(T_0)$ is the quantum efficiency sensitivity integrated for a source spectrum.

The CCD response is measured on the test bench for variations of –40°C +/- 15°C, and for tree different leds. We deduce α_{CCD} which is the slope of this evolution at $T_0 =$ –40°C. We find a negative coefficient at 470 and 740 nm, and a positive coefficient at 880 nm. Typical values at three different leds for all CCDs are given in Table 1. According to Eq. (2), $A_{Qe}(T_0)$ can be obtained by subtracting $\alpha_g(T_0)$ from $\alpha_{CCD}(T_0)$.

Table 1. CCD response sensitivity to temperature ($\alpha_{CCD}(T_0$=-45 °C)).

λ (nm)	470	640	880
Mean value (ppm/K)	-510	-400	2500
Accuracy (ppm/K)	50	50	80
Dispersion (ppm/K)	200	118	360

4.6 CCD Sensitivity to Bias Voltages

For each CCD we verified that operation is optimal with nominal values of bias voltage. These nominal values come from data sheet and optimization made on engineering model CCDs. When bias voltages vary some characteristics of the CCDs are modified. In particular, CCD gain is sensitive to Vod (output drain), Vog (output gate) and Vrd (reset drain). For each voltage we measured the slope of the evolution of the video signal amplitude versus each voltage at the nominal value. These slopes represent the sensitivity to each voltage.

Sensitivity to bias voltages measured are reported in Table 2.

Table 2. CCD gain sensitivity to bias voltages.

λ (nm)	Vod	Vrd	Vog
Mean value (ppm/mV)	-34.4	-13.0	22.0
Dispersion (ppm/mV)	3.6	4.0	5.0
Bias voltage value (V)	26.4	13.2	-1.9

5. CONCLUSION

Corot is a high accuracy photometer, and the core of this instrument is based on four CCDs (e2v-4280), AIMO and back illuminated. Some characteristics of these CCDs have an impact on photometric performance: PRNU combined with jitter produces photometric noise, dark current brings shot noise, pixel capacity limits saturation. Others have an impact on photometric stability: gain and quantum efficiency are sensitive to temperature, gain is sensitive to bias voltages.

For the selection of CCDs for the Corot mission, criteria are based on characteristics affecting photometric performances. The main limitation is pixel capacity, and principally the weakness of capacity in the center of the CCD. On the four selected CCDs the pixel capacity varies from 95 ke$^-$.pix^{-1} in the center of the worst CCD, to 125 ke$^-$.pix^{-1} at the edges of the best CCD. The presence of defects (dark and PRNU) are very rare on the selected CCDs.

Characteristics affecting stability are considered as calibration parameters. They are used to estimate the perturbation amplitude due to variation of temperature and bias voltages and to make corrections. In the case of Corot, the main perturbation comes from sensitivity to bias voltages and precisely to Vod (34 ppm.mV^{-1}). With a Vod variation of 1 mV (due to orbital temperature stability of 1 K of the electronic generating the bias), we obtain a perturbation of 34 ppm on the photometric curve. While CCD response temperature sensitivity is lower than 300 ppm.k^{-1} and with an orbital CCD temperature variation of 5 mK, the perturbation on photometric curve is lower than 2ppm.

6. REFERENCES

[1] Baglin A. et al., 1998, *Asteroseismology from space - The Corot experiment,* IAUS, **185**, 301.

[2] Rouan et al., 2000, *The extrasolar planets program of the Corot satellite*, EM&P, **81**, 79.

[3] Auvergne et al., 2003, *COROT-high-precision stellar photometry on a low Earth orbit: solutions to minimize environmental perturbations*, SPIE, **4854**, 170A.

[4] Jorden P.R., Deltorn J.M., Oates A.P., 1994, *Nonuniformity of CCDs and the effects of spatial undersampling*, SPIE, **2198**, 836.

[5] Piterman A., Ninkov Z., 2002, Opt. Eng. **41**, 1192.

[6] Janesick, James R. 2001, Scientific charge-couple devices, SPIE press.

SECTION VII:

ELECTRONICS

NGC DETECTOR ARRAY CONTROLLER BASED ON HIGH SPEED SERIAL LINK TECHNOLOGY

Manfred Meyer, Dietrich Baade, Andrea Balestra, Claudio Cumani, Sebastian Deiries, Christoph Geimer, Reinhold Dorn, Siegfried Eschbaumer, Gert Finger, Leander Mehrgan, Alan Moorwood, Roland Reiss, Javier Reyes, Joerg Stegmaier
European Southern Observatory

Abstract: *Progress in FPGA technology has made it possible to build a very compact, versatile, low power detector array controller based on high speed serial link technology. All data and communication transfers run between back-end and front-end, and within the front-end over high speed serial links with transmission rates of 2.5 GBit/s. The serial-bus architecture offers high performance and system scalability for modular controller set-up.*

Key words: *Detector readout electronics, data acquisition system, focal plane arrays.*

1.   INTRODUCTION

The conventional approach to build data acquisition systems is based on parallel bus architectures. A parallel bus in the front-end connects the detector video data digitizing modules to a communication module for further transfer to the back-end. This bus already poses serious design challenges when the number of modules varies between systems, especially if the bus clock frequency is high. In addition, the bus busy time may determine the maximum sample rate for large systems because during bus transfer conversion accuracy may be affected by coupling digital artifacts into the analog chain. For system setup and communication an additional structure is needed, which adds complexity to the system. On the New

General detector Controller (NGC) the parallel buses are replaced with high speed point to point serial links carrying data and communication transfers.

2.   PROTOTYPE OF NGC

NGC is a modular system for IR detector and CCD readout with a back-end and a basic front-end containing a complete four channel system on one card. In future additional boards like multi-channel ADC units, routers and interfaces for applications like interferometry and   adaptive optics are foreseen (see Fig. 1).
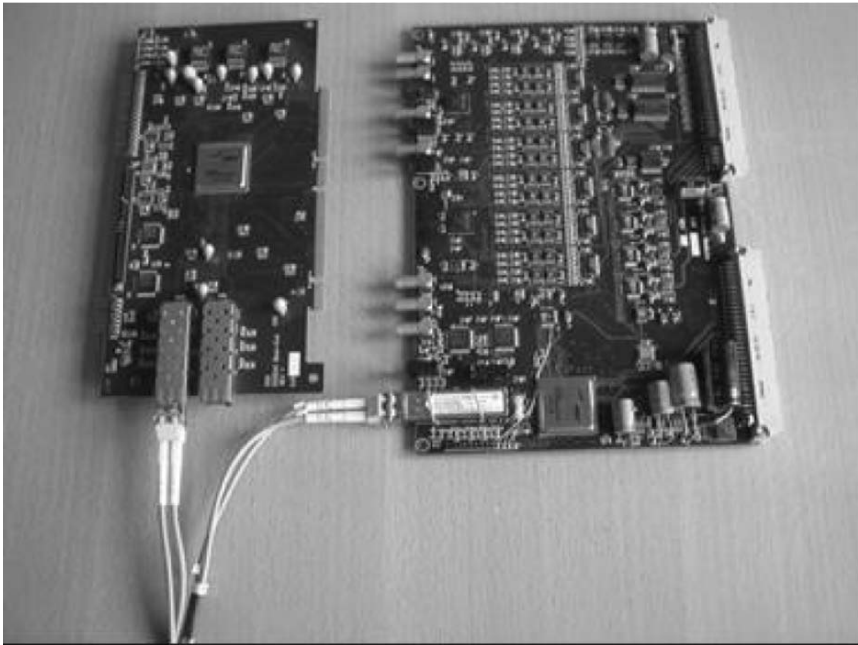
Figure 1. Prototype NGC.

There is no processor or parallel inter-module data bus on the front-end side. Advanced FPGA (VirtexPro 2VP7) link technology is used to replace conventional logic. The back- and front-ends are connected by fibers with high speed links (2.5 GBit/s). The modules inside the front-end are connected with high speed copper links (2.5 GBit/s). The links are derived from the Rocket I/O transceivers of the VirtexPro chip. The data rate on one channel between front and back-ends is ~200 MByte/s. The module functions on the boards are addressed directly from the FPGA without glue

logic. Results are minimum disturbance for the anticipated low noise operation on the low level detector signals, small size and low power consumption. The power consumption of the basic front-end is less than 10 Watts (excluding power supply). Thus the front-end system does not require big cooling boxes.

3.   BACK-END

All functions are based on the XILINX Virtex Pro FPGA XC2VP7 FF 672. The back-end is a 64 Bit PCI board (see Fig. 2). The FPGA contains the PCI interface for communication functions, the video data DMA channel and the RocketIO transceivers for link transfer. The interface from PCI to FPGA does not have glue logic. PCI master (data) and PCI slave (communication) interfaces are independent and can work concurrently. All communication and data transfers are on serial links. Scatter /Gather DMA is used for data taking, all communication runs with a handshake protocol.
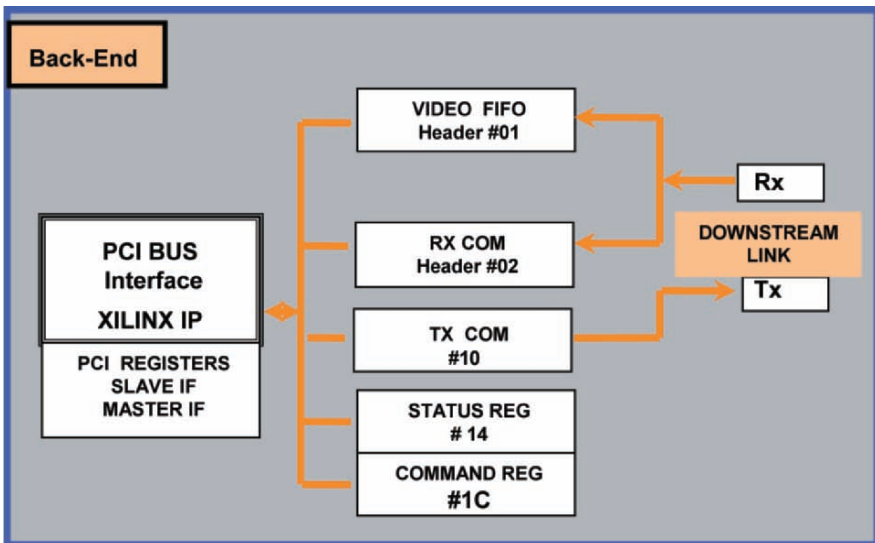
Figure 2. Back-end block.

4.   FRONT-END BASIC MODULE
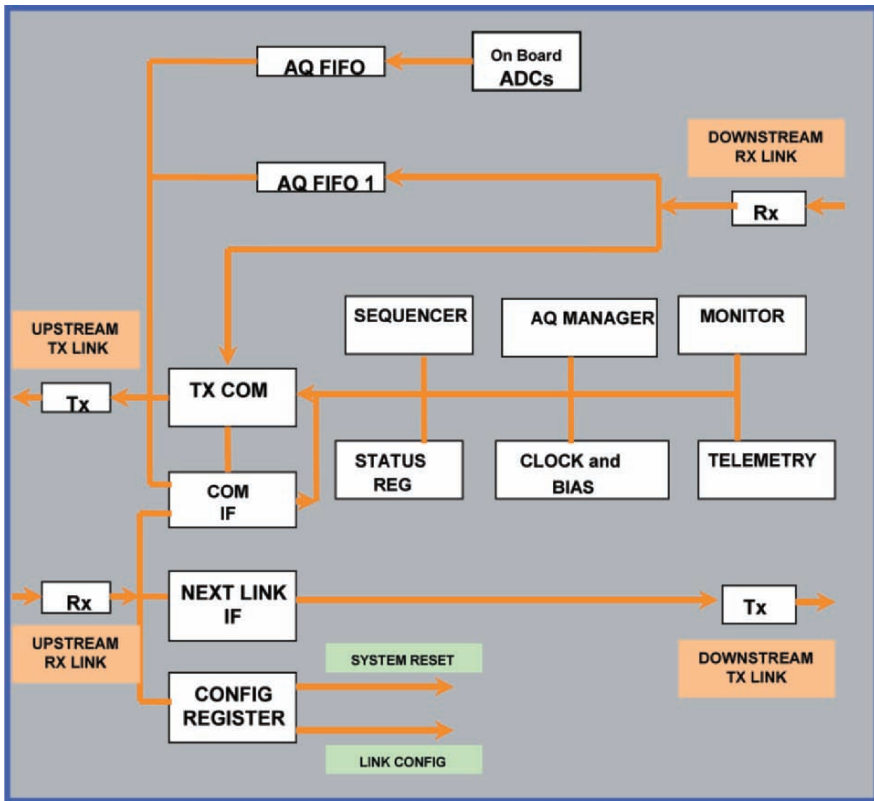
Figure 3. Front-end basic block.

All functions are based on the XILINX Virtex Pro FPGA XC2VP7 FF 672 (see Fig. 3). The FPGA contains the link interface for communication and data transfer with RocketIO transceivers, sequencer, system administration, interface to acquisition, clock and bias, telemetry and monitoring. The board contains four ADC channels (with 16- or 18-Bit Analog Devices Pulsar ADCs), 16 clocks and 20 biases, all remotely programmable, Telemetry with 16-Bit accuracy, monitor outputs of video input, ADC input, clock signals, convert strobe and digital marker signals. There are galvanic isolated trigger input and control output signals. LVDS signals are provided to connect to detector ASIC's - all communication and data transfer to the back-end is handled with the same firmware used for conventional detector read-out.

5. PROTOTYPE SYSTEM NOISE

System noise measurements look promising. A double correlated readout with 100 Ohm terminated inputs shows 0.7 ADU RMS (readout noise * SQRT 2). The noise on a channel with 10 KOhm termination differs as expected (see Fig. 4).
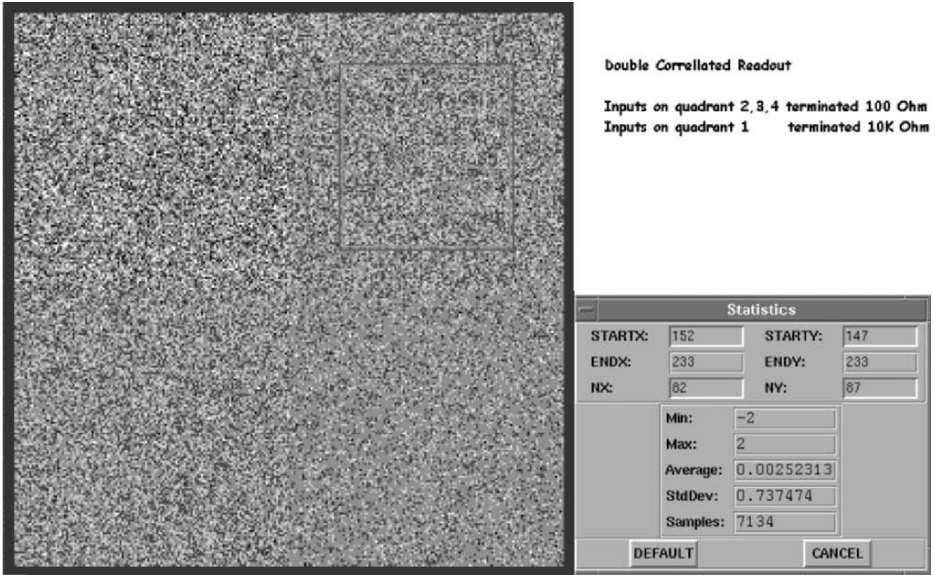
Figure 4. System noise.

6. APPLICATIONS AND ARCHITECTURES

The minimum system (see Fig. 5) consists of the back-end and front-end to readout a four channel IR detector or a CCD. If more bandwidth is required an additional link can be added. If more clocks/biases are needed or a synchronized readout of more than one or an additional/different detector must be performed this can accommodated by adding additional basic units (see Fig. 6).
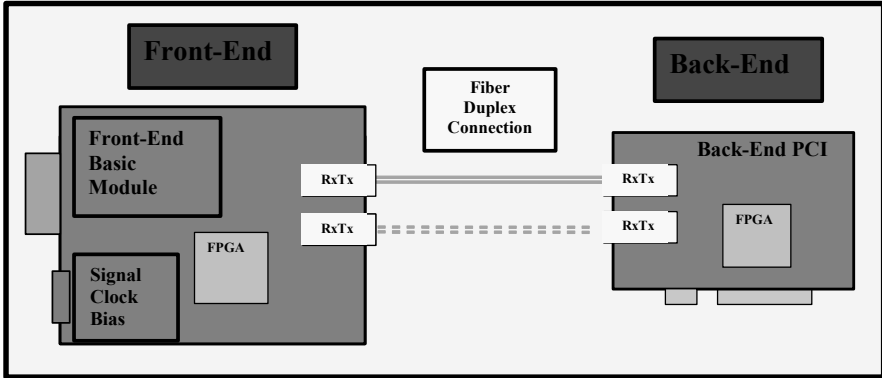
Figure 5. Minimum system.
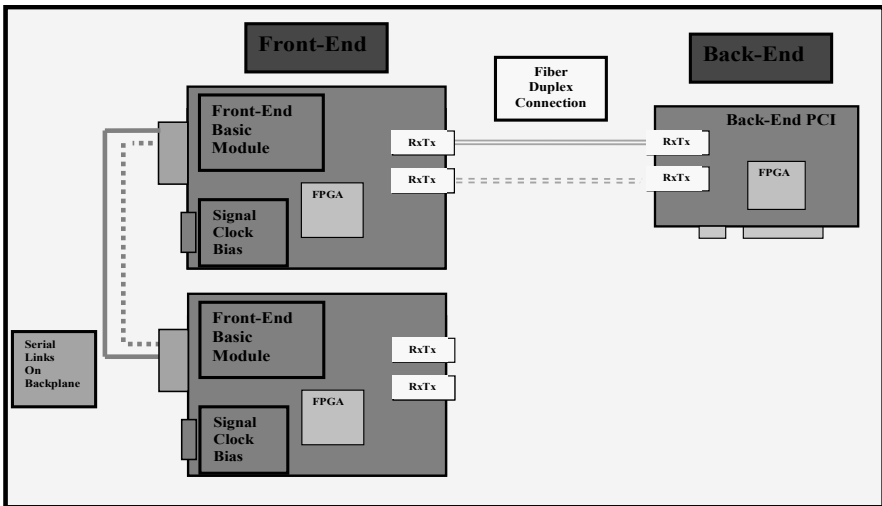
Figure 6. Synchronized readout of detectors.

Multi-channel applications for mosaics of detectors are easy to accommodate by adding additional multi-channel modules with serial links.

Applications like interferometry or adaptive optics can be connected with high speed serial links. The big advantage is that data arrives with minimum latency directly at the processing node, the FPGA. The implemented Power PC's or dedicated DSP's have direct access to the data buffers containing the image data. The processing node can be located remotely and close to functions like deformable mirrors or others (see Fig. 7).
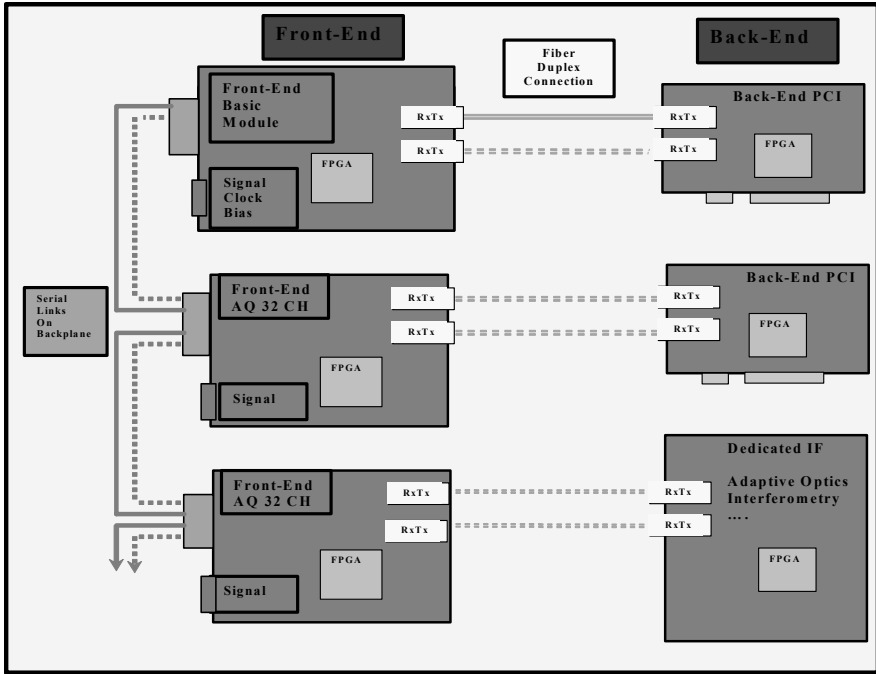
Figure 7. Multi-channel system for special applications.

7.   CONCLUSIONS

Advanced FPGA technology allows building low power and compact data acquisition systems for a wide range of applications like single detector or mosaic detector readout as well as different detectors: from the visible to the mid-infrared.

Veni, vidi, non vinci. Though he tried, Manfred Meyer has not been selected as spokesperson for Murgo Winery.

NGC FRONT-END FOR CCDS AND AO APPLICATIONS

Javier Reyes, Mark Downing, Leander Mehrgan, Manfred Meyer and Ralf Conzelman
European Southern Observatory

Abstract: *The New General detector Controller (NGC) at ESO aims at single-handedly covering optical, infrared and wavefront sensing applications. However, the detector requirements for optical, infrared and Adaptive Optics (AO) have increasingly diverged in the past years, presenting challenges in the design of the electronics. This paper extends the description of the general architecture of the controller [1] towards the specific front-end electronics to drive and read-out CCDs both for optical instruments and AO applications. In addition, the adaptation of the NGC front-end to the future ESO CCD head for AO and the control of the L3 devices are presented.*

Key words: *Adaptive optics, sensing applications, real time computer, RocketIO serial link, L3CCD, Xilinx Virtex-II Pro.*

1.   INTRODUCTION

For the first time at ESO we are trying not only to combine forces and resources to control IR and CCDs focal planes with a universal controller, but also to cover Adaptive Optics (AO) applications with the same controller. The challenges of the design results from the choice of L3CCD technology for the AO systems of VLT second generation instruments and the limited volume of the AO head [2].

The new controller at ESO must therefore seamlessly drive both scientific applications, e.g. HAWAII-2RG and e2v or MIT CCDs, and sensing applications heads, e.g. L3Vision CCDs or OTAs.

2.   NGC FOR SCIENTIFIC APPLICATIONS

Figure 1 shows a typical connection of the NGC to a cryostat on scientific applications. The front-end electronics is based on a standard 19-inch rack hosting 6U-size boards with compact-PCI connectors for the analog signals (video input, clock and bias outputs) and high-speed Erni ERmet ZD connectors for the board-to-board communication via the RocketIO serial links [3,4].
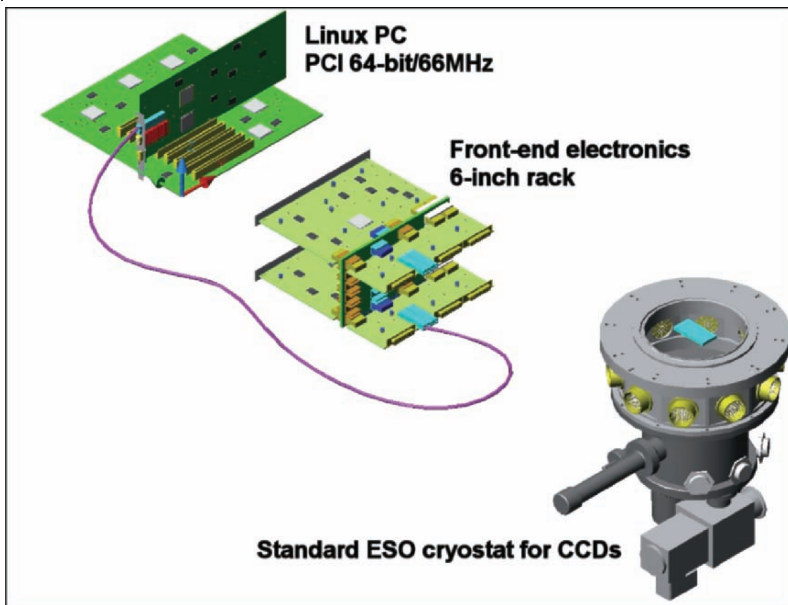
Figure 1. NGC for scientific applications.

3.   NGC FOR SENSING APPLICATIONS

By contrast, Fig. 2 shows how the NGC will be connected to a head for AO. In Fig. 2, the same Linux PC is used, but the functionality of the front-end electronics shown in Fig. 1 has been reduced to a volume of only 100×200×40 mm. The complete NGC front-end electronics needed to drive the L3Vision CCDs will be repackaged in two Eurocard size PCBs (160×100 mm) connected via high-speed serial links at 3.125 Gbps. The connection of the AO head to the back-end electronics is done through optical fiber and via the Front Panel Data Port (FPDP) protocol [4].

In the configuration of Fig. 2 the AO head sends the pixel data directly to the real-time computer for number crunching. However, another possible alternative to connect the AO head to the RTC is shown in Fig. 3. In this figure the back-end computer receives the pixel data from the front-end head and transmits it to the RTC for processing. The RTC is a multi-processor VME-based board with a commercial FPGA03 piggy-back daughter card for pre-processing, image calibration and centroiding [5].
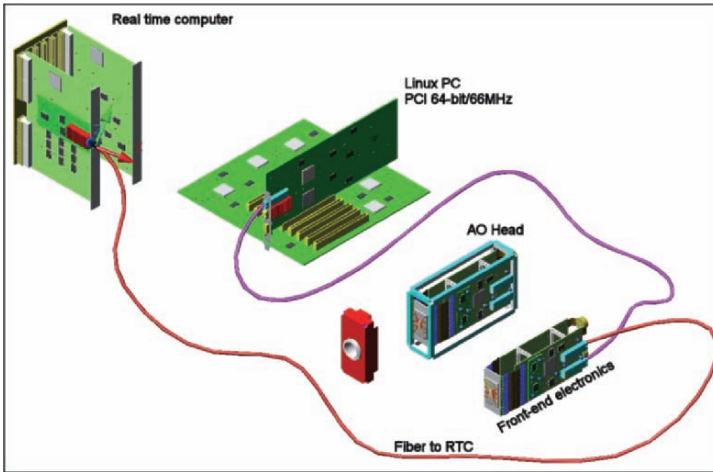
Figure 2. NGC for sensing applications. Direct connection of the AO head to the Real Time Computer (RTC).
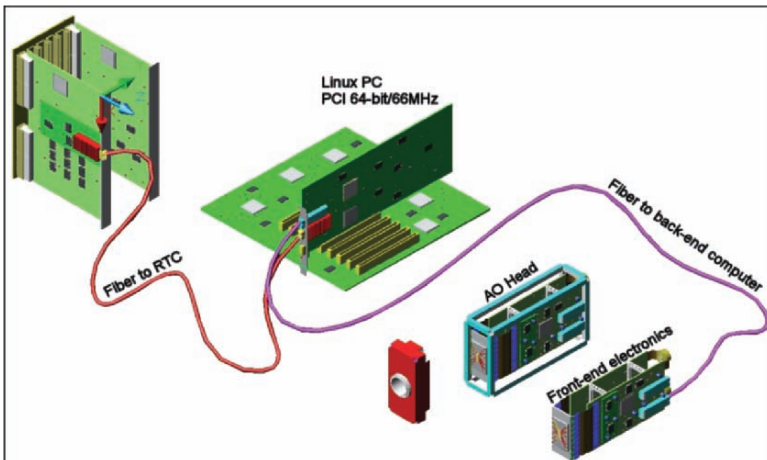
Figure 3. NGC for sensing applications (second alternative). Pixel data is sent to back-end computer. Back-end computer sends the data to the RTC.

4.   ESO HEAD FOR ADAPTIVE OPTICS

We plan to condense the functionality of the NGC front-end in two Eurocard PCBs (see Fig. 4). These PCBs will contain the high-speed high-voltage clock driver to control the L3Vision chip, the 8 fast 14-bit ADCs (for scientific applications we are currently using 18-bit ADCs) and a Xilinx Virtex-II Pro as the only digital electronics on the board.

The AO head must be compact and the electronics must be in close proximity of the CCD to avoid reflections on the high-speed clock lines driving the chip. Similarly, the fast ADCs input tracks must be shielded and as close as possible to the output ports of the CCD to avoid pick-up noise and interference from the high-speed electronics in the surrounding. Especially challenging is the generation of phase voltages close to 50 V and currents peaks of several amps [6].
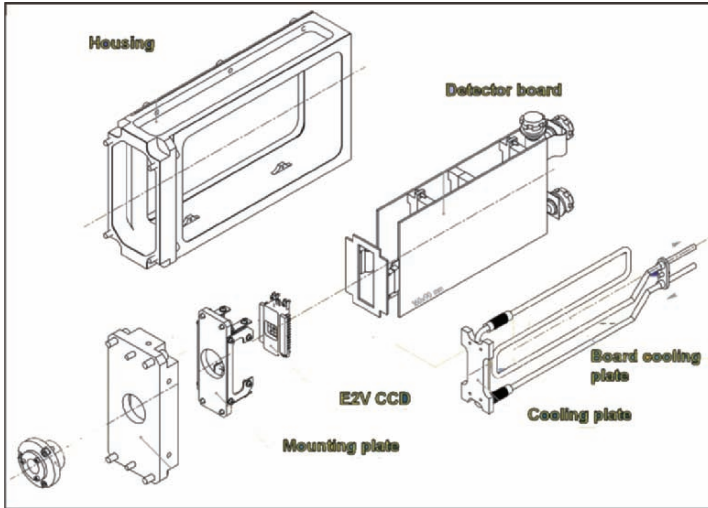
Figure 4. New ESO head for adaptive optics.

From an electronics point of view, the challenges in driving an L3CCD can be summarized as [1,7]:

- Fast reading of up to 10 Mlines per second,
- 8 output ports, 14-bit ADCs,
- Frame rate of up to 1.2 kHz,
- High-voltage, high-speed clock driver generation,
- Sampling of high-speed video with RON < 1 (0.1) e$^-$/pixel.

5. NGC FRONT-END FOR CCDS

ESO aims at reading CCDs by applying multiple sampling rather than a more laborious analog technique like dual-slope or clamp-and-sample. However, the performance obtained with multiple sampling, and principally read-out noise, is still uncertain and needs investigation.

To validate multiple sampling, the readout noise must be in the order of 2 to 2.5 electrons at 50 kpix/s; 4 to 4.5 electrons at 225 kpix/s and about 6 electrons at 625 kpix with an e2V CCD-44 chip. If multiple sampling does not achieve the desired performance, we plan to develop a dedicated board for CCDs with dual-slope or clamp-and-sample as currently implemented in FIERA (ESO's CCD controller).

6. CONCLUSIONS

The new controller at ESO, NGC, covers both scientific applications and sensing applications indistinguishably with the same controller and the same core electronics. The design challenges of driving L3Vision CCDs are various and intrinsic to the characteristics of the new chip. Moreover, additional constraints arise from the available space for the electronics inside. NGC plans to read-out CCDs by using digital multiple sampling, but the performance is still to be validated.

7. ACKNOWLEDGEMENTS

8. REFERENCES

[1] Meyer, M., et al., 2005, *ESO's New General detector Controller*, these proceedings.
[2] Downing, M., et al., 2005, *A dedicated L3CCD for Adaptive Optics applications*, these proceedings.
[3] High-speed connector information http://www.erni.com/.
[4] RocketIO information at Xilinx web site. http://www.xilinx.com/products/virtex2pro/rocketio.htm.
[5] Transtech FPGA03 board, http://www.transtech-dsp.com/io/pmc-fpga03.asp
[6] Gach, J-L., 2005, *A dedicated controller for adaptive optics L3CCD developments*, these proceedings.
[7] Mackay, C., 2005, Near *Diffraction Limited Visible Imaging on 10m class telescopes*, these proceedings.
[8] Tulloch, S., 2005, *L3CCD Wavefront Sensor Developments at the ING*, these proceedings.

Javier Reyes presented his poster with enthusiasm!

The participants enjoyed the demonstration of
Champagne corking at the Murgo Winery.

SOFTWARE FOR THE ESO NEW GENERAL DETECTOR CONTROLLER

Claudio Cumani, Andrea Balestra, Joerg Stegmeier
European Southern Observatory

Abstract: *An introductory overview is given of the control software for the ESO New General detector Controller (NGC), which will handle the detectors of both optical and infrared new instruments at the ESO telescopes.*

Key words: *CCDs, optical and infrared detectors, detector controllers, software.*

1. INTRODUCTION

NGC is the ESO New General detector Controller, designed to handle the detectors of both optical and infrared instruments, for scientific imaging as well as for advanced signal sensing applications. It is being developed on the basis of experience with the actual ESO standard controllers, FIERA for the optical domain [1,2] and IRACE for the infrared [3], and the provisions of a new generation of detectors.

2. NGC HARDWARE

NGC is a modular system consisting of back-end and front-end modules based on the XILINX Virtex Pro FPGA XC2VP7 FF 672. The back-end modules are connected to the acquisition computer (the so called LCU or Local Control Unit) via a 64 bit PCI bus interface.

The front-end modules, which create and receive the detector signals, are connected to the back-end modules via fiber optic links with transmission rates of 2.5 Gbit/s. Clock signals for the detectors are generated by the

sequencers which are completely implemented inside the FPGA of the front-end modules. The communication between all system modules is based on packet transmission over high speed serial links [4,5].

3. NGC SOFTWARE REQUIREMENTS

3.1 High-Level Requirements

The VLTSW (Very Large Telescope control SoftWare) environment defines the software standards to be used or fulfilled, in terms of programs, utilities, protocols and interfaces. At high level, the NCG software must be able to replace the FIERA and IRACE software: all the interactions with the instrument and telescope software will be performed in the same way as is performed for FIERA and IRACE (VLT message, error and logging system, SETUP files and image files in FITS format, etc.).

Experience has shown that it is important that the same code that is used for operating the telescope is also used in the laboratory for rapid prototyping, testing and calibration. This requires detector control software which is flexible enough to let engineers test a system extensively, but at the same time defines different levels of operational freedom well and carefully, to ensure safety during the normal operation.

As defined by the VLT paradigm, operations through observation blocks will drive the NGC software at the telescope, adding another level of protection from operational errors.

3.2 Intermediate-Level Requirements

Particularly at the LCU level, the merging of optical and infrared detector controllers is also an interesting challenge from the software point of view. The NGC software must consider a variety of requirements originating from different domains:

- huge on-the-fly processing of the acquired data (infrared detectors)
- shutter handling and cryostat vacuum and temperature control (optical detectors - see Geimer, et al. [6])
- strict timing requirements (interferometry or high time resolution imaging or spectroscopy - see [7])
- synchronization with external signals (multiple cameras, va-et-vien, nodding, chopping)
- interface to real-time-computers (adaptive optics)

- fast image assembly and storage in FITS files (big detector mosaics)
- continuous readout and storage in FITS files (drift-scanning).

All these functions must be achieved along with stiff performance requirements.

3.3   Low-Level Requirements

The interface with the NGC modules defines the requirements for the low-level part of the NGC software.

Signals to be sent to the detectors must be loaded into the sequencer RAM of the FPGA of each so-called NGC front-end "Basic Module", following a well defined structure (see Meyer, et al. [4]).

4.   NGC SOFTWARE DEVELOPMENT ENVIRONMENT

The EUP (Enterprise Unified Process) iterative approach is being used, following the standard development phases of requirements: analysis & design, development, testing, and commissioning.

Extensive utilization of "use cases" has been the basis for software design.

In order to guarantee reusability, the use cases and design patterns which are being defined for NGC should become the future "building blocks" in the ESO detector control software area.

DOORS is being used during the life-cycle of the NGC software. DOORS is a widely used requirement management tool, which allows easy management of all documents, with mutual references and easy traceability (requirements vs. design vs. implementation vs. test).

The possibility of using XML language is currently being explored. XML may be used for the configuration description of systems. In a later stage it may also be conceivable to use XML files for code generation.

Version control is enforced by using standard ESO tools (e.g., CMM).

5.   NGC SOFTWARE DEVELOPMENT AND STATUS

The core of the NGC software is developed with C/C++, while Java and Tcl/tk are used for graphical user interfaces or standalone applications.

The NGC LCU will run Linux. At the moment, a device driver for Red Hat Linux 2.4.20 has been developed for the NGC prototype, together with

part of the NGC Base Software, which contains functionalities such as a transparent threads interface, priority control, etc. Porting to Scientific Linux and kernel 2.6.x is under way.

The pre-processing framework for the multi-threaded Acquisition Process, which is required only for IR applications, has been taken over from IRACE.

The sequencer is the code used to load elementary detector timings (stored in patterns), voltages (stored in configuration files) and programs into the sequencer of the NCG. Patterns can be executed in series and/or loops, at different speeds (i.e., clock frequencies), with different intervals. Changes in pattern execution can be performed on the fly. A graphic tool for the pattern creation is under development.

A Controller Interface provides modular objects to control the Sequencer and the ADCs on the front-end modules, for interfacing to the acquisition process and for the asynchronous data reception. The objects can be assembled in an arbitrary way to reflect all functionalities of any NGC hardware configuration.

Test code is developed in parallel as an integrated part of the NGC software and is integrated in the ESO modular test procedures. Concerning the code on the LCU, analysis has shown that the differences between optical and infrared operations suggest different designs for infrared and visual in order to achieve higher efficiency and to avoid unneeded complexity.

The goal is a control software which is robust, modular (for fast prototyping and easy maintenance), safe (the same software must run in the laboratory and at the telescope, with different levels of operational freedom) and flexible (to handle any future development in hardware and software).

6. REFERENCES

[1] Beletic, J.W., Gerdes, R., DuVarney, R.C., *FIERA: ESO's New Generation CCD Controller*, Kluwer, ASSL, vol. **228**, pp. 103-114.
[2] Cumani, C., Donaldson, R., 1998, *The Architecture for two Generations of ESO VLT CCD Controllers*, Kluwer, ASSL, vol. **228**, pp. 115-122.
[3] Meyer, M., Mehrgan, H., Nicolini, G., Stegmeier, J., 1998, *The ESO Infrared Detector High Speed Array Control and Processing Electronic IRACE*, SPIE, vol. **3354**, pp. 134-138.
[4] Meyer, M., et al., these proceedings.
[5] Reyes, J. et al., these proceedings.
[6] Geimer, C., et al., these proceedings.
[7] Cumani, C., Mantel, C. H., 2000, *Phase resolved High Speed Photometry and Spectroscopy of Pulsars*, Kluwer, ASSL, vol. **252**, pp. 311-317.

KEEPING CONTROL: PULPO 2
ESO's New Cryostat Housekeeping Unit

Christoph Geimer, Claudio Cumani, Nicolas Haddad, Javier Reyes, Javier Valenzuela, Bernhard Lopez
European Southern Observatory

Abstract: *PULPO 2 is ESO's new housekeeping unit to monitor and control temperature, pressure and shutter of the CCD systems. In particular, it can monitor up to 125 temperature sensors and control the focal plane temperature with up to 8 independent heaters. PULPO 2 features a set of configurable alarm outputs for temperature and vacuum, which can be connected to a central alarm system and/or a dialer. A self recovery feature ensures that the CCDs are protected in case of an alarm condition. System monitoring and debugging is guaranteed by intensive sensor data logging.*

Key words: *CCD, vacuum control, temperature control, shutter control, safety.*

1.   INTRODUCTION

Mosaics put tough requirements on temperature control and housekeeping functions. Thus far, ESO has used PULPO [1] for this purpose. 33 units have been built for 16 instruments, but contemporary mosaics, like ESO's OmegaCAM [2] with 36 CCDs in the focal plane, require a new approach [2,3]. For this reason, ESO has developed a new housekeeping unit, PULPO 2 (see Fig. 1) [4].

Key features of PULPO 2 are:
- Monitoring of 29 PT100 sensors (4 wire system) by default and up to 125 with external multiplexer boards.
- Temperature control of the focal plane with up to 8 independent heaters.

- Monitoring of the vacuum in the cryostat (by means of Balzers or Edwards vacuum gauges).
- Separate alarm outputs for temperature and vacuum.
- Shutter handling with control of the exposure time and measurement of open and close delays.
- Internal logging of numerous system parameters over time (up to 65000 records), thereby making PULPO 2 a valuable trouble shooting and optimizing tool.
- Backward compatibility with PULPO.

The PULPO 2 control software exploits all capabilities of the hardware to implement further functionality for system monitoring and recovery to a safe state in case of failure.
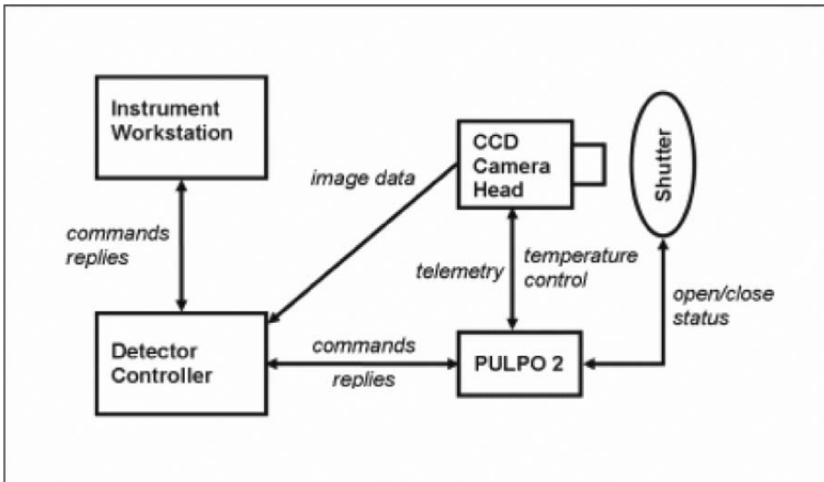
Figure 1. PULPO 2 in the VLT environment.

2.   DESCRIPTION

PULPO 2 is a compact unit (230mm×105mm×120mm) containing two Eurocard-size (160mm×100mm) boards. The CPU board contains an embedded PC running the PULPO 2 control software under Linux and provides power to the rest of the unit. The peripheral board contains all circuitry needed to fulfill the required housekeeping functions: PT100 inputs, amplifiers and 16-bit ADC, shutter interface, alarm output, vacuum monitoring and temperature regulation. The communication between the two

boards follows the ISA bus standard (as defined in the "IBM PC/AT Technical Reference Manual").

3.   THE HARDWARE

The PULPO 2 CPU board (see Fig. 2) is a Eurocard-size board. The core component is a credit card sized embedded PC module from Compulab. It hosts a complete PC with 486 processor, integrated 16 MB flash disk, 32 MB of RAM, Ethernet controller and all standard PC peripherals (serials, parallel port, IDE controller, etc).
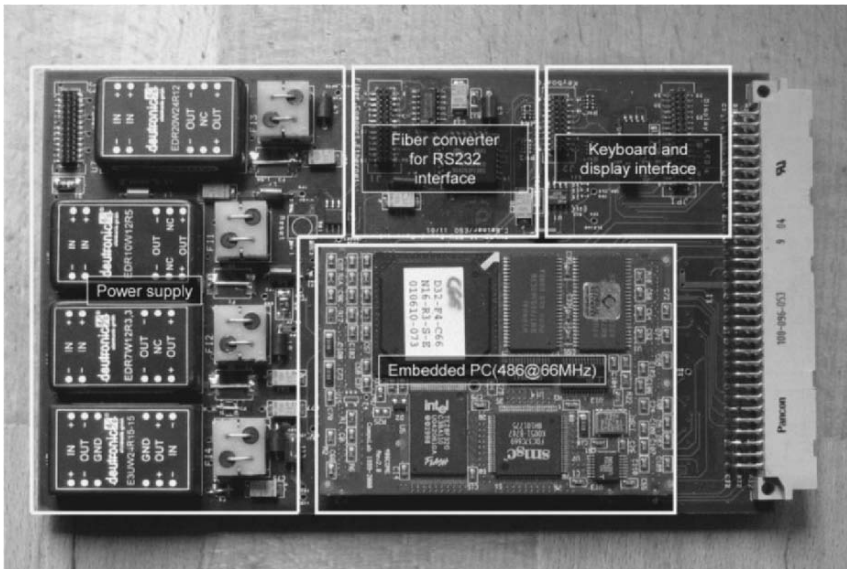
Figure 2. PULPO 2 CPU Board.

PULPO 2 is supplied with +24V from the FIERA [5] linear power supply. All internal voltages (+5V, +3.3V, ±15V and +12V) are generated on the CPU board by means of DC/DC converters. Each voltage has auto-resetting SMD fuses. Standard bypassing plus additional PI filters are used to smoothen the supply voltages. A voltage supervisor, MAX814, on the 5V supply is used to generate a reset on power-up and in the case of power failure. The MAX814 also provides the option of a manual reset via a button on the front panel. A 3V lithium battery with 3 years lifetime is used to keep the RTC (Real Time Clock) on the 486Core running in case of a power failure.

The RS232-to-fiber interface is built around a ML4624 chip. It drives an Agilent HFBR 1414 transmitter and receives commands via a HFBR 2416 receiver. The fiber can be up to 1500 m long. The display on the front panel is a Varitronix MGLS 12864T.

The PULPO 2 Peripheral Board (see Fig. 3) contains all interfaces to the cryostat and the shutter. The core component here is a PLD that controls all the interfaces on the board and handles the communication to the CPU board.

The sensor interface contains a multiplexer group with 32 inputs. One channel is used for monitoring the vacuum in the cryostat (Balzers or Edwards gauges, set by software), another for the onboard sensing of the heater current and another for an internal calibration resistor. The other 29 channels can be used to connect external PT100 sensors (4-wire system).

The output of the multiplexers travels via a two-stage amplifier with programmable gain into a 16-bit ADC. Low gain (G=8) is used for heater current and vacuum sensing. High gain (G=72) is used for PT100 input.
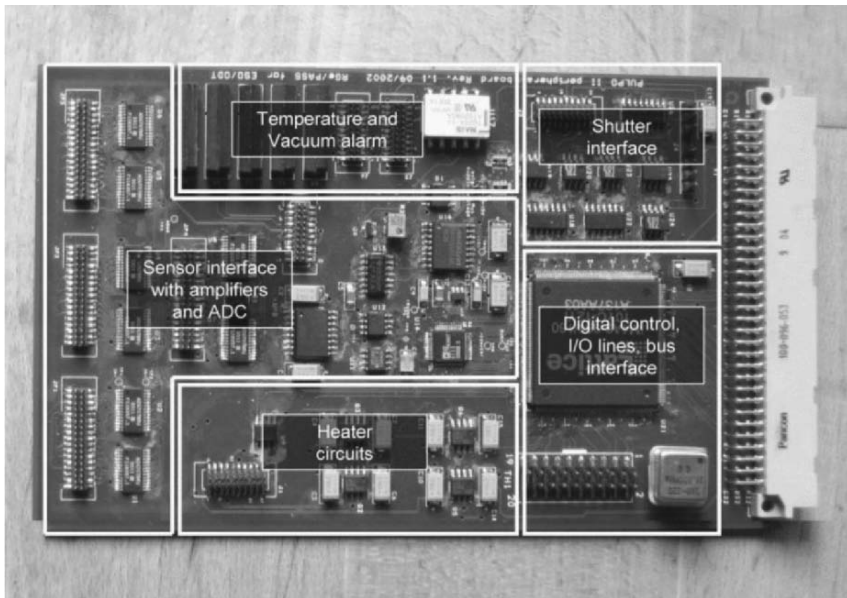
Figure 3. PULPO 2 peripheral board.

PULPO 2 uses PWM (Pulse Width Modulation) for the heater control. The power dissipation inside the unit is therefore very small (~30 mΩ per heater). A total of 8 independent or jointly used heaters are available. The heaters are operated with the linear +24V supply in order to avoid switching

noise (from the DC/DC converters) in the focal plane. The maximum heater current is 3A, giving a maximum heating power of up to 72W.

PULPO 2 also features a set of alarm outputs for temperature and vacuum. Four independent alarm outputs are available (2 for temperature and 2 for vacuum problems). The alarm values for temperature and vacuum can be configured by software and can be connected to a Central Alarm System and/or a dialer.

Optical detectors normally require a mechanical shutter to control a shutter. PULPO 2 offers 1 output (open command) and 4 inputs (open status, close status, remote, and fail). All of them are optically isolated in order to avoid ground loops. Exposure time counting and the measurement of the open and close delays are handled by the PLD. The logic for the I/O lines is programmable via the software, enabling PULPO 2 to interface with almost any type of shutter.

4.   THE SOFTWARE

PULPO 2 runs a customized version of embedded Linux. The code has been written in C and assembler. Different threads keep control of the temperature sensors and heaters, the shutter, the user interfaces (serial port, display, keyboard), using on average 4% of the CPU.

Most of the features offered by PULPO 2 are implemented via the control software on the CPU Board.

The communication between the SLCU (FIERA's host computer) and PULPO 2 goes through a simple serial link (RS232).

The protocol consists of a two character commands followed by several parameters (e.g., the command *SP,1,153* sets the temperature control for heater 1 to 153 K). Currently there are 60 commands available. Several status bytes can be retrieved via the serial link to get information about the current status of the device.

The software controls the peripherals via a set of registers that are implemented in the PLD. The PID tuner that is required for accurate temperature control is also implemented in software. The accuracy of the temperature regulation is typically ±0.1 K for the control sensor assigned to a heater. Other valuable software features are data logging and self recovery.

4.1   Data Logging

The 486Core runs embedded Linux. Therefore, only 60% of the flash disk is used for the OS, leaving approximately 9MB free to store the data from the connected sensors. The logging interval is adjustable. The number

of records that can be stored on the flash disk is currently 65000. In the case of OmegaCAM this is sufficient to log all 101 sensors for almost 7 days if the log interval is set to 15 minutes.

The log file is cyclic, which means that the first entries will be overwritten as soon as the number of 65000 records is reached. It is written in plain ASCII format and can be easily analyzed through standard tools like Microsoft Excel.

4.2   **Self Recovery**

The self recovery feature ensures that the CCDs are protected in case of an alarm condition. One of the sensors connected to PULPO 2 can be selected to trigger this feature. As soon as the alarm from this sensor is triggered, PULPO 2 will start to heat the CCDs to ensure that the CCDs are always warmer than the rest of the cryostat. This will avoid contamination.

5.   **STATUS**

Thus far, two PULPO 2 units have been assembled and intensively tested with the OmegaCam instrument [2]. Temperature control through 103 sensors and 4 heaters in the CCD camera head has shown a good level of temperature distribution (±1,25 K across the mosaic), while the alarm and self recovery system has proven to be safe and reliable.

6.   **REFERENCES**

[1] Haddad, N., Sinclaire, P., 1998, *PULPO: Temperature, Vacuum, Shutter, LN ₂Level, All in One Box*, Kluwer, ASSL Vol. **228**, p. 131-134.

[2] Iwert, O., et al., 2005, *The OmegaCAM 16K×16K CCD Detector System for the ESO VLT Survey Telescope (VST)*, these proceedings.

[3] Reyes-Moreno, J., Geimer, C., Balestra, A., Haddad, N., 2004, *Upgrade of ESO's FIERA CCD Controller and PULPO subsystem*, Kluwer, ASSL, vol. **300**, pp. 449-452

[4] Cumani, C., Geimer, C., Haddad, N., Lopez, B., Reyes-Moreno, J., Valenzuela, J., 2004, *PULPO 2 Manual*, ESO, VLT-TRE-ESO-13630-3490

[5] Beletic, J.W., Gerdes, R., DuVarney, R.C., 1998, *FIERA: ESO's New Generation CCD Controller*, Kluwer, ASSL, vol. **228**, pp. 103-114

WE MUST BE MAD
Pushing FIERA to its Limits

Roland Reiss, Andrea Balestra, Claudio Cumani, Christoph Geimer, Javier Reyes, Enrico Marchetti, Joana Santos
European Southern Observatory

Abstract: *MAD (Multi conjugate Adaptive optics Demonstrator) is an MCAO pathfinder experiment for both OverWhelmingly Large (OWL) 100 m telescopes and ESO VLT 2nd generation instrumentation. MAD's Wave Front Sensor (WFS) employs five thermo-electrically cooled e2v CCD39-01 devices operating in two modes: the multi Shack-Hartmann (SH) WFS consists of three CCDs with 80×80 pixels which are read in parallel at up to 400 frames per second delivering a pixel rate of 4.8 Mpix/sec at lowest noise. The Layer Oriented (LO) WFS is constructed with two CCDs of the same type but both detectors are read simultaneously with different frame rates and binning factors using a single FIERA controller. This paper discusses the concept of both SH and LO wave front sensors and gives first performance results from laboratory tests. We report on techniques used to implement and improve clock patterns and the lessons learned during the development phase.*

Key words: *Adaptive optics, CCD, multi conjugate, Shack-Hartmann, thermo-electrical cooling, wavefront sensor.*

1.   OVERVIEW

   MAD will investigate two different approaches of MCAO correction with two independent techniques: the Star Oriented MCAO with a Multi Shack-Hartmann Wavefront Sensor (SHWFS) and the Layer Oriented MCAO with a Layer Oriented Wavefront Sensor (LOWFS). The design of the MUSE WFS was driven by the requirement to re-use as many key components (e.g., the FIERA controller) as possible. The design is simplified by the fact that the FIERA controller [1] must operate in only one WFS mode at a time.

The detector system is based on five CCD39-01 devices from e2v technologies. These devices have split frame transfer architecture with 80×80 active pixels and four outputs and are available in a hermetically sealed package which includes a thermo-electrical (Peltier) cooler.

Table 1 shows the hardware configuration for both operating modes of the FIERA controller. Each video board has four channels, each clock board can provide 14 fully programmable clocks (only 10 are used for MAD) and the bias board can provide a total of 32 DC voltages to the CCD chips.

Table 1. FIERA configuration for MAD.

Item	SHWFS	LOWFS
Bias board	CCD1, 2, 3	CCD4, 5
Clock driver I	CCD1	CCD4
Clock driver II	CCD2	CCD5
Clock driver III	CCD3	Not used
Video board I	CCD1	CCD4
Video board II	CCD2	CCD5
Video board III	CCD3	Not used
Communications board	Required	Required

2.   SHACK-HARTMANN WAVEFRONT SENSOR MODE (SHWFS)

The timing for the three SHWFS CCDs is straightforward (see Fig. 1). All three CCDs operate with the same frame rate and binning factors (1×1 or 2×2). In principle, the three CCDs could be operated by a single clock driver board because their timing is identical. However, in practice the wiring is more complex and performance is reduced due to longer cable lengths and larger capacities. Therefore each CCD is now driven by its own clock driver board, which allows chip specific settings of clock levels.

The frame rate required for the SHWFS mode is 400 Hz (for a 64×64 window). A timing budget was established given the constraints of the CCD39-01 for maximum vertical and horizontal clocking rates and of the FIERA controller for maximum pixel rate. Table 2 shows this budget, assuming four horizontal prescans, one "pipeline" and two overscan pixels (to clean the horizontal register) per CCD quadrant. Similarly, two overscan lines for each half of the CCD are factored in.

Unfortunately, in executing the CCD clock patterns the FIERA controller created unexpected clocking overhead, which slowed the frame rate in SHWFS windowed mode from a theoretically possible 480 Hz to a much lower value of approx. 370 Hz. One kind of overhead was identified in the execution of loops, another was observed when executing very short clock patterns (i.e. vertical line shift with 2 μs duration, but ~9 μs of excess

overhead). The loop overhead was reduced by unrolling the inner loops of the timing patterns which are executed 32 times in the case of windowed SHWFS mode. The second measure combined the short patterns for line shifting and skipping pre- and overscan pixels into one single pattern. After these modifications, the "execution" time of 4000 frames has been measured at 10.2 s, which corresponds to a frame rate slightly below 400 Hz.
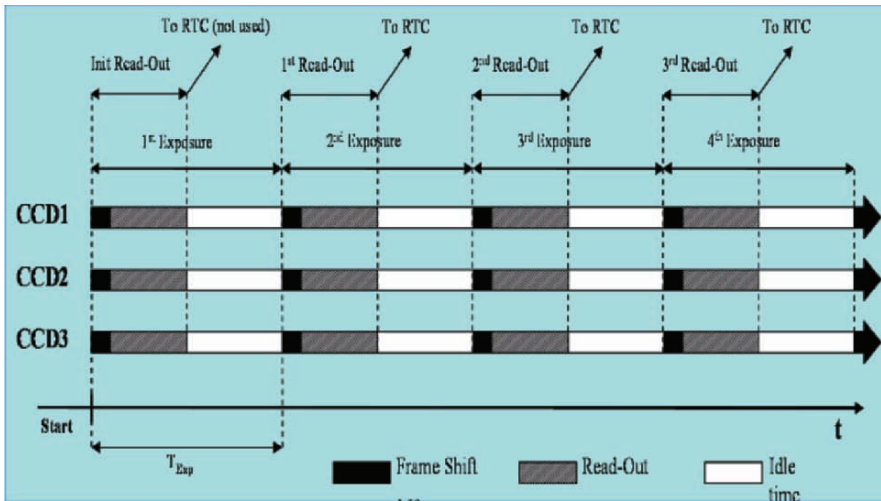
Figure 1. Shack-Hartmann readout sequence.

Table 2. Timing budget for SHWFS and LOWFS modes.

Chip format	
No. of outputs hor.	2
No. of outputs ver.	2
Total hor. pixels	94
Total ver. pixels	84

3.   LAYER ORIENTED WFS (LOWFS)

The timing for the LOWFS mode is more complex (see Fig. 2). Not only do the two CCDs read with different frame rates (1:2 or 1:4), but both CCDs require different binning factors. The FIERA controller makes use of local microsequencers on each clock and video board. These microsequencers are loaded, triggered and monitored by the DSP controlling the complete readout sequence, allowing each board to have different timing. The only constraint is that the lengths of these clock patterns must be identical.

The issue of different horizontal binning factors for the two CCDs was addressed by a clock pattern that bins four pixels on one CCD, but only two pixels on the other by omitting clock transitions on the latter. As the standard FIERA software expects an equal number of pixels to be read from all CCDs, dummy pixels are read from the CCD with the higher binning factor. They are ignored by the subsequent image processing routines. A similar method is applied for the vertical binning. While the first CCD is subject to four line shifts two of them are skipped on the second device.

Different frame rates are executed in such a way that a virtual frame is defined which contains two or four frames, depending on the frame ratio of 1:2 or 1:4. While each frame of the CCD with the higher rate is "clocked", the CCD with the lower rate skips one out of two or three out of four. The result is a frame with many dummy pixels which are ignored by the software.

Table 3. Timing budget for SHWFS and LOWFS modes.

Mode	SHWFS 1×1	SHWFS 1×1 windowed	LOWFS 2×2	LOWFS 4×4
No. active hor. pixels	94	64	94	94
No. active ver. pixels	84	64	84	84
Binning hor.	1	1	2	4
Binning ver.	1	1	2	4
No. active pixels	7896	4096	7896	7896
Inactive hor. pixels	0	1920	0	0
Inactive ver. lines	0	20	0	0
System timing	**µs**	**µs**	**µs**	**µs**
Pixel period	1,60	1,60	1,60	1,60
Horizontal shift	0,60	0,60	0,60	0,60
Vertical shift	2,00	2,00	2,00	2,00
Results	**µs**	**µs**	**µs**	**µs**
Frame transfer	84,00	84,00	84,00	84,00
Clear line	56,40	56,40	56,40	56,40
Read active pixels	3158,40	1638,40	789,60	197,40
Binning overhead	0,00	0,00	296,10	222,08
Skip inactive pixels	0,00	288,00	0,00	0,00
Skip lines	0,00	20,00	0,00	0,00
FIERA overhead	n/a	600,00	n/a	n/a
Frame period	3298,80	2686,80	1226,10	559,88
Max. frame rate [Hz]	303,14	372,19	815,59	1786,11
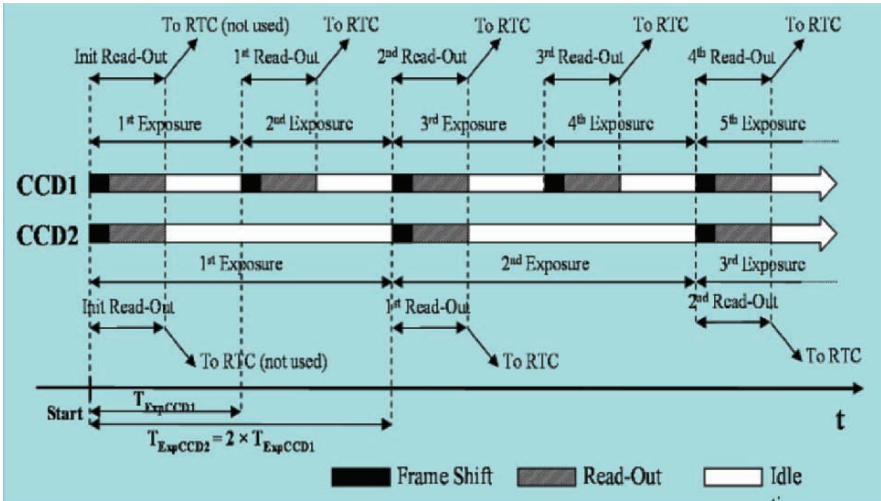
Figure 2. Layer oriented readout sequence.

4.   MECHANICAL CONSTRAINTS

The size of the complete detector head is limited to a volume of $96 \times 68 \times 30$ mm^3. The electrical connections must be very flexible because the heads are mounted on motorized x-y-tables. The adopted solution is a rigid-flex Printed Circuit Board (PCB) which contains clock filters, junction FET buffers and constant current loads for each CCD output (see Fig. 3). The e2v Peltier package is tightly attached by screws to the aluminum base plate. The base plate has mating connectors for water cooling. With an input power of eight Watts to the Peltier cooler, a temperature difference between hot and cold surfaces of about 45°C was measured. With a liquid coolant temperature of typically 10°C a CCD temperature of -35°C can be reached.

5.   PERFORMANCE DATA (SHWFS)

Figure 4 shows a typical example of a SHWFS image with three CCDs reading out simultaneously. A frame rate of 400 Hz with a total of 64×192 pixels was achieved. This corresponds to an average pixel rate of 4.9 Mpixel/sec and a burst pixel rate of 7.5 Mpixel/sec. The noise level for all 12 channels is ~6 e$^-$ RMS, with a conversion factor of 1.7 e$^-$/ADU.
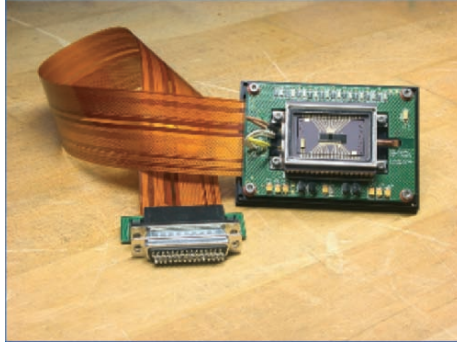
Figure 3. Rigid-flex PCB.
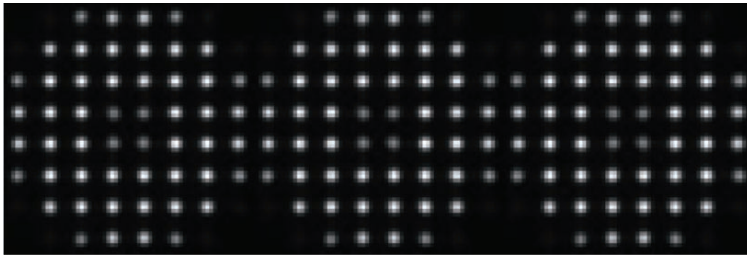
Figure 4. Sample image, Shack-Hartmann mode, 3×64×64 pixels.

6.   REFERENCES

[1] Gerdes, R., Beletic J. W., and Duvarney, R. C., 1998, *Design concepts for a fast-readout low-noise CCD controller,* Optical Astronomical Instrumentation, Sandro D'Odorico (Ed.), Proc. SPIE Vol. **3355**; p. 520-528.

256 CHANNEL DATA ACQUISITION SYSTEM FOR VISTA FOCAL PLANE TO READOUT SIXTEEN 2K×2K RAYTHEON VIRGO DETECTORS

Largest System of its Kind

Leander H. Mehrgan[1], Nagaraja Bezawada[2], Reinhold Dorn[1], Siegfried Eschbaumer[1], Gert Finger[1], Manfred Meyer[1], Joerg Stegmeier[1], Guy Woodhouse[3]

[1]European Southern Observatory, [2]UK Astronomy Technology Centre, [3]Rutherford Appleton Laboratory

Abstract: *The ESO standard Infrared Array Control Electronics, IRACE, is used to read out the VISTA focal plane, which contains sixteen 2K×2K VIRGO detectors. Each detector has 16 parallel video output channels. In total 256 video channels must be processed resulting in a readout time for the complete focal plane of less than 1 sec. The IRACE system is modular and can be adapted for VISTA. It contains 27 VME size boards, which are distributed in three separate VME crates. Sixteen boards are ADC-type, each accommodating 16 video channels. All three boxes are connected by digital isolated differential signal cables to avoid any timing jitter and to trigger all ADCs simultaneously. An additional module must be designed, which uses digital isolators to distribute the main signals like system clock, trigger pulse, reset signal and status bus control signals. The number cruncher of the data acquisition system needed for data capturing and preprocessing is realized by three high speed Linux-PC's with dual 3 GHz CPU's*

Key words: *Data acquisition system, IRACE, VISTA, Raytheon Virgo detector, NGC.*

1. INTRODUCTION

The Visible and Infra-Red Survey Telescope for Astronomy (VISTA) is a 4 m diameter wide field survey telescope, which is in development for delivery by late 2006. When completed it will be the world's largest

telescope dedicated to ground-based survey work and will become part of ESO's Cerro Paranal Observatory. The VISTA IR Camera will use a mosaic array of 16 Raytheon 2K×2K VIRGO detectors at its focal plane (see Fig. 1) [1, 2]. Each detector has 16 parallel video output channels. In total 256 video channels must be processed, resulting in a readout time for the complete focal plane of less than 1 sec. In order to control these detectors, ESO's standard Infrared Array Control Electronics, IRACE, is used to control and read out the VISTA focal plane. The IRACE system is modular and has been adapted for VISTA IR camera requirements.
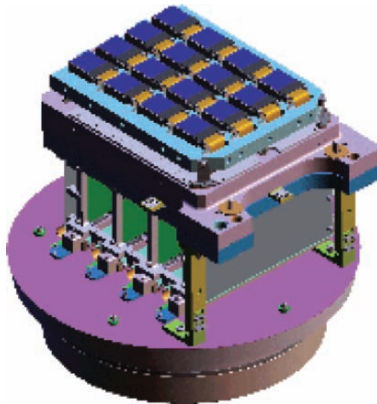
Figure 1. VISTA focal plane accommodating 16 2K×2K Raytheon VIRGO detectors.

2.   SYSTEM DESCRIPTION

To build a 256-channel system, all boards, in total 27, are distributed over three separate racks 19 inch wide (see Fig. 2). The main rack, called master rack, contains clock- and bias-driver boards, sequencer, Giga-Link and sync boards. The other two racks, called slave racks, contain sixteen ADC boards, eight boards per rack. Each board accommodates 16 video channels. Because of the bandwidth limitation of the IRACE-PCI card (up to 65 MB/s) it was necessary to split the backplane into two groups. Each group contains four ADC boards and one Giga-Link board, which captures and transmits the data over the fiber optic to the host PCI card. To avoid any timing jitter of ADC convert pulses, the master clock and convert pulses are distributed by the master rack to two slave racks.
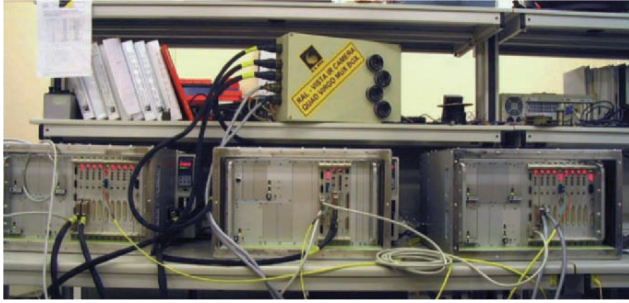
Figure 2. In the test phase the system has been operated with four VIRGO bare multiplexers at RAL (Rutherford Appleton Laboratory).

2.1 Master Rack

The master rack contains two clock- and bias-drivers, one sequencer, one sync and one Giga-Link module. The Giga-Link module is only used for the command interface to the whole system (i.e. downloading configuration-files, setting voltages, reading telemetry data and status bus controlling). To reduce the number of required boards, several clock- and bias-voltages must share one source. The sync-board distributes the 20 MHz system clock, the convert pulses, the reset signal and four status bus signals to the slave racks.

2.2 Slave Rack

The slave rack contains eight ADC-boards divided into two groups by splitting the backplane. Each ADC-board accommodates 16 ADCs with a resolution of 16 bits at 500 ksps from Linear Technology. The ADC-board can also be operated in simulation mode, which means that each board can send its channel number or counter value over the backplane. In that way the digital chain can easily monitored, which is essential for the maintenance of a system with such a high number of channels.

2.3 Digital Isolator

To avoid ground loops between the racks, an additional sync-board has been developed. The main component is a digital isolator based on Analog Devices iCoupler® technology (ADuM1401). These isolation components provide outstanding performance characteristics that are superior to alternatives such as optocoupler devices, operating at 100 Mbps. The signals

have also been driven by a deferential line driver to be able to use long cables (up to 8 meters).

2.4   Cooling Box

ESO has designed a new compact and very efficient water cooling box for VISTA, which will also be used for all new instruments (see Fig. 3).
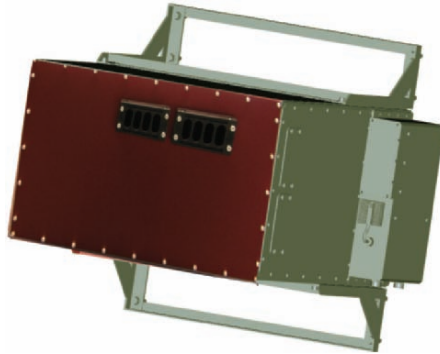
Figure 3. ESO's new cooling box.

3.   LINUX PC

The Linux PC is a rack mountable PC (double 3 GHz CPUs and 3 Gbytes of memory). It contains at least three PCI-cards, which are the host interface of the system, equipped with a full-duplex optical link, operating at one GBaud. One is used for the command interface and the other two just for data capturing. The PCI-card has a 32 bit, 33 MHz interface with a net data rate of 65 MB/s. All three PCs are connected together via Gigabit ethernet in a ring topology.

4.   DETECTOR CONTROL SOFTWARE

The IRACE software has been expanded and adapted to the requirements of VISTA. The Detector Control Software (DCS) controls all five PCI cards. Two data acquisition tasks are launched on each Linux PC. Special effort needs to be taken to guarantee data integrity on the four parallel data streams (see Fig. 4).
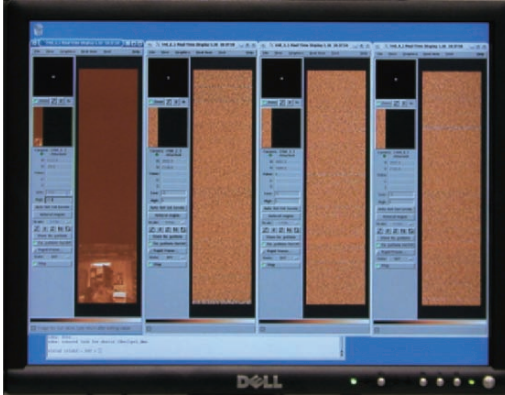
Figure 4. Four real time displays simultaneously visualize incoming data. Each display shows a group of four detectors.

5. CONCLUSIONS

IRACE is a highly flexible and modular data acquisition system, which can easily be configured to read out the 256 channels of the VISTA focal plane. The ESO's New General detector Controller, NGC, will use the accumulated experience of the IRACE system [3]. Up to 18 instruments at ESO are using IRACE to readout a large variety of infrared detectors.

6. REFERENCES

[1] Finger, G., Dorn, R., Meyer, M., Mehrgan, L., Stegmeier, J., Moorwood, A.F.M., 2005, *Performance and Evaluation of Large Format 2K×2K MBE-grown HgCdTe Hawaii-2RG Arrays Operating in 32-channel Mode*, these proceedings.
[2] Bezawada, N., 2005, *Performance Overview of VISTA IR Detectors*, these proceedings.
[3] Meyer, M., et al, 2005, *ESO's New General detector Controller NGC,* these proceedings.

Continuing to demonstrate his internationalism, AG Davis Phillips (second from left) is joined by (left to right) Nagaraja Bezawada, David Carter, Geoff Evans and Simon Tulloch.

Vyshi Suntharalingam demonstrates her new CMOS imager.

MONSOON IMAGE ACQUISITION SYSTEM PROJECT SUCCESSES AND REALITIES
"Rain drops keep falling on our heads"

Peter Moore[1] and Gustavo Rahmer[2]

[1]*National Optical Astronomy Observatory,* [2]*Cerro Tololo International Observatory*

Abstract: *The MONSOON development program reports on the current status and future plans of this project. The warm deluges of success have been followed by cold showers of reality. Future MONSOON events will be prognosticated and, because of its open source nature, readers are invited to take a shower together.*

Key words: *MONSOON, detector controller, image acquisition system, open source.*

1. INTRODUCTION

MONSOON, so named as an analogy to Tucson autumn storms which are like the intermittent but massive pixel data flux of large focal plane arrays, is now being produced to support several important instruments for NOAO facilities. The layered and extensible architecture of the MONSOON image acquisition system is being successfully applied to instruments operating in the 350 nm to 5 μm wavelength range and supporting from 1 to 64 detectors in the focal plane. The highest data rate so far achieved is 33 Mpix/sec for the NEWFIRM instrument. This requires an array of four Orion InSb detectors to be read out in a half second through a total of 256 video channels. The One Degree Imager, due to be on sky in 2009, requires an array of 64 OTA (Orthogonal Transfer Array) detectors to be read out in 2 seconds for a total data rate of 512 Mpix/sec through 512 video channels. Four MONSOON image acquisition systems are currently being used in three different laboratories as flexible controllers for hybrid IR and CCD detector characterization systems.

2.   CURRENT SYSTEMS DEVELOPMENT

MONSOON now has image acquisition capabilities for both hybrid (IR & VIS) and CCD type detectors. These capabilities have been tested in the laboratory using various detectors requiring the acquisition of 1 to 64 video signals. The structuring of the architecture into layers that are interfaced through concise Interface Control Documents (ICDs) has enabled a high degree of commonality to be used in supporting the different detector requirements. These interface documents describe the communication method and protocol between each functional layer as illustrated in Fig. 1.
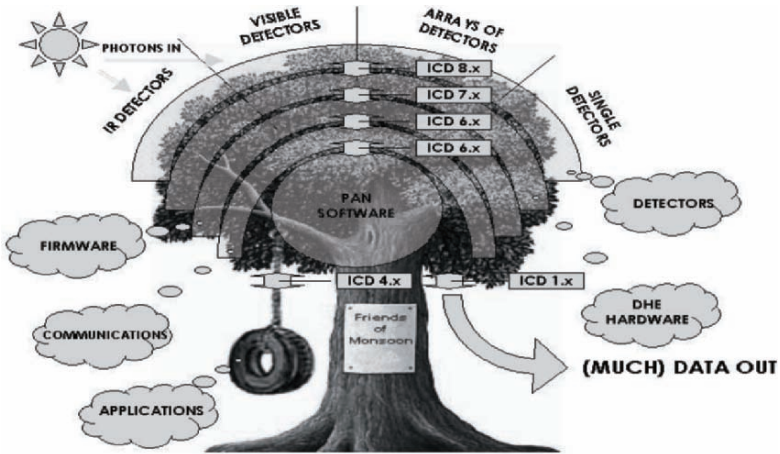
Figure 1. MONSOON function layers and interfaces.

Using the technique of layer re-use through ICDs we have delivered 5 MONSOON image acquisition systems for CCD and IR detectors and have another 9 systems that are in the development and/or construction phase. A brief description of these systems is presented in Table 1.

Table 1. MONSOON Systems Characteristics.

System Name	Detector Types	Video Count	Bias Count	Clock Count	Pixel Rate[1]	DHE Power[2]	Delivery Date
Tucson Eng	IR/CCD	36 / 8	44	32	8 / 6	37	Aug '03
Chile Eng	IR/CCD	36 / 8	44	32	8 / 6	37	Sept '03
Orion Test	IR	64	44	32	13	38	July '04
Tucson DetLab	CCD	8	44	32	6	37	Dec '04
Newfirm	IR	256	88	64	36	192	Sep '05
DES Test 1	CCD	8	44	32	6	37	Oct '05
DES Test 2	CCD	8	44	32	6	37	Oct '05
Chile DetLab	CCD	8	44	32	6	37	Oct '05
KPNO CCD	CCD	8	44	32	6	37	Nov '05
FhiRE	CCD	4	44	32	3.5	27	Nov '05
QUOTA	CCD	32	44	32	8	63	Jan '06
WHIRC	IR	32	44	32	16	26	Jan '06
DESCam	CCD	124	176	128	31	274	Mar '06
One Degree Img	CCD	512	768	1792	512	320	Mar '07

[1]Expressed as system gross pixel rate in Mpixels/sec during focal plane readout.
[2]Expressed as average power dissipation in watts.

3.   SYSTEM PERFORMANCE LEVELS

Typical video signal performance is shown in Table 2. The performance indicated by the ORION device is limited by the choice of low system gain dictated by the request of the detector development team. Typically, MONSOON allows system performance to be detector limited in terms of noise, linearity, and readout speed.

Table 2. Video signal performance metrics.

	Detector Type	System Gain	System Noise	Pixel Rate	Lin.	Dynamic range	Total noise
CCD	ST0510	6	2.7 ADU	350	< 0.1%	18 Bit	5 e⁻ rms.
		3μv/ADU	rms	Kpix	INL	1:262144	10 ADU
IR	ORION	2.54	1.3 ADU	132	< 0.1%	16 Bit	12 e⁻ rms.
		15μv/ADU	rms	Kpix	INL	1:65536	4 ADU

By using an 18 bit A/D converter on the CCD acquisition board, we can accommodate the full well dynamic range required by most detectors in one system gain setting with sufficient resolution to adequately resolve the detector noise floor. This board allows 18 bit pixel data to be sent to the image file or one of the 3 sixteen bit truncated sub-products to be acquired. In this way the conversion factor of the system (in e⁻/ADU) remains calibrated by a digital factor of two function as the system noise contribution decreases by the same amount.

4.   AN EXAMPLE OF 'CUT AND PASTE' DEVELOPMENT

The layered structure and clean interfaces of the architecture of MONSOON allows the re-use of existing hardware, firmware, and software modules. This concept was realized during the development of the CCD Acquisition Board. Table 3 lists the basic requirements for this board.

Table 3. CCD Acquisition Board Requirements.

Number of video channels	8 @ < 10μv input ref. noise
Dynamic range	18 bits linear to < 0.1% INL
Acquisition rate	800 Kpixels/sec/chan.
Detector types	P & N channel devices
Bias channels	32 @ +/- 35v low noise
High speed data port	32 bits @ 1 Mword/sec

During the design of this board, an example of a classic dual slope CDS front end design was modified to suit our purposes. This was combined with the existing IR Acquisition board A/D converter and acquisition logic module that is supported by the acquisition firmware and software modules of MONSOON for that board. In addition, the design of the bias channels used in the existing clock and bias board was modified for operation at higher voltages and then glued in a similar manner to the same firmware and software support modules used for the clock board. This was greatly facilitated by the common architecture and common hardware components used on both of these MONSOON boards. The design and production of the prototype board was completed and the functionality of the design confirmed in approximately 10 person-months of effort. However, we then discovered that while this functionality was achieved comparatively easily, the detailed optimization of the acquisition front end to meet the tight requirements took the same amount of resources as for the previous system. The entire project took a lot longer than expected (approx. 24 person-months). This was a cold shower of reality at the time.

5.   CURRENT SOFTWARE AND HARDWARE STATUS

In the three years of development by NOAO, MONSOON has reached a level of maturity and is now ready to be released for use with operational instrumentation. The requirements for detector support on these instruments (see Table 1) have been met by the layered architecture which has resulted in

a hierarchy of functional modules at the software, firmware, and hardware levels. These modules and their current release status are illustrated in Figure 2. The coupling of MONSOON hardware to different detectors used in these instruments is physically achieved through a small transition board that typically accommodates detector safety circuitry and cable connectors appropriate for each instrument. In this way, commonality of hardware and software systems among the different instruments is achieved and a common pool of spares for observatory operations is possible.
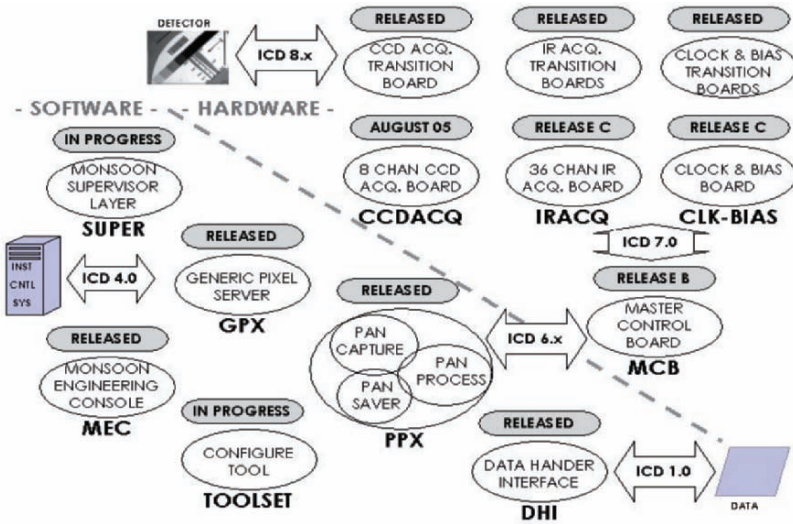
Figure 2. Module release status.

The software modules are generic to all observing and detector testing applications of MONSOON that range from IR to visible, 1 to 256 detectors per node. A small detector function library (written in C), a sequencer code module, and a system configuration file is all that is required to adapt a MONSOON system to a different detector type. For system configurations in which multiple nodes are required (for example, to support very large focal plane arrays or very high gross pixel rates), a supervisor node is established and controls the system in the same manner as a single node would appear to the instrument control system. Synchronization of events in this configuration is guaranteed to maintain noise performance with no specific software required. System and board level functional testing and general detector testing functions can be automated and performed using the MONSOON engineering Console interface. This module uses the same communication protocols as the Instrument Control System interface (ICD 4.0) and provides a stand-alone capability for engineering and systems

development use. The Data Handler Interface (DHI) provides a simple FITS format image file or a more sophisticated shared memory interface for real time pipeline processing or data offload via other media types.

6.   OPEN SOURCE RELEASE OF TECHNOLOGY

MONSOON technology was released to the public using a modified Mozilla open source license in November 2004. The principle motive for this release is to support the concept of common image acquisition architecture for astronomical observatories. Successful software products released into the public domain have seen the synergy that can be obtained through peer review, reuse and adaption of existing designs, and pooled knowledge resources. In this context we encourage other institutions to adopt and enhance the system architecture to their requirements. It is our desire to see MONSOON become a versatile image acquisition system used for technical and scientific, visible and NIR, small and large arrays of detectors. To accomplish this we ask others to take ownership of the design and eliminate the single source for detector controller paradigm. The group of users (and abusers) of MONSOON is called "Friends of Monsoon" and the establishment of a common engineering environment is being considered. Currently, access to the MONSOON technology is via agreement to the conditions of the license which essentially asks that NOAO be blameless for anything you attempt to do with the technology and that you do not license the technology as your own intellectual property. This agreement allows anyone to access the complete software, firmware, hardware, and mechanical source and technical documentation. The URL for MONSOON technical documentation is http:/www.noao.edu/ets/monsoon.

7.   MONSOON COLLABORATION HISTORY

Once the Operational Concepts Definition Document for MONSOON (OCDD) had been drafted, the document was sent to several organizations for review. It was then ascertained that similar requirements were being pursued at several of the review organizations under the code name ASTEROID. It was considered advantageous to combine the two projects and the MONSTEROID project was born. During a brief period of intense work, the requirements for this amplified project were refined and milestones were set. At this point it was discovered that sufficient funding did not exist and this multi-organization collaboration fell dormant. The first cold shower of reality: that collaboration always requires resources to be

spent by all parties but will not always bear fruit! After the successful "first light" of MONSOON hardware in the laboratory (August 2003), a collaboration was established with the WIYN observatory to co-develop the image acquisition system for the One Degree Imager (ODI). In this regard WIYN engineers have been active in the development and testing in the CCD area, specifically to support the OTA detector development project, through hardware and firmware design.

At one point we were encouraged to study the application of MONSOON to the LSST project. It was ascertained that requirements could be met by the architecture and indeed, apart from a greater number of detectors in the focal plane, the system complexity was less than that of ODI. However, funding for the camera and acquisition system was found through other agencies and this opportunity was lost by MONSOON.

Recently, collaborations have been established with the Fermi National Laboratory (FNAL) and the University of Illinois at Urbana-Champaign (UIUC). There collaborations are to develop an image acquisition system for the proposed Dark Energy Survey Camera (DES) and with the Space Telescope Science Institute (STScI) to develop code and hardware for using MONSOON with the VIRGO detectors in the WIYN high-resolution infrared camera instrument (WHIRC). Both FNAL and STScI have taken ownership of the design and construction of their respective acquisition projects while using existing components of MONSOON where appropriate. As an example of this, work is in progress at FNAL to design and construct a 12 channel CCD acquisition board based on the re-use of current functional modules from the existing 8 channel version. MONSOON systems will also be built and used to test and characterize the LBL detectors chosen for the DES project. These successful collaborations therefore give us the excuse to quote Henry Ford: "Coming together is a beginning. Keeping together is progress. Working together is success."

8.   FUTURE DEVELOPMENT PLANS

The cliché "The proof is in the pudding" will be applicable to MONSOON. Until there are operational instruments on sky with some useful history to exploit, MONSOON will not be adopted in the sense that it is intended to be: as a generic architecture for detector image acquisition systems. This will occur in early 2007 when NEWFIRM, QUOTA, a KPNO instrument, and the DES test facility will be operational. All of these instruments will be equipped with the current technology MONSOON image acquisition systems. This current technology is called MONSOON "Orange", since the hardware modules carry orange anodized front panels.

Meanwhile, the development of MONSOON will continue for future NOAO projects. The ODI instrument configuration requires a very dense Detector Head Electronics (DHE) package that is currently under development. This repackaging also involves a redesign of the front-end hardware to reduce the power dissipation in the DHE. The goal of this work is to fit the hardware support required by four OTA detectors into a footprint covered by the shadow of the four detectors themselves. When this is achieved, MONSOON will be capable of efficiently supporting arbitrary large focal planes using similar dimensioned detectors. This development is called MONSOON "Green" for the same reason as explained above.

Development for ODI is running in parallel as a small scale version of the same redesigned hardware modules as a replacement detector controller for obsolete controller technology at the national observatories. This development, code named "TORRENT", will offer the advantage of common image acquisition systems to existing instrumentation at observatories that will reduce maintenance overhead caused by disparate detector controller systems in use at the observatories. Of course, the MONSOON developments explained here are likely in harmony with many other developments in the field of astronomy and imaging. We invite others to involve themselves in this common goal to provide detector-limited performance through common and easily maintained systems. This involvement can be through direct collaboration with the project at NOAO or through the simple adoption of MONSOON technology through the open license agreement. Finally, we wish to thank all those people who have so far in the past contributed to this project through peer review, constructive commentary, or just by listening. Through you we have been able to come this far without resorting to the use of an umbrella!

Peter Moore, the most prolific questioner at the workshop,
even found a way to ask himself a question.

MONSOON IMAGE ACQUISITION SYSTEM CONFIGURATION

Gustavo Rahmer[1] and Peter C. Moore[2]

[1]Cerro Tololo International Observatory, [2]National Optical Astronomy Observatory

Abstract: *With the development of image acquisition systems designed to accommodate large mosaics of detectors, the management of documentation and the generation of configuration data sets has become increasingly complex. We present work carried out within the context of the MONSOON project that conceals this complexity within a self-documenting configuration management tool set. Following the open-source philosophy of MONSOON, the configuration data sets are based on the XML standard, making it platform-independent and easily accessible through standard web browsers.*

Key words: *MONSOON, detector controller, image acquisition, configuration, XML.*

1.   INTRODUCTION

The MONSOON image acquisition system is being developed to handle NOAO's present and future requirements for serving focal plane pixel data to higher-level software. It is designed to handle both optical and infra-red data seamlessly, independent of science acquisition instrument. When fully developed, MONSOON may be applied to single chip CCD or IR detectors, large area mosaics, photometric imaging, spectroscopy and technical imaging (the latter, for example, comprises fast guiding and wavefront sensing).

Such a wide variety of uses requires a common configuration of the system, while allowing a high degree of flexibility. This flexibility must be achieved without confusing the system user, and implemented without requiring extensive knowledge of how the configuration process works.

With simple generic data entry, following a hierarchical structure, the system should automatically generate the configuration file required by the system software.

A MONSOON system has several hierarchical levels: supervisor, Detector Head Electronics (DHE) boards, PAN-DHE pairs, transition boards, focal plane, software, etc. Most of these levels are defined at their corresponding design time (e.g., the DHE board functionality or software functions). The links between them are defined at integration time (e.g., the correspondence between hardware functions and actual Focal Plane signals) by concise Interface Control Documents (ICDs).

In our system, the configuration information is encapsulated within XML files at each of these levels. XML (eXtensible Markup Language) is a markup language for documents containing structured information. Structured information contains both content (words, pictures, etc.) and some indication of what role that content plays, i.e. context. A markup language is a mechanism to identify structures in a document. The XML specification defines a standard way to add markup to documents. There are other files that are used together with the XML files in the configuration process:

- DTD (Document Type Definition): describes the structure and contents of the XML documents.
- XSL (eXtensible Stylesheet Language): describes a translator for the XML documents [1]. In our case, we use them to convert the XML documents into HTML format for display on a web browser, and to generate the configuration record required by the MONSOON software, as explained in Sec. 2.

2.   THE MONSOON CONFIGURATION PROCESS

An overview of the main steps of the MONSOON configuration process is shown in Fig. 1. These steps are not necessarily sequential, and each step is typically the responsibility of a different person: the DHE board designer, software designer, and system integrator.

The **System Configuration** level defines how many PAN-DHE pairs are required, the partitions of the focal plane, and determines the need for a supervisory node (i.e., when there is more than one PAN-DHE pair).

The **DHE Configuration** level defines the number and type of DHE boards/modules for every specified DHE, taking in consideration that the selection and configuration of DHE boards will depend on the specific application.

The **Board Configuration** level defines the intrinsic functionality of every DHE board/module. It provides the definition of every function contained in a DHE board, where each function is assigned a generic name. This level also defines the specifics of special board settings (like adjustable voltage ranges or any special function not common to every board of its type). Every independent board or module will have its own configuration file at this level.

The **Hardware Function Assignment** level is where the generic functions of the DHE are linked to specific functions of the focal plane.

The **Software Configuration** level is where the software specific functions are defined, and where the hardware functions are assigned meaningful ("human-readable") names.

For all these levels the configuration information is contained in structured XML files, one for every module. A common MONSOON document descriptor file defines the allowed tags and rules for those files. It is a standard DTD file that applies to all the XML files. There is also a common XSL file (a "display translator") to produce the HTML code required for display in any XML-capable web browser (the configuration viewer), and another XSL translator file for tools. This scheme allows us to neatly separate data from presentation.
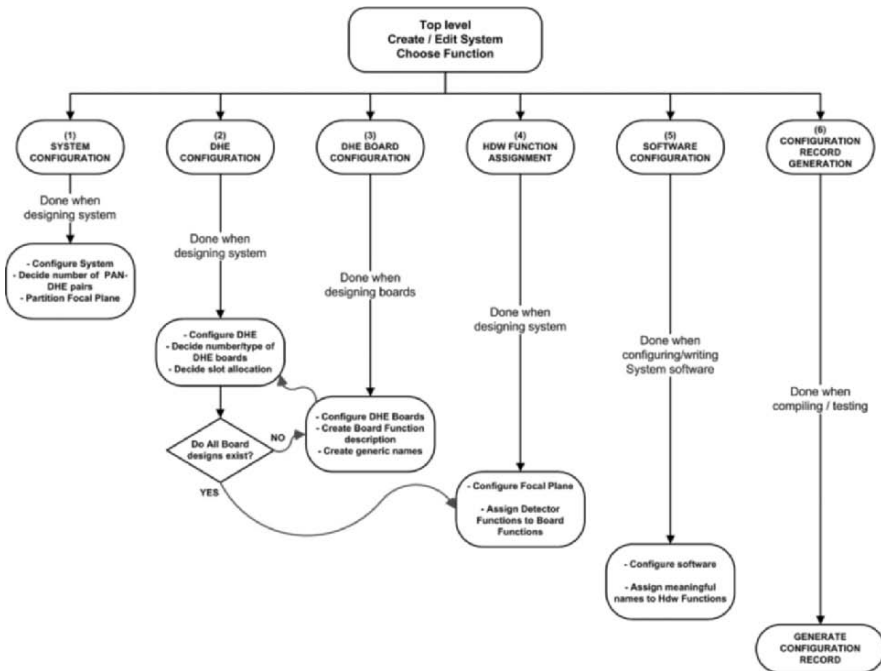
Figure 1. The MONSOON configuration process.

The **Configuration Record Generation** level is the last step of the process. This level is where all the information contained in the previous levels is automatically translated and correlated to produce a configuration record file that is used by the MONSOON software to setup the user interface and the functionality of the system.

In the current implementation of MONSOON, this record file is a standard CSV (Comma Separated Values) file.

The processing rules are defined in a special XSL file ("Configuration Generator"), which is applied to the XML data to generate the configuration record file.

3. THE MONSOON CONFIGURATION DATA HIERARCHY

The hierarchical structure of the MONSOON configuration data begins with a unique configuration root entry (MONSOON ROOT), under which all the MONSOON systems are listed. Every system defines a hierarchical tree, where its nodes correspond to the modules previously defined, as shown in Fig. 2. The relationships between the nodes inside the system tree are established through "signals". A "signal" is an element within an XML file that describes a connection point to a function. Signals from different modules are connected together through "logical" (for software signals) or "physical" (for hardware function signals) CONNECTOR:PIN name matching.

The MONSOON software resides at the top level of the hierarchy because it has one-to-many correspondences (in the different systems) [2]. Code that applies to specific systems is linked through logical signals connections.

4. THE MONSOON CONFIGURATION TOOLBOX

Although the XML files are simple text files, their internal structures are complex enough to make proper input/edit tools mandatory. The tools provide basic HTML forms in which configuration information is filled in according to templates (also in XML format). These templates have been previously defined for each level of the process, along with the tools required to create/edit the corresponding XML files.

There are specific DTD and XSL files that apply to the template XML files. The XSL file contains HTML display rules to produce the

corresponding forms, including the posting of the form data to the configuration tools processing server.

The processing is performed by a Java servlet running on an application server, which receives the data from the HTML forms and generates the corresponding XML files. By using templates to define the form structures, we allow for changes in form content without the need to modify the underlying Java code.

Figure 3 shows the complete configuration data flow when the toolbox set is used. It shows how the toolbox is used to generate and edit the configuration data XML files.
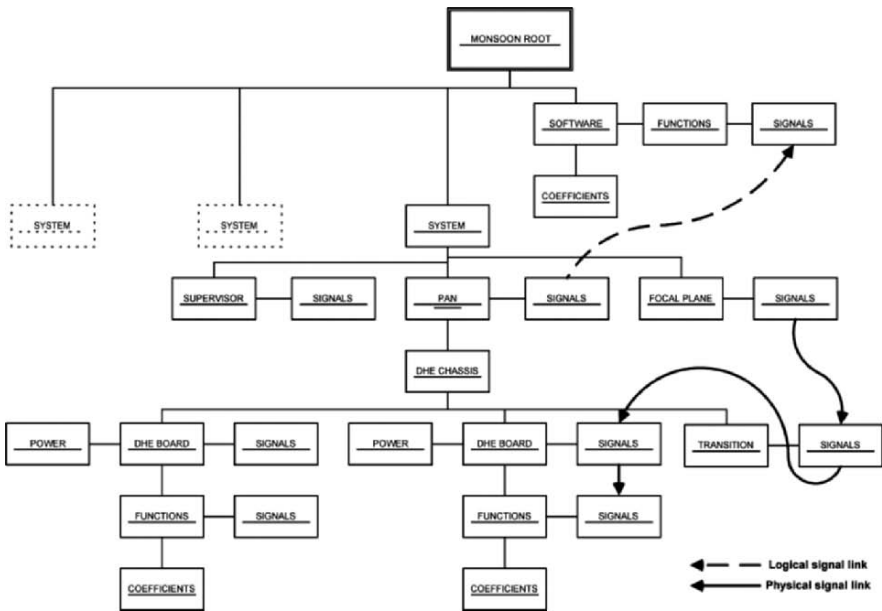
Figure 2. An example of a data hierarchy tree.
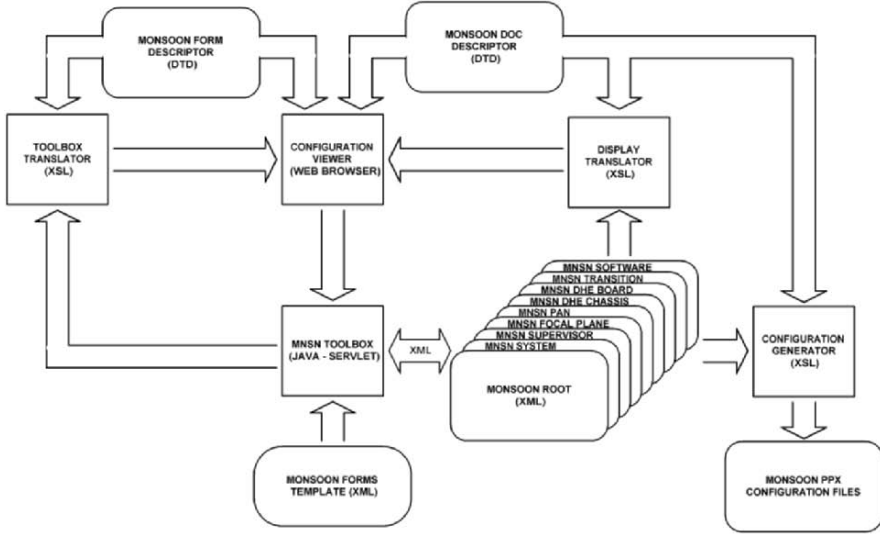
Figure 3. The configuration data flow when using the toolbox set.

5.   REFERENCES

[1]   Wlash, N., 1998, *A Technical Introduction to XML*,
       (http://www.xml.com/pub/a/98/10/guide0.html).
[2]   Daly, P. N., Buchholz, N.C., and Moore, P., *Automated Software Configuration in the
       MONSOON System*, (http://www.noao.edu/ets/monsoon/papers/spie04/5496-43.pdf).

CURRENT STATUS OF THE OSIRIS-GTC INSTRUMENT CONTROL SYSTEM

Enrique Joven[1], José V. Gigante[1], Marta Aguiar[1], José C. López-Ruiz[1], Alberto Herrera[1], Guillermo A. Herrera[1], Ángeles Pérez[1], Jordi Cepa[1] and Francis Beigbeder[2]

[1]*Instituto de Astrofísica de Canarias (IAC),* [2]*Observatoire Midi-Pyrénées (OMP)*

Abstract: *OSIRIS (Optical System for Imaging and low/intermediate-Resolution Integrated Spectroscopy) is an instrument designed to obtain images and low resolution spectra of astronomical objects in the optical domain (from 365 through 1000 nm). It will be installed on day one at the Nasmyth focus of the 10 m Spanish GTC Telescope. It is expected to be in operation in mid-2006. The mosaic is composed of two abuttable E2V44-82 CCDs providing a total of 4K×4K pixels, 15 microns/pixel, 0.125" plate scale. The control system performances are described. To manage the mosaic some HW modifications have been done in a classical ARC-GenII controller, and also major SW DSP programming. This new arrangement allows us to link the electronics to a PMC, VxWorks driven, standard frame-grabber. In such a way, it is possible to run any of the complex observing modes (direct or tunable imaging, long slit spectroscopy, multiple object spectroscopy, long slit fast photometry or fast spectroscopy), programming the atomic operations into the controller's DSP code and the rest in the CORBA driven, VME Local Control Unit. The software architecture allows us to synchronize critical operations, for example, charge shuffling, wavelength ethalons tuning, or filters and grism wheels movements. Some tests and their results carried out during the assembly and the verification phase at the integration laboratories are given.*

Key words: *E2V44-82, ARC-GenII, VxWorks, CORBA.*

1.   OVERVIEW

OSIRIS is an imaging system and a low-resolution long slit and multi-object spectrograph for the 10.4 m Gran Telescopio Canarias (GTC), covering the wavelength range 0.365-1.0 μm with an unvignetted field of view of 8.53'×8.67' and 8.53'×5' in direct imaging and low-resolution spectroscopy, respectively. The mosaic is composed of two abuttable 2K×4K CCDs which provides a total 4K×4K pixels, 15 microns/pixel, 0.125" plate scale. Day one arrays will be E2V44-82 (2-channels, frame-transfer, 20-1000 kHz readout rate).

The OSIRIS control is embedded into the so called GTC Control System (GCS). According to this fact, we have used some hardware and software standards, summarized in the following Tables 1 and 2:

Table 1. OSIRIS hardware standards.

Unit	Model
CPU	Motorola MVME 2400/5100 with internal PCI bus (two)
Crate	Two backplane Wiener VME bus, CAN controlled
CCD controller	ARC-Gen II (modified)
CCD controller output	RS422 to fiber optics
Standard motors	DC servo motors (Parker)
Standard motion controller	Delta tau turbo PMAC
Peripheral	Multiport technobox PMC serial card
Communication	PMC-dual 1 Giga ethernet
Temperature control	Lakeshore, USA
Vacuum control	Pfeiffer, Germany

Table 2. OSIRIS Software Standards.

Tool	Type
Environment	GTC Control System (GCS)
Modeling	UML & RUP
Main tools	GCS release
Aid tools	JBuilder, Rational Rose, Doxygen
Languages	GNU-C++, C, JAVA
Operating systems	VxWorks (Real Time), Solaris
Distributed technology	CORBA & TAO-ACE
Platforms	SUN

Implemented distributed component model technology (see López-Ruiz, et al. for details [1]) allows developers to build applications as a set of components. These components may be physically distributed, executed under different operating systems, and written in different programming languages. Each distributed component has a network addressable interface. Some of the advantages of using the distributed component model are a

more simplified software communication and an easier way to access to common services provided by the GCS, such as logs, alarms, or monitoring and configuration systems. This GCS-distributed component model is based on CORBA middleware.

2. CURRENT STATUS OF THE OSIRIS CONTROL

The principal component of the OSIRIS control is the Data Acquisition System (DAS). It is explained in some detail in Sec. 2.1. Most of the other subsystems must be connected or synchronized with it in order to perform the implemented observing modes listed in Table 3.

Table 3. OSIRIS observing modes.

High-level observing modes
Direct imaging
Tunable imaging
Long-slit spectroscopy
Multiple-object spectroscopy
Fast spectro-photometry

2.1 OSIRIS Data Acquisition System (DAS)

The DAS is based on a classical ARC-GenII controller, using a timing board with parallel cable linked to a digital PMC-type commercial frame grabber plugged into a VME-crate running VxWorks OS (see Figures 1 and 2). The cable supports very high data rates and is presently implemented at 6.25 Mpixels/s (only 4 MHz is needed in a 4-channel configuration). A fiber optics link has been added. More details about this configuration can be found in Joven, et al. [2]. Table 4 summarizes the main elements of the OSIRIS DAS.

Table 4. OSIRIS Data Acquisition System

Element	Model
Mosaic	Two - E2V44-82 back-illuminated CCDs (4096×4102 pixels)
Controller	Modified ARC-Gen II (San Diego, USA)
Output	RS422 to fiber optics (Arvoo, Netherlands)
Interface	PMC-digital frame grabber (Datacell, UK)
Operating system	VxWorks real time operating system (Wind River, USA)
Shutter	Bonn University (Germany)
Cryostat	LN2-based (TTM, Valencia, Spain)
Control crate	VME-bus (Wiener, Germany) with MVME2400/5100 Motorola CPUs
Communication	PMC Dual-Giga ethernet

Figure 1. *(left)* OSIRIS DAS including a couple of eng-E2V44.82 CCDs in the test bench. *(right)* Main control crate.
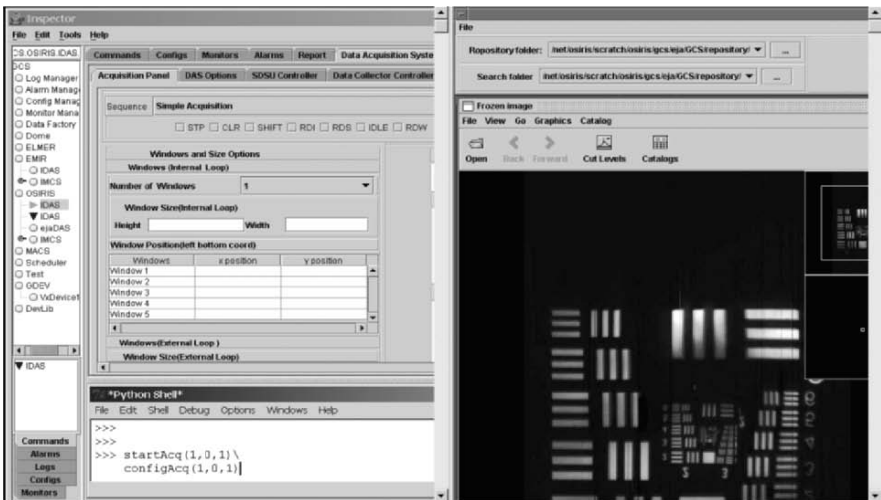
Figure 2. *(left)* One of the OSIRIS control panels of the DAS, included in the Inspector-GCS and showing a Python Shell for scripting. *(right)* VISADO Program, real time JSkyCat-based image visualization application.

2.2   Other Related OSIRIS Subsystems

The OSIRIS control architecture allows the coordination and synchronization of critical operations (for example, charge shuffling and wavelength tuning) with real time constraints (see Figures 3 and 4).

Figure 3. (left) Filter wheels. They include pupil masks, conventional filters and light dispersive elements (grisms). *(right)* Main elements mounted in the last wheel are the two tunable filters, which convert OSIRIS into a very versatile instrument. Development of the four wheels has been carried out by NTE (Barcelona, Spain). Tunable filters are made by ICOS (London, UK), with a new entire FPGA-based control developed by the OSIRIS team (see Gigante, et al. [3]).
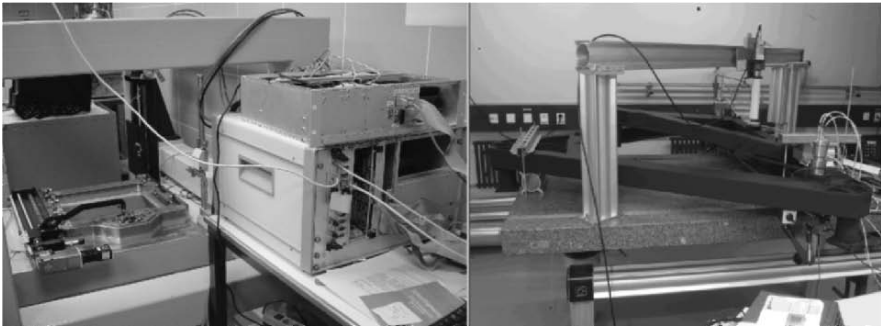
Figure 4. (left) Mask loader, including control, mounted at the test bench in the IAC facilities. All the mechanisms are driven by DC servo motors (Parker). *(right)* Collimator frame support. The collimator mirror has been manufactured by SESO (France), and its support and micro-actuators by CSEM (Switzerland).

3. ACKNOWLEDGEMENTS

4.   REFERENCES

[1] López-Ruiz, J.C., Aguiar M., Joven E., Herrera A., Gigante J., Cruz-López A. and González-Serrano I, 2002, *OSIRIS Software: An Overview*, Advanced Telescope and Instrumentation Control Software II, Lewis, H.(editor*),* Proceedings of the SPIE, Volume **4848**, pp. 545-552.

[2] Joven E., Gigante J. and Beigbeder F, 2004, *OSIRIS Detectors: First tests and Control System*, Scientific Detectors for Astronomy, Amico, P., Beletic, J.W. and Beletic, J.E. (editors) Astrophysics and Space Science Series Vol. **300**, Kluwer Academic Press, p. 345.

[3] Gigante, J.V., et al., 2005, *Improved Control Electronics for OSIRIS-GTC Commercial Tunable Filters,* these proceedings.

Workshop participants received "pupi" (puppets) of Renaldo and Orlando in their souvenir bags (see Mark Downing at left). In Toarmina Gemma and Chiara Figer and Molly McLeod find "lifesize" pupi (see below).

EMIR DETECTOR DATA ACQUISITION ELECTRONICS

José Javier Díaz[1], Fernando Gago[1], Pablo López[1], Francis Beigbeder[2], Francisco Garzón[1,3], Jesús Patrón[1]

[1]*Instituto de Astrofísica de Canarias (IAC),* [2]*Observatoire Midi-Pyrénées (OMP),* [3]*Departamento de Astrofísica, Universidad de La Laguna*

Abstract: *EMIR is a multiobject intermediate resolution near infrared (1.0-2.5 microns) spectrograph with imaging capabilities. The instrument is to be mounted on the 10 m Gran Telescopio Canarias (GTC), located on the Spanish island of La Palma.*

This paper gives an overview of the EMIR detector data acquisition electronics. The detector is an HAWAII-2 array. First, a description of the detector fan-out electronics is given, which involves the use of commercial components (resistors, capacitors and operational amplifiers) working under cryogenic conditions (~77K). The particulars of the cold electronics, the thermal considerations as well as the cabling design, detector controller architecture and data handling system are reviewed.

Key words: *Electronics, HAWAII-2, infrared.*

1. EMIR ELECTRONICS BLOCK DIAGRAM

Figure 1 shows a simplified view of the EMIR electronics. The data acquisition system consists of a workstation, connected to a VME crate by means of the telescope Gbit ethernet network. This crate connects to the detector controller with fiber optics by means of a PMC card.
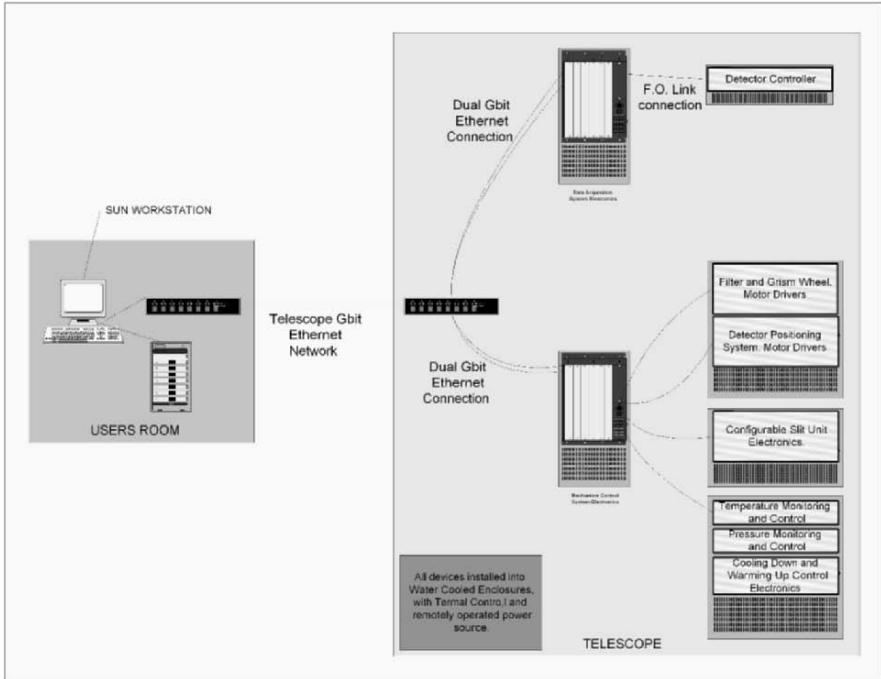
Figure 1. EMIR electronics block diagram.

2.   FAN-OUT DESIGN

Two versions of the fan-out board have been used with the HAWAII-2 detector. Figure 2 (left) shows the 32-channel version while Fig. 2 (right) shows the architecture used to operate the Detector with the 4-channel configuration.   Both versions have the same physical dimensions, match with the same mechanical support, and share the same design philosophy to ensure the correct operating temperature and stability during operation.

The electronic design, although basically identical, has suffered some adjustments based on the results of the initial tests performed with the 4-channel architecture. The circuit layout has also been adapted to minimise the total area and to reduce the number of active components used per channel.
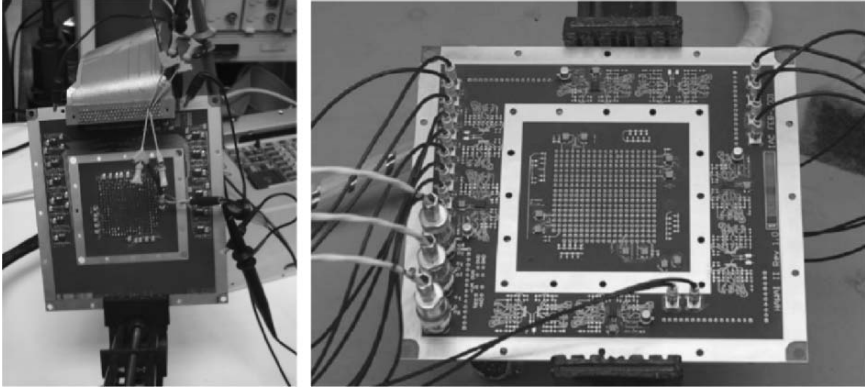
Figure 2. Fan-out board configurations, *(left)* 32-channel and *(right)* 4-channel.

3. FAN-OUT THERMAL DESIGN

Figure 3 shows the thermal contact used for the 4-channel version of the detector fan-out board. This version has been used to check electrical, mechanical and thermal behaviour. The initial design was adopted after successful testing. Only minor modifications to the electrical circuitry were required to adapt the structure to the 32-channel fan out board.

A mechanical layer has been included to facilitate heat dissipation and ensure an almost uniform temperature distribution. As shown in Fig. 3, the detector area is thermally shielded from the amplifiers area by a cold barrier connected to flexible thermal links. All active components are placed on the side of the board opposite the detector to avoid any spurious source of radiation.

Temperature stabilization is achieved using a PID control loop, based on a temperature sensor and a heater, placed on the back of the detector inside the thermally shielded area.

4. DETECTOR FRONT END ELECTRONICS

The operational amplifier (see Fig. 4) in the fan-out, the OPA350, is a single-supply rail-to-rail amplifier functioning from 0-5 volts. Its behaviour at cryogenic temperatures (77 K) is adequate for this application and it has proven to be reliable and repetitive after many thermal cycles.
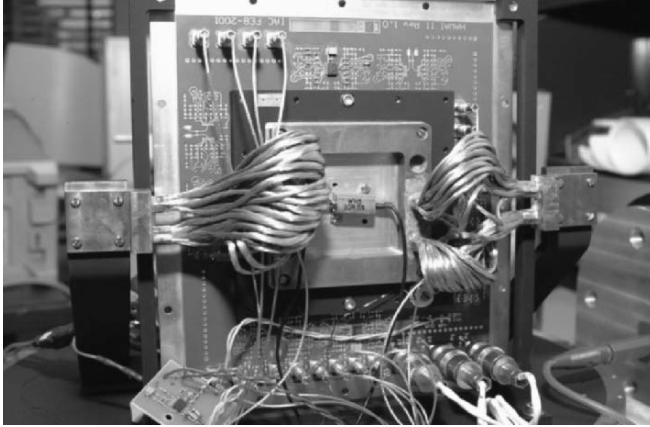
Figure 3. Thermal considerations of the fan-out board.
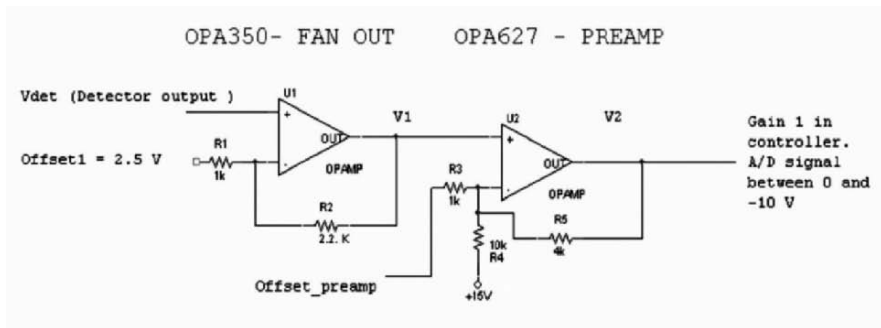
Figure 4. Cold preamplifier schematic.

5.   ARC/IRL CONTROLLER

The detector controller (see Fig. 5) used by EMIR is based on a Generation III Leach Controller. Some modifications have been introduced to make it more robust. The boards have been interconnected using a flex-rigid circuit. Also a direct connection is made to the cryostat vacuum sealed connector with no cable.

Some boards have been adapted, which is the case of the slew rate of the clock signals, the analog chain previous to the A/D conversion, etc., to match with the characteristics of the detector.

The controller consists of:
- 1 FO timing board,
- 4 video boards with 8 channels each,

- clock driver board,
- 1 back panel with power board,
- 1 power supply,
- Rigid flex interconnection with additional electronics to achieve high slew rates for the pixel clock, and
- Fan and water cooled system to allow installation in a hermetic enclosure.

Figure 5. Detector controller.

6. VME MAIN BOARD AND FO PMC

The detector controller is connected to a VME crate by means of a fiber optic link (see Fig. 6). On the VME crate there is a processor board with two mezzanine cards. One of these cards is a custom board from Leach to facilitate connection with the controller. The second card, with a dual Gbit Ethernet connection, allows data transmission to a workstation located in the observation room using the telescope Gbit network.

Due to the high data transmission rate available it is not required to introduce any real-time reduction in the VME crate. The reduction will occur

afterwards at the workstation. If it were necessary, data handling algorithms could be implemented in the VME crate and, if required, additional hardware modules, such as memory cards, could be added inside the VME crate.
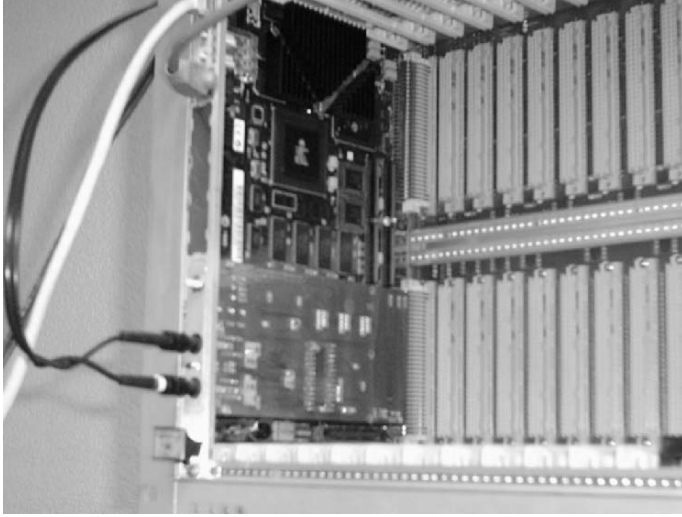
Figure 6. VME and PMC cards.

7.   ACKNOWLEDGEMENTS

IMPROVED CONTROL ELECTRONICS FOR OSIRIS-GTC COMMERCIAL TUNABLE FILTERS

José V. Gigante[1], Guillermo A. Herrera[1], José L. Rasilla[1], Enrique Joven[1], Marta Aguiar[1], Alberto Herrera[1], José C. López[1], Victor González[1], Fernando Gago[1], Ángeles Pérez[1], M. Rodríguez Valido[2] and Jordi Cepa[1]
[1]Instituto de Astrofísica de Canarias (IAC,. [2]Universidad de La Laguna (SPAIN)

Abstract: *OSIRIS (Optical System for Imaging and low/intermediate-Resolution Integrated Spectroscopy) is an instrument designed to obtain images and low-resolution spectra of astronomical objects in the optical domain (from 365 to 1000 nm). It will be installed on Day One at the Nasmyth focus of the 10 m Spanish GTC Telescope. One of its key elements is two ICOS ET100 tunable filters, which will be used for several scientific programs. ICOS delivered the CS100 controller, a standard controller for these devices. This controller has several specifications that do not satisfy our project requirements. A plug-in electronic module for the CS100 controller is being developed at IAC to address these issues. The main features of this improved module are: capability to scan the full range of the etalon from a remote host, an improved resolution >15 bits, a table to store a pre-defined set of cavity spacing points allowing quicker gap spacing change, and the possibility of synchronizing that change with an external trigger signal. Currently, an initial prototype has been developed and is operating successfully. The control electronics are based upon a microcontroller embedded in a FPGA. We have started the detailed design of the final product, whose completion and testing is expected by the end of 2005.*

Key words*: Etalon, tunable filter, electronics, FPGA, ICOS, CS100.*

1.   INTRODUCTION

OSIRIS (Optical System for Imaging and low/intermediate-Resolution Integrated Spectroscopy) is an instrument designed to obtain images and low-resolution spectra of astronomical objects in the optical domain (from 365 to 1000 nm). It will be installed on Day One at the Nasmyth focus of the 10 m Spanish GTC Telescope. One of its key elements is two ICOS ET100 tunable filters (see Fig. 1), which will be used for several scientific programs. The tunable filters are basically two partially plated parallel mirrors acting as an Etalon. When a polychromatic light crosses the cavity between the mirrors only specific wavelengths are able to pass through, depending on the gap width. One of the mirrors is movable which permits changing of the cavity width. The mirror is moved by three high voltage piezoelectric actuators, while the gap width and parallelism is measured using several capacitors on the internal side of the mirrors. An electronic module, called the CS100 controller, controls the mirrors' positions. This controller has several specifications that do not meet the OSIRIS project requirements. We have developed an improved plug-in electronic module in order to improve both the CS100 performance and to meet the OSIRIS specifications.
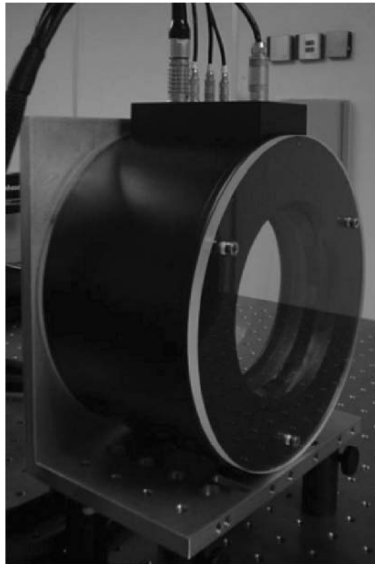
Figure 1. ET100 tunable filter.

2. THE CS100 CONTROLLER

The CS100 is a standard controller produced by ICOS for their tunable filters (see Fig. 2). This device is an accurate position servo-controller that applies correct voltage to each piezoelectric actuator to adjust gap width and parallelism between the mirrors. It can be controlled manually from its front panel, or remotely through a RS-232 serial port. Although the system is very reliable, it is a dated design and its specifications do not completely satisfy the OSIRIS requirements:

- The CS100 is only capable of remotely controlling the gap between the mirrors with a resolution of 2 μm. OSIRIS needs to control the cavity width of the entire filter range (8-10μm), and with a resolution >0.5 nm.
- The CS100 allows remote control of some frontal panel switches and buttons. OSIRIS needs to control all front panel elements, and be able to read the front panel gauges.
- OSIRIS also needs to quickly adjust the cavity width and to synchronize with an external CCD controller trigger signal. The CS100 controller does not have this function.

Figure 2. The CS100 controller.

3. AN IMPROVEMENT MODULE FOR THE CS100 CONTROLLER

In order to improve CS100 performance the electronics were upgraded by reusing its useful modules: parallelism servo control, position sensing and high voltage circuitry. A new plug-in module was developed to suit the

OSIRIS requirements. This new control module will be connected to the original CS100 by taking advantage of pre-existing testing and interface connectors. Using these connectors allows easy installation of the module without any modifications of the CS100 internal electronics.

The new control electronics has two main elements: the application board and the control board. The application board is the principal component of the new design (see Fig. 3). It includes several functional modules:

- 16 bit position control module
- automatic quadrature control module
- front panel control module
- gauge reading module
- CCD synchronization module
- interface and communication module
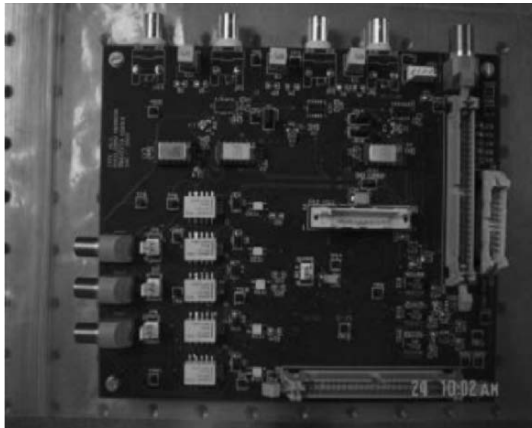
Figure 3. The application board.

All these functional modules are operated by the control board. An Avnet FPGA evaluation board has been used for this prototype. This board, very powerful and flexible, is based on a Xilinx Spartan IIE FPGA. The use of microcontroller embedded technology speeds the software development. All the functions of the improved system can be controlled with a remote terminal using a complete set of commands.

4. THE PERFORMANCE OF THE IMPROVED CS100 CONTROLLER

Several test bench arrangements have been developed in order to test the functionality and validate the specifications of the new electronics. The results have been very successful:

- It is now possible to control the tunable filters over their entire wavelength range with a resolution greater than 0.5 nm. Measurements made in two different ways (optical spectrum analyzer and photometry), have shown that the 16 bit resolution of the improved CS100 controller can be resolved. This resolution is equivalent to 0.15 nm of mirror displacement.
- The quadrature error is compensated automatically without the use of the front panel quadrature control.
- It is possible to control all the front panel elements remotely, as well as the reading of the gauges.
- It is possible to synchronize the tunable filter with an external trigger signal. The set of programmable gap widths is stored in a table in the control board memory, allowing quick gap changes.

Based on this prototype (see Fig. 4), we are currently developing the final product of the improvement module for the CS100. This final version will be a 3U plug-in module, and is planned to be completed and tested by the end of 2005.
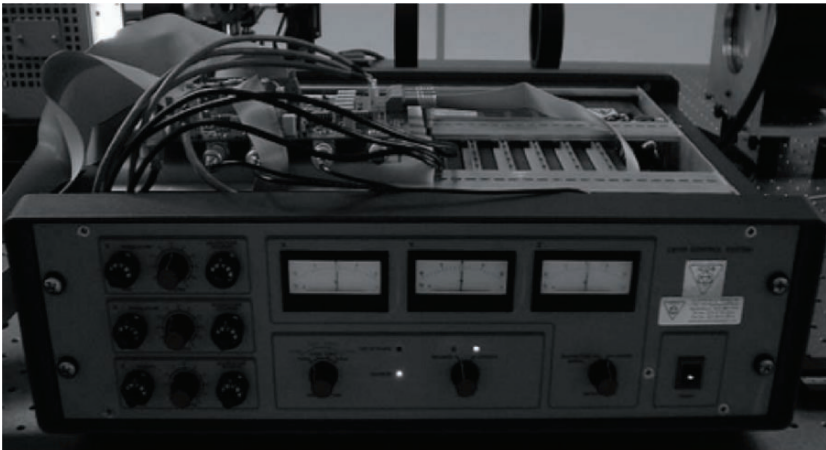
Figure 4. The prototype working with the CS100.

5. ACKNOWLEDGEMENTS

Coffee breaks were a valuable time for interaction.

Guided tours were given during the Monday visit to Taormina.

A DEDICATED CONTROLLER FOR ADAPTIVE OPTICS L3CCD DEVELOPMENTS

Jean-Luc Gach[1], Philippe Balard[1], Olivier Boissin[1], Mark Downing[2], Philippe Feautrier[3], Christian Guillaume[4], Eric Stadler[3]

[1]*Observatoire de Marseille,* [2]*European Southern Observatory,* [3]*Observatoire de Grenoble,* [4]*Observatoire de Haute Provence*

Abstract: *We present the dedicated controller in development for the OPTICON JRA2 programme "Fast Visible Detectors for Adaptive Optics" [1]. The CCD developed within this programme is a highly specialized chip using e2v's Low Light Level Charge Coupled Device (L3CCD) technology capable of outstanding capabilities [2]. It is not possible to extrapolate existing controller techniques since the chip needs radiofrequency signals (more than 10 MHz) for clocking, and gives a high frequency video output. Compactness is of prime importance to deal with these high frequency signals and is also important for future integration in next generation adaptive optics systems. Developing such a controller is very challenging and needs to utilize innovative techniques to fulfill the requirements. We will summarize the JRA2 and detector requirements, derive the controller requirements, present guidelines of the controller, and highlight the challenges of this controler.*

Key words: *Wavefront sensor, Charge Coupled Device (CCD) controller, Low Light Level Charge Coupled Device (L3CCD).*

1.   OPTICON AND THE JRA2 DETECTOR (CCD220)

The Optical Infrared Co-ordination Network for Astronomy (OPTICON) is a European Union funded network bringing together national funding agencies and users with common interests in optical and infrared astronomy. The aim of the OPTICON Joint Research Activity 2 (JRA2) is to develop visible detectors that fulfill the requirements of Adaptive Optics (AO) wavefront sensors for 10 m class telescopes. These detectors do not yet exist; current detectors have frame rates that are too slow and too noisy for the

second generation of AO systems [1]. The main characteristics of the developed CCD (named CCD220) are summarized in Table 1.

Table 1. CCD220 Main Characteristics.

Item	Specification
Detector format	240×240 pixels of 24 μm, 8 L3 outputs, Frame transfer
Frame rate	25-1500 Hz
Parallel transfer rate	10 Mlines/s
Read noise	<1e⁻ at 1.2 kHz

2.   IMPACT OF REQUIREMENTS ON CCD CONTROLLER

2.1   Data Throughput

Assuming a 1500 Hz frame rate with necessary overhead to shift the charge from the storage section to the serial register, the necessary pixel rate with 8 outputs is 13.7 Mpixels/s per output, giving a throughput of ~110 Mpixels/s. The data is digitized with 14 bits, giving a useful transfer rate of 220 Mbytes/s. This is much higher than the standard throughput rate a classical computer bus can accept. Several solutions were considered for data transmission, including networked standards (Gigabit ethernet, IEEE1394, USB2.0, etc.). The Cameralink industrial standard has been selected. It has been developed by major camera suppliers for large and/or fast sensors and a lot of grabbers and other accessories are avalaible on the market. The full specifications of the cameralink exhibit a data throughput rate of 680 Mbytes/s with standard grabbers on PCI-X bus or PCI-Express.

2.2   Sequencer Resolution

Using frequencies up to 13.7 MHz for the generation of clock phases gives a phase period of 73 ns. This has a big impact on the necessary sequencer resolution. Since the chip is using a L3 output, it is necessary to adjust the phases of the CCD very precisely in order to have good electron multiplication in the gain register [3]. At this frequency, the phase scale is 5°/ns. A 20° phase shift in a case of a sine HV phase gives 6% of phase voltage decrease. This effect can be canceled by increasing the HV clock voltage, but it is limited by the HV phase breakdown voltage. Also, since the multiplication occurs when the sine is not at its maximum level, small jitters

in the serial clock will produce gain variations. Therefore a sequencer resolution down to 1 ns would be necessary. The foreseen technical solution is to use several very fast master clocks (up to 400 MHz) finely skewed from each other with a specialized circuitry.

2.3   Data Acquisition

At a rate of 13.7 Mpixels/s, it is very tricky to build a Correlated Double Sampling (CDS) system that has a suitable performance. The goal is to have 14 bit dynamics since analog to digital converters sufficiently fast are only now coming onto the market. The baseline is to use an integrated Analog Front End (AFE) with embedded CDS, built by classical integrated circuit suppliers. This has the advantage of offering a very compact system (insensitive to EMI/RFI) with a lot of built-in features such as programmable gain amplifiers. The other alternative is to use an oversampled system and a digital CDS. Using selected weighted coefficients, it would also be possible to reduce the overall readout noise [4,5]. These two approaches will be developed in parallel.

2.4   Phases Drive

The required bandwidth for any periodic square-like signal is given by the classical formula in Eq. 1:

$$BW = \frac{0.35}{\tau} \qquad (1)$$

where τ is the rise/fall time. Serial phases require 5 ns rise time, this gives a required bandwidth of 70 MHz and, with a 15 V amplitude, a slew rate of 3kV/µs.

The parallel phase drivers have lower constraints on bandwidth, but since the phases of a CCD behave electrically as capacitors, it's necessary to drive a large capacitor at high speed. The parallel phase capacitance will be approximately 2 nF, giving a mostly reactive impedance of 8 Ω at 10 MHz. This is likely the main issue of the controller since it is necessary to provide several amperes of current to the CCD. To avoid current flow through the VSS pin, a symmetrical two phase parallel register will be used to balance the current flows.

The HV phase needs a 50 V amplitude sine drive. The sine wave is preferred to avoid thermal dissipation in the chip. This is very hard to achieve with classical circuits because of the necessary current drive of the

HV phase. The impedance of the HV phase at 13.7 MHz is 116 Ω, therefore the peak current in the phase is 430 mA. The driver dissipation in this case is several watts. The solution is to use a resonnant clocking system that uses the energy transfer between an inductor and the capacitor of the phase. Using this technique the driver power dissipation drops to less than 1W.

3.   THE CONTROLLER DESIGN

3.1   General Architecture

Dealing with such high frequencies is very uncommon for an astronomical CCD controller. The classical approach consisting of putting all the drive electronics into a box one meter from the cryostat head is not applicable in this case. With such high bandwidths, a strict impedance matching would be necessary to avoid ringings of the signals through the cables. But a CCD phase is a pure reactive load, therefore impedance matching is not possible. The only way to proceed is to arrange all the drive electronics close to the detector.

3.2   Inductance of PCB Traces

The inductance of a PCB trace is given by the formula in Eq. 2:

$$LT \approx 0.2L\left[\ln\left(\frac{L}{w+h}\right)+1.2+0.22\left(\frac{w+h}{L}\right)\right] \tag{2}$$

where, LT is the inductance in nH, L is the length of the track, w is the width and h is the thickness of copper; all in millimeters. This shows a weak dependence on trace thickness (10 nH/cm for a 200 μm track, 7 nH/cm for a 1 mm track). This series inductance will create overshoots and undershoots since it makes an oscillator with the CCD phase capacitances. These overshoots are proportional to the variation of current, and in the case of parallel phases, a small wire of a few centimeters adds an unacceptable overshoot. Figure 1 shows a SPICE simulation of the effect of a 4nH parasitic inductance due to a 0.5 cm wire or PCB trace on the drive waveform of the parallel phases of CCD220.

The only way to reduce the parasitic inductance is to increase the mutual inductance of the phase drive track and its returning path by minimizing the distance of these two tracks. Practically, the inductance can be divided by a factor 2.5 to 5. Another method, which could be used in conjunction with the previous one, is to use a shape controlled drive waveform to counterbalance

the oscillation, but in this case the phase drivers can't be simple switches, but have to be amplifiers. Figure 2 shows the effect of controlled drive with a parasitic inductance of 10 nH. Finally, driving CCD220 parallel phases with sine waves is also possible due to the symmetric 2 phase structure and would have the advantage of minimizing clock induced charge [6].
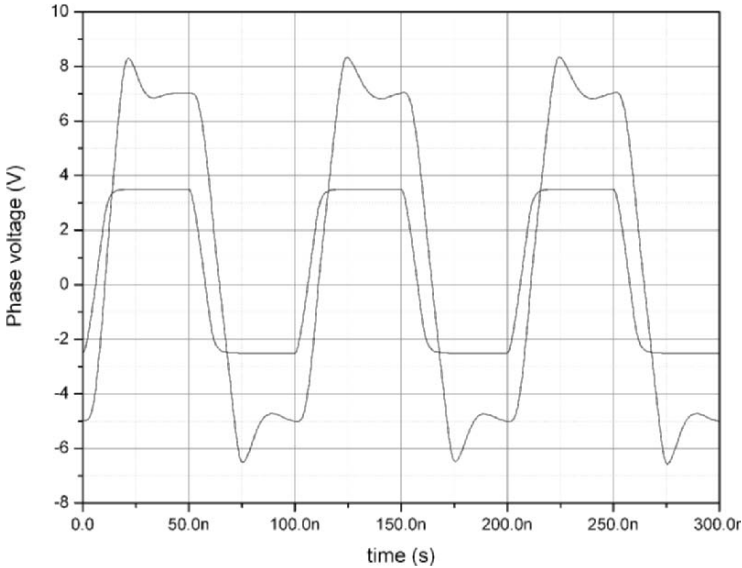
Figure 1. Effect of 4 nH parasitic inductance on the parallel clocks. Lowest amplitude signals refer to the drive waveform,the highest waveform refer to the clock signal (the buffer has a gain of 2).

4. CONCLUSION

Designing a CCD controller for CCD220 requires the use of high frequency techniques usually nonessential in scientific CCD controllers due to the low readout speed. Particular care has to be taken with wire length that introduces parasitic inductance, especially when high current flows are present. The approach of classical CCD controllers with separate control electronics connected to the CCD head by long wires are widely used in astronomy but are not applicable in this case. A fully integrated approach must be used to place all the CCD drive electronics close to the chip and therefore in close conjunction with mechanical and cryogenic design.
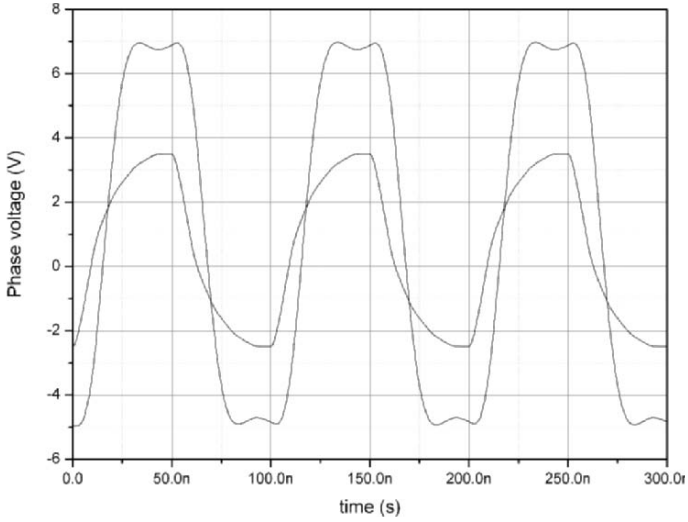
Figure 2. Overshoot cancellation (large trace) with a controlled drive shape (small trace) and a parasitic capacitance of 10 nH.

5. REFERENCES

[1] Feautrier, P., et al., 2005, *Zero Noise Wavefront Sensor Development within the Opticon European Network,* these proceedings.
[2] Downing, M., et al., *A dedicated E2V-L3Vision CCD for Adaptive Optics Applications*, 2005, these proceedings.
[3] Jerram P., et al., 2001, SPIE Vol. **4306**, p. 178.
[4] Gach, J. L., et al., 2003, PASP Vol. **115**, p. 1068.
[5] Gach, J. L., et al., 2004, *Scientific Detectors for Astronomy*, ASSL Vol. **300**, p. 603.
[6] Daigle O., Gach J-L., Guillaume C., Carignan C., Balard P., Boissin O., 2004, SPIE Vol. **5499**, p. 219.

CHARACTERIZATION OF THE OPA350 OPERATIONAL AMPLIFIER AT CRYOGENIC TEMPERATURES

Fernando Gago, José J. Díaz, Francisco Garzón and Jesús Patrón
Instituto de Astrofísica de Canarias (IAC)

Abstract: *As part of the development of EMIR, an infrared multiobject spectrograph for the Gran Telescopio de Canarias (GTC), the OPA350 operational amplifier is being successfully used at cryogenic temperatures (77K). The use of off-the-shelf electronics (not specifically designed for cryogenics) is advantageous since it allows us to get signal amplification very close to the detector without the need of special components.. This helps to keep the signal integrity along the analogue chain at the very low cost of commercial components. However, since commercial components are not specified for cryogenics, some tests have to be performed to check if their main parameters are kept within acceptable values and if the chips behave in a reliable way.*

In this paper, both the procedures and the results of the OPA350 tests are presented. They will be used not only to confirm the good performance of the chip in cryogenics, but also as a guideline for the tests to be carried out in other chips for future instruments.

Key words: *Cryogenics infrared, OPA350, EMIR, GTC.*

1.   INTRODUCTION

The OPA350 is a single-supply rail-to-rail CMOS operational amplifier. Its main parameters (low noise, very low bias current and relatively high speed) together with being single-supply (and, therefore, having a low power consumption) make it an ideal component to be used with infrared detectors. That is why during the development of EMIR, an infrared instrument for the

Gran Telescopio de Canarias (GTC), it was considered as a possibility for the amplification of the detector analogue output in the fan-out board, where a HAWAII-2 detector is being used at 77K.

Using amplification so close to the detector eases a lot of the difficulties in keeping noise and interference under control. Since the OPA350 is a commercial component not specified for cryogenics its cost is very low ($1.30 per unit). However, some questions immediately arise. Will it work in cryogenics? Even if it is successful, what will be the amplifier parameters when cold?

We have been using the OPA350 for more than 3 years with good results and with the certainty that possible changes in the parameters were not affecting the detector science data. Even so, we have performed some detailed tests to obtain the exact chip parameters in cryogenics. This allowed us not only to establish those parameters, but also to validate the test circuits so that they can be applied to other chips in the future. Our idea is to create a database of commercial chips working in cryogenics so that they can be used with conviction.

2.   THE OPA350 OPERATIONAL AMPLIFIER

Manufactured by Burr-Brown (now part of Texas Instruments), this CMOS amplifier is available in various formats. For EMIR, the space-saving SSOP-16 surface mount OPA4350 chip was used. There are 4 amplifiers per chip. The results in this paper refer to that particular format.

The main parameters at room temperature are a white noise of 5 nV/√Hz, a bandwidth of 38 MHz, a slew rate of 22 V/μs, a bias current of 0.5 pA and a voltage offset of around ±150 μV (maximum 500 μV)

The tests to obtain chip parameters were initially performed at room temperature. The results were, as expected, similar to those on the datasheet, which allowed us to validate the test circuits. Then, the chips were cooled and the tests repeated to obtain the cryogenic parameters.

In Fig. 1 a detail of a previous version of the EMIR fan-out board populated with an OPA4350 chip is shown.

3.   COOLING CONSIDERATIONS

The OPA4350 has shown reliable and repetitive behavior at 77K. However, some considerations must be taken into account. If the chip is kept off when cooled it is possible to encounter problems when attempting to power-up the chip at 77K. The chip will either consume a lot of current or

very little. However, after some attempts it will consume the correct value. From that moment forth, if a soft-start voltage regulator is used (we are using a REG103 from Burr-Brown), which rises the voltage slowly (in ~1 ms), it will be possible to turn on the chip as many times as desired in repetition (see test bench in Fig. 2).

However, requiring multiple attempts is not desirable. The solution is as simple as keeping the chip on while cooling. If we use a soft-start voltage regulator when cold, the chip can be turned on and off in a repeatedly manner without requiring previous attempts. It appears that keeping the chip powered during cooling minimized the lattice distortion resulting from possible thermal stresses.
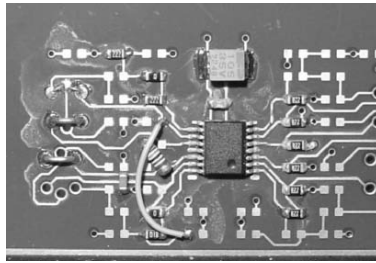
Figure 1. OPA4350 in a previous version of the EMIR fan-out board.

Figure 2. Test bench used to obtain parameters in cryogenics.

4.   TEST CIRCUITS AND RESULTS

The chip has been working correctly for almost 3 years at 77K. However, the results presented in this section were obtained at 115K, the temperature of the Printed Circuit Board (PCB) containing the chips. Tests will be

repeated in the future for a PCB temperature of 77K (that is not necessarily the chip's internal temperature, whose value is unapparent).

4.1   Noise

The circuit in Fig. 3 allows us to obtain the input noise density of the amplifier. The offsets are used to guarantee that the output is within range. The noise at the output is basically due to the input noise of the first amplifier. The noise due to the remainder of the amplifiers and to the offsets is negligible in this circuit.
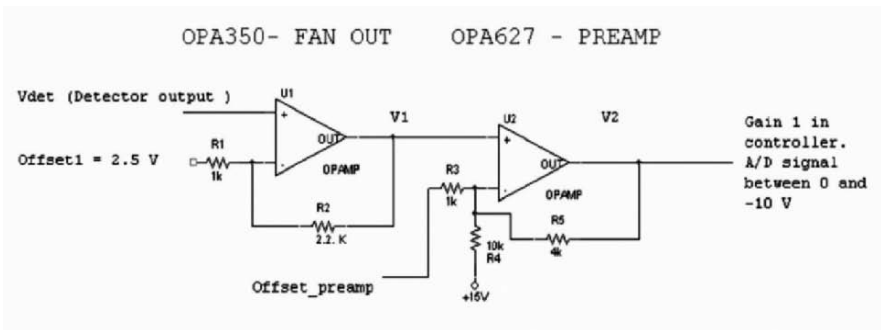
Figure 3. Circuit used for obtaining the amplifier input noise density.

The total amplification is so high (~68000) that even a low resolution digitizer such as a digital oscilloscope is enough to obtain the data. The noise density is obtained by calculating a Fourier transform of the data. Sharing the total gain among several amplifiers allow us to keep the system bandwidth at a relatively high value. By doing so the noise density can be calculated at frequencies of at least 100 kHz in order to ensure that it is white noise.

The main result is that the noise variations are small. When cold, there seems to be a very slight increase in the 1/f noise of the amplifier and a decrease (around 25%) in the white noise.

4.2   Offset Voltage and Bias Current

The nominal bias current at room temperature is so low (0.5 pA) that no tests were carried out in cryogenics. Although there could be small changes, they are not expected to vary the bias current in an appreciable way, in the sense that it will be kept in the range of a few pA or less.

As for the offset voltage, in this chip it depends appreciably both on the common mode voltage at the inputs of the amplifier and the temperature. Even though there is a clear dependence of the offset on temperature, the

maximum voltage offset observed at the input is kept at a similar value (700 µV at 115K versus 500 µV at room temperature). In the future, tests must be performed to determine if the offset drift with temperature is similar under the chip nominal temperatures and in cryogenics.

4.3   Bandwidth and Slew Rate

For this test, the operational amplifier was configured as a non-inverting amplifier with a gain of 2. The Bode Diagram of this non-inverting amplifier was obtained, both at room temperature and at 115K. The bandwidth for small signal is similar at both temperatures (see Fig. 4).
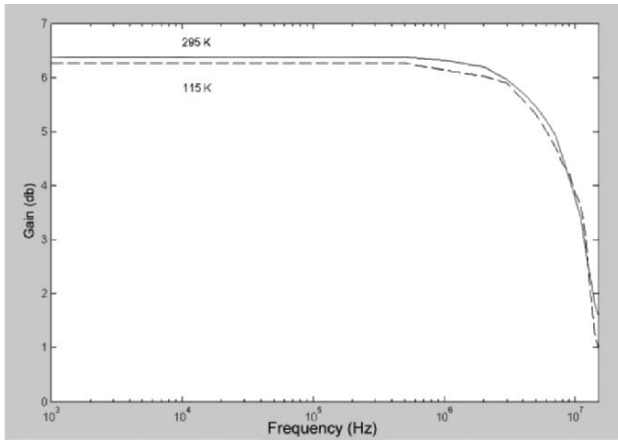
Figure 4. Bode diagram at 295K and 115K.

However, the slew rate decreases with temperature. At 295K a value of 24.7 V/µs was measured (the datasheet value is 22 V/µs). At 115K the slew rate was only 13.0 V/µs.

5.   CONCLUSIONS

The main conclusions of our tests are:

- The chip behaves in a repetitive and reliable way provided that it is kept on during cooling and a soft-start regulator is used to power up the chip at cryogenic temperatures.
- The amplifier input noise when cold increases very slightly regarding 1/f noise, while white noise decreases in around a 25% at 115K.

- The maximum offset voltage increases slightly at 115K but is kept in the same order of magnitude.
- The bandwidth for small signal is kept at a similar value, but the slew rate decreases appreciably when cooling the amplifier (it is approximately divided by 2 at 115K).
- The test circuits used to obtain the parameters, although simple, give the correct results. They have been, therefore, validated at room temperature.

6.   FUTURE WORK

The good results obtained for the OPA350 working under cryogenic conditions make us optimistic about the use of other commercial chips for near-infrared instruments. More detailed tests will be performed on the OPA350 at 77K (the current parameters were obtained at 115K) and several other chips will be tested in the near future at the Instituto de Astrofísica de Canarias (IAC). We aim at getting a database of commercial off-the-shelf components that behave correctly in cryogenics, so that we can use them in the future with guarantee and knowing their detailed behavior (that is, their parameters and reliability).

Barry Burke (left) receives his asteroid citation (see Lifetime Achievement Awards, p. xxiii) from James Beletic as Jenna Beletic watches, and Charlotte Cumani (in back) tries to escape.

A SIMPLE TECHNIQUE FOR THE SUPPRESSION OF LINE FREQUENCY NOISE IN IR ARRAY SYSTEMS

Bruce Atwood, Jerry A. Mason, and Daniel Pappalardo
Ohio State University

Abstract: *A description of a simple system to suppress low levels of line frequency noise in data taken with IR array cameras is given. Dark frames taken with the MDM/Ohio State infrared camera (MOSAIC) are shown to illustrate the effectiveness of the system.*

Key words: *Noise reduction, IR detector electronics.*

1. INTRODUCTION

Mux-Readout IR arrays and CCD-type detectors are both routinely operated in systems that can produce images with only a few electrons RMS noise. Obtaining a low noise image from either type of detector requires subtracting a baseline image during the readout process. Within CCD detectors baseline information is obtained on a pixel-by-pixel basis, usually by measuring the level of the output node after resetting it and immediately before the signal charge packet is transferred to the output node. In IR Mux-Readout type arrays a baseline image is normally acquired prior to the exposure to the signal of interest. In either case the baseline sample (or image) is subtracted from the signal sample (or image) to form the final image. This subtraction process creates a high pass filter which rejects signals with long periods compared to the time between the two samples. Since the time between signal and baseline in CCD detectors is typically a few to a few tens of microseconds, disturbances at the power line frequency

(PLF) are attenuated by a factor of order 100. Mux readout type IR arrays, on the other hand, require that a pixel be reset prior to exposure. Thus the time between the baseline sample and the signal sample is longer than the exposure time, typically by a few to many seconds and PLF disturbances are in the resulting bandpass. Even when the wide dynamic range signal chains used for these systems are engineered (or trimmed) to be insensitive to PLF electric or magnetic fields, small changes in the environment can cause this disturbance to reappear. We describe a simple way to greatly reduce the sensitivity of such systems to PLF disturbance.

2.   IR ARRAY READOUT

The typical IR array read sequence begins by reading a frame with nearly zero exposure, in the case of the Ohio State ICIMACS systems [1,2] with Hawaii arrays, by resetting a full line, reading that line, and advancing to the next line. This "pre-read" is stored digitally. The exposure timer is started at the beginning of this pre-read process. When the desired exposure time is complete the process is repeated, with the exception of using dummy delays instead of the line resets, to form the post-read frame. The pre-read frame is then subtracted from the post-read frame. Structure in the pre-read frame is dominated by the offsets from the individual preamplifiers associated with each pixel, and these offsets subtract out. There is also, inevitably, a small amount of coherent noise at the PLF and harmonics. The image in Fig. 1, from the Ohio State MOASIC/TIFKAM [3], was obtained by subtracting two frames taken as outlined above.
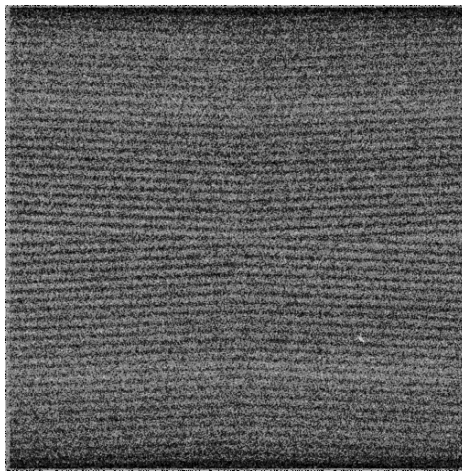
Figure 1. Image without synchronization to the power line frequency.

The diagonal banding is the result of the random phase of the line frequency disturbance with respect to the read process. The bands point toward the center because this type of device reads out in quadrants arranged so that the read process proceeds from the corners toward the center. Figure 2 was taken in an identical fashion with the exception that the start of both pre-reads and post reads are synchronized to the PLF phase. The RMS in Fig. 1 is 2.74 data numbers while the RMS in Fig. 2 is 2.67 data numbers. Thus the improvement in noise level is largely cosmetic.
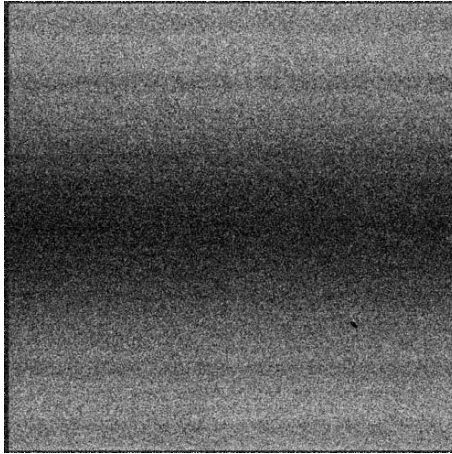
Figure 2. Image with synchronization to the power line frequency.

Figure 3 shows the circuit used to generate the synchronizing signal. The output of a small 12 volt transformer is clipped with d1 and d2. A low pass filter formed form R1 and C1 attenuates any spikes. Comparator U1 then detects the sign of the resulting signal. This square wave is applied to the RI (ring input) pin of a UART, though any available digital input that can be poled could be used. A hardware interrupt could also be used. In our case the RI input is sampled at ~50 kHz and the read process is started when a zero is detected on sample n and a one on sample n+1.

Note that the scheme fails if the line frequency is changing rapidly enough that the total number of power line cycles in a pre-read and a post-read are different. The effect would be good cancellation of the PLF disturbances in the pixels read first, where the phases match due to the active synchronization, and decreasing cancellation as the read process continues. If the pre-read PLF were dramatically different for the pre and post reads there would be bands of good and bad cancellation as the pre and post PLF beat.
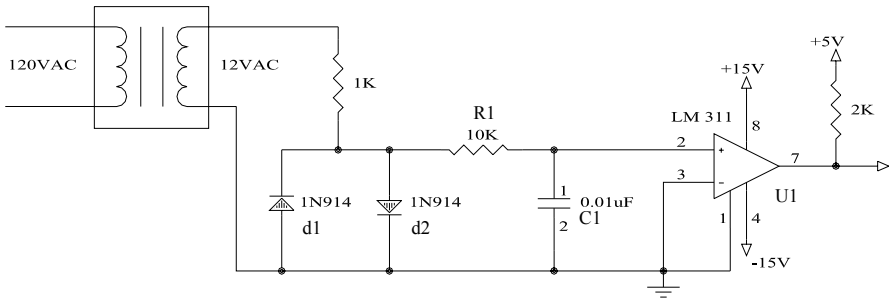
Figure 3. The circuit used to generate the synchronizing signal.

3.   REFERENCES

[1] Atwood, B. et al., 1998, Proc. SPIE **3355**, p. 560.
[2] Atwood, B. et al., 2000, Further Developments in Scientific Optical Imaging, M. Bonner Denton (ed.), The Royal Society of Chemistry, Cambridge, UK, p. 80.
[3] Pogge, R. W., et al., 1998, Proc. SPIE **3354**, p. 414.

SCUBA-2 CCD-STYLE IMAGING FOR THE JCMT
Readout electronics for detectors at 100mK

Maureen Ellis
UK Astronomy Technology Centre

Abstract: *SCUBA-2 will replace SCUBA (Submillimetre Common User Bolometer Array) on the James Clerk Maxwell Telescope in 2006 and will be the first CCD-style camera for submillimetre astronomy. The instrument will simultaneously image at 850 and 450 microns using two focal plane arrays of 5120 pixels each. SCUBA-2 will map the submillimetre sky 1000 times faster than SCUBA to the same signal-to-noise ratio. This paper introduces the detector technology and the challenges faced in reading out a detector array cooled to ~120 mK.*

Key words: *SCUBA-2, submillimetre, superconducting, Transition Edge Sensor (TES).*

1.   INTRODUCTION

The submillimetre wavelength (200 µm to 1 mm) is of great interest to astronomers as it allows them to study galaxy formation and evolution in the early universe to understanding star and planet formation in our own galaxy.

SCUBA (Submillimetre Common User Bolometer Array), the existing submillimetre camera, mounted on the James Clerk Maxwell Telescope (JCMT) consists of a 128-element feedhorn array. Each pixel must be individually assembled. Although this first generation multi-element array instrument has had a huge impact on submm astronomy, the limitations of 128 pixels are being felt. Surveying large areas of sky, or imaging to any great depth, is still very slow but to fill the 8×8 arcmin field of view of the JCMT would require many thousands of pixels and when using this conventional bolometer technology is clearly impractical [1].

SCUBA-2 is the next generation wide-field submillimetre camera which utilizes recent advances in superconducting detector technology, to demonstrate that large format arrays of many thousands of pixels are now possible.

2.   DETECTOR ARCHITECTURE

The detector will be formed from state-of-the-art Transition Edge Sensors (TES) while the multiplexing readout will be implemented using Superconducting Quantum Interference Devices (SQUIDs).

The low heat dissipation of SQUID multiplexers allows them to be at the same temperature as the detectors. The use of the cryogenic SQUID multiplexer is crucial since it makes possible to instrument the full field-of-view with a practical number of wires. The array will be formed by an upper detecting layer and lower multiplexing layer hybridized together using indium bump bonds, as is common practice with IR arrays.

The architecture must be compatible with processing and wafer sizes of the semi-conductor industry to allow fabrication by relatively standard techniques to make the realization of many thousands of pixels practical and affordable. The common Si wafer processing size is 3 inches. The design and physical size of these pixels limits the number on a wafer to 40×32 [2].

2.1   Pixel Geometry

The unit cell of a SCUBA-2 pixel consists of a silicon outer frame that provides the support for the silicon nitride membrane on which the TES and the absorbing bricks are suspended. The TES forms the backshort of a quarter-wave silicon "brick" with an implanted absorber at the front, which is ion-implanted to give a surface impedance match to free space [3]. This layer is then bump bonded to the SQUID MUX wafer. Figure 1 shows a representation of a group of detectors while Figure 2 shows a completely diced array.

3.   SIGNAL READOUT

Incoming submm radiation produces a small amount of heat in the absorber. The TES detects this temperature rise and translates it into a signal current which is then measured by a SQUID ammeter. The TES is voltage biased on the normal-superconducting transition. The resistance of the TES

has a very steep dependence on temperature in the transition region resulting in a very sensitive detector.
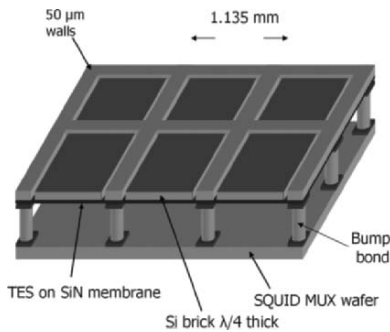
Figure 1. Schematic of detector pixels   *Figure 2.* Detector hybridized to mux
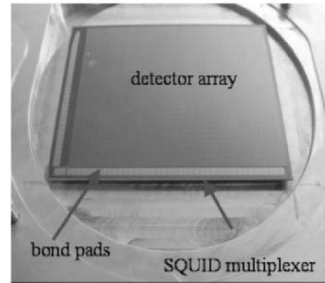
Each pixel is connected to a SQUID via an input transformer to form a two-dimensional array of SQUIDs that make up an array of 32 columns × 40 rows. Address currents are applied sequentially to turn on each row, one at a time. The output is inductively coupled to a summing coil, common to all SQUIDs in a column. The output is tracked to the molybdenum wire bonding pads at the edge of the detector where it is routed through to the 1K pcb which supports the SQUID Series Array Amplifiers (SSA).

The detector is wire bonded onto a ceramic pcb which matches the thermal contraction of the detectors. The tracking is silver-plated as aluminum wire bonding is required for the molybdenum pads. Niobium flex cables provide thermal isolation and carry the signals to the 1K pcb which supports four magnetically shielded cans, each of which contain eight SSAs.

To manage the high-density of connections, a method commonly found in mobile phone technology was used. The flexes are attached to the ceramic pcb and the 1K pcb using an anisotropically-conductive adhesive. After applying a combination of heat and pressure to the adhesive, conducting particles within the adhesive are aligned in the z-axis therefore conducting vertically but not horizontally.

As the SQUIDs used for multiplexing and amplification are extremely sensitive magnetometers they must be well shielded from magnetic fields. Shielding is incorporated, but material having any magnetic properties is excluded from the subassembly. At these temperatures (<10K) nickel, which is used in gold-plating for example, becomes magnetic.

3.1   Cooling

To cool the array to ~120 mK a good thermal contact has to be made to the back of the MUX wafer, while at the same time relieving stresses caused by differential contraction that could shatter the wafer. The solution adopted on the SCUBA-2 project is to use a beryllium copper 'hairbrush' (see Figure 3). There is one tine under each pixel and a few under the second-stage SQUIDs. The wafer is attached to the hairbrush using Stycast 1266. A controlled amount of epoxy is deposited onto each individual tine using a commercial liquid deposition system then the wafer lowered onto the hairbrush. The hairbrush is then bolted to the copper cold finger that leads to the mixing chamber of the dilution fridge [4]. A completed subassembly, lying flat, is shown in Figure 4.
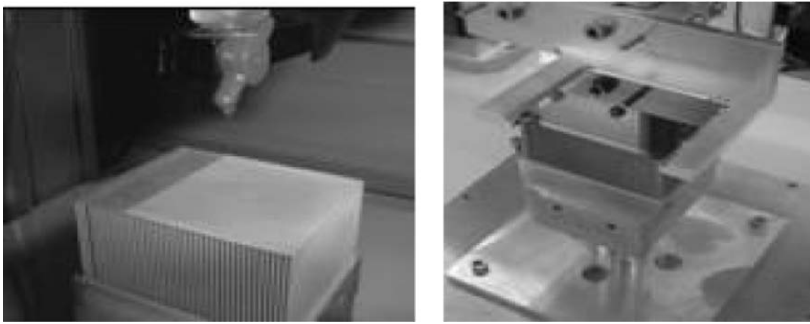
Figure 3. Depositing epoxy onto individual tines and attaching detector wafer.
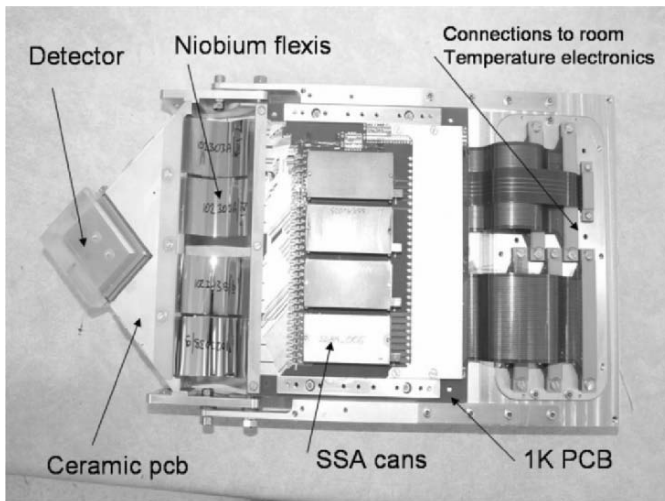
Figure 4. Complete subassembly.

The output of 1K pcb is routed to the room temperature readout electronics through a woven cable constructed from superconducting niobium titanium wires weaved with a nomex fibre.

Figure 5 shows the SCUBA-2 focal plane unit which consists of 4 detector subassemblies butted together, to fill most of the 60 arcmin^2 field-of-view of the JCMT. There will be two focal plane units to cover the 850 μm and 450 μm wavelengths.
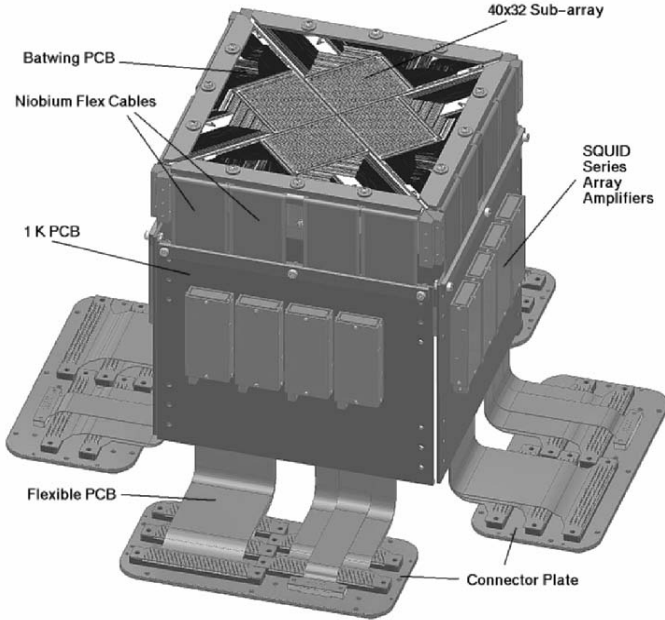
Figure 5. Focal plane unit.

4. CONCLUSIONS

Two complete subassemblies have been assembled and tested. One has been fitted with an 850 μm prototype detector and the other with a 450 μm prototype detector. The 850 μm prototype detector has been successfully tested showing that noise performance has been met, uniformity of the array is good and operation is reproducible. Test results will be published shortly. The 450 μm prototype subassembly is currently being tested. SCUBA-2 is scheduled to be commissioned on the JCMT in 2006.

5.   ACKNOWLEDGEMENTS

6.   REFERENCES

[1] W.S. Holland, W.D. Duncan, B.D. Kelly, K.D. Irwin, A.J. Walton, P.A.R. Ade, E.I. Robson, 2002, *SCUBA-2: A large format submillimetre camera on the James Clerk Maxwell Telescope*, Millimeter and Submillimeter Detectors for Astronomy, Phillips, Thomas G., Zmuidzinas, Jonas (editors), Proceedings of the SPIE, Volume **4855**, pp. 1-18.

[2] W.D. Duncan, W.S. Holland, M.D. Audley, M. Cliffe, T. Hodson, B.D.Kelly, Xiaofeng Gao, D. Gostick, M. MacIntosh, H.M. McGregor, T.Peacocke, K.D. Irwin, G. Hilton, S. Deiker, J. Beyer, C. Reintsema, A.J. Walton, W. Parkes, T. Stevenson, A. Gundlach, C. Dunare, P.A.R. Ade, 2002, *SCUBA-2: Developing the detectors, in Millimeter and Submillimeter Detectors for Astronomy*, Phillips, Thomas G., Zmuidzinas, Jonas (editors), Proceedings of the SPIE, Volume **4855**, pp. 19-29.

[3] J. Walton, W. Parkes, J.G. Terry, C. Dunare, et al., 2002, *Design and fabrication of the detector technology for SCUBA-2*, IEE Proceedings on Science, Measurement and Technology **151** no.2, 110-120.

[4] Michael D. Audley, Wayne . S. Holland, Trevor Hodson, Mike MacIntosh , Ian Robson, Kent Irwin, Gene Hilton,, William Duncan, Carl Reintsema, Anthony Walton, William Parkes, Peter Ade, Ian Walker, Michel Fich, Jan Kycia, Mark Halpern, David A. Naylor, George Mitchell, Pierre Bastien, 2004*, An update on the SCUBA-2 project*, Millimeter and Submillimeter Detectors for Astronomy II, Zmuidzinas, Jonas, Holland, Wayne. S., Withington, Stafford (editors), Proceedings of the SPIE, Volume **5498**, pp. 63-77.

THE ASTRONOMICAL ARRAY CONTROL & ACQUISITION SYSTEM AT NAOC

Zhaowang Zhao and Binxun Ye
Research Labs for Astronomy, National Astronomical Observatories

Abstract: *The Astronomical Array Control & Acquisition System (AACAS) has been completed at the Research Labs for Astronomy of the National Astronomical Observatories of China (NAOC). Ethernet network is used for interface, ensuring that the AACAS can be accessed and controlled around the globe. Various CCD chips, e.g. e2v, Kodak, SITE, Fairchild, etc., can be controlled by the AACAS in many operation modes, e.g. full frame, frame transfer, drift scan, windows and binning.*

One of the key components of the AACAS is a NIOS II family of embedded processors, which is Altera's second-generation soft-core embedded processor for FPGAs. The powerful embedded processors provide AACAS features to satisfy continuously appearing new CCDs and observational requirements. AACAS is very flexible and allows easy implementation of new functions with the help of NIOS II processors. Since FPGA and other peripheral logic signals are triggered by a single master clock, the whole system is perfectly synchronized. By maintaining synchronization, the AACAS camera noticeably reduced the noise.

Keywords: *CCD array sensor, universal controller, ethernet interface, FPGA, NIOS embedded processors.*

1.   INTRODUCTION

The AACAS in development at NAOC is aimed for potential application at many large telescopes in China such as the Large Sky Area Multi-Object Fiber Spectroscopic Telescope (LAMOST), the New Generation Telescope, Yunnan new telescope and Xing Long telescopes.

The AACAS Image Acquisition System was conceived as a scalable, network-based, multi-speed data acquisition system. AACAS will address IR, optical and UV detector needs. To accomplish this, the system requires a modular, scalable hardware and software architecture [1-3]. Different subassemblies for device interface or processing will be added and developed as needed. AACAS is based on a scalable network of powerful NIOS embedded processors, each supporting a 10Mb/100Mb ethernet link. AACAS can be used as a multi-channel data acquisition system. Each data acquisition system can be easily connected to one host control computer. The host computer acts as a supervisor, combining data from each data acquisition channel. In this design, data acquisition channels can be added as needed. We designed the AACAS to be a universal controller for any kind of CCDs such as inter-line CCDs, Low Light Level CCDs (L3CCDs), frame transfer CCDs and full frame CCDs. Thus any observational station can employ an AACAS controller with small modifications.

The CCD controller uses a 16 bit 1 MHz ADC, which can be read out on two or four channels. The pixel read out rate is programmable to be 250 K, 500 K or 1 Mhz. The gain is programmable in four levels. The read out modes are full frame, frame transfer, drift scan, binning, and windows. The binning is among $\times 1$, $\times 2$, $\times 4$, and $\times 8$. High frame rate is achieved in window readout mode utilizing both vertical dump and horizontal high-speed skip. It is useful for fast tracking of a guide star and quick set up of instruments. All of the voltages for clocks and bias are programmable with an accuracy of 1 mV. To protect the CCDs, all of the voltages for DC power, electric biases and clock amplitudes are monitored by individual ADCs. An Altera development kit, which uses a Cyclone FPGA embedded with a NIOS soft core CPU, controls the AACAS.

The NIOS embedded processor board features a Cyclone EP1C20F400C7 device with 20,060 logic elements (LEs) and 294 Kbits of on-chip memory. The NIOS embedded processor board comes pre-programmed with a 32-bit NIOS processor reference design. In this paper, we will give an overview of the AACAS controller and its unique controlling method.

2.   THE AACAS IMAGE ACQUISITION SYSTEM ARCHETECTURE

The AACAS's image acquisition system [4] electronics (see Fig. 1) is typically comprised of four boards as shown in Fig. 2: (1) Embedded

processor board, (2) Driver clock board, (3) Analog (bias) boards, (4) A/D and data acquisition board. All of the electronics boards are inserted into a 6U pseudo-VME backplane.
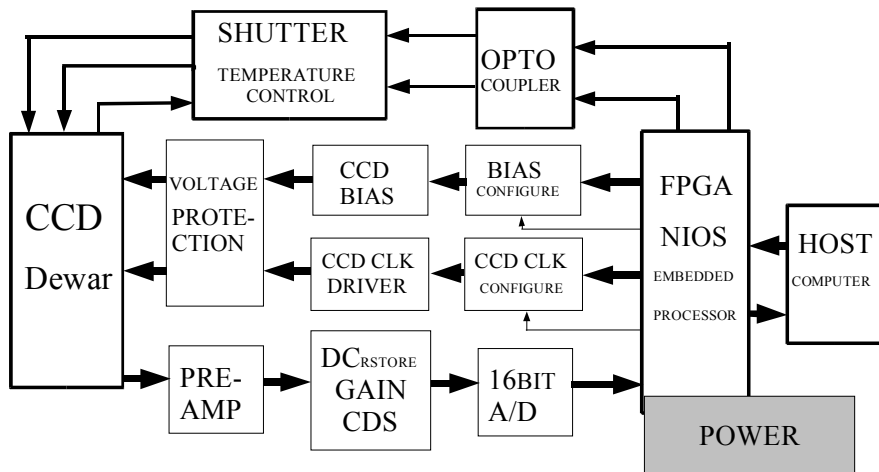
Figure 1. The AACAS image acquisition system architecture.

The standard VME backplane does not meet our AACAS controller requirements, because standard VME backplane does not support more than five types of power supply pins. The width of a signal trace of a standard VME backplane is only about 10 mil (0.25 mm). If the signal pins in the standard VME backplane are used for power, it could become overheated. Thus we designed a 6U pseudo-VME backplane with a 6-layer PCB and a standard 96 Pin connector. 10 power pins are available within. The power supply wire in the pseudo-VME backplane was chosen to be greater than 40 mil (1 mm). Individual layers are allocated for the most important DC power supplies, such as +/-5 V and +/-15 V. We carefully isolated the analog ground plane from the digital ground in the pseudo-VME backplane

The embedded processor board produces all of the AACAS image acquisition system signals, such as clocks and control signals. The clock driver board can produce 8 horizontal and 8 vertical clocks. The clock amplitudes, which are provided by 12-bit DACs, are adjustable in the range of +/-12V. There are sixteen DC analog biases on an analog (bias) board. Each output voltage is provided by a 12-bit DAC and is adjustable in the range of +/-15 V or +/-30 V.

All the voltages of the clock levels and biases are monitored by individual 12-bit ADCs. If any voltage failure is detected, the system protection procedure is executed and the power is cut off.

Figure 2. The AACAS image acquisition system.

3.   AACAS SYSTEM DESIGN

3.1   Top Level Design

The system uses an Aletera Cyclon family FPGA. All of the design is performed by the Quartus II FPGA development software from Altera. The Quartus II design software provides the most advanced suite of tools for system-level design, embedded software programming, FPGA and CPLD design, synthesis, place-and-route, verification, and device programming.

The top level (see Fig. 3) consists of user logic, NIOS embedded processor, master clock and control signals. In the user logic all of the CCD clocks and control signals are produced. This is accomplished by VHDL.
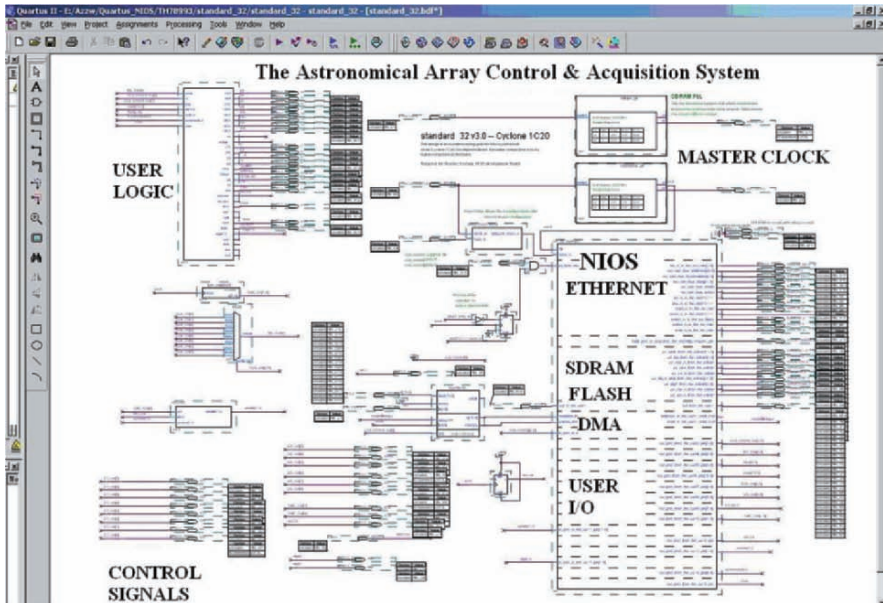
Figure 3. The top level of the AACAS acquisition system.

Since all of the signals produced by a single FPGA, simulation can be used in the design stage at any time. Most of the design should be simulated multiple times and adjusted carefully. In our case we can check all the waveforms in the computer. Any mistake can be found and corrected in the design stage. After completing these components, an oscilloscope will determine if the simulator had correct timing for all waveforms.

Cyclone devices have up to two enhanced Phase-Locked Loops (PLLs). They provide advanced clock management capabilities such as frequency synthesis, programmable phase shift, external clock output, programmable duty cycle, lock detection, and high-speed differential support on the input and output clocks. The master clock of AACAS uses PLLs and can supply very flexible and accurate clocks, reducing the difficulty of the system design. The control signals including ADC control signals, readout modes, control signals, CDS and gain control signals.

SOPC (System On a Programmable Chip) Builder is an automated system development tool that dramatically simplifies the task of creating high-performance SOPC designs. SOPC Builder is included as part of Quartus II software products. The NIOS embedded processor is designed with this tool.

When the design of all the above parts is completed, the Quartus software compiles the project and then downloads the programming code into the FPGA device.

3.2   NIOS Embedded Processor Design

The embedded processor is the most powerful and convenient soft CPU core embedded in a FPGA in recent years. We selected Altera's NIOS embedded processor as the system control CPU. Combining logic, memory, and a processor core, Altera created the industry's first embedded processor FPGA solution that allows engineers to integrate an entire system on a single device.

The NIOS embedded processor [5] provides the flexibility to integrate memory, processors, peripherals, and other Intellectual Property (IP) for SOPC designs. This configurable, general-purpose RISC processor can be easily integrated with user logic and programmed into an Altera FPGA. The processor features a 16-bit instruction set, user-selectable 16- or 32-bit data paths, and a library of standard soft peripherals configurable for a wide array of applications. The development kit [6] provides everything needed for SOPC development based on Altera's NIOS family of embedded processors. The main parts included in the development board [7] are:

- High-volume low-cost Cyclone FPGA EP1C20f400 device
- MAX® EPM7128AE CPLD configuration control logic
- SRAM (1 Mbyte in two banks of 512 Kbytes, 16-bit wide)
- SDR SDRAM (16 Mbytes, 32-bit wide)
- Flash (8 Mbytes)
- EPCS4 serial configuration device (4 Mbits)
- 10/100 Ethernet physical layer/media access control (PHY/MAC)
- Ethernet connector (RJ-45)
- 2 serial ports
- 82 user define I/O ports

4.   ETHERNET DESIGN AND APPLICATION

AACAS is based on a scalable network of powerful NIOS embedded processors, each supporting a 10Mb/100Mb ethernet link [8]. AACAS can be used as a multi-channel data acquisition system. Each data acquisition system can be easily connected to one host control computer. The main diagram is shown in Fig. 4.

The host computer is a supervisor and acts to combine data from each acquisition channel. In this design, data acquisition channels can be added as needed up to an arbitrarily large limit.

When the SOPC Builder development tool generates a system that includes an ethernet peripheral, SOPC Builder includes the plug routes in the Software Development Kit (SDK) for the system. SOPC builder customizes

the Plugs Ethernet library with low-level drivers to match the network hardware used in the custom system. To function on a network (either LAN or point-to-point), the AACAS system must have an IP address.
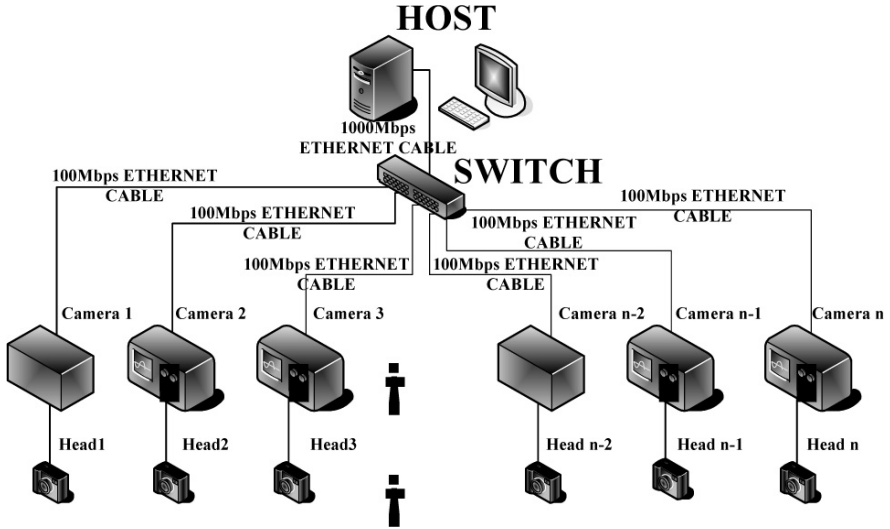
Figure 4. Scheme for the multi-channel AACAS application.

After connecting the AACAS system to a LAN, the camera will either obtain a dynamic IP address using DHCP, or a static IP address stored in flash memory. Once the AACAS system obtains a valid IP address, we can access the board via a web browser (e.g., Microsoft Internet Explorer) by typing the IP address of the camera in the URL address input field.

When a network has more than one CCD camera, an ethernet switcher is needed, which can automatically combine multiple narrow data streams into a broad one. In this case, the connection between the switcher and embedded module is 100 Mbps, and the connection between the switcher and the host computer is 1000 Mbps. Thus one monitor computer can manage numerous CCD cameras.

5.   CONCLUSION AND DISCUSSION

In this paper we described the AACAS image acquisition and process system based on ethernet. We also carried out a test observation successfully. The AACAS used the Atmel TH7899M CCDs and Kodak

KAF-4301 CCDs producing satisfactory results. The flexibility of the AACAS allows changing a CCD with small modifications.

Ethernet and TCP/IP make the expansion of the system very easy. Installation of multiple CCD cameras or the replacement of one is established without any further development of the program in the current system. The beauty of network architecture is the non-interrupt replacement of a CCD camera.

6.   ACKNOWLEDGEMENTS

7.   REFERENCES

[1] Shang, Y., Ye, B., Song, Q., 2004, *A CMOS camera with extended dynamic range*, Advanced Software, Control, and Communication Systems for Astronomy, The International Society for Optical Engineering, Proceedings of SPIE, vol **5496**, p 414-422.
[2] Wei, M., Stover, R., 2002, *A New CCD Controller at UCO/LICK Observatory*, Scientific Detectors for Astronomy, P.Amico, J. W. Beletic and J. E. Beletic (eds), Astrophysics and Space Science Lib., Vol. **300**, Kluwer Academic Publishers, pp 463-465.
[3] Binxun Ye and Binhua Li, *System Design of Detector Systems for a Major CHINESE Multi-Object Spectroscopic Sky Surveyor*, these proceedings.
[4] Barry M. Starr et al, 2002, *MONSOON Image Acquisition System*, Scientific Detectors for Astronomy, eds. P.Amico, J. W. Beletic and J. E. Beletic, Astrophysics and Space Science Lib., Vol. 300, Kluwer Academic Publishers, pp 269-276.
[5] NIOS Embedded Processor Software Development Reference Manual.
[6] NIOS Development Kit, Cyclone Edition Getting Started User Guide.
[7] NIOS Development Board Reference Manual.
[8] Keliang Hu, Yuanyong Deng, Xuelian Ma, 2004, *Data Acquirement and Process System Based on Ethernet for Multi-Channel Solar Telescope*, Proceedings of SPIE - The International Society for Optical Engineering, v **5496**, Advanced Software, Control, and Communication Systems for Astronomy, p 489-496.

HIAC

A High Speed Camera Controller for Avalanche-Gain CCDs

Marc Baril and Tim Hardy
National Research Council, Herzberg Institute of Astrophysics

Abstract: *A new controller tailored to the operation of avalanche-gain CCDs is described. The design utilizes the PC104 standard for compact computer systems allowing the controlling host computer to be embedded within the camera. This controller provides a low-cost, compact solution for implementing small custom CCD cameras.*

Key words*:   High-speed readout, avalanche-gain, embedded system, CCD controller.*

1.   INTRODUCTION

The HIAC camera controller was originally conceived as part of a Kuiper-Belt Object (KBO) detection program using the 1.2 m and 1.8 m telescopes at the Dominion Astrophysical Observatory in Victoria, BC, Canada. The program required the monitoring of a wide field of stars for chance occultations by KBOs, preferably on multiple instruments, at frame rates above 40 Hz. Avalanche-gain CCDs, such as e2v's line of L3Vision sensors, were identified as providing a means of achieving relatively low-noise readout at the required pixel rate of 10 MHz.

Another important consideration was the total deployment system cost per camera. The idea was to use the well established PC104 standard for embedded computer systems and build a camera around this form-factor. The camera could interface either to an external host computer or to a processor embedded within the camera. USB 2.0 was selected as the interface to the host due to its ease of implementation and its widespread commercial use.

Conceivably this controller would be useful in any program requiring monitoring at multiple locations (e.g. meteor cameras) where unit system cost is important, or where a distributed control approach is convenient (e.g. a fast guiding camera). The advantage of architecture with an embedded processor is evident in the example of a fast guiding camera. In this case the processing could be performed by the embedded computer and the appropriate correction signals sent directly to the telescope control system. This architecture obviates the need for a high-speed data link between the camera and a remote host computer. This distributed-control approach for operating the camera is particularly attractive for wavefront sensing in adaptive optics. With a sufficiently powerful processor (or sufficiently low-order adaptive optics) reduction of the data could be performed at the camera level and the control signals sent directly to the deformable mirror driver. Since magnetic storage can be easily embedded in the camera, a night's data could be stored in the camera for slow download to a server the following day.

2.   ARCHITECTURE

The CCD controller consists of four boards: an interface and timing board, a clock driver board, a video processor and bias board, and a board to mount the CCD (see Fig. 1). Typically, these boards would be stacked on top of each other using the PC104 ISA bus connector, which is only used here to bus power between the boards.
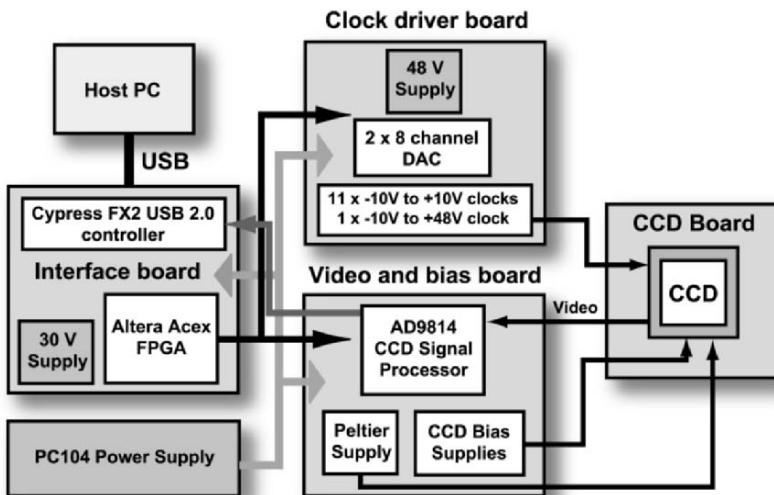
Figure 1. Architecture of the HIAC controller. Each large block represents an individual board module in the PC104 stack.

The interface board uses an Altera Acex FPGA operating at 100 MHz to generate the CCD clock sequences (see Fig. 2). Cypress's FX2 chip is used to implement the USB 2.0 interface to the FPGA and to the output port of the ADC on the video-processor board. The FX2 has a built in 8051 microcontroller that is only used to interface the FPGA circuit to the USB.

The video board uses an Analog Device, AD9814 CCD signal processor to perform correlated double sampling and effectively 13.5 bit digitization of the CCD signal at 7 MHz. The video board also provides 11 programmable fixed bias lines for operating the CCD and a programmable supply for running a Peltier element. Each clock board provides 11 clocks with levels between –10V and +10V and a single clock with a range of –10V to +48V. Up to two clock boards can be incorporated in the system. The CCD board contains no active components, serving only to mount the CCD and clock line terminations.
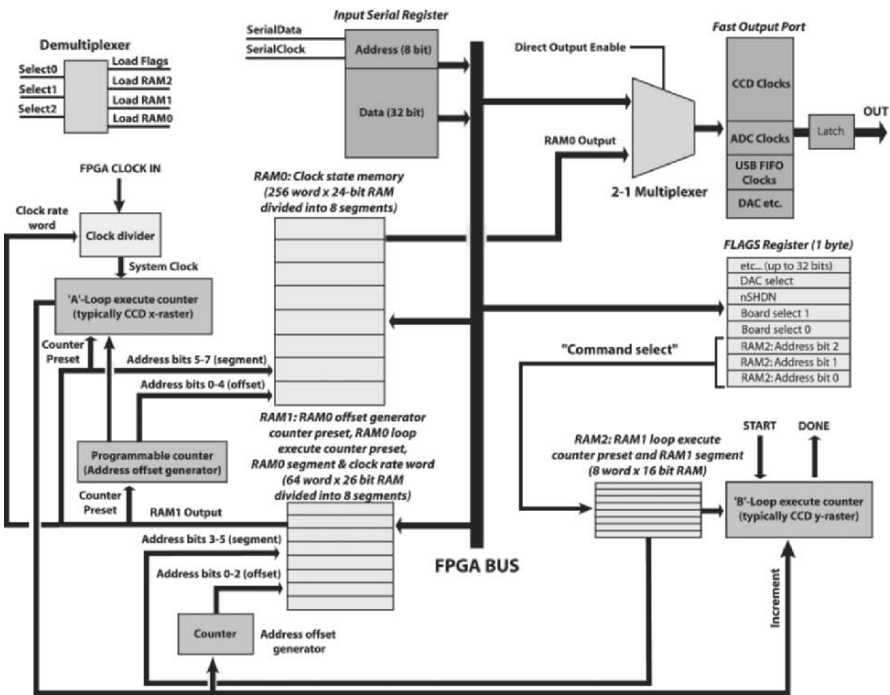
Figure 2. Simplified schematic of the FPGA clock sequencing circuit. The circuit allows the user to switch quickly between different clocking sequences.

3.   SOFTWARE AND FPGA DESIGN

   The FPGA design consists of a state-machine that fully encompasses the clocking sequences required to read out a full frame, a sub-frame or clear the CCD. The frame "readout" or "clear" is triggered by a single "start" strobe. Three on-chip RAM memories hold the clock patterns, the iteration numbers for the various patterns and the clock rate to use for a given pattern. A GUI was developed for the Windows platform to easily create the RAM memory map file to control the circuit, set the biases on the DACs and program the AD9814 CCD processor. The state-machine is sufficiently flexible that for most applications, the user will not need to modify the FPGA circuit or the FX2 microcontroller code. In other words, the user is shielded from the low-level details of the system

   It is anticipated that the first version of the camera will be operational before the end of 2005. This initial version will use the Texas Instruments TC253SPD sensor. Future enhancements may include a "slow-scan" version of the video board which would use a 16-bit CCD signal processor to operate conventional, low-noise CCDs, at slower data rates.
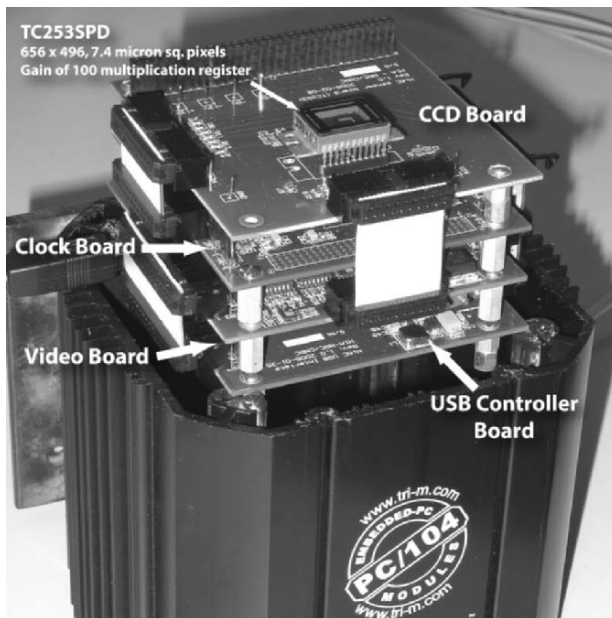
Figure 3. The HIAC camera board stack sitting on a PC104 container.

THE ANTARCTIC NIR/MIR CAMERA AMICA

Fabio Bortoletto[1], Maurizio D'Alessandro[1], Carlotta Bonoli[1], Daniela Fantinel[1], Enrico Giro[1], Demetrio Magrin[1], Leonardo Corcione[2], Danilo Pelusi[3], Croce Giuliani[3], Amico di Cianno[3], Vincenzo de Caprio[4] and Alberto Riva[4]

[1]INAF, Osservatorio Astronomico di Padova, [2]INAF, Osservatorio Astronomico di Torino; [3]INAF, Osservatorio Astronomico di Teramo, [4]INAF, Osservatorio Astronomico di Brera

Abstract: *The near/medium infrared camera (AMICA) is expected to be operational in 2007 at the Dome-C site at the Antarctic pole as a result of the cooperation of several Italian institutions (OAMI, OATO, OAPD) led by the Teramo Observatory and the Istituto Nazionale di Astrofisica (INAF). The camera, to be mounted at the Nasmyth focus of the 80 cm IRAIT telescope, will provide the first astronomical data with scientific content from this site both in the near IR (1-5 μm) and medium IR (5–27 μm) spectral regions via two independent channels equipped with InSb and SiAs detectors respectively. The goal of this instrument is a direct estimate of the observational quality of this new, highly promising astronomical observational site.*

Key words: *Antarctica, infrared camera, robotic telescope.*

1.   THE ANTARCTIC SITE

The high Antarctic plateau appears to have exceptional observing conditions: low wind speed, poor humidity, good meteo conditions and the possibility to perform observations up to several months long. These conditions promise significant gain over temperate latitude sites. Site-testing campaigns have been undertaken in recent years, first at South Pole [1] with only partially encouraging results. These tests suggested that the highest points of the plateau, such as Domes A and C could offer improved seeing due to lower wind speeds and a thinner inversion layer [2, 3].

Recent measurements at Dome C [4], combining data from MASS (Multi-Aperture Scintillation Sensor) and SODAR (Sonic Detection And

Ranging) report exceptional seeing with a median value of 0.27 arcsec. Moreover, Antarctica is much less dusty than Chilean and Hawaiian summits and could substantially reduce the emissivity of telescope surfaces. These conditions are extremely favourable for infrared observations in particular, where the ambient thermal background usually overpowers the objects studied (see [5] for a review of the current capabilities in infrared astronomy and a comparison with the opportunities presented at Antarctic sites).

Figure 1 shows a simulation of the principal background components (left) and of the total contribution (right) in the NIR-MIR spectral range with a resolving power of 3. The simulations are in agreement with recent semi-empirical models [4] indicating that the atmosphere can be at least a factor of 10 darker than mid-latitude sites.
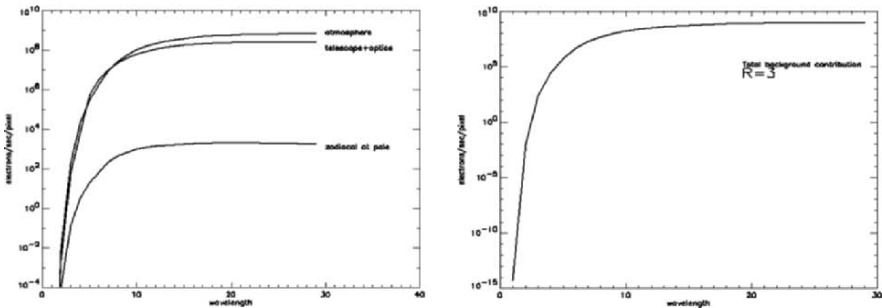
Figure 1. *(left)* Separated (zodiacal, telescope + optics, and atmosphere) and *(right)* total background contribution in a typical camera observation with 3% bandwidth.

Observations in the NIR bands could also benefit from extremely low humidity and consequent airglow reduction.

The opening of the Italian-French base Concordia at Dome C [6] offers a unique opportunity for the Italian astronomical community. The possible advantages offered by the Antarctic plateau are in someways counterbalanced by the actual difficulties of building and maintaining a telescope in such a remote and severe environment.

A number of issues, both technical and logistical, must be taken into consideration when designing instrumentation for operation in Antarctica. It is the most remote place on Earth. Dome C is particularly remote, being 1200 km inland from Terra Nova Bay; it is more difficult to reach than the coastal regions. Telescopes and instruments must be left without any possible maintenance for long periods during the long Antarctic night. Weather conditions are extremely severe. In wintertime temperatures fall to −90°C, while summer highs are −30°C. These temperatures make both human and instrumentation operations difficult.

2. THE IRAIT TELESCOPE AND THE MIR/NIR AMICA CAMERA

The IRAIT project is part of an international collaboration (Italy-Spain-France) led by the Perugia University and is based on a fully robotic 80 cm ALT-AZ telescope. The final optical and mechanical configuration of the telescope is now defined and a preliminary sketch is given in Figure 2. The telescope is integrated into a modified ISO20 container and a hydraulic system provides the opening and closing mechanism of the structure. The telescope secondary will allow the chopper function to be commanded by the camera controller.

One of the Nasmyth focal stations will be equipped with AMICA (Antarctic Multiband Infrared Camera), a NIR/MIR double armed camera operating in the J, H, K, L, M, N, Q photometrical bands.
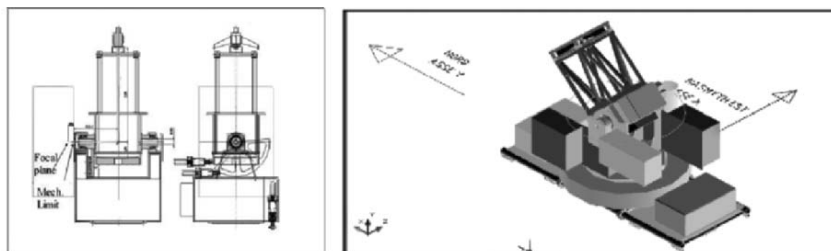
Figure 2. The Perugia University IRAIT Antarctic telescope. The complete structure fits a standard container.

A preliminary optomechanical design of the camera is shown in Figure 3. Taking advantages from the large difference in pixel size between the NIR and MIR detectors, a single TMA (Three Mirror Anastigmatic) system with fixed magnification has been designed to illuminate the selected detector. Detector selection is commanded by a simple step-motor driven flat flip-mirror. A second advantage of this simple optical system is a single step-motor driven filter wheel placed in the reimaged pupil that switches between filters for both channels. Both mechanisms, flip-mirror and filter-wheel, are driven by cryogenic motors (Phytron) working at optical bench and radiation shield temperatures (about 55 K°) and avoiding the presence of mechanical feed-through.

Detectors will be mounted on dedicated housings cooled by conductive straps connected to the second stage of a Sumitomo GM cryocooler. The optical-bench and shield will be cooled by the first stage of the cryocooler. Resulting electro-optical parameters of the camera are given in Table 1.

Under these conditions the MIR detector provides diffraction-limited Rayleight sampling at λ=8.57 μm.
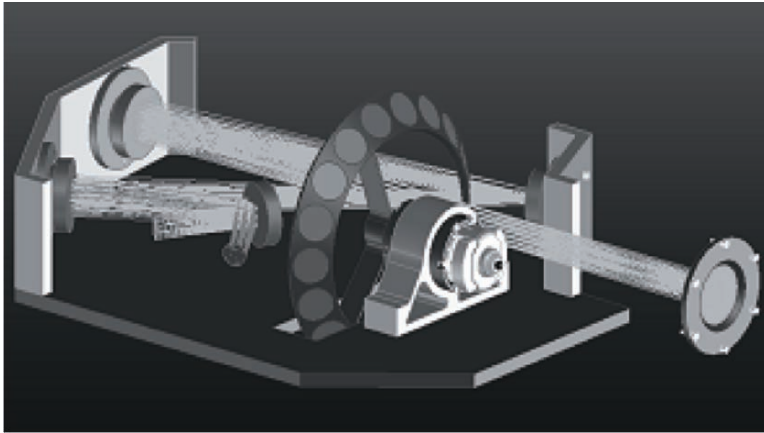
Figure 3. A preliminary sketch of AMICA showing the entrance window, the TMA mirror system and the two motor driven parts: a flip-mirror and the single filter wheel.

Table 1. Main electro-optical parameters for the NIR/MIR channels of AMICA.

MODE	Detector	Pixel number	Pixel size	Pixel sampling	Well capacity	Work Temp.
NIR	Raytheon In:Sb	256×256	30 μ	0.54" /pixel	1.5×10^5 e/pixel	7 K°
MIR	DSR Si:As	128×128	75 μ	1.34" /pixel	10^7 e/pixel	30 K°

3.   THE AMICA CONTROL SYSTEM

There are two specific problems complicating the operation of an autonomous instrument in Antarctica:

- The presence of unusually low ambient temperatures
- The unexpected low capacity to dissipate heat from electrical components due to air rarefaction (Dome-C is at an altitude of 3280 m corresponding to a barometric altitude of about a thousand meters higher)

These problems demand balloon/space techniques that guarantee reliable margins. For AMICA it was decided to split the system in two sections, with controls and electronics in a controlled temperature ambient (-10/+10 C°), and the camera system at the external temperature (see Fig. 4).
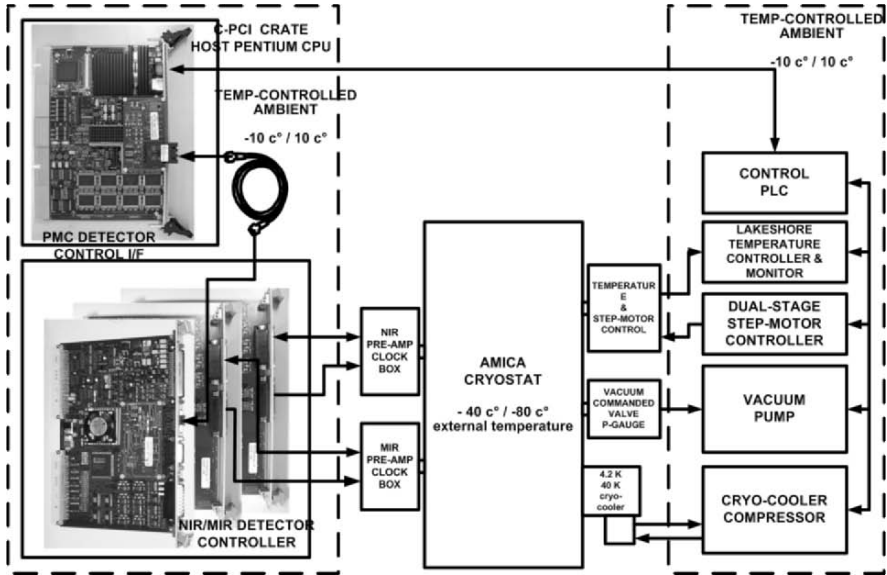
Figure 4. The overall AMICA control system subdivided in cold and warm ambient temperatures.

In such conditions electrical and optical flanges on the cryostat will be sealed with indium wire due to the low external temperature. The cryo-cooler head will remain open at operating temperature, which is usually higher (5/35 C°). All the control electronics (CPCI computer, detector controller, PLC master control system) and the cryo-mechanisms (vacuum pump, cryo-cooler compressor and temperature controllers) will be placed in the thermalized rack. The PLC interface to the CPCI host provides high level system control, i.e., system ON/OFF cycles, vacuum and cryocooling cycles, temperature monitoring (inside and outside the dewar), racks temperature control and cryogenic step-motors control.

Both NIR and MIR detectors are built around 4 output multiplexers and are served by an eight independent channel electronics [7] based on a CPCI-Pentium host and a SKYTECH PMC control I/F.

4. CONCLUSIONS

While there are surely challenges to operating in Antarctica, the advantages for astronomy appear more and more compelling. Here we presented a NIR/MIR camera to be operated on a fully robotic telescope that will be placed at Dome C. The project is on-going and some parts are defined and acquired: one of the two detectors was acquired and tested in the laboratory in combination with a cryo-motor driven filter wheel at a temperature of 18K.

5. REFERENCES

[1]   M.A. Chamberlain, et al, 2000, Ap.J. **535**, p. 501.
[2]   J.S. Lawrence, 2004, PASP, **116**, p. 482.
[3]   R.D. Marks, 2002, A&A **385**, p. 328.
[4]   J.S. Lawrence, M.C.B. Ashley, A. Tokovin & T. Travouillon, 2004, Nature, **431**, p. 278.
[5]   P.F. Roche, 2003, Mem. S.A.It. Suppl. **2**, p. 74.
[6]   M. Candidi, A. Lori, 2003, Mem. S. A. It., **74**, p. 29.
[7]   F. Bortoletto, et al, 2005, these proceedings.

Catania Observatory Director Santo Catalano was a gracious host and excellent partner for organizing this workshop.

A NEW GENERATION OF DATA AND CONTROL INTERFACES FOR DIGITAL DETECTORS

Fabio Bortoletto[1], Maurizio D'Alessandro[1], Enrico Giro[1], Rosario Cosentino[2], Massimiliano Belluso[2], Alessandro Carbone[3], Marco Gemma[3]
[1]INAF - Osservatorio Astronomico di Padova, [2]INAF - Osservatorio Astronomico di Catania, [3]SKYTECH

Abstract: *The purpose of this project, started in 2002 with the support of a two year grant from the Agenzia Spaziale Italiana (ASI), was the development of a modular detector-controller and data-handler compatible with present industrial and consumer bus/interfaces, i.e., VME, CPCI and PCI. As a second, but no less important, instance the system here described has been developed as an upgrade for the out of date VME/transputer interfacing systems still in operation at various Italian astronomical sites and also as a platform for more complicated detection systems (NIR/MIR cameras or large detector mosaics) to be implemented in the future. As a consequence this paper is intentionally focused on the digital structure of the system (data-flow, controls and telemetry), being the usual analog electronics typically embedded on a classical detector controller (i.e. pulse and voltage adapters, amplifiers etc.). This paper is less concerned with the overall architecture, which is only marginally mentioned herein. Several implementations of this system are already in operation in different astronomical applications, some of them presented during this meeting.*

Key words: *Detectors, control systems, electronics.*

1.   INTRODUCTION

It is from the advent of modern CCD area detectors (in the second half of seventies) that the need for flexible detector controllers has emerged. The life-time for such control systems is determined not only by the evolution of

detectors and by the technological evolution of electronic components (converters, gate-arrays, printed circuit technology, etc.), but also by the need to have better connectivity in terms of throughput and ease of system insertion inside computers and advanced data networks. Looking back, we can estimate that the life-time of a detector controller system is typically between 5 and 10 years before it is obsolete. This project, named VISIR-C (Visual Infrared Controller), belongs to the third and last generation of controllers constructed by the authors of this paper. This evolution spans 25 years activity beginning with the first generation of detector control systems created in order to support small and medium ground-based observatories [1] and a second generation of systems constructed to support the Galileo National Observatory [2].

2. SYSTEM REQUIREMENTS

As a direct result of previously made considerations and by comparison with the present advancements in the field of detector controllers we derived the following requirements for the VISIR-C project [3,4]:

1. Upgrades for the previous generation of transputer based VME/VSB boards ensuring compatibility with high level SW (table editors)
2. Compatibility with modern bus architecture, i.e., PCI, CPCI, VME and use of dedicated single-chip modern bus-adapters (AMCC chips in this case)
3. Use of host computer memory for data storage via PCI fast data transfers assuring an easy upgrade path
4. Use of fast throughput, full-duplex, data & controls link between host interface and remote electronics (1.2 Gbaud in the present case)
5. On board (host interface) generation of detector clock sequences and transmission through the fast control link
6. A simple expansion scheme for the controller adding boards to the system.

3. THE PMC/PCI CONTROLLER INTERFACE

In order to achieve a high level of compatibility with modern bus structures, the PCI bus model has been used as a base for reference due to its presence at the CPU board level, as well as in different 'industrial' structures like the VME bus and the CPCI. It was thus possible to cover a wide range of bus standards with the construction of the two basic detector host-adapters shown in Fig. 1:

- the PCI model, covering low-cost PC based systems, and
- the PMC model, covering more professional structures like CPCI and VME

Both systems are built around a standard AMCC PCI bus adapter and are served by a Motorola DSP53301 processor acting as a programmable clock sequencer. The processor is compatible with the existing off-line software for clock waveforms design and run-length encoding. Clocks produced by the DSP at a stable tick time of 50 nSec are serialized, sent to the remote controller board and de-serialized. The same is done for commands and operands, so that the remote electronics are completely passive and a unique system clock is used at 40 Mhz on the remote head.
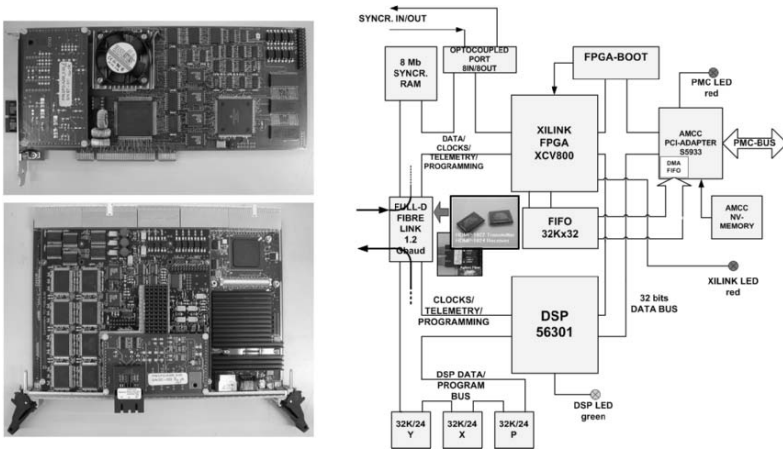
Figure 1. PCI and PMC interfaces. The PMC interface is based on a 'piggy-back' module (two PMC slots) typically mounted on the top of a CPU board (a Motorola CPV-5375 in the bottom picture) or in a PMC carrier board.

The more complex PMC module adds the presence of a large FPGA array, custom programmable from the host computer, to implement fast algorithms on the detector data flow.

The DSP 56301 and the FPGA have their own memory for data and programs; both can use the output channel to the remote unit for commands and readout sequences. This means that both can be used as clock-sequence generators. Conversely, the input fast channel for data can be used only by the FPGA. It is then possible to process data from the detector 'on the fly' using wired functions on the FPGA (co-adding, computation of event centroids, tracking of objects, etc.). The configuration of the FPGA can be changed so the controller interface can be remotely reprogrammed by downloading the micro-code into the dedicated memory from the host-

computer. Both boards are provided with an opto-coupled I/O port acting as a general services port or, if required, as a synchronization link for expanded systems (see Fig. 2).

4.   THE REMOTE CONTROLLER INTERFACE

The remote unit is completely 'passive' in that no computing power has been implemented to reduce the clock/interference jitter on the system to a minimum.
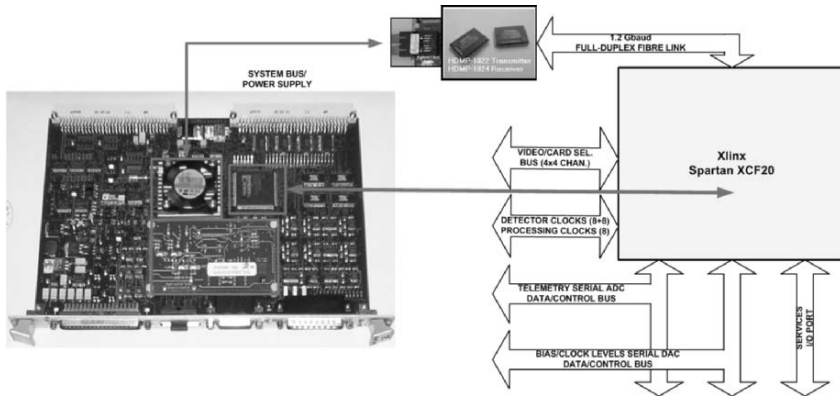
Figure 2.   A single FPGA (Glue Logic chip) allows remote interfacing with the PMC/PCI set
of host computer interfaces. A specific remote unit can be constructed around this
embedded logic only by adding the specific analog functions required.

The central 'core' of this system is a Glue Logic chip that implements all the logic functions needed to drive a set of general-purpose analog boards customized for a given detector on an FPGA (Xilink Spartan series), i.e.:

- handling of a command/data/telemetry link to the PCI/PMC interface board,
- reformatting of detector clocks coming from the PCI/PMC interface board (8+8 programmable clock lines plus 8 pixel processing lines),
- handling of video channel data-flow (up to 4×4 16 bit channels),
- handling of serial DACs control lines for BIAS/CLOCK programming,
- handling of serial ADCs control lines for Telemetry acquisition, and
- handling of services (temperature and shutter control).

In our specific implementation, the basic remote unit has been mounted in a VME format board allowing compatibility with existing analog boards. Different implementations can be also imagined, for example a single,

compact, remote unit where the Glue Logic chip is directly embedded with the analog electronics.

The system is, in this way, customizable for a given application and/or detector focal plane, in that only the insertion of a specific set of analog boards is needed to configure it.

The requirement to expand the system with more complex control architecture (detector mosaics, multiple service cameras, etc.) has been satisfied by making use of host-computers. Figure 3 shows simple architecture based on PCI interface, where a common synchronization line driven by a master interface allows the building of a large system with no dedicated hardware other than the simple insertion of extra boards. The same architecture and configuration is valid for PMC interfaces.
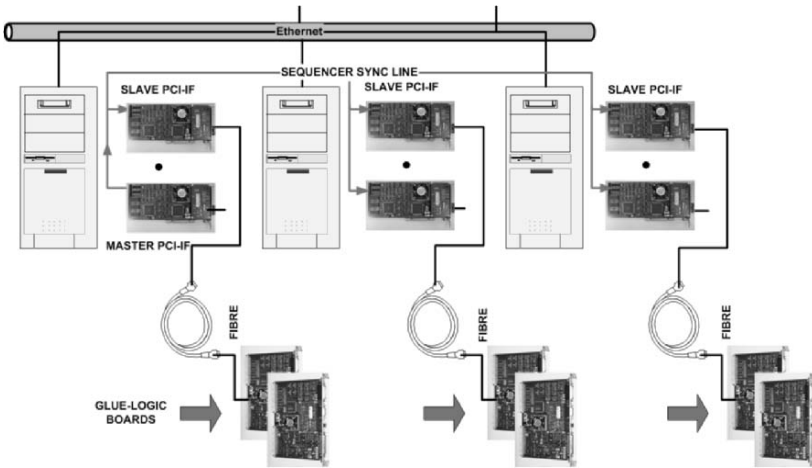
Figure 3. Expansion tree for the system based on a common synchronization line handled by a master host-computer interface.

5. CONCLUSIONS

A modular, general purpose detector control system has been studied, developed and tested. The system allows the handling of a variety of image detector configurations based on contemporary dominant technologies (CCD and CMOS multiplexer readout). The hardware can be remotely controlled, reconfigured, and asynchronous telemetry on every detector-crucial parameter captured. The system is compatible with a wide range of PCI, CPCI and VME host computer interfaces and it can be easily expanded inside this ambient to complex configurations.

6.   REFERENCES

[1] Bortoletto, F., D'Alessandro M., 1986, Rev. Sci. Instruments, **57**, p.253

[2] Bortoletto, F., Bonoli, C., D'Alessandro, M., Fantinel, D., Farisato, G., Bonanno, G., Bruno, P., Cosentino, R., Bregoli, G., Comari, M., 1996, SPIE Proc. **2654**, P. 248

[3] Bortoletto, F., D'Alessandro, M., Fantinel, D., Giro, E., Corcione, L., Bonanno, G., Bruno, P., Cosentino, R., Carbone, A., Evola, G, Mem. SaIt **74**, 2003

[4] Cosentino, R., Belluso, M., Bonanno, G., Bruno, P., Bortoletto, F., D'Alessandro, M., Fantinel, D., Giro, E., Corcione, L., Carbone, A., Evola, G., 2003, Scientific Detectors for Astronomy, The Beginning of a New Era, Amico, P. , Beletic, J. W. , Beletic, J. E. (eds.), p. 423.

Fernando Pedichini and Roberto Speziali holding their breath and eating pizza
at the the same time.

McDONALD OBSERVATORY *n*RG DETECTOR ELECTRONICS

Joseph R. Tufts and Phillip J. MacQueen
The University of Texas at Austin, McDonald Observatory

Abstract: *The McDonald Observatory detector group recently added IR capability to their Version 2 (V2) CCD controller. With minimal hardware and software modifications, we are operating HAWAII-nRG devices. Principally modified to support a HAWAII-1RG detector for LRS-J, a J-band extension to the HET's low-resolution spectrograph, our existing system can be used to operate 2RG devices in 4-amplifier mode as well. LRS-J, based on a cryogenic prime focus camera optical design, uses an unusual approach to mounting a 1RG device, and it requires custom cryostat circuitry to minimize heat load, obscuration, and changes to the CCD-based electronics. It takes advantage of the nRG's programmability and makes dual use of the serial interface programming lines. AC coupling the preamplifier to the detector requires line-by-line DC restoration, but yields stable reference pixel values between frames. The performance of the reference amplifier and reference pixels are under investigation for use in long integration time, low background spectrometry.*

Key words: *LRS-J, McDonald Observatory V2 Controller, HAWAII-1RG.*

1.   INTRODUCTION

Presently, the McDonald Observatory only operates one modern near-IR ($0.9\,\mu\text{m} \leq \lambda \leq 2.5\,\mu\text{m}$) instrument, LRS-J, and thus this paper focuses strongly on the specifics of that instrument and its HAWAII-1RG detector. In practice, we can operate any *n*RG device without modification and many other near-IR detectors by only implementing new gain settings within the preamplifier stages.

The LRS-J detector controller is based on the McDonald Observatory V2 CCD controller, with minor modifications to two modules: the Penthouse/preamplifier (PH) module, and the Clock Driver (CD) module (see Fig. 1).

The V2 controller is a true 18-bit 2/4 channel 100 kpix/s system. Although the 1RG doesn't require an 18-bit system, because of its limited dynamic range, these modules exist and operate fast enough to acquire 16-bit data by simply not using the 2 LSBs. System noise in this configuration is essentially non-existent.
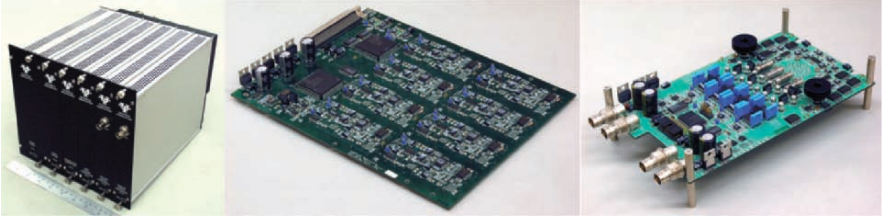
Figure 1. (left) McDonald Observatory V2 controller. *(middle and right)* The HAWAII-*n*RG specific clock driver and Penthouse modules.

With few exceptions, the required modifications were made simply to decrease risk to the array. For example, in the CD module, the Thaler VRE310 was replaced with a 3.000 V VRE303J to limit the allowable voltage swing of the nRG clock inputs to a range of 0–3.3 V, all settable with 12-bit ADCs. In the PH module a similar philosophy (VRE402J) was employed. Gain in the preamp went up to ~28.0 V from the 8–20 V we use for CCDs. The PH module now outputs 0–10 V depending upon the 1RG detector signal.

The most esoteric change required bypassing (by occasionally lifting an SMD foot and soldering another component between the foot and its pad) the unused negative clock supplies required for CCD operation. Aside from the vacuum circuitry, no new Printed Circuit Boards (PCBs) were required to accommodate the new detector.

2. VACUUM ELECTRONICS

Typical instruments require custom vacuum circuitry usually implemented in micro-coax of exotic materials, or, as in LRS-J, a rigid-flex PCB designed to accommodate unique instrumental geometry (see Fig. 2). In the LRS-J implementation, the vacuum circuitry is implemented in two custom four-layer polyimide flex circuits with rigid Kapton stiffeners

bonded to the component side of the flex circuits at each end. We minimize the number of required control lines by utilizing as much of the programmability of the 1RG device as possible. We carry out four of the 32 *n*RG outputs. Two of these, OutputB[7] and OutputB[15], are defined, while the other two can be selected via on board jumpers to the WindowOutB and RefOutB outputs, available on both the 1 and 2RG devices, and respectively OutputB[23] and OutputB[31], available only on the 2RG. The flex circuit was manufactured by Flex Interconnect Technologies in California. It is a four layer polyimide construction of 2 mil DuPont Pyralux AP with 1 mil Pyralux LF as a coverlay. The acrylic adhesive in the coverlay is vacuum degassed for 8 hours at 105ºC as per the manufacturer's instructions.
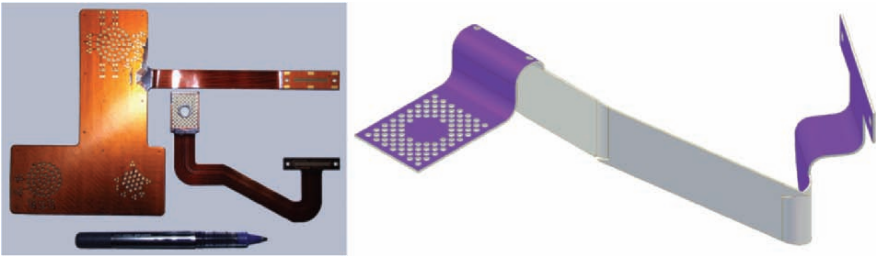
Figure 2. LRS-J HAWAII-1RG vacuum circuitry. This was designed in Inventor as if it were made of sheet metal.

Components are soldered to the flex through a 1.5 mm thick Kapton stiffener located at each end of the two flexible boards. Excepting the four analog outputs, all traces are 0.5 oz (18 µm) thick copper by 5 mil wide on 20 mil centers. Each signal trace is one layer separated from an 8 mil trace on a grounding grid. The ground grid is meant to mimic the functionality of a ground plane without the penalty of high thermal conductivity.

The four analog outputs are passed over 5 mil wide traces and coupled to 12 mil ground traces. Thus, they would be well shielded if they could be interpreted as running over a semi-infinite ground plane.

Using industry standard approximations for high speed signals over flex circuitry (IPC-2251, Feb 2001) we calculate the impedance to be 36.9 Ω at 1 MHz. The signal lines have a capacitance of 1.414 pF/cm (46 pF total). Note that the approximation is made so that the ground trace is significantly wider, compared to their separation, than the signal trace. Observing the analog output signal just after the first preamplifier stage on an oscilloscope we see a full scale transition (10 V) followed by a 100 mV overshoot which decays to 0 V (16-bit precision) within 5 µs. For comparison, the ASP integration time is 7.5 µs.

The flex is fabricated in two pieces allowing straightforward instrument assembly/disassembly. The MDM-37 intermediate connection on the outer flex is thermally bonded to the optical assembly at 120 K, and the instrument sees a conductive load of 40 mW from the ambient temperature vacuum housing (insignificant compared to the conductive load through G10-CR structural supports). A similar (but more geometrically complex) flex circuit isolates the ~40 K drop between the optical and detector assemblies with a 10 mW load seen by the detector cold link.

3.   DETECTOR ASSEMBLY

In an unusual approach, LRS-J (see Fig. 3) places the detector in a sandwich-like assembly between the field flattener and copper cooling plate.

Matching the instrumental pupil (142 mm) to the 18 µm pixels of the 1RG at a plate scale of 2 µrad/pix required an unusually fast f/1 camera. The final optical element in this assembly is a PK50 field flattener (a meniscus shape with outer convex r_1=50.5969 mm and inner concave r_2=−461.0109 mm). The PK50 material was chosen to sharpen 1RG's long wavelength cutoff. At f/1 the overall size of the FF is approximately that of the 1RG package. Coincidentally, this nearly matched the HET central obscuration and, on axis, the detector assembly does not obscure the beam by using the oversized 1RG package in a Schmidt camera configuration. However, we were not afforded much room beyond the package to make the assembly. We were also restricted to a very short (25 mm) overall length by the separation between the detector's active layer and cavity face of the J-band blocking filter.

To constrain the separation between FF and detector, we make use of the 1RG's mask features, 4 1-72 blind tapped holes located next to the detector island. Using precision turned vented pins threaded to fit these tapped holes, we locate a spacer with a hole/slot combination, on the front surface of the 1RG package. The spacer, of stress relieved SST 416, has a spherical surface precision machined to match the concave final FF surface. Its CTE was chosen to match the PK50 rather than that of the molybdenum 1RG package so that it would not move, during thermal cycling, relative to the FF. Regardless, the total relative movement during a thermal cycle, between detector and spacer, is 28 µm.

The SST spacer and field flattener are together clamped into a die-form EDM machined aluminum retaining shell with a 25 µm thick SST shim. This is only necessary for alignment and assembly purposes as the final assembly is preloaded together. The shell itself is 0.5 mm larger than the elements it

contains to allow a small amount of tip/tilt alignment tolerance between the axis of the FF and that of the detector.

The FF is constrained in three DOF by the geometry of the spherical retaining shell, and in the remaining three, *xy* translation and *z* rotation by a frictional force equal to many hundreds of times its weight. Likewise the SST spacer is constrained to the FF in the same manner. The H1RG is constrained to the spacer in all six DOF with the aforementioned locating pins, and the copper cold block to it in *z* by spring preload.

Three McMaster-Carr 9435K11 springs are compressed approximately 1.5 mm yielding a force of 125 N keeping the assembly together, allowing thermal conduction between its members, and to allow for CTE mismatches between the Al gimbal assembly and the various low CTE components which make up the detector assembly.
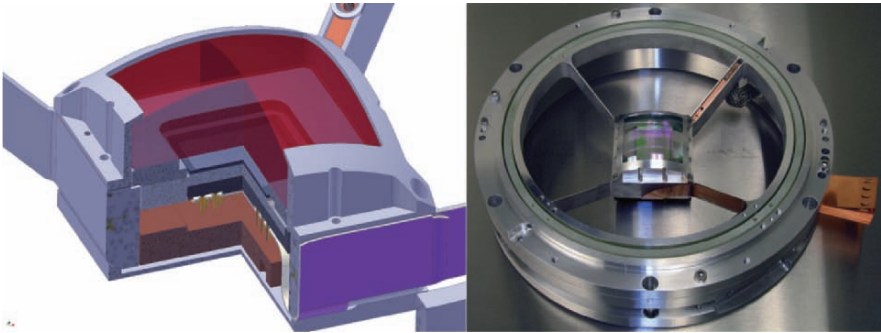
Figure 3. LRS-J detector assembly. Note the custom rigid flex folded along the spider vane, large copper cooling conductors, and G10-CR middle gimbal ring for thermal isolation. Also note the unusual use of the 1RG mask features to constrain the FF spacer.

4. GIMBAL ASSEMBLY

The innermost of three gimbal rings supports the detector assembly via five spider vanes 1 by 15 mm in cross section. Two of these vanes straddle the Cu cold finger and are separated by 4 mm; the remaining three are equally spaced at right angle intervals from this initial pair. Viewed edge-on the detector assembly is not flat. It is wire-EDM machined from a conical form which allows us to place the intersection of the gimbal axes at the outer vertex of the field flattener allowing gimbal adjustment without affecting instrumental focus.

The two gimbal axes are achieved through four Lucas/Goodrich 6008-400 flex-pivots which, when coupled with a G10-CR middle gimbal ring, help reduce the thermal conductivity between the ~80 K detector assembly and the ~120 K optical assembly to < 50 mW.

5.   SOFTWARE

The V2 controller interfaces to the user through an implementation of IRAF/ICE. C routines are used for host-based detector operations, and the controller microcode is in DSP assembler. Significant changes were required to the CCD-oriented ICE and microcode software to program the array through its serial interface, and to offer a full range of data taking and reduction capabilities for spectrometry.

A H1RG array can be readout with either 1 or 2 amplifiers, in full-frame or window mode, with pixel (0, 0) in any corner of the array, and with the reference amplifier read also. The pixel rate, 100 kpix/s per output, yields 10.5 or 5.2 s frame readout times, respectively, for 1 or 2 output reads. Global or line-by-line reset is optional.

The optional readout modes are reset-read, up-the-ramp, and Fowler sampling. The data for the different modes can be reduced as part of the readout, optionally using both the reference pixels and the reference amplifier. A checksum is generated on a per-line basis, and each line of a multi-frame readout is uniquely tagged to ensure that the data can be correctly reduced should some data integrity issue arise. Saving each of the raw and reduced data is optional, as are different modes of shutter control for the various readout modes.

A full-featured waveform generator can be selected under software control instead of the preamplifier. This allows much of the hardware to be exercised and tested in most of the readout and data reduction modes. This has proved valuable during software development, and in verifying many aspects of the hardware during use.

INTEGRATING SIGNAL PROCESSING AND A/D CONVERSION IN ONE FOCAL PLANE MOUNTED ASIC

Turning Photons into Bits in the Cold

Armin Karcher, Christopher J. Bebek, Maximilian Fabricius, Brad Krieger, Hendrik von der Lippe, Markus Redelstab, Jean Pierre Walder
E.O. Lawrence Berkeley National Laboratory

Abstract: *The CRIC (CCD Readout IC) ASIC has been designed to meet the power, space and radiation requirements of the SNAP satellite. It incorporates four channels consisting of a pre-amplifier, double correlated sampler and pipeline A/D converter with integrated voltage reference. The CRIC chip has been specifically designed to operate both at room temperature and at typical focal plane temperatures down to 130 K. This minimizes wiring complexity while maintaining signal integrity on complex focal planes. CRIC is half of a two ASIC CCD readout system. The other ASIC in development is a bias and clock voltage generator. Also in development are 16 and 32 channel versions of CRIC for use with hybrid photodiode and near infrared pixel arrays.*

Key words: *ASIC, CCD readout, cryogenic, radiation tolerant, low power.*

1.   INTRODUCTION

A four-channel custom chip designed for reading out Charge Coupled Devices (CCD) is presented. This design is part of the research and development program for the SNAP (Super Nova/Acceleration Probe) project. SNAP is an international satellite proposal dedicated to understanding the dark energy responsible for the accelerating expansion of our universe. It has a 2 meter telescope with a large field of view. CCDs and near infrared detectors are located on the focal plane for imaging and spectroscopy. The primary goal of the CRIC circuit is to cover a 16-bit

dynamic range with a readout noise of 7 µV rms (2 electrons) referred to the input at 100 kpixel/s readout speed.

The circuit described is intended to operate close to the CCDs to reduce interconnect heat-load and complexity as well as minimize pick-up noise. This adds additional constraints to the circuit such as low power consumption, operation at 140 K and radiation tolerance to a total dose of 10 krad. To simplify the testing and characterization of the chip, full operation at room temperature is desirable. The chip was designed with standard 0.25 µm CMOS technology using only 3.3 V transistors. This technology was chosen since it is mature, but far from obsolescent. The choice of 3.3 V transistors also increases the design portability to other foundries, further improving manufacturability and longevity of the circuit design.

This chip described here is CRIC II. CRIC I [1] was a proof-of concept chip that implemented the basic analog signal path of the circuit and was used to validate the signal path architecture and to gain insight into low temperature operation.

2.   CIRCUIT OVERVIEW
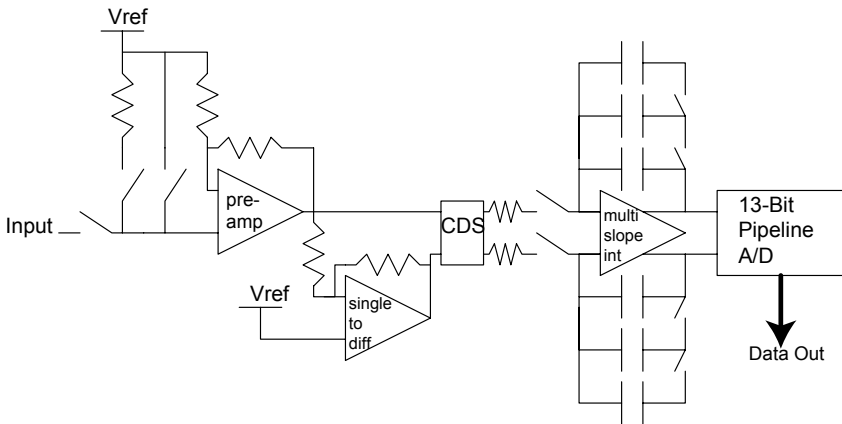
Figure 1. The block diagram of the CRIC II chip.

The circuit consists of four major components, which can be seen in Fig. 1:
- The input stage with preamplifier and single-ended to differential conversion.
- The signal processing stage with its Correlated Double Sampler (CDS).

- The Analog to Digital Converter (A/D).
- The band-gap based voltage reference for both the input stage and A/D.

2.1 The Input Stage

The CCD will be AC coupled to the readout chip with a large external capacitor. This is necessary to eliminate the influence of the parasitic capacitance of the input node due to ESD protection circuitry. To charge this capacitor to its operating voltage upon CCD power-up, the CRIC II has a dedicated input clamp switch that connects its input to the voltage reference with a low resistance. After power-on, the switch is disabled.

During normal operation, two other switches control the input signal. One switch disconnects the input during CCD clocking transitions to prevent amplifier saturation. The last switch is responsible for setting the DC operating point of the input amplifier. During the sampling of the CCD reset level, this switch is closed. It connects the input to the reference voltage through a large (200 kΩ) resistor. Together with the input coupling capacitor, this resistance creates a time constant for change of the input voltage that is much longer than a single pixel sampling time. Since the CCD reset level is independent of the CCD signal, averaging over the reset level only creates a consistent DC baseline for the signal processor.

The central part of the input stage consists of an ultra low noise preamplifier with a gain of four. The gain is chosen to minimize the noise contribution of downstream system components, while maintaining a large dynamic range using only 3.3 V operating voltage. The opamp input is biased at 200 μA to achieve a thermal noise spectral density of about 4 nV/Hz$^{1/2}$. The output settling time to 16-bit linearity is about 200 ns. The input stage is one of the main power consumers of the chip, but lower power can only be achieved at the price of higher noise. The output of the first stage is connected to a unity gain inverter, generating a differential signal of 2 V from a 500 mV full-scale CCD signal input, effectively doubling the available dynamic range.

2.2 The Correlated Double Sampler

It has been shown [2] that a dual slope integrator is efficient at eliminating reset transistor noise, and also attenuates noise that is significantly higher or lower in frequency than the CCD pixel rate. Such a dual slope integrator integrates the reset signal level at one polarity and then integrates the image signal level at the opposite polarity, in effect subtracting the reset level from the pixel signal level. Since the input stage already generates a differential signal, changing the polarity of the input signal for

the integrator merely requires a cross-over switch. Care has to be taken that the resistive miss-match of the switch is much smaller than the integration resistor (see Fig 1.) to obtain the full benefit of the CDS noise rejection.

The gain of the integrator is directly dependant on the value of the integration resistors, while the input stage gain is dependant only on the ratio of feedback resistors. Therefore, the integration resistors require particular attention to reduce the temperature coefficient.

2.3   The Multi Slope Integrator

The dynamic range requirement is 16-bit, derived from 2 electrons CCD readout noise and 130K electrons full well capacity. The requirement for the signal to noise ratio, however, is driven by the Poisson process of the light interacting in the sensor, which has a variance equal to $\sqrt{N}$, where N is the number of incoming photons [3]. The signal can be digitized with an LSB size that depends on the signal amplitude such that the A/D quantization noise is still below the Poisson noise, allowing the implementation of a dynamic range compression without the loss of data. Since the implementation of a radiation tolerant 16-bit A/D converter in the required power budget seemed unrealistic, a means of dynamic range compression had to be adopted. The CRIC II chip is intended for use in high precision photometry, so the compression scheme has to allow for simple yet precise calibration.

In the CRIC chip a novel compression was implemented; the integrator has three integration capacitors. Initially only the smallest capacitor is connected. A comparator at the integrator output triggers a flip-flop if the voltage on the integration capacitor rises above a set-point. This switches in an additional larger capacitor. A third capacitor can be switched for larger signals. Fig. 2 shows the signal at the output of the integrator for a signal close to full-scale. Traces two and three show the flip-flop outputs that drive the gain selection. These two gain bits are transmitted along with the A/D conversion result for each CCD pixel to allow full reconstruction of the image signal.

There are several advantages of a multi-slope integrator over a logarithmic gain amplifier for dynamic range compression. A non-linear preamplifier requires extensive data sets for gain and offset calibration, and radiation induced parameter shifts will likely require on-orbit recalibration. For the multi-slope integrator this is much easier. When the second gain stage is triggered and the additional capacitor is turned on, the charge stored on the integration capacitor is redistributed and none of it is lost. Additional charge injection from switching is carefully eliminated. This means that in each section the gain is different, yet they all share a common offset. To

fully characterize the system one needs only two points in the first slope to determine its gain and offset, then one point each in the following slopes to determine their gain.

In Fig. 3 the noise margin between the photon shot noise on the CCD and the quantization noise due to the bit size of the A/D converter is shown. The plot also demonstrates the advantage of a multi-slope integrator followed by a 12-bit A/D over a standard linear 16-bit converter for small signals. Since the dynamic range of modern CCDs is often greater than 16 bits, a linear converter is forced to a larger number of bits or to undersample the read noise.
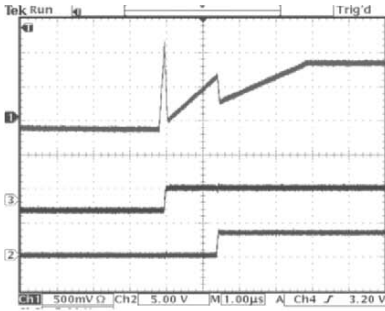
Figure 2. A large signal on the auto-gain integrator.
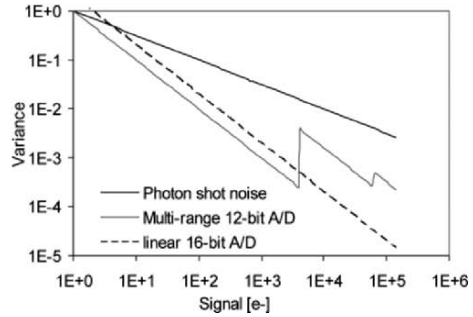
Figure 3. Comparing shot noise and quantization noise.

2.4 The Pipeline A/D Converter

To sample the output of the multi-slope integrator a 13-bit A/D converter has been implemented. We chose a 13-bit range with a fixed negative offset of 4K electrons to eliminate the need to remove the CCD offset voltage. The range of the 13-bit A/D converter is adequate to fully sample the CCD output signal, and any offset subtraction can be done later in the digital domain.

After studying several A/D architectures, we decided on pipeline architecture for the CRIC II chip. This architecture achieves high resolution while maintaining low power consumption. It also has the advantage of 12 identical stages, greatly reducing layout efforts. Pipeline A/D converters have excellent linearity by design, as can be seen in the test results section. To prevent the digital noise from degrading the signal, the A/D converter is clocked at pixel read rate and the timing is designed so that no transitions occur during either integration period. Since any digital noise is generated while the integrator is off, such noise is completely rejected.

2.5   The Voltage Reference

The primary function of the voltage reference is to generate a low-noise ultra-stable reference for the input stage. The same voltage is used in the A/D converter, but requirements are less strict. The voltage reference has been optimized to give very similar performance at room temperature and at the planned operating temperature of -130°C, not to give the minimal temperature coefficient at the designed operating temperature. The plot in Fig. 4 shows excellent stability, ~0.1 mV/K at both room and operating temperature.
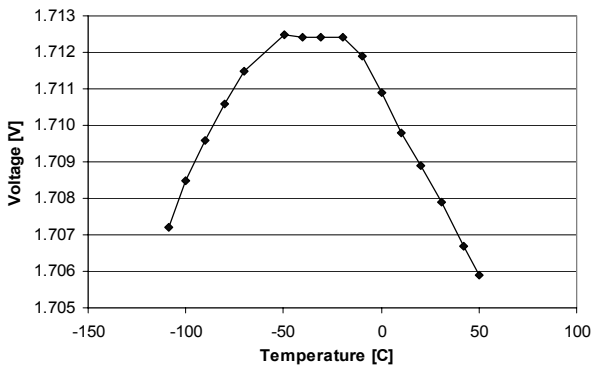
Figure 4. Voltage reference performance over temperature.

Since band-gap based voltage references are notoriously noisy, a trick was used to achieve the required noise performance. A sample and hold circuit was implemented at the output of the voltage reference. At the beginning of each pixel read the reference voltage is 'frozen' on the sample capacitor and the voltage reference is disconnected for the entire duration of the pixel read. Therefore the entire voltage reference noise is rejected by the CDS. Only the buffer amplifiers distributing the reference voltage over the chip contribute to the reference voltage noise.

3.   MEASUREMENT RESULTS

Proving the low noise capabilities of the CRIC II chip was one of the main testing goals. Figure 5 shows 1.9 ADU rms noise that was measured running the chip at -110°C and at 100K samples per second. This translates to about 6.5 µV rms noise, or slightly less than two electrons. The warm

performance is slightly worse due to higher thermal noise. At room temperature, we measured 2.3 ADU or 8.3 µV rms noise. All noise measurements were done using the highest integrator gain. For larger signals at lower integrator gains, the noise is no longer dominated by the input stage, but by the A/D converter. For signals greater than 4K electrons, we measured 0.8 ADU or 12.8 electrons rms noise. For signals above 64K electrons we measured 0.9 ADU or 28.8 electrons rms noise, both very close to the quantization noise plotted in Fig. 3.
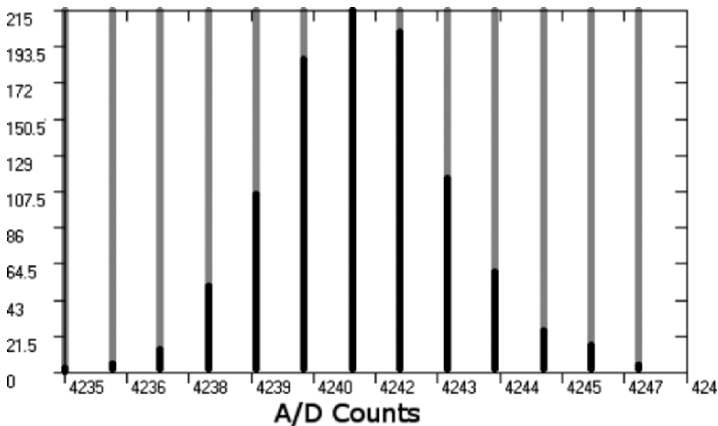
Figure 5. Noise histogram from 10000 samples at -110°C.

The linearity of a pipeline A/D converter is very good by design. Figure 6 shows 1 ADU rms nonlinearity for a signal that varies over the full scale of the middle slope of the multi-slope integrator.

The power consumption of the system is 17 mW/channel at 100 KHz. The power draw is roughly equally distributed among the analog input stage and the pipeline A/D. Our CCDs typically dissipate just as much power in the source follower load.

4. OUTLOOK

We are very pleased with the performance of the CRIC II chip. The third generation chip is in design. This will incorporate internal time sequencing and a 14-bit A/D with auto calibration. This will greatly simplify the interface and pinout of the chip. We also continue to develop a second ASIC that contains DC bias voltage DACs, timing generation and clock line drivers.
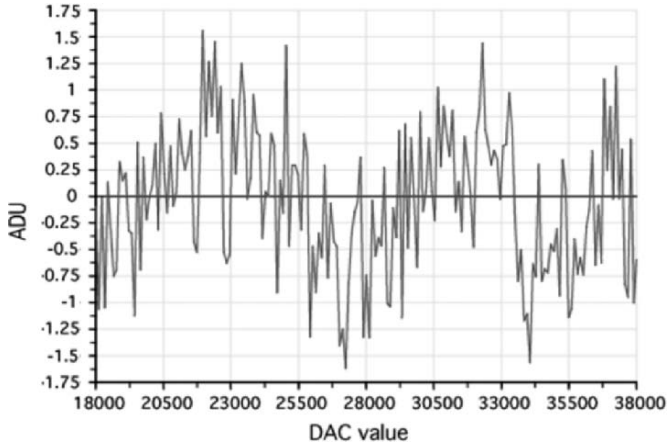
Figure 6. The integral nonlinearity is shown as the deviation from a line fit as a function of the injected charge.

5.   REFERENCES

[1] Walder, J.-P., Chao, G., Genat, J.-F., Karcher, A., Krieger, B., Kurz, S., Steckert, J., von der Lippe, H., 2004*, A low power, wide dynamic range multigain signal processor for the SNAP CCD*, IEEE Trans. Nuc Sci. Vol. **51**, Issue 5, pp. 1936-1941.
[2] Hopkinson, G. R., Lumb, D. H., 1982, Noise *Reduction Techniques for CCD Image Sensors*, J.Phys. E:Sci. Instrum., Vol **15**, p. 1212.
[3] Walder, J. P., Bussat, J. M.,   Denes, P., Mathez, H., Pangaud, P., 2001, *Custom Integrated Front-End Circuit for the CMS Electromagnetic Calorimeter,* IEEE Transactions on Nuclear Science, Vol. **48,** No 6, pp. 2375-2379.

SIDECAR ASIC - CONTROL ELECTRONICS ON A CHIP

Markus Loose[1], James W. Beletic[1], John Blackwell[1], Don Hall[2] and Shane Jacobsen[2]
[1]Rockwell Scientific Company, [2]Institute for Astronomy

Abstract: *The SIDECAR ASIC is a custom-designed integrated circuit for controlling high performance focal plane arrays. It includes 36 parallel analog input channels, each providing pre-amplification coupled with 12-bit or 16-bit A/D converters. In addition, the micro-controller based SIDECAR ASIC provides full programmability for bias and clock generation as well as a number of digital processing features. It has been developed for space-based as well as ground-based applications. Excellent performance has been demonstrated both at room temperature and at cryogenic temperatures down to 37 K in conjunction with the HAWAII-2RG multiplexer. The ASIC has been selected by NASA for use in all three JWST near-infrared instruments and is in the process of full space qualification.*

Key words: *ASIC, SIDECAR, FPA controller, control electronics, HAWAII-2RG.*

1. INTRODUCTION

Conventional high performance Focal Plane Arrays (FPAs), also called detectors or image sensors, require significant external control electronics. To reduce the amount of external overhead, more and more modern image sensors include drive electronics on the sensor chip itself. This approach has been strongly endorsed by the consumer market where cost and miniaturization are strong drivers. In the scientific arena, however, performance and flexibility remain the highest priority. Most astronomy detector systems are still based on analog FPAs operated by a dedicated controller box.

To offer an alternative to discrete electronics, RSC has developed a new approach known as the SIDECAR™ Application-Specific Integrated Circuit (ASIC) as presented in Loose, et al. [1]. The SIDECAR design includes all capabilities required to operate the FPA, including bias and clock generation and A/D conversion. The interface to the outside world is fully digital, thereby simplifying the design of the instrument while guaranteeing constant low noise performance. Overall, the ASIC approach leads to a hundredfold reduction in space, weight and power consumption.

2.   SIDECAR ARCHITECTURE

The SIDECAR ASIC represents a fully programmable control and digitization system for analog image sensors. It is designed to operate at room temperature as well as at cryogenic temperatures down to 30 K. The architecture can be divided into the following major blocks, which are shown in Fig. 1: analog bias generator, A/D converter, digital control and timing generation, data memory and processing, and digital data interface.
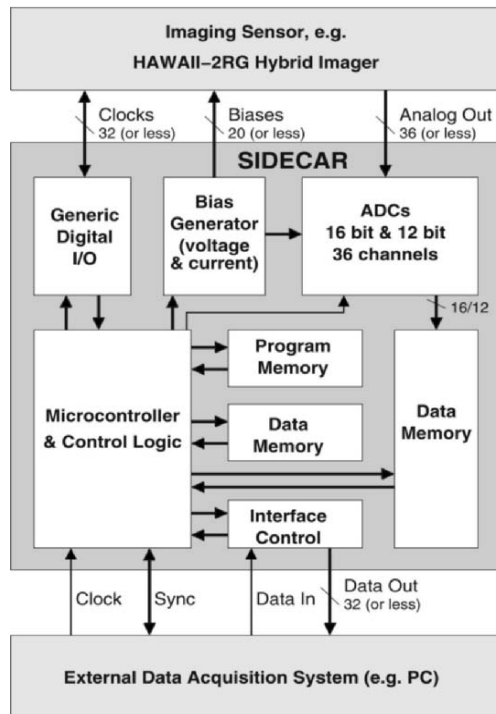
Figure 1. Block diagram of the SIDECAR ASIC.

The analog bias generator consists of 20 independent channels, each of which is composed of a 10-bit digital-to-analog converter and an output buffer with adjustable driver strength. They are basically programmable current and voltage sources. For reading out the analog detector signals, the SIDECAR provides 36 analog input channels. Each channel can be digitized by on-chip ADCs offering 16-bit resolution at sample rates up to 500 kHz and 12-bit resolution at sample rates up to 10 MHz. A fully programmable and application optimized micro-controller is responsible for overall ASIC control and for generating specific timing patterns of the image sensor clocks. A total of 32 digital I/O channels can be individually adjusted for driver strength and signal direction. Additional on-chip memory permits simple data processing functions like pixel averaging or data sorting. Finally, a serial and a parallel data interface are implemented to read the digitized pixel values and to program the ASIC.

The primary driver for this controller-on-a-chip approach was the development of the James Webb Space Telescope (JWST), successor to the Hubble Space Telescope. Requiring 16-bit accuracy at a temperature of 37 K without active cooling, the JWST put stringent requirements on the performance and power consumption of the ASIC. The JWST goal is 16-bit conversion on 4 parallel channels at a power consumption of less than 10 mW, including bias generation, clock generation and data transmission. As the next section on measurement results describes, this goal has been achieved, and the SIDECAR ASIC is fully suitable for JWST and other space-based applications, in addition to ground-based applications.

Figure 2 shows a micrograph of the SIDECAR chip as well as a packaged ASIC in a 337-pin µPGA package. A summary of the important properties is given in Table 1.
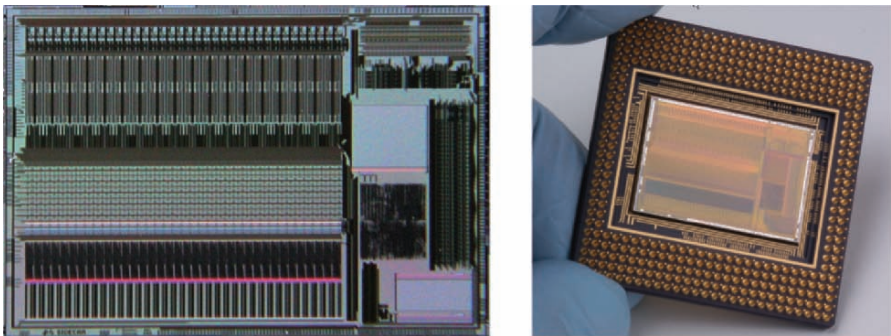
Figure 2. (left) Micrograph and *(right)* packaged SIDECAR ASIC.

Table 1. Summary of the SIDECAR ASIC properties.

Die Dimension	22×14.5 mm²
Technology	0.25 μm CMOS
Analog Input	36 independent channels, fully differential
Preamplifiers	Programmable gain (-3 to 27 dB) and bandwidth
16 bit ADCs	(1 mW / channel at 100 kHz). Up to 500 kHz sample rate
12 bit ADCs	(10 mW / channel at 5 MHz). Up to 10 MHz sample rate
Bias Outputs	20 output channels, selectable voltage or current DACs
Digital I/O	32 channels, fully programmable
Micro-controller	16 bit RISC, low power, excellent arithmetic capabilities
Program Memory	16 kwords (16 bit / word)
Data Memory (μC)	8 kwords (16 bit / word)
Data Memory (ADC)	36 kwords (24 bit / word)
Array-processor	Adding & multiplying and DMA control per ADC channel
Digital Interface	LVDS or CMOS, custom serial protocol, up to 32 lines
Operating Temperature Range	30 K – 300 K
Radiation	Complete design is single event upset protected

3.   MEASUREMENT RESULTS

The performance and functionality of the SIDECAR ASIC have been examined at room temperature [2] and at cryogenic temperatures down to 37 K. Room temperature performance is important for applications that operate detectors at or near room temperature (visible light and/or high background) as well as for convenient testing and verification of the ASIC itself. Whereas cryogenic performance is essential for low background detector systems that benefit from analog to digital conversion close to the FPA.

The test results will be presented in the following two sections. Sec. 3.1 describes the performance of individual ASIC components such as ADCs and preamplifiers. In Sec. 3.2 measurement results from a complete system test comprising the SIDECAR ASIC and the HAWAII-2RG will be discussed. Both types of results have been obtained using a PC-based environment with a custom-built test board. Room temperature tests have been carried out at Rockwell Scientific; cryogenic tests have been performed at the Institute for Astronomy in Hilo, Hawaii.

3.1   SIDECAR Functionality and Performance Results

The purpose of the first set of tests included the verification of the correct functionality and the measurement of the analog performance of all integrated building blocks. As part of these initial tests, the test environment had to be completed and various ASIC micro-code programs had to be written. Aside from a leakage problem in one of the integrated memory modules, all digital and analog components were fully functional. Subsequently, fabrication of a second ASIC revision has completely solved the problem in the memory module. The following paragraph lists all building blocks that have been measured and verified:

- Serial/parallel data interface to and from SIDECAR
- Micro-controller plus program & data memories
- Timer/Counter modules
- Digital I/O block for clock generation
- Array processor for parallel data processing
- Analog bias generator for internal/external voltage & current biases
- Integrated 2.5 V voltage regulator for digital supply voltage
- 12-bit ADC, DNL < ± 0.3 LSB, INL < ± 0.8 LSB, noise < 0.4 LSB
- 16-bit ADC, DNL < ± 0.4 LSB, INL < ± 2.3 LSB, noise < 3 LSB
- Preamplifiers, noise at T=300K: 20µV, noise at T=40K: 12 µV

The analog performance of the two types of on-chip ADCs has been examined with respect to linearity and noise. In the case of the 12-bit ADC, the Differential and Integral Non-Linearities (DNL and INL) at a sample rate of 7.5 MHz are shown in Fig. 3. At room temperature and at T=40K, the 12-bit ADCs exhibit excellent DNL and INL as well as low temporal noise of less than 0.4 LSB. No significant difference in performance has been observed for sampling rates of 10 MHz.
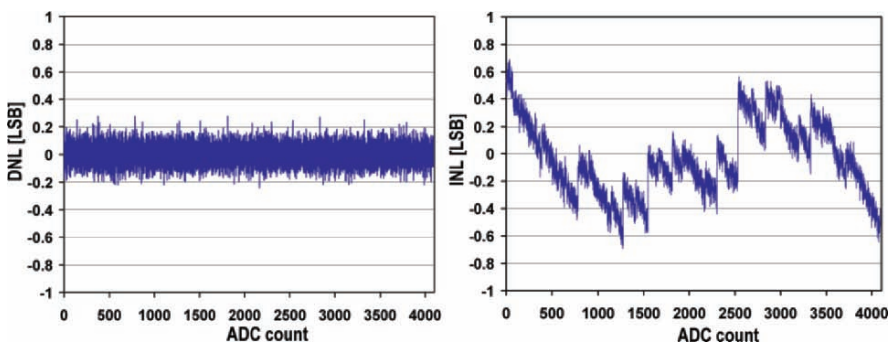
Figure 3. (left) DNL and *(right)* INL of the integrated 12-bit ADC (7.5 MHz).

Likewise, the 16-bit ADC shows good performance with respect to DNL and INL (see Fig. 4). In terms of noise, a compromise between the noise level and the power consumption suitable for JWST was required. At a power level of 1.3 mW and a sampling rate of 100 kHz, the ADC noise is 5 LSB at room temperature and 2.5 LSB at T=40K. This performance fulfills JWST requirements with margin. The noise can be reduced by increasing the ADC bias current at the cost of higher power consumption. However, no measurements at higher bias conditions have been undertaken.
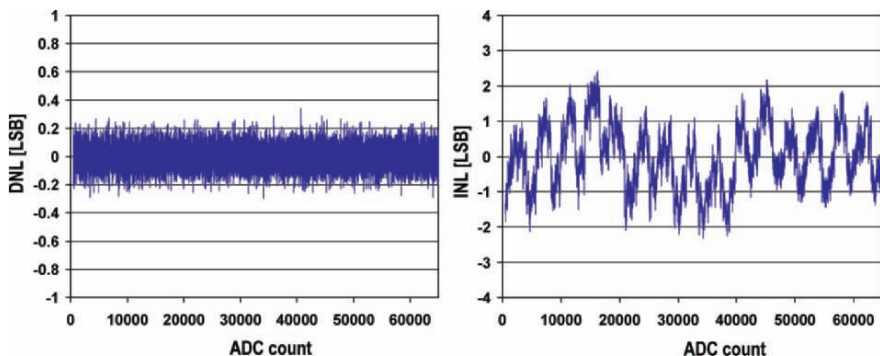
Figure *4*. *(left)* DNL and *(right)* INL of the integrated 16-bit ADC (100 kHz).

The preamplifier provides control over the analog signal gain and the analog signal bandwidth by means of programmable capacitors and resistors. Its performance has been evaluated under JWST conditions for 100 kHz pixel rate, using a bandwidth of 300 kHz and a gain of 27 dB. The measured noise is 20µV (input-referred) at room temperature and less than 12µV at 40K. This combines the noise of the preamplifier and the noise of the 16-bit ADC results in a total analog noise of 18µV for cryogenic operation. As mentioned above for the ADC, increasing the bias current (power consumption) can further reduce the amplifier noise.

3.2   Performance of SIDECAR + HAWAII-2RG

As illustrated in the block diagram in Fig. 1, a complete detector system consisting of the SIDECAR ASIC and the HAWAII-2RG multiplexer has been assembled. The HAWAII-2RG, hybridized to a short-wave infrared detector with 2.5 µm cutoff frequency, was mounted next to the ASIC inside the dewar and was operated in unbuffered mode. The SIDECAR ASIC was programmed to generate the required bias voltages and clock signals. At the

same time, the SIDECAR digitized the four analog FPA outputs at 100 kHz pixel rate and sent the digital data to the host PC.

Figure 5 shows a full field CDS frame with a total noise of 16 e⁻. This is comparable to or better than results obtained with a conventional discrete controller system. To demonstrate suitability for the JWST instruments, the total noise was measured for a Fowler-8 sampling scheme (NIRCam) and for the sampling-up-the-ramp scheme with 22 groups of 4 averaged frames (NIRSpec). The gray-scale images and the corresponding histograms are shown in Fig. 6. All JWST noise requirements have been met with margin.
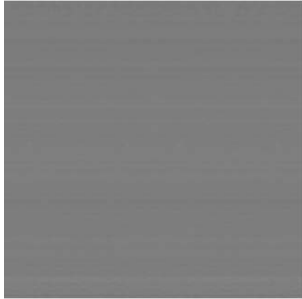
Figure 5. CDS frame acquired by the SIDECAR ASIC shows 16 e⁻ noise.
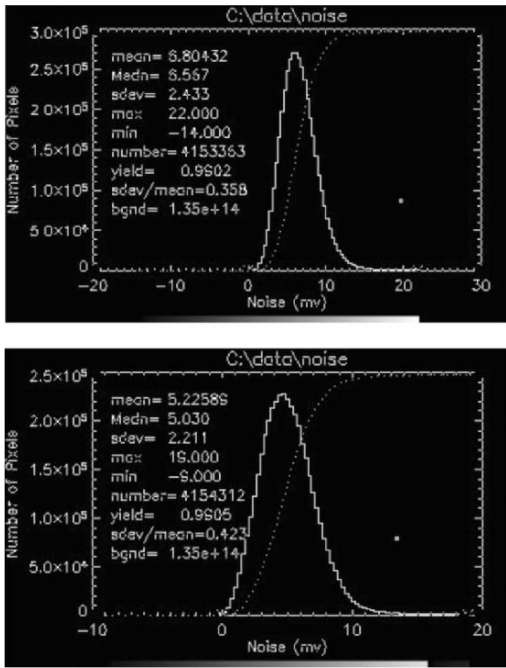
Figure 6. (top) Fowler 8-8 over a 1000s integration yields a total noise of 6.5 e⁻-,
        (bottom) sampling-up-the-ramp over 1000s integration yields a total noise of 5 e⁻.

Besides noise performance, power consumption is important in many cryogenic detector systems. For JWST, a total budget of less than 10 mW has been allocated for each 2K×2K detector to allow for passive radiative cooling. Table 2 summarizes the measured power consumption for all contributors inside the SIDECAR and the HAWAII-2RG. A total power of 9.4 mW has been demonstrated.

Table 2. Power consumption for operation with 4 channels including H2RG detector.

Component	Power Consumption
HAWAII-2RG	0.4 mW
16-bit ADCs (4 channels)	5.2 mW (1.3 mW / channel)
Preamplifiers (4 channels)	1.0 mW (0.25 mW / channel)
Bias generator	1.2 mW
Micro-controller & Clocking	1.5 mW
LVDS Driver	0.1 mW
Total Power	**9.4 mW**

4.   CONCLUSION

Based on the demonstrated test results, the SIDECAR ASIC has been selected by NASA for use in all three JWST near-infrared instruments. Recently, a second ASIC revision has been produced to correct a leakage problem with the on-chip dual-port memory. The first SIDECAR ASICs of the new revision are being tested at Rockwell Scientific. So far, no excess leakage could be found indicating that the memory leakage issue has been solved. The SIDECAR is in the process of becoming fully space qualified, which includes the development of suitable packaging, application specific micro-code and further performance tests. The SIDECAR ASIC has proven to be an attractive alternative to conventional controllers for ground-based and space-based applications.

5.   REFERENCES

[1] Loose, M., et al., 2003, *SIDECAR low-power control ASIC for focal plane arrays incl. A/D conversion and bias generation*, Instrument Design and Perform. for Optical/IR Ground-based Telescopes, Proc. SPIE, Vol. **4841**, pp. 782-794.
[2] Wong, S., et al., 2004, *Advanced Technology Trends for Astronomy at Rockwell Scientific*, Optical and Infrared Detectors for Astronomy, Proc. SPIE, Vol. **5499**, pp. 258-268.

BLACK & WHITE PHOTO GALLERY

Charlotte Cumani arrives to the joy of the workshop registration staff.

The workshop began with a Sunday evening reception where old friends caught up on news and new friendships began.

Charlotte Cumani with her mother Sara Hoffman.

Olaf Iwert modeling the workshop souvenir bag.

Markus Loose (with microphone) defends CMOS turf during the CCD-CMOS roundtable. Also shown (from left to right) are Paul Vu, Alan Hoffman, Vyshi Suntharalingam and Morley Blouke.

Klaus Reif is overjoyed to hear of another wide field imager that needs one of his special shutters (plus a spare!).

Welcoming remarks from the University of Catania.

University of Catania student helpers with Rosario Cosentino (middle).
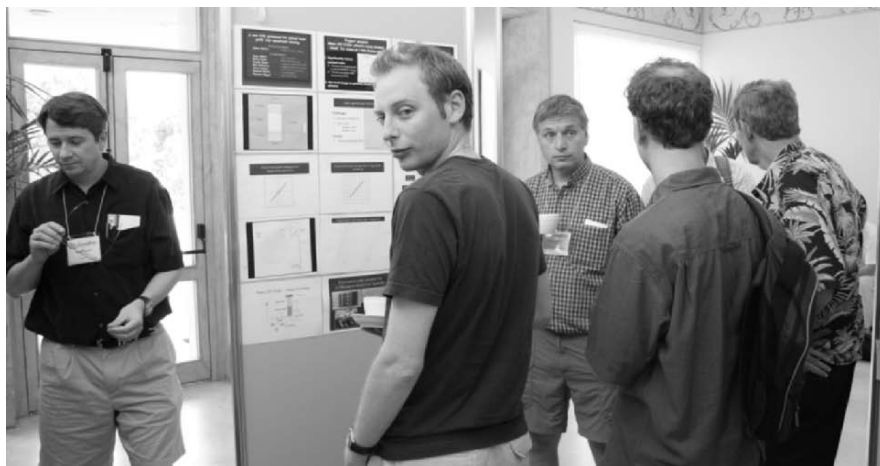
Paul Berry (center, looking at the camera) seems to be thinking, "Do these guys have the slightest idea what they are talking about?".

Like a lion waiting to pounce, Roger Smith looks for an opening to speak his turn at the CCD-CMOS roundtable. The records show that he supports both technologies as long as his laboratory gets the cutting edge devices to test.

Always ready with a smile and good conversation, Craig Mackay visited many tables during the week. Here Craig is with Diana Ashman and Mark Downing.

Young Explorers of the Photon Odyssey
Jason Henning, Jenna Beletic, Thomas Craven-Bartle and Juliet Beletic (l. to r.).

So much champagne, and so little time.   Giovanni Bonanno checks out the new vintage at Murgo Winery.

Isabel Mujica, Ricardo Schmidt and Marco Bonati at the Murgo Winery.

Diana Ashman and wine chef.

Peter Sinclaire, Derrick Salmon and Doug Simons.

Giovanni Bonanno, Giovanna Cimino and James Beletic on the hike to the castle
at the top of the hill in Forza d'Agró.

Marcela Del Villar and Nicolas Haddad in Forza d'Agró.

Bruce Atwood at the pizza dinner.

Louise Choquette, Robert Lamontaigne and Celine Boisvert.

I got one! Gert Finger holds his asteroid citation up high.

At the end of the night, the pizza restaurant owner Fortunato and Jim Beletic relax.
(Note that Fortunato and Jim both mean "lucky".)

Martina and Philipp Müller.

Alexandrina Stoyanova and Fabrice Christen.

Rainer and Heidi Kramm, Ira and Roland Reiss.

Kevin and Susan Ho.

Gustavo Rahmer and Mariana Casal.

Festa Paesana!
(left to right: Colin Earle, Paul Harding, Philip MacQueen, unidentified
CMOS designer, Martin Roth, Roger Smith, Fred Harris, Paul Vu)

Maureen Ellis accepts the award for Best Poster.

Paul Jorden reacts after receiving the traditional Sicilian kiss when accepting the corporate sponsorship award on behalf of e2v technologies.

The session chairs accept their bottles of Murgo champagne.

Roger Smith waves to the crowd as he accepts the Most Loquacious award for the second straight workshop.

The crowd reacts to Roger's short speech.

Catching some shade in Agrigento are Maureen Ellis, Roger Smith, Marco Bonati, Derek Ives and Paul Berry.

Coolest Agrigento look goes to ……. Ray DuVarney.

Sebastian Deiries truly enjoyed the nature in Sicily.

Jenna Beletic, Thomas Craven-Bartle and Joseph Tufts

Jason Henning worked 16 hour days with the editors to ensure the proceedings
were completed on time. What a guy!

APPENDIX A

INSTRUMENTATION DATABASE FOR GROUND-BASED TELESCOPES

This appendix contains an extract of the instrument database that was developed for the overview paper on instrumentation and detectors of large ground-based telescopes (Simons and Amico, et al.). The complete database, can be downloaded from: http://www.sc.eso.org/~pamico/sdw2005.

The data is presented twice, with different sorting: (a) sorted according to telescope name, and (b) sorted according to instrument name. The ID sequence repeats twice. The column heading are elaborated below.

ID	Running ID number. Repeated
Institute, Telescope, Instrument, Mode	Institute, Telescope name, Instrument name and main observing modes.
λ min and λ max	Wavelength range expressed in nanometers [nm].
Multiplex	Multiplexer gain.
Year	Year of first light (for future instrument, estimated year of first light).
Spatial Res.	Spatial resolution. When not indicated, it is seeing limited.
Min λ/Δλ, Max λ/Δλ	Min and Max resolution for instruments with spectroscopic capabilities.
Manufacturer	Name of manufacturer and type of detector. Only CCDs and IR arrays are listed.
Format, # Det. Size X and Size Y	Format, Number of detectors, size in X and Y [pixels].
Pixel scale	Expressed in [arcsecs/pixel].
FOV	Field Of View. Expressed in arcsecs [″] or prime of arc [′].
Electronics	Brand/name of electronics controller.
Noise min, Noise Max	Min and Max noise [e⁻ rms], linked to Max and Min readout times respectively.
Min and Max Readout Time	Expressed in [sec].
Dark Current	In Units of Dark Current (UDC): [e⁻/pix/hr] for CCDs and [e⁻/sec] for IR arrays.
Full Well	Expressed in [e⁻].
Buttability	Number of buttable sides.
Pixel Cost , Inst. Cost	Costs expressed in US$/10⁶US$ respect. Exchange rate used: Euro/Dollar=1.

ID	Institute	Telescope	Instrument	Mode	λ min	λ max	Multiplex	Year	Spatial Res.	Min λ/Δλ	Max λ/Δλ	Manufacturer	Format	# Det.	Size X	Size Y
1	AAO	AAT	2df	MOS	350	1050	400	1998		400	2500	Tektronix	Mosaic	2	2048	4096
2	AAO	AAT	AAOmega	MOS	370	950	400	2006		1300	8000	e2v	Mosaic	2	2048	4096
3	AAO	AAT	IRIS-2	Imaging, Longslit, MOS	1000	2500	200	2001		2400		Rockwell Hawaii-2	Single	2	1024	1024
4	AAO	AAT	UCLES	Longslit	310	1100	1	1988		40000	120000	e2v or MIT/LL CCID20	Mosaic	3	2048	4096
5	AAO	AAT	UHRF	Longslit	310	1100	1	1990		150000	940000	e2v	Single	1	2048	4096
6	AAO	AAT	WFI	Imaging	320	1000	1					MIT/LL	Mosaic	8	2048	4096
7	NOAO	Blanco	DECam	Imaging	320	1100	1	2009				LBNL	Mosaic	62	2048	4096
8	NOAO	Blanco	HYDRA	MOS	330	1100	130	1999		300	15000	SITe ST002A	Single	1	2048	4096
9	NOAO	Blanco	ISPI	Imaging	1000	2400	1	2002				Rockwell Hawaii-2	Single	1	2048	4096
10	NOAO	Blanco	Mosaic-2	Imaging	320	1100	1	1999				SITe ST002A	Mosaic	8	2048	4096
11	NOAO	Blanco	RC Spec	Longslit	320	1100	1	1995		300	5000	Loral 3K	Single	1	2048	4096
12	CAHA	Calar Alto	Laica	Imaging	350	1000	1	2002	0.22			BAE	Mosaic	4	4096	4096
13	CAHA	Calar Alto	Mosca	Imaging, MOS	350	1000	1	1996	0.32			SITe #16	Single	1	4092	2048
14	CAHA	Calar Alto	Omega2000	Imaging	1000	2500	1	2003	0.45			Rockwell Hawaii-2	Single	1	2048	2048
15	CAHA	Calar Alto	OmegaCass	Imaging, Longslit, Polarimetry	1000	2500	1	1996	0.10			Rockwell Hawaii-1	Single	1	1024	1024
16	CAHA	Calar Alto	PMAS	IFU	350	900		2002	0.50			SITe ST002A,	Single	1	2048	4096
17	CAHA	Calar Alto	Pyramir	AO, NIR wavefront sensor	1000	2500	1	2006				Rockwell Hawaii-1	Single	1	1024	1024
18	CAHA	Calar Alto	TwinB	Longslit	500	1100	1	1988	0.56			SITe #6	Single	1	2048	800
19	CAHA	Calar Alto	TwinR	Longslit	320	550	1	1988	0.56			SITe #12	Single	1	2048	800
20	CFHT	CFHT	CFHTIR	Imaging	1000	2500	1	2001	0.40			Rockwell Hawaii-1	Single	1	1024	1024
21	CFHT	CFHT	Espadons	Polarimetry, Longslit	370	1050	1	2004		68000	81000	e2v CCD42-90	Single	1	2048	4500
22	CFHT	CFHT	Gecko	Coude' Spectroscopy	350	950	1	1992		70000	190000	MIT/LL CCID-20	Single	1	2048	4096
23	CFHT	CFHT	KIR	AO Imaging	1000	2500	1	1997	0.10			Rockwell Hawaii-1	Single	1	1024	1024
24	CFHT	CFHT	MegaCam	PF Imaging	350	1100	1	2002	0.40			e2v 42-90	Mosaic	36	2048	4500
25	CFHT	CFHT	MOS	Imaging, MOS	350	900	120	1992		100	700	MIT/LL CCID-20	Single	1	2048	4096
26	CFHT	CFHT	WIRCam	PF Imaging	900	2500	1	2005	0.40			Rockwell Hawaii-2RG	Mosaic	4	2048	2048
27	Lowell	DCT	Prime Focus Camera	Imaging	320	1100	1	2010				e2v CCD42-82BI	Mosaic	40	2048	4096

ID	Institute	Telescope	Instrument	Mode	λ min	λ max	Multiplex	Year	Spatial Res.	Min λ/Δλ	Max λ/Δλ	Manufacturer	Format	# Det.	Size X	Size Y
28	ESO	ESO 3.6m	CES	Longslit spectroscopy	346	1028	1	1982		220000		e2v CCD44-82	Single	1	2048	4096
29	ESO	ESO 3.6m	EFOSC2	Imaging, Coronography, Polarimetry Longslit, MOS	350	1000	25	1997		150	1500	Loral/Lesser	Single	1	2048	2048
30	ESO	ESO 3.6m	HARPS	Longslit	380	690	1	2003		120000		e2v CCD44-82	Mosaic	2	2048	4096
31	ESO	ESO 3.6m	TIMMI2	Imaging, Imaging Polarimetry, Spectroscopy	3000	24000	1	2000		160		Raytheon HBIBC Si:As	Single	1	320	240
32	AURA	Gemini	bHROS	Longslit	500	900	1	2006	0.90	1500000		e2v	Mosaic	2	2048	4096
33	AURA	Gemini	EXAOC	Coronagraph/IFU	1000	2500	100	2009	0.02		40	Rockwell Hawaii-2RG	Single	1	2048	2048
34	AURA	Gemini	FLAMINGOS-2	Imaging, Longslit, MOS	1000	2500	50	2006	0.40			Rockwell	Single	1	2048	2048
35	AURA	Gemini	GMOS-N	Imaging, Longslit,MOS,IFU	400	900	100	2002	0.40	700	4400	e2v	Mosaic	3	2048	4096
36	AURA	Gemini	GMOS-S	Imaging, Longslit,MOS,IFU	400	900	100	2003	0.40	700	4400	e2v	Mosaic	3	2048	4096
37	AURA	Gemini	GNIRS	Longslit, X-Disp, IFU	1000	5000	150	2004	0.40	1700	18000	Raytheon	Single	1	1024	1024
38	AURA	Gemini	GSAOI	Imaging	1000	2500	1	2006	0.04			Rockwell	Mosaic	4	2048	2048
39	AURA	Gemini	MICHELLE	Imaging, Longslit	5000	25000	1	2003	0.40	200	30000	Raytheon	Single	1	240	320
40	AURA	Gemini	NICI	Imaging, Coronography	1000	5000	1	2006	0.04			Raytheon	Single	2	2048	1024
41	AURA	Gemini	NIFS	IFU	1000	2500	100	2006	0.10	5000		Rockwell	Single	1	2048	2048
42	AURA	Gemini	NIRI	Imaging, Longslit	1000	5000	1	2002	0.40	500		Raytheon	Single	1	1024	1024
43	AURA	Gemini	T-RecS	Imaging, Longslit	5000	25000	1	2003	0.40	1000		Raytheon	Single	1	240	320
44	GMT	GMT	MID IR High Res. Spect.	Longslit	5000	25000	1	2010		30000	100000					
45	GMT	GMT	MID IR Imaging Spect.	MOS/IFU	5000	25000		2010		1500	3500					
46	GMT	GMT	Near IR Imager (AO)	Imaging, MOS/IFU	1000	2500		2010		1500	3500					
47	GMT	GMT	Near IR Imaging Spect.	MOS	1000	2500		2010		4000		Rockwell Hawaii-2RG	Mosaic	4	2048	2048
48	GMT	GMT	Optical High Res. Spect.	Longslit Echelle	320	1000	1	2010		30000						
49	GMT	GMT	Optical Imaging Spect.	Imaging, MOS	320	1000		2010				e2v?	Mosaic	2	3000	6000
50	IAC	GTC	A&G (Guacamole)	Imaging, Wavefront sens.	380	1000	1	2006	0.60			e2v 47-20	Single	2	1024	1024
51	IAC	GTC	CanariCam	Imaging, Corona., Polarimetry, Longslit	8000	25000	1	2007	0.16	60	1300	Raytheon Si:As IBC	Single	1	320	240
52	IAC	GTC	CIRCE	Imaging, Polarimetry, Longslit	900	2400	1	2007	0.50	410	1500	Rockwell Hawaii-2	Single	1	2048	2048
53	IAC	GTC	Commissioning Instrument	Imaging, Wavefront sens.	380	1000	1	2006	0.60			e2v 47-20	Single	1	1024	1024
54	IAC	GTC	ELMER	Imaging, Longslit, MOS, fast phot., slitless spect.	365	1000	25	2007	0.60	80	2500	e2v 44-82	Single	1	2048	4096

ID	Institute	Telescope	Instrument	Mode	λ min	λ max	Multiplex	Year	Spatial Res.	Min λ/Δλ	Max λ/Δλ	Manufacturer	Format	# Det.	Size X	Size Y
55	IAC	GTC	EMIR	Imaging, Longslit, MOS	900	2500	20	2008	0.60	3500	4250	Rockwell Hawaii-2	Single	1	2048	2048
56	IAC	GTC	FRIDA	Imaging,Coronography,IFU	900	2500	1	2010	0.03	500	25000	Rockwell Hawaii-2	Single	1	2048	2048
57	IAC	GTC	NAHUAL	Imaging, Longslit	900	2500	1	2010	0.03	30000	100000	Rockwell Hawaii-2	Single	1	2048	2048
58	IAC	GTC	OSIRIS	Tunable Filter (TF) Imaging, MOS, Longslit, Fast Spectr.	360	1000	60	2007	0.60	250	2500	e2v 44-82	Mosaic	2	2048	4096
59	IAC	GTC	UES	IFU	330	1000	1	2008	0.60	80000		e2v 44-82	Single	1	2048	2048
60	Palomar	Hale	COSMIC	Imaging, Longslit	390	1100	1					SITe	Single	1	2048	2048
61	Palomar	Hale	Double Spect. Polarimeter Red	Longslit, MOS, Polarimetry	470	1000	8									
62	Palomar	Hale	Double Spect. Polarimeter Red	Longslit,MOS,Polarimetry	310	700	8						Single	1	1024	1024
63	Palomar	Hale	LFC	Imaging	390	1100	1					SITe SI-002	Mosaic	6	2048	4096
64	Palomar	Hale	WIRC	Imaging	1100	2300	1	2001				Rockwell Hawaii-2	Single	1	2048	2048
65	NOAO	HET	HRS	Longslit, Echelle	420	1100	1	2002		15000	120000	e2v	Mosaic	2	2048	4096
66	NOAO	HET	LRS	Imaging, Longslit, MOS	415	1010	13	1999		600	1900	Ford Aerospace	Single	1	3072	1024
67	NOAO	HET	MRS	Longslit, Echelle	450	1300	1	2002		5000	20000	Rockwell Hawaii-1, e2v	Single	2	2048	4096
68	CARA	Keck	DEIMOS	Imaging, Longslit, MOS	400	1100	1200	2003	0.40	1200	10000	MIT/LL CCID-20	Mosaic	8	2048	4096
69	CARA	Keck	ESI	Longslit, Imaging, Echelle	390	1100	1	1999	0.40	1000	6000	MIT/LL CCID-20	Single	1	2048	4096
70	CARA	Keck	HIREs	Echelle	320	1100	1	1994		30000	80000	MIT/LL	Mosaic	3	2048	4096
71	CARA	Keck	KALI	Fringe Spectroscopy	10000	28000	1	2005				Boeing Si:As	Single	1	128	128
72	CARA	Keck	LRISb	Imaging, Longslit, MOS, Polarimetry	320	560	30	2002	0.40	200	5000	e2v	Mosaic	2	2048	4096
73	CARA	Keck	LRISr	Imaging, Longslit, MOS, Polarimetry	560	1100	30	1993	0.40	200	5000	SITe	Single	1	2048	2048
74	CARA	Keck	LWS	Imaging, Longslit	3000	25000	1	1996	0.25	100	1400	Boeing Si:As	Single	1	128	128
75	CARA	Keck	MOSFIRE	MOS, Imaging	1100	2500	40	2010								
76	CARA	Keck	NIRC	Imaging, Longslit	800	5500	1	1994	0.40	150		Raytheon InSb	Single	1	256	256
77	CARA	Keck	NIRC2	Imaging, Longslit, Coronography	1000	5500	1	2002	0.04			Raytheon Aladdin-3 InSb	Single	1	1024	1024
78	CARA	Keck	NIRES	Echelle	1100	2500	1	2006								
79	CARA	Keck	NIRSPEC	Imaging, Echelle, Longslit	950	5500	1	2000		2000		Raytheon Aladdin-3 InSb, Rockwell PICNIC	Single	2	1024	1024
80	CARA	Keck	OSIRIS	IFU, Imaging	1000	2200	3000	2005	0.02	35	4400	Rockwell Hawaii-1, Rockwell Hawaii-2	Single	2	2048	2048

ID	Institute	Telescope	Instrument	Mode	λ min	λ max	Multiplex	Year	Spatial Res.	Min λ/Δλ	Max λ/Δλ	Manufacturer	Format	# Det.	Size X	Size Y
55	IAC	GTC	EMIR	Imaging, Longslit, MOS	900	2500	20	2008	0.60	3500	4250	Rockwell Hawaii-2	Single	1	2048	2048
56	IAC	GTC	FRIDA	Imaging,Coronography,IFU	900	2500	1	2010	0.03	500	25000	Rockwell Hawaii-2	Single	1	2048	2048
57	IAC	GTC	NAHUAL	Imaging, Longslit	900	2500	1	2010	0.03	30000	100000	Rockwell Hawaii-2	Single	1	2048	2048
58	IAC	GTC	OSIRIS	Tunable Filter (TF) Imaging,MOS, Longslit, Fast Spectr.	360	1000	60	2007	0.60	250	2500	e2v 44-82	Mosaic	2	2048	4096
59	IAC	GTC	UES	IFU	330	1000	1	2008	0.60	80000		e2v 44-82	Single	1	2048	2048
60	Palomar	Hale	COSMIC	Imaging, Longslit	390	1100	1					SITe	Single	1	2048	2048
61	Palomar	Hale	Double Spect. Polarimeter Red	Longslit, MOS, Polarimetry	470	1000	8									
62	Palomar	Hale	Double Spect. Polarimeter Red	Longslit,MOS,Polarimetry	310	700	8						Single	1	1024	1024
63	Palomar	Hale	LFC	Imaging	390	1100	1					SITe SI-002	Mosaic	6	2048	4096
64	Palomar	Hale	WIRC	Imaging	1100	2300	1	2001				Rockwell Hawaii-2	Single	1	2048	2048
65	NOAO	HET	HRS	Longslit, Echelle	420	1100	1	2002		15000	120000	e2v	Mosaic	2	2048	4096
66	NOAO	HET	LRS	Imaging, Longslit, MOS	415	1010	13	1999		600	1900	Ford Aerospace	Single	1	3072	1024
67	NOAO	HET	MRS	Longslit, Echelle	450	1300	1	2002		5000	20000	Rockwell Hawaii-1, e2v	Single	2	2048	4096
68	CARA	Keck	DEIMOS	Imaging, Longslit, MOS	400	1100	1200	2003	0.40	1200	10000	MIT/LL CCID-20	Mosaic	8	2048	4096
69	CARA	Keck	ESI	Longslit, Imaging, Echelle	390	1100	1	1999	0.40	1000	6000	MIT/LL CCID-20	Single	1	2048	4096
70	CARA	Keck	HIREs	Echelle	320	1100	1	1994		30000	80000	MIT/LL	Mosaic	3	2048	4096
71	CARA	Keck	KALI	Fringe Spectroscopy	10000	28000	1	2005				Boeing SI:As	Single	1	128	128
72	CARA	Keck	LRISb	Imaging, Longslit, MOS, Polarimetry	320	560	30	2002	0.40	200	5000	e2v	Mosaic	2	2048	4096
73	CARA	Keck	LRISr	Imaging, Longslit, MOS, Polarimetry	560	1100	30	1993	0.40	200	5000	SITe	Single	1	2048	2048
74	CARA	Keck	LWS	Imaging, Longslit	3000	25000	1	1996	0.25	100	1400	Boeing SI:As	Single	1	128	128
75	CARA	Keck	MOSFIRE	MOS, Imaging	1100	2500	40	2010								
76	CARA	Keck	NIRC	Imaging, Longslit	800	5500	1	1994	0.40	150		Raytheon InSb	Single	1	256	256
77	CARA	Keck	NIRC2	Imaging, Longslit, Coronography	1000	5500	1	2002	0.04			Raytheon Aladdin-3 InSb	Single	1	1024	1024
78	CARA	Keck	NIRES	Echelle	1100	2500	1	2006								
79	CARA	Keck	NIRSPEC	Imaging, Echelle, Longslit	950	5500	1	2000		2000		Raytheon Aladdin-3 InSb, Rockwell PICNIC	Single	2	1024	1024
80	CARA	Keck	OSIRIS	IFU, Imaging	1000	2200	3000	2005	0.02	35	4400	Rockwell Hawaii-1, Rockwell Hawaii-2	Single	2	2048	2048

ID	Institute	Telescope	Instrument	Mode	λ min	λ max	Multiplex	Year	Spatial Res.	Min λ/Δλ	Max λ/Δλ	Manufacturer	Format	# Det.	Size X	Size Y
81	CAS	LAMOST	HRS	MOS	370	900	250	2009		2000		e2v 203-82	Single	2	4096	4096
82	CAS	LAMOST	LRS	MOS	370	900	4000	2007	3.30	1000		e2v 203-82	Single	32	4096	4096
83	LBT	LBT	LBC Blue	Imaging	320	550	1	2005				e2v 42-90	Mosaic	4	2048	4600
84	LBT	LBT	LBC Red	Imaging	550	1100	1	2005				e2v 42-90	Mosaic	4	2048	4600
85	LBT	LBT	LBTI-NOMIC	Nulling, Fizeau Interferometry	8000	13000	1	2008	0.01			SI:As BIB	Single	1	256	256
86	LBT	LBT	LINC-Nirvana	Fizeau Interferometry	1250	2500	1	2008				Rockwell Hawaii-2	Single	1	2048	2048
87	LBT	LBT	LUCIFER 1	Imaging, Longslit, MOS, AO	900	2500	1	2007		5000	10000	Rockwell Hawaii-2	Single	1	2048	2048
88	LBT	LBT	LUCIFER 2	Imaging, Longslit, MOS, AO	900	2500	1	2007		5000	10000	Rockwell Hawaii-2	Single	1	2048	2048
89	LBT	LBT	MODS Blue 1	Imaging, Longslit, MOS	320	600	1	2007		1000	10000		Mosaic	4	4096	4096
90	LBT	LBT	MODS Blue 2	Imaging, Longslit, MOS	320	600	1	2007		1000	10000		Mosaic	4	4096	4096
91	LBT	LBT	MODS Red 1	Imaging, Longslit, MOS	600	1100	1	2007		1000	10000		Mosaic	4	4096	4096
92	LBT	LBT	MODS Red 2	Imaging, Longslit, MOS	600	1100	1	2007		1000	10000		Mosaic	4	4096	4096
93	LBT	LBT	PEPSI	Fiber fed Spectroscopy, Polarimetry	390	1050	1	2008		40000	300000	ITL/STA	Single	2	4096	4096
94	LBT	LBT	PEPSI HR	Fiber fed Spectroscopy, Polarimerty	390	1050	1	2008		40000	300000	AIP/UoA	Single	1	10000	10000
95	LSST	LSST	LSST	Imaging	320	1100	1	2012					Mosaic	250	4096	4096
96	UBC	LZT	Prime Focus Camera	Drift Scan Imaging	320	10000	1	2004		5	22	Site	Single	1	2048	2048
97	Las Campanas	Magellan	4-Star Imager	Imaging	1100	2500	1	2100				Rockwell Hawaii 2-RG	Single	1	2048	2048
98	Las Campanas	Magellan	B&C Spectrograph	Longslit	320	1000	1	2001				e2v	Single	1	2046	515
99	Las Campanas	Magellan	EMS	Echelle	320	900	1	2006		5600		Broadband	Single	1	1024	2048
100	Las Campanas	Magellan	IMACS	Imaging, Longslit, MOS, IFU, Echelle	365	1000	800	2003	0.40	2000	20000	SITe STA-002A	mosaic	8	2048	4096
101	Las Campanas	Magellan	LDSS-3	Imaging, Longslit, MOS	360	1000	200	2005	0.50	850	3000	ITL STA0500A	Single	1	4060	4060
102	Las Campanas	Magellan	MagIC	Imaging	320	1000	1	2001	0.21			SITe SI424a	Single	1	2048	2048
103	Las Campanas	Magellan	MIKE Blue	Echelle Longslit	320	500	1	2004	0.25	28000	83000	MIT/LL CCID-20	Single	1	2048	4096
104	Las Campanas	Magellan	MIKE Red	Echelle Longslit	490	1000	1	2002	0.25	22000	65000	SITe ST002A	Single	1	2048	4096
105	Las Campanas	Magellan	MMIRS	Imaging, MOS	1100	2500		2006		3000		Rockwell- Hawaii-2	Single	1	2048	2048
106	Las Campanas	Magellan	PANIC	Imaging	1000	2500	1	2003	0.19			Rockwell Hawaii-1	Single	1	1024	1024

ID	Institute	Telescope	Instrument	Mode	λ min	λ max	Multiplex	Year	Spatial Res.	Min λ/Δλ	Max λ/Δλ	Manufacturer	Format	# Det.	Size X	Size Y
107	NOAO	Mayall	Echelle	Echelle Spectroscopy	320	1100	1	1995		300	1500	Tektronix 2B	Single	1		
108	NOAO	Mayall	FLAMINGOS	Imaging, Longslit, MOS	900	2500		2000		18000	65000	Rockwell Hawaii-2	Single	1		
109	NOAO	Mayall	MARS	Imaging, Longslit, MOS	340	1100		2001		300	5000	LBNL	Single	1		
110	NOAO	Mayall	MOSAIC-1	Imaging	320	1100	1	1998		1000	1800	SITe ST002A	Mosaic	8		
111	NOAO	Mayall	NEWFIRM	Imaging	900	2500	1	2006				Raytheon ORION InSB	Mosaic	4		
112	NOAO	Mayall	RC Spec	Longslit, MOS	320	1100		1995				Tektronix 2B, LB1A	Single	2		
113	NOAO	Mayall	SQIID	Imaging	1000	4000	1	2000				Raytheon Aladdin InSb	Single	4	1024	1024
114	MMT	MMT	ARIES (AO)	Imaging, Longslit	1100	5000	1	1800				HgCdTe	Single	1	1024	1024
115	MMT	MMT	Binospec	Imaging, Longslit, MOS	390	1000	150	2006								
116	MMT	MMT	Hectospec	MOS, Echelle	350	1000	300	2002	1.50	32000		e2v	Mosaic	2	2048	4096
117	MMT	MMT	Megacam	Imaging	320	1100	1	2003				e2v 42-90	Mosaic	36	2048	4096
118	MMT	MMT	MIRAC3 (AO)	Imaging	2000	26000	1	2000				Rockwell HF16 As:Si	Single	1	128	128
119	MMT	MMT	MMT Spectrograph Blue	Longslit	320	800	1					ITL/STA	Single	1	2688	512
120	MMT	MMT	MMT Spectrograph Red	Longslit	500	1000	1					ITL/STA	Single	1	1200	800
121	MMT	MMT	SPOL	Imaging, Longslit, pol.	380	900	1	1990				Loral W11-C	Single	1	1200	800
122	MMT	MMT	Spectrograph red	Echelle	430	890	1				345	ITL STA0510A	Single	1	1200	800
123	MMT	MMT	Spectrograph blue	Echelle	320	800	1				10000	ITL STA0520A	Single	1	2688	512
124	MMT	MMT	SWIRC	Imaging	1100	1600	1	2004				Rockwell Hawaii-2	Single	1	2048	2048
125	ESO	NTT	EMMI Blue	Imaging, Longslit	300	500	30	1990		800	9000	Tektronix 1024 AB	Single	1	1024	1024
126	ESO	NTT	EMMI Red	Echelle	400	1000	30	1990		280	70000	MIT/LL CCID-20	Mosaic	2	2048	4096
127	ESO	NTT	SOFI	Polarimetry, Longslit	800	2500	1	1998		1000	2200	Rockwell Hawaii 1	Single	1	1024	1024
128	ESO	NTT	SuSI2	Imaging	300	1000	1	1998				e2v CCD44-82	Mosaic	2	2048	4096
129	SAAO	SALT	PFIS	Fabry-Perot	320	850	100	2005		500	6000	e2v 44-82	Mosaic	3	2048	4096
130	SAAO	SALT	SALT-HRS	High Res Spectroscopy	370	900	1	2007			80000					
131	SAAO	SALT	SALTICAM	imaging	320	950	1	2005	1.20			e2v 44-82	Mosaic	2	2048	4096
132	RAS	SAO Bolschoi	LYNX	Echelle	390	850	1	1991		30000	50000	ISD017A	Single	1	1024	1024
133	RAS	SAO Bolschoi	MOFS	MOS	360	960	72	1998	1.80	400	1600	e2v CCD42-40 BI	Single	1	2048	2048
134	RAS	SAO Bolschoi	MPFS	2D Spectroscopy	360	960	256	1998	0.50	400	1600	e2v CCD42-40 BI	Single	1	2048	2048
135	RAS	SAO Bolschoi	MSS	Longslit	330	900	1	1992		2000	13000	e2v CCD42-40 BI	Single	1	2048	2048
136	RAS	SAO Bolschoi	NES	Echelle	310	1100	1	1998		40000	75000	Loral	Single	1	2048	2048

ID	Institute	Telescope	Instrument	Mode	λ min	λ max	Multiplex	Year	Spatial Res.	Min λ/Δλ	Max λ/Δλ	Manufacturer	Format	# Det.	Size X	Size Y
137	RAS	SAO Bolschoi	PFES	Echelle	390	880	1	1997		14000		Electron-Optronic ISD017A	Single	1	1024	1024
138	RAS	SAO Bolschoi	SCORPIO	Imaging, Longslit, MOS, 2D Spectroscopy	320	1000		2000		250	2500	e2v CCD42-40 BI	Single	1	2048	2048
139	RAS	SAO Bolschoi	Specle	Speckle IF	500	800		2000	0.02			3-stage image intens. + 1Kx1K CCD	Single	1	1024	1024
140	RAS	SAO Bolschoi	UAGS	Longslit	350	900	1	1995		400	1600	Tektronix 1024	Single	1	1024	1024
141	NOAO	SOAR	Goodman	Imaging, MOS	320	850	40	2005		1400	6000	MIT/LL CCID20	Mosaic	2	2048	4096
142	NOAO	SOAR	OSIRIS	Imaging, Longslit	1000	2200	1	2005		3000		Rockwell Hawaii-1	Single	1	1024	1024
143	NOAO	SOAR	SIFS	IFU	370	1000		2006		1000	40000	e2v 44-82, MIT/LL CCID20	Mosaic	2	2048	4096
144	NOAO	SOAR	SOI	Imaging	310	1050	1	2004				e2v 44-82	Mosaic	2	2048	4096
145	NOAO	SOAR	Spartan	Imaging	1000	2200	1	2006				Rockwell Hawaii-2	Mosaic	2	2048	2048
146	NAOJ	Subaru	CIAO	Imaging	900	5500	1	2000	0.40			Raytheon InSb	Single	1	1024	1024
147	NAOJ	Subaru	CISCO/OHS	Imaging, Longslit	900	2500	1	1999	0.40	300	500	Rockwell Hawaii-1	Single	1	1024	1024
148	NAOJ	Subaru	COMICS	Imaging, Longslit	8000	25000	1	1999	0.30	250	8000	Raytheon SiAs IBC	ngle, Mosa	6	320	240
149	NAOJ	Subaru	FOCAS	Imaging, Longslit, MOS, polarimetry,	365	980	50	2000	0.40	250	5500	MIT/LL CCID20	Mosaic	2	2048	4096
150	NAOJ	Subaru	HDS	Longslit	300	1000	1	2000		100000	160000	e2v 42-80	Mosaic	2	2048	4096
151	NAOJ	Subaru	IRCS	Imaging, Longslit	900	5500	1	2000	0.40	5000	20000	Raytheon InSb (ALADDIN3)	Single	2	1024	1024
152	NAOJ	Subaru	Suprime-Cam	Imaging	350	1000	1	1999	0.40			MIT/LL CCID20	Mosaic	10	2048	4096
153	INAF	TNG	DOLORES	Imaging, Longslit, MOS	320	1100	70	2000		200	7000	Loral	Single	1	2048	2048
154	INAF	TNG	NICS	Imaging, Longslit, Polarimetry	900	2500	2	2000		40	2500	Rockwell Hawaii-1 HgCdTe	Single	1	1024	1024
155	INAF	TNG	OIG	Imaging	320	1100	1	1997				e2v 42-28	Mosaic	2	2048	4096
156	INAF	TNG	SARG	Longslit	370	1000	1	2000		30000	164000	e2v 42-28	Mosaic	2	2048	4096
157	PPARC	UKIRT	CGS 4	IFU, Echelle,Longslit	1000	5000				500	37000	Raytheon Aladdin InSb	Single	1	1024	1024
158	PPARC	UKIRT	UFTI	Imaging	800	2500	1	1998			0	Rockwell Hawaii 1 HgCdTe	Single	1	1024	1024
159	PPARC	UKIRT	UIST	Imaging, Longslit, Polarimetry, IFU	1000	5000	1	2002	0.50			Raytheon Aladdin InSb	Single	1	1024	1024
160	PPARC	UKIRT	WFCAM	Imaging	1000	2500	1	2004	0.40	500		Rockwell Hawaii 2	Mosaic	4	2048	2048

Douglas A. Simons, Paola Amico, et al.

ID	Institute	Telescope	Instrument	Mode	λ min	λ max	Multiplex	Year	Spatial Res.	Min λ/Δλ	Max λ/Δλ	Manufacturer	Format	# Det.	Size X	Size Y
161	ESO	VISTA	VISTA IR Camera	Imaging	850	2500	1	2006				HgCdTe Raytheon VIRGO (science)	Mosaic	16	2048	2048
162	ESO	VISTA	VISTA OPT	Wavefront sensing	850	1100	1	2006				e2v CCD42-40	Mosaic	4	2048	2048
163	ESO	VLT	AMBER	Interferometric Imaging, Spectroscopy	1000	2400	1	2005		30	10000	Rockwell Hawaii-1	Single	1	512	512
164	ESO	VLT	CAMCAO	Imaging	1200	2500	1	2011				Rockwell Hawaii-2	Single	1	2048	2048
165	ESO	VLT	CONICA	Polarimetry, Longslit, Spectral diff-imaging	800	5500	1	2001		60	1500	Raytheon Aladdin 3	Single	1	1024	1024
166	ESO	VLT	CRIRES	Longslit	1000	5000	1	2006			100000	InSb	Mosaic	5	1024	1024
167	ESO	VLT	FINITO	Fringe tracking	1500	1800	1	2005				Rockwell MBE PICNIC	Single	1	256	256
168	ESO	VLT	FLAMES (Giraffe)	MOS, IFU	370	950	132	2003		5600	45000	e2v CCD 44-82	Single	1	2048	4096
169	ESO	VLT	FORS1	Imaging, MOS, Longslit, Polarimetry	330	1100	19	1999		520	3300	Tektronix 2048EB4-1	Single	1	2048	2048
170	ESO	VLT	FORS2	Imaging, MOS, Longslit,	330	1100	80	2000		520	5120	MIT/LL CCID-20	Mosaic	2	2048	4096
171	ESO	VLT	GALACSI/GRAAL	Wavefront Sensing	450	950	1	2011				e2v L3 CCD220	Mosaic	5	240	240
172	ESO	VLT	HAWK-1	Imaging	850	2500	1	2006				Rockwell Hawaii-2RG	Mosaic	4	2048	2048
173	ESO	VLT	IRIS	Tip-tilt correction	1000	2500	1	2005				Rockwell PICNIC	Single	1	256	256
174	ESO	VLT	ISAAC - LW	Imaging, Imaging polarimetry, Longslit	2500	5000	1	1999		250	5120	Raytheon Aladdin 2 InSb	Single	1	1024	1024
175	ESO	VLT	ISAAC - SW	Imaging, Imaging polarimetry, Longslit	1000	5000	1	1999		250	11000	Rockwell Hawaii 1	Single	1	1024	1024
176	ESO	VLT	KMOS	IFU	1000	2450	1	2009		3500		Rockwell Hawaii-2RG	Mosaic	3	2048	2048
177	ESO	VLT	MAD	Wavefront Sensing	450	950	1	2006				e2v CCD39	Single	5	80	80
178	ESO	VLT	MIDI	Interferometric Imaging, Spectroscopy	8000	13000	1	2003		30	230	Raytheon CRC 774 Si:As IBC	Single	1	320	240
179	ESO	VLT	MUSE	IFU	465	930		2011		3000			Mosaic	24	4096	4096
180	ESO	VLT	NAOS IR	Wavefront Sensing	800	2500	1	2001				Rockwell Hawaii 1	Single	1	1024	1024
181	ESO	VLT	NAOS OPT	Wavefront Sensing	450	1000	1	2001				e2v CCD50	Single	1	128	128
182	ESO	VLT	PRIMA	Fringe tracking; astrometry	2000	2500	1	2006				Rockwell PICNIC	Mosaic	2	256	256

ID	Institute	Telescope	Instrument	Mode	λ min	λ max	Multiplex	Year	Spatial Res.	Min λ/Δλ	Max λ/Δλ	Manufacturer	Format	# Det.	Size X	Size Y
183	ESO	VLT	SINFONI	IFU	1050	2450	32	2004		1500	4000	Rockwell Hawaii-2RG	Single	1	2048	2048
184	ESO	VLT	UVES blue	Echelle	320	500	1	1999			80000	e2v CCD 44-82	Single	1	2048	4096
185	ESO	VLT	UVES Red	Echelle	420	1100	8	1999			110000	e2v CCD 44-82, MIT/LL CCID-20	Mosaic	2	2048	4096
186	ESO	VLT	VIMOS	Imaging, MOS, IFU	350	1100	1000	2002		200	2500	e2v CCD 44-82	Single	4	2048	4096
187	ESO	VLT	VISIR	Imaging, Longslit	8000	24000	1	2004		150	30000	Boeing DRS BIB	Single	2	256	256
188	ESO	VLT	X-Shooter NIR	Longslit, IFU	1100	2400	1	2008		6400	11000	Rockwell Hawaii-2RG	Single	1	2048	2048
189	ESO	VLT	X-Shooter OPT Blue	Longslit, IFU	320	500	1	2008		6400	11000	e2v CCD44-82	Single	1	4096	2048
190	ESO	VLT	X-Shooter OPT Red	Longslit, IFU	500	1100	1	2008		6400	11000	MIT/LL CCID-20	Single	1	4096	2048
191	ING	WHT	AF2/WYFFOS	MOS	350	1000		2004		10000		e2v 42-80	Mosaic	2	2048	4096
192	ING	WHT	AG1-7	Autoguider/TV	400	900	1	2004				CCD4720/5710	Single	1	1024	1024
193	ING	WHT	AUX	Imaging	350	1000	1	1987				TEK 1024	Single	1	1024	1024
194	ING	WHT	INGRID	AO Imaging	800	2500	1	2000				Rockwell Hawaii-1	Single	1	1024	1024
195	ING	WHT	ISIS Blue	Longslit	350	1000	1	1987		4000		e2v 42-80	Single	1	2048	4096
196	ING	WHT	ISIS Red	Longslit	350	1000	1	1987		4000		e2v 42-90	Single	1	2048	4500
197	ING	WHT	LIRIS	Imaging, Longslit, MOS	800	2500		2004		1000	3000	Rockwell Hawaii-1	Single	1	1024	1024
198	ING	WHT	OASIS	AO IF Spectroscopy, Imaging	350	1000	1100	2004	0.30	1000	4000	MIT/LL CCID20	Single	1	2048	4096
199	ING	WHT	PFIP	Imaging	350	1000	1	1999				e2v 42-80	Mosaic	2	2048	4096
200	ING	WHT	QUCAM2	Rapid Spectroscopy	400	900	1	2005				MIT/LL CCD201	Single	1	1024	1024
201	WIYN	WIYN	DensePak	IFU	340	1100	82	1998		700	22000	SITe	Single	1	2048	2048
202	WIYN	WIYN	HYDRA II	MOS	340	1100	100	2004		200	5000	SITe	Single	1	2048	2048
203	WIYN	WIYN	MiniMo	Imaging	320	950	1	1999		700	22000	SITe	Mosaic	2	2048	4096
204	WIYN	WIYN	ODI	Imaging	320	1100	1	2009				STA/Dalsa OTAs	Mosaic	16	3840	3952
205	WIYN	WIYN	OPTIC	Imaging	350	1050	1	2002				OTCCD	Mosaic	2	2048	4140
206	WIYN	WIYN	QUOTA	Imaging	320	1100	1	2006				STA/Dalsa OTAs	Mosaic	4	3840	3952
207	WIYN	WIYN	SparsePak	IFU	340	1100	90	2002		700	22000	SITe	Single	1	2048	2048
208	WIYN	WIYN	WHIRC	Imaging	950	2500	1	2006				Raytheon VIRGO	Single	1	2048	2048
209	WIYN	WIYN	WTTM	Imaging	320	950	1	2003				e2v	Single	0	2430	2048

ID	Instrument	Pixel scale	FOV	Electronics	Noise min	Noise max	Read-time Max	Read-time Min	Dark Current	Full Well	Buttability	Pixel Cost	Inst. cost
1	2df		120' x 120'	AAO2	4	6	402	41		385000	0	0.008	
2	AAOmega		120' x 120'	AAO2	2.2	2.8					3		
3	IRIS-2	0.45	7.7' x 7.7'	AAO2	2	12	1	0.6	0.1	212000	0		
4	UCLES	0.16		AAO2	5	14	428	4.8	1.2	200000	0		
5	UHRF	0.16		AAO2	2	10.5	54	10	1.2	200000	0		
6	WFI	0.23	30' x 30'	Leach Gen II	5			60	25	80000	3		
7	DECam	0.27	132'	Monsoon	5			3	7.2	300000	4		
8	HYDRA	0.30	40'	Arcon	3.1			130	<1	60000	0		
9	ISPI	0.30	11' x 11'	Leach Gen II	15			3.2	0.1	55000	0		
10	Mosaic-2	0.27	36' x 36'	Arcon	5	8		100	1	80000	3		
11	RC Spec	0.50	5.5'	Arcon	7			138	<1	80000	0		
12	Laica	0.22	60' x 60'	MPI Hd Vis	6			60	<5	100000	0		3
13	Mosca	0.33	21.8' x 10.9''	MPI Hd Vis	5.5			240	<5	55000	0		1
14	Omega2000	0.40	15.4' x 15.4'	MPI Hd IR				1.6	29000	100000	0		3
15	OmegaCass	0.20	5.1' x 5.1'	MPI Hd IR	22			0.842	40000	230000	0		1.5
16	PMAS	0.50	16'' x 16''	ACE	5			240			0		5
17	Pyramir	0.08		MPI Hd IR	10			0.006	40000	100000	0		20
18	TwinB			MPI Hd Vis	5.6			50	<5	60000	0		1
19	TwinR			MPI Hd Vis	5.5			50	<5	65000	0		1
20	CFHTIR	0.21	3.6' x 3.6'	Leach Gen II	<20			1	0.15	100000	3	0.03	0.165
21	Espadons			Leach Gen II	<3			25	1.8	150000	3		0.8
22	Gecko		single star	Leach Gen II	<7.5			50	60	150000	3		0.4
23	KIR	0.04	36'' x 36''	Leach Gen II	<20			9	0.15	100000	3	0.03	1.9
24	MegaCam	0.19	60' x 60'	Custom CEA	<5			40	1.8	150000	3		5
25	MOS	0.31	9.3' x 9.3'	Leach Gen II	<7.5			50	60	150000	3		0.5
26	WIRCam	0.30	20.5' x 20.5'	Leach Gen II	<30			1	0.01	100000	3	0.131	5.5
27	Prime Focus Camera	0.32	120' x 120'	Leach or Monsoon	<10			10	0.01	200000	3	0.033	11

ID	Instrument	Pixel scale	FOV	Electronics	Noise min	Noise max	Read-time Max	Read-time Min	Dark Current	Full Well	Buttability	Pixel Cost	Inst. cost
28	CES			FIERA	3	4	51	26	2	150000	3		
29	EFOSC2	0.16	5.4' x5.4'	FIERA	10	11	160	70	3.5	100000	3		
30	HARPS			FIERA	3	7	180	25			3		
31	TIMMI2	0.60	96'' x 72''	IRACE	950			0.006	100	30000000	0		
32	bHROS		1''	Leach Gen II	5		100	30	3	100000	0	0.01	2
33	EXAOC	0.02	3'' x 3''	Leach Gen III							0	0.1	24
34	FLAMINGOS-2	0.18	2' x 6'	MCE-4	15			1	0.1	200000	0	0.09	5
35	GMOS-N	0.07	5.5'	Leach Gen II	5		150	70	3	100000	3	0.01	6
36	GMOS-S	0.07	5.5'	Leach Gen II	5		150	70	3	100000	3	0.01	6
37	GNIRS	0.15	5''	GNAAC	40			1	0.3	200000	0	0.05	6
38	GSAOI	0.02	80''	Leach Gen III	15			10	0.03	200000	0	0.01	5
39	MICHELLE	0.01	32'' x 24''	EDICT	2000			0.01	100	10000000	0	1.3	10
40	NICI	0.02	20''	MKIR	40			5	0.3	200000	0	0.05	5
41	NIFS	0.05	3'' x 3''	Leach Gen III	15			10	0.03	200000	3	0.1	3
42	NIRI	0.12	120''	GNAAC	40			1	0.3	200000	0	0.05	4.5
43	T-RecS	0.09	22'' x 29''	MCE-4	1000			0.01	100	10000000	0	1.3	2
44	MID IR High Res. Spect.												
45	MID IR Imaging Spect.												
46	Near IR Imager (AO)												
47	Near IR Imaging Spect.		25' x 25'										
48	Optical High Res. Spect.												
49	Optical Imaging Spect.		50' x 50'										
50	A&G (Guacamole)	0.10	12'' x 12''	GTC Guider	4	6	5	2	360	60000	0		
51	CanariCam	0.08	25.6'' x 19.2''	MCE-4	1000	2800			100	3000000	0		
52	CIRCE	0.10	3.4' x 3.4'	MCE-3							0		
53	Commissioning Instrument	0.06	1' x 1'	GTC Guider	4	6	5	2	360	60000	0		
54	ELMER	0.19	4.2'	Leach Gen II	2	6	90	9	5	100000	3		

ID	Instrument	Pixel scale	FOV	Electronics	Noise min	Noise max	Read-time Max	Read-time Min	Dark Current	Full Well	Buttability	Pixel Cost	Inst. cost
55	EMIR	0.20	6' x 6'	Leach Gen III	12			1	0.1	130000	0		
56	FRIDA	0.01	54" x 54"	Leach Gen III	12			1	0.1	130000	0		
57	NAHUAL	0.08		Leach Gen III	12			1	0.1	130000	0		
58	OSIRIS	0.10	8.5' x 8.5'	Leach Gen II	2		90	4.5	9	100000	3		
59	UES	0.10		Leach Gen II							3		
60	COSMIC	0.29	9.7' x 9.7'		12			149		21000000	0		
61	Double Spect. Polarimeter Red										0		
62	Double Spect. Polarimeter Red	0.47									0		
63	LFC	0.18	24' x 24'					115			0		
64	WIRC	0.25	8.7' x 8.7'	Custom Cornell 32 chan.		15		3.25	0.26		0		
65	HRS	0.00	4' x 3'								0		
66	LRS	0.25	4' x 3'								0		
67	MRS	0.00	4' x 3'								0		
68	DEIMOS	0.12	16.7' x 5'	Leach gen II	2.2	2.8	80	40	4.7	116000	3		12
69	ESI	0.15	2' x 8'	Leach Gen II	2.7		70	30	2	105000	0		
70	HIREs			Leach Gen II	2.9	4.2			0	100000	2	6	
71	KALI	75.00		Custom Wallace Elec.+JPL	640						0		
72	LRISb	0.14	6' x 8'	Leach Gen II	4	6		42	5	150000	1		3
73	LRISr	0.21	6' x 8'	Leach Gen I		6.3		70	0	125000	2		6
74	LWS	0.08	10" x 10"	BCE Custom	1100			0.01	550000	9000000	0	122	2
75	MOSFIRE										0		
76	NIRC	0.15	5.3' x 5.3'	IRE	1500			9	50000	11000000	0		
77	NIRC2	0.01	40" x 40"	UCLA transputer	60			0.18	0.1	50000	0	9.5	10
78	NIRES	0.00									0		
79	NIRSPEC	0.14	46" x 46"	UCLA transputer	25			6	2	120000	0		6
80	OSIRIS	0.02	1.6" x 6.4"	Leach Gen III	8.5	10			0.09	90000	0		

ID	Instrument	Pixel scale	FOV	Electronics	Noise min	Noise max	Read-time Max	Read-time Min	Dark Current	Full Well	Buttability	Pixel Cost	Inst. cost
81	HRS	0.41	300' x 300'	AACAS	5			100	<5	100000	0	0.008	12
82	LRS	0.41	300' x 300'	AACAS	5			60	<5	100000	0		6
83	LBC Blue	0.23	27' x 27'	Elettromare							0	0.1	3.6
84	LBC Red	0.23	27' x 27'	Elettromare							0	0.1	3.6
85	LBTI-NOMIC	0.10	25" x 25"	MPIA							0		
86	LINC-Nirvana	0.01	10" x 10"	Leach Gen III							0		
87	LUCIFER 1	0.12	4' x 4'	MPIA							0	0.78	6.5
88	LUCIFER 2	0.12	4' x 4'	MPIA							0	0.78	6.5
89	MODS Blue 1	0.15	6' x 6'	OSU Custom							0	0.09	6
90	MODS Blue 2	0.15	6' x 6'	OSU Custom							0	0.09	6
91	MODS Red 1	0.15	6' x 6'	OSU Custom							0	0.09	6
92	MODS Red 2	0.15	6' x 6'	OSU Custom							0	0.09	6
93	PEPSI	0.17	0.5" x 1.4"	Magellan	< 3						0		
94	PEPSI HR	0.17	0.5" x 1.4"								0		
95	LSST	0.20	210'x210'		6			2	2	90000	0	0.03	80
96	Prime Focus Camera	0.50	16.9' x 16.9'	Pixel Vision				100	neg.	300000	0	0.02	
97	4-Star Imager	0.15									0		
98	B&C Spectrograph	0.25		Custom?	3.9	5.7					0		
99	EMS	0.31									0		
100	IMACS	0.20	27.5'x27.5'	OCIW BASE	3.5		94		1	78000	3		
101	LDSS-3	0.19	8.3 ' x 8.3'	OCIW BASE	3.6	6.2	72	32	1	47000	0		
102	MagIC	0.07	2.35' x 2.35'	Leach Gen II	4.6	5.9		23	1	130000	0		
103	MIKE Blue	0.13	5"x5"	OCIW BASE	2			190	4	5000	0		
104	MIKE Red	0.12	5"x5"	OCIW BASE	3.5			65	1	60000	0		
105	MMIRS	0.20	6.8' x 6.8'	Custom							0		
106	PANIC	0.13	2.13' x 2.13'	OCIW Custom	15			1.5	0.03	60000	0		

ID	Instrument	Pixel scale	FOV	Electronics	Noise min	Noise max	Read-time Max	Read-time Min	Dark Current	Full Well	Buttability	Pixel Cost	Inst. cost
107	Echelle		2'	2901_controller	4.5			120	4	220000	0		
108	FLAMINGOS		10' x 10'	MCE-4	40			2	0.1	30000	0		
109	MARS		5.4'	2901_controller	7			80	70		0		
110	MOSAIC-1		36' x 36'	Arcon	6			154	5	70000	3		
111	NEWFIRM		27' x 27'	Monsoon	20			1	1	170000	2		
112	RC Spec		5.4'	2901_controller	4			120	4	220000	0		
113	SQIID	0.39	3.3' x 3.3'	Wildfire	40			1	30	170000	0		
114	ARIES (AO)	0.04	40" x 40"								0		
115	Binospec		16' x 15'								0		
116	Hectospec										0		
118	Megacam	0.08	24' x 24'	Custom	4	13	34	10			3		
119	MIRAC3 (AO)		44" x 44"							30000000	0		
120	MMT Spectr. Blue										0		
121	MMT Spect. Red										0		
117	SPOL	0.19	19"x19"				45	13			0		
122	Spectrograph red				2.8			15		110000	0		
123	Spectrograph blue				2.8			15		140000	0		
124	SWIRC	0.15	5' x 5'								0		
125	EMMI Blue	0.37	6'x6'	ACE	5	8.5	50	33	7	245000	0		
126	EMMI Red	0.17	9' x 10'	FIERA	4	7	48	10	0.5	100000	3		
127	SOFI	0.28	4.8' x 4.8'	IRACE	11			1.2	0.01	100000	0		
128	SuSI2	0.08	5.5' x 5.5'	FIERA	4	5	56	0.5		150000	3		
129	PFIS	0.16	8' x 8'	Leach Gen II	3.3	<5	11	5	<1	>150000	3	0.03	
130	SALT-HRS					0		0		0	3		
131	SALTICAM	0.14	8' x 8'	Leach Gen II	3.3	<5	11	5	<1	>150000	0	0.03	
132	LYNX	0.13	4"	SAO Gen III	6			90	1	140000		0.15	0.15
133	MOFS	0.25	12' x 12'	DINACON I	2.3			234	.5	100000	0	0.04	0.15
134	MPFS	0.25	16"	DINACON I	2.3			234	.5	100000	0	0.05	0.2
135	MSS	0.16	30"	DINACON I	2.3			234	.5	100000		0.05	0.2
136	NES	0.16	16"	IJAF	7.7			100	2	150000	0	0.1	0.4

ID	Instrument	Pixel scale	FOV	Electronics	Noise min	Noise max	Read-time Max	Read-time Min	Dark Current	Full Well	Buttability	Pixel Cost	Inst. cost
137	PFES	0.18	4"	SAO Gen III	6			90	1	140000		0.05	0.05
138	SCORPIO	0.18	6.1' x 6.1'	DINACON I	1.7			90	.5	100000		0.02	0.075
139	Specle	0.05	23"					0.02	30			0.2	0.2
140	UAGS	0.43	2" x 140"	Photometrics	3.5			50	.65	325000	0	0.1	0.1
141	Goodman	0.15	5' x 5'	Leach Gen II	3			20	1	100000	1		
142	OSIRIS	0.14	1.5' x 1.5'	Ohio Controller	15			10	0.15	33000	0		
143	SIFS	0.30	7.8' x 15 '	Leach Gen III	3	3.8		20	2	100000	1		
144	SOI	0.08	5.25' x 5.25'	Leach Gen II	3.8			20	2	100000	1		
145	Spartan	0.07	2.5' x 5'	Ed Loh Controller	15			2.6	0.1	55000	1		
146	CIAO	0.01	21.8"	Redstar (MK IR)	60			0.18	6	60000	0		
147	CISCO/OHS	0.10	108" x 108"	Messia3+	7	16		1.4	<0.1	70000	0		
148	COMICS	0.13	42" x 32"	Custom				0.03	100	5700000	0		
149	FOCAS	0.10	6'	Messia5 + Mfront (NAOJ)	4			152	2	40000	3		
150	HDS	0.14	1'	Messia5 + Mfront (NAOJ)	4.4			46	10	80000	3		
151	IRCS	0.02	24" x 59"	Redstar (MK IR)	43	68		0.12	0.1	129000	0		
152	Suprime-Cam	0.20	34' x 27'	Messia5 + Mfront (NAOJ)	5	10		49	3	100000	3		
153	DOLORES	0.28	9.4' x 9.4'	Elettromare	9			71	6	150000	0		
154	NICS	0.25	4.3' x 4.3'	Custom	24			1	<1	100000	0	0.15	0.5
155	OIG	0.07	4.9' x 4.9'	Elettromare	4			220	6	150000	2	0.0062	0.18
156	SARG	0.16		Elettromare	7.5			200	6	150000	2	0.014	0.88
157	CGS 4	0.60									0		
158	UFTI	0.09	92" x 92"	Astrocam 4100 (PerkinElmer)	10	26				85000	0		
159	UIST	0.12	2' x 2'	EDICT Custom	40	80					0		
160	WFCAM	0.40	45' x 45'	Leach Gen III	4					180000	2		0

ID	Instrument	Pixel scale	FOV	Electronics	Noise min	Noise max	Read-time Max	Read-time Min	Dark Current	Full Well	Buttability	Pixel Cost	Inst. cost
161	VISTA IR Camera	0.34	71' x 71'	IRACE	17			0.7	2.7	150000	3		
162	VISTA OPT	0.23		Leach Gen III				0.09			2		
163	AMBER		0.05	Bonn Controller Custom		11		0.005	0.01	120000	0		
164	CAMCAO	0.03	1' x 1'	IRACE	12			1	0.04	100000	0		
165	CONICA	0.06	56"x56"	IRACE	10	40	2	0.7	1	250000	0		
166	CRIRES	0.10		IRACE	10	40		0.11	<0.1	200000	3		
167	FINITO	0.01		IRACE	15	40		0.000125	0.01	250000	0		
168	FLAMES (Giraffe)	0.30	25'	FIERA		4		42	1	100000	3		
169	FORS1	0.20	6.8' x 6.8'	FIERA	5	6		25	8	160000	0		
170	FORS2	0.13	6.8' x 6.8'	FIERA	3	4	62	31	2	100000	3		
171	GALACSI/GRAAL	0.00		NGC		1		0.001	1	100000	0		
172	HAWK-1	0.11	7.5' x 7.5'	IRACE		20		0.88	0.01	100000	3		
173	IRIS	0.03		IRACE		40		0.001	0.01	250000	0		
174	ISAAC - LW	0.07	2.5' x 2.5'	IRACE	10	40		0.1	0.1	200000	0		
175	ISAAC - SW	0.15	2.5' x 2.5'	IRACE	5	11		1.8	0.01	120000	0		
176	KMOS	0.20	24x2.8"x2.8"	NGC	5			0.88	0.01	100000	3		
177	MAD	0.30	19.2" x 19.2"	FIERA		6.5		0.002	500	30000	0		
178	MIDI	0.08	0.3	GEIRS (MPA Heidelberg)	850	2400		0.002	10000	33000000	0		
179	MUSE	0.20	1' x 1'	NGC		3	60	10	2	100000	0		
180	NAOS IR	0.40	7x7x4.8"x4.8"	Perkin-Elmer	10	20		0.01	0.8	100000	0		
181	NAOS OPT	0.30	7x7x4.6"x4.6"	FIERA	5	6		0.002	10000	100000	0		
182	PRIMA	0.00		IRACE	14	50		0.0008	0.01	250000	0		

ID	Instrument	Pixel scale	FOV	Electronics	Noise min	Noise max	Read-time Max	Read-time Min	Dark Current	Full Well	Buttability	Pixel Cost	Inst. cost
183	SINFONI	0.25	8'' x 8''	IRACE	7	20	1		0.01	110000	3		
184	UVES blue	0.22		FIERA	2	4		37	1	100000	3		
185	UVES Red	0.16		FIERA	2	4		37	1	80000	3		
186	VIMOS	0.20	28' x 32'	FIERA		5	24	0	1	150000	0		
187	VISIR	0.13	32'' x 32''	IRACE	300	1700	2		0.01	7000	18000000	0		
188	X-Shooter NIR	0.31		IRACE	3			1		0.01	80000	2		
189	X-Shooter OPT Blue	0.14		FIERA	2	3	70		.2	120000	3		
190	X-Shooter OPT Red	0.14		FIERA	2	3	70		1.1	120000	3		
191	AF2/WYFFOS	1.60	40'	Leach Gen II	4	6	60	45	<1	100000	3		
192	AG1-7	0.30	4' x 4'	Leach Gen II	4			5	0.1	50000	3		
193	AUX	0.11	1.8'	Leach Gen II	4	6	35	22	6	200000	0		
194	INGRID	0.04	40'' x 40''	Leach Gen II	20			0.8		30000	0		
195	ISIS Blue	0.20	5'	Leach Gen II	4			60	3	120000	3		
196	ISIS Red	0.20	5'	Leach Gen II	4			60	3	120000	3		
197	LIRIS	0.25	4.3' x 4.3'	Leach Gen II	10			0.9	0.03		0		
198	OASIS	0.00	37.6' x 37.6'	Leach Gen II	2.3	2.8	60	39	3	100000	3		
199	PFIP	0.24	16.2' x 16.2'	Leach Gen II	4	6	60	45	<1	100000	0		
200	QUCAM2	0.00		Leach Gen II	<1			2	<1	50000	0		
201	DensePak	0.50	0.5' x 0.75'	KPNO 2091	4.5			160	4.5	125000	2	0.02	0.038
202	HYDRA II	0.50	60' x 60'	KPNO 2091	4.5			160	4.5	125000	2	0.02	0.655
203	MiniMo	0.14	9.6' x 9.6'	ARCON	6			160	4.5	125000	2	0.02	0.17
204	ODI	0.10	60' x 60'	MONSOON	8			4	<4	>70000	3	0.02	6.6
205	OPTIC	0.14	10' x 10'	Leach Gen II	4			4	3	>80,000	2	0.01	0.25
206	QUOTA	0.10	16' x 16'	MONSOON	8			4	<4	>70000	3	0.02	0.76
207	SparsePak	0.50	1.2' x 1.2'	KPNO 2091	4.5			160	4.5	125000	2	0.02	0.08
208	WHIRC	0.12	4' x 4'	MONSOON		15		2	0.2	300000	2	0.05	1.15
209	WTTM	0.11	3.8' x 4.7'	ARCON	4.5			160	7	95000	2	0.02	2.1

APPENDIX B

OVERVIEW PAPER - DETECTORS FOR SPACE SCIENCE

Editors Note: Due to the late submission of this paper we were unable to include it in Section I: Observatory Status and Plans, where it properly belongs.

This page intentionally left blank

DETECTORS FOR SPACE SCIENCE
Future requirements and considerations for flight detectors

Mark Clampin[1], David Lumb[2], Marco Sirianni[3] and Edward Smith[4]
[1]NASA/GSFC, [2]ESA/ESTEC, [3]ESA/STScI, [4]NASA/HQ

Abstract: *The design of detector systems for flight applications requires the consideration of a number of issues unique to space instrumentation. Flight detectors must endure hostile radiation environments and thermal extremes. Paramount importance is given to reliability since inflight replacement is at best difficult and usually impossible. Flight detectors are also significant cost and design drivers since they often determine key requirements for flight instruments such as volume, mass, power consumption, heat dissipation and communications budgets. In this paper we describe the primary concerns in developing flight detector systems, and review the challenges posed by future NASA and ESA space science missions for detector development.*

Key words: detectors, space science

1.   INTRODUCTION

The last two decades saw major progress in the development of large format detector systems for visible and near-infrared astronomy. Detector developments for planned NASA and ESA space science missions reflect this progress, albeit on a smaller scale, since detector developments must pass many more hurdles to gain acceptance for space science missions. In this paper we summarize the primary considerations for developing detector systems and maturing their technology to meet acceptable standards for flight. We also discuss the challenges posed by future space science mission concepts under consideration by NASA and ESA for their respective programs.

2.   FLIGHT DETECTORS: SPECIAL CONSTRAINTS

The design of detector systems for flight applications requires the consideration of a number of issues unique to space instrumentation. In addition to the primary task of developing a detector that meets the demands of a space environment, it is necessary to consider the impact of the detector on the science payload. In this section we will address these issues in turn.

The most significant difference between detector systems for ground instrumentation is the issue of reliability. Flight detector systems cannot be easily replaced in the event of a failure. Furthermore, they must perform to the required specifications over the design lifetime of the mission. In addition, to the subsystem or component failures, the mission orbit and its associated radiation environment is one of the main lifetime concerns for solid state detectors. In the case of photon counting detectors employing microchannel plates (MCPs), or intensifier technologies the lifetime is more likely to be a function of phosphor or MCP ageing. Carefully designed prelaunch integration and testing (I&T) plans are required to fully validate flight detector system performance in an environment matching that in which they will operate.

Flight detector systems must have reached sufficient technical maturity that the detector design concept has been fully validated prior to its adoption as the baseline technology for a given application. In order to evaluate the readiness of a flight technology NASA employs the concept of technology readiness levels (TRL), which we summarize in Table 1 [1].

Table 1. A summary of Technology Readiness Level (TRL) definitions.

Level	Definition
TRL 1	Basic principles observed and reported
TRL 2	Technology concept and/or application formulated
TRL 3	Analytical and experimental critical function and/or characteristic proof of concept
TRL 4	Component and/or breadboard validation in laboratory environment
TRL 5	Component and/or breadboard validation in relevant environment
TRL 6	System/subsystem model or prototype demonstration in a relevant environment (ground or space)
TRL 7	System prototype demonstration in a space environment
TRL 8	Actual system completed and "flight qualified" through test and demonstration (ground or space)
TRL 9	Actual system "flight proven" through successful mission operations

A program is required to demonstrate that a technology has reached TRL 6 by the completion of Phase B, a program's design phase. TRL level 8 is achieved by completion of system level integration and test. Ideally, technology development paths in the early phases of a program should incorporate some redundancy, such as alternate approaches and/or different

vendors. This approach has proved valuable in the case of near-IR detectors for the James Webb Space telescope where two alternate technologies were pursued until early in Phase B, when a selection was made between the competing HgCdTe and InSb technologies [2,3]. This approach helps mitigate the risk of locking in a technology before the real program requirements are fully understood.

It has been noted elsewhere in this conference that ground observatories tend to develop instruments after deployment of their telescopes, as the perception of science needs and facility capabilities changes. With the sole and very expensive exception of HST, this luxury is not afforded to space-borne instruments; optics and detectors have to be developed together and ideally matched in performance. This is surely the explanation behind Luppino's version of Moores Law – that the increasing number of pixels in a CCD camera, which exponentially increases with time, is retarded by a factor ~5 years in a space observatory, compared with the ground facility. Aditionally we note that space technology especially favours wavebands that are not accessible from ground, with a further delay in "learning curve".

Flight detector systems face a major challenge from the radiation environment in the orbit into which they are launched. The primary sources of energetic radiation of concerns for flight detectors are summarized in Table 2. In addition to the orbit, the impact of radiation on flight detector systems depends upon other factors such as the solar cycle, detector architecture and detector shielding. In general, solid state detectors are more susceptible than MCP and intensifier-based systems. Detailed descriptions of the effects of radiation on detectors, and silicon devices, in particular, are given by Pickel, et al. [4], Srour, et al. [5], and Hopkinson, et al. [6].

Table 2. Sources of Energetic Radiation

Radiation Source	Affected Orbits
Trapped protons	Low earth orbits, Highly Elliptical Orbits Transfer Orbits
Galactic Cosmic Ray Ions	Low earth orbits, Geostationary orbits, Highly Elliptical Orbits, Drift-Away, L2, Interplanetary
Solar Flare Protons	Low earth orbits $(I > 45^o)$, Geostationary orbits, Highly Elliptical Orbits, Drift-Away, L2Interplanetary
Solar Flare Heavy Ions	Low earth orbits, Geostationary orbits, Highly Elliptical Orbits, Drift-Away, L2, Interplanetary

Damage to solid state devices takes the form of ionizing and non-ionizing damage. Ionizing damage mechanisms involve the buildup of trapped charges and the generation of trapping sites. Short term effects include single event soft and/or permanent errors. Long term ionizing damage mechanisms include flat band voltage shifts, surface leakage current, amplifier noise and linearity changes. The ionizing damage can generally be managed. For example, since the dark current of buried channel Charged Coupled Devices

(CCDs) is dominated by carrier generation at the Si/SiO2 interface if the CCD is bias inverted, holes from the channel stop regions fill traps in the interface and suppress the generation of dark current.

Non-ionizing damage generally takes the form of long-term displacement damage where atoms are displaced from their position in the lattice structure creating defects which act as trapping or emission sites. This leads to bulk leakage current, hot spikes, and in the case of charge coupled devices (CCDs)   charge transfer inefficiency. In Fig. 1 we show the relative degradation of charge transfer effiency in CCDs flown in Hubble Space Telescope (HST) instruments [7].
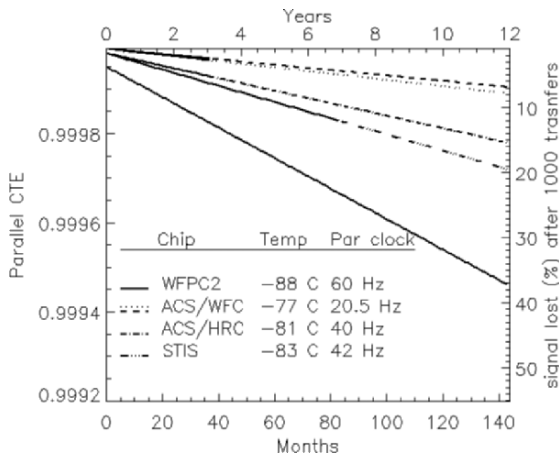

Figure 1. Degradation of charge transfer efficiency in HST CCD cameras.

Appropriately designed packages to shield focal plane arrays can mitigate damage from lower energy protons, but cannot protect from high energy protons or neutrons generated by collisions in the shielding. Typical materials used for shielding include, tantalum, molybdenum and Alloy 52. In addition, as focal plane arrays grow in size it becomes more important to ensure the solid angle subtended by the window of the focal plane array is appropriately shielded by appropriate design of the instrument. Operational planning (such as splitting or dithering observations and annealing of hot spikes) may also provide mitigation to radiation damage but it may also increase overheads and data volume.

Detector packaging is another area where the demands of space hardware differ widely from those of ground-based instrumentation. Firstly, mass is a precious commodity and detector sub-systems must stay within their allocations. Of particular concern is radiation shielding for solid-state detectors, which becomes significant as focal plane array requirements grow.

Figure 2 shows the HST Advanced Camera for Surveys (ACS) flight detector package, which houses a 4K×4K CCD focal plane. The mounting assembly for individual detectors is also an area where proven techniques have to be revisited for flight detectors. Epoxies used for mounting detectors have to be compliant with stringent contamination requirements, and thermal extremes encountered during thermal processing of flight assemblies. Detector assemblies have to be thermal matched to the materials used in the detector package. Finally, the detector assemblies have to pass environmental and vibration testing which mandates more robust designs and attention to aspects of the detector packaging design.
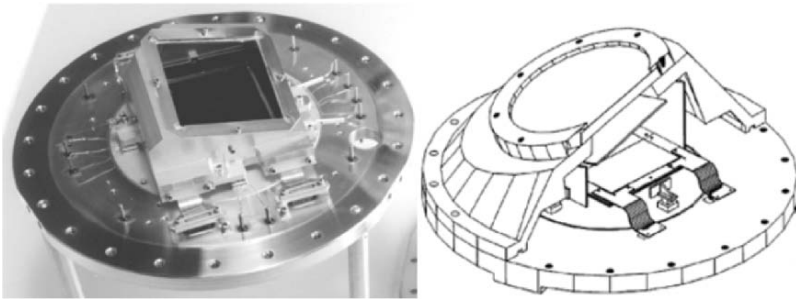

Figure 2. The right figure shows a schematic of the ACS 4K×4K CCD dewar. It comprises an inner shell, and an outer shell of alloy-52 with a Molybdenum baseplate. The left hand figure shows the baseplate, the inner dewar shell, and the CCD array seen through the inner shell's window.

Cooling a detector to the required temperature can also be a challenge in space missions. Passive cooling of detector arrays is the most desirable solution, however, this is not always possible. Thermal management of flight detector systems can be a major driver for a spacecraft's thermal design. Thermo electric coolers have been recently the main cooling mechanism for large visible and near-IR arrays. Although not very efficient, TECs are a relatively small, and can be combined in sequence to reach low temperature. For example a four stage TEC keeps the 4K×4K CCD FPA of the HST/ACS at -77 C, and a six stage TEC is employed in the HST/WFC3 to cool the 1kx1k HgCdTe array to -123°C. Quite often the generated heat need to be transferred by means of heat pipes to a radiator and dissipated.

Mechanical cryocooling systems (e.g., the Turbo Brayton mechanical cooler) are an established technique for cooling instruments to few 10s K. Although their use in space has been so far very successful [8], mechanical systems increase reliability issues and require dissipation of the generated heat. The James Webb Space Telescope is also baselined to employ a mechanical cooling system for its Mid-Infrared Camera (MIRI).

Cooling detectors using stored cryogen coolers is a straightforward approach, but it has the limitation of limited lifetime, and relatively high mass and volume requirements. In free-flying spacecraft venting cryogen needs to be managed and it cryogens also place constraints on launch operations.

Flight detector systems often play a major role driving mission subsystem definition, for example spacecraft communications, and mission operation concepts. The size of detector focal planes has now reached the situation where detector data volume is the major driver in the determination of communication requirements. Focal plane arrays of ≥100 Mpixel taking exposures every 1000 seconds can produce significant data volumes which need to be stored and downlinked before storage space is allocated. Actual observational overheads are driven by considerations such as cosmic ray rates, detector performance, calibration needs and observing strategies. In the case of detector systems with limited dynamic range, specialized observation program planning may be required to prevent catastrophic over-illumination or accelerated aging of the detector.

2.1   NASA Space Science Missions

In discussing detectors for future NASA missions we will limit our discussion to relatively large programs and some selected smaller programs. Smaller programs such as MIDEX, SMEX and Discovery class missions are competed, and are specifically identified in long term planning. Typically, the smaller, fast-track missions have to show a relatively high level of technology maturation compared with larger, long lead time programs. Our discussion is also primarily limited to astronomical missions; we do not discuss Solar System mission requirements.

2.1.1   Current Status

The current state of the art for UV to near-IR flight detectors is summarized in Table 3, using a selection of current missions. Visible detectors currently have the largest focal plane array sizes reflecting the investment in large CCD focal planes developed for ground-based astronomy through the 1990s [9,10], and the benefits of continued servicing of the Hubble Space Telescope. The lag of flight detectors behind ground-based instrumentation is readily demonstrated by the ACS 4K×4K focal plane array. The ACS instrument was proposed in 1994, and flew in 2002, encompassing several cycles of ground based instrumentation development.

Infrared arrays on current missions such as HST and the Spitzer Space Telescope (SST) feature relatively small formats, since these detector technologies precede the recent growth in the size of IR detectors. SST in particular has demonstrated the successful performance of a range of IR technologies from the near-IR to the far-IR.

Table 3. Summary of current NASA mission detector highlights

Mission	Camera	Detector System
HST	**ACS**	4K×4K CCDs: 400-1000 nm
		1K×1K CCDs: 200–1000 nm
	NICMOS [11]	256×256 HgCdTe
	STIS [12]	1K×1K MAMA array: 121–180 nm
		1K×1K MAMA array: 200–400 nm
	COS [13]	1k×1k MCP/Delay line detector: 120–180 nm
		1K×1K MAMA array: 200-400 nm
	WFC3 [14]	4K×4K CCD: 200-1000 nm
		1K×1K HgCdTe array: 1.0-1.7 μm
Spitzer	**IRAC** [15]	Two 256×256 InSb: 3.6-4.5 μm
		Two 256×256 SiAs IBC: 5.8-8.0 μm
	IRS [16]	Two 128×128 Si:As: 5-20 μm
		Two 128×128 SiSb: 19-40 μm
	MIPS [17]	128×128 SiAs (IBC): 24 μm
		32×32 Ge:Ga: 50-100 μm
		2×20 Stressed Ge:Ga: 160 μm
GALEX	**GALEX** [18]	4K×4K MCP/Cross delay line anode: 115-180 nm
		4K×4K MCP/Cross delay line anode: 165-300 nm

UV detectors still cover a range of technologies, ranging from MCP-based photon counting detectors, with delay-line or similar readouts, to CCDs optimized for the UV. Photon counting detectors have traditionally dominated UV imaging and spectroscopy. The combination of low UV to optical flux ratios in astronomy, combined with their high visible QE places CCDs at a disadvantage. The primary technical problem in UV imaging with CCDs is the red light rejection problem. UV optimized CCDs have high visible QEs. While near-UV filters can be designed with effective red blocking, the problem for far-UV imaging remains a challenge. Filters with visible light suppression factors of at least $\sim 10^{6}$ are required for effective far-UV imaging. Woods filters can achieve these suppression levels, but at the cost of relatively low far-UV throughput. More work is required to develop technologies for efficient visible-light rejection technologies such as Wood's filters, made with sodium, lithium and potassium [19].

2.2   Future Space Missions

NASA current plans for scientific goals are summarized by its strategic roadmap planning documents. The new Universe Science and Advanced Telescope Searches for Earth-like Planets and Habitable Environments roadmap document was assembled by committees during 2005. The science outlined in these roadmaps follows many of the objectives previously found in the Origins, and The Structure and Evolution of the Universe (SEUS) roadmaps.   These roadmaps contained notional timelines for science goals and missions directed at achieving those goals. Below we discuss some of these missions.

To examine how these roadmaps can drive detector technologies it is useful to look at a few specific examples. The stated goals of the Universe Exploration Roadmap are:

1. Find out what powered the Big Bang.

2. Observe how black holes manipulate space, time and matter.

3. Uncover the nature of the mysterious dark energy pulling the universe apart.

4. Determine how the infant universe grew into the galaxies, stars and planets, setting the stage for life.

A major mission planned to address the final question in this roadmap is the James Webb Space Telescope (JWST). JWST is a 6.5 meter, segmented mirror space telescope planned to be launched into an L2 orbit for a ten year mission. The primary science goal for JWST is to detect and study the first galaxies. It will also study the assembly of galaxies, the birth of stars and protostellar systems, and planetary systems and the origins of life.

JWST will operate at wavelengths from 0.6 μm to 29 μm, although it will be optimized to provide diffraction-limited image quality at 2μm. The telescope will be passively cooled to 40K, although the Mid-Infrared Imager (MIRI) focal planes will be further cooled using a cryocooler. Four science instruments will share the JWST focal plane. The detector complement of the JWST mission is summarized in Table 4. The core detector technology for JWST is the near-IR detector, which was developed on a dual technology development path. The downselect to HdCdTe was madewas made early in Phase B of the mission development program. Progress with the near-IR and mid-IR arrays for JWST is well under way and should provide many smaller missions with high-TRL IR detectors which can be scaled to larger focal plane sizes for the next decade.
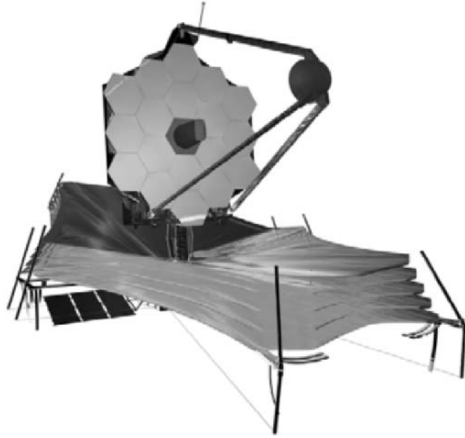
Figure 3. JWST is a passively cooled telescope.

Table 4. Infrared detector complemen for the James Webb Space Telescope

Instrument	Wavelength Range	Detector System
NIRCam	0.6 – 2.3 μm	Eight 2048×2048 HdCdTe
	2.3 – 5.0 μm	Two 2048×2048 HdCdTe
NIRSpec	0.6 – 5.0 μm	Two 2048×2048 HdCdTe
MIRI	5.0 – 29 μm	Three 1024×1024 SiAs
TF	1.7 – 4.2 μm	2048×2048 HdCdTe
FGS	0.8 – 2.5 μm	Two 2048×2048 HdCdTe

Another concept from the roadmapping effort that addresses question 3 above is the Joint Dark Energy Mission (JDEM). JDEM is a program that will seek to address the nature of dark energy by setting accurate constraints on the expansion history of the universe through observations of distant supernovae. JDEM is currently planned as a joint program between NASA and the Department of Energy. A number of concepts exist for the JDEM mission including the Supernova Acceleration Probe (SNAP) [20], JEDI (Joint Efficient Dark-energy Investigation) [21], and the Dark Energy Space Telescope (Destiny). These telescope concepts typically feature a 2 meter class telescope providing wide field imaging and/or spectroscopy. In Fig. 4 we show the a schematic illustrating the SNAP mission.
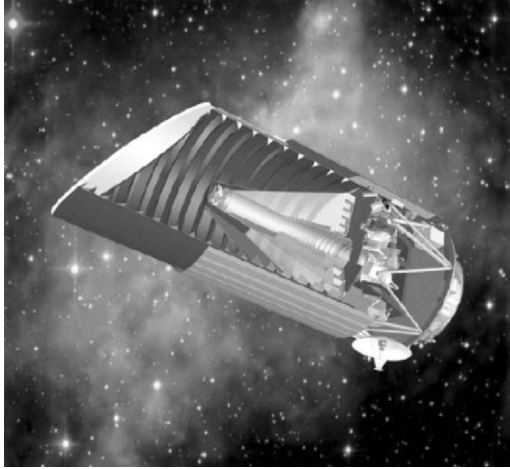
Figure 4. The Supernova Acceleration Probe

The SNAP concept illustrates some of the detector technologies currently being considered for this mission concept. The visible bandpass wide field imager might comprise as many as 36 CCDs. LBL have developed deep depletion p-type CCDs for SNAP [22], which feature improved red response, ease of production, and improved radiation hardness. The LBL CCDs are fully depleted through epitaxial thicknesses of 200 μm – 300 μm, yielding high quantum efficiency up to the Si bandgap cutoff at 1.1 μm. This approach has the benefit that CCD thinning is not required, offering reduced processing, higher device yields and reduced processing costs. Long wavelength fringing due to interference found in thinned, 13-25 μm epitaxial thickness CCDs is also avoided with this approach to the CCD architecture. The very high resistivity ensures that there is no field free region, so there is little charge diffusion to adjacent pixels. Due to the device thickness cosmic rays leave relatively long trails compared to thinned CCDs with 10 – 40 μm thickness. In flight, these CCDs will incur higher cosmic rate contamination rates for a given exposure time, which will need to factored into mission planning. P channel CCDs are an option for increasing the radiation tolerance of CCDs. The P channel design prevents the formation of silicon-E centers, the primary cause of trapping and CTI.

SNAP will also likely capitalize on the development of near-IR arrays for JWST to provide a near-IR focal plane of 36 2K×2K HdCdTe arrays. The possibility of using InGaAs arrays is also under consideration for a shorter near-IR cutoff (~1.4 μm). The primary challenge for SNAP is accommodating the large number of focal planes planned for this mission concept, within the spacecraft communications, mass, power, and volume allocations.

2.2.1   SAFIR

The Single Aperture Far-Infrared Telescope (SAFIR) is a ~10 meter aperture telescope designed to be operated at a temperature of <15 K, to achieve zodi-limited imaging performance over a wavelength range of 20 μm - 500 μm. In appearance, strawman SAFIR architectures are similar to JWST, only larger. SAFIR is designed to deliver 2" angular resolution at a wavelength of 100 μm. Detectors are a key technology for SAFIR, which will require large format arrays (~10^4 pixels) of Ge and Si BIB photoconductors, together with semi- and superconducting TES bolometers. Currently, the largest challenges are achieving the required array sizes and improving sensitivities by an order of magnitude. In addition to the challenges posed by the detectors, the infrastructure for the SAFIR detectors is also challenging. Low power dissipation is required from the focal plane arrays, together with thermal isolation. The detectors will also require superconducting electronics and high performance cryocoolers to achieve their operating temperatures.

2.2.2   LUVO

The Large Optical Ultraviolet Observatory (LUVO) is an 8-10 meter aperture UV/Optical telescope design for wide field (15'×15') UV and visible imaging and spectroscopy. The technologies for large format UV sensitive focal planes need considerable development to meet the demands of such a mission. The two competing approaches to large format UV imaging and spectroscopy are solid state and MCP-based detectors.

MCP-based detectors have advanced a long way in the last decade with large format detectors flown on FUSE, STIS [14] and Galex. These detectors typically employ glass MCPs, combined with CsI or KBr photocathodes deposited on the MCP surface for the far-UV (100 nm- 200 nm), or semi-transparent photocathodes such CsTe deposited on a detector front window. In the case of larger missions with complicated integration programs, it has also been useful to seal even the FUV detector packages with a window to permit effective management of contamination. Readout techniques for the charge cloud leaving the MCP fall into the categories of time delay or charge division event controiding anodes, or phosphors coupled to rapid readout detectors such as the CMOS [14].
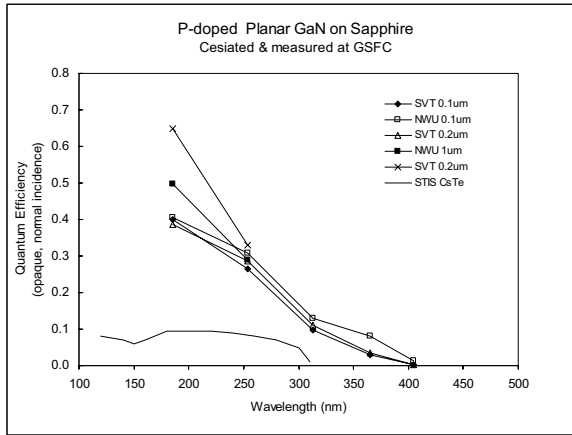
Figure 5. Meaured GaN photocathode QEs compared to a STIS CsTe photocathode
(Courtesy B. Woodgate and T. Norton)

Recently there have been two major advances in MCP-based detectors in the areas of photocathodes and new approaches to MCP fabrication. Silicon MCPs [12, 18] are fabricated using microlithographic techniques and offer a number of benefits compared to glass MCPs. Silicon MCps are not sensitive to contamination by photocathodes, so a larger range of opaque photocathode materials can be deposited onto their front surface. This produces high QE and spatial resolution than is available with semi-transparent photocathodes. Silicon MCPs also exhibit superior global and local dynamic range compared to glass MCPs [9]. The fabrication technique for Silicon MCPs also allows smaller channel diameters and customized front surface architectures which maximize the open channel to web area ratio. This provides an additional boost to overall sensitivity. Recent developments in MCP photocathodes have focused on new materials such as Diamond, GaN and AlGaN [12,18]. In Fig. 6 we show the quantum efficiencies currently being achieved with these new technologies. One of the major challenges for these technologies will be achieving the level of scalability required for future missions such as LUVO.

The alternative to MPC-based detectors are solid state arrays. Clampin has discussed the issues associated with UV imaging with CCDs. Currently, near-UV CCD imaging is possible, as demonstrated by ACS [9], but the far-UV remains elusive because while CCDs can be optimized for far-UV performance, the problem of red-leak remains predominant (solar blind problem). Solid state UV imaging which offers solar blind performance has focused on GaN and AlGaN photodiode arrays hybridized to CMOS readouts. Formats are currently 256×256, and the major limitation is dark current resulting from material fabrication defects. With continued long term

development to improve the material purity, these technologies are potentially very scalable and would offer all of the benefits of solid state imaging for wide field UV imaging and spectroscopy.

The stated goals of the "Search for Earth-Like Planets" Roadmap are:

1. Do other stars harbor planets like Earth?
2. What are the properties of these planets?
3. How will we detect the presence of life?
4. How does star formation lead to planet formation?
5. How do the components of life come to reside on terrestrial planets?

The centerpiece missions for this roadmap are Kepler, the Space Interferometry Mission, and the Terrestrial Planet Finder missions.

2.2.3 Kepler

Kepler is a Discovery class mission designed to determine the frequency of terrestrial and larger planets, in or near the habitable zone, of a wide variety of spectral types of stars. Kepler will specifically search for the photometric signature of transits, with a 0.95 meter telescope feeding a wide field imager. From the perspective of detector systems Kepler will set a new flight record for the size of its CCD focal plane array, comprising forty two 2200×1024 CCDs, and is a pathfinder for many new missions concepts which would employ focal plane arrays of similar, or larger sizes.

2.2.4 Terrestrial Planet Finder

The Terrestrial Planet Finder (TPF) is a mission concept designed to detect and characterize terrestrial planets. TPF has recently been divided into two missions, the Terrestrial Planet Finder Coronagraph (TPF-C), and Terrestrial Planet Finder Interferometer (TPF-I). It is planned that TPF-C will fly first and address the following science goals:

1. Search for and directly detect terrestrial planets that may exist in the habitable zone around nearby stars.
2. Characterize the atmospheres of these planets in search for signatures of biological activity.
3. Direct detection and characterization of the other constituents of planetary systems (Comparative Planetology).
4. Carry out a program of revolutionary general astrophysics investigations (General Astrophysics).

The mission concept for TPF is under-development, and is planned to enter Phase A development in 2008. The current TPF-C design calls for a space telescope with an elliptical, 8 meter primary mirror with an off-axis secondary mirror. It is shown in Fig. 6. TPF-C must achieve extremely high

contrast levels (10^{-10}) in order to be able to detect terrestrial planets. A stray light suppression system (SSS) follows the telescope optics. The current SSS design is a coronagraph employing deformable mirrors for phase and amplitude correction of the wavefront, and shaped apodizers for diffraction suppression to achieve the required contrast levels. Two focal plane instruments following the SSS are currently planned, a camera and a spectrograph. A general astrophysics instrument is also envisaged with a focal plane located outside of the SSS optical train. NASA concept studies are currently in progress to evaluate concepts for the focal plane instruments and the general astrophysics instrument.
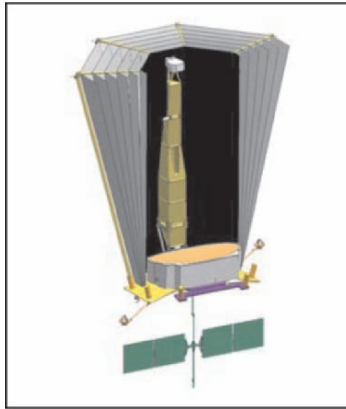

Figure 6. Schematic of the TPF-C

The Coronagraphic Camera will likely have a relatively small format detector of ≤2K×2K with a wavelength response of 500-1000 nm. There is considerable interest in being able to image out to 1.4 μm to provide coverage for observations of extrasolar giant planets (EGPs), and possibly terrestrial planets. The camera must also be able to handle high dynamic range, to facilitate initial target acquisition, to assist placement of extremely bright stellar targets behind the occulting masks. It must also be able to recover from anomalies such as loss of guide star lock, when the detector might be exposed to sudden and extreme changes in incident flux. Despite the bright central targets, the sources being detected are very faint (V~30 mag), and so minimizing dark current and read noise is mandatory. Exposure times are also likely to be very long, which requires careful consideration of the operation strategy from the perspective of detector operations, and in particular, cosmic ray management. The TPF-C mission is currently baselined for an L2 orbit. The spectrograph requirements are similar to the camera, however, the issue of read noise is even more important since current concepts call for an integral field approach, where each focal plane

image element is dispersed. With resolutions of ~100, it will be mandatory to have a photon counting capability where read noise is zero.

Current options for TPF-C detectors include photon counting CCDs, avalanche photodiode arrays (APD) and CMOS hybrid detectors. The photon counting CCDs developed by e2v are extensively discussed in these proceedings and show promise for TPF imaging and spectroscopic applications. APD arrays are not yet available in large formats and their performance and TRL needs to be quantified for space applications. CMOS hybrid detectors do not deliver photon counting performance, but may be suitable for the camera, since they can be configured for long exposures, with readout modes optimized for cosmic ray removal.

The TPF-C general astrophysics instrument is likely to be a wide field visible imager. Large format array options include CCDs and CMOS hybrid detectors. In the long-term, planet detection missions will be interferometric and will require high sensitivity near-IR and mid-IR large format arrays.

2.3   European Space Agency Technology Planning

The Science Payloads and Advanced Concepts Office of the European Space Agency (SCI-A) is charged with promoting and developing future technologies for science missions. The European Space Agency science programme is generally scoped by funding limits to 1 or 2 missions per year. Then given the constraints for accommodating all the disciplines of planetary, solar and fundamental physics missions, the period of time between astrophysics missions in a given wavelength domain can be as large as one decade. This raises a difficult proposition that instrument development cannot be sustained from the budgets of successive approved projects. The investment in next generation instrumentation is always beyond the current life cycle of the science programme projects. Conversely unless appropriate developments are made in a timely manner, innovative science missions are unlikely to be approved due to the risks posed by an immature technology development status. Worse still a mission may proceed to implementation phase while this development is in progress, with a consequent risk to schedule and cost.

Breaking this stranglehold requires some imagination in pursuing future technology. Generically, one can forecast that technology should address a major enhancement of capability (for example an order of magnitude improvement in a certain aspect of performance), or the introduction of a new technique (for example new imaging techniques, introduction of spectroscopy, polarimetry or timing domain capability or analysis of a new particle species etc.). To promote a more focused development activity, the SCI-A office uses the concept of the "Technology Reference Mission"

(TRM) which takes note of future mission ideas promoted by the community, but selected particularly for those that demand significantly new technology that has broad application.

Increasingly complex science instrumentation requires a corresponding investment in technologies for spacecraft infrastructure. For example, increasingly high angular resolution telescopes demand an improvement in spacecraft pointing stability and knowledge; increased data density and cadence demand more sophisticated on-board data processing and storage capability. Notwithstanding the needs for spacecraft infrastructure support, the funding for science payload sub-systems by ESA remains the most critical and costly sectors for the Agency, as shown in Figure 7.
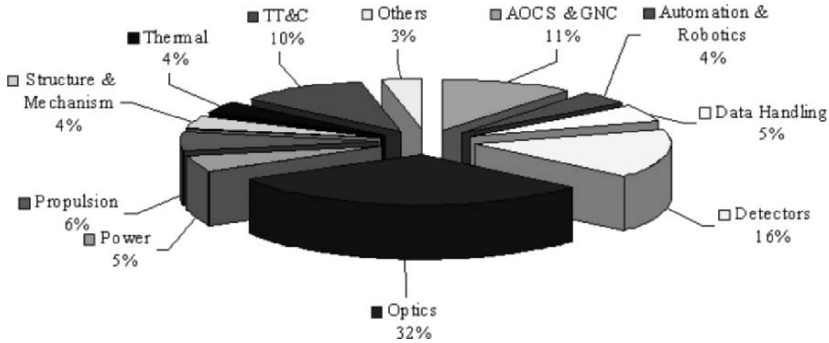

Figure 7.   Investment by ESA on various domains of spacecraft and instrument technology. Almost half of the technology development activity is concentrated on optics and sensors.

2.4   Future ESA Missions

Next we discuss some of the up-coming missions that are in development or conceptual stage, highlighting some of the technologies being actively qualified for space projects in the ESA programme.

2.4.1   Herschel

This far-IR observatory class mission [23] is designed for discovering the earliest epoch of proto-galaxies, studying the cosmologically evolving AGN-starburst symbiosis, and mechanisms involved in the formation of stars and planetary system bodies. At its heart is a 3.5 metre diameter passively cooled telescope optimized for the 60 - 670μm band. To date it is easily the largest space borne mirror to be fabricated [24]. The science payload complement includes two cameras/medium resolution spectrometers (PACS and SPIRE)

and a very high resolution heterodyne spectrometer (HIFI), that will be housed in a superfluid helium cryostat. Herschel will be placed in a transfer trajectory to the L2 Lagrangian point in 2007 and in this stable environment should have an active lifetime of ~3 yrs.

PACS (Photoconductor Array Camera & spectrometer [25]) comprises 3 Ge:Ga photoconductor linear arrays for spectroscopy and 2 Si bolometers. The whole instrument includes 50 passive and active optical elements and 4 precision mechanisms. The field of view subtends 1.75×3.5 arcmin. An internal ^{3}He sorption cooler will provide the 300 mK environment needed by the bolometers. SPIRE [26] is a 3-band imaging photometer providing simultaneous observations at wavelengths of 250, 350 and 500 μm. Within a 4×8 arcmin field of view 4×8 arcmin the beam will be 71, 24, and 35 arcsec FWHM. Again the instrument relies on ^{3}He cooling. Spectroscopy is provided by an Imaging Fourier Transform Spectrometer (FTS) giving simultaneous imaging observations of the whole spectral band, in a wavelength range of 200-400 μm over a field of view ~2.0 arcminutes, and with a spectral resolution of ~1 cm^{-1}. Finally HIFI (Heterodyne Instrument for the Far-IR [27]) is a spectrometer operating from 480 – 1250 GHz and 1410 – 1910 GHz with a frequency resolution of 134 kHz to 1 MHz. It employs both superconductor/insulator/superconductor and hot electron bolometers, together with new technology for mixers and local oscillators, etc.

This combination of a large He observatory cryostat and complex thermal interfaces with the instrument coolers has been a huge programme risk. This has been compounded in that HERSCHEL is to launch with the PLANCK observatory, meaning developments are tied to those of another platform (to reduce launch cost to <<$150M). All instruments have required substantial development and qualification (especially in areas of thermal design and vibration). From an over-riding concern about limited lifetime, future space missions with cryogenic instruments will receive critical attention, and these lessons indicate that in the future the Agency may prefer to take on the load of the cryogenic developments from PI teams. This may reduce risk in cryogenics hardware development but possibly makes the testing interface more complex. Again this is a development/risk trade-off that does not need to be so critical for ground-based instrumentation.

2.4.2 Gaia

Gaia [28] aims to provide astrometric measurements for the whole sky to magnitude V < 20, implying detection, measurement and cataloguing of 10^9 stars. The required accuracy of 10-20 μarcsec at 15 mag compares with the previous Hipparcos mission [29] where 1 milliarcsec at magnitude 9 was achieved. GAIA will be a scanning satellite, with two viewing directions.

Radial velocity measurements to V<16-17 will provide the third component of space motion, perspective acceleration. The science impact will be significant in the areas of dynamics, population studies, binaries spectra: chemistry, rotation. Additionally, photometry (V<20) will give astrophysical diagnostics (5 broad + 11 medium-band) and chromaticity data.

The overview of the GAIA payload is provided in Fig. 8. The key element is a large focal plane of CCDs comprising ~Gigapixel. The two separate fields of view focus onto the array, and a set of mapping CCDs identify target stars for tracking (see Fig. 9). The images are TDI mapped across subsequent sets of CCDs, but each CCD has complex readout sequences generated after real-time target selection to read out only selected windows. The focal plane also contains broad-band photometer rows for colour information.
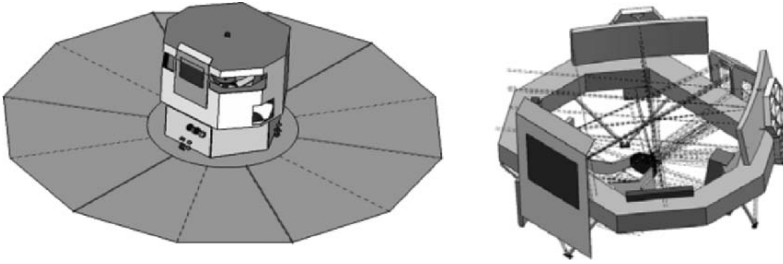

Figure 8. The GAIA spacecraft spins about its axis so that the two telescope axes scan slowly across the sky (left). Close up of the complicated optics trains underneath the spacecraft covers (left). Two mirrors (~1 metre) at top and right eventually focus onto the same CCD focal plane.

Mass limitations originally dictated rather thin exterior light shades, but analysis showed that for a reasonable number of solar flares, this would lead to a very large proton dose, and consequent severe degradation of CTI. Now the project has requested the measuring of prototype CCD performance after 10^9 protons/cm^2. The efficient transfer over thousands of pixels is critical, because a smeared response would prevent star centroids being accurately calculated. The performance then depends upon the history of stars transferred within a column and it was decided that a "thin zero" charge background needs to be injected at the top of each CCD readout column to ensure stable response.
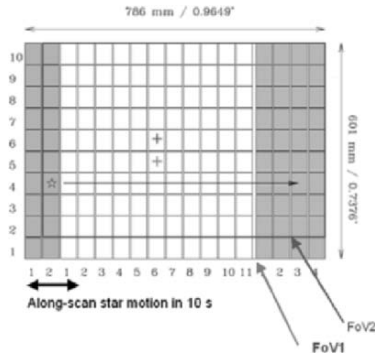
Figure 9. GAIA Astrometric Focal Plane. An array of 11×10 CCDs are sandwiched by two rows of mapper CCDS (left) and 4 broad band photometer rows (right). The focal planes of the two telescope trains are slightly displaced vertically on the array.

Compared with most envisaged ground-based gigapixel focal planes, the GAIA application is unique in its requirement for radiation tolerance, and the additional complexity of multiple parallel readout sequencers acting out of synchronization. The latter demands a very early development of CCDs together with their front-end electronics, and comprehensive testing of envisaged readout modes.

2.4.3 BepiColombo

The BepiColombo mission to Mercury [30] aims to perform mineralogy measurements at the spatial scale of large craters. This requires a combination of visible, IR and X-ray imaging. The payload must survive through the environment of solar irradiation, and cruise period of several years with no performance degradation, yet the X-ray instruments can map fluoresence emission with high resolution only at times of high solar flare fluence. The optical and IR instruments require Active Pixel Sensor technology, in order to allow ~room temperature operation, together with a radiation hard capability. In the medium IR, the inability to provide significant cooling leads to the adoption of uncooled broadband IR arrays using Si MEMS technology. These micro-bolometers use a ¼ wave cavity for good response at the chosen wavelength, and are produced with polymer lift-off technique. For the required resolution, an array of format ~256×320 pixels mated to ASIC is to be used to allow pushbroom readout.
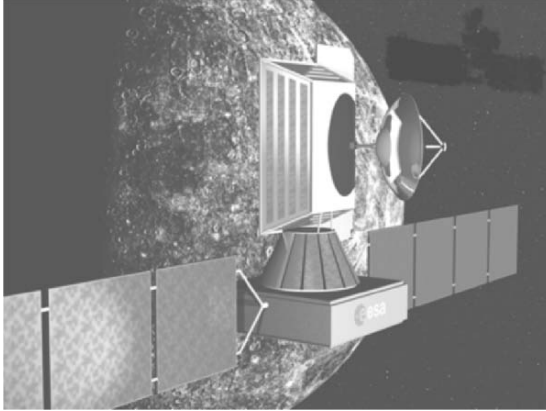
Figure 10.   The instruments for the BepiColombo mission to Mercury have to be optimized for very low resources and radiation hardness. High performance features, such as angular resolution are not as strong a driver as might be the case for other science missions.

2.4.4   Solar Orbiter

Solar Orbiter will be placed to make observations at a distance 0.2 AU from the Sun where it will co-rotate with solar surface features to follow their evolution for many days [31]. The most important challenges for the experiments will be the 25 Solar constants heat load and the intense radiation environment. The latter requirement forces a choice for Active Pixel Sensors, because CCD sensors would suffer intolerable radiation damage at 0.2 AU. CMOS based APS are a key need for the mission for all the remote sensing instrument package.

Particular developments being pursued for the instrument package include heat rejecting entrance windows and EUV filters. The key need to reject the heat before it reaches the spacecraft requires technologies like foils and supporting grids. To select a narrow and tunable spectral band baseline a double Fabry-Perot structure followed by a band pass interference filter will be used. The spectral tuning of both Fabry Perot is to be achieved by applying a high voltage. To select one of four independent input polarisation states Liquid Crystal Variable Retarders will be applied. A requirement for the near-UV detecting systems is a solar-blind detector, using either wide band gap semiconductors or a development of an intensified CMOS APS. Just as with BepiColombo, the environmental concerns and unusual space-accessible wavelengths combine to drive instrument design in a different direction than for ground based instruments.
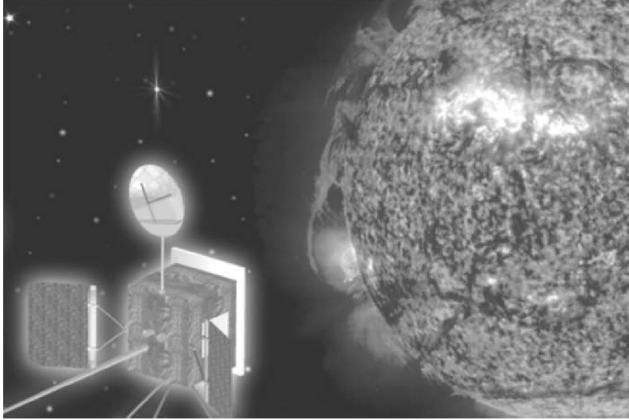
Figure 11. The Solar Orbiter spacecraft will orbit the Sun at a distance of only 0.2 AU, suffering a factor 25 higher heat load than an equivalent spacecraft in low Earth orbit.

For both missions to the inner reaches of the solar system the special developments of spacecraft sub-systems are as important. They include thermal protection, steerable high-gain antennae, high temperature solar panels, etc.

2.4.5 Darwin

Darwin is designed to detect extrasolar planets and measure the mid-IR spectral signatures of life processes in their atmospheres [32]. The method relies on precise interferometric nulling of the parent star's light by a factor of 10^{-8}. The present baseline design relies on four spacecraft placed at a halo L2 orbit. Three of the spacecraft deploy 2 m class telescopes, and the fourth spacecraft contains the beam combining optics. The method requires maintaining baselines in the range from 50 m to 200 m, sometimes while rotating the whole constellation. Therefore the four spacecraft must maintain their constellation via formation-flying techniques with sufficient accuracy so that optical path differences can be established to 20 nm within the beam combiner spacecraft. The selection of the waveband of interest is determined by the spectral features of molecules such as water and ozone, and a wide range of technology developments are required for integrated optics and detectors for 4-20μm for spectroscopy. In principle the detectors could rely on JWST technology for this 5-20 μm band, e.g., a linear array of BIB Si:As detectors [33]. However, to date these need an 8K operating temperature, compared with the optics that will operate at 40K. The possible problems with vibrations from an additional mechanical cooler affecting the optical path stability at the nm level are severe [34]. The mandatory development of

formation-flying spacecraft technologies represent a very demanding aspect of the Agency-provided mission critical items that would not be necessary on-ground.
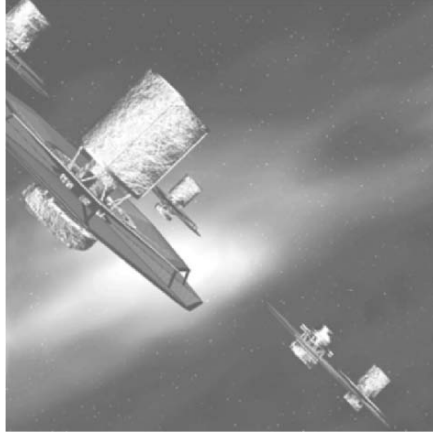
Figure 12.   Darwin will be implemented as a constellation of satellites flying in formation with 3 or 4 collecting telescopes and a hub combining spacecraft.

2.4.6   XEUS (X-ray Early Universe Spectroscopy)

XEUS will be based around a novel focusing technology, providing a huge mirror area ~10m^2, in order to access the faintest distant AGN-forming objects [35]. The mission is expected to fly in a halo L2 orbit, with mirror and detector spacecraft flying in formation 50 m apart. The imaging and spectroscopy measurements require new detectors developments. With this large effective area, photon counting detectors have to exhibit very fast readout to avoid pile-up. The proposed Wide Field Imager offers a silicon CCD class X-ray energy resolving capability. The mirror depends in part for its capable performance on a long focal length, and this translates into requirements for ~100μm pixels. These constraints have forced the project to look towards novel non-CCD technologies. It is proposed to use a DEPFET version of APS technology, that offers non-destructive in-pixel readout with few electrons noise [36].

Other instruments rely on cryogenic sensors to achieve non-dispersive spectroscopy with E/δE ~ 1000. These will include STJ [37] and/or a Transition Edge Sensor [38] readout of bolometers. These advanced sensors need commensurate developments in Adiabatic Demagnetisation coolers (to achieve operating temperatures ~50 mK), efficient light and IR-blocking filters, RF SQUID multiplexors etc. Specific science requirements on maximizing the fields of view would eventually pay off in terms of finding

more utility in ground-based optical applications for colour-resolved photon-counting detectors.
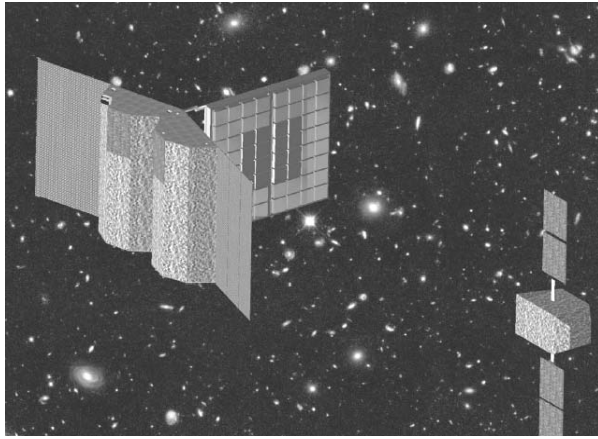
Figure 13. The XEUS mission envisages a Mirror and a Detector Spacecraft flying at 50 m focal distance. This implies large focal plane scale and significantly new developments in instrumentation necessary to fill a reasonable field of view.

2.5 Summary of Required Developments

Despite a wide variety in requirements, wavelengths and applications, there are a number of common themes that emerge needing development:

- The "pixel" version of Moore's Law continues to demand ever larger focal planes, but with space radiation effects, readout speed and electronics integration all at a premium, the push is to promote APS-like readout at all wavelengths.
- The demands of TPF-C and future interferometry missions mandate new solid state detectors with zero read noise, photon counting capabilities.
- Parallel investment in novel optics and mechanical coolers will be equally important. Fast optics with low mass and deployable technology to secure large apertures, offer performance comparable to large focal planes. As we have seen above, the optics and detectors must be developed together as space missions cannot rely on changing outmoded detector packages.
- With long durations between successive missions, a productive and long life-span is necessary. For cryogenic instruments, lifetime is a serious concern, so that development of mechanical coolers is

mandatory. Although qualification for spaceflight is difficult, this trend is inevitable, and follows the ground-based trend for adopting "cryotiger"-like solutions, whether or not the motives are entirely similar.

- Early identification of the required technology is important, but sensible levels of investment must be followed through, in a project implementation phase to enable early testing in appropriate environment. The harsh realities of respecting constraints of a launch date have to be tempered with an early appreciation of building-in appropriate calibration time, and developing efficient operation procedures.

- A common location for future observatories is the halo around L2. Longer wavelength observatories should not ignore existing experience of operations in the outer magnetosphere with respect to radiation damage and prompt cosmic ray effects.

3.   REFERENCES

[1]   Mankins, John C., 1995, Technology Readiness Levels: A White Paper, NASA, Office of Space Access and Technology, Advanced Concepts Office
[2]   Figer, D., Rauscher, B. J., Regan, M. W., Morse, E., Balleza, J., Bergeron, L., Stockman, H. S. 2004, Proc. SPIE 5167, 270
[3]   Rauscher, B. J. 2005, these proceedings.
[4]   Pickel, J.C., Kalma, A.H., Hopkinson, G.R., and Marshall, C.J. 2003, IEEE Trans. Nucl. Sci. vol 50, 671.
[5]   Srour, J.R., Marshall, C.J., and Marshall, P.W. 2003, IEEE Trans. Nucl. Sci. vol 50, 653
[6]   Hopkinson, G.R., Dale, C.J., and Marshall, P.W. 1996, IEEE Trans, Nucl. Sci. vol 43, 614
[7]   Sirianni, M. and Mutchler, M. 2005, this proceedings
[8]   Boeker, T., Bergeron, E., Mazzuca, L. M., Sosey, M., and Xu, C. 2003, Proc. SPIE 4850, 935
[9]   Clampin, M. 2002, Opt. Eng. 41(6) 1185
[10]   Luppino, G. A., Tonry, J. L. and Stubbs, C. W. 1998, Proc. SPIE 3355, 469
[11]   Thompson, R. I. and Schneider, G. 1998, Proc. SPIE 3356, 215
[12]   Woodgate, B. E., et al. 1998, PASP, 752, 1183
[13]   Green, J. C., Wilkinson, E., and Morse, J. A. 2003, Proc. SPIE 5164, 17
[14]   Kimble, R. A., MacKenty, J. W. and O'Connell, R. W. 2004, Proc. SPIE 5487, 266
[15]   Fazio, G. G., Hora, J. L., Willner, S. P., Stauffer, J. R., Ashby, M. L., Wang, Z., Tollestrup, E. V., Pipher, J. L., Forrest, W. J., McCreight, C. R., Moseley, S. H., Hoffmann, W. F., Eisenhardt, P., Wright, E. L. 1998, Proc. SPIE 3354, 1024
[16]   Houck, J. R., Roellig, T. L., van Cleve, J., Forrest, W. J., Herter, T., Lawrence, C. R., Matthews, K., Reitsema, H. J., Soifer, B. T., Watson, D. M., Weedman, D., Huisjen, M., Troeltzsch, J., Barry, D. J., Bernard-Salas, J., Blacken, C. E., Brandl, B. R., Charmandaris, V., Devost, D., Gull, G. E., Hall, P., Henderson, C. P., Higdon, S. J. U., Pirger, B. E., Schoenwald, J., Sloan, G. C., Uchida, K. I., Appleton, P. N., Armus, L.,

Burgdorf, M. J., Fajardo-Acosta, S. B., Grillmair, C. J., Ingalls, J. G., Morris, P. W., Teplitz, H. I., 2004, ApJS, 154, 18

[17] Rieke, G. H., Young, E. T., Engelbracht, C. W., Kelly, D. M., Low, F. J., Haller, E. E., Beeman, J. W., Gordon, K. D., Stansberry, J. A., Misselt, K. A., Cadien, J., Morrison, J. E., Rivlis, G., Latter, W. B., Noriega-Crespo, A., Padgett, D. L., Stapelfeldt, K. R., Hines, D. C., Egami, E., Muzerolle, J., Alonso-Herrero, A., Blaylock, M., Dole, H., Hinz, J. L., Le Floc'h, E., Papovich, C., Pérez-González, P. G., Smith, P. S., Su, K. Y. L., Bennett, L., Frayer, D. T., Henderson, D., Lu, N., Masci, F., Pesenson, M., Rebull, L., Rho, J., Keene, J., Stolovy, S., Wachter, S., Wheaton, W., Werner, M. W., Richards, P. L. 2004, ApJS 154, 25

[18] Siegmund, O. H. W., Welsh, B. Y., Martin, C., Barlow, T., Bianchi, L., Byun, Y-I., Forster, K., Friedman, P. G., Jelinsky, P. N., Madore, B. F., Malina, R., Milliard, B., Morrissey, P. F., Neff, S. G., Rich, M. R., Schiminovich, D., Small, T., Szalay, A., and Wyder, T. K. 2004, Proc. SPIE 5488, 13.

[19] McCandliss, S. R., Feldman, P. D., McPhate, J. B., Burgh, E. B., Pankratz, C., Pelton, R., Nikzad, S., Siegmund, O. and Vallerga, J. 1999, in Ultraviolet-Optical Space Astronomy Beyond HST, ASP Conference Series 164, Jon A. Morse, J. Michael Shull, and Anne L. Kinney, Eds., p. 437–445 ~1999

[20] Lampton, M. et al. 2004, SPIE 5166, 113

[21] Wang, Y., Crotts, A., Garnavich, P., Priedhorsky, W., Habib, S., Heitmann, K., Kutyrev, A., Moseley, H., Squires, G., Tegmark, M., Wright, N. 2004 BAAS 131.07

[22] Bebek, C. J., Groom, D. E., Holland, S. E., Karcher, A., Kolbe, W. F., Palaio, N. P., Roe, N. A., Turko, B. T., Wang, G. 2004, Proc. SPIE 5499, 140

[23] Pilbratt, G., 2003, Proc SPIE 4850, 586

[24] Sein, E., Toulemont, Y., Safa, F., Duran, M., Deny, P., de Chambure, D. et al.. 2003, Proc SPIE 4850, 606

[25] Poglitsch, A., Waelkens, C. and Geis, N., 2003, Proc SPIE 4850, 662

[26] Griffin, M., Swinyard, B. and Vigroux, L., 2003, Proc SPIE 4850, 686

[27] Pearson, J., Mehdi, I., Schlecht, E., Maiwald, F., Maestrini, A., Gill, J. et al., 2003, Proc SPIE 4850, 650

[28] Perryman, M. in GAIA Spectroscopy: Science and Technology, ASP Conference Proceedings, Vol. 298, Ed. U Munari.

[29] Perryman, M , 1998, Physics Today, 51, pt 6, 38

[30] Schulz, R. 2005 in Proceedings 35th Cospar Assembly, p1289

[31] Fleck, B., Harrison, R., Marsden, R., Wimmer-Schweingruber, R. 2004, Proc SPIE 5171, 123

[32] Fridlund, C.V.M, 2004, Advances in Space Research, 34, 613

[33] Campbell, R. 2002, Exp Astron, 14, 57

[34] Ross R., 2003, Proc SPIE 5052, 1

[35] Bavdaz, M., Lumb, D., Peacock, A. 2004, Proc SPIE 5488, 530

[36] Treis, J., Fischer, P., Hälker, ., Harter, M., Herrmann, S., Kohrs, R et al., 2004, Proc SPIE,5501, 89

[37] Verhoeve, P., Lumb, D., Peacock, A., Brammertz, G., den Hartog, R., and Martin, D. 2004 Proc SPIE 5488, 291

[38] de Korte, P., Hoevers, H., den Herder, J-W., Bleeker, J.,.; Tiest, W., Bruijn, M., Ridder, M., 2003, Proc SPIE 4851, p. 779.